Spring 2021

Disentangling the Vibrational Spectra of Water with Cryogenic Water Clusters: from Isolated Static OH Oscillator to Temperature Dependent Spectral Dynamics

Nan Yang
Yale University Graduate School of Arts and Sciences, nan.yang@aya.yale.edu

Abstract

Disentangling the Vibrational Spectra of Water with Cryogenic Water Clusters: from Isolated Static OH Oscillator to Temperature Dependent Spectral Dynamics

Nan Yang

2021

Water is arguably the most important solvent and reactant on earth. It has many special properties compare to other liquids thanks to its hydrogen bonding. Understanding the interaction between water molecules as well as with other solutes in aqueous solutions is of great importance for studying reactions that happens in aqueous environments. Water in its many forms is heavily investigated by many experimental and theoretical methods including rotational, vibrational and electronic spectroscopy, ultrafast spectroscopy, interface specific spectroscopy, neutron scattering, X-ray diffraction, atomic force microscopy, mass spectrometry, nuclear magnetic resonance spectroscopy and so on. With improvements in instrumentation and computation power, our knowledge of water's special properties keeps advancing toward a more accurate molecular level understanding. Among the experimental techniques, vibrational spectroscopy is widely used in several variations including linear absorption spectroscopy, ultrafast multidimensional spectroscopy, and interface specific spectroscopy, among others. The advantage of using vibrational spectroscopy to study water is its sensitivity towards structural information as well as relatively high time resolution. Linear absorption spectroscopy is the most common ways of studying isolated water clusters in the gas phase and provides highly resolved fundamental frequencies that are useful for theoretical calibration. The non-linear methods are mostly used in the condense phase to provide structural and dynamical information

about water and aqueous systems. However, these approaches each have their own limitations. For the traditional cluster study, the cluster size are usually small and the hydrogen bond environments are less complex compared to those in the condense phase. Several studies of very large water cluster run into another problem, where the large number of overlapping bands masks detailed structural information about the OH oscillators. The condense phase study suffers from a similar problem, where even with isotopic dilution, many thousands of oscillators are sampled every time. Hence, it is impossible with the current experimental sensitivity in the condense phase to isolate a single water molecule's spectral feature and information about its specific hydrogen bond environment. In this thesis, I report new experiments that tracks single OH oscillators or single intact water molecules imbedded in an extended hydrogen bond network made of D_2O molecules. Such experiment allowed unprecedented molecular level insight into the OH spectral mechanics including hydrogen bond environment's effect on the OH frequency as well as linewidth up to the second hydration shell, the intra- and intermolecular couplings, and Fermi resonances. After establishing the correlation between the OH frequency and the structural information, a new type of experiment was developed to observe spectral diffusion inside a water cluster via water reorientation. Various pathways were activated at different temperatures, which display different rate constants, and hence allowing the determination of activation energy of each pathway. Together with the OH frequency of interest, detailed reorientation pathway can be inferred to reveal what type of water molecules are involved in the H-bond rearrangement. It was observed that the water molecule at the surface of the cluster starts to move first at lower temperature which resembles the surface melting phenomena.

Disentangling the Vibrational Spectra of Water with Cryogenic Water Clusters: from Isolated Static OH Oscillator to Temperature Dependent Spectral Dynamics

A Dissertation
Presented to the Faculty of the Graduate School
of
Yale University
in Candidacy for the Degree of
Doctor of Philosophy

by

Nan Yang

Dissertation Director: Mark A. Johnson

June 2021

TABLE OF CONTENTS

Abstract i

List of Figures xi

List of Tables xliii

Acknowledgments xlvi

Chapter 1 – Introduction 1

References 10

Chapter 2 – Experimental: Principles of Cryogenic Ion Vibrational Predissociation Spectroscopy and the Development of MS^4IR^3 Instrumentation with Time Dependent Spectroscopy Capabilities 26

2.1 The 'Mini Machine': New Generation Compact Yale Tandem Time of Flight Photofragmentation Mass Spectrometer 27

1. Generation of Gas Phase Ions Using Electrospray Ionization 27
2. Trapping, Mass selection, and Cryogenic Processing of the Ions 34
3. In-trap Mass Separation of the Ion Packet and In-trap Laser Excitation 38
4. TOF Mass Separation of the Ion Packet 45
5. Generation of Infrared Light 41
6. Generation of the Cryogenic Ion Vibrational Predissociation Spectrum 66

2.2 References 67

Chapter 3 – Spectroscopic Signatures of the Ground State and the Vibrationally Excited Iodide-Water Binary Complexes 68

3.1 Spectroscopic Signatures of Mode-Dependent Tunnel Splitting in the Ground State Iodide-Water Binary Complex 112
1. Introduction 112
2. Results and Discussion 114

3.3 References 124

Chapter 4 – Development of Various Generic Two Laser Experiments and Isolation of Site-specific Anharmonicities of Individual Water Molecules in the $I^-\cdot(H_2O)_2$ Complex Using Tag-free, Isotopomer Selective IR-IR Double Resonance 129

4.1 Introduction 130

4.2 Implementation of the IR-IR scheme in a new triple focusing TOF photofragmentation mass spectrometer 134

4.3 Applications of two-color IR-IR photofragmentation to isotopologues of $I^-\cdot(H_2O)_2$ 136
1. Tag-free detection of the linear absorption spectrum: $I^-\cdot(D_2O)_2$ 136
2. Intermolecular coupling and soft mode activity in the DD and AD binding sites through isotopomer selective spectroscopy of the $I^-\cdot(H_2O)\cdot(D_2O)$ isotopomers 155
3. Determination of the local vs normal mode character of the OH stretches in the $I^-\cdot(HOD)\cdot(D_2O)$ and $I^-\cdot(DOH)\cdot(H_2O)$ isotopologues 172
4. Temperature-dependent spectral diffusion as a probe of large amplitude motion 177

4.4 Summary 181

4.5 References 182

Chapter 5 – Capturing Intrinsic Site-dependent Spectral Signatures and Lifetimes of Isolated OH Oscillators in Extended Water Networks as well as Their Temperature Dependent Behavior 192

5.1 Introduction 193

5.2 Experimental Methods and Computational Methods 196

5.3 Results and Discussion 197

5.4 Fit and Simulation Methods 223

5.5 Summary 225

5.6 References 226

Chapter 6 – Deconstructing Water's Diffuse OH Stretching Vibrational Spectrum with Cold Clusters: Unmasking the Factors Controlling the Anharmonic Spectral Response of a Single Water Molecule Embedded in a Two-dimensional Cage 234

6.1 Introduction 235

6.2 Experimental and Computational Methods 236

1. Experimental Methods 236

2. Computational Methods 237

6.3 Results and Discussion 238

6.4 Summary 259

6.5 References 260

Chapter 7 – Unraveling the Controlling Factors of OH Frequency: Isolating the Contributions of Specific Network Sites to the Interfacial Vibrational Spectrum of Water with Isotopomer-Selective Spectroscopy of Cold Clusters 267

7.1 Introduction 268

7.2 Results and Discussion 273

7.3 Summary 296

7.4 References 297

Chapter 8 – Demonstration of Temperature Dependent Spectral Diffusion Experiment: Unmasking Rare, Large-Amplitude Motions in $I^-\cdot(H_2O)_2$ Isotopomers 302

8.1 Introduction 303

8.2 Experimental Details 305

8.3 Results and Discussion 309

8.4 Summary 333

8.5 References 333

Chapter 9 – From Temperature Dependent Spectral Diffusion to Time Dependent Kinetics Measurements: Mapping the Temperature-Dependent and Network-site-specific Onset of Hydrogen Bond Rearrangement a Water Cluster Nano-cage 341

9.1 Introduction 342

9.2 Experimental and Computational Methods 346

1. Computational Methods 346

2. Computational Methods for the Structures and Vibrational Frequencies of $H^+(D_2O)_{21}$ 355

9.3 Results and Discussion 358

9.4 Summary 388

9.5 References 389

LIST OF FIGURES

2.1 Schematic of the compact Yale Tandem Time of Flight Photofragmentation Mass Spectrometer (MS^4IR^3). There are two ion sources. One of them (shaded green) is the newly integrated LTQ Orbitrap Velos Pro instrument, which includes high-resolution mass spectrometry (Orbitrap) and collisional-induced dissociation (CID) functions. It can send mass-selected ions or their CID fragment ions to the existing photofragmentation instrument to carry out vibrational spectroscopy experiments. Additional new capabilities (shaded blue) include in-trap laser excitation and in-trap mass isolation. In-trap mass isolation is achieved by sweeping the mass-dependent secular frequency using custom electronics. The isolated ions are then irradiated by the in-trap laser to achieve photoactivation or photobleaching. The storage time in the temperature-controlled ion trap can be varied from 10-500 ms to achieve long delay times between pump (bleach) and probe laser pulses, a feature used to obtain intra-cluster reaction kinetic measurements. 28

2.2 Picture of a working ESI source. The charged liquid forms a cone on the exit of the needle (50 micron diameter) and electro sprays into a cone of mist which enters the capillary entrance. 29

2.3 Simulated trajectory of ions passing through a bent octapole ion guide. The red traces are the ion trajectories. This simulation was performed using SIMION with a user program written for this simulation to apply time-dependent voltage and collision from gas molecules. 33

2.4 A cutaway view of the quadrupole Paul-type trap and surrounding components that are used in the new generation Yale tandem time of flight photofragmentation spectrometer. The ion packet enters from the left through the octapole ion guide and is focused by the aperture and tube lens into the Paul trap. The trap consists of an entrance cap, a center ring, and an exit cap, and is cooled by the cryohead. Buffer gas is pulsed in through a hole on the insulator between the entrance cap and the center ring. 36

2.5 Ion intensity of $EMIM^+$ as a function of the pulsed buffer gas timing in the cryogenic Paul trap. Ions are pre-accumulated in the first ion guide before being injected into the trap. The time axis labels the delay between when the ions are extracted from this pre-accumulation and when the pulsed valve is triggered. 37

2.6 (a) Resonance response curve of damped driven oscillators where A marks the amplitude of the damped driven oscillation and ω/ω_0 marks the driving frequency relative to its natural frequency. (b) Mass spectrum of protonated water clusters with no secular frequency excitation. (c,d) Mass spectra of protonated water clusters with secular frequency excitation. 40

2.7 Triggering scheme for generating the secular frequency sweep pulse for mass isolation inside the Paul trap. An SRS function generator serves as the master clock running at 20 Hz (a). This 20 Hz trigger is then down converted to a 10 Hz clock pulse (b) that triggers the rest of the experiment. The SRS delay generator running at 10 Hz feeds an AM pulse back into the amplitude modulation input of the function generator, which is running in frequency sweep mode (d). The AM pulse controls the frequency at which the output waveform (e) is turned on or off. The output waveform looks "blocky" instead of sinusoidal due to the high frequency compared to the overall time scale of the figure. 42

2.8 Triggering scheme and circuit diagram for generating the secular frequency sweep pulse for mass isolation inside the Paul trap. An SRS function generator serves as the master clock running at 20 Hz. This 20 Hz trigger is then down converted to a 10 Hz clock pulse that triggers the rest of the experiment. The SRS delay generator running at 10 Hz feeds an AM pulse back into the amplitude modulation input of the function generator, which is running in frequency sweep mode. The SRS delay generator also triggers the trap RF generator (labeled "Jordan"), which turns off the RF waveform applied to the Paul trap and sends out a trigger at the zero-crossing point of the RF. This trigger is then used to trigger the exit bias. 43

2.9 Schematic of a windowed secular frequency sweep applied to a Paul trap to achieve mass isolation (a). The oscillation period is exaggerated for ease of viewing. The high frequency waveform is more realistically depicted in Figure 2.7e. (b) shows the mass spectrum of protonated water clusters with no mass selection and (c) shows the mass spectrum that results when a secular frequency sweep is applied to isolate the m/z 379 ion. 44

2.10 Evaporation of isotopically substituted water clusters over time, observed in Paul trap at 100 K. The small splitting of the peaks is caused by hydrogen substitution of the perdeuterated cluster. 46

2.11 (a) A cutaway view of the quadrupole Paul-type trap and its surrounding components. The ion packet enters from the left in the octapole ion guide

and is focused with the aperture and tube lens into the Paul trap, which consists of an entrance cap, a center ring, and an exit cap. (b) A SIMION simulation of the electric field and equipotential contours. Only the equipotential contours are plotted. The potential surface around the center axis is close to that produced by a set of parallel plates typically used in Wiley-McLaren time of flight mass spectrometers. 48

2.12 Wiley-McLaren configuration controlling the temporal focal point of identical mass ions with exit cap voltage. The higher potential gradient inside the trap results in a temporal focal point that is closer to the trap along the flight path. The spatial distribution of the ion packet inside the trap results in a different starting point for the time of flight, which is compensated by the kinetic energy difference. The identical mass ions that are closer to the entrance cap lag behind distance wise but obtain a higher velocity (kinetic energy). They will catch up with the ions that start closer to the exit cap but obtain lower velocity. 49

2.13 CAD model (a) and SIMION simulation (b) of the entire instrument. The inset in (a) is a simulated mass spectrum of EMIM and its ^{13}C isotopologue (m/z 111 and 112). 50

2.14 Cross section schematic (a) and photo (b) of newly designed mesh grid holder plate. 51

2.15 (a) Photo of a newly installed nickel electroformed mesh grid. (b) Nickel electroformed mesh grid after 6 months of operation. The holes are caused by ion etching. (c) Newly installed tungsten wire mesh grid. (d, e) Ion beam profile after passing through a grid imaged by a MCP detector and imaging phosphor screen. The grid lines are caused by ions colliding into the mesh grid. (f) The etching effect of the ion beam on the tungsten grid. The left portion is the area where the ion beam did not impact. The black color is the oxidized layer whereas on the right is the area where the ion beam did impact. The metallic color is the exposed tungsten with its oxidized layer etched away by the ion beam. The etching of the tungsten metal, however, is not significant and this mesh grid has been in operation for more than one year without the failure seen for the nickel grid shown in (b). 52

2.16 CAD model (right) and SIMION simulation (left) of the reflective mass gate. At 2.5 keV beam energy and 100 m/z, the gap between the plates corresponds to about 100 ns flight time, which limits the mass resolution. In this simulation, the grid on the back side is removed to increase ion

transmission (~10% loss per grid). However, this creates fringe fields on the right side that can diverge the ion beam when the gate voltage is turned back on after the desired mass ions pass through. That can be compensated by opening the time window wider on the later side to allow some heavier mass ions to come through. This is typically not a problem. Otherwise, the three grids can be carefully aligned so that the nearly parallel beam can pass through the three grids and only suffer 10% loss. 54

2.17 (a) A red diode laser is used to align the multipass assembly using condensed water vapor from liquid nitrogen to show the beam path. (b) The beam path shown in the CAD model. (c) The actual multipass assembly. 55

2.18 Two stage gridless reflectron. The 1st stage is kept at ground and the second stage voltage (repulsive, ±500 to ±1500 V) is tuned according to the distance of the next temporal focal point. The back plate is kept at a repulsive voltage (±2600 V) slightly above the beam energy. The rings are connected via a resistor chain to achieve a linear voltage gradient. 57

2.19 SIMION simulation of the arrival time profile at 1200 mm and 2400 mm distance from the two stage reflectron with various second stage voltages (100 V apart). The optimal temporal focusing can be achieved by tuning the second stage voltage. Higher voltages are required for longer focal distances. 58

2.20 SIMION simulation of the arrival time profile at 2400 mm distance from the two stage reflectron with various second stage voltages. The second stage voltage tunes the arrival time width. About 1700 V is optimal for the 2400 mm distance. Each peak is a different voltage spaced by 100 V. The top panel compares the effect of the Einzel lens. The Einzel lens does not influence the ion packet time profile significantly - it only shifts the entire ion packet earlier in time (running in attractive mode). The bottom panel compares the time profile with and without grids on the two stage reflectron. The grid mesh does have some effect on the time profile but can be readily compensated by tuning the voltage. 59

2.21 SIMION simulation of the focusing effect of the Einzel lens on the reflectron stack (blue trace) compared with experimentally measured results (red trace). The two results generally agree with each other. The simulated result displays higher divergence when the beam diameter is larger due to the sensitivity of the ion imager. Only the high intensity part of the beam can be seen; thus, when the beam is focused, the experimental

results agree very well with the simulation. When the beam is large, the ions distributed near the edge are not detected by the imager, leading to underestimation of the beam radius. 60

2.22 SIMION simulation of the reflectron stack with different ring distances. The colored lines are the equipotential contours and the black short lines are the electric field lines. Excessively large spacing results in significant fringe fields that can distort the beam. 61

2.23 Extension of the instrument with a linear reflectron for detecting various fragmentation channels at the same time. The actual linear reflection is pictured at right bottom. 64

2.24 Schematic of the tunable IR laser system. 64

3.1 Asymmetric minimum-energy structure of $I^-\cdot H_2O$ and its vibrational predissociation spectrum. (A) Minimum-energy structure of $I^-\cdot H_2O$ from the MB-nrg potential (ref. 7) (B) Vibrational predissociation spectrum of $I^-\cdot H_2O$ at 20 K with low laser power to ensure the maximum number of photons absorbed at any transition is one (linear regime). The inset highlighted by the gray background is an Ar-messenger, tagged predissociation spectrum in the same region to reflect transitions to states that lie below the dissociation threshold. 70

3.2 Excited State Spectra of $I^-\cdot H_2O$. Vibrational predissociation spectra obtained with (B) and without (A) Ar messenger tag. The smaller binding energy of Ar tag allows the observation of bands below the H_2O's binding energy whereas the tag-free experiment allows the observation of the quartet pattern. By fixing the first laser on one member of the quartet and scanning the second laser, the excited state's spectral features were obtained (C-F). Even though the first laser excitation puts the system slightly above the dissociation threshold, the lifetime is extremely long and the majority of the excited clusters remains undissociated at the second laser interaction point. Lower energy bands can now be observed due to the sum of the two absorbed photon exceeding the dissociation limit by more than 1000 cm^{-1} which results in faster dissociation of the cluster. 76

3.3 Energy level diagram for the excited state spectra displayed in Fig. 3.2. The black arrows indicate the pump laser transition that creates the excited state, the red and orange arrows indicate HOH bend and OH stretch transitions originating from the excited state, respectively. The quantum number is denoted as |Bend, Stretch, νs> where Bend represents the quantum number of HOH bending mode, Stretch represents the OH

stretching mode quantum number and vs denotes the soft mode quantum numbers in general. (A) displays the transitions originating from the v=2 level of the HOH bend where the dashed transitions are not allowed on the harmonic level, (B) displays the transitions with the v=1 level of the OH stretch as the initial state and (C) shows the situation when the superposition state of the bend and stretch as a result of Fermi resonance is prepared as the initial state, the transitions initiating from such state can access both the bend and the stretch levels manifold. 77

3.4 Comparison between simulated FOH spectra at different tunneling splittings with the experimental spectrum at 20 K. (A, B) Simulated rovibrational spectrum based on a 20-cm^{-1} ground-state tunneling splitting for transitions originating from K_a levels built off of the GS(-) and GS(+) states, respectively. (C) Simulated spectrum with a 20-cm^{-1} ground-state tunneling splitting initiated from all thermally populated GS(±) and K_a levels, including nuclear spin statistical effects. (D) Experimental IR predissociation spectrum. (E) Simulated spectrum obtained with a 0-cm-1 tunneling splitting, based on thermally populated GS(±) and K_a levels. (F) Energy level diagram illustrating the transitions involved, in which the solid and dashed lines are used to differentiate between states that are symmetric (solid) and antisymmetric with respect to exchange of the two hydrogen atoms. The tunneling splitting between GS(-) and GS(+) is indicated with the double-sided arrow. 80

3.5 Double-resonance spectra, probing specific K_a levels of the ground vibrational state(s). (A) Linear infrared photodissociation spectra obtained with low laser power (0.7 mJ/pulse, 8 ns pulse width, 5 mm beam diameter) at 20 K. (B) The high-power (20 mJ/pulse) IRMPD experimental spectrum at 20 K. (C) Experimental state-specific double-resonance spectra obtained by probing the peak indicated by the purple arrow, which putatively includes population from both GS(+) and GS(-) states. The main contribution is nonetheless attributed to GS(+), arising from the β_7 transition, and the remaining contribution of GS(-) arises from the β_8 transition. (D,E) Double-resonance spectra obtained by probing the peaks indicated by the color-coded arrows, which reflect the GS(+) and GS(-) population, correspondingly. 84

3.6 GS(+/-) double resonance comparison. Solid traces are the experimental data obtained by probing different positions (probing β_2 for red trace, β_4 for blue trace and $\beta_{7,8}$ for the purple trace) corresponding to transitions initiated in GS(-), GS(+) and GS(+/-), respectively. The relative intensity represents the amount of remaining probe signal after the pump laser

excitation normalized to the probe signal when pump laser is off. The dotted line in (B) corresponds to the admixture of 73% GS(+) spectrum and 27% GS(-) spectrum which suggests the relative population of GS(+) and GS(-) contributing to the solid purple trace in (B) is close to 3:1. 88

3.7 Energy-level diagram of the IHB region, based on previous spectral observations. The left inset is an IRPD spectrum reproduced from figure 3.1B. The blue color of the energy level lines denotes the quantum states with (+) symmetry; the red color denotes (–) symmetry. The solid lines represent real energy levels, whereas dotted lines are shifted down by an equal amount such that the initial state in the IR transitions is aligned with the (+) ground state for ease of comparison of transition energies (arrows). The shift (20 cm-1) is the ground-state tunneling splitting, and the energies used to make the energy-level diagram are based on ref. 8. The grey box shows the range of energies that correspond to the quartet feature in the spectrum (reproduced in inset). 93

3.8 Mode-dependent tunnel splittings and adiabatic potential energy surfaces. (inset) Definition of the IP bend coordinate, along with (B) ZPE, (A) 2HOH, IHB, and FOH frequency-response curves added to the underlying double-well potential energy surface along the IP bend coordinate. 99

3.9 Comparison between the state-specific experimental spectra and the calculated infrared spectrum. (A) Linear infrared photodissociation spectra obtained with low laser power (1 mJ/pulse, 8 ns pulse width, 5 mm beam diameter) at 20 K. (B) Calculated rovibrational spectrum at 20K. (C) Calculated spectrum initiated from both members of the ground-state tunneling pair, with the intensity scaled by 73% for GS(+) K_a =1 and 27% for GS(-) K_a=0. (D) Experimental state-specific, double-resonance spectra obtained by probing the peak indicated by the purple arrow, which includes population from both GS(+) and GS(-). (E, G) Calculated spectrum with the initial state being GS(+) and GS(-), respectively. (F, H) Double-resonance spectra obtained by probing the peaks indicated by the color-coded arrows, which reflect the GS(+) and GS(-) population, correspondingly. All calculated traces (B,C,E,G) in the FOH region are magnified ×20. 108

3.10 Decomposition of the main transitions underlying the FOH band. The calculated line widths have been homogeneously broadened by a Lorentzian line shape with a width of 5 cm^{-1}. The calculated spectrum has been shifted by +36 cm^{-1} to compare with the experiment. (A) Full decomposition of the calculated FOH band. (B) Perpendicular band out of

GS(+). (C) Perpendicular band out of GS(+). (D) Parallel band out of GS(+). (E) Perpendicular band out of GS(-). 109

3.11 Asymmetric minimum-energy structure of I^-·HDO and its vibrational predissociation spectrum at different temperatures. (A) Vibrational predissociation spectrum obtained using weakly bound Ar as messenger tag. On the right is the minimum-energy structures of the two isotopomers of I^-·HDO from the MB-nrg potential (ref. 7) (B) IRPD spectrum of I^-·HDO at 30 K, the IDB feature is observed through two photon absorption process. (C,D) IRPD spectrum of I^-·HDO at 50 K and 100 K. 115

3.12 Excited state spectra of I^-·HDO exciting the bound OH/OD band. (A) IRPD spectrum of I^-·HDO at 30 K, the IDB feature is observed through two photon absorption process. (B, C) excited state spectra with the IDB(v=1) and IHB(v=1) as initial states, respectively. (D) Initial excitation of the vibrational levels of the two isotopomers where GS denotes the ground state and (1) and (2) denotes the first and second vibrational levels. 117

3.13 Energy level diagrams for different regimes in the excited state spectra's behaviors. Regime I is when the excitation connects two stationary states and no IVR can happen, the strongest contribution will arise from the 1 to 2 transition. Regime II is when IVR rate is slow (in other words, density of state or coupling is low) and only a few energy levels are populated close to the transition energy, several transitions can arise from those states results in a spectrum that has finite features. Regime III is when the density of state is high and IVR rate is fast, the original excitation quickly relaxes and energy is redistributed into low frequency modes, the spectra would appear as a broadened peak around the frequency of the 0 to 1 transition. 119

3.14 Two-dimensional map of the pump-probe spectra. (A) Displays the single laser one color spectra of I⁻·H2O. (B) Displays the 2D map where the pump and probe lasers are fixed at two frequencies and the time delay between the two lasers is fixed at 30 microseconds. The diagonal line labels the points where the pump and the probe lasers are at the same frequency. The dotted lines are the slices at specific pump frequencies labeled by number 1-5. 121

3.15 Excited state spectra of I^-·H_2O at various pump frequencies. The experimental spectra (upwards) and the calculated spectra (downwards) color coded by their initial states are displayed together. GS represents

grounds state and GS(Ar) represents the ground state of the Ar tagged $I^-\cdot H_2O$ complex. The quantum state labeling scheme is the same as that in the Chapter 3.1. 123

4.1 (a) Calculated minimum energy structure of $I^-\cdot(H_2O)_2$ at the MP2/aug-cc-pVTZ-PP level of theory 31 and (b) D_2-predissociation spectrum of $I^-\cdot(H_2O)_2\cdot D_2$ at a trap temperature of 20 K. The main OH stretching fundamentals are identified by their dominant contributions to the displacement vectors at the harmonic level: the free OH (FOH), inter-water hydrogen bonded OH group (IH), ionic H-bonded (IHB) OH group on the AD water (IHB_{AD}), and the corresponding IHB on the DD water (IHB_{DD}). The HOH bend overtone (2vHOH) is also identified, 32,33 along with several weaker transitions (denoted an) with energies and assignments included in Table 1. (c) Infrared photo- dissociation (IRPD) spectrum of $I^-\cdot(H_2O)_2$ at 300 K trap temperature. The baseline is indicated by the gray dashed line. The loss of the pattern of four fundamentals in (b) is interpreted to indicate that the H-bond between the two water molecules is broken in the hot ensemble. 30 131

4.2 Diagram of the temperature controlled cryogenic ion vibrational spectrometer with two laser capabilities at Yale. The mass selected ions intersect the first laser crossing (pump, $h\nu_1$), yielding photo excited ions and/or photofragments. Parent and fragment ions, together with metastable decay products, are separated by the Zajfman-inspired[34], coaxial, dual-stage gridless retro-reflectron (R_1) and intersect with the second laser crossing (probe, $h\nu_2$) where either parent or fragment ions can be irradiated. The ion beam is then turned 90° by the pulsed DC turning quad (Q) into the second reflectron (R_2) to separate photofragments produced by the probe laser. Lastly, the ion beam emerging from R_2 crosses the main ion beam axis at 90° and moves toward the MCP detector where parent, pump laser fragments and probe laser fragments appear at different arrival times. This design offers great versatility by allowing the probe laser to interact with the ion packet either before or after mass separation by R_1 by simply changing the timing sequence. In particular, one can obtain isotopomer-selective dip spectra (Fig. 4.3e),[35] tag-free linear spectra by two-color IR-IR photodissociation of bare ions (Fig. 4.3d), or the spectrum of the excited clusters generated by resonant excitation of cold clusters by the pump laser below their dissociation thresholds (Fig. 4.3c). Finally, spectra of tagged clusters (Fig. 4.3a) can be obtained with very low background in a single laser mode where the probe laser interacts with parent ions after mass selection by R_1 to isolate them from fragments

arising from metastable decay along the flight tube en route to R_1. Details about these components and their design are discussed in Chapter 2. 133

4.3 Schematics for various experiments that can be executed on the platform introduced in Fig. 4.2. including schemes for obtaining (a) tag predissociation (denoted IR1PD for single-color, one photon) spectra where the tag is chosen to have a low binding energy (blue dotted line) such as D_2 in this specific case, and bare (i.e. tag free) predissociation IR1PD spectra above the water cluster binding energy (red dashed line); (b) single-color IR two photon dissociation (IR2PD) spectra of the bare molecule below the water cluster dissociation energy by sequential absorption of two photons of the same color before dissociation; (c) two-color IR2PD spectra of photoexcited molecules obtained by fixing the first laser ($h\nu_1$) on a strong transition below the dissociation threshold and scanning the second laser ($h\nu_2$); (d) two-color IR2PD linear spectra of the cold molecules obtained by fixing the second laser ($h\nu_2$) on a transition unique to the excited state molecule and scanning the first laser ($h\nu_1$); and (e) double resonance depletion spectra obtained by fixing the second laser ($h\nu_2$) on a transition unique to one of the isomers and removing population from the ground state using the first laser (scanned). The difference in ground state energy of the two isomers in (e) is governed by zero-point energy. 135

4.4 Comparison between the predissociation spectra of $I^-\cdot(H_2O)_2$ obtained with (a) D_2, (b) H_2, and (c) Ar tags. 137

4.5 The black curve is the calculated (MP2/aug-cc-pVTZ-PP) potential energy as a function of the O-O distance in the $I^-\cdot(D_2O)_2$ cluster with other parameters relaxed, where region (I) corresponds to the cyclic ring structure at the global minimum, region (II) indicates more open structures where the inter water H-bond is broken to yield freely rotating water monomers, and (III) refers to dissociation of a water monomer.[30] The blue arrow represents the pump laser fixed on a known transition while the green arrows represent the scanning probe laser. $\sigma_0(\nu)$ and $\sigma_{ex}(\nu)$ are the ground state and excited state absorption cross sections as functions of photon energy, respectively. 140

4.6 (a) IR1PD D_2 predissociation spectrum of D_2 tagged $I^-\cdot(D_2O)_2$. The color-coded arrows indicate the pump laser ($h\nu_1$) energies leading to excited ions with the photodissociation spectra displayed in traces (b), (c), (d), (more pump frequencies are shown in Fig. 4.7). In addition, traces (e) and (f) are

single laser IR1PD spectra of bare $I^-\cdot(D_2O)_2$ at trap temperatures of 160 and 300 K, respectively. 141

4.7 The (a) two-color IR2PD (probe at 2589 cm^{-1}) and (b) single-color IR2PD spectra obtained by the methods described in Fig. 3d and Fig. 3b, respectively. The colored spectra were gathered by the method outlined in Fig. 3c where the pump laser was parked at (c) 2475 cm^{-1}, (d) 2547 cm^{-1}, (e) 2589 cm^{-1}, (f) 2685 cm^{-1}, and (g) 2721 cm^{-1}. When there is no absorption (blue arrow) the probe laser ($h\nu_2$) simply reproduces the single color IR2PD spectra (d). When the cross section for absorption of the pump laser is low (e.g., at 2721 cm^{-1}), the probe laser sees a distribution of both photoexcited and ground state ions. The resulting spectrum (g) therefore resembles a composite of the single- and two-color IR2PD spectra (e.g., b + c). 142

4.8 (a) The black trace is the single color IR2PD spectra of $I^-\cdot(D_2O)_2$ [see Fig. 4.3b], while the green trace is the spectrum of the cluster after excitation at 2589 cm^{-1} [see Fig. 4.3c]. The arrow in (a) indicates the probe laser position used to obtain the two-color IR2PD spectrum (b). (c) is the predissociation spectrum of D_2 tagged $I^-\cdot(D_2O)_2$. $2\nu_{DOD}$ is the D_2O bend overtone. IDB, ID and F_{OD} are the OD stretch frequencies which can be found in Table 4.1 together with the assignment of combination band e_0. 144

4.9 D_2-predissociation spectrum of $I^-\cdot(H_2O)(D_2O)$. The position of the D_2 transition is indicated by ν^{D_2}, which appears at 2957 cm^{-1} as opposed to the unperturbed position at 2993.6 cm^{-1}. 146

4.10 Calculated minimal energy structure of $I^-\cdot(H_2O)_2\cdot D_2$ using VPT2 at the MP2/aug-cc-pVTZ-PP level of theory. 147

4.11 (a) Single laser IRPD spectra of $I^-\cdot(H_2O)_2$ at trap temperature 15 K. The yellow dotted line indicates the dissociation energy, above this line the spectrum is an IR1PD spectra and below this line the spectra is a IR2PD spectrum. (b-k) are the two laser spectra obtained by fixing the first laser (pump) at a specific frequency and scanning the second laser, the second laser detects both the clusters that absorbed one photon and do not dissociate and the clusters that did not absorb any photon and remains cold. 149

4.12 (a) Single laser IRPD spectra of $I^-\cdot(H_2O)_2$ at trap temperature 15 K. The yellow dotted line indicates the dissociation energy, above this line the spectrum is an IR1PD spectra and below this line the spectra is a IR2PD spectrum. (b-k) are the two laser spectra obtained by fixing the first laser

(pump) at a specific frequency indicated by the blue arrows in (a) and scanning the second laser, the second laser detects both the clusters that absorbed one photon and do not dissociate (red trace) and the clusters that did not absorb any photon and remains cold (sharp features). The overall spectra are displayed as black traces. 150

4.13 Experimental data (orange points) and simulated curves (blue) of the laser power dependence of the cluster population that absorbs only one photon (a), the excited cluster population that already absorbed one photon absorbing a second photon (b), and the cluster population that absorbs two photons at the same frequency when interacting with one single laser (c). 153

4.14 The IR dissociation spectra of (a) D_2 tagged $I^-\cdot(H_2O)_2$, (b) D_2 tagged $I^-\cdot(H_2O)\cdot(D_2O)$, and (c) bare $I^-\cdot(H_2O)\cdot(D_2O)$, where the black arrow indicates the thermochemical dissociation enthalpy.[42] Trace (c) is a hybrid spectrum where bands below D_o are single color IR2PD (Fig. 4.3b) while above D_o they are obtained by IR1PD (Fig. 4.3a). The gray trace in (b) is 3 times magnified in intensity. See Fig. 4.1 caption for labeling scheme. All labeled transitions can be found in Table 4.1. The shoulder on the IHB_{DD} band (*) was traced to a D_2 tag effect as illustrated in Fig. 4.15. 156

4.15 (a) IR2PD spectrum of $I^-\cdot(HOD)\cdot(D_2O)$ obtained by scanning the pump and probe on 3458 cm^{-1} (Fig 4.3d) which is unique to the photoexcited molecule cluster compared with (b) the D_2 tagged predissociation spectrum. 157

4.16 (a) The black trace is the D_2-predissociation spectrum of both isotopomers of $I^-\cdot(H_2O)\cdot(D_2O)$. The isotopomer-specific dip spectra are presented for the bare $I^-\cdot(H_2O)\cdot(D_2O)$ complex with the H_2O molecule at (b) the DD position (H_2O_{DD}), obtained by probing on the IH transition (red arrow), and (c) the AD position (H_2O_{AD}), obtained by probing on free OH (blue arrow). The black arrow is reproduced from Fig. 4.14c. The brackets represent calculated (VPT2, MP2/aug-cc-pVTZ-PP) combination bands with intensities greater than 1 km/mol, which are discussed in the text. Assignments and peak positions are collected in Table 4.1. 159

4.17 The black trace shows the relative cross section of $I^-\cdot(H_2O)_2\cdot D_2$ (obtained using single-color IR1PD Fig. 4.3a), while the blue trace displays the relative cross section of $I^-\cdot(H_2O)\cdot(D_2O)$ with the H_2O molecule on the AD position obtained by probing the free OH transition indicated by the blue arrow (described further in Fig. 4.3e) and the red trace is for the H_2O molecule on the DD position. The blue and red traces are inverted and

normalized to the peak intensities of the probe position peaks in the black trace to show that these features recovered from the double resonance experiments (when combined) closely match the spectra of the two isotopomers (black trace). 160

4.18 IR2PD spectra of (a) $I^-\cdot(HOD)_2$ and (b) $I^-\cdot(H_2O)\cdot(D_2O)$, the difference in fragment masses enabled selective detection of one isotopologue or the other. All peak positions can be found in Table 4.1. 169

4.19 Displacement vectors (MP2/aug-cc-pVTZ-PP) of (ν_{14}) antisymmetric O-I-O stretch with rock action centered on AD water molecule. (ν_{14}) antisymmetric O-I-O stretch with rock action centered on DD water molecule. The band numbering scheme is based on Herzberg notation. [60] 171

4.20 (a) is the predissociation spectrum of D_2 tagged $I^-\cdot(H_2O)\cdot(D_2O)$. (b) is the predissociation spectrum of D_2 tagged $I^-\cdot(HOD)\cdot(D_2O)$. The dotted lines indicate the peak position for those in the $I^-\cdot(H_2O)_2$ case. The brackets indicate the combination bands of the IHB_{AD} and IHB_{DD} fundamentals with ν_{15} (green), and ν_{14} (blue), which are displayed in Fig. 4.19. Peak positions and assignments are collected in Table 4.1. The blue and gray arrows in (c) indicate the splitting between the IHB_{DD} and IH band in $I^-\cdot(HOD)\cdot(D_2O)$ and $I^-\cdot(H_2O)\cdot(D_2O)$, respectively. The difference between these values ($\Delta\nu$) reflects the strength of coupling between the two OH oscillators, as discussed further in the text. 173

4.21 The linear spectra of (a) $I^-\cdot(D_2O)_2$, (c) $I^-\cdot(H_2O)\cdot(D_2O)$, (d) $I^-\cdot(DOH)\cdot(H_2O)$ obtained by two-color IR2PD (Fig. 4.3d) and (b) D_2 tagged spectra of $I^-\cdot(HOD\cdot(D_2O)\cdot D_2$ compared with their calculated frequencies (inverted stick spectra) using VPT2 at the MP2/aug-cc-pVTZ-PP level of theory. All labeled transitions can be found in Table 4.1. 175

4.22 (a) Predissociation spectrum of D_2 tagged $I^-\cdot(H_2O)\cdot(D_2O)$. (b-g) Isotopomer selective double resonance dip spectra at various trap temperatures. The blue traces represent the spectra of H_2O_{AD} obtained by probing on the free OH indicted by the blue arrow in (a), while red traces represent the spectra of H_2O_{DD} acquired by probing on the IH transition labeled by the red arrow. The color-coded droplines indicate the cold cluster transition frequencies associated with each isotopomer. 180

5.1 Representative structures of the pentagonal dodecahedron (PD_0) water cages. The representative $Cs^+\cdot(H_2O)_{20}$ cluster structure [30] (a) and the minimal energy structure [31] (b) of $H_3O^+\cdot(H_2O)_{20}$. These structures contain three classes of network sites: AAD (red), ADD (orange) and AADD

(purple), that differ by the number of H-bond acceptors (A) and donors (D) associated with each water molecule. 195

5.2 Comparison between vibrational spectra of $Cs^+\cdot(H_2O)_{20}\cdot D_2$ and $Cs^+\cdot(HDO)(D_2O)_{19}\cdot D_2$. Displayed here are the vibrational predissociation spectra of $Cs^+\cdot(H_2O)_{20}\cdot D_2$ (a) and $Cs^+\cdot(HDO)(D_2O)_{19}\cdot D_2$ (b) and its isotopomer-specific spectra (c) where, purple, light blue and red represents the bound OH (OH^b_{AAD}), HOH bend overtone ($2\nu_{HOH}$) and the free OH (OH^{free}_{AAD}) on the AAD water molecules, respectively, whereas yellow labels identify the bound OH stretches (OH^b_{ADD}) on the ADD water molecules. Isotopomer selective spectra in the gray box (c1-c16) of $Cs^+\cdot(HDO)(D_2O)_{19}$ were obtained by probing at various locations indicated by the color-coded arrows. The structure shows one example of the single OH group that is in a configuration that contributes to one of the yellow OH^b_{ADD} features. Trace (c12) is expanded to show more detail in Figure 5.5. The symbol * in (c15) denotes a sharper feature that is embedded in the broader lineshape. Spectral assignments, probe positions and widths are reported in Table 5.1 and Table 5.2. Trace c16 was taken with extensive averaging at representative points due to low signal intensity in this energy range. 200

5.3 (**a**) Predissociation spectra of all isotopomers of $Cs^+\cdot(HDO)(D_2O)_{19}\cdot D_2$ in the OH stretching region for the structure PD_0 in Fig. 5.1A. Bands colored red, orange, and purple denote the free OH stretch (OH^{free}_{AAD}), bound OH stretch on an ADD water (OH^b_{ADD}), and the bound OH stretch on an AAD water (OH^b_{AAD}), respectively. (**b**) Harmonic spectra of all isotopomers of $Cs^+\cdot(HDO)(D_2O)_{19}\cdot D_2$ computed at the B3LYP/6-31+G** level of theory and basis with the LANL2DZ pseudopotential for Cs scaled by a 0.973 scaling factor. 203

5.4 Comparison of the vibrational predissociation sepctra of $Cs^+\cdot(H_2O)_{20}\cdot D_2$ (a) and $Cs^+\cdot(HDO)(D_2O)_{19}\cdot D_2$ (c), with expanded views of the OH features associated with the ADD water molecules in (e) and (f), respectively. The spectral contribution from each single H_2O molecules can be extracted via with isotopomer selective spectroscopy of the $Cs^+\cdot(H_2O)(D_2O)_{19}\cdot D_2$ isotopologue (b), whereas contribution from each single OH oscillator can be extracted from the isotopomer specific spectra of $Cs^+\cdot(HDO)(D_2O)_{19}\cdot D_2$ (d) where intramolecular coupling between the two OH groups and the bend overtone is removed. 204

5.5 Vibrational predissociation spectrum of $Cs^+ \cdot (HDO)(D_2O)_{19} \cdot D_2$ (a) and $D_3O^+ \cdot (HDO)(D_2O)_{19} \cdot D_2$ (d) as well as isotopomer selective spectra of them (b, c) respectively. Some of the lower energy OH stretches (orange feature in b3, b4 and pink feature in c2) have combination bands built on top of them (small feature on the higher energy side indicated with the brackets). The higher energy OH stretch (blue/orange and blue/pink features on the high energy side in b1, b2 and c1) are accidentally degenerate with the combination bands. The contribution to the predissociation spectra from the lower energy OHs and their combination bands as well as the higher energy OH stretches are depicted with smooth solid lines in (a, d), with the sum of the two isotopomers colored black. The higher energy features have contribution from multiple isotopomers. As a result, when the probe laser is fixed on the higher energy peaks, features from both isotopomers are detected, hence displaying a distorted intensity profile (b1, b2 and c1). Conversely, when the probe laser is fixed on the lowest energy peak (orange arrow in b4 and pink arrow in c2), only one isotopomer is detected and the intensity profile displays the typical fundamental and combination band pattern. 206

5.6 Expanded display highlighting the appearance of a second feature in the isotopomer-specific spectra of $D_3O^+ \cdot (HDO)(D_2O)_{19} \cdot D_2$ with OH oscillators near 3400 cm^{-1}. Non-selective spectra are displayed in (a), while (b1-b4) are the isotopomer-selective photobleach scans obtained with the probe laser positions labeled by the arrows. The combination bands are labeled by brackets displaced from the OH stretching fundamentals on the lower energy side (b3). The simulated traces (colored in b2, b3) are overlaid on top of experimental data (gray traces), with a detailed explanation of the photoexcitation scheme included in Figure 5.5. Details about the simulation are included in the Chapter 5.4. Probe positions and widths are reported in Table 5.3. 209

5.7 Predissociation spectra (a) and isotopomer selective spectra (b) of all isotopomers of $D_3O^+ \cdot (HDO)(D_2O)_{19} \cdot D_2$ in the OH stretching region. The contribution from each OH group is isolated with isotopomer selective spectroscopy and the results are fitted with a Gaussian profile to obtain the peak position and FWHM. The residues for each fit are plotted below each trace in blue. The mean, FWHM, and error of the Gaussian fits are collected in Table 5.3. For trace b3, the * band is a result of the OH stretch feature in b2 having a combination band that has the same frequency as the main feature in b3. Detailed analysis on the extra band in b3 is included in figure 5.5. 212

5.8 Predissociation spectra (a) and isotopomer selective spectra (b) of all isotopomers of $Cs^+ \cdot (HDO)(D_2O)_{19} \cdot D_2$ in the OH stretching region. The contribution from each OH group is isolated with isotopomer selective spectroscopy and the results are fitted with a Gaussian profile to obtain the peak position and FWHM. The residues for each fit are plotted below in blue. The mean, FWHM and error of the Gaussian fits are collected in Table 5.1. The * in trace b15 (blue) indicates a sharper transition embedded in the broad feature whose assignment is not known. Spectra in b16 was obtained by extensive averaging at several representative frequencies due to limitation in signal intensity. 213

5.2 Illustrations of the two low-frequency modes used in the seven-dimensional model Hamiltonian. The mode on the left (mode 2) has a frequency of 92.4/94.5 cm^{-1} (unscaled) and corresponds to primarily ring breathing with some contribution from the H_3O^+ translation within the cage. The mode on the right (mode 1) has a frequency of 205.5/206.1 cm^{-1} (unscaled) and corresponds to primarily H_3O^+ translation with some contribution from ring breathing. Both modes are nearly doubly degenerate, and would correspond to the two components of an E vibration if the cluster had perfect C_3 symmetry. A8

5.9 Dependence of experimental linewidths of OH stretch features on red shift. The included features can be found in figure 5.2c and figure 5.7 on the red shift of the OH frequency from the gas phase uncoupled free OH stretch value at 3607 cm^{-1}. The error bars correspond to the confidence interval associated with the Gaussian fits used to obtain the spectral width (Fig. 5.7). Triangle symbols refer to the bound OH group (△) and 0→2 overtone of the intramolecular HOH bend (▲) in $Cs^+ \cdot (H_2O)(D_2O)_{19} \cdot D_2$. The error bars are drawn at ± one standard deviation from the data points. All data are collected in Table 5.1 and 5.3. 215

5.10 Infrared two photon dissociation (IR2PD) spectra of $D_3O^+ \cdot (HDO)(D_2O)_{19}$ at three different temperatures (11, 60 and 100 K). The spectral feature remains unchanged below 60 K. Slight broadening starts to become observable at 100 K suggesting the thermal fluctuation below 60 K is minimal. 217

5.11 Dependence of experimental linewidths of OH stretch features on redshift in figure 5.2c and figure 5.7b, and widths of calculated frequency distributions for neutral $(H_2O)_6$ cage cluster at 40 K (ref. 18), on the red shift of the OH frequency from the gas phase uncoupled free OH stretch value at 3607 cm^{-1}. The error bars correspond to the confidence interval

associated with the Gaussian fits used to obtain the spectral width (Fig. 5.7). Triangle symbols refer to the bound OH group (△) and $0 \rightarrow 2$ overtone of the intramolecular HOH bend (▲) in $Cs^+ \cdot (H_2O)(D_2O)_{19} \cdot D_2$. 220

5.12 Temperature dependent OH spectra of $D_3O^+ \cdot (HDO)(D_2O)_{19}$. Temperature dependent vibrational spectra of $D_3O^+ \cdot (HDO)(D_2O)_{19}$ with temperature color coded (a,b). Isotopomer selective spectra of $D_3O^+ \cdot (HDO)(D_2O)_{19}$ at various temperatures with the same coloring scheme (c.d). 221

6.1 Minimum energy structure [42] of the distorted pentagonal dodecahedron (PD) cage formed by the $Cs^+ \cdot (H_2O)_{20}$ cluster, denoted PD_0. On the top is a static picture of the PD_0 structure and on the bottom is an interactive 3D model which can be rotated in Adobe Reader. This structure has two classes of network sites (AAD, red and ADD, orange) that differ by the number of H-bond acceptors (A) and donors (D) associated with the water molecules at each location. 235

6.2 Comparison of SFG spectra from the ice and liquid water surfaces with the experimental vibrational spectra of $Cs^+(40H) \cdot D_2$ and its isotopologue incorporating an intact H_2O molecule. SFG spectra of ice-vapor (A) [34] and water-air (B) [33] interfaces (used with permission) obtained using ssp polarization combinations. (C) and (D) were obtained by predissociation of the (C) $Cs^+ \cdot (H_2O)_{20} \cdot D_2$, and (D) $Cs^+ \cdot (H_2O)(D_2O)_{19} \cdot D_2$ cluster ions. The δ label indicates assignment of intramolecular HOH bending overtone from the literature.[33] The frequencies of features labeled a_n and b_n are included in Tables 6.1 and 6.2. 239

6.3 (**A**) Predissociation spectra of all isotopomers of $Cs^+(2H,38D) \cdot D_2$ in the OH stretching region. Bands colored red, orange, purple and blue denote the free OH stretch (OH^{free}_{AAD}), bound OH stretch on an ADD water (OH^{b}_{ADD}), bound OH stretch on an AAD water (OH^{b}_{AAD}), and the intramolecular HOH bend overtone ($2\nu_{HOH}$), respectively. Harmonic spectra of all isotopomers of $Cs^+(2H,38D)$ computed at the (**B**) B3LYP/6-31++G**, (**C**) CAM-B3LYP/6-31++G** and (**D**) M06-2X/6-31++G** levels of theory and basis with the LANL2DZ pseudopotential for Cs. The calculated transitions are categorized according to the nomenclature suggested by Skinner and coworkers [44] where the number indicates the total number of H-bonds that an individual water molecule is involved in (1-4) and the letter indicates the number of OH groups on that water molecule that are donating H-bonds (N for none, S for single and D for double). Finally, a specific OH oscillator is indicated by a pair of water molecules connected with a dash where the H-

bond donor resides on the left and acceptor on the right (e.g. 3_D-3_S means the OH group on an ADD water that donates to an AAD water, see Fig. 6.4 for more examples). 244

6.4 Expanded views of several donor-acceptor pairs in the calculated structure of $Cs^+(40H)$ computed at the B3LYP/6-31++G**level of theory and basis with the LANL2DZ pseudopotential for Cs. The bound OH on AAD water molecules (OH^b_{ADD}), indicated by purple halos on red molecules, can be categorized by their H-bond acceptors into two classes: 3_s-3_s with an AAD water as acceptor (**A**) and 3_s-3_d with an ADD water (Orange, (**B-E**)). The 3_s-3_d class can be further differentiated according to the types of water molecules that the acceptor ADD water binds to. The case where the acceptor ADD water binds to two AAD waters (**C**) results in the acceptor ADD water displaced slightly out of the cage towards the free OH (**B**), whereas when the acceptor ADD water binds to one AAD and one ADD water (**E**), the acceptor ADD water is displaced inward, away from the free OH (**D**). These three motifs result in different OH^b_{ADD} transition frequencies on the donor AAD water molecule. The motif in (**A**) yields the highest calculated frequency whereas that displayed in (**D,E**) results in the lowest frequency.. 246

6.5 Product mass spectrum arising from condensation of H_2O molecules onto preformed $Cs^+\cdot(D_2O)_n$ clusters at an H_2O pressure of approximately 10^{-4} Torr in an octopole ion guide. 248

6.6 Isolation of the contributions of the AAD (red) and ADD (orange) water molecules to the spectrum of the $Cs^+(2H, 38D)\cdot D_2$ isotopologue. Vibrational predissociation spectrum of (A) $Cs^+\cdot(2H,38D)\cdot D_2$ and two-color, IR-IR double resonance hole burning spectra of $Cs^+\cdot(2H,38D)\cdot D_2$ with the probe laser fixed on (B) the a_0 (red arrow) and (C) the a_1 (orange arrow) features, thus isolating the signatures of H_2O in AAD and ADD sites, respectively. 250

6.7 Isolation of band patterns associated with spectroscopically distinct sites occupied by an intact H_2O molecule in the Cs+(2H,38D)$\cdot D_2$ cluster, obtained by fixing the probe laser at the photon energies indicated by downward arrows while scanning the pump laser through the OH stretching region. (A) Non-selective predissociation spectrum of Cs+(2H,38D)$\cdot D_2$, (B-D) bands due to ADD sites (orange), (E-H) bands arising from AAD sites. The AAD contributions are further resolved into excitations of free OH (red), bound OH (purple) and intramolecular bend overtones (blue). The solid lines in (E) and (F) are fits to a 2×2 coupling

scheme between the OH stretch and intramolecular bend described in detail in Fig. 6.9. 253

6.8 (A) Predissociation spectra of all isotopomers of $Cs^+(2H,38D)\cdot D_2$. . See caption in Fig. 6.3 for notation. The free OH region is expanded and presented as inverted gray traces in (B) and (C). The red depletion traces are two-color, isotopomer-selective IR-IR double resonance hole burning spectra of $Cs^+(2H,38D)\cdot D_2$ in the free OH region, obtained by probing on the position indicated by the red arrows in (B) and (C). 254

6.9 Fits (solid lines) of the multiplet structures in Figs. 6.7E (**A**) and 6.7F (**B**) to a 2×2 Fermi resonance model. Each trace displays the spectral features associated with one H_2O molecule: the free OH, the bound OH partner (purple) and the intramolecular bend overtone (turquoise). The probe positions are indicated by the red arrows. The fit results are reported below: **A**. OH^b_{ADD} band center (3364 ± 4 cm^{-1}) with area of 92 ± 4 a.u. and width (56 ± 3 cm^{-1}) whereas the nominal $2\nu_{HOH}$ band is centered at 3234 ± 4 cm^{-1} with area 11 ± 2 a.u. and width (10 ± 2 cm^{-1}). The fitted Lorentzians result from a coupling constant of 40 cm^{-1} between the two states. **B**. OH^b_{ADD} band center (3320 ± 4 cm^{-1}) with area 115 ± 5 a.u. and width (64 ± 3 cm^{-1}) whereas the nominal $2\nu_{HOH}$ band is centered at 3202 ± 4 cm^{-1} with area 58 ± 3 a.u. and width 36 ± 3 cm^{-1}. These were obtained with a coupling constant of 53 cm^{-1} between the two states. These values were obtained by solving

$$H = T^+ \nu T$$

for the elements of H (e.g. the unperturbed frequencies of the OH stretch, ν^0_{str}, and the HOH bend overtone, $2\nu^0_{bnd}$, as well as the Fermi resonance coupling term, λ_{sbb}. To do this we express the three matrices as

$$H = \begin{pmatrix} 2\nu^0_{bnd} & \lambda_{sbb} \\ \lambda_{sbb} & \nu^0_{str} \end{pmatrix}, T = \begin{pmatrix} T_{11} & T_{12} \\ -T_{12} & T_{11} \end{pmatrix} \text{ and } \nu = \begin{pmatrix} \nu_L & 0 \\ 0 & \nu_H \end{pmatrix}$$

where ν_L and ν_H represent the centers of the blue and purple features in the above spectra, while T_{11} and T_{12} provide the square roots of the normalized areas under these features. The value of λ_{sbb} is obtained through simple matrix multiplication of these 2×2 matrices. 256

7.1 Theoretical decomposition of the SFG $\chi^{(2)}$ spectrum of the air-water interface to reveal the contributions of water molecules in specific local network sites. (A) Complex $\chi^{(2)}$ spectra of water with the real part in black and imaginary part in red, reproduced from ref.19 with permission. (B) Theoretical analysis of contribution from different types of water to $\chi^{(2)}$ spectra's the imaginary part reproduced from ref.8 with permission. (C-H)

example structures of different types of water molecules on the interface where A denotes H-bond acceptor and D denotes H-bond donor. 269

7.2 SFG intensity spectra of the air water interface compared to the spectra of various water clusters in the OH region. (A) SFG intensity ($|\chi^{(2)}|^2$) spectra of water reproduced from ref.5 with permission. δ denotes the bend overtone ($2\nu_{HOH}$) transition and α denotes the controversial 3500 cm^{-1} region. (B-E) Vibrational predissociation spectra recorded with an D_2 messenger tag and representative structures of $NH_4^+\cdot(H_2O)_{22}$, $Cs^+\cdot(H_2O)_{20}$, $Na^+\cdot(H_2O)_{20}$, and $Li^+\cdot(H_2O)_{20}$. OH bands and water molecules in the structures are color coded according to their types. 271

7.3 Theoretically calculated OH frequency distribution at the air water interface compared with examples of each type of water molecule's spectra obtained with finite size water clusters. (A) OH frequency distribution at the surface reproduced from ref.8 with permission. (B) Vibrational predissociation spectra of $H_3O^+\cdot(H_2O)_5$. (C-G) Spectra of each type of water molecules present on the surface obtained with isotopomer selective double resonance hole burning technique applied to various water clusters with the probe laser position labeled with the colored arrows. 274

7.4 SFG intensity spectra compared with various types of water molecule's spectra obtained with finite size water clusters. (A) OH frequency distribution at the surface. (B) OH band regions divided by types of water molecules summarized from the isotopomer specific hole burning spectra in (C-T). (C-T) Spectra of various types of water molecules imbedded in various water clusters with the probe laser position labeled with colored arrows. Bands are colored according to the water molecule's types and mixing color indicates mixed feature from different origins. 278

7.5 Frequency distribution of different types of H_2O molecules imbedded in $(D_2O)n$ cages. The harmonic frequencies of all isotopomers of $Li^+\cdot(H_2O)(D_2O)_{19}$, $Na^+\cdot(H_2O)(D_2O)_{19}$, $Cs^+\cdot(H_2O)(D_2O)_{19}$, and $CH_3NH_3^+\cdot(H_2O)(D_2O)_{20}$ are calculated at the B3LYP/6-31++G** level of theory and basis with the LANL2DZ pseudopotential for the Cs atom. The calculated frequencies are scaled by a 0.973 scaling factor. Multiple structural isomers are included for some of the species. Details of the harmonic frequencies for each cluster are displayed in Fig. 7.6-7.9. 280

7.6 Comparison between the experimental and theoretical vibrational spectra of $Cs^+\cdot(H_2O)(D_2O)_{19}$. (A) Representative low energy structure of

$Cs^+\cdot(H_2O)_{20}$ (B)Single laser vibrational predissociation spectra of all isotopomers of the $Cs^+\cdot(H_2O)(D_2O)_{19}$. (C)Harmonic spectra calculated at the B3LYP/6-31++G** level of theory and basis with the LANL2DZ pseudopotential for the Cs atom. The calculated frequencies are scaled by a 0.973 scaling factor. The labels consist of the water molecule type the OH group of interest is residing on and the water molecule's type that the OH group of interest is donating to. For example, **AAD**-ADD denotes the OH group on an AAD molecule donating to an AAD molecule. 281

7.7 Comparison between the experimental and theoretical vibrational spectra of $Na^+\cdot(H_2O)(D_2O)_{19}$. (A)Single laser vibrational predissociation spectra of all isotopomers of the $Na^+\cdot(H_2O)(D_2O)_{19}$. (B-D) Harmonic spectra calculated at the B3LYP/6-31++G** level of theory and basis. The calculated frequencies are scaled by a 0.973 scaling factor. (E-G) Representative structures of $Na^+\cdot(H_2O)_{20}$ with their relative energies. The spectrum in (B) corresponds to the structure displayed in (E), the spectrum in (C) corresponds to the structure in (F) and the spectrum in (D) corresponds to the structure in (G). 282

7.8 Comparison between the experimental and theoretical vibrational spectra of $Li^+\cdot(H_2O)(D_2O)_{19}$. (A)Single laser vibrational predissociation spectra of all isotopomers of the $Li^+\cdot(H_2O)(D_2O)_{19}$. (B,C) Harmonic spectra calculated at the B3LYP/6-31++G** level of theory and basis. The calculated frequencies are scaled by a 0.973 scaling factor. (D,E) Representative structures of $Li^+\cdot(H_2O)_{20}$ with their relative energies. The spectrum in (B) corresponds to the structure displayed in (D), and the spectrum in (C) corresponds to the structure in (E). 283

7.9 Comparison between the experimental and theoretical vibrational spectra of $CH_3ND_3^+\cdot(H_2O)(D_2O)_{19}$. (A) Representative low energy structure of $CH_3NH_3^+\cdot(H_2O)_{20}$ (B)Single laser vibrational predissociation spectra of all isotopomers of the $CH_3ND_3^+\cdot(H_2O)(D_2O)_{19}$. (C)Harmonic spectra calculated at the B3LYP/6-31++G** level of theory and basis. The calculated frequencies are scaled by a 0.973 scaling factor. 284

7.10 Dependence of OH oscillator's frequency on the H-bond environments. The OH of interest is labeled by solid O-H bond. The black dots indicate frequency of the OH oscillator where bottom is lowest frequency and top is the highest frequency. The small red arrows are the direction of the hydrogen pushing. 286

7.11 Dependency of OH frequency on the H-bonding environment. The colored arrow indicates blue shift and red shift, the A and D labels the type of the water molecule that the OH is residing on. For example, a single donor (D) water's OH stretch is generally lower in frequency compared to the double donor (DD) water molecule. The 'donate to' and 'accept from' labels denote the type of water molecule the OH group of interest is connected to. And the 'partner donates to' labels the H-bond environment the other OH group on the same water molecule is residing in. 288

7.12 Dependence of OH oscillator's frequency on the second shell water H-bond environments. The OH of interest is labeled by solid O-H bond with H highlighted in red spherical shade. The first shell water molecule is also in black whereas the second shell water molecules are in gray. The black dots indicate frequency of the OH oscillator where bottom is lowest frequency and top is the highest frequency. The small red arrows are the direction of the hydrogen pushing. 290

7.13 Dependence of OH oscillator's frequency on the second shell water H-bond environments. The OH of interest is labeled by solid O-H bond with H highlighted in red spherical shade. The first shell water molecule is also in black whereas the second shell water molecules are in gray. The black dots indicate frequency of the OH oscillator where top is lowest frequency and bottom is the highest frequency. The small red arrows are the direction of the hydrogen pushing. 291

7.14 Dependence of OH oscillator's frequency on the second shell water H-bond environments. The OH of interest is labeled by solid O-H bond with H highlighted in red spherical shade. The first shell water molecule is also in black whereas the second shell water molecules are in gray. The black dots indicate frequency of the OH oscillator where bottom is lowest frequency and top is the highest frequency. The small red arrows are the direction of the hydrogen pushing. 292

7.15 Regression tree of OH oscillator's frequency on the H-bond environments. The frequencies are in cm^{-1}. 294

8.1 (a) Calculated (MP2/aug-cc-pVTZ-PP, ref. 20) minimum energy structure of $I^-\cdot(H_2O)_2$ and D_2-predissociation spectra of (b) $I^-\cdot(H_2O)_2\cdot D_2$, (c) $I^-\cdot(H_2O)\cdot(D_2O)\cdot D_2$ and (d) $I^-\cdot(HDO)\cdot(D_2O)\cdot D_2$. The H atoms and the vibrational bands are color coded according to the corresponding local OH oscillators, denoted free OH (F_{OH}, blue), inter-water hydrogen bonded OH (IH, yellow), ionic H-bonded (IHB) OH on the AD water (IHB_{AD}, pink),

and the corresponding IHB on the DD water (IHB_{DD}, green). The HOH bend overtone ($2v_{HOH}$) is also identified, which disappears in the $I^-\cdot(HDO)\cdot(D_2O)$ isotopologue, while (*) identifies combination bands involving soft modes of the complex (ref. 25). Traces b, c and d are adapted from data in Chapter 4 or ref. 25. 304

8.2 Diagram of the temperature controlled cryogenic ion vibrational spectrometer with two laser capabilities at Yale. The mass selected ions are intersected by the pump laser (hv_1) at the first laser crossing, yielding photo excited ions and/or photofragments while depleting the ground state parent ion. Parent and fragment ions are separated by the coaxial, dual-stage gridless retro-reflectron (R_1) and intersected by the probe laser (hv_2) at the second laser crossing where a certain isomer/isotopomer within the parent ions is interrogated by the probe laser. The ion beam is then turned 90° by the pulsed DC turning quad (Q) into the second reflectron (R_2) to separate photofragments from the probe laser interaction. Lastly, the ion beam emerging from R_2 crosses the main ion beam axis at 90° and moves toward the MCP detector where parent, pump laser fragments and probe laser fragments appear at different arrival times. By scanning the pump laser and fixing the probe laser on a transition unique to one of the isotopomers and monitoring the photofragment signal which exclusively reflects the population in the selected isotopomer, one can obtain isotopomer selective dip spectra. In addition, spectra of tagged clusters can be obtained with very low background in a single laser mode where the probe laser interacts with parent ions after mass selection by R_1 to isolate them from fragments arising from metastable decay along the flight tube en route to R_1. The schematic is reproduced from the work by Yang et al (ref.1). 307

8.3 (a) Schematic of the flip motion that exchanges the DD_{2H} and AD_{2H} sites, where the gray atoms label the deuterated positions; (b) and (c) are the calculated time-dependent population changes in the 2H-D_2 (b) AD_{2H} and (c) DD_{2H} sites in the regime II limit under the condition that the pump laser completely removes the local population in one of the two sites (see text) at t=0. The horizontal lines indicate the equilibrium population before interaction with the pump laser. The displacements between the dotted horizontal lines and the solid traces correspond to the expected time-dependent population changes. The traces are color coded according to the pump laser excitation of AD_{2H} (blue) and DD_{2H} (red). The population changes at the probe timing (vertical dashed gray line in (b)

and (c)) are plotted as dashed drop arrows. See text for numerical values used in the simulation. 310

8.4 (a) The predissociation spectrum of D_2 tagged $I^-\cdot(H_2O)\cdot(D_2O)$. (b) through (g) are the double resonance hole burning experiment spectra of bare $I^-\cdot(H_2O)\cdot(D_2O)$ at various trap temperatures. The blue traces represent the spectra of AD_{2H} obtained by probing on the free OH indicted by the blue arrow in (c,e,g), while red traces represent the spectra of DD_{2H} acquired by probing on the IH transition labeled by the red arrow. The color-coded droplines indicate the cold cluster transition frequencies associated with each isotopomer. The traces are reproduced from the work by Yang et al (ref.1). 312

8.5 (a) D_2-predissociation spectrum of all four isotopomers of $I^-\cdot(HDO)(D_2O)\cdot D_2$. (b-f) Double resonance hole burning dip spectra of bare $I^-\cdot(HDO)(D_2O)$ at various temperatures. The traces are color coded according to the probe position: yellow corresponds to probing the IH position and blue corresponds to probing the free OH position. Dips other than the probe position indicates the H atom migrated during the time between pump and probe laser. The migration happens around 60-75 K. 313

8.6 Calculated (MP2/aug-cc-pVTZ-PP, ref.2) relaxed potential energy scan along the (right) flipping (Fig. 8.13f) coordinate and the (left) rocking (Fig. S8.13g) coordinate for $I^-\cdot(H_2O)_2$. These are generated by rotating the AD water molecule through a C_{2v} geometry to exchange protons bound to the ion in the rocking pathway and moving the free OH into the IH position for the flipping pathway. The two minima resemble the minimal energy structure in Fig. S8.13h whereas the peak height in the center represents the barrier height of the two pathways as described in the main text. Note that in the deuterated systems tunneling is not possible due to the isotopic substitution. 314

8.7 Rotatable PDF on the previous page displays the calculated structure of $I^-\cdot(H_2O)_2\cdot D_2$ at the MP2/aug-cc-pVTZ-PP level of theory and basis function (ref. 2). A static version is displayed on this page. 315

8.8 (a) calculated (MP2/aug-cc-pVTZ-PP, ref. 2) fundamental intensities of the four OH oscillators in the two $I^-\cdot(H_2O)(D_2O)$ isotopomers according to whether the H_2O molecule resides in the AD (AD_{2H}, blue) or DD (DD_{2H}, red) positions, (b) calculated population ratio of the four OH oscillators which reflects population of the two isotopomers at 30 K, ‘x’ here is the population of the less dominant DD_{2H} isotopomer and K here is the

equilibrium constant of the $DD_{2H} \rightleftharpoons AD_{2H}$ reaction. (c) Calculated predissociation yield obtained by multiplying oscillator strength by population for each OH oscillator. (d,e,f) Demonstrations of double resonance hole burning spectra under different regimes when probing on a specific isotopomer, where probe positions are indicated by the colored arrows. The two oscillators chosen have high oscillator strength hence insure 100% dissociation upon excitation. Conversion refers to the interchange of the H_2O molecule between the AD and DD sites, $\tau_L = 8$ ns is the pump laser pulse width and $\tau_w = 40$ μs is the time delay between pump and probe laser and K is the same equilibrium constant as the one in (b). 317

8.9 Vibrational predissociation spectrum of $I^-\cdot HDO$ at trap temperature 15K. The features are the rotational K transitions on the free OH fundamental and they are assigned according to the calculated (MP2/aug-cc-pVTZ-PP, ref. 2) rotational constants and vibrational fundamental. Temperature was extracted using Boltzmann factor between population in the K= 0 and K= 1 state which can be obtained by integrating the peak area of the K= 0 → 1 and K= 1 → 2 transitions and correcting for the difference in transition moments (ref.3). 318

8.10 (a) and (b) are the time-dependent population changes at the AD and DD sites in the regime II limit under the condition that the pump laser removes the local population in one of the two sites. The population time behavior was simulated with reversible unimolecular kinetics. Panel (a) applies to the case where the pump laser removes population from the DD site, and (b) pertains to the case when the pump laser removes population from the AD site. AD(0) and DD(0) are the populations before the pump laser interaction, which reflect steady state equilibration before excitation by the pump laser. The displacements between the dotted horizontal lines and the solid lines correspond to the expected time-dependent population changes. AD(t) and DD(t) are the populations obtained by the probe laser at time t after the pump, while AD(∞) and DD(∞) are the populations when the equilibrium is re-established. 325

8.11 (a) D_2-predissociation spectrum of the two $I^-\cdot(H_2O)\cdot(D_2O)\cdot D_2$ isotopomers. The features associated with the AD_{2H} isotopomer are colored blue and those associated with DD_{2H} are colored red. (b) and (d) are MS^3IR^2 dip spectra obtained by probing on the bare $I^-\cdot(H_2O)\cdot(D_2O)$ ion at the positions indicated by the black arrows, while (c) and (e) are obtained by probing on the D_2 tagged $I^-\cdot(H_2O)\cdot(D_2O)$ ion at the positions indicated by the black arrows. The colored arrows indicate the H

migration that causes the extra dip features in the spectra and the gray arrow indicates that the expected feature was not resolved at the current signal to noise. The dashed drop lines indicate the depletions predicted by the first order unimolecular kinetics model in Fig 8.3. See text for numerical values used in the simulation. 326

8.12 (a) Schematic of the rocking pathway for H migration. (b) MS^3IR^2 dip spectra of $I^-\cdot(HDO)\cdot(D_2O)\cdot D_2$ obtained by probing on free OH position. The black arrow labels the probe laser position and the colored arrow indicates the H migration to yield absorption at the IHB_{AD} site. (c) D_2-predissociation spectrum of all four $I^-\cdot(HDO)\cdot(D_2O)\cdot D_2$ isotopomers. Features are color-coded by the H sites (see caption Fig. 8.1). 329

8.13 (a,b,c,d) Double resonance hole burning dip spectra of $I^-\cdot(HDO)(D_2O)\cdot D_2$ obtained by probing on four different OH positions. The tails of the arrows label the probe laser position and arrow heads indicate the H migrations. Arrows are color coded by the H sites and gray means the signal to noise was not enough to resolve the feature. (e) D_2-predissociation spectrum of all four isotopomers of $I^-\cdot(HDO)(D_2O)\cdot D_2$. (f,g) Schematics of the possible pathway for H migration. (h) Minimum energy (MP2/aug-cc-pVTZ-PP, ref. 2) structure of $I^-\cdot(HDO)(D_2O)$. 330

8.14 On the left is the heat capacity of $I^-\cdot(H_2O)_2$ (blue) and $I^-\cdot(H_2O)_2\cdot D_2$ (black) calculated from harmonic frequencies obtained with the MP2/aug-cc-pVTZ-PP level of theory and basis function (ref. 2). The addition of the weakly bonded D_2 molecule increase the low energy degrees of freedom hence increase the heat capacity significantly. On the right is the internal energy obtained by integrating the heat capacity over temperature. Th green dash indicates the calculated barrier and corresponding Boltzmann temperatures of the flip motion. The calculation using harmonic oscillator partition function will underestimate the heat capacity but it provides a qualitative sense of the effect of D_2 tag molecule on the internal energy of the system. 332

9.1 Comparison of the isotope-diluted SFG spectrum of the air-water interface with vibrational predissociation spectra of $D_3O^+\cdot(HDO)(D_2O)_{19}$ at temperatures in the range 10-200 K. (a) Representative low-energy structure of the $H_3O^+\cdot(H_2O)_{20}$ cluster. The stick spectra of the clusters with the OH group in each of the possible sites of the cluster are included in Supplementary Fig. 9.14. (b) SFG spectrum of HDO at the water-air interface (*4*) reproduced with permission. (c-g) Vibrational spectra of $D_3O^+\cdot(HDO)(D_2O)_{19}$ from 200 to 10 K. OH^b and OH^{free} represent

hydrogen bonded OH and free OH. The A/D notation labels the number of hydrogen bond acceptors and donors on one water molecule. (h) displays the calculated spectrum based on 400 isotopomers of the 10 lowest energy structural isomers of the $D_3O^+ \cdot (HDO)(D_2O)_{19}$ cluster. The contribution from each type of water molecule (or site) is displayed as a color-coded trace. 344

9.2 MS^4IR^3 Instrument for the temperature controlled variable delay time hole burning experiment. The second ion guide is capable of storing ions and ejecting them as an ion packet into the Paul trap in which the secular frequency mass selection (MS^1) is performed. The bleach laser (IR^1) is introduced into the ion trap after ion cooling and mass selection. The bleached ion ensemble is stored for a variable delay time, then mass selected again with a TOF mass selection (MS^2). In the TOF region there are two additional stages of mass selection with two reflectrons (MS^3 and MS^4). In between $MS^{2,3 \text{ and } 4}$ there are two IR lasers that can serve as the probe laser (IR^2 and IR^3). In this study, we use the in-trap laser and the third laser as the bleach and probe laser, respectively. 347

9.3 Time sequence for the in-trap mass selection and variable delay two laser experiment. (a) The experiment starts with pulsed buffer gas and ion injection. After the ions are introduced and cooled in the Paul trap, an amplitude-modulated frequency sweep in the ion secular frequency range is introduced to select the desired mass. The frequency sweep (d) starts from low frequency that corresponds to the higher masses (b) and sweeps to high frequency (c) that removes the lower masses. The output waveform is modulated to zero when the frequency matches the desired mass to allow the target species to remain in the trap. After mass selection, the bleach laser is introduced to the trap at variable delay time. Finally, the ions are extracted from the ion trap for TOF mass analysis and probe laser detection. 348

9.4 Time dependent population behavior of a two isotopomer system at two different temperatures**.** (a-c) At low temperature, bleaching isotopomer B does not influence the population in A whereas bleaching A results in depletion of A's population at the frequency corresponding to A. (d-f) At higher temperatures where interconversion between the two isotopomers can happen, bleaching B will result in a decrease in A's population over time to refill the hole burned in B. Bleaching A will result in a large initial depletion in A, which is then refilled by B. This behavior manifests in the hole-burning spectra of A as two dips at both A's and B's positions. 351

9.5 Comparison between the ensemble behavior and the individual cluster ion's behavior at elevated temperature where interconversion between two isotopomers is possible. (a) The overall behavior of the ensemble including population in A and B isotopomers with an equilibrium constant of 2, which results in an equilibrium population ratio of 1:2 for A:B. (b) Behavior of individual clusters where interconversion between A and B can happen. The identity of the cluster is traced over time. Interconversion is depicted as a sudden jump from dotted line labeled A to B or vice versa. At t=15 ms, a bleach laser pulse is introduced at a frequency corresponding to absorption in isotopomer A, which destroys all instantaneous population in isotopomer A. At t=55 ms, the probe laser can be introduced to count the population in A or B isotopomers. 353

9.6 Thermal and photo induced evaporation kinetics of the $D_3O^+ \cdot (HDO)(D_2O)_{19}$ clusters. (a) Thermal evaporation kinetics at 200 K measured in the Paul trap held at 200 K. The evaporation time is about 16.7ms. The exponential behavior indicates a canonical condition in the ion trap. (b) Photoinduced evaporation kinetics at 120 K with a vibrational excitation at 3,686 cm^{-1} measured in the Paul trap held at 120 K. The evaporation time is about 450 ms without laser excitation and 9.7 ms with the laser excitation. The vibrational excitation heats the cluster to about 200 K considering the harmonic heat capacity (Figure 9.5). The experimentally measured rates agree with the theoretically calculated rate constants (c) at 200 K [14]. Panel (c) is reproduced with permission. 354

9.7 Structure of all 10 low energy isomers of the $H_3O^+ \cdot (H_2O)_{20}$ species. These geometries are optimized at the DF-MP2/aug-cc-pVTZ level. The relative energies are included in Table 9.1. 356

9.8 Comparison between the vibrational spectra of $H_3O^+ \cdot (H_2O)_{20}$ and $D_3O^+ \cdot (HDO)(D_2O)_{19}$. Single laser vibrational predissociation spectra of the all-H isotopologue (a) and the $D_3O^+ \cdot (HDO)(D_2O)_{19}$ isotopologue (b) obtained with the D_2 messenger tagging technique at 13.5 K. The single laser spectrum in (b) contains contributions from various isotopomers that are isolated with the isotopomer-specific double resonance hole burning technique and displayed in (c-i) where the probe position is listed in (b) and color coded in the same scheme as other figures. The appearance of the lower energy feature in (e) was discussed previously in ref. 28 and attributed to combination band activity. 361

9.9 Comparison of OD and OH intensities of the $D_3O^+ \cdot (HDO)(D_2O)_{19}$ cluster. The red trace is a scaled up (by 20 times) version of the black trace in the

OH region. The low intensity in the OH region is caused by isotopic dilution. As a result, each individual cluster displays 42 OD features and only one OH feature. 362

9.10 Comparison between calculated and experimental vibrational spectra of all isotopomers of the $D_3O^+\cdot(HDO)(D_2O)_{19}$ isotopologue. (a) Calculated spectra including summed contributions (black trace) from all 400 isotopomers of the 10 low energy structural isomers shown in Figure 9.7 where scaled (0.96 scaling factor) harmonic frequencies are convolved with experimentally determined linewidths (28). Contributions from the various types of water molecules are displayed in color coded traces that corresponds to the scheme depicted in the representative structure. (b) Calculated stick spectra. (c) Experimental spectra at 10 K including contributions of all isotopomers present. 363

9.11 Structures and vibrational predissociation spectra of $D_3O^+\cdot(HDO)(D_2O)_{19}$ and $CH_3ND_3^+\cdot(HDO)(D_2O)_{19}$. Representative low energy structure of (a) $D_3O^+\cdot(HDO)(D_2O)_{19}$ and (b) $CH_3ND_3^+\cdot(HDO)(D_2O)_{19}$. Vibrational predissociation spectra of D_2 tagged (c) $D_3O^+\cdot(HDO)(D_2O)_{19}$ and (d) $CH_3ND_3^+\cdot(HDO)(D_2O)_{19}$. 366

9.12 Vibrational spectra of $CH_3ND_3^+\cdot(H_2O)(D_2O)_{19}$ and $CH_3ND_3^+\cdot(HDO)(D_2O)_{19}$. Vibrational spectra of D_2 tagged (a) $CH_3ND_3^+\cdot(HDO)(D_2O)_{19}$ and (c) $CH_3ND_3^+\cdot(H_2O)(D_2O)_{19}$. Double resonance spectra (d,e,g,i,k) and calculated spectra (c,f,h,j) of) $CH_3ND_3^+\cdot(H_2O)(D_2O)_{19}$ probing various positions indicated by the color coded arrow. Some has contribution from more than one type of water molecule (g has ADD and ADD', i has ADD' and AADD). 367

9.13 Overall assignment scheme of $CH_3NH_3^+\cdot(H_2O)_{20}$ and $H_3O^+\cdot(H_2O)_{20}$ cluster and their isotopologues containing one HDO or one H_2O molecules. Vibrational spectra of (a) $H_3O^+\cdot(H_2O)_{20,}$ (b) $D_3O^+\cdot(HDO)(D_2O)_{19,}$ (c) $CH_3ND_3^+\cdot(HDO)(D_2O)_{19,}$ (d) $CH_3ND_3^+\cdot(H_2O)(D_2O)_{19}$ and (e) $CH_3NH_3^+\cdot(H_2O)_{20}$ where vertical lines indicates how peaks of the same assignments (color coded) shifts from one species to another. The two structures are reproduced from figure 9.11. Comparison between calculated spectra (g,i,k) with contributions from each type of water molecules color coded and the experimental spectra (f,h,j) of $D_3O^+\cdot(HDO)(D_2O)_{19,}$ $CH_3ND_3^+\cdot(HDO)(D_2O)_{19,}$ and $CH_3ND_3^+\cdot(H_2O)(D_2O)_{19}$. 369

9.14 Scheme describing the onset of spectral diffusion by site exchange in a temperature controlled, cluster using selective photodissociation. The populations in the five spectroscopically distinct sites, color coded to match those identified in Fig. 9.1g and 9.1h, are indicated by the fractional filling of the circles. The panels correspond to three temperature regimes: (a) a low temperature, static ensemble in which the red isotopomer is removed at t=0, and subsequent interrogation of the ensemble after a delay time Δt reveals persistent removal of the red species from the ion packet, (b) an intermediate temperature where only two sites, red and brown, undergo interconversion on the timescale of the experiment. In this case, initial depletion of the red species, and hence its vibrational signature band, partially recovers after time Δt while the population of the brown isotopomer decreases to restore equilibrium with red, and (c) a sufficiently high temperature that all sites interconvert after initial depletion of red such that, after delay Δt, the red population is largely restored while those in the other four sites exhibit minor depletions upon returning to steady state. 370

9.15 Harmonic heat capacity curve and internal energy as a function of temperature of all isotopomers of $D_3O^+ \cdot (HDO)(D_2O)_{19}$. The heat capacity (a) and internal energy (b) are similar among all isotopomers. 374

9.16 Vibrational Internal energy distribution of $D_3O^+ \cdot (HDO)(D_2O)_{19}$. The internal energy distribution is obtained by random sampling of all he normal modes harmonically following Boltzmann distribution. The ZPE is subtracted such that the ground state energy is at 0. 375

9.17 Time dependence of the PD_{OH} IR spectrum following photodepletion of the isotopomer with the isotopically labeled OH group in the non-bonded (red) site (OH_{AAD}^{free}) at T = 120 K. Double resonance spectra were obtained at bleach-probe delay times of: (a) 0.04 ms, and (b) 50 ms. The purple trace in (b) closely reproduces the single laser spectrum of the entire isotopologue (all sites occupied) from Fig. 1e. The time evolutions of the OH_{AAD}^{free} population modulation by the bleach laser at two frequencies (OH_{AAD}^{b} and OH_{AAD}^{free} in (a)) are presented in (c) and (d), respectively. The time constants t_{diff} were extracted from exponential fits to the observed data. Negative delay times in (c) and (d) correspond to experiments with the bleach laser off. 376

9.18 Temperature dependent evolution of the photobleaching spectra corresponding to a bleach-probe delay of 50 ms and fixing the probe laser

to monitor population of the isotopomer with isotopically labeled OH group in the non-bonded (red) site (OH_{AAD}^{free}). (a) Vibrational spectrum of all isotopomers at 10 K and (b)-(f) hole burning spectra at 10-120 K. The red trace in (f) reproduces the single laser spectrum of the entire isotopologue (all sites occupied) from Fig. 1e. The vertical red arrow in (b) indicates the probe laser frequency, whereas the curved arrows in (d) and (e) indicate that the appearance of additional dips arise from OH migration from the OH_{AAD}^{free} site to various other sites when their populations are depleted by the bleach laser, (g) a representative low energy PD structure, (h) a possible pathway for OH migration at 100 K, and (i) schematic illustration of more complex pathways that likely operate at higher temperatures, where the ribbon arrows indicate the directions of OH group rotations. 379

9.19 The lowest energy pathways for rotation of each of the AAD molecules of $(H_2O)_{21}$. The relative energies are calculated with MBPol. The barrier heights are included in Table 9.2. 381

9.20 Schlegel diagrams for the lowest energy rotational pathway of water 3 of $(H_2O)_{21}$. The blue dots denote the water molecules with a free OH group, the arrows label the OH groups and the thinner lines represents hydrogen bonds. The water molecule labeled AAD in the reactant panel is the water molecule of interest that is involved in the rearrangement that exchange the free OH with its bound OH group. One of the original AAD water molecule's OH (black arrow) forms an additional hydrogen bond to the original AADD water molecule to form a four-membered ring involving a five coordinated AAADD water molecule. 382

9.21 Fractional depletion obtained at specific bleach-probe frequencies as a function of temperature. (a)Temperature dependent fractional depletion obtained at 50 ms delay time by probing the free OH position (3686 cm^{-1}) and bleaching the bound OH position of one of the AAD water molecule. This position has the lowest onset temperature for H-bond rearrangement and yield an apparent activation energy (E_0) of 2.9 kcal/mol (1000 cm^{-1}). (b, c) Temperature dependent fractional depletion obtained at 50 ms delay time by probing the free OH position (3686 cm^{-1}) and bleaching the bound OH position of one of the AADD water molecule (b) and bleaching the free OH position of all AAD water molecules (c). Both results yield apparent activation energy (E_0) about 4.7 kcal/mol (1670 cm^{-1}) which is consistent with the higher onset temperature (120 K) for all the other rearrangement pathways. 383

9.22 Temperature dependent evolution of the photobleaching spectra corresponding to a bleach-probe delay of 50 ms and fixing the probe laser to monitor population of the isotopomer of $Cs^+\cdot(HDO)(D_2O)_{19}$ with isotopically labeled OH group in the AAD (orange) site (OH_{ADD}^{free}). (a) Representative minimal energy structure of $Cs^+\cdot(H_2O)_{20.}$ (b) Vibrational spectrum of all isotopomers at 10 K and (c)-(e) hole burning spectra at 20-150 K. 387

LIST OF TABLES

3.1 Parameters for rotational structure simulation of the free-OH stretch band 81

3.2 Computed level structure with six-dimensional vibrationally averaged rotation constants of each normal-mode degree of freedom with qualitative assignments. The $\widetilde{\mathbf{A}}$ constants lie along the C_{2v} symmetry axis. The parenthesis after the quantum state labels denotes quantum numbers in the in-plane bend degree of freedom. Specifically, (+) and (-) denotes the ground-state tunneling partners, respectively. In addition, (1+) and (1-) denotes the first excited-state tunneling pair including the symmetric and antisymmetric states. 89

3.3 Computed transition frequencies (shifted by +36 cm^{-1}), comparison with experiment, and qualitative assignments for the simulated rovibrational water-iodide spectrum at 20 K. The assignments were made by projecting the calculated states onto the basis states listed in tables 3.4 and 3.5. The || notation represents a parallel transition with $\Delta K_a=0$. 101

3.4 Chosen symmetry-adapted configuration state functions and symmetry labels for the basis states used in the assignment of the anharmonic six-dimensional vibrational eigenstates. The functions are constructed from harmonic oscillator basis states with the order $|\nu_{IP}, \nu_{IO}, \nu_{OOP}, \nu_{HOH}, \nu_{SS}, \nu_{AS}\rangle_{Harm}$. 103

3.5 Corresponding SA-CSF's for the ion-hydrogen and free-OH basis states expressed as a linear combination of the symmetric and antisymmetric stretch SA-CSF's. 106

4.1 This table includes the experimentally observed frequencies in various isotopologues of the iodide water dimer and their assignments. For some isotopologues there are multiple isotopomers and the contribution is attributed in the isotopomer column in which case a range of frequency is reported to cover different frequencies for various isotopomers. Calculated frequencies were obtained from VPT2 calculations with the MP2/aug-cc-pVTZ-PP level of theory and basis function. 161

5.1 Experimental frequencies, redshifts from the gas phase free OH frequency (±4 cm^{-1}) and FWHM of OH features in $Cs^+ \cdot (HDO)(D_2O)_{19}$. Each row contains the features detected by fixing the probe laser on the experimental frequency except for peak 11* and 12*. Those two features where obtained when probing on peak xi and peak 12 and attributed to combination band activities, detailed explanation was included in figure

5.5. The assignments of the features are denoted such that AAD and Free refer to the bound OH and free OH on the AAD water molecules, respectively, whereas ADD refers to the bound OH groups on the ADD water molecules. Additionally, ADD combo. refers to the combination band in figure 5.2 (trace c12) and figure 5.8 (trace b12) and AAD* refers to the sharp band labeled with * in figure 5.2 (trace c15) and figure 5.8 (trace b15). The peak number corresponding to the peaks labeled in figure 5.2 (trace c1-c16) and figure 5.8 (trace b1-b16). 201

5.2 Experimental frequencies (±4 cm^{-1}) observed for $Cs^+(H_2O)_{20}$. Peak labels are defined in Table 5.1 and $2\nu_{HOH}$ denotes the HOH bend overtone feature. 202

6.1 Experimental frequencies (±4 cm^{-1}) of Cs^+(2H,38D), each column contains the features detected by fixing the probe laser on the probe position (colored red with frequency listed on top of the column). The text in the cells are the assignments of the features, where AAD, F and $2\nu_{HOH}$ refer to the bound OH, free OH, and bend overtones on the AAD water molecules, respectively whereas ADD refers to the bound OH groups on the ADD waters. *Denotes multiplet structure within main peak identified in Fig. 6.2. 240

6.2 Experimental frequencies (±4 cm^{-1}) observed for Cs^+(40H). Peak labels are defined in Fig. 6.2C. 241

6.3 Calculated frequencies of H_2O molecules in the **PD_0** structure in a 2-dimensional coupled (normal mode) and uncoupled (local mode) representation of the OH vibrations. The splittings ($\Delta\omega$) provide the frequency difference between the two OH stretch vibrations (between ω_L and ω_H or ω_1 and ω_2) on a single water molecule, when the vibrations are expressed in a normal or local mode representation, while coup. (λ_{12}) provides the intramolecular coupling between the two local mode stretches. The water molecules are classified into AAD and ADD types. All numbers are in wavenumbers (cm^{-1}). 241

8.1 Experimentally observed frequencies ($\pm 4\ cm^{-1}$) for the four OH sites in the $I^-\cdot(HDO)\cdot(D_2O)$ and $I^-\cdot(H_2O)\cdot(D_2O)$ cluster ions along with their vibrational zero point energies. Calculated frequencies were obtained from VPT2 calculations with the MP2/aug-cc-pVTZ-PP level of theory and basis function as reported in Ref. 1, which did not include the ZPE values. 320

9.1 Relative energies of the lowest energy isomers of $H_3O^+ \cdot (D_2O)_{20}$. Energies are calculated at the DF-MP2/aug-cc-pVQZ level of theory, using geometries optimized at the DF-MP2/aug-cc-pVTZ level. 357

9.2 Energies (kcal/mol) of transition states and intermediates for rotating the water molecules of $(H_2O)_{21}$ with a free OH group. Energies are referenced relative to the global minimum. 384

ACKNOWLEDGMENTS

The last six years at Yale have been an amazing experience for me. And I want to thank everyone around me for making this journey fun and exciting. First, I want to thank Mark Johnson who has been a great mentor. On the scientific front Mark was there to provide guidance and great ideas whenever needed and also left me great amount of freedom when I want to explore new approaches. I'm always amazed by Mark's vast collection of knowledge and fun stories that puts some personal touch behind the discoveries and the real people behind them. Also, Mark is also a great story teller and everyone in the group comes out with a great deal of that influence. Mark also gave us exposure to the inner mechanics of academia from how to navigate the scientific community to how to run a great research group. Thanks, Mark, for taking care of so many things so we can enjoy the worry-free research experience!

To Gary Weddle, thank you for taking us out on the sailing trips every summer and brining spicy jokes to the ski trips in the winter. Your great knowledge for all things radio frequency was super helpful and my favorite story was the talking tree in your back yard!

To Anne McCoy, thanks for being the best collaborator over countless projects! You feel more like part of the same group than a collaborator at this point. You know the instrumentation and experiment so well that you could suggest new schemes to try at times in addition to the great theoretical insights. You are always enthusiastic about our work and caring for young folk's career development. Thanks for all the help and also for making our community a welcoming one!

I still remember the first one I talked to in the Johnson lab was Stephanie Craig. It was the visiting day and I asked Steph ‘So, do you guys modify instruments a lot?’ and Steph told me ‘Yeah! We take things apart and machine new parts for modifications all the time!’ and that pretty much made up my mind for joining the group. Your passion for instrumentation and great mechanical skill were very impressive and thanks for teaching me all about the cryogenic parts of our instruments. Also, thanks for introducing all the students from other research groups at my first GRC to us ‘young kids’ in the group, it made the conference experience a lot foreign for a first timer!

To Olga Gorlova, Olga you are my first desk mate in the group when I was still rotating. Thanks for navigating me through all things I needed to know as a new graduate student joining the group and all the tips to success! Pointing me to the water related projects turned out to be the best advice I can ask for, I stepped into a real fun five years thanks to you! Also, I always had something special for Russian culture and you were the only one I can share the laugh when it comes to funny Russian TV shows.

To Conrad Wolke, thanks for brining me on to the iodide water train. I remember you trying to teach me how to run a double resonance experiment on Tinman in one day and explaining what that experiment means in terms of studying spectral diffusion. It was the day before spring break and you were heading to Germany afterwards and you were machinegunning out bits and tips about the machine that I tried to cram all into my poor memory. The dream experiment of spectral diffusion turned out to be the most important goal that I worked towards throughout my graduate school time and has led to many great results. Thanks for all the guidance and great project you handed me and also thanks for the very insightful advice when I asked you ‘How did you get so good at tuning the

machine?', 'Just spend a lot of time on it! I spend many hours a day tweaking and come tweak on it on the weekend when I'm bored.'

To Fabian Menges, I have learned so much from you about the instruments as well as computations. You were the default to turn to for help when me and Chinh runs into a snug. I'm always amazed by how you know how to run pretty much everything in the lab from orbitrap to ICR, from electronics to laser. Getting ions out of an commercial instrument without breaking anything was just a awesome achievement. It has been fun working together! I've always been a big fun of German engineering! Thanks for all the great knowledge scientific wise and also the fresh international view you always bring around! It's been fun laughing together about how ridiculous this place can get at times.

To Joseph DePalma, you were in charge of the test bed instrument at the back of SCL8 when I joined the group and that became a great opportunity for me to learn all about our instrument by taking it apart. Thanks for patiently teaching me all the details about the mini-machine, I learned a lot of details of vacuum flanges, pumps, gauges and power supplies from you. And thanks for passing down the machine to me and Chinh which will later on become our work horse for two laser experiments.

To Patrick Kelleher, you are probably the most calm and peaceful person I know who can always keep your cool regardless of what is happening. I learned so much about lasers from you and thank you for keeping the lasers on our machine in top shape! I missed the fun chats in office as well as skiing together on the group ski trip. Also I missed the after hour CS games a lot!

To Chinh Duong, needless to say, we spend pretty much all our time together in and outside of lab. It wouldn't have been possible without you to make the great machine

we have. I remember countless times we look at the clock and decides to modify something at 6 PM and of course there is a leak or something doesn't fit and then it's midnight. And also, the long hauls we pulled of many times taking spectra of several ions per shot. And it isn't just work, we probably watched every new movie coming out on the half price Thursdays at North Haven or the CT post. We also tried out so many different restaurants as dinner break during our 6 PM projects. We also rode the up and down and down and downs on the crypto moon shot (the down part is mainly for me). You are a great scientist and a great friend that's always there to turn to. I can't imagine making it this far without doing it together. I hope you make it and fund your own private research lab soon!!

To Joanna Denton, your attention to detail and patience for getting to the bottom of a problem is inspiring. You always brought some new perspective to the table and expanded my horizon. You've always been very friendly and kind and it wouldn't have been as fun without you!

To Helen Zeng, it has been a great deal of fun hanging out in the office after dark between us 'three nuts'. You brought so much fun to lab as well as the extended hours. Your ability to manage so many collaborations and to bring people together is always inspires me. You always come to the rescue at occasions like department social hours, especially when I stand in the far corner trying to figure out who is who. On the scientific front your great work of all the ionic liquid systems ever was always fun and your skills to tailor molecular interactions is like no others. Thanks for all the help during the past six years!

To Evan Perez, your great knowledge of organic and inorganic chemistry has been a great addition to the group. Your passion for chemical reactions and pushing our tool sets to do interesting reactions has always brought new and exciting perspectives. You are always open to try new stuff scientific wise and culture wise. I'll never forget the many Saturday dim-sums and dinners at Lao's. Thanks for all the fun!

To Anton Lachowicz, you are the only one that I know that drive as crazy as I do and ski faster than I do! It has been so much fun exploring the glades and clocking speed records on the slope. I'm so lucky to have you around. I always admire your mechanical skills and perseverance for putting together the now Enterprise machine in the magnet lab, bringing a new machine with new design is no easy task yet you managed it. I'll never forget the great time, and also our tight competition over whose desk is more chaotic.

To Sayoni Mitra, you have advanced so far so quickly coming from a theoretical background. Now you've mastered the machine as well as the lasers, no one can stop you anymore. The instrument we built are in good hands and soon enough you'll catch those shuttling protons! It has been a great deal of fun in and outside lab to have you around. You always had fun and spicy stories to share and can laugh at my terrible jokes. We are the chaotic evils in the group after all. You are always around when I'm about to burn my computer over Linux script problems. Thanks for cheering me up all the time and helping me!

To Thien Khuu, it's reassuring to see someone bright and driven to be interested in the water project. You've been a very fast learner and mastered the instrument in

weeks. And you also managed to learn how to do MD simulations which has been out of our group's reach for the longest time. It has been great fun to work with you!

To Santino Stropoli, you have picked up the new trap to trap instrument so quickly. It's great to see a new generation of cluster magician rising and keeping on exploring the fun world of all things aqueous at molecular level. It was a pleasure to be able to overlap with you.

To Sean Edington, we have pulled off the dream experiment together. It is so nice to have someone that are on the exact same frequency. And you have been that person for me, we would always arrive at the same idea or conclusion at the same time. It is frictionless communication most of the time which will probably work with key words only. I always looked up to your great wealth of knowledge as well as self-discipline. Also, you are a lot of fun to be around and I'll miss you a lot when I leave the group.

I'd also like to thank my committee members and all who I've had the privilege of learning from in grad school. Thank you, Charlie Schmuttenmaer, Patrick Vaccaro and Ziad for taking the time to chat with me about my research and my progress. I'd also like to thank Rosario Bernardo and Vincent Bernardo for making all the parts for the instrument I built in the fastest time possible with the greatest precision, also for teaching me about all the details about materials selection and machining techniques to keep in mind when designing a part to be manufactured. I always loved going down to the shop to see you and chat. Thank you also to Dave Johnson, Ed Ginter, for all the help and knowledge you gave me.

I also want to thank James Farrar, my undergraduate research advisor who introduced me to the world of quantum mechanics and experimental physical chemistry. I

wouldn’t have been here without you and also, I quite literally would not have been here if you haven’t suggested me to put Yale on my application list.

Finally, I give the most enormous of thanks to my family. Thanks for all the support and freedom you’ve given me. You made me who I am today!

"I'm a scientist; because I invent, transform, create, and destroy for a living, and when I don't like something about the world, I change it."
Pickle Rick, Rick and Morty. 2017

CHAPTER 1

Introduction

Water mediates and participates in many important reactions: from water oxidation in photosynthesis where it is the reactant, to aqueous proton transfer reactions where water acts as a medium to carry the mobile proton from one protonation site to the other.[1-4] Understanding neat water itself as well as hydration is important for understanding reactions in aqueous environments. In addition, the interfacial water also displays properties that deviate from the bulk behavior which becomes particularly important for atmospheric chemistry surrounding droplets as well as electrochemistry at the electrode surface.[5-10] A great variety of experimental techniques had been utilized to study all forms of water including gas phase water, water clusters, liquid water, ice and aqueous interfaces. For example, rotational, vibrational and electronic spectroscopy, ultrafast spectroscopy, interface specific spectroscopy (sum frequency generation (SFG) and second harmonic generation (SHG)), neutron scattering, X-ray diffraction, atomic force microscopy, mass spectrometry, nuclear magnetic resonance spectroscopy and so on.[11-37] In the meantime, lots of theoretical efforts are also being made with ab initio calculations for minimum energy structure, obtaining accurate potential energy surfaces, and force fields which forms the basis for larger scale molecular dynamic simulations, as well as spectroscopic predictions.[38-53]

Among the experimental techniques mentioned above, vibrational spectroscopy has been widely utilized in many forms to investigate water thanks to its ability to provide detailed structural and dynamical insights. For liquid water, the early studies use linear spectroscopy techniques such as infrared absorption spectroscopy as well as Raman spectroscopy.[9, 38, 54-55] However, these techniques are limited to probing only the averaged response in bulk since it probes a large number of molecules over a period of time much

longer than the timescale for molecular motions. The introduction of non-linear spectroscopic technique opened the possibility to probe ultrafast dynamics (time resolved infrared spectroscopy with pump-probe method), anharmonicities and vibrational mode couplings (two-dimensional infrared spectroscopy, 2DIR), as well as surface specific features with molecular orientation information (SFG and SHG).[29, 56-62] More recently, the development of two-dimensional heterodyne-detected sum frequency generation spectroscopy (2D-HD-SFG) allows for direct observation of ultrafast dynamics, anharmonicity and coupling specific to interfaces.[19, 63-65] Great progress were made in observing the spectral dynamics of water. It was discovered that the spectral diffusion in water has several different processes. Each of those processes has their own characteristic time constants including faster processes attributed to vibrational relaxation, energy transfer or delocalization, as well as liberation reorientation, and a slower process that is attributed to H-bond reorientation through a jump mechanism proposed through molecular dynamic studies.[13, 29, 53, 56-57, 66-80] Similarly, at the air-water interface, the spectral diffusion has different timescales.[27, 61, 63-65, 81-85] In addition, there is a controversy over whether the reorientation dynamics is slower for some frequencies and what those OH frequencies correspond to in terms of hydrogen bond environments.[63, 84] Due to the broad nature of hydrogen bonded OH vibrational features and the large sample size of these condense phase techniques, causing many overlapping features in the experimental spectra, it is challenging to gain a detailed molecular level understanding of these aqueous systems by comparing these spectra to the theoretical predictions from molecular dynamics (MD) simulations. Furthermore, for the interfacial water experiments, the bleaching of the ground state negative signal and excited state absorption of positive signal are effectively

indistinguishable. This signal cancelation between opposite phases in the imaginary second order susceptibility in SFG spectra makes the correlation of the observed OH frequency to a specific hydrogen bond environment and subsequent interpretation of the 2D spectra even more challenging.[64, 86]

Among the currently active experimental techniques, gas phase vibrational spectroscopy offers highly accurate structural details about isolated water molecule or clusters on the molecular level and serves as the most rigorous benchmark for calibrating computational methods. The early spectroscopic studies of neutral and ionic water cluster provided more thorough structural information for smaller water clusters. However, as the cluster size increases, the broad overlapping bands cause spectral congestion and the spectra become less informative.[11, 22-23, 87-94] The continuous advances in spectroscopic techniques over the past decades has pushed the limit of spectral resolution and interpretability. The introduction of messenger tag predissociation in place of IRMPD technique allows for a more reliable detection of low energy vibrational transitions without the drawback of IRMPD transparency and while also narrows down spectral line width.[95-96] The introduction of ESI ion source together with ion trap cooling in place of jet expansion cooling yields a greater variety of ions that can be studied as well as controllable and consistent low temperatures.[97-99] In terms of neutral water cluster, chirp pulse rotational spectroscopy with natural abundance isotope analysis provided unprecedented structural precision for smaller clusters while the newly introduced IR-EUV detection scheme allows for size selective and tag-free detection of neutral cluster IR spectrum.[24, 100-108]

The Johnson lab has a long history investigating water cluster's vibrational spectra. Early studies with supersonic jet expansion and messenger tag technique provided

structural insight into many cluster systems. The introduction of ion trapping technique later made isotopic tracing studies more accessible[109-110] and expanded the scope of these studies,[11, 87, 89, 109, 111-115] reaching beyond static structural information into temperature dependent study of dynamical systems.[116]

This thesis introduces a new instrument configuration, which significantly improved the signal to noise ratio and ease of use on multiple resonance experiments (Discussed in detail in Chapter 2). This new instrument opened up various new possibilities which were previously prohibitively time consuming. With the new instrument we first revisited a long-standing problem regarding one of the earliest studied system in ion-water complex, namely the iodide water complex first studied by Okumura in 1996.[117] We deployed various two laser techniques to dissect the complicated band pattern arising from combination bands, Fermi resonances, tunneling splitting as well as rovibrational structures. One exciting development is probing the spectra of the vibrationally excited ions. Such experiment gives us extra information regarding the identity of the transition being studied since each excited state have a distinct set of allowed transition further up the state ladder allowing for identification of nearly degenerate states/transitions. The results served as a rigorous benchmark for newly developed high accuracy theoretical model. It was found that the experimentally measured vibrational transition energy is sensitive to the electronic potential energy surface along the tunneling coordinate down to ten wavenumbers. These results are discussed in Chapter 3.

After the study of monohydrate systems, we showcased more techniques on the iodide dihydrate system in Chapter 4. This system was studied before by the Johnson group. It was determined that both water molecules each form one hydrogen bond with the iodide

ion, while one of the water molecules forms an additional hydrogen bond to the other water molecule.[118] Such configuration results in four unique OH transitions that couple to each other through intra and intermolecular couplings. By employing isotope substitution technique, we were able to isolate the spectral feature of single OH oscillator by embedding HDO molecule in a D_2O cluster. Such operation results in mass degenerate isotopomers which have the OH group occupying different sites. By employing IR-IR hole burning technique, the spectrum of each individual OH position (isotopomer) is obtained. This allows us to remove all inter and intramolecular couplings between OH oscillators and study only the spectral response as a result of the hydrogen bonding environment. We then embed a H_2O molecule in a D_2O cluster to isolate the spectra of single water molecules, which contain information about the intramolecular couplings as well as Fermi resonance. By comparing the single H_2O spectrum with the all-H_2O spectrum, we recovered the intermolecular couplings between water molecules.

To explore OH features in more varieties of hydrogen bonding environments and extended H-bond networks, we turn to larger clusters. First, we explored the protonated water 21 'magic' number cluster, where we imbedded an HDO molecule in a fully deuterated scaffold. With the same IR-IR hole burning technique mentioned above, we were able to isolate the OH stretching feature of an isolated OH oscillator in various H-bond environments across the entire typical spectral range for liquid water OH stretching envelope. For the most part, the OH oscillator displays a single peak which has been the common approach for modeling liquid water spectrum. However, for one of the positions, the OH group produces a combination band which yields two peaks. In addition, the peak width of the OH feature almost linearly increases with respect to the redshift from the free

OH frequency. We attributed this trend to the life time broadening of the hydrogen bonded OH group having shorter lifetime as it is strongly bound to the neighboring water molecule. These results are discussed in detail in Chapter 5.

In Chapter 6 and 7, we utilized a variety of charge carrier ions for the water clusters under investigation to produce an even greater variety of H-bond network topologies. That allowed us to study all the H-bonding types present at the air-water interface and in bulk water, namely A (acceptor), AD (acceptor-donor), ADD, AAD, AADD water molecules. They each have their characteristic range of frequencies. We again employ trace isotope technique where we exchange one of the D_2O molecules in a perdeuterated cluster with an H_2O molecule. The H_2O remains intact as long as there is no excess proton or hydroxide ion present in the cluster. We can then obtain the correlated absorption of the two OH groups on the same water molecule as well as the Fermi resonance feature with the bend overtone. We observed that as the bound OH frequency approaches the bend overtone frequency, the intensity borrowing strengthens to yield a 50-50 intensity pattern. As they depart from each other, the intensity of the bend overtone feature weakens until it eventually become unobservable when they are more than 200 cm^{-1} apart. We also use the diverse collection of H-bond environments to refine an index where the H-bond in the first and second hydration shell of an OH group is counted and used to map to an OH frequency that reflects this specific H-bond arrangement. This index reflects the cooperativity in hydrogen bonding which can be explained with a charge transfer picture.

With the detailed understanding of the spectroscopic characteristics of water molecules in extended H-bond networks, we then move forward to explore the dynamic nature of water via spectral diffusion. In the proof-of-concept experiment discussed in

Chapter 8, we carried out the experiment on a smaller system first. It has been illustrated before that we can embed an HDO molecule in a D_2O cluster, which results in various isotopomers with distinctive spectral features in the OH region. By monitoring one specific OH feature after it is photobleached with a fixed time delay, we can observe spectral diffusion in the form of "hole-filling" if the OH frequency can change in the same time interval. Such change reflects the H-bond network rearrangement or, in other words, water molecule reorientation processes. In the isotopically labeled iodide dihydrate system, we were able to observe the water molecule rotating around a hydrogen bond. This motion involves the rearrangement of the free OH group to become a bound OH group on the time scale of tens of microseconds at low temperature (~10 K). These motions are very fast and rare, which leaves the OH stretch spectral features intact from exchange broadening or extra spectral feature arising from long-lived intermediates. As a result, the OH frequency changes from one frequency to another in a 'blinking' fashion, and the ensemble averaged behavior displays first order kinetics.

In Chapter 9, building on top of the successful demonstration of spectral diffusion experiment in Chapter 8, we developed a new instrument that is capable of varying the time delay between the photobleaching laser and the probe laser from tens of microseconds to hundreds of milliseconds, which allows time dependent and temperature dependent kinetics measurements. We use such technique on a well-characterized larger water cluster from Chapter 5, namely the protonated water 21 cluster, which provides significant structural diversity for various pathways of water reorientation to happen. We embed a single HDO molecule inside a perdeuterated water cluster, which then results in 43 different isotopomers. Each isotopomer represents a unique site that is occupied by the OH

group while all other sites are occupied by OD groups. Some of the sites are very similar in terms of their H-bond environment, which results in spectral degeneracy and yielding a 6 bands pattern with each band representing a unique type of hydrogen bond environment. The experiment is carried out by first loading the clusters into a temperature controlled cryogenic ion trap where the ion temperature reaches equilibrium with the trap temperature by collision cooling from the buffer gas. The clusters are then mass selected by secular frequency excitation which ejects ions that are in resonance with the excitation waveform. The only cluster ions left in the ion trap are the ones with a specific mass. A laser pulse is then introduced to bleach out a specific set of isotopomers with the same OH frequency (representing similar H-bond environments) and after a certain time delay the ions are introduced to a time-of-flight mass spectrometer where a probe laser is used to read out the ion population of a chosen OH frequency. If the depletion in population caused by the first laser remains the same over time, there is no observable spectral diffusion on the experimental time scale, which is the case for clusters below 100 K. However, at 100 K, one specific pathway activates and we observed that the free OH group can rotate to exchange with its partner bound OH on the same water molecule and vice versa. Such process has a time constant of about tens of milliseconds. And at 110 K, many other H-bond rearrangement pathways activates. This suggests that the water reorientation pathways have different activation energies and the water molecule at the surface starts moving first. This dynamics is, in a way, similar to the surface melting phenomena where the surface layer melts at lower temperature compared to the core or bulk.

This thesis explores various aspects of the mechanics behind the broad OH stretching envelope of water on a molecular level from the static structural origin to the

dynamical nature. Smaller model systems were first studied to demonstrate the experimental concept and gain understanding of the simpler systems. Larger systems were then used to explore the full complexity caused by the diversity in the hydrogen bond environments as a result of extended networks. The low temperature static spectra were first studied to provide detailed correlation between the OH frequency and the hydrogen bond environment as well as mechanisms that further complicate the spectra such as intra and intermolecular couplings, lifetime broadening, combination band activity and Fermi resonance between the OH fundamental and the bend overtone transition. These systems were then studied at a higher temperature with a time dependent approach where the water reorientation kinetics is measured through spectral diffusion.

References:

1. Costentin, C.; Louault, C.; Robert, M.; Saveant, J.-M. Evidence for Concerted Proton-Electron Transfer in the Electrochemical Oxidation of Phenols with Water as Proton Acceptor. Tri-tert-butylphenol. *J. Am. Chem. Soc.* **2008,** *130*, 15817-15819.

2. Brudvig, G. W.; McEvoy, J. P.; Gascon, J. A.; Batista, V. S. The mechanism of photosynthetic water splitting. *Photochem. Photobiol. Sci.* **2005,** *4* (12), 940-949.

3. Day, T. J. F.; Schmitt, U. W.; Voth, G. A. The mechanism of hydrated proton transport in water. *J. Am. Chem. Soc.* **2000,** *122* (48), 12027-12028.

4. Siwick, B. J.; Bakker, H. J. On the role of water in intermolecular proton-transfer reactions. *J Am Chem Soc* **2007,** *129* (44), 13412-13420.

5. Dewan, S.; Carnevale, V.; Bankura, A.; Eftekhari-Bafrooei, A.; Fiorin, G.; Klein, M. L.; Borguet, E. Structure of Water at Charged Interfaces: A Molecular Dynamics Study. *Langmuir* **2014,** *30* (27), 8056-8065.

6. Abbatt, J. P. D. Interaction of HNO3 with water-ice surfaces at temperatures of the free troposphere. *Geophys Res Lett* **1997,** *24* (12), 1479-1482.

7. Bertram, T. H.; Thornton, J. A. Toward a General Parameterization of N_2O_5 Reactivity on Aqueous Particles: The Competing Effects of Particle Liquid Water, Nitrate and Chloride. *Atmos Chem Phys* **2009,** *9* (21), 8351-8363.

8. Enami, S.; Hoffmann, M. R.; Colussi, A. J. Proton Availability at the Air/Water Interface. *J Phys Chem Lett* **2010,** *1* (10), 1599-1604.

9. Falk, M.; Ford, T. A. Infrared Spectrum and Structure of Liquid Water. *Can J Chemistry* **1966,** *44* (14), 1699-&.

10. Hirshberg, B.; Molina, E. A. R.; Gotz, A. W.; Hammerich, A. D.; Nathanson, G. M.; Bertram, T. H.; Johnson, M. A.; Gerber, R. B. N_2O_5 at Water Surfaces: Binding Forces, Charge Separation, Energy Accommodation and Atmospheric Implications. *Physical chemistry chemical physics : PCCP* **2018,** *20* (26), 17961-17976.

11. Ayotte, P.; Weddle, G. H.; Kim, J.; Johnson, M. A. Mass-Selected "Matrix Isolation" Infrared Spectroscopy of the $I^-\cdot(H_2O)_2$ Complex: Making and Breaking the Inter-Water Hydrogen-Bond. *Chem. Phys.* **1998,** *239*, 485-491.

12. Bakker, H. J.; Kropman, M. F.; Omta, A. W. Effect of ions on the structure and dynamics of liquid water. *J. Phys-Condens. Mat.* **2005,** *17* (45), S3215-S3224.

13. Bakker, H. J.; Rezus, Y. L. A.; Timmer, R. L. A. Molecular Reorientation of Liquid Water Studied with Femtosecond Midinfrared Spectroscopy. *J. Phys. Chem. A* **2008,** *112* (46), 11523-11534.

14. Bakker, H. J.; Skinner, J. L. Vibrational spectroscopy as a probe of structure and dynamics in liquid water. *Chem. Rev.* **2010,** *110* (3), 1498-1517.

15. Baldelli, S.; Schnitzer, C.; Shultz, M. J.; Campbell, D. J. Sum frequency generation investigation of water at the surface of H2O/H2SO4 binary systems. *J. Phys. Chem. B* **1997,** *101* (49), 10435-10441.

16. Barnett, R. N.; Landman, U. Structure and Energetics of Ionized Water Clusters: (H2O)n+, n = 2-5. *J. Phys. Chem. A* **1997,** *101*, 164-169.

17. Benedict, W. S.; Gailar, N.; Plyler, E. K. Rotation-Vibration Spectra of Deuterated Water Vapor. *J. Chem. Phys.* **1956,** *24*, 1139-1165.

18. Blanton, W. B.; Gordon-Wylie, S. W.; Jordan, K. D.; Wood, J. T.; Clark, G.; Collins, T. J. A cube of water: sythesis and X-ray structure of an $(H_2O)_8$ clathrate complex. *J. Am. Chem. Soc.*, In press.

19. Bonn, M.; Nagata, Y.; Backus, E. H. G. Molecular Structure and Dynamics of Water at the Water-Air Interface Studied with Surface-Specific Vibrational Spectroscopy. *Angewandte Chemie-International Edition* **2015,** *54* (19), 5560-5576.

20. Boulon, J.; Braud, I.; Zamith, S.; Labastie, P.; L'Hermite, J. M. Experimental Nanocalorimetry of Protonated and Deprotonated Water Clusters. *J. Chem Phys.* **2014,** *140* (16), 164305.

21. Bowman, J.; Wang, Y. M.; Liu, H. Ab initio potential and dipole moment surfaces for water and applications from the water hexamer to models of ice. *Abstr Pap Am Chem S* **2013,** *246*.

22. Brudermann, J.; Buck, U.; Buch, V. Isomerization and melting-like transition of size-selected water nonamers. *J. Phys. Chem. A* **2002,** *106* (3), 453-457.

23. Buch, V.; Bauerecker, S.; Devlin, J. P.; Buck, U.; Kazimirski, J. K. Solid water clusters in the size range of tens-thousands of H_2O: a combined computational/spectroscopic outlook. *Int. Rev. Phys. Chem.* **2004,** *23* (3), 375-433.

24. Cole, W. T. S.; Farrell, J. D.; Sheikh, A. A.; Yonder, O.; Fellers, R. S.; Viant, M. R.; Wales, D. J.; Saykally, R. J. Terahertz VRT spectroscopy of the water hexamer-d_{12} prism: Dramatic enhancement of bifurcation tunneling upon librational excitation. *Journal of Chemical Physics* **2018,** *148* (9), 094301.

25. Cole, W. T. S.; Saykally, R. J. Hydrogen bond network rearrangement dynamics in water clusters: Effects of intermolecular vibrational excitation on tunneling rates. *Journal of Chemical Physics* **2017,** *147* (6), 064301.

26. Buch, V.; Tarbuck, T.; Richmond, G. L.; Groenzin, H.; Li, I.; Shultz, M. J. Sum frequency generation surface spectra of ice, water, and acid solution investigated by an exciton model. *J. Chem. Phys.* **2007,** *127* (20), 204710.

27. Cyran, J. D.; Backus, E. H. G.; Nagata, Y.; Bonn, M. Structure from Dynamics: Vibrational Dynamics of Interfacial Water as a Probe of Aqueous Heterogeneity. *Journal of Physical Chemistry B* **2018,** *122* (14), 3667-3679.

28. Cavalleri, M.; Ogasawara, H.; Pettersson, L. G. M.; Nilsson, A. The interpretation of X-ray absorption spectra of water and ice. *Chem. Phys. Lett.* **2002,** *364* (3-4), 363-370.

29. Fecko, C. J.; Eaves, J. D.; Loparo, J. J.; Tokmakoff, A.; Geissler, P. L. Ultrafast Hydrogen-Bond Dynamics in the Infrared Spectroscopy of Water. *Science* **2003,** *301* (5640), 1698-1702.

30. Felicissimo, V. C.; Guimaraes, F. F.; Gel'mukhanov, F.; Cesar, A.; Agren, H. The principles of infrared-x-ray pump-probe spectroscopy. Applications on proton transfer in core-ionized water dimers. *J. Chem. Phys.* **2005,** *122* (9).

31. Fishman, E.; Saumagne, P. Near-Infrared Spectrum of Liquid Water from 30 to 374º. *J. Phys. Chem.* **1965,** *69* (10), 3671.

32. Fox, J. J.; Martin, A. E. Investigations of infra-red spectra (2.5-7.5m). Absorption of water. *Proc. R. Soc. Lond. A* **1940,** *174*, 234-262.

33. Geissler, P. L. Water Interfaces, Solvation, and Spectroscopy. *Annu Rev Phys Chem* **2013,** *64*, 317-337.

34. Gruenloh, C. J.; Carney, J. R.; Arrington, C. A.; Zwier, T. S.; Fredericks, S. Y.; Jordan, K. D. Infrared Spectrum of a Molecular Ice Cube: The S_4 and D_{2d} Water Octamers in Benzene-$(Water)_8$. *Science* **1997,** *276*, 1678-1681.

35. Heine, N.; Fagiani, M. R.; Asmis, K. R. Disentangling the contribution of multiple isomers to the infrared spectrum of the protonated water heptamer. *J Phys Chem Lett* **2015,** *6* (12), 2298-2304.

36. Ludwig, R. Water: From Clusters to the Bulk. *Angew. Chem., Int. Ed.* **2001,** *40* (10), 1808-1827.

37. McDonald, D. C.; Wagner, J. P.; McCoy, A. B.; Duncan, M. A. Near-Infrared Spectroscopy and Anharmonic Theory for Protonated Water Clusters: Higher Elevations in the Hydrogen Bonding Landscape. *J Phys Chem Lett* **2018,** *9* (19), 5665-5671.

38. Auer, B. M.; Skinner, J. L. IR and Raman Spectra of Liquid Water: Theory and Interpretation. *J. Chem. Phys.* **2008,** *128* (22).

39. Ayala, R.; Martinez, J. M.; Pappalardo, R. R.; Marcos, E. S. On the halide hydration study: Development of first-principles halide ion-water interaction potential based on a polarizable model. *Journal of Chemical Physics* **2003,** *119* (18), 9538-9548.

40. Bajaj, P.; Gotz, A. W.; Paesani, F. Toward Chemical Accuracy in the Description of Ion-Water Interactions through Many-Body Representations. I. Halide-Water Dimer Potential Energy Surfaces. *Journal of Chemical Theory and Computation* **2016,** *12* (6), 2698-2705.

41. Bajaj, P.; Wang, X.-G.; CarringtonJr., T.; Paesani, F. Vibrational spectra of halide-water dimers: Insights on ion hydration from full-dimensional quantum calculations on many-body potential energy surfaces. *The Journal of Chemical Physics* **2018,** *148* (10), 102321.

42. Bankura, A.; Karmakar, A.; Carnevale, V.; Chandra, A.; Klein, M. L. Structure, Dynamics, and Spectral Diffusion of Water from First-Principles Molecular Dynamics. *J Phys Chem C* **2014,** *118* (50), 29401-29411.

43. Batista, E. R.; Xantheas, S. S.; Jonsson, H. Electric fields in ice and near water clusters. *J. Chem. Phys.* **2000,** *112*, 3285-3292.

44. Boero, M.; Terakura, K.; Ikeshoji, T.; Liew, C. C.; Parrinello, M. Car-Parrinello simulation of water at supercritical conditions. *Prog Theor Phys Supp* **2000,** (138), 259-261.

45. Bukowski, R.; Szalewicz, K.; Groenenboom, G.; Avoird, A. v. d. Interaction potential for water dimer from symmetry-adapted perturbation theory based on density functional description of monomers. *J. Chem. Phys.* **2006,** *125* (4), 044301.

46. Burke, L. A.; Jensen, J. O.; Jensen, J. L.; Krishnan, P. N. Theoretical study of water clusters. I. Pentamer. *Chem. Phys. Lett.* **1993,** *206*, 293-296.

47. Burnham, C. J.; Xantheas, S. S. Development of transferable interaction models for water. III. Reparametrization of an all-atom polarizable rigid model (TTM2-R) from first principles. *J. Chem. Phys.* **2002,** *116*, 1500-1510.

48. Calvo, F.; Douady, J.; Spiegelman, F. Accurate evaporation rates of pure and doped water clusters in vacuum: A statistico-dynamical approach. *Journal of Chemical Physics* **2010,** *132* (2).

49. Ceriotti, M.; Cuny, J.; Parrinello, M.; Manolopoulos, D. E. Nuclear quantum effects and hydrogen bond fluctuations in water. *Proc. Natl. Acad. Sci.* **2013,** *110* (39), 15591-15596.

50. Ceriotti, M.; Fang, W.; Kusalik, P. G.; McKenzie, R. H.; Michaelides, A.; Morales, M. A.; Markland, T. E. Nuclear Quantum Effects in Water and Aqueous Systems: Experiment, Theory, and Current Challenges. *Chem. Rev.* **2016,** *116* (13), 7529-7550.

51. Dang, L. X.; Chang, T.-M. Molecular dynamics study of water clusters, liquid, and liquid-vapor interface of water with many-body potentials. *J. Chem. Phys.* **1997,** *106*, 8149-8159.

52. Hermansson, K. Electric-field effects on the OH vibrational frequency and infrared absorption intensity for water. *J. Chem. Phys.* **1993,** *99*, 861-868.

53. Laage, D.; Stirnemann, G.; Sterpone, F.; Hynes, J. T. Water Jump Reorientation: From Theoretical Prediction to Experimental Observation. *Accounts Chem Res* **2012,** *45* (1), 53-62.

54. Walrafen, G. E. Raman spectral studies of the effects of temperature on water structure. *J. Chem. Phys.* **1967,** *47*, 114.

55. Medders, G. R.; Paesani, F. Infrared and Raman Spectroscopy of Liquid Water through "First-Principles" Many-Body Molecular Dynamics. *Journal of Chemical Theory and Computation* **2015,** *11* (3), 1145-1154.

56. Eaves, J. D.; Loparo, J. J.; Fecko, C. J.; Roberts, S. T.; Tokmakoff, A.; Geissler, P. L. Hydrogen bonds in liquid water are broken only fleetingly. *Proc. Natl. Acad. Sci. USA* **2005,** *102* (37), 13019.

57. Asbury, J. B.; Steinel, T.; Kwak, K.; Corcelli, S. A.; Lawrence, C. P.; Skinner, J. L.; Fayer, M. D. Dynamics of water probed with vibrational echo correlation spectroscopy. *J. Chem. Phys.* **2004,** *121* (24), 12431-12446.

58. Du, Q.; Superfine, R.; Freysz, E.; Shen, Y. R. Vibrational Spectroscopy of Water at the Vapor/Water Interface. *Phys. Rev. Lett.* **1993,** *70* (15), 2313-2316.

59. Yeremenko, S.; Pshenichnikov, M. S.; Wiersma, D. A. Hydrogen-bond dynamics in water explored by heterodyne-detected photon echo. *Chemical Physics Letters* **2003,** *369* (1-2), 107-113.

60. Stiopkin, I. V.; Weeraman, C.; Pieniazek, P. A.; Shalhout, F. Y.; Skinner, J. L.; Benderskii, A. V. Hydrogen Bonding at the Water Surface Revealed by Isotopic Dilution Spectroscopy. *Nature* **2011,** *474* (7350), 192-195.

61. Smits, M.; Ghosh, A.; Sterrer, M.; Muller, M.; Bonn, M. Ultrafast vibrational energy transfer between surface and bulk water at the air-water interface. *Phys. Rev. Lett.* **2007,** *98* (9).

62. Nihonyanagi, S.; Kusaka, R.; Inoue, K.; Adhikari, A.; Yamaguchi, S.; Tahara, T. Accurate determination of complex c(2) spectrum of the air/water interface. *Journal of Chemical Physics* **2015,** *143* (12).

63. Inoue, K.; Ishiyama, T.; Nihonyanagi, S.; Yamaguchi, S.; Morita, A.; Tahara, T. Efficient Spectral Diffusion at the Air/Water Interface Revealed by Femtosecond Time-Resolved Heterodyne-Detected Vibrational Sum Frequency Generation Spectroscopy. *Journal of Physical Chemistry Letters* **2016,** *7* (10), 1811-1815.

64. Inoue, K.; Nihonyanagi, S.; Singh, P. C.; Yamaguchi, S.; Tahara, T. 2D heterodyne-detected sum frequency generation study on the ultrafast vibrational dynamics of H_2O and HOD water at charged interfaces. *Journal of Chemical Physics* **2015,** *142* (21).

65. Hsieh, C. S.; Okuno, M.; Hunger, J.; Backus, E. H. G.; Nagata, Y.; Bonn, M. Aqueous Heterogeneity at the Air/Water Interface Revealed by 2D-HD-SFG Spectroscopy. *Angewandte Chemie-International Edition* **2014,** *53* (31), 8146-8149.

66. Fecko, C. J.; Loparo, J. J.; Roberts, S. T.; Tokmakoff, A. Local hydrogen bonding dynamics and collective reorganization in water: Ultrafast infrared spectroscopy of HOD/D_2O. *J. Chem. Phys.* **2005,** *122* (5).

67. Loparo, J. J.; Roberts, S. T.; Tokmakoff, A. Multidimensional Infrared Spectroscopy of Water. I. Vibrational Dynamics in Two-Dimensional IR Line Shapes. *J. Chem. Phys.* **2006,** *125* (19), 194521.

68. Loparo, J. J.; Roberts, S. T.; Tokmakoff, A. Multidimensional Infrared Spectroscopy of Water. II. Hydrogen Bond Switching Dynamics. *J. Chem. Phys.* **2006,** *125* (19), 194522.

69. Nicodemus, R. A.; Corcelli, S. A.; Skinner, J. L.; Tokmakoff, A. Collective Hydrogen Bond Reorganization in Water Studied with Temperature-Dependent Ultrafast Infrared Spectroscopy. *J. Phys. Chem. B* **2011,** *115* (18), 5604-5616.

70. Schmidt, J. R.; Roberts, S. T.; Loparo, J. J.; Tokmakoff, A.; Fayer, M. D.; Skinner, J. L. Are water simulation models consistent with steady-state and ultrafast vibrational spectroscopy experiments? In *Chem. Phys.*, 2007; Vol. 341, pp 143-157.

71. Tokmakoff, A. Shining light on the rapidly evolving structure of water. *Science* **2007,** *317* (5834), 54-55.

72. Nienhuys, H. K.; van Santen, R. A.; Bakker, H. J. Orientational relaxation of liquid water molecules as an activated process. *J. Chem. Phys.* **2000,** *112* (19), 8487-8494.

73. Woutersen, S.; Bakker, H. J. Resonant intermolecular transfer of vibrational energy in liquid water. *Nature* **1999,** *402* (6761), 507-509.

74. Woutersen, S.; Emmerichs, U.; Bakker, H. J. Femtosecond mid-IR pump-probe spectroscopy of liquid water: Evidence for a two-component structure. *Science* **1997,** *278*, 658-660.

75. Laage, D.; Hynes, J. T. Reorientional dynamics of water molecules in anionic hydration shells. *Proc. Natl. Acad. Sci. USA* **2007,** *104* (27), 11167-11172.

76. Laage, D.; Hynes, J. T. On the molecular mechanism of water reorientation. *J. Phys. Chem. B* **2008,** *112* (45), 14230-14242.

77. Laage, D.; Stirnemann, G.; Sterpone, F.; Rey, R.; Hynes, J. T. Reorientation and Allied Dynamics in Water and Aqueous Solutions. *Annual Review of Physical Chemistry* **2011,** *62*, 395-416.

78. Moller, K. B.; Rey, R.; Hynes, J. T. Hydrogen bond dynamics in water and ultrafast infrared spectroscopy: A theoretical study. *J. Phys. Chem. A* **2004,** *108* (7), 1275-1289.

79. Moilanen, D. E.; Fenn, E. E.; Lin, Y. S.; Skinner, J. L.; Bagchi, B.; Fayer, M. D. Water inertial reorientation: Hydrogen bond strength and the angular potential. *Proc. Natl. Acad. Sci. USA* **2008,** *105* (14), 5295-5300.

80. Skinner, J. L. Following the Motions of Water Molecules in Aqueous Solutions. *Science* **2010,** *328* (5981), 985-986.

81. Perakis, F.; De Marco, L.; Shalit, A.; Tang, F. J.; Kann, Z. R.; Kuhne, T. D.; Torre, R.; Bonn, M.; Nagata, Y. Vibrational Spectroscopy and Dynamics of Water. *Chem Rev* **2016,** *116* (13), 7590-7607.

82. Seki, T.; Yu, C. C.; Yu, X.; Ohto, T.; Sun, S.; Meister, K.; Backus, E. H. G.; Bonn, M.; Nagata, Y. Decoding the molecular water structure at complex interfaces through surface-specific spectroscopy of the water bending mode. *Phys Chem Chem Phys* **2020,** *22* (19), 10934-10940.

83. Sun, S. M.; Tang, F. J.; Imoto, S.; Moberg, D. R.; Ohto, T.; Paesani, F.; Bonn, M.; Backus, E. H. G.; Nagata, Y. Orientational Distribution of Free O-H Groups of Interfacial Water is Exponential. *Phys Rev Lett* **2018,** *121* (24).

84. van der Post, S. T.; Hsieh, C. S.; Okuno, M.; Nagata, Y.; Bakker, H. J.; Bonn, M.; Hunger, J. Strong frequency dependence of vibrational relaxation in bulk and surface water reveals sub-picosecond structural heterogeneity. *Nat Commun* **2015,** *6*.

85. Ishiyama, T.; Morita, A.; Tahara, T. Molecular dynamics study of two-dimensional sum frequency generation spectra at vapor/water interface. *Journal of Chemical Physics* **2015,** *142* (21).

86. Nihonyanagi, S.; Kusaka, R.; Inoue, K.; Adhikari, A.; Yamaguchi, S.; Tahara, T. Accurate determination of complex chi((2)) spectrum of the air/water interface. *Journal of Chemical Physics* **2015,** *143* (12).

87. Duong, C. H.; Gorlova, O.; Yang, N.; Kelleher, P. J.; Johnson, M. A.; McCoy, A. B.; Yu, Q.; Bowman, J. M. Disentangling the Complex Vibrational Spectrum of the Protonated Water Trimer, H+(H2O)(3), with Two-Color IR-IR Photodissociation of the Bare Ion and Anharmonic VSCF/VCI Theory. *Journal of Physical Chemistry Letters* **2017,** *8* (16), 3782-3789.

88. Fagiani, M. R.; Knorke, H.; Esser, T. K.; Heine, N.; Wolke, C. T.; Gewinner, S.; Schollkopf, W.; Gaigeot, M.-P.; Spezia, R.; Johnson, M. A.; Asmis, K. R. Gas Phase Vibrational Spectroscopy of the Protonated Water Pentamer: The Role of Isomers and Nuclear Quantum Effects. *Physical chemistry chemical physics : PCCP* **2016,** *18* (38), 26743-26754.

89. Fournier, J. A.; Wolke, C. T.; Johnson, C. J.; Johnson, M. A.; Heine, N.; Gewinner, S.; Schollkopf, W.; Esser, T. K.; Fagiani, M. R.; Knorke, H.; Asmis, K. R. Site-Specific Vibrational Spectral Signatures of Water Molecules in the Magic $H_3O^+(H_2O)_{20}$ and $Cs^+(H_2O)_{20}$ Clusters. *Proc. Natl. Acad. Sci.* **2014,** *111* (51), 18132-18137.

90. Fournier, J. A.; Wolke, C. T.; Johnson, M. A.; Odbadrakh, T. T.; Jordan, K. D.; Kathmann, S. M.; Xantheas, S. S. Snapshots of proton accommodation at a microscopic

water surface: understanding the vibrational spectral signatures of the charge defect in cryogenically cooled $H^+ \cdot (H_2O)_{n=2-28}$ clusters. *J. Phys. Chem. A* **2015,** *119* (36), 9425-9440.

91. Steinbach, C.; Andersson, P.; Melzer, M.; Kazimirski, J. K.; Buck, U.; Buch, V. Detection of the book isomer from the OH-stretch spectroscopy of size selected water hexamers. *Phys. Chem. Chem. Phys.* **2004,** *6*, 3320-3324.

92. Williams, E.; DiTucci, M.; Stachl, C. Effects of temperature on long range ion-water interactions in aqueous nanodrops. *Abstr Pap Am Chem S* **2019,** *257*.

93. Ayotte, P.; Johnson, M. A. Electronic absorption spectra of size-selected hydrated electron clusters: $(H_2O)_n^-$, n=6-50. *J. Chem. Phys.* **1997,** *106*, 811-814.

94. Shin, J.-W.; Hammer, N. I.; Diken, E. G.; Johnson, M. A.; Walters, R. S.; Jaeger, T. D.; Duncan, M. A.; Christie, R. A.; Jordan, K. D. Infrared signature of structures associated with the $H^+ \cdot (H_2O)_n$ (n = 6 to 27) clusters. *Science* **2004,** *304* (5674), 1137-1140.

95. Johnson, M. A. Vibrational Predissociation Ion Spectroscopy. In *Encyclopedia of Mass Spectrometry*, Armentrout, P. B., Ed. Elsevier: San Diego, 2003; Vol. 1.

96. Weber, J. M.; Kelley, J. A.; Nielsen, S. B.; Ayotte, P.; Johnson, M. A. Isolating the Spectroscopic Signature of a Hydration Shell using Clusters: Superoxide Tetrahydrate. *Science* **2000,** *287*, 2461-2463.

97. Robertson, W. H.; Kelley, J. A.; Johnson, M. A. A Pulsed Supersonic Entrainment Reactor for the Rational Preparation of Cold Ionic Complexes. *Rev. Sci. Instrum.* **2000,** *71* (12), 4431-4434.

98. Kamrath, M. Z.; Garand, E.; Jordan, P. A.; Leavitt, C. M.; Wolk, A. B.; Van Stipdonk, M. J.; Miller, S. J.; Johnson, M. A. Vibrational Characterization of Simple

Peptides Using Cryogenic Infrared Photodissociation of H_2-tagged, Mass-selected Ions. *J. Am. Chem. Soc.* **2011,** *133* (16), 6440-6448.

99. Wolk, A. B.; Leavitt, C. M.; Garand, E.; Johnson, M. A. Cryogenic Ion Chemistry and Spectroscopy. *Acc. Chem. Res.* **2014,** *47* (1), 202-210.

100. Dyke, T. R.; Muenter, J. S. Microwave Spectrum and Structure of Hydrogen-bonded Water Dimer. *J. Chem. Phys.* **1974,** *60* (7), 2929-2930.

101. Page, R. H.; Frey, J. G.; Shen, Y. R.; Lee, Y. T. Infrared predissociation spectra of water dimer in a supersonic molecular-beam. *Chem. Phys. Lett.* **1984,** *106*, 373-376.

102. Huang, Z. S.; Miller, R. E. High-resolution near-infrared spectroscopy of water dimer. *J. Chem. Phys.* **1989,** *91*, 6613.

103. J.B. Paul, R. A. P., C. Chapo, A. Petterson, R.J. Saykally. Infrared cavity ringdown spectroscopy of water clusters: O-D stretching bands. *J. Chem. Phys* **1998,** *109* (23), 10201-10206.

104. Keutsch, F. N.; Cruzan, J. D.; Saykally, R. J. The water trimer. *Chem. Rev.* **2003,** *103* (7), 2533.

105. Perez, C.; Muckle, M. T.; Zaleski, D. P.; Seifert, N. A.; Temelso, B.; Shields, G. C.; Kisiel, Z.; Pate, B. H. Structures of Cage, Prism, and Book Isomers of Water Hexamer from Broadband Rotational Spectroscopy. *Science* **2012,** *336* (6083), 897-901.

106. Perez, C.; Lobsiger, S.; Seifert, N. A.; Zaleski, D. P.; Temelso, B.; Shields, G. C.; Kisiel, Z.; Pate, B. H. Broadband Fourier transform rotational spectroscopy for structure determination: The water heptamer. *Chem. Phys. Lett.* **2013,** *571*, 1-15.

107. Perez, C.; Zaleski, D. P.; Seifert, N. A.; Temelso, B.; Shields, G. C.; Kisiel, Z.; Pate, B. H. Hydrogen Bond Cooperativity and the Three-Dimensional Structures of Water

Nonamers and Decamers. *Angewandte Chemie-International Edition* **2014,** *53* (52), 14368-14372.

108. Zhang, B.; Yu, Y.; Zhang, Z.; Zhang, Y. Y.; Jiang, S.; Li, Q.; Yang, S.; Hu, H. S.; Zhang, W.; Dai, D.; Wu, G.; Li, J.; Zhang, D. H.; Yang, X.; Jiang, L. Infrared Spectroscopy of Neutral Water Dimer Based on a Tunable Vacuum Ultraviolet Free Electron Laser. *J Phys Chem Lett* **2020,** *11* (3), 851-855.

109. Yang, N.; Duong, C. H.; Kelleher, P. J.; Johnson, M. A.; McCoy, A. B. Isolation of site-specific anharmonicities of individual water molecules in the $I^-\cdot(H_2O)_2$ complex using tag-free, isotopomer selective IR-IR double resonance. *Chem. Phys. Lett.* **2017,** *690*, 159-171.

110. Wolke, C. T.; Fournier, J. A.; Miliordos, E.; Kathmann, S. M.; Xantheas, S. S.; Johnson, M. A. Isotopomer-Selective Spectra of a Single Intact H_2O Molecule in the $Cs^+(D_2O)_5H_2O$ Isotopologue: Going Beyond Pattern Recognition to Harvest the Structural Information Encoded in Vibrational Spectra. *J. Chem. Phys.* **2016,** *144* (7), 074305.

111. Ayotte, P.; Nielsen, S. B.; Weddle, G. H.; Johnson, M. A.; Xantheas, S. S. Spectroscopic Observation of Ion-Induced Water Dimer Dissociation in the $X^-\cdot(H_2O)_2$ (X = F, Cl, Br, I) Clusters. *J. Phys. Chem. A* **1999,** *103*, 10665–10669.

112. Ayotte, P.; Weddle, G. H.; Bailey, C. G.; Johnson, M. A.; Vila, F.; Jordan, K. D. Infrared spectroscopy of negatively charged water clusters: Evidence for a linear network. *J. Chem. Phys.* **1999,** *110*, 6268-6277.

113. Campagnola, P. J.; Lavrich, D. J.; DeLuca, M. J.; Johnson, M. A. Photodestruction spectra of the anionic water clusters, $(H_2O)_n^-$, n=18 and 30: absorption to the red of e^-_{aq}. *J. Chem. Phys.* **1991,** *94*, 5240.

114. Roscioli, J. R.; Diken, E. G.; Johnson, M. A.; Horvath, S.; McCoy, A. B. Prying Apart a Water Molecule With Anionic H-Bonding: A Comparative Spectroscopic Study of the $X^{-}\cdot H_2O$ (X = OH, O, F, Cl, and Br) Binary Complexes in the 600−3800 cm^{-1} Region. *J. Phys. Chem. A* **2006,** *110* (15), 4943-4952.

115. Yang, N.; Duong, C. H.; Kelleher, P. J.; McCoy, A. B.; Johnson, M. A. Deconstructing Water's Diffuse OH Stretching Vibrational Spectrum With Cold Clusters. *Science* **2019,** *364* (6437), 275-278.

116. Wolke, C. T.; Menges, F. S.; Totsch, N.; Gorlova, O.; Fournier, J. A.; Weddle, G. H.; Johnson, M. A.; Heine, N.; Esser, T. K.; Knorke, H.; Asmis, K. R.; McCoy, A. B.; Arismendi-Arrieta, D. J.; Prosmiti, R.; Paesani, F. Thermodynamics of Water Dimer Dissociation in the Primary Hydration Shell of the Iodide Ion with Temperature-Dependent Vibrational Predissociation Spectroscopy. *J. Phys. Chem. A* **2015,** *119* (10), 1859-1866.

117. Johnson, M. S.; Kuwata, K. T.; Wong, C. K.; Okumura, M. Vibrational Spectrum of $I^{-}(H_2O)$. *Chem. Phys. Lett.* **1996,** *260* (5-6), 551-557.

118. Ayotte, P.; Weddle, G. H.; Kim, J.; Johnson, M. A. Mass-Selected "Matrix Isolation" Infrared Spectroscopy of the $I^{-}\cdot(H_2O)_2$ Complex: Making and Breaking the Inter-Water Hydrogen-Bond. *Chem. Phys.* **1998,** *239* (1-3), 485-491.

CHAPTER 2

Experimental:

Principles of Cryogenic Ion Vibrational Predissociation Spectroscopy and the Development of MS^4IR^3 Instrumentation with Time Dependent Spectroscopy Capabilities

This chapter will provide an overview of the custom-built instrument that incorporates several types of multiple-laser cryogenic ion vibrational predissociation (CIVP) spectroscopy, which is the essential platform enabling the experiments performed in this Dissertation. Briefly, this method generates vibrational spectra of cryogenically cooled and mass selected ions through action spectroscopy.

2.1 The 'Mini Machine': New Generation Compact Yale Tandem Time of Flight Photofragmentation Mass Spectrometer

2.1.1. Generation of Gas Phase Ions Using Electrospray Ionization

A schematic of the new generation compact Yale tandem time of flight photofragmentation mass spectrometer is displayed in Fig. 2.1. The first component of the instrument is the electrospray ionization (ESI) source, which was developed in the late 1980's by Yale's own John Fenn.[1] The ion source includes an ESI needle held at high voltage and surrounded by a capsule whose atmospheric composition is controlled by a controlled gas purge (Fig. 2.2). Ion generation begins with a millimolar solution of analyte dissolved in an appropriate solvent such as acetonitrile, methanol, or water. This solution is then transferred to a 0.5 mL glass syringe that is discharged at a rate about 0.16 mL/hr by a syringe pump. This solution flow feeds the ESI needle. A constant voltage of ±2500-4000 V is applied to the needle in order to generate a fine mist of the charged droplets. As the droplets' charge overcomes their surface tension, they undergo Coulombic explosion. This creates smaller and smaller droplets until no more solvent remains and bare ions are extracted.[2] The capsule surrounding the ESI needle can be used

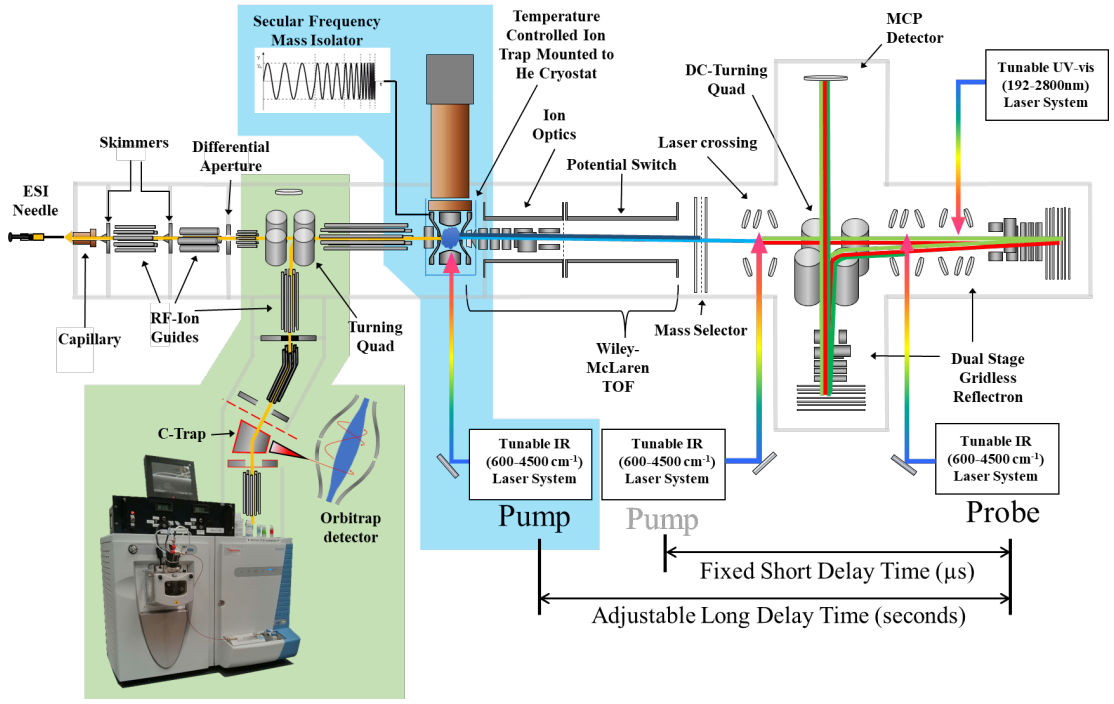

Figure 2.1. Schematic of the compact Yale Tandem Time of Flight Photofragmentation Mass Spectrometer (MS^4IR^3). There are two ion sources. One of them (shaded green) is the newly integrated LTQ Orbitrap Velos Pro instrument, which includes high-resolution mass spectrometry (Orbitrap) and collisional-induced dissociation (CID) functions. It can send mass-selected ions or their CID fragment ions to the existing photofragmentation instrument to carry out vibrational spectroscopy experiments. Additional new capabilities (shaded blue) include in-trap laser excitation and in-trap mass isolation. In-trap mass isolation is achieved by sweeping the mass-dependent secular frequency using custom electronics. The isolated ions are then irradiated by the in-trap laser to achieve photoactivation or photobleaching. The storage time in the temperature-controlled ion trap can be varied from 10-500 ms to achieve long delay times between pump (bleach) and probe laser pulses, a feature used to obtain intra-cluster reaction kinetic measurements.

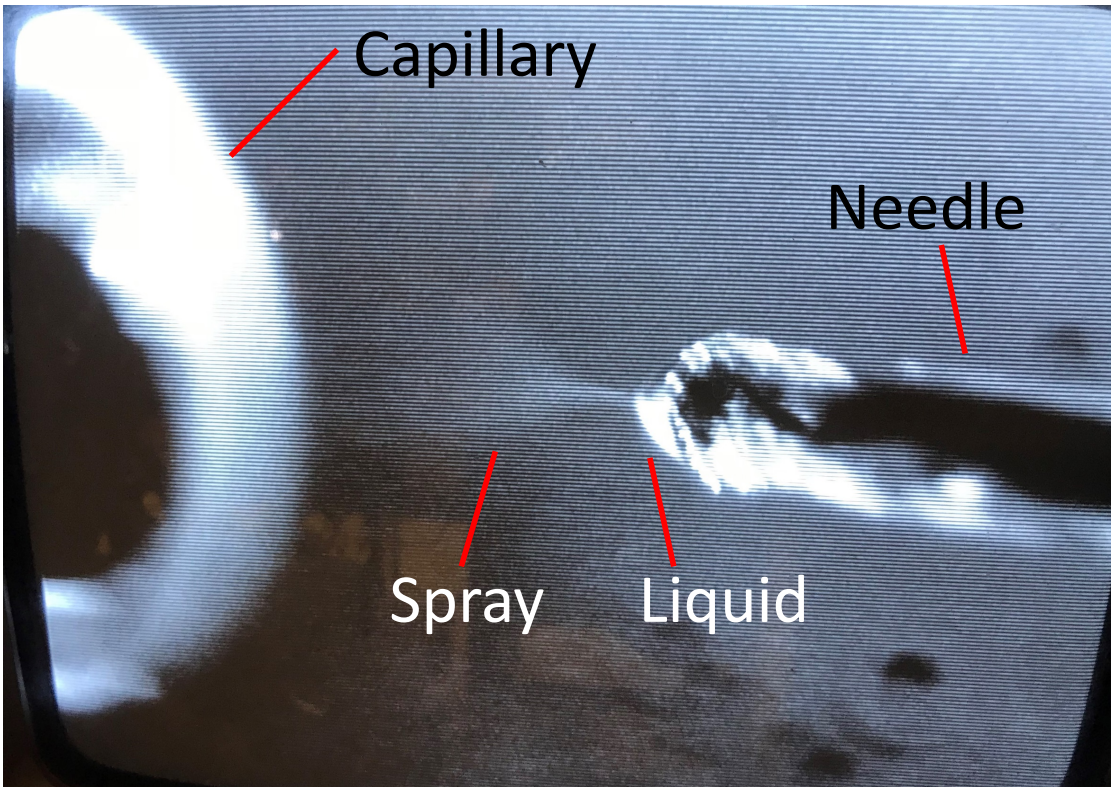

Figure 2.2. Picture of a working ESI source. The charged liquid forms a cone on the exit of the needle (50 micron diameter) and electro sprays into a cone of mist which enters the capillary entrance.

to either control the relative humidity of the spray source by adding small amounts of water to the capsule or purged with N_2 gas in order to create an oxygen- and water-free environment, which is crucial for the formation of air-sensitive species. In addition to the ESI mode, the source can also be operated with a metallic needle in a humid atmosphere to generate protonated water clusters via corona discharge. Such operation requires no solution inside the needle. When the ESI needle voltage surpasses a critical value, regardless of the solution, the spray transitions into the discharge mode and produces protonated water cluster under humid conditions. A slight purple glow can be seen when ambient lighting is turned off. Increase of needle voltage much beyond this point will result in electric breakdown and produce arcing between the needle and the copper capillary that admits ions into the vacuum envelope. This condition draws large currents and can melt the needle tip.

After entering the gas phase, ions produced by the electrospray are attracted towards the capillary. This capillary has a diameter of 1.6 mm and is held at room temperature and a potential of ±100-300 V. As ions pass through the capillary, they move from the atmospheric pressure regime of the capsule to the 2.2-2.6 Torr environment immediately before the first skimmer, which is held at a potential of around 30 V. The skimmer has a small aperture (1.5 mm) that creates the first region of differential pumping and keeps the pressure in the first ion guide around 2-5 mTorr.

After entering the first skimmer, the ions enter the first quadrupole ion guide, which is held at a pressure of $2\sim5\times10^{-3}$ torr. This ion guide consists of four stainless steel rods with a diameter of 12.7 mm that are held parallel to one another in a square configuration. A 1 MHz radio frequency (RF) waveform with a peak-to-peak amplitude of 100~600 V is

applied to the rods such that adjacent rods have opposite phase. This creates a parabolic effective potential centered around the symmetry axis of the guide that confines the ions to the center axis of the machine.[3] In order for the ions to travel from one region of differential pumping to the next, the ion guides are floated at a potential that is generally 15-30 V lower than the previous element, thus attracting the ions down the machine. Attempts were made to use this quadrupole ion guide as a mass selective quadruple by applying a DC offset between the two sets of rods. Unfortunately, the performance was not ideal due to limited machining and assembly precision. The assembly tolerance needs to be controlled within 10 micron to achieve mass resolution comparable to commercial quadrupole mass spectrometers[citation?].

During the development of this instrument, various capillary diameters, skimmer diameters, and pumping speeds were explored. Larger capillary diameters result in higher pressure in the region before the first skimmer and result in loss of cluster signal, possibly through collision induced dissociation (CID). Larger skimmer diameters, or smaller separations between the end of the capillary and the skimmer, result in elevated pressure in the first ion guide and consequent loss of cluster signal due to CID processes. Adding additional turbo-molecular vacuum pumps on the first ion guide chamber can lower the pressure down to 1 mTorr and also reduces signal intensity. This is due to the gas in the first ion guide, which also plays the role as a buffer gas that reduces the ions' transverse velocity and focuses them in the direction perpendicular to the machine axis. This allows more ions to pass though the small aperture on the second skimmer. Such processes are often referred to as "phase space quenching" of the ion packet. Excessively low pressures inhibit this process and result in loss in signal. For water cluster ion production, a slight

increase of temperature from room temperature to about 313 K can improve the cluster ion signal by about 10-20% dependent on cluster size.

After passing through the first ion guide (an octapole ion guide), the ions pass through a second skimmer and into the second region of differential pumping (around 10^{-5} torr). The ions are then guided down several octapole ion guides. These each comprise eight rods of 3.175 mm diameter arranged in a mutually parallel circular configuration. Each successive octapole guide is held at a lower potential than that of the preceding ion guide. This draws ions towards the aperture at the end of each guide. These apertures have a diameter of 1.5 mm and are held at an attractive potential to the ions. Similar to the skimmer, the aperture separates the second region of differential pumping from the third, which is around 10^{-6} torr.

The ions pass through the aperture into the third ion guide. This guide operates in an identical manner to the quadrupole guide and no major effect is experimentally observed. The ions are then pulled to the end of the octapole guide by another aperture before entering the low-speed ion turning quad and another set of octapole guides, which deliver the ions to the Paul trap.

To allow integration of multiple ion sources into the same instrument, a turning quadrupole is inserted between the third and fourth ion guides. The turning quadrupole consists of four rods that lie orthogonal to the octapole guides. Diagonal rods are held at equivalent DC voltages and adjacent rods are held at inverted values (similar to the polarity scheme in a quadrupole RF ion trap). The specific voltages required for turning depend on the kinetic energy of the ions under study. This creates an electric field that

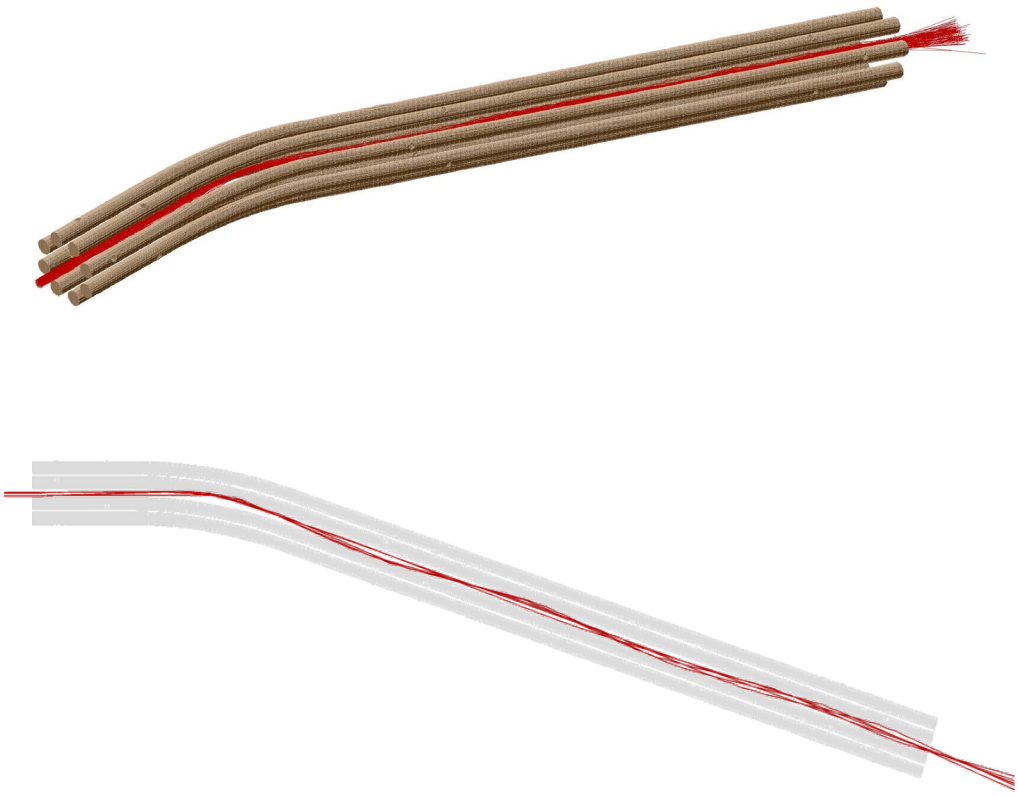

Figure 2.3. Simulated trajectory of ions passing through a bent octapole ion guide. The red traces are the ion trajectories. This simulation was performed using SIMION with a user program written for this simulation to apply time-dependent voltage and collision from gas molecules.

causes the incoming ions from the bottom of Fig 2.2 (shaded green) to be turned at 90° towards the Paul trap (shaded blue). For the ions from the ESI source on the left of Fig. 2.1, the two sets of poles of the turning quadrupole are kept at uniform attractive voltage to allow the ion packet to fly straight through. After exiting the turning quadrupole, the ions pass through an octapole ion guide and are focused by an aperture on the heat shield immediately outside of the Paul trap. The ions subsequently pass through a tube lens on the exterior of the Paul trap and enter the cryogenically cooled trap interior, where they are collisionally cooled. It is important to note that the kinetic energy of the ions is set by the sequence of voltages (from the first skimmer voltage to the final octapole ion guide float voltage) that sends the ions into the trap. The ion kinetic energy is often a crucial variable determining the efficiency of the ion trapping and tagging processes that occur within the trap.

Additionally, for ions from the secondary ion source (commercial ThermoFisher Orbitrap, shaded green in Fig. 2.2), a bent ion guide was designed to correct for the angle between the axes of the two instruments. Simulations were performed to validate the design following the principle that the turning radius of the ion guide should be at least 5 times larger than the wavelength of the ion's oscillatory trajectory. The simulated trajectory is shown Fig. 2.3).

2.1.2. Trapping, Mass selection, and Cryogenic Processing of the Ions

The next phase of the experiment occurs in the cryogenically cooled ion trap (highlighted in green in Fig. 2.1). The ions first pass through the entrance aperture on the

heat shield, which serves to reduce heating via black body radiation, before they encounter the ion trap. The aperture also serves as an ion beam lens, compensating for the divergence of ion beam in the transverse direction after exiting an ion guide (right side of Fig. 2.3). The ion trap used in the New Generation Yale tandem time of flight photofragmentation mass spectrometer is a quadrupole Paul-type ion trap[4] (shown in Fig. 2.4). The Paul trap begins with the entrance trap and exit trap apertures held at a DC potential similar (within 5 V) to that of the center electrode (referenced to ground, 0 V).

The slight DC offset creates some mass selectivity and helps exclude unwanted ions. Such selectivity improves ion signal by preventing unwanted ions from saturating the ion trap's finite capacity. An RF voltage (800 kHz to 1 MHz, 100-2000 V_{pp}) is applied to the center electrode in order to trap the ions. Pulsed buffer gas is used to collisionally (ca. 10^5 collisions) cool the ions both kinetically and internally.[5-6] The effective trapping window, during which the buffer gas pressure is sufficient to trap ions, is about 10 ms (Fig. 2.5) at a repetition rate of 10 Hz using a pulsed valve. One important note is that this window depends heavily on both the conductance of the gas pipe connecting the pulsed valve to the trap and the pumping speed. A gas pipe longer than 100 mm will result in a 'smoothed out' pulse which effectively turns the pulsed gas into a continuous gas load as if a leak valve were used instead of a pulsed valve. A short Teflon tube is used to maximize conductance while thermally insulating the trap from the heat shield and the pulsed valve. This reduces heat load on the cryohead, which has limited cooling capacity. After the ion packet is trapped and cooled, a secular frequency sweep pulse can be applied to the entrance cap to achieve higher resolution mass selection (about 1/100 mass

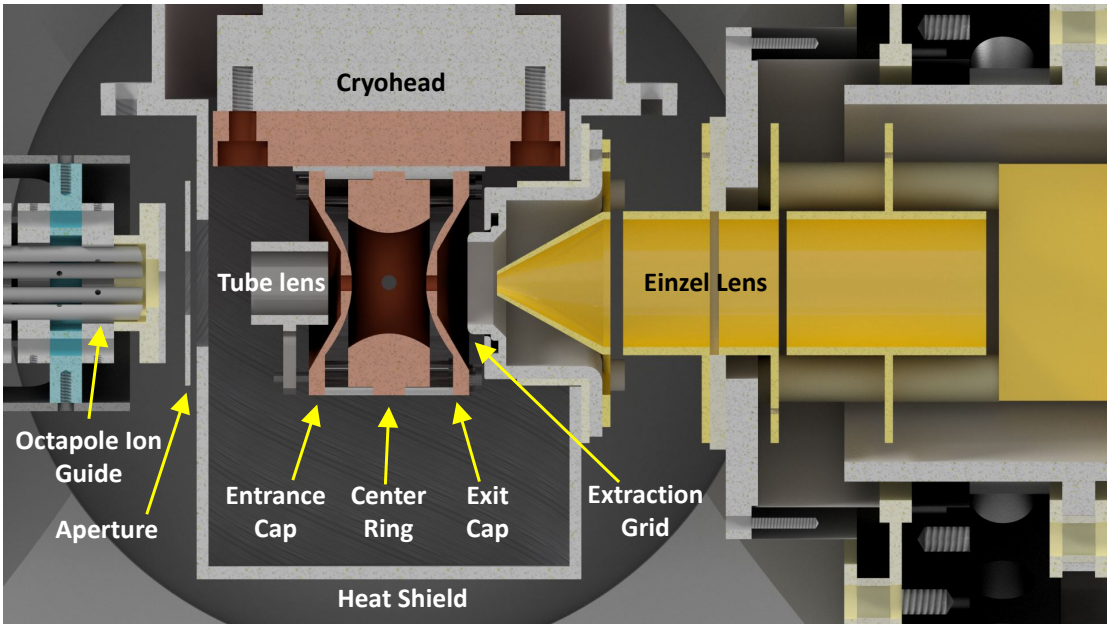

Figure 2.4. A cutaway view of the quadrupole Paul-type trap and surrounding components that are used in the new generation Yale tandem time of flight photofragmentation spectrometer. The ion packet enters from the left through the octapole ion guide and is focused by the aperture and tube lens into the Paul trap. The trap consists of an entrance cap, a center ring, and an exit cap, and is cooled by the cryohead. Buffer gas is pulsed in through a hole on the insulator between the entrance cap and the center ring.

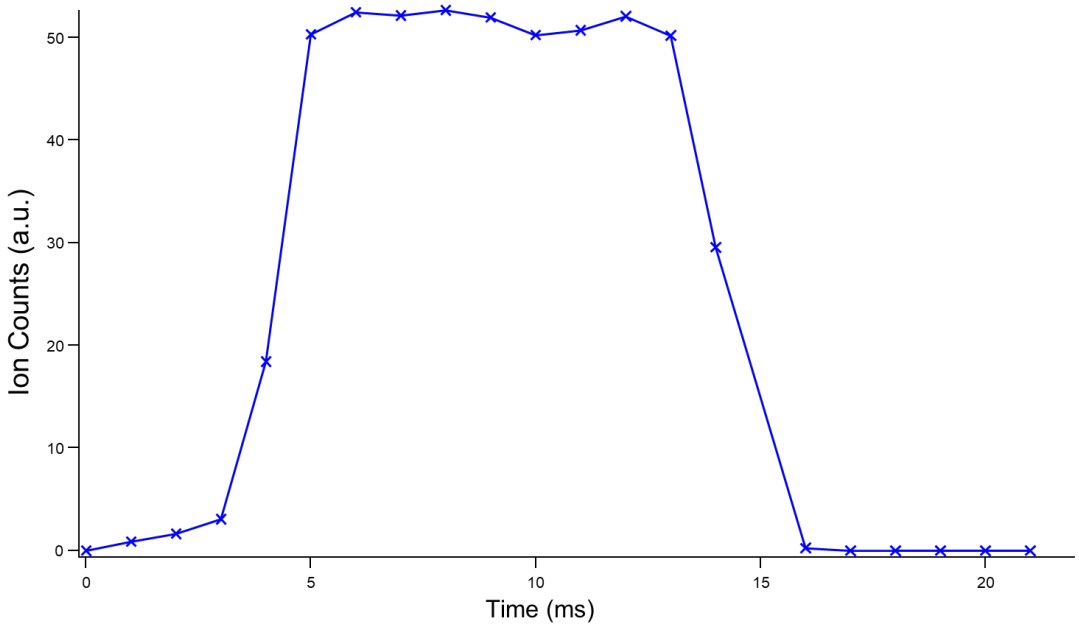

Figure 2.5. Ion intensity of $EMIM^+$ as a function of the pulsed buffer gas timing in the cryogenic Paul trap. Ions are pre-accumulated in the first ion guide before being injected into the trap. The time axis labels the delay between when the ions are extracted from this pre-accumulation and when the pulsed valve is triggered.

resolution limited by the short duty cycle (~30 ms) and the precision of the mechanical parts). This is discussed later in this chapter.

The ion trap is held anywhere from 4-300 K, depending on the aims of the experiment, by a closed-loop Sumitomo cryohead and compressor. Cooling is achieved with Gifford-McMahon cycle and helium cooling media inside the cryohead. A heater is installed between the trap and the cryohead to regulate the temperature by heating against the cryohead. Temperature diodes monitor the temperatures of both the Paul trap and the cryohead, which has up to 100 W of cooling power above 50 K and up to 1.5 W at 4 K. The heating element is chosen accordingly, and is able to provide up to 100 W of heating power.

During the trapping and cooling process, the helium buffer gas can be doped with a secondary gas (H_2, D_2, Ne, N_2, CO, CO_2, etc.). When the trap is at an appropriate temperature, based on the vapor pressure of the dopant or tagging gas, some number of tag molecules condense onto the trapped ions.[7-8] When the ions of interest do not need to be tagged, pure helium gas is used to minimize the operational temperature without excessive condensation within the trap.

2.1.3. In-trap Mass Separation of the Ion Packet and In-trap Laser Excitation

After the ions are cooled and the buffer gas pressure is lowered (roughly 20 ms after "t_0" when the pulse valve fires, a secular frequency pulse can be applied to the entrance cap to achieve higher resolution mass selection (about 1/100 mass resolution limited by the 30 ms duty cycle and the precision of the mechanical parts). The simplest operation is using one specific secular frequency, which will excite one particular m/z. The

excitation has width to it in terms of m/z ratio (Fig. 2.6a) which depends on the gas pressure, duration of the pulse, and the pulse amplitude. The secular motion can be modeled as a damped driven oscillator where the damping term comes from the friction caused by buffer gas collision and the driving term is the secular frequency excitation pulse. The greater the damping term the wider the excitation profile is (Fig. 2.6a). Such excitation of the secular motion causes the driven ion to be ejected out of the ion trap (Fig. 2.6c). When the excitation pulse is applied with buffer gas pressure still high, ejection can also be caused by collision-induced dissociation of the ion (CID) as illustrated in Fig. 2.6d, where an $H^+(H_2O)_{21}$ cluster is dissociated to form $H^+(H_2O)_{20}$ and $H^+(H_2O)_{19}$.

However, selective ejection of ions with one specific m/z is not our goal in the laser experiments. We want to isolate one specific m/z by ejecting all other m/z ions. This is done by applying a sweeping frequency instead of a fixed frequency pulse. The frequency sweep (50-200 kHz log sweep, 30 ms duration, from t_0 + 20 ms to t_0 + 50 ms) is generated with an SRS arbitrary waveform generator. We chose to sweep from low frequency to high frequency so that the potential fragment products of unintentional collision induced dissociation (lighter mass, higher secular frequency) will be removed later by the sweeping frequency. We use a log sweep because this scheme spends equal amounts of time at each frequency, thus maximizing excitation efficiency across all m/z. In order to preserve the desired m/z ion while ejecting all others, an amplitude modulation (AM) was applied to the sweeping frequency: when the frequency sweeps near the secular frequency of the m/z that is to be preserved, the AM control pulse goes to 0 V (edge B of Fig. 2.7c). This effectively turns off the excitation waveform (edge B of

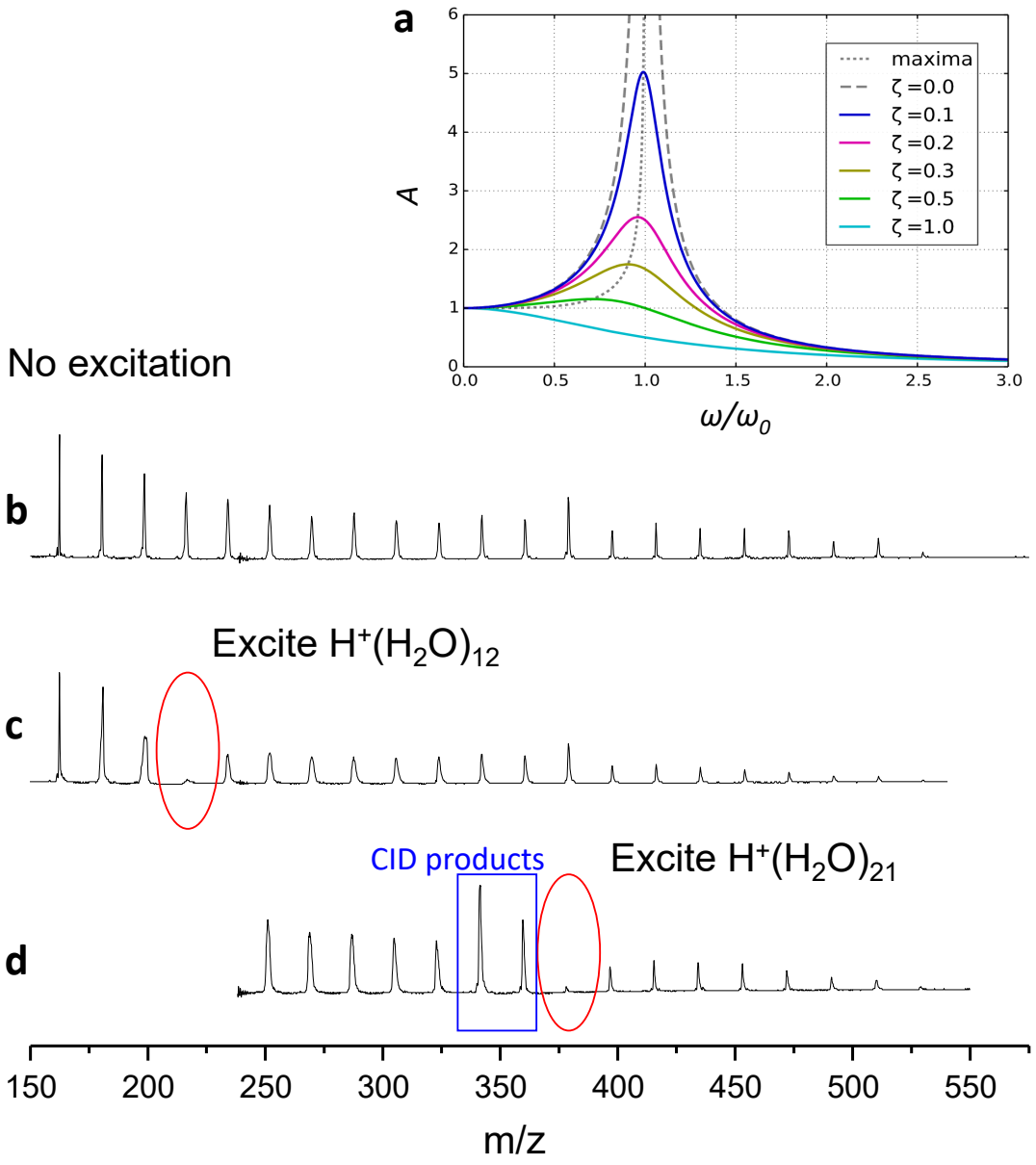

Figure 2.6. (a) Resonance response curve of damped driven oscillators where A marks the amplitude of the damped driven oscillation and ω/ω_0 marks the driving frequency relative to its natural frequency. (b) Mass spectrum of protonated water clusters with no secular frequency excitation. (c,d) Mass spectra of protonated water clusters with secular frequency excitation.

Fig. 2.7e). Once the frequency sweeps pass the secular frequency specified, the AM control pulse goes back to 5 V (edge C of Fig. 2.7c), which turns the excitation waveform back on (edge C of Fig. 2.7e). The resulting waveform has a window at the frequency corresponding to the mass to be isolated.

The secular frequency sweep is carried out within the first half of the 100 ms period dictated by the 10 Hz experiment frequency. The latter half of the 100 ms period is reserved for laser interaction. Hence, the frequency sweep needs to be completed before t_0 + 50 ms. In order to match the experimental frequency of 10 Hz, the function generator is triggered at 20 Hz and sweeps from 1 kHz to 200 kHz. The 20 Hz clock (Fig. 2.7a) is then fed into a delay generator that down converts it to yield a 10 Hz trigger (Fig. 2.7b) that runs the rest of the experiment. The delay generator also generates a square wave whose high and low (0 or 5 V, respectively) correspond to the on and off of the secular frequency excitation. This square wave (Fig. 2.7c) is fed into the AM input channel of the function generator to gate the sweeping frequency output. The resulting frequency sweep waveform (Fig. 2.7e) is only turned on in the first half of the experiment after the buffer gas is pumped out (edge A in Fig. 2.7c,e). Then there is the window where the frequency sweeps nears the secular frequency of the desired m/z, where the output waveform is turned off then back on (edge B and C in Fig. 2.7c,e). Finally, the waveform is turned off right before the end of the first half 50 ms (edge D in Fig. 2.7c,e). The produced wave form is then capacitively coupled onto the entrance cap of the Paul trap (Fig. 2.8). A demonstration of the resulting mass isolation is shown in Figure 2.9, where a specific water cluster is isolated inside the Paul trap.

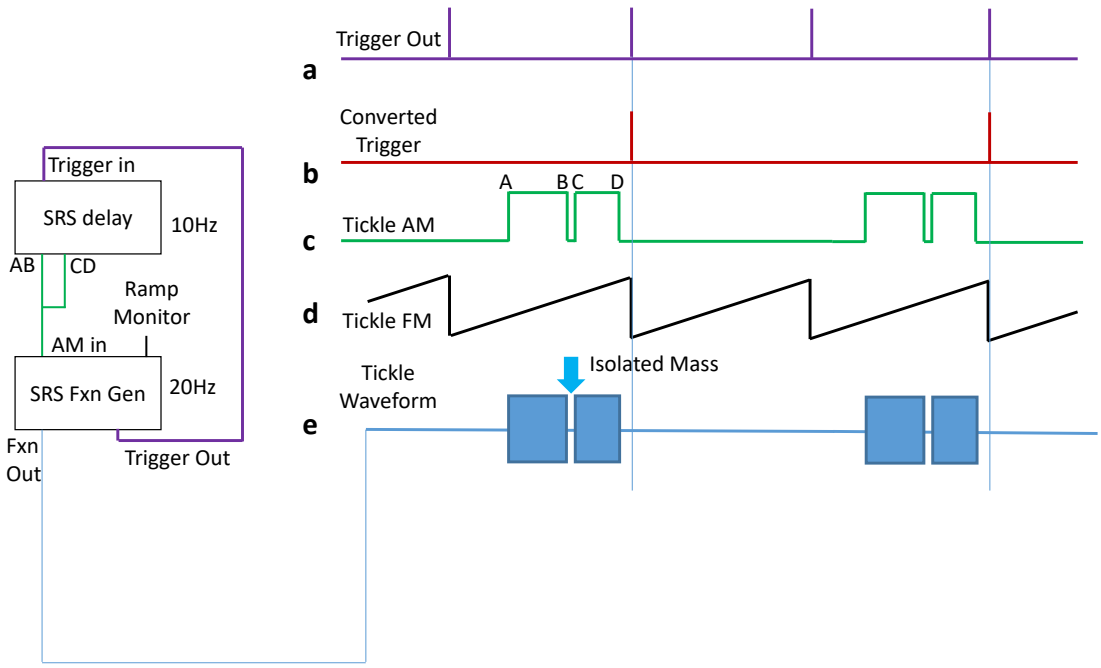

Figure 2.7. Triggering scheme for generating the secular frequency sweep pulse for mass isolation inside the Paul trap. An SRS function generator serves as the master clock running at 20 Hz (a). This 20 Hz trigger is then down converted to a 10 Hz clock pulse (b) that triggers the rest of the experiment. The SRS delay generator running at 10 Hz feeds an AM pulse back into the amplitude modulation input of the function generator, which is running in frequency sweep mode (d). The AM pulse controls the frequency at which the output waveform (e) is turned on or off. The output waveform looks "blocky" instead of sinusoidal due to the high frequency compared to the overall time scale of the figure.

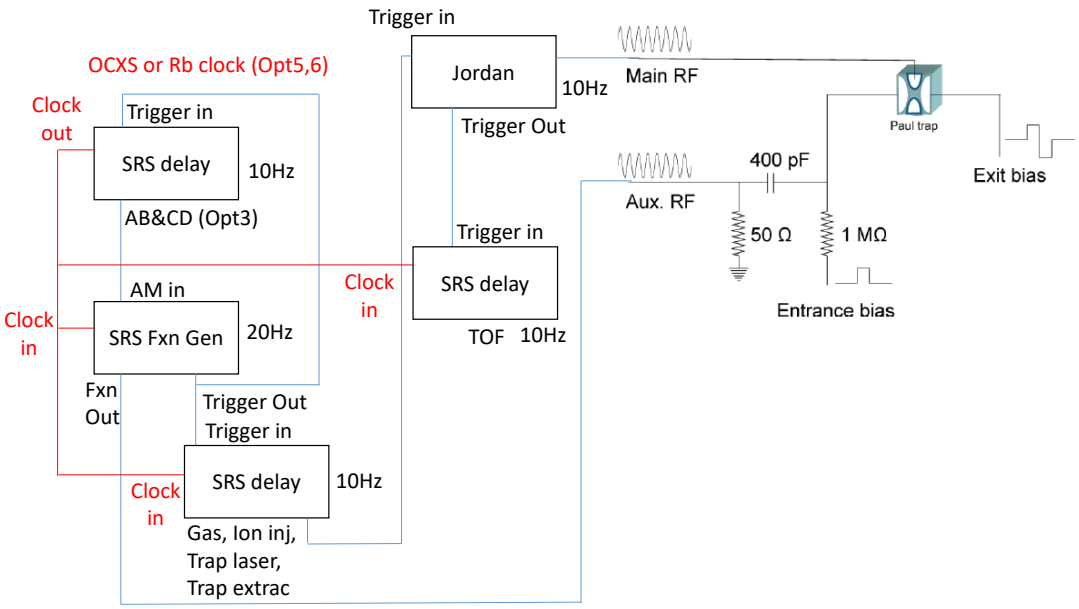

Figure 2.8. Triggering scheme and circuit diagram for generating the secular frequency sweep pulse for mass isolation inside the Paul trap. An SRS function generator serves as the master clock running at 20 Hz. This 20 Hz trigger is then down converted to a 10 Hz clock pulse that triggers the rest of the experiment. The SRS delay generator running at 10 Hz feeds an AM pulse back into the amplitude modulation input of the function generator, which is running in frequency sweep mode. The SRS delay generator also triggers the trap RF generator (labeled “Jordan”), which turns off the RF waveform applied to the Paul trap and sends out a trigger at the zero-crossing point of the RF. This trigger is then used to trigger the exit bias.

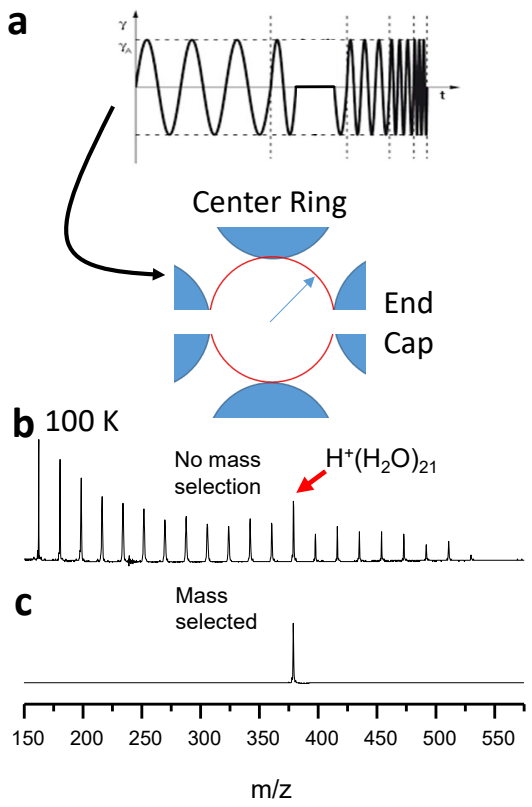

Figure 2.9. Schematic of a windowed secular frequency sweep applied to a Paul trap to achieve mass isolation (a). The oscillation period is exaggerated for ease of viewing. The high frequency waveform is more realistically depicted in Figure 2.7e. (b) shows the mass spectrum of protonated water clusters with no mass selection and (c) shows the mass spectrum that results when a secular frequency sweep is applied to isolate the m/z 379 ion.

Once the desired ion is successfully isolated, a laser can be introduced into the trap to carry out photo-bleaching or photo-excitation experiments. The advantage of a 3D Paul trap is that the parabolic effective potential concentrates ions at the center of the trap, allowing for effective laser excitation. The in-trap laser interaction allows easily variable delay times between the different lasers in multi-laser experiments, including photo-bleaching ambient kinetics measurements as well as laser-induced kinetics measurements. These experiments are discussed in detail in Chapter 9. In addition to the laser experiment, the mass isolated ions can also be used to measure temperature-dependent reaction kinetics such as evaporation kinetics. For example, size selected protonated water clusters are observed to evaporate over time, and the time-dependent relative abundance of the product and parent species can be observed by varying the delay between the secular frequency excitation and the time-of-flight mass spectrum sampling (Fig. 2.10).

2.1.4. TOF Mass Separation of the Ion Packet

Towards the end of the 100 ms time period, the ions are extracted out of the Paul trap towards the extraction grid (Fig. 2.11), which is arranged in the Wiley-McLaren[9] configuration to carry out time of flight mass spectrometry. The entrance cap and the center electrode are kept at ground (0 V), the exit cap is pulsed to an attractive voltage of ± 400 V (depending on ion polarity), and the extraction grid is kept at an attractive voltage of ± 2500 V. The three voltages form a Wiley-McLaren[9] configuration (drawn as a schematic in Fig. 2.12 and actual potential contours drawn in Fig. 2.11b) and control the temporal focal point of the ion beam where the ion packet is at minimum width in terms of arrival time at a fixed plane. The exit cap voltage is fine tuned to change the

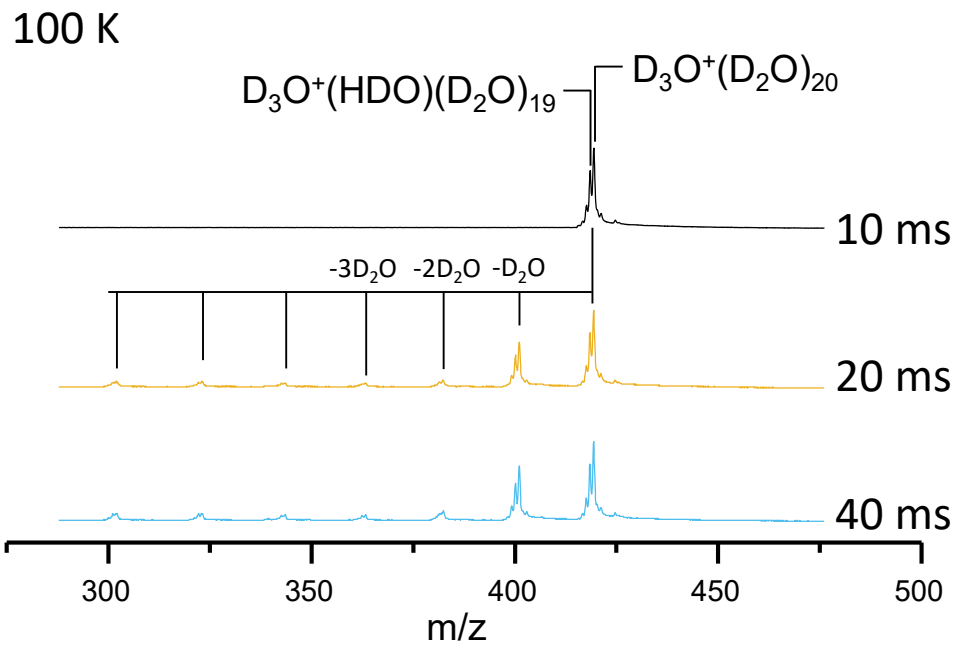

Figure 2.10. Evaporation of isotopically substituted water clusters over time, observed in Paul trap at 100 K. The small splitting of the peaks is caused by hydrogen substitution of the perdeuterated cluster.

temporal focal point's position to best overlap with the first laser interaction region outside the trap (labeled as "pump" with gray text in Fig 2.1). The entire instrument is simulated using AutoCAD Inventor and SIMION. The ion beam trajectory is shown in Fig. 2.13. Details of the design and simulation of each component are discussed in following sections.

The very first component the ion encounters is the extraction grid (Fig. 2.11), which creates a parallel field between the exit cap and the grid to accelerate the ions without distorting the energy distribution and direction of velocity. It is crucial that the mesh grid is kept flat. Traditionally, the mesh grid is either glued on with conductive epoxy or spot welded. These methods have several limitations: grids made with these methods are hard to manufacture given the flatness required; the epoxy glue could fail at low temperature (the extraction grid cools down to 50 K); spot welding only works for certain metals (stainless steel is typically the best for spot welding, while copper is very difficult to spot weld). Given these limitations, we designed a new construction for fixing grids onto an electrode where the grid mesh is held down with a rubber O-ring (Fig. 2.14a). Such designs are easy to machine and assemble, achieve great flatness throughout the working temperature range (Fig. 2.14b) with pre-tension created by the O-ring, and retains mechanical strength through a wide temperature range (50 K to 350 K).

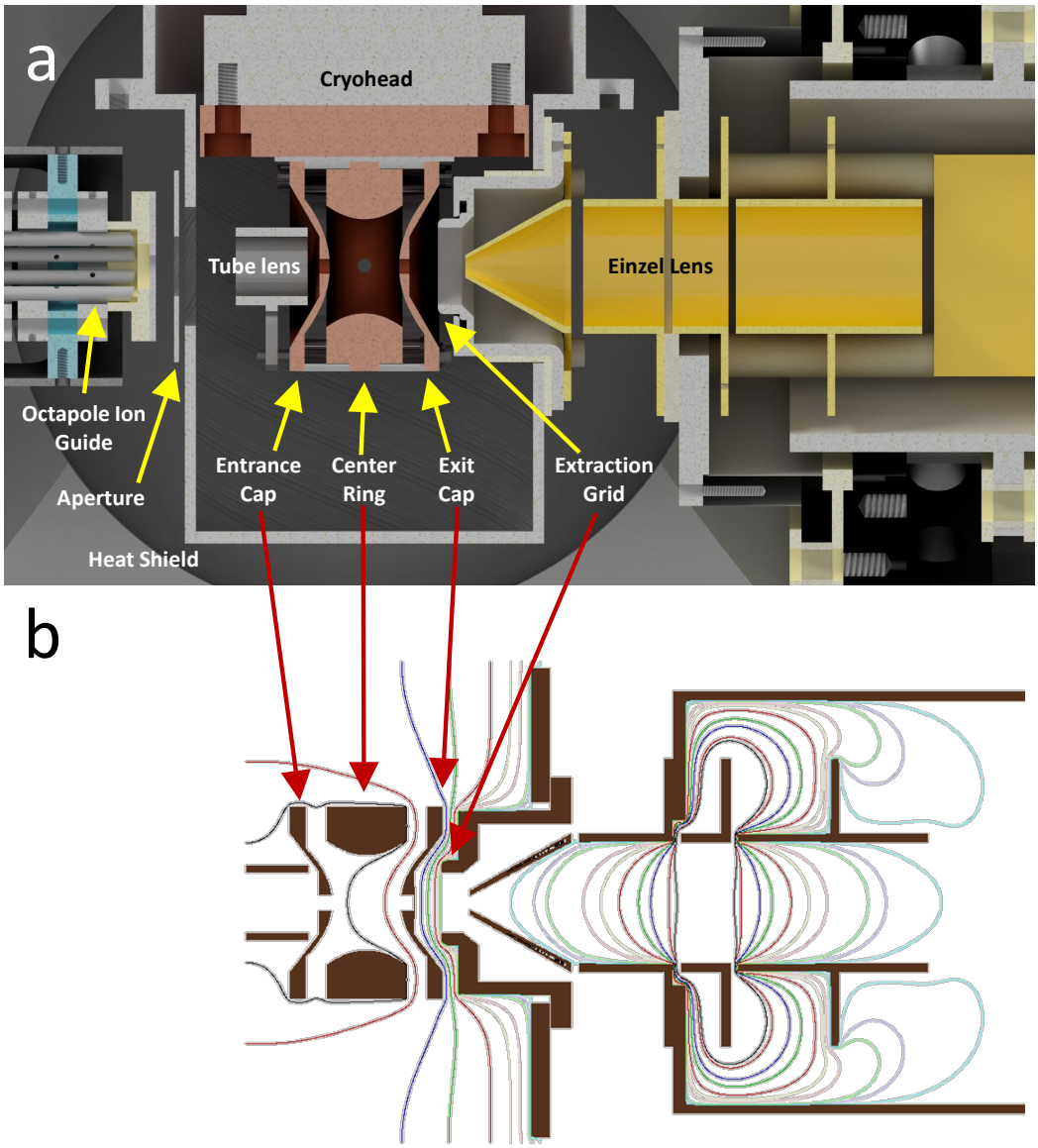

Figure 2.11. (a) A cutaway view of the quadrupole Paul-type trap and its surrounding components. The ion packet enters from the left in the octapole ion guide and is focused with the aperture and tube lens into the Paul trap, which consists of an entrance cap, a center ring, and an exit cap. (b) A SIMION simulation of the electric field and equipotential contours. Only the equipotential contours are plotted. The potential surface around the center axis is close to that produced by a set of parallel plates typically used in Wiley-McLaren time of flight mass spectrometers.

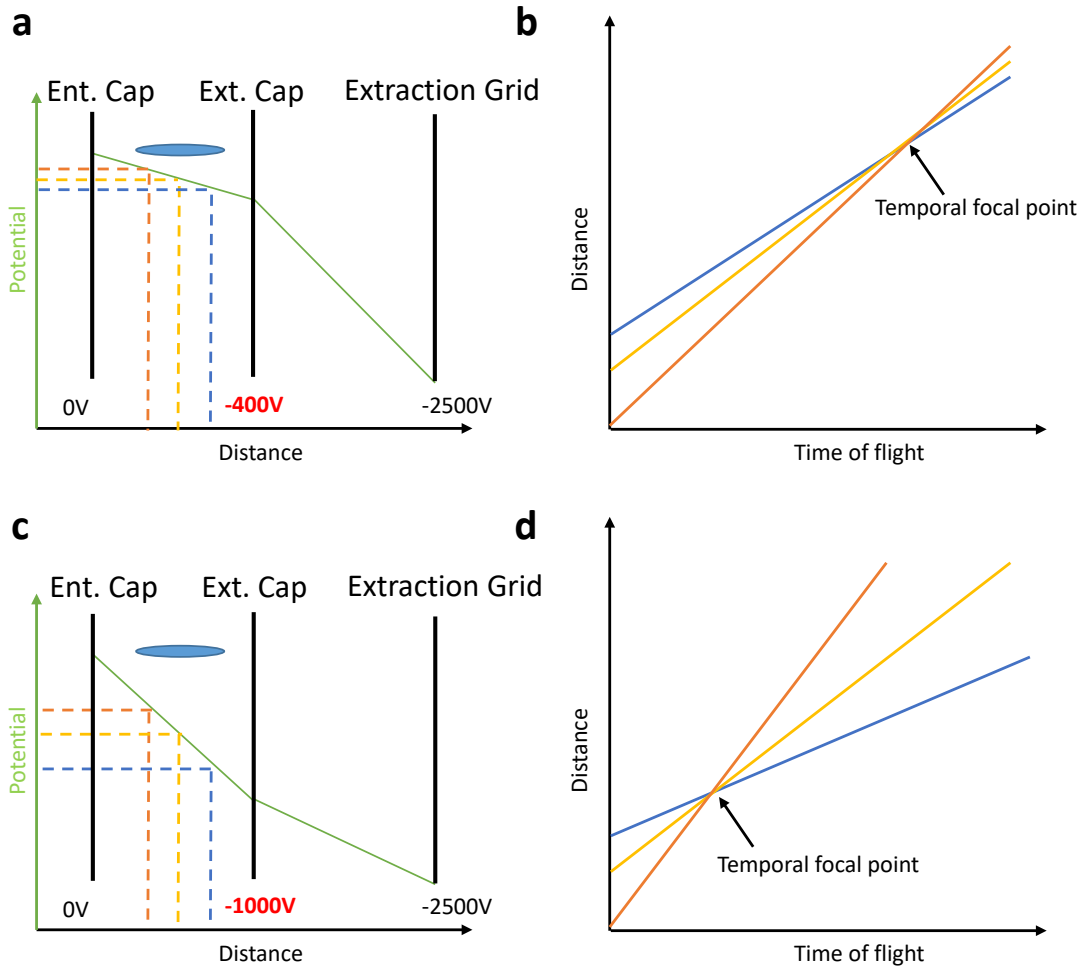

Figure 2.12. Wiley-McLaren configuration controlling the temporal focal point of identical mass ions with exit cap voltage. The higher potential gradient inside the trap results in a temporal focal point that is closer to the trap along the flight path. The spatial distribution of the ion packet inside the trap results in a different starting point for the time of flight, which is compensated by the kinetic energy difference. The identical mass ions that are closer to the entrance cap lag behind distance wise but obtain a higher velocity (kinetic energy). They will catch up with the ions that start closer to the exit cap but obtain lower velocity.

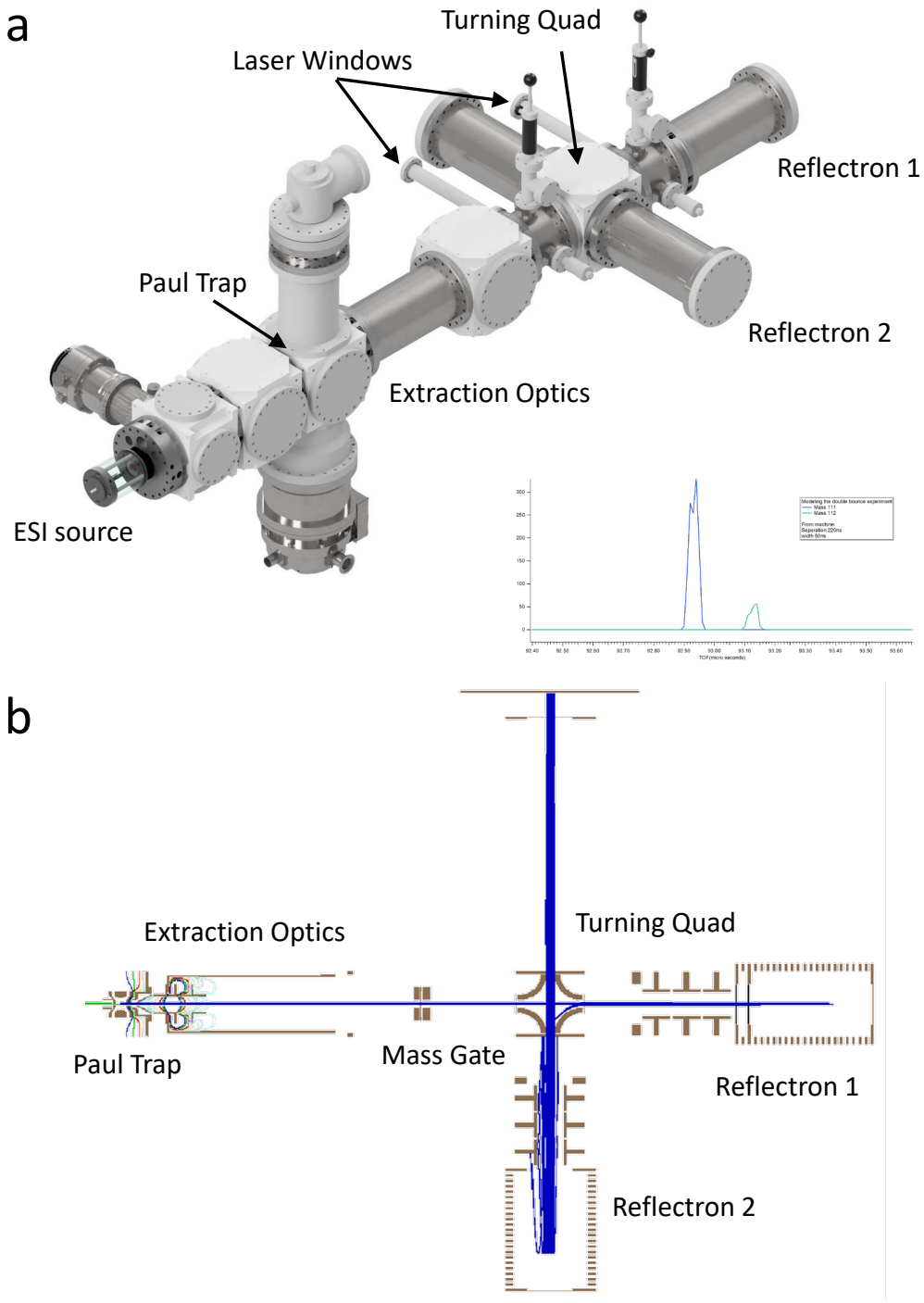

Figure 2.13. CAD model (a) and SIMION simulation (b) of the entire instrument. The inset in (a) is a simulated mass spectrum of EMIM and its ^{13}C isotopologue (m/z 111 and 112).

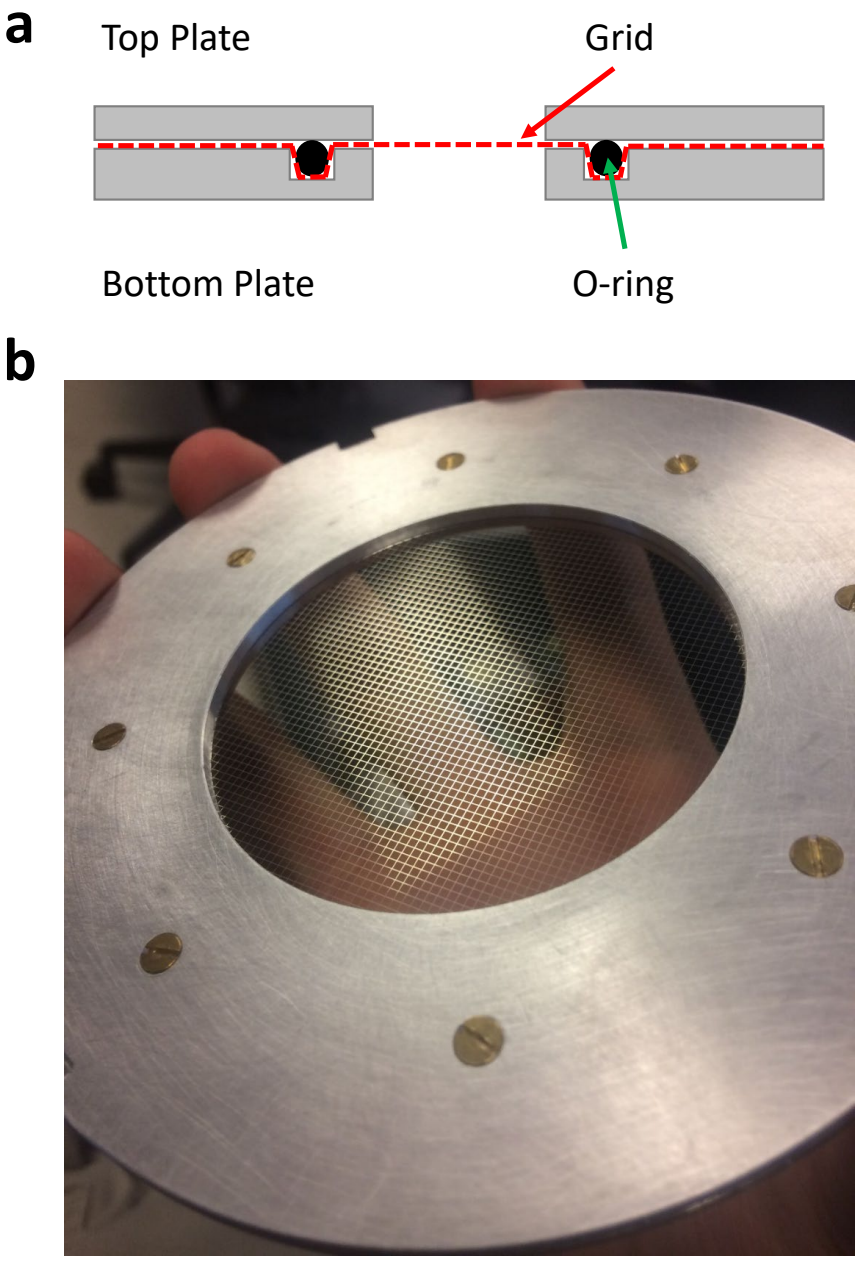

Figure 2.14. Cross section schematic (a) and photo (b) of newly designed mesh grid holder plate.

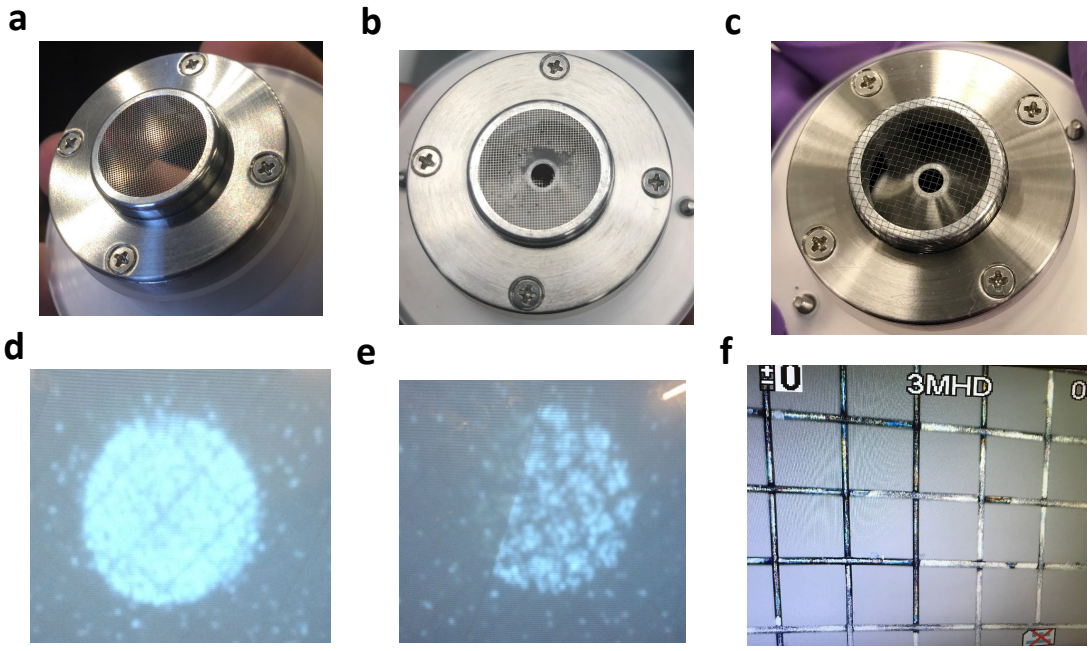

Figure 2.15. (a) Photo of a newly installed nickel electroformed mesh grid. (b) Nickel electroformed mesh grid after 6 months of operation. The holes are caused by ion etching. (c) Newly installed tungsten wire mesh grid. (d, e) Ion beam profile after passing through a grid imaged by a MCP detector and imaging phosphor screen. The grid lines are caused by ions colliding into the mesh grid. (f) The etching effect of the ion beam on the tungsten grid. The left portion is the area where the ion beam did not impact. The black color is the oxidized layer whereas on the right is the area where the ion beam did impact. The metallic color is the exposed tungsten with its oxidized layer etched away by the ion beam. The etching of the tungsten metal, however, is not significant and this mesh grid has been in operation for more than one year without the failure seen for the nickel grid shown in (b).

In addition to the construction of the grid holder, the grid material and manufacturing method also need close attention. Initially, 75 and 100 LIP (lines per inch) electroformed nickel grids were used. The thickness of these grids is thin, and nickel does not resist ion beam etching very well. These mesh grids have a lifespan of around 3 months of operation; a hole eventually forms in the ion beam path (Fig. 2.15 a, b). The ion imaging results confirm that the ions indeed collide with the grid (Fig. 2.15 d, e). A tungsten wire mesh is chosen instead due to tungsten's high resistance to ion etching (Fig. 2.15f, only the oxidized layer is etched off). The thicker material yielded by wire weaving instead of electroforming also increases the service life of the mesh grid. The tungsten wire mesh has been in service for more than a year without breakdown.

The ions are accelerated to 2.5 keV upon exiting the extraction grid. The Einzel lens and deflectors (Figs. 2.11 and 2.13) parallelize the beam divergence and steer the beam towards the laser interaction point. A potential switch is then used to re-reference the ion beam to ground as opposed to the ±2.5 kV float so that the rest of the machine does not need to be floated. Upon exiting the potential switch and before the first laser interaction region, a reflective mass gate is installed. The mass gate consists of three mesh grids. The two exterior grids are held at ground and the center grid is kept at a repulsive voltage (±2.7 kV) higher than the beam kinetic energy to block unwanted ion. The center grid is pulsed to ground (0 V) when the desired mass ion comes through.

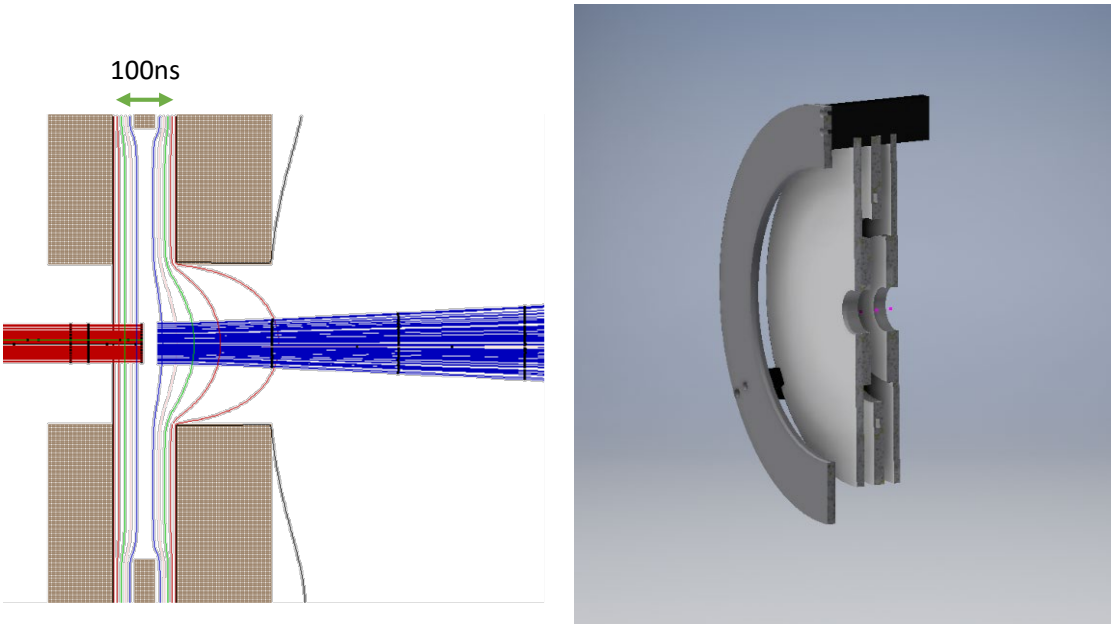

Figure 2.16. CAD model (right) and SIMION simulation (left) of the reflective mass gate. At 2.5 keV beam energy and 100 m/z, the gap between the plates corresponds to about 100 ns flight time, which limits the mass resolution. In this simulation, the grid on the back side is removed to increase ion transmission (~10% loss per grid). However, this creates fringe fields on the right side that can diverge the ion beam when the gate voltage is turned back on after the desired mass ions pass through. That can be compensated by opening the time window wider on the later side to allow some heavier mass ions to come through. This is typically not a problem. Otherwise, the three grids can be carefully aligned so that the nearly parallel beam can pass through the three grids and only suffer 10% loss.

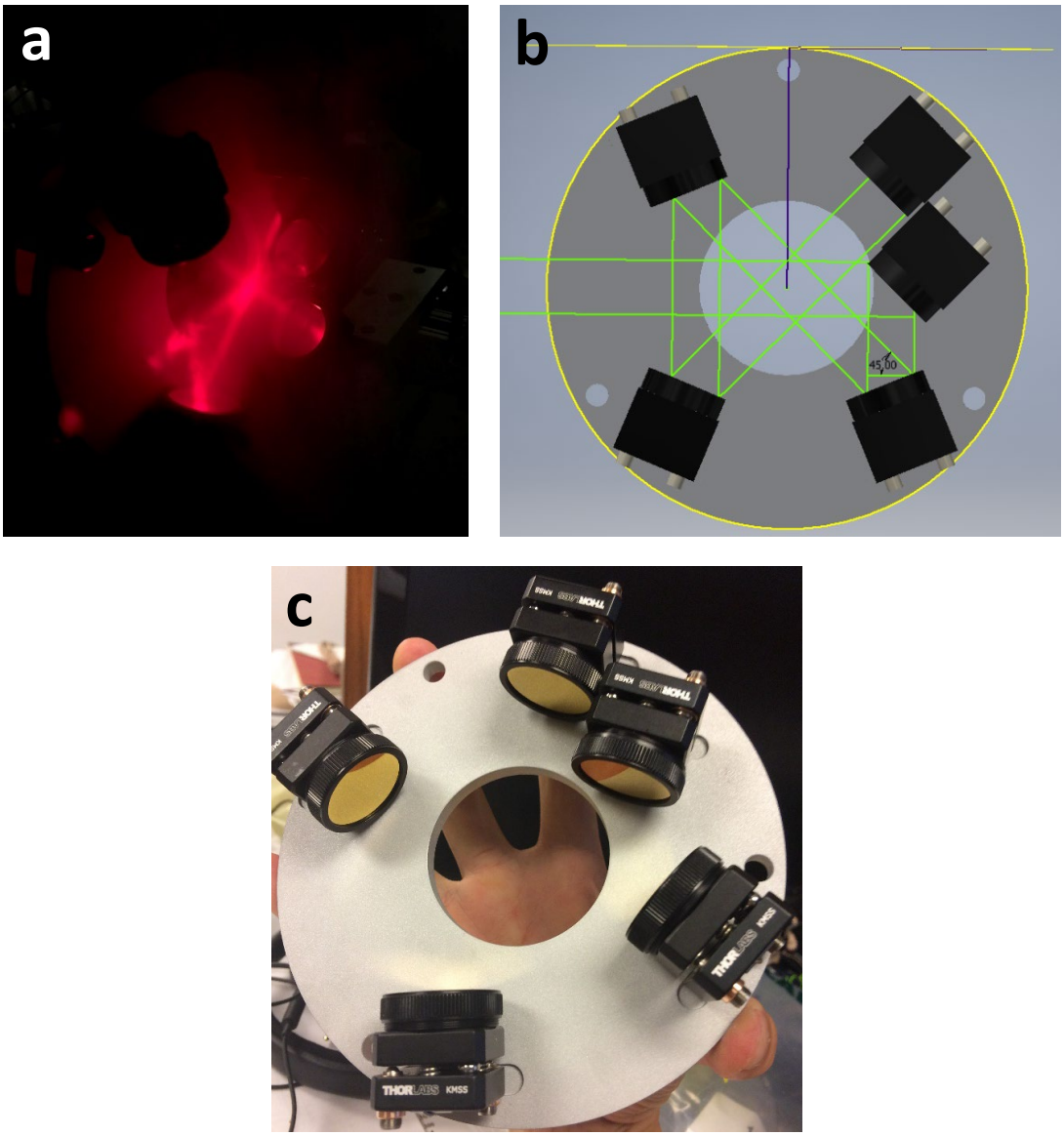

Figure 2.17. (a) A red diode laser is used to align the multipass assembly using condensed water vapor from liquid nitrogen to show the beam path. (b) The beam path shown in the CAD model. (c) The actual multipass assembly.

Once the ion beam is mass selected at the mass gate, the ion packet arrives at the laser interaction region. Due to the compact size of the instrument, the laser crossing is designed to fit within an 8-inch conflat vacuum flange. 1inch diameter gold mirrors on Thorlab KMS compact mirror mounts (Fig. 2.17 c) are used to minimize the size of the optical assembly. The laser passes 6 times through the ion beam axis, tripling the fragment yield compared to one single pass (Fig. 2.17a, b).

A miniature MCP detector is mounted on a translation vacuum feedthrough, allowing it to be moved into the ion beam at the laser interaction point to optimize the ion beam's spatial and temporal profile. It also provides a reference point for laser timing. Notice that the IR laser can create photoelectrons and cause a large signal on the MCP detector. For this reason it is important to ensure that the laser is blocked when lowering the MCP detector into the ion beam axis.

The ion packets containing the laser fragments and the undissociated parent ions fly at the same velocity towards the first reflectron (Fig. 2.1 and 2.13). The first reflectron is a two-stage gridless reflectron (Fig. 2.18), which creates a voltage gradient similar to that of the Wiley-McLaren configuration (Fig. 2.12). Two stage reflectrons allow better mass

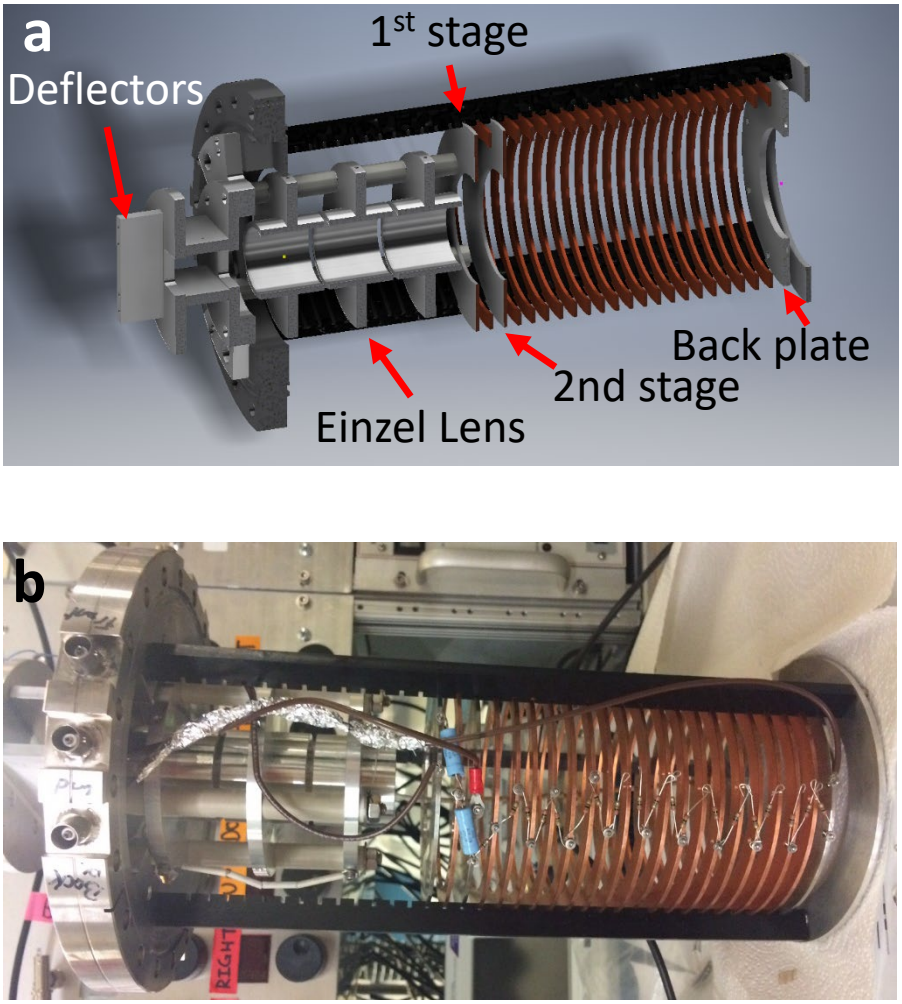

Figure 2.18. Two stage gridless reflectron. The 1st stage is kept at ground and the second stage voltage (repulsive, ±500 to ±1500 V) is tuned according to the distance of the next temporal focal point. The back plate is kept at a repulsive voltage (±2600 V) slightly above the beam energy. The rings are connected via a resistor chain to achieve a linear voltage gradient.

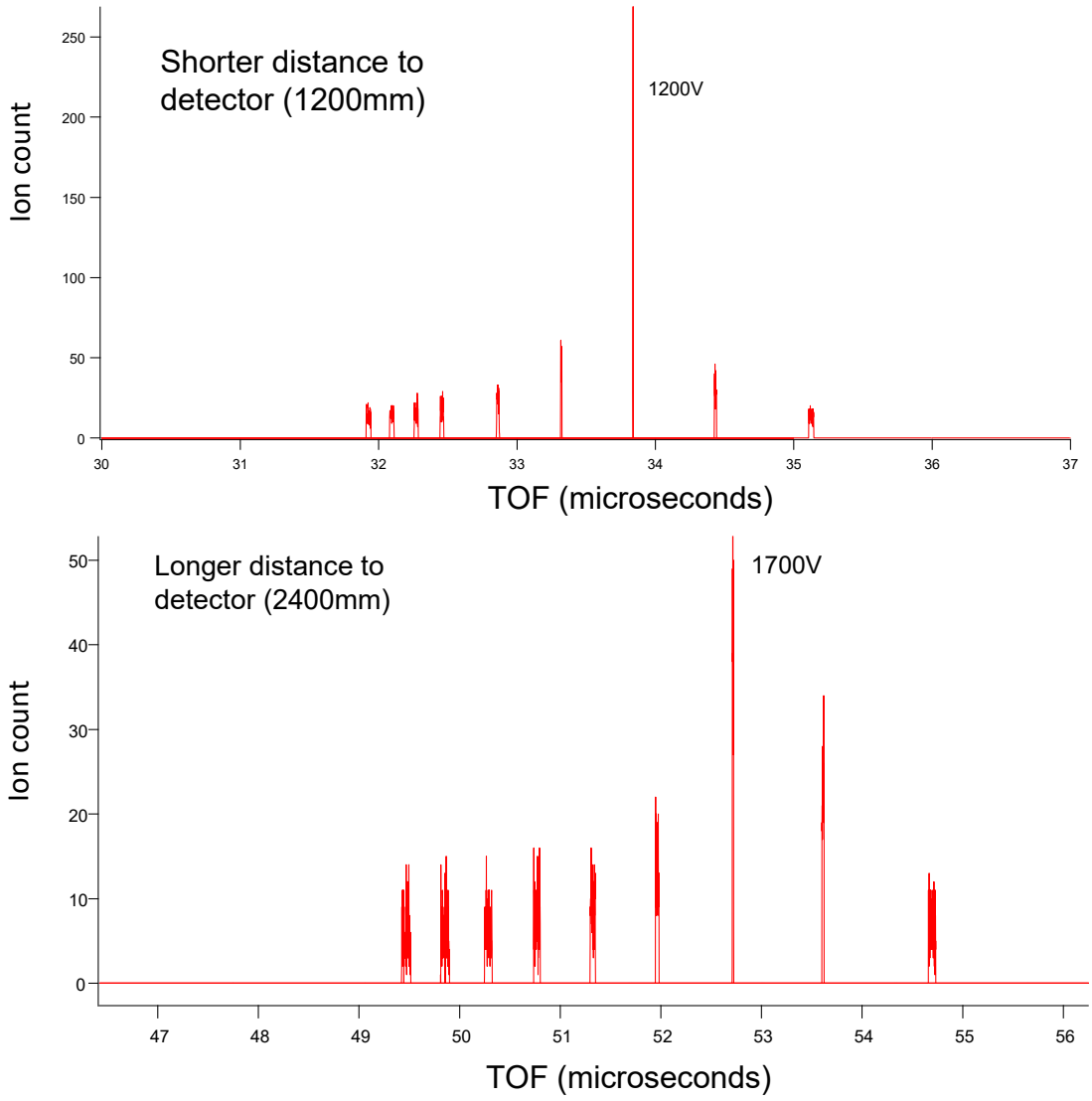

Figure 2.19. SIMION simulation of the arrival time profile at 1200 mm and 2400 mm distance from the two stage reflectron with various second stage voltages (100 V apart). The optimal temporal focusing can be achieved by tuning the second stage voltage. Higher voltages are required for longer focal distances.

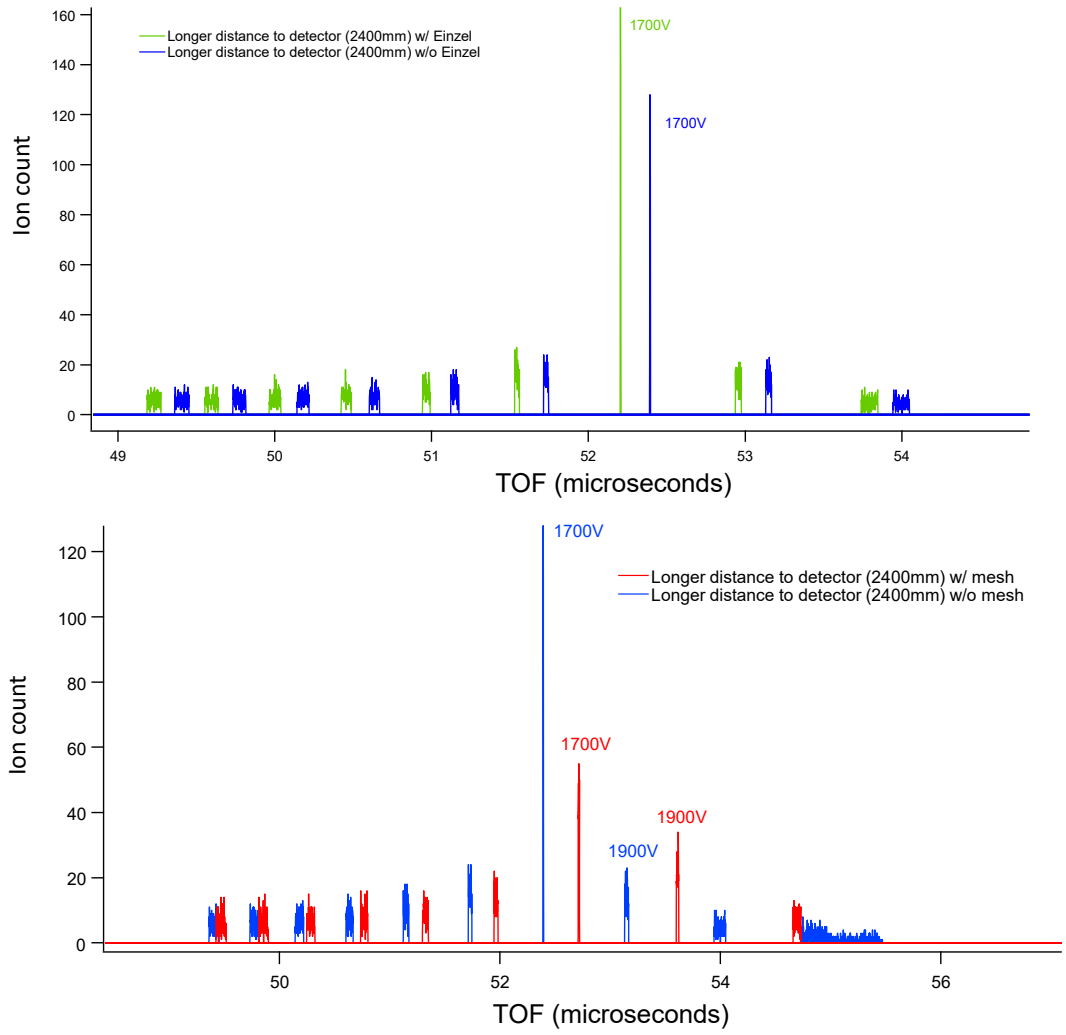

Figure 2.20. SIMION simulation of the arrival time profile at 2400 mm distance from the two stage reflectron with various second stage voltages. The second stage voltage tunes the arrival time width. About 1700 V is optimal for the 2400 mm distance. Each peak is a different voltage spaced by 100 V. The top panel compares the effect of the Einzel lens. The Einzel lens does not influence the ion packet time profile significantly - it only shifts the entire ion packet earlier in time (running in attractive mode). The bottom panel compares the time profile with and without grids on the two stage reflectron. The grid mesh does have some effect on the time profile but can be readily compensated by tuning the voltage.

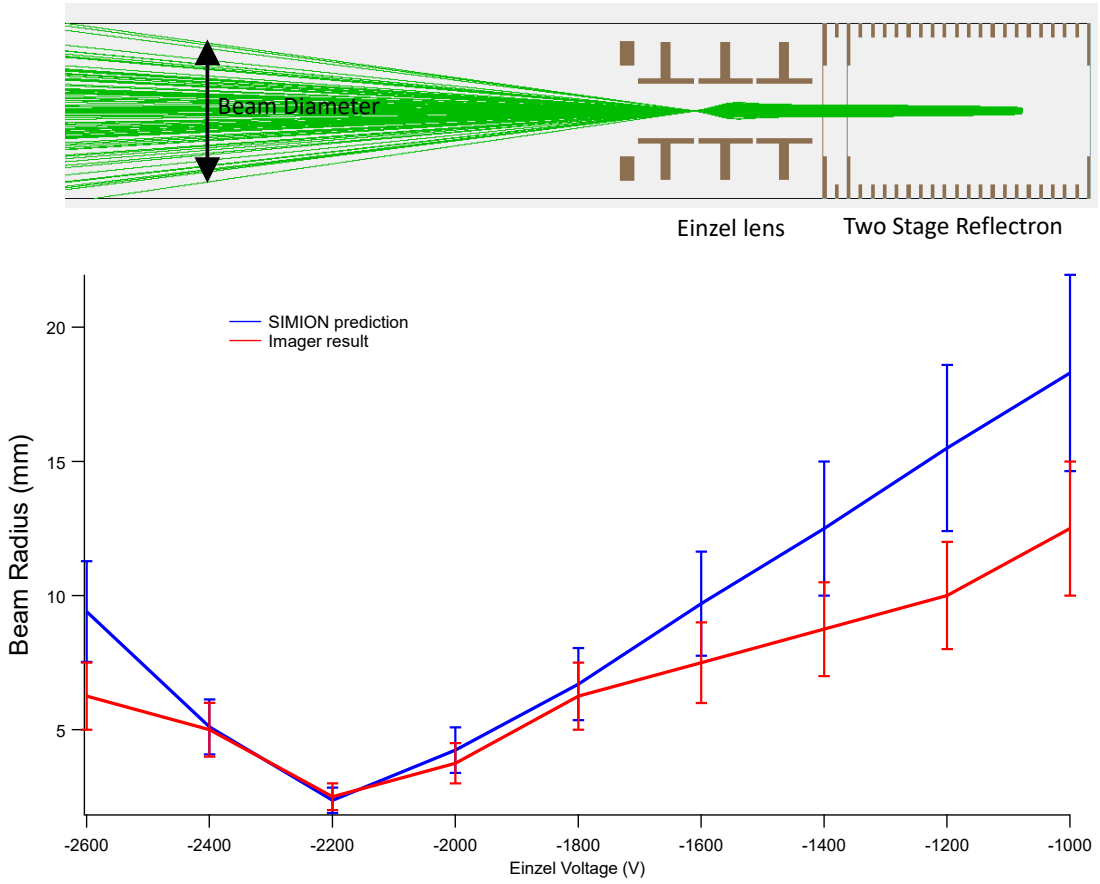

Figure 2.21. SIMION simulation of the focusing effect of the Einzel lens on the reflectron stack (blue trace) compared with experimentally measured results (red trace). The two results generally agree with each other. The simulated result displays higher divergence when the beam diameter is larger due to the sensitivity of the ion imager. Only the high intensity part of the beam can be seen; thus, when the beam is focused, the experimental results agree very well with the simulation. When the beam is large, the ions distributed near the edge are not detected by the imager, leading to underestimation of the beam radius.

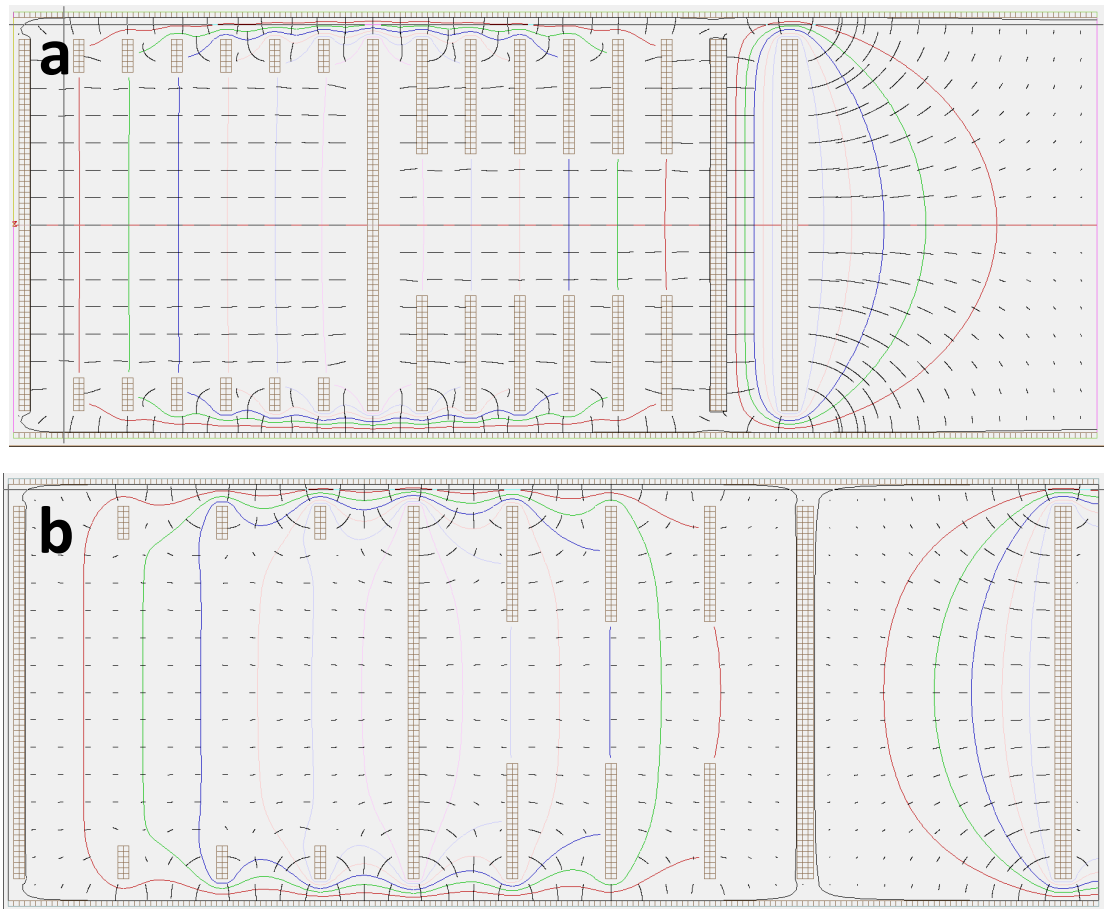

Figure 2.22. SIMION simulation of the reflectron stack with different ring distances. The colored lines are the equipotential contours and the black short lines are the electric field lines. Excessively large spacing results in significant fringe fields that can distort the beam.

separation and provides the ability to tune the position of the temporal focal point relative to the front plate of the reflectron (Fig. 2.19). In contrast, a linear reflectron has to be placed at the right distance relative to the laser crossing and the final detector. The gridless construction is designed to minimize ion signal loss (10% loss per grid pass, 40% loss when entering and exiting the two grids on the two stage reflectron). Gridless reflectrons operate comparably to their gridded counterparts and require only some compensation on the second stage voltage (Fig. 2.20). However, the gridless construction does create curvature in the electric field lines and potential surface, which creates divergence in the ion beam. Such divergence is compensated by the Einzel lens in front of the reflectron entrance (Fig. 2.21). The Einzel lens does not impact the time profile of the ion packet when correcting the spatial profile (Fig. 2.20), which is ideal.

One other detail pertinent to the design of the reflectron is the distance between the rings in the stack. If the spacing is too large, the fringe field can create divergence in the ion beam and result in signal loss (Fig. 2.22).

The first reflectron is tuned so that the temporal focal point overlaps with the second laser interaction point. The laser-irradiated ion packet is then turned towards the second reflectron, which has a temporal focal point at the position of the final MCP detector (Fig.2.1 and 2.13).

This design, incorporating a turning quad and two reflectrons, has one limitation due to the energy selectivity of the turning quad. The laser fragment has lower kinetic energy compared to that of the parent ion and is thus turned more, direction wise, by the turning quadruple. This results in mass selectivity on the final detector. A big mass change

upon photofragmentation is accompanied by a big energy change. Thus, when photofragments lose more than 10% mass compared to their parent ions, the turning quad needs to be tuned in voltage to detect the fragment. This is not ideal for UV-Vis laser experiments where various fragment channels exist and should be detected simultaneously. To achieve that goal, a dedicated laser interaction region, linear reflectron, and detector are attached behind reflectron 1. When operating with the linear reflectron, the reflectron 1 voltages are turned off to let the ion packet fly through (Fig. 2.23). The ion packet is then irradiated by a UV-Vis laser and passed into a tilted reflectron that is offset 2 degrees relative to the machine axis (Fig. 2.23).

2.1.5. Generation of Infrared Light

Photofragmentation of tagged ions is induced by a tunable optical parametric oscillator/amplifier (OPO/OPA) (*LaserVision*), which is able to scan from 600-4500 cm^{-1}. The OPO/OPA is pumped with ~600 mJ, 7 ns pulses at 1064 nm and a repetition rate of 10 Hz by a Nd:YAG laser (*Continuum Surelite EX* or *Spectra-Physics GCR-4*).. The 1064 nm light is first split into two beams using a beam splitter. The first of these beams is frequency doubled to 532 nm in a potassium titanyl phosphate (KTP) crystal in order to pump the OPO. In the OPO, the 532 nm light generates two new beams such that the energy of the input beam is conserved: a signal beam that ranges from 720 nm – 860 nm and an idler beam that ranges from 1400 nm – 2100 nm. Both the signal and idler beams are tunable because the proper phase matching conditions determined by nonlinear optics[10] are met based on the rotation of the KTP crystals in the OPO chain. The signal beam is monitored by a wavelength meter in order to determine the wavelength of the final beam produced. The tunable OPO idler beam is sent to the OPA system,

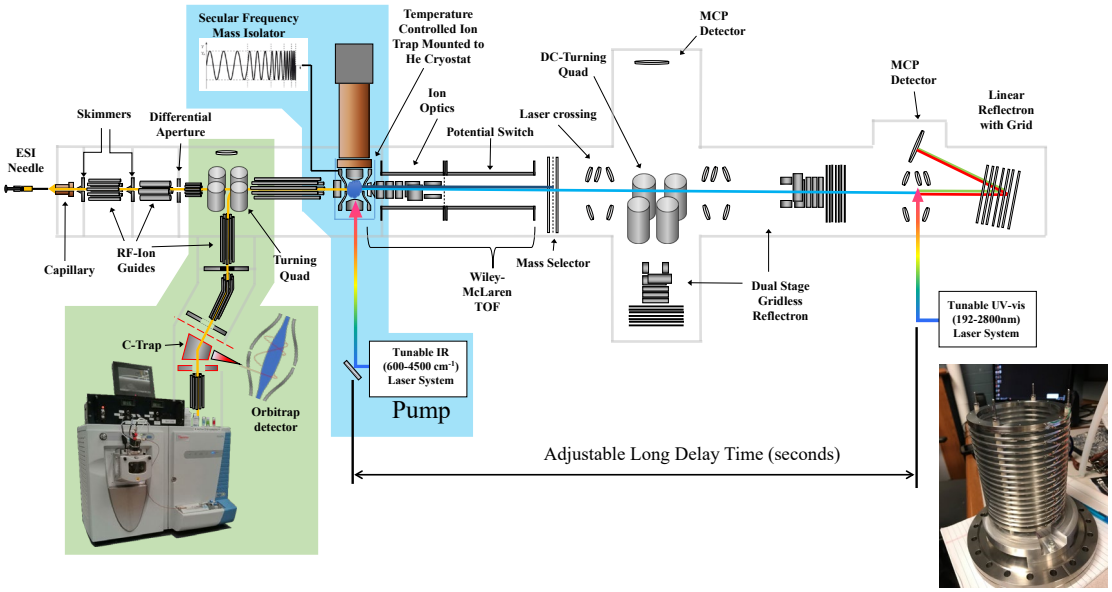

Figure 2.23. Extension of the instrument with a linear reflectron for detecting various fragmentation channels at the same time. The actual linear reflection is pictured at right bottom.

LaserVision tunable OPO/OPA Setup:

- 1064nm fundamental of Nd:YAG (9398 cm^{-1})
- 532nm 2nd harmonic of Nd:YAG (18797 cm^{-1})
- 710 - 860nm OPO signal (11630 cm^{-1} - 14080 cm^{-1})
- 1.4 – 2.1µm OPO idler (4800-7100 cm^{-1})
- 2.2 – 4.4µm OPA idler (2300-4700 cm^{-1})

$$\omega_{Pump} = \omega_{Signal} + \omega_{Idler}$$
$$k_{Pump} = k_{Signal} + k_{Idler}$$

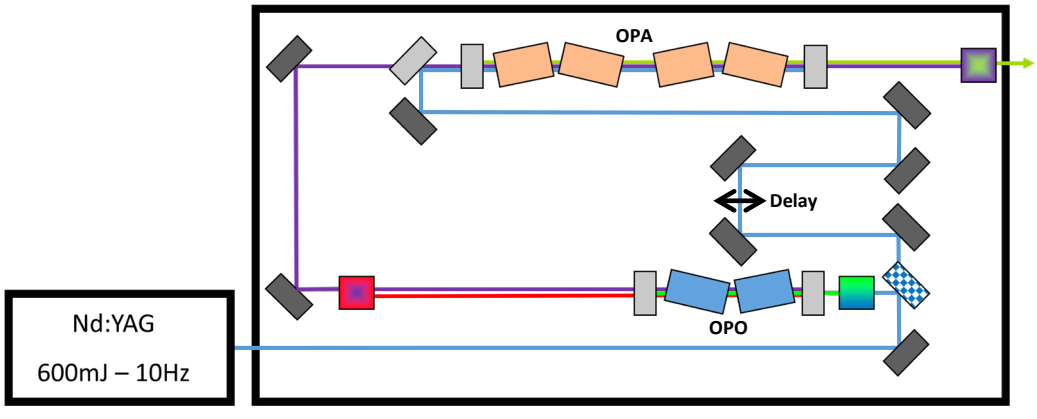

Figure 2.24. Schematic of the tunable IR laser system.

which is pumped by the second leg of the 1064 nm beam split off from the Nd:YAG laser. Here, the idler undergoes difference-frequency generation (DFG) in a chain of potassium titanyl arsenate (KTA) crystals to produce light from 2100-4500 cm^{-1} with a typical power output of 20 mJ/pulse at 4000 cm^{-1} once excess 1064 nm and OPA signal light are removed. To access the lower energy region, the OPA signal and idler are allowed to mix in a silver gallium selenide ($AgGaSe_2$) crystal. Here, DFG is used once again to generate light from 600-2400 cm^{-1}, with typical output power of 1 mJ/pulse. The entire set up is enclosed in a box that is purged with dry, CO_2-free air in order to avoid absorption of the IR beam by atmospheric water vapor and CO_2.

2.1.6. Generation of the Cryogenic Ion Vibrational Predissociation Spectrum

In order to generate the vibrational spectrum of the mass-selected ions, the loss channel of the messenger tag (that is, the formation of the photofragment) is monitored as a function of photon energy. This form of action spectroscopy is used rather than the nominal absorption spectroscopy (i.e. FTIR) because the ion density is too low to absorb observable quantities of laser light. Other action spectroscopy techniques, such as infrared multiphoton predissociation (IRMPD), infrared two-photon predissociation (IR2PD), and infrared predissociation (IRPD) serve as alternatives to messenger spectroscopy described in this Chapter and are discussed in Chapter 4. Other multi-laser experiments to obtain linear spectra, isomer/isotopomer selective spectra, rotational state selective spectra, and excited state spectra are also developed and discussed in various chapters. Some measurements require extensive averaging. These experiments require a data collection

mode where one laser is turned on and off every other shot to actively monitor the laser induced modulation free of signal intensity fluctuation. This is achieved by modulating the laser's Q-switch with an SRS delay generator while still firing the flash lamp at 10 Hz. The power meter signal is used to sort the data into 'laser on' and 'laser off' bins, which are then subtracted to obtain the net modulation caused by the laser interaction.

2.2 References

1. Yamashita, M.; Fenn, J. B. Negative-ion production with the electrospray ion-source. *J. Phys. Chem.* **1984,** *88*, 4671-4675.

2. Fenn, J. B.; Mann, M.; Meng, C. K.; Wong, S. F.; Whitehouse, C. M. Electrospray Ionization-Principles and Practice. *Mass Spectrom. Rev.* **1990,** *9* (1), 37-70.

3. Gerlich, D. Inhomogeneous RF-Fields - A Versatile Tool for the Study of Processes with Slow Ions. *Adv. Chem. Phys.* **1992,** *82*, 1-176.

4. Paul, W. Electromagnetic Traps for Charged and Neutral Particles. *Rev. Mod. Phys.* **1990,** *62* (3), 531-540.

5. Asvany, O.; Schlemmer, S. Numerical simulations of kinetic ion temperature in a cryogenic linear multipole trap. *International Journal of Mass Spectrometry* **2009,** *279* (2-3), 147-155.

6. Mikosch, J.; Fruhling, U.; Trippel, S.; Otto, R.; Hlavenka, P.; Schwalm, D.; Weidemuller, M.; Wester, R. Evaporation of trapped anions studied with a 22-pole ion trap in tandem time-of-flight configuration. *Phys. Rev. A* **2008,** *78* (2).

7. Kamrath, M. Z.; Relph, R. A.; Guasco, T. L.; Leavitt, C. M.; Johnson, M. A. Vibrational Predissociation Spectroscopy of the H_2-Tagged Mono- and Dicarboxylate Anions of Dodecanedioic Acid. *Int. J. Mass Spectrom.* **2011,** *300* (2-3), 91-98.

8. Wolk, A. B.; Leavitt, C. M.; Garand, E.; Johnson, M. A. Cryogenic Ion Chemistry and Spectroscopy. *Acc. Chem. Res.* **2014,** *47* (1), 202-210.

9. Wiley, W. C.; Mclaren, I. H. Time-of-Flight Mass Spectrometer with Improved Resolution. *Review of Scientific Instruments* **1955,** *26* (12), 1150-1157.

10. Demtroder, W. *Laser Spectroscopy - Basic Concepts and Instrumentation*. 4 ed.; Springer-Verlag: Berlin, Heidelberg, New York, Vol. 2.

CHAPTER 3

Spectroscopic Signatures of the Ground State and the Vibrationally Excited Iodide-Water Binary Complexes

The material in this chapter is adapted with permission from

Talbot, Justin J.*, Nan Yang*, Meng Huang*, Chinh H. Duong, Anne B. McCoy, Ryan P. Steele, and Mark A. Johnson. "Spectroscopic Signatures of Mode-Dependent Tunnel Splitting in the Iodide–Water Binary Complex." The Journal of Physical Chemistry A 124, no. 15 (2020): 2991-3001.

and

Nan Yang, Talbot, Justin J., Ryan P. Steele, and Mark A. Johnson. "Infrared spectroscopy of vibrationally excited iodide-water complex: a stringent test for vibrational state assignments and their anharmonicities" *In preparation*

3.1 Spectroscopic Signatures of Mode-Dependent Tunnel Splitting in the Ground State Iodide-Water Binary Complex

3.1.1 Introduction

The vibrational spectrum of the iodide-water binary complex, $I^- \cdot H_2O$, was the first of this class of halide monohydrate ions to be reported in 1996 by Okumura and co-workers.[1] This seminal study ushered in a new field that has shaped our understanding of ion hydration.[1-2] Subsequent studies of the $X^- \cdot H_2O$ $(X = F, Cl, Br, I)$ systems and their isotopologues, over the expanded frequency range of 600-4000 cm^{-1}, have provided a detailed picture of their vibrational level structures, which, in turn, have yielded stringent constraints on the potential energy surfaces that drive halide ion hydration.[3-13] Although many of the $X^- \cdot H_2O$ spectral features have been convincingly assigned to the expected normal-mode fundamentals, overtones, and combination bands based on C_s equilibrium structures, such as the configuration depicted in Figure 3.1A, the $I^- \cdot H_2O$ spectrum, recorded in the course of this work and displayed in Figure 3.1B, stands out as one of the most complex of the halide series with many labeled features in Figure 3.1B remaining unassigned after more than two decades of study.

A partial assignment emerges from temporarily overlooking the detailed multiplet structures and focusing instead on the two sets of transitions centered near 3400 and 3700 cm^{-1}. Specifically, the asymmetric equilibrium structure of the $I^- \cdot H_2O$ complex (Figure 3.1A) qualitatively accounts for the widely split oscillator position in the OH stretching region: a strong set of bands (β_{13-16} near 3400 cm^{-1}) have been nominally assigned to the

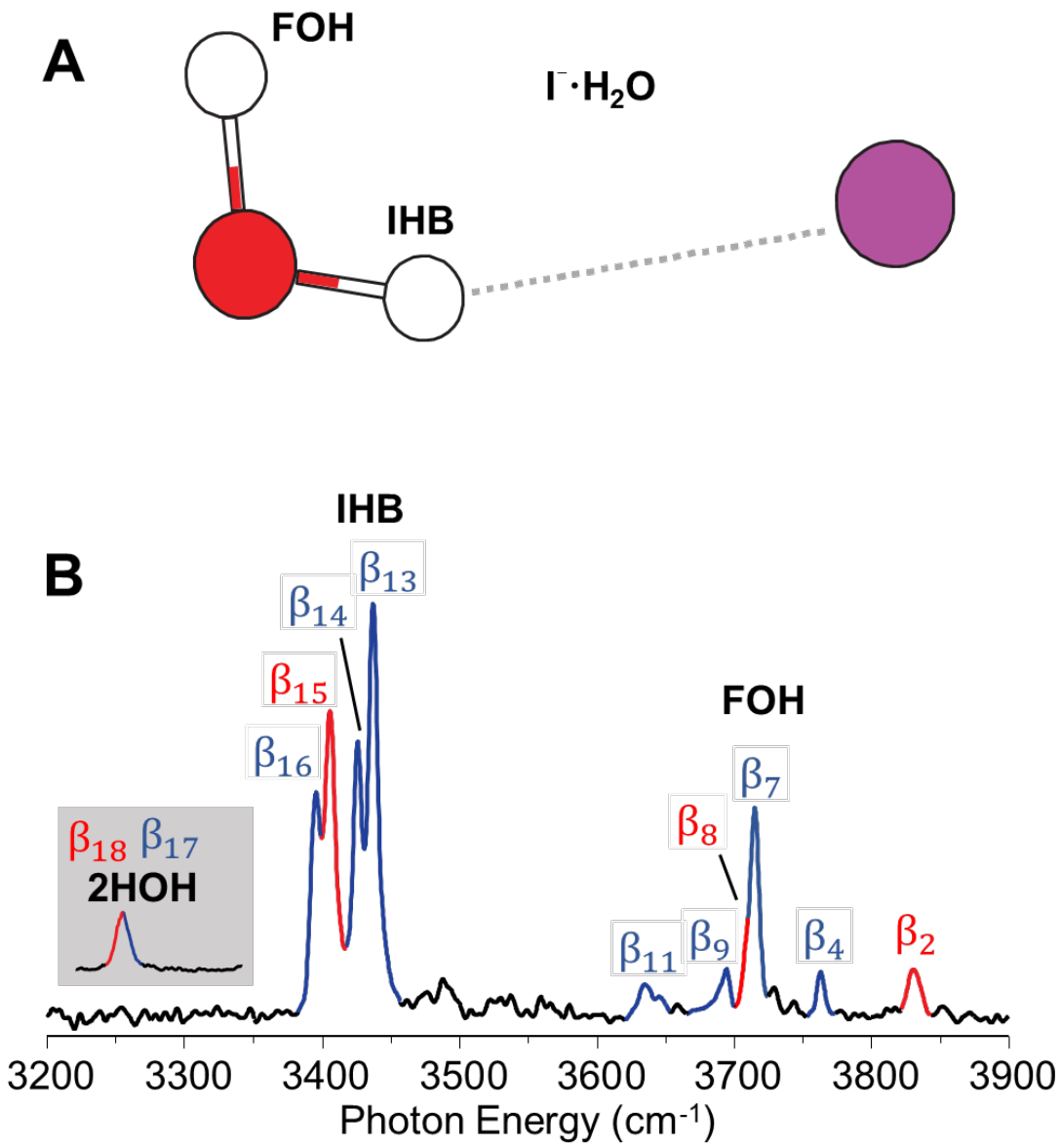

Figure 3.1: Asymmetric minimum-energy structure of $I^-\cdot H_2O$ and its vibrational predissociation spectrum. (A) Minimum-energy structure of $I^-\cdot H_2O$ from the MB-nrg potential (ref. 7) **(B)** Vibrational predissociation spectrum of $I^- \cdot H_2O$ at 20 K with low laser power to ensure the maximum number of photons absorbed at any transition is one (linear regime). The inset highlighted by the gray background is an Ar-messenger, tagged predissociation spectrum in the same region to reflect transitions to states that lie below the dissociation threshold.

red-shifted OH group that is bound to the ion (hereafter denoted IHB for "ionic hydrogen-bonded"),[5-6] and weaker features centered at 3714 cm^{-1} (labeled β_{2-11}) have been attributed the free-OH group (denoted FOH). Some of the differences in the fine structure associated with these motions can then be attributed to the differences in the transition types associated with the two bands, with the transition to the fundamental in the IHB being primarily parallel, while the transition to the fundamental in the FOH has mixed parallel and perpendicular character. Spectroscopically, the two different transition types lead to primarily $\Delta K_a = 0$ rovibrational transitions carrying most of the intensity for the IHB motion, which would result in a single feature (at this rather modest resolution of ~3 cm^{-1}) in the lower-energy region. The component of the transition moment that is perpendicular to the IO axis for the FOH transition would lead to strong transitions with $\Delta K_a = \pm 1$, and, indeed, the extra peaks in the FOH region have been attributed to partially resolved rotational structure.[6] This difference in transition types can be traced to the angles between the two OH bonds (which are roughly the orientations of the transition moments) and the IO axis (which is approximately the a rotational axis for this ion), as well as the expected partial locality of the OH stretching motions.

While the above description qualitatively accounts for some of the observed fine structure, it does not explain the curious quartet structure (β_{13-16} in Figure 3.1B) of the IHB region near 3400 cm^{-1}, which was first reported by Okumura and coworkers;[1] this feature is absent in other halide-water complexes,[10] as well as the Ar-tagged spectrum of $I^- \cdot H_2O$.[5] One aspect of the ion-water interaction that complicates the $I^- \cdot H_2O$ spectrum relative to the smaller halides is that its barrier to exchanging the bound OH group with the free OH group is smallest in the halide series. Earlier calculations[8, 14] placed this barrier at

105-185 cm^{-1}, while more recent work[7] supports the smaller value, reporting a barrier of 102 cm^{-1}. These values can be compared to the frequency (~160 cm^{-1}) attributed to the in-plane bending mode,[8] which is the motion that connects the two equivalent minima on the potential surface through the C_{2v} transition-state structure. The similarity of this frequency to the height of the barrier points to a scenario in which the ground vibrational state should exhibit relatively large tunneling splittings. These splittings would be expected to be partially quenched with OH stretch excitation, however, due to the larger effective barrier when an anharmonic v=1 state is accessed. This behavior could account for doublets in the OH-stretching regions, but it nevertheless does not explain the quartet structure observed in the IHB region of the spectrum nor the series of transitions in the FOH region.

In the present study, the $I^- \cdot H_2O$ spectrum is revisited using tools that have been developed over the past decade. On the experimental side, these developments include the ability to control clusters' internal energy using cryogenic ion traps and the ability to obtain linear spectra without the need for a weakly bound adduct (mass tag), using two-color IR-IR double-resonance spectroscopy.[15] These approaches are combined with knowledge of the frequencies of the six vibrations in this ion from the argon-tagged $I^- \cdot H_2O$ spectrum over a broader spectral range,[8] along with theoretical predictions of the level structure by application of a fully coupled, six-dimensional eigensolver model[16-19] on a new, MB-nrg many-body potential energy surface.[3, 7, 11] These methods yield a consistent assignment scheme and reveal how vibrational mode-dependent tunneling splittings, soft-mode combination bands, and partially resolved rotational fine structure (modified by nuclear

spin statistics) all combine to yield the observed multiplet patterns in the spectrum of the cold $I^- \cdot H_2O$ complex.

3.1.2 Overview of Experimental and Computational Approaches

Experimentally, the $I^- \cdot H_2O$ cluster was prepared with electrospray ionization and cooled in a temperature-controlled ion trap that has been described previously,[15, 20] and its vibrational spectrum was recorded by infrared photodissociation with several complementary laser configurations.[15, 20]

Specifically, The $I^- \cdot H_2O$ cluster ions were obtained by electrospraying 5 mM $EMIM^+I^-$ acetonitrile solution in a humidity-controlled purge capsule. Subsequently, the ions were loaded into a temperature-controlled Paul trap kept at 20 K with helium buffer gas to cool and store the ions. The IRPD and IRMPD spectra were obtained by irradiating the mass-selected ions with a pulsed (10Hz, 8ns) tunable OPO/OPA IR laser (Laservision) which results in dissociation of the iodide-water complex upon resonant excitation by single-photon or multiphoton absorption, respectively. The fragment ion (I^-) is separated from the parent ion ($I^- \cdot H_2O$) with a secondary mass spectrometer and detected to monitor IR absorption by the parent ion. For the IRPD experiment, the laser power was tuned to about 0.7 mJ/pulse to avoid multiphoton absorptions, and the vibrational features below the dissociation threshold will not be observed in this mode. For the IRMPD experiment, the laser power was tuned to 20 mJ/pulse to maximize multiphoton absorptions.

The dissociation energy of this complex has been reported to be in the range 3410-3510 cm^{-1} using threshold electron photodetachment of the anion,[21] which lies in middle of the OH stretching range. As such, a changeover from one- to two-photon dissociation will occur, depending on whether the upper state in the transition lies above

or below the dissociation energy and, in the case of the former, the dissociation lifetime of the metastable state. This effect was explored by reducing the laser pulse energy to avoid multiphoton absorption so that transitions to states with energies below the dissociation threshold (after accounting for residual internal energy) are suppressed in the spectrum. For example, the bend overtone mode near 3200 cm^{-1} is missing in the low-power, linear predissociation (PD) spectrum (complete trace in Figure 3.1B) but can be observed using Ar-tagging methods (gray inset in Figure 3.1B); this observation establishes that the effective dissociation energy at the experimental temperature lies between 3200 and 3400 cm^{-1}. As discussed below, this apparent discrepancy between these values and the previously reported dissociation energy[21] is likely due to the fact that the excited states accessed in the transitions shown in Figure 3.1 near 3400 cm^{-1} ($\beta_{13\text{-}16}$) are situated just above dissociation threshold but are surprisingly long-lived.[22] Steps taken to confirm that the spectrum shown in Figure 3.1 results from the absorption of a single photon are discussed in the Supporting Information. Two-photon processes could be observed by increasing the laser fluence above that used to obtain the spectrum in Figure 3.1 by about a factor of three.

When a PD spectrum is heterogeneous (because of isomers, rotational and/or vibrational state populations, and, in this case, tunneling splittings), overlapping spectral contributions from different ground-state populations can be isolated with two-color, IR-IR double-resonance, hole-burning spectroscopy.[15] These spectra were measured using the IR^2MS^3 capability of the photofragmentation mass spectrometer,[15] where mass-selected ions were irradiated with the pump laser first and mass-separated in the secondary mass spectrometer to eliminate the photofragment from the pump. The remaining parent ion

was then irradiated by the probe laser and mass-separated again in the third mass-separation stage, where the fragment from the probe laser was monitored. When acquiring a ground state-selective, double-resonance dip spectrum, the probe laser was fixed on a frequency that is potentially unique to one of the components that contribute to the overall spectrum. The pump laser was then scanned through the entire spectrum, and when it excited transitions originating from the level monitored by the probe laser, the probe-laser fragment yield was decreased. These depletions were recorded as a function of pump-laser frequency, and the resulting "dip" trace revealed the spectrum associated with the rovibrational state selected by the probe laser. More complicated patterns, including those featuring photoinduced enhancement of the fragment from the probe laser, were also observed when the states excited by the pump laser were either stable or exhibited longer dissociation lifetimes than the time between the pump and probe excitations (about 30 microseconds). This scenario is relevant to the present IR-IR studies because, as mentioned above, many of the upper levels in the OH stretching region of the $I^- \cdot H_2O$ spectrum are sufficiently long-lived to display such enhancement. Although excited-state dynamics are complex and likely state-dependent, this situation was exploited to gain qualitative insight into the quantum composition of the levels involved in the quartet, as discussed in the Figures 3.2 and 3.3. More detailed discussion of the excited state spectra are included in Chapter 3.2.

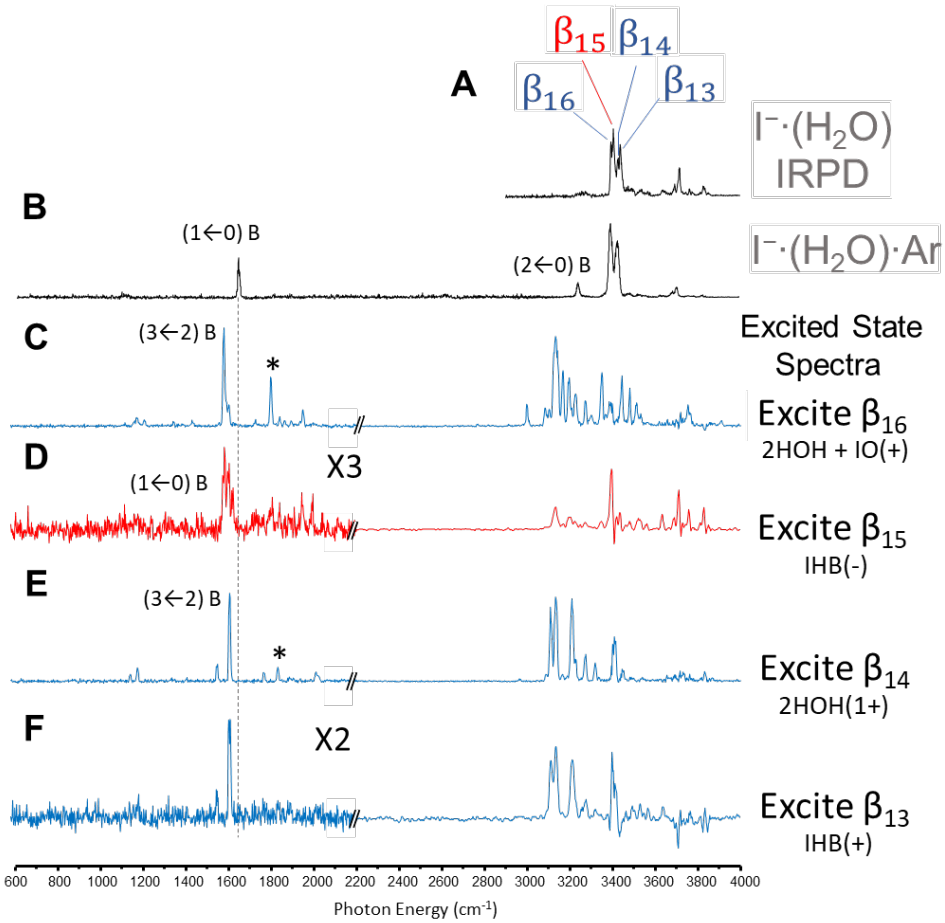

Figure 3.2: Excited State Spectra of $I^-\cdot H_2O$. Vibrational predissociation spectra obtained with **(B)** and without **(A)** Ar messenger tag. The smaller binding energy of Ar tag allows the observation of bands below the H_2O's binding energy whereas the tag-free experiment allows the observation of the quartet pattern. By fixing the first laser on one member of the quartet and scanning the second laser, the excited state's spectral features were obtained **(C-F)**. Even though the first laser excitation puts the system slightly above the dissociation threshold, the lifetime is extremely long and the majority of the excited clusters remains undissociated at the second laser interaction point. Lower energy bands can now be observed due to the sum of the two absorbed photon exceeding the dissociation limit by more than 1000 cm^{-1} which results in faster dissociation of the cluster.

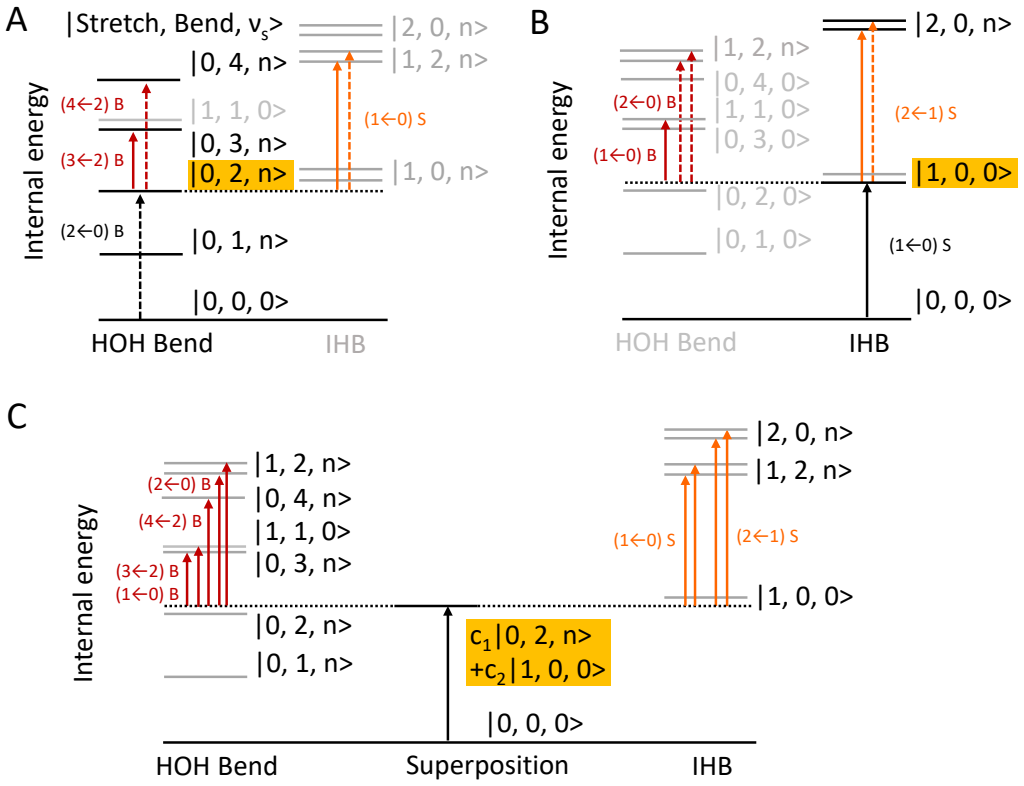

Figure 3.3: Energy level diagram for the excited state spectra displayed in Fig. 3.2. The black arrows indicate the pump laser transition that creates the excited state, the red and orange arrows indicate HOH bend and OH stretch transitions originating from the excited state, respectively. The quantum number is denoted as |Bend, Stretch, ν_s> where Bend represents the quantum number of HOH bending mode, Stretch represents the OH stretching mode quantum number and ν_s denotes the soft mode quantum numbers in general. **(A)** displays the transitions originating from the v=2 level of the HOH bend where the dashed transitions are not allowed on the harmonic level, **(B)** displays the transitions with the v=1 level of the OH stretch as the initial state and **(C)** shows the situation when the superposition state of the bend and stretch as a result of Fermi resonance is prepared as the initial state, the transitions initiating from such state can access both the bend and the stretch levels manifold.

The rovibrational state-selective two-color IR-IR double-resonance hole-burning dip spectra were measured in an IR^2MS^3 instrument, where mass-selected ions were irradiated with the pump laser first and mass-separated in the secondary mass spectrometer to eliminate the fragment. The remaining parent ion was then irradiated by the probe laser and mass-separated again in the third mass-separation stage, where the fragment from the probe laser was monitored. When acquiring a state-selective, double-resonance dip spectrum, the probe laser was fixed on a frequency that was potentially unique to one or several states that share the same transition. The pump laser was scanned through the entire spectrum, and when it was on resonance with the parent ions selected by the probe, the parent ions were photodissociated and the photodissociation fragment signal generated by the probe laser decreased. This depletion was recorded as a function of pump laser frequency, and the resulting trace revealed the spectrum associated with the population in the rovibrational state selected by the probe laser. However, in the $I^- \cdot H_2O$ system, the binding energy is close to the photon energy and the ions that absorbed one photon exhibited a long lifetime compared to the delay between the two lasers; therefore, some of the ions could have absorbed one photon and not dissociated prior to interacting with the probe laser. Such processes add extra complexity to the two-laser experiment since, if the first photon absorption results in a new spectral feature of the ion at the probe frequency, the pump laser excitation can *enhance* the probe laser in photodissociation and create an enhancement feature in the double-resonance dip spectrum (Fig. 3.5D). Specifically, the enhancement is a result of making the population that was previously transparent to the probe laser absorb at the probe frequency. In this experiment different rovibrational states' populations have different spectral features, and, by fixing the probe laser on a unique

feature, one can detect the population in a specific rovibrational state; however, if the pump laser excitation changes the spectral feature of the other states that are not being probed and makes them absorb at the probe frequency, the population that absorbs at the probe frequency increases, hence creating an increase in detected population.

Calculations of the rovibrational spectra were performed via numerical solution of the Schrödinger equation in a basis set of six-dimensional harmonic oscillators and prolate symmetric top basis functions. In this calculation, five of the six available internal degrees of freedom were represented as normal-mode coordinates that were computed at the C_{2v} reference structure. The sixth degree of freedom, the in-plane bend, was described by a rigid, curvilinear rotation of the water molecule about the principal axis that is perpendicular to the plane of the molecule and intersects the molecule at its center of mass. Eight quanta of excitation were included in all normal-mode coordinates except the in-plane bend, which, as a result of the double-well anharmonicity, required ten quanta for convergence. Gauss-Hermite quadrature was used for evaluating the potential-energy and dipole-moment integrals. The large size of the resulting vibrational Hamiltonian matrix required the use of the PRIMME iterative diagonalization routine.[18] After exhaustive benchmarking, the six-dimensional potential energy calculations of $I^- \cdot H_2O$ were performed with the analytic MB-nrg potential energy surface.[23] The dipole moment hypersurfaces were calculated using the MP2 level of theory with the aug-cc-pVTZ-PP basis set within the frozen-core approximation.[24] All dipole moment calculations were performed using a development version of the Q-Chem software package.[17] The rotation constants were computed for each vibrational state by averaging over the fully coupled, six-dimensional vibrational wavefunctions. The axes were defined, starting from the C_{2v}

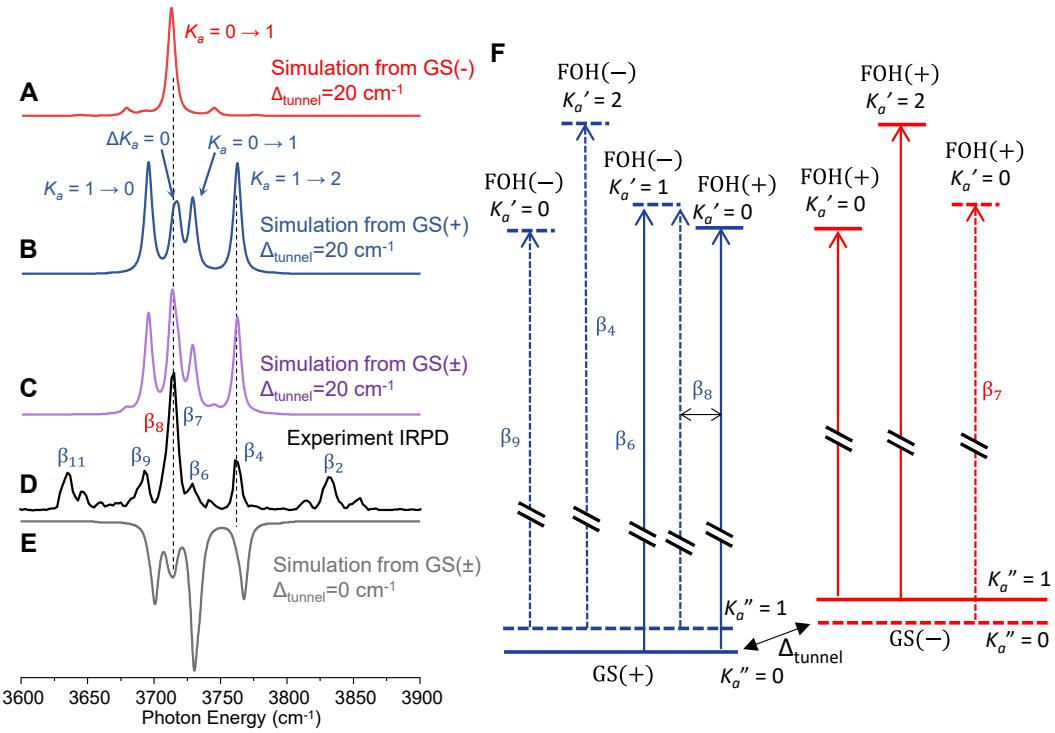

Figure 3.4: Comparison between simulated FOH spectra at different tunneling splittings with the experimental spectrum at 20 K. (A, B) Simulated rovibrational spectrum based on a 20-cm^{-1} ground-state tunneling splitting for transitions originating from K_a levels built off of the GS(−) and GS(+) states, respectively. **(C)** Simulated spectrum with a 20-cm^{-1} ground-state tunneling splitting initiated from all thermally populated GS(±) and K_a levels, including nuclear spin statistical effects. (**D**) Experimental IR predissociation spectrum. (**E**) Simulated spectrum obtained with a 0-cm^{-1} tunneling splitting, based on thermally populated GS(±) and K_a levels. (**F**) Energy level diagram illustrating the transitions involved, in which the solid and dashed lines are used to differentiate between states that are symmetric (solid) and antisymmetric with respect to exchange of the two hydrogen atoms. The tunneling splitting between GS(-) and GS(+) is indicated with the double-sided arrow.

reference structure, by aligning the *a* axis with the C_2 symmetry axis and the *c* axis perpendicular to the plane of the molecule.[25] Full details of these calculations, including extension to a vibrationally adiabatic approach, are provided in the Supporting Information.

3.1.3 Assignments of partially rotationally resolved vibrational bands

The spectroscopic assignments in the following discussion are made in two parts. In the first, an analysis of the rotational structure of the bands near 3700 cm^{-1} is performed in order to obtain an approximate ground-state tunneling splitting. This discussion is then followed by an analysis of the quartet feature near 3400 cm^{-1}.

Figure 3.4D presents an expanded version of the experimental spectrum in the region of the FOH fundamental. Above the spectrum (purple trace, 3.4C) are the results of a spectral simulation, performed using PGOPHER[26] with parameters that are provided in Table 3.1.

Table 3.1: Parameters for rotational structure simulation of the free-OH stretch band

	Energy (cm^{-1})	$\widetilde{A}$ **(cm^{-1})**	$\widetilde{B}$**(cm^{-1})**	$\widetilde{C}$ **(cm^{-1})**	$D_{GS(+)}$ **(a.u.)**	$D_{GS(-)}$ **(a.u.)**
GS(+)	0	16.785	0.085	0.085	--	--
GS(−)	20	17.202	0.085	0.084	--	--
FOH(+)	3714	16.526	0.085	0.085	-0.0075(a)	-0.0165(b)
FOH(−)	3712	16.734	0.085	0.085	0.014(b)	0.0027(a)

These parameters include the transition dipole moments and vibrationally averaged rotational constants, which were obtained from the six-dimensional calculation, described

above, as well as the tunneling splitting and FOH transition frequency, which were adjusted to obtain agreement with the measured spectrum. This purple trace is the sum of traces 3.4A (red) and 3.4B (blue). Those traces isolate the contributions from transitions originating from the lower [GS(+), blue] and upper [GS(-), red] members of the tunneling doublet. Figure 3.4F depicts the rovibrational level structure corresponding to these transitions. In this panel, solid and dashed lines are used to differentiate states that are symmetric (solid) and antisymmetric (dashed) with respect to exchange of the two hydrogen atoms. When the ground-state tunneling splitting is small, the lowest-energy state that is antisymmetric with respect to exchange of the hydrogen atoms is the $K_a'' = 0$ level of the GS(-) member of the tunneling doublet, and this level will have three times the population of the $K_a'' = 0$ level in the GS(+) manifold, due to nuclear spin statistics. On the other hand, when the tunneling splitting is larger than the energy of the $K_a'' = 1$ level of the GS(+) member, the $K_a'' = 1$ level of the GS(+) tunneling member will become the lowest-energy antisymmetric state and have three times the population of the $K_a'' = 0$ level of the GS(+) manifold. The latter situation is illustrated in panel 2F. The population of higher-energy states within either symmetry class (with respect to exchange of the hydrogen atoms) will be determined by the usual temperature-dependent Boltzmann factor.

Since the tunneling splitting is expected to be mostly quenched by excitation of one of the OH stretches, the red pattern of transitions in Figure 3.4 will shift relative to the blue pattern by roughly the value of the ground-state tunneling splitting. This shift is the origin of the difference between traces 3.4C and 3.4E, while the 3:1 nuclear spin weighting for population of the K_a'' levels is the reason for the different intensity patterns of the blue and

red traces in Figure 3.4. The important point is that, when the GS(±) tunneling splitting is taken to be small (trace 3.4E), the simulated trace does not match the recorded trace (3.4D). The agreement improves dramatically when a ground-state tunneling splitting is 20 cm^{-1} and an excited state tunneling splitting of -2 cm^{-1} are used. The 20 cm^{-1} value for the ground-state tunneling splitting is accidentally close to the ~17 cm^{-1} energy difference between $K_a'' = 1$ and $K_a'' = 0$ levels in this ion. Therefore, the main component of the FOH rovibrational profile can be captured by a combination of vibrational tunneling in the soft in-plane bend mode, rotational fine structure, and nuclear spin-weighted state populations.

To further explore the magnitude of the tunneling splitting and the assignment of the spectrum in the region of the quartet, the results of two-color, IR-IR double-resonance experiments have been analyzed. In this part of the study, the probe laser was fixed at three features in the rotational contour of the FOH feature. The resulting spectra are shown in panels C to E of Figure 3.5, where the probe frequency is indicated by the colored arrow. These spectra were obtained at higher laser power (Fig. 3.5B) than the trace reported in Figure 3.1B, which has been reproduced (Fig. 3.5A) for comparison. The patterns in the two power regimes differ in the region of the lower-energy bands in the bend overtone and IHB regions (β_{13-18}), while the FOH structure generally remains intact. As mentioned above, the appearance of $\beta_{17,18}$ at higher power in a single-laser experiment is due to the fact that the excited state (the v =2 level of the bending mode) lies below the dissociation threshold of the ion. The power-dependent intensity profiles of the β_{13-16} features that make up the quartet are more complicated. These effects arise because the involved excited states are long-lived and exhibit highly structured, mode-dependent absorption spectra that

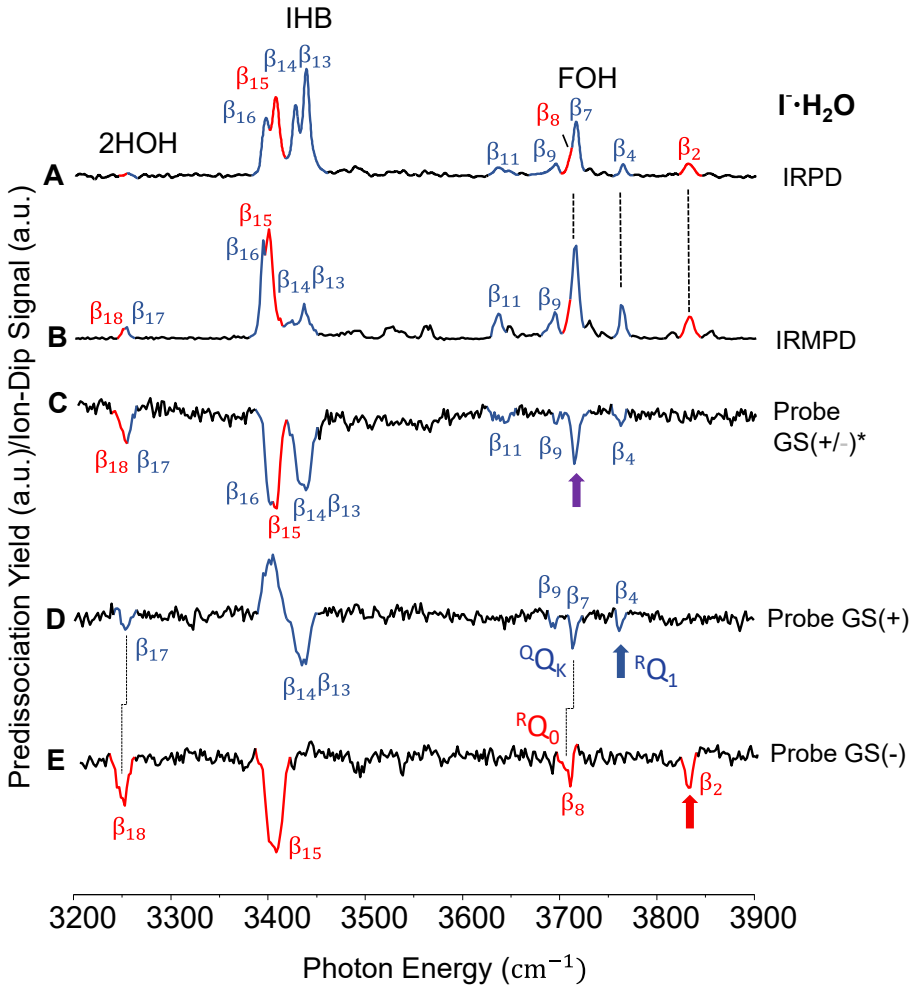

Figure 3.5: Double-resonance spectra, probing specific K_a levels of the ground vibrational state(s). (A) Linear infrared photodissociation spectra obtained with low laser power (0.7 mJ/pulse, 8 ns pulse width, 5 mm beam diameter) at 20 K. **(B)** The high-power (20 mJ/pulse) IRMPD experimental spectrum at 20 K. **(C)** Experimental state-specific double-resonance spectra obtained by probing the peak indicated by the purple arrow, which putatively includes population from both GS(+) and GS(-) states. The main contribution is nonetheless attributed to GS(+), arising from the β_7 transition, and the remaining contribution of GS(-) arises from the β_8 transition. **(D,E)** Double-resonance spectra obtained by probing the peaks indicated by the color-coded arrows, which reflect the GS(+) and GS(-) population, correspondingly.

mediate the cross section for absorption of a second photon at the excitation frequency, which is needed to accelerate dissociation sufficiently to yield a strong fragment signal (Figure 3.2).

Importantly, two distinct spectral patterns of transitions are revealed in the IR-IR double resonance scans between 3600 and 3900 cm^{-1}, which are consistent with spectra that originate from contributions of two different symmetry classes in the ground-state population. This effect is immediately evidenced by the character of the dips in traces 3.5D/3.5E that arise from the two peaks comprising the doublet feature near 3400 cm^{-1} in traces 3.5A/3.5B. (The closely spaced doublet characters of this feature—$\beta_{13,14}$ and $\beta_{15,16}$ in trace 3.5A—are lost due to the saturation conditions required to observe the dip pattern.) In trace 3.5E, only the lower-energy member of the main IHB doublet is depleted when the probe is set at β_2 (3831 cm^{-1}), while in trace 3.5C, with a probe set at a possible overlap of β_7 and β_8 (3714 cm^{-1}), both members of the 3400 cm^{-1} doublet are depleted similarly. Probing at 3763 cm^{-1} (β_4, trace 3.5D) yields a more complicated pattern in which the lower member of the main doublet is enhanced, indicating that excitation by the pump creates an excited state that exhibits absorption at the probe frequency (see Figure 3.2C, where excitation of β_{16} creates new absorption around the β_4 band). These features of the IR-IR study that reveal state-selective spectra and excited-state dynamics warrant further study and analysis, but the present investigation is mostly concerned with the implications of these more advanced measurements on assignment of the linear spectrum of the cold, ground-state complex.

Turning to the quartet and bend-overtone regions at the lower-energy part of the spectral range covered in Figure 3.5, the results of the double-resonance experiment were

found to be consistent with the conclusions described above regarding the symmetry assignments of the rotational bands. Specifically, trace 3.5E exclusively records lower-frequency features of the tunneling doublet transitions (originating in GS(-), which is higher in energy), and only the lower-energy IHB peak yields a dip in the probe signal. As this trace also includes the β_8 peak that was assigned in the rotational analysis (Figure 3.4C) to correspond to the $K_a = 1 \leftarrow 0$ transition from GS(-), this trace is associated with transitions originating from the GS(-) level with $K_a'' = 0$. On the other hand, traces C and D include contributions from the GS(+) level, and the fact that trace 3.5D shows a dip feature at the location of the higher-energy member of the doublet ($\beta_{13,14}$) in the IHB region indicates that it originates the from GS(+) manifold. Due to the positive signal in the energy range of the lower member ($\beta_{15,16}$), an assignment of this feature to one or both members of the ground-state tunneling doublet cannot be made based on this double-resonance response alone. Additional evidence that the transitions probed in panel 3D arise from GS(+), while those in panel 3.5E arise exclusively from GS(-), however, comes from the small (4 cm^{-1}) but significant shift of the position of the feature that is assigned to the overtone in the HOH bend (β_{17} and β_{18}). If the tunneling splitting for this excited bending state is identical to that for the ground state, these two transitions would appear at the same energy in these two IR^2MS^3 traces. This small observed shift is, therefore, consistent with a slightly smaller tunneling splitting (by ~4 cm^{-1}) for the v=2 level of the HOH bend, compared to the ground-state tunneling splitting. Accordingly, traces 3.5D and 3.5E likely originate solely from different members of the GS tunneling pair.

Trace 3.5C is more complex in that it shows a broadened feature near 3250 cm^{-1}, compared to traces 3.5D and 3.5E, indicating that both GS(+) and GS(-) levels contribute

to the probed transition at 3714 cm^{-1}. The relative contributions are complicated, however, by the admixture in the absorption at the probe wavelength (3714 cm^{-1}) and the efficiencies with which transitions excited by the pump laser remove population from the two lower levels under partially saturated excitation conditions (Figure 3.6). For example, the behavior of the rotational bands in the FOH region is most similar to the behavior displayed by the GS(+) ground state, indicating that the contribution from GS(-)to the probe fragmentation yield is less than that of GS(+). This conclusion is consistent with the analysis of the FOH band contour in Figure 3.4, where transitions from both GS(-) and GS(+) were found to contribute to the transition selected by probe identified as $\beta_{7,8}$. The smaller contribution from transitions arising from GS(-) is also consistent with the absence of the β_2 feature from trace 3.5C and the redshift of the β_8 feature in trace 3.5E, relative to the position of the β_7 feature in trace 3.5D.

With this experimental confirmation of the assignments in place, an estimate of the tunneling splitting for both the ground and excited states can be made. In the rotational band assignments, the two features near the FOH band origin in trace D of Figure 3.5 were assigned to the $K_a = 0 \leftarrow 0$ (β_7) and $K_a = 1 \leftarrow 0$ (β_4) transitions that originated from the GS(+) level. As such, the shift between these two peaks is roughly the A rotational constant for the state with one quantum of excitation in the FOH vibration. In the absence of tunneling splitting in both vibrational states, the $K_a = 0 \leftarrow 0$ transition originating from GS(+) and the $K_a = 1 \leftarrow 0$ transition originating from GS(-) (β_8) should also be shifted by the value of the A rotational constant, which is approximately 17 cm^{-1} (Table 3.2).

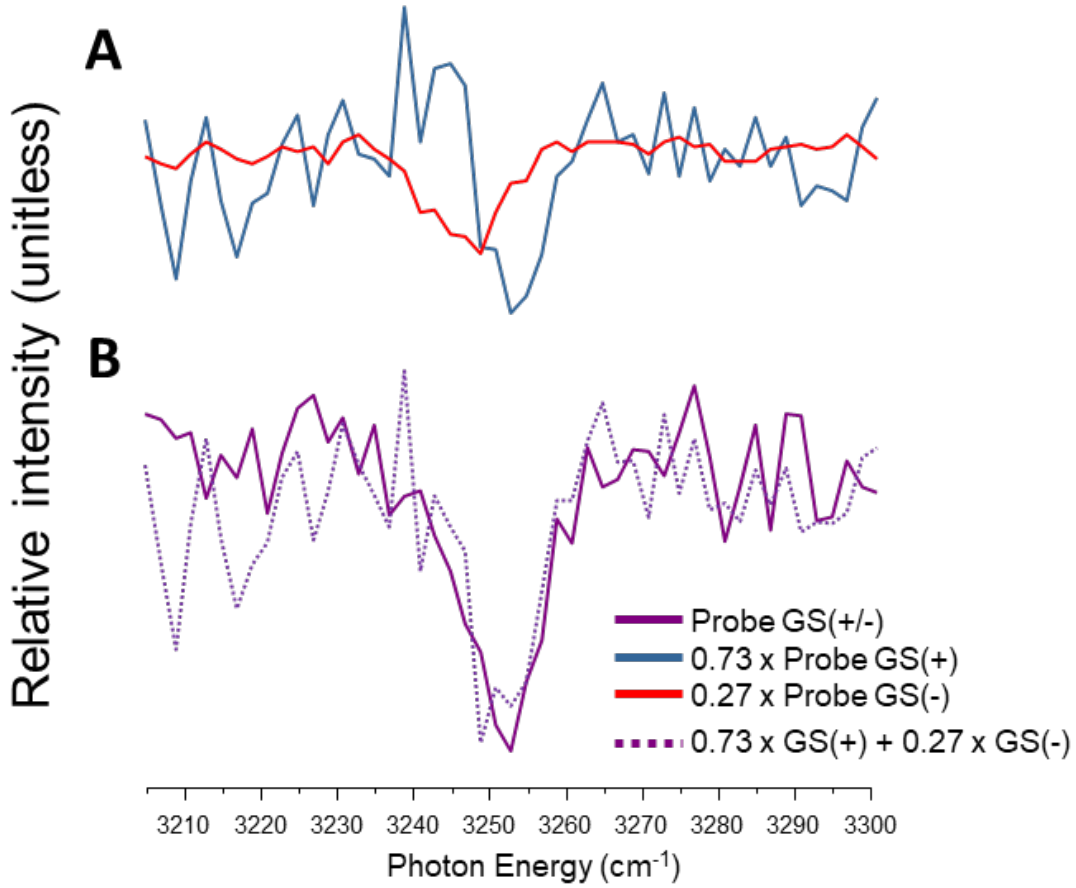

Figure 3.6: GS(+/-) double resonance comparison. Solid traces are the experimental data obtained by probing different positions (probing β_2 for red trace, β_4 for blue trace and $\beta_{7,8}$ for the purple trace) corresponding to transitions initiated in GS(-), GS(+) and GS(+/-), respectively. The relative intensity represents the amount of remaining probe signal after the pump laser excitation normalized to the probe signal when pump laser is off. The dotted line in **(B)** corresponds to the admixture of 73% GS(+) spectrum and 27% GS(-) spectrum which suggests the relative population of GS(+) and GS(-) contributing to the solid purple trace in **(B)** is close to 3:1.

Table 3.2: Computed level structure with six-dimensional vibrationally averaged rotation constants of each normal-mode degree of freedom with qualitative assignments. The $\widetilde{\mathbf{A}}$ constants lie along the C_{2v} symmetry axis. The parenthesis after the quantum state labels denotes quantum numbers in the in-plane bend degree of freedom. Specifically, (+) and (-) denotes the ground-state tunneling partners, respectively. In addition, (1+) and (1-) denotes the first excited-state tunneling pair including the symmetric and antisymmetric states.

Label	Energy (cm^{-1})	% Character	$\widetilde{A}$ (cm^{-1})	$\widetilde{B}$ (cm^{-1})	$\widetilde{C}$ (cm^{-1})
GS(+)	0.0	84 %	16.78	0.09	0.08
GS(−)	15.0	78 %	17.20	0.08	0.08
GS + IP(+)	161.0	66 %	16.76	0.09	0.08
GS + IP(−)	256.9	63 %	17.74	0.08	0.08
IO(+)	98.7	58 %	16.96	0.08	0.08
IO(−)	113.0	56 %	17.33	0.08	0.08
IO + IP(+)	264.0	46 %	16.78	0.08	0.08
IO + IP(−)	351.9	38 %	17.77	0.08	0.08
2IO(+)	195.0	51 %	17.10	0.08	0.08
2IO(−)	208.6	45 %	17.46	0.08	0.08
2IO + IP(+)	364.1	50 %	16.87	0.08	0.08
2IO + IP(−)	537.2	51 %	18.04	0.08	0.08
OOP(+)	448.4	64 %	16.76	0.08	0.08

OOP(−)	454.6	66 %	17.02	0.08	0.08
OOP + IP(+)	615.7	47 %	16.17	0.08	0.08
OOP + IP(−)	683.3	46 %	17.41	0.08	0.08
2OOP(+)	875.9	35 %	16.92	0.08	0.08
2OOP(−)	873.8	32 %	17.67	0.08	0.08
2OOP + IP(+)	1058.1	21 %	16.17	0.08	0.08
2OOP + IP(−)	1097.4	19 %	18.23	0.08	0.08
HOH(+)	1624.0	70 %	16.88	0.09	0.08
HOH(−)	1637.0	65 %	18.64	0.09	0.09
HOH + IP(+)	1783.6	56 %	16.86	0.09	0.08
HOH + IP(−)	1873.4	52 %	17.88	0.08	0.08
2HOH(+)	3222.1	53 %	16.98	0.09	0.08
2HOH(−)	3232.4	47 %	17.29	0.08	0.09
2HOH + IP(+)	3387.4	27 %	17.24	0.09	0.08
2HOH + IP(−)	3463.9	38 %	16.40	0.08	0.08
2HOH + IO(+)	3318.9	53 %	17.09	0.09	0.08
2HOH + IO(−)	3328.0	44 %	16.92	0.09	0.09
2HOH + IO + IP(+)	3488.7	43 %	17.32	0.08	0.08
2HOH + IO + IP(−)	3656.1	35 %	17.98	0.08	0.08

IHB(+)	3371.9	60 %	17.37	0.09	0.09
IHB(−)	3377.9	79 %	17.70	0.09	0.09
IHB + IP(+)	3632.0	57 %	17.28	0.09	0.09
IHB + IP(−)	3623.0	54 %	16.96	0.09	0.09
2HOH + 2IO(+)	3413.1	37 %	17.55	0.08	0.08
2HOH + 2IO(−)	3421.0	38 %	17.63	0.08	0.08
2HOH + 2IO + IP(+)	3585.4	24 %	17.57	0.08	0.08
2HOH + 2IO + IP(−)	3737.3	41 %	18.36	0.09	0.08
FOH(+)	3677.8	78 %	16.53	0.09	0.08
FOH(−)	3681.9	72 %	16.73	0.09	0.08
FOH + IP(+)	3817.2	60 %	17.02	0.09	0.08
FOH + IP(−)	3808.4	61 %	16.96	0.09	0.08

As noted above, these two transitions contributed to the broadening evident in the peak ($\beta_{7,8}$) near 3715 cm^{-1} in trace 3.5C. The small displacement between the two dip peaks observed in the IR^2MS^3 spectra in this region (traces 3.5D/3.5E) indicates that the difference between the tunneling splitting in the ground state and the tunneling splitting in the state with one quantum in the FOH is only slightly larger than 17 cm^{-1}. Analysis of the peak positions in the FOH region of the spectrum (Supporting Information section S3)

results in a ground-state tunneling splitting of approximately 20 cm^{-1} and a splitting for the level with one quantum in the FOH of -2 cm^{-1}, which are the parameters that were used to obtain traces B-D in Figure 3.4. Assuming similar tunneling behavior for the $\nu = 1$ levels of the IHB and FOH modes, these splittings at least qualitatively account for the ~30 cm^{-1} separation between the features assigned to the IHB near 3400 cm^{-1} in traces A and B of Figure 3.5.

To this point, two of the four features in the IHB quartet can be understood as a consequence of a tunneling splitting in the ground vibrational state, which is manifest as a widely split doublet when recorded at high laser power (Figure 3.5C). These peaks are attributed to the two transitions involving excitation to the IHB(+/-) fundamental levels from the corresponding GS(+/-) states. The quartet then emerges in the lower-power spectrum (Figure 3.1B) as the two more widely spaced band centers ($\beta_{13,14}$ and $\beta_{15,16}$) split into two closely spaced doublets (by ~10 cm^{-1}). The roles of both electrical and mechanical anharmonicities in the generation of pervasive "extra" peaks in the spectra of the $X^- \cdot H_2O$ systems has been discussed at length,[8, 10] and these resonance effects serve as a backdrop for the present analysis of the smaller splittings in the quartet feature. In a previous study of the spectrum of Ar-tagged $I^- \cdot H_2O$,[8] for example, the vibrational frequencies of the six vibrational degrees of freedom in $I^- \cdot H_2O$ were identified as band fundamentals or combination bands excited along with either the OH stretches or the overtone of the HOH bend. Based on the reported spectra, the soft modes associated with the IO stretch, in-plane water bend, and out-of-plane water bend modes were assigned at 131, 160 and 549 cm^{-1}, respectively. Using these values, both members of the tunneling doublet in states with two quanta in the HOH bend and one quantum in the IO stretch

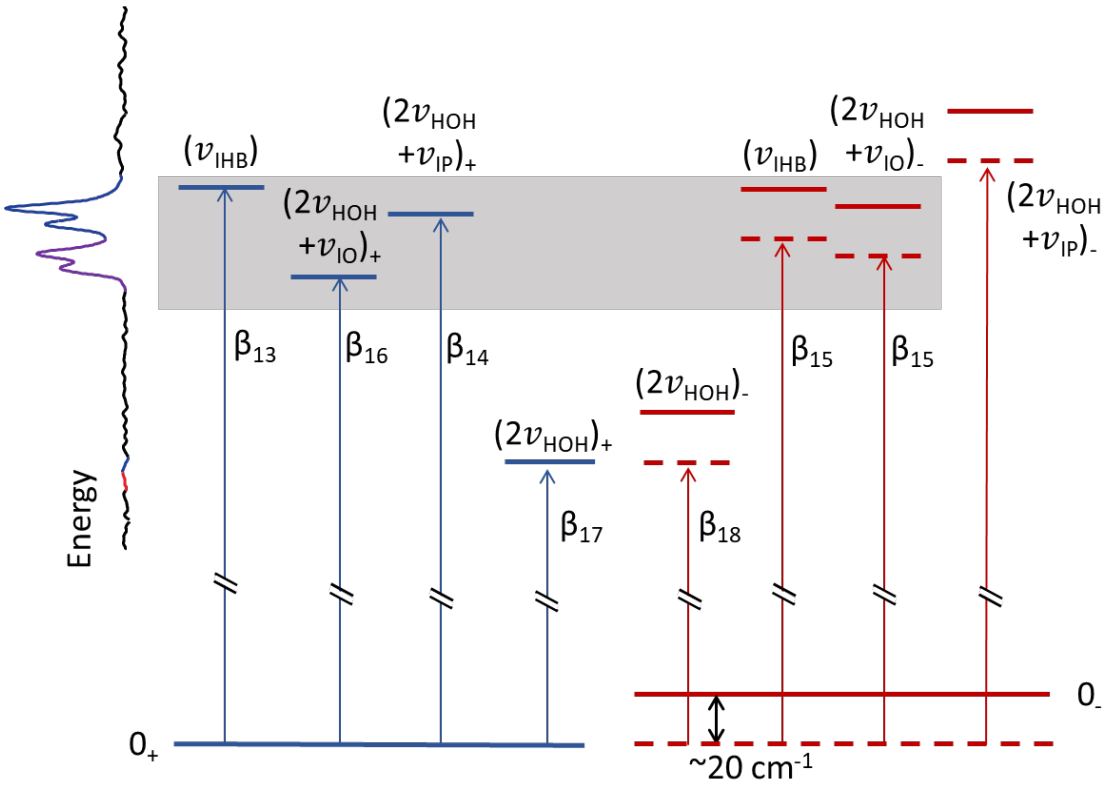

Figure 3.7: Energy-level diagram of the IHB region, based on previous spectral observations. The left inset is an IRPD spectrum reproduced from figure 3.1B. The blue color of the energy level lines denotes the quantum states with (+) symmetry; the red color denotes (–) symmetry. The solid lines represent real energy levels, whereas dotted lines are shifted down by an equal amount such that the initial state in the IR transitions is aligned with the (+) ground state for ease of comparison of transition energies (arrows). The shift (20 cm^{-1}) is the ground-state tunneling splitting, and the energies used to make the energy-level diagram are based on ref. 8. The grey box shows the range of energies that correspond to the quartet feature in the spectrum (reproduced in inset).

should lie close in energy to the corresponding IHB(-) fundamental. Similarly, the IHB(+) level lies close in energy to the state with two quanta in the HOH bend and one quantum of excitation in the in-plane bend $(2\nu_{HOH} + \nu_{IP})_+$. The frequencies of the transitions to these four states, based on the frequencies derived from Ref. 8, are plotted to-scale in the grey box in Figure 3.7. Combination-band activity has also been observed in both of these modes in many of the $X^- \cdot H_2O$ systems.[8] As such, the two transitions expected from tunneling splitting in the IHB fundamental are here proposed to be further split by coupling to nearby, nominally dark levels composed of two quanta in the HOH bend plus one quantum of either the in-plane bend or IO stretch.

One way to address the composition of vibrationally excited states that involve coupling between two or more contributions from the separable normal-mode basis is to monitor the absorption spectra arising from the upper energy level in question. If the harmonic basis correctly describes this level, for example, the absorption spectrum will simply yield a spectrum that is identical to that of the ground state, but with slightly shifted transition energies that reflect the anharmonic coupling between modes. When the upper level is a superposition of zero-order states, however, its absorption spectrum should contain contributions from ~~of~~ the two spectra arising from the two zeroth-order states that are coupled. The relevance of this in the present case is that, if the close doublet features ($\beta_{13,14}$ and $\beta_{15,16}$) arise from coupling of the IHB fundamentals to states based on the bend overtone along with v =1 levels of one or more soft modes, then the absorption spectrum should reflect the selection rules governing excitations from the v =1 level of the IHB as well as those from the v =2 of the bend along with soft mode activity as required to bring the v=2 of the bend into resonance with v=1 of the IHB stretch. The level diagram

describing the spectra expected for the limiting (harmonic approximation) case as well as that arising from mixed levels is presented in Fig. 3.3.

A survey of the photofragmentation spectra, arising from excitation of each member of the quartet, is presented in Figure 3.2. In this experiment, the first laser was fixed at the frequency of one of the quartet bands, while the second laser was scanned from 600 to 4000 cm^{-1}. At first glance, one might expect that such a measurement would not yield any signal since the approach taken to obtain the spectra in Figure 3.1 and in trace A of Figure 3.5 relies on the states that are accessed by the transitions that are probed by the first laser being dissociative. The fact that such depletions were observed, even though a significant fraction of the excited-state population survives the 30 microsecond time between pump and probe lasers, is consistent with a scenario where the lifetimes of these excited states are surprisingly long ($\geq$ 30 microseconds). With these timescale considerations in mind, the excited-state spectra of the upper levels of the four transitions (Figure 3.2) that make up the quartet are different in the region of the fundamental in the bend (~1600 cm^{-1}). In particular, traces D and F in Figure 3.2 exhibit one dominant feature, while traces C and E show a series of transitions separated by about 200 cm^{-1}. This behavior is consistent with the bands labeled β_{13} and β_{15} being assigned to the tunnel-split fundamental in the IHB, while the bands labeled β_{14} and β_{16} are better described as combination bands built off of the overtone in the HOH bend. When the spectra above 3400 cm^{-1} are compared, traces C, E, and F appear more similar to each other than they do to trace D (red trace in Figure 3.2). This trend is suggests that the transition that is probed by the fixed excitation laser in trace D originates from GS(-), whereas the transitions that are initially probed in the other three traces all originate from GS(+). A detailed analysis

of the complex set of sharp bands displayed across the spectral range is beyond the scope of this paper, but the qualitative character of the state-specific spectra further supports the assignments of these four bands discussed above.

3.1.4 Comparison to the spectrum predicted by full-dimensional anharmonic calculations

The above discussion has been primarily based on the empirical analysis of the $I^- \cdot H_2O$ spectrum by fitting the rotational pattern and verifying the symmetries involved in the assignment scheme using IR-IR double resonance. But this approach did not consider the strength of the couplings between the various zeroth-order excited states that govern the level pattern. Furthermore, the density of states stemming from combination bands and overtones of soft modes provides many additional possibilities for explaining the appearance of "extra" bands in the spectrum. The results of the full-dimensional vibrational eigensolver calculations—and adiabatic approximations thereof—are considered here, in order to further explore these interactions and their influence on the motions most responsible for the variety of observed bands.

An adiabatic treatment of the $I^- \cdot H_2O$ vibrations provides a conceptual (and semi-quantitative) framework for understanding the mode-dependent tunneling behavior. This approach examines the manner in which the soft-mode potentials depend on the degree of excitation in the high-frequency motions. In this approximate treatment, the five-dimensional Schrödinger equation was solved as a function of the in-plane bend angle, θ_{ip}, which was defined as the angle between the vector that connects the oxygen and iodine atoms and the bisector of the HOH angle. These vectors intersect at the center of mass of HOH, as illustrated in the inset to panel B of Figure 3.8. The potential for the in-plane

bend coordinate was calculated in the approximation that its potential energy is parametrically dependent on the eigenvalues of the other normal modes. The energy differences between the vibrationally adiabatic potential curves were then constructed as a function of θ_{ip} by including the θ_{ip}-dependence of the energies of states with varying degrees of excitation in the high-frequency modes.[27] In this manner, the four potential curves shown in Figure 3.8 can be considered analogous to the Born-Oppenheimer potentials in electronic structure calculations that differ according to the bonding character of the various electronic states. The one-dimensional Schrödinger equation, with an appropriate effective mass for the hindered in-plane rotation as defined in Eq 3.1,[28]

$$I(\theta_{\mathrm{IP}}) = A_{\mathrm{R}}(\theta_{\mathrm{IP}})\left(1 - \frac{\lambda_{R,c}^2(\theta_{\mathrm{IP}})}{I_c(\theta_{\mathrm{IP}})}\right) \qquad (Eq.\,3.1)$$

can then be solved for each of these potentials, yielding tunneling splittings in the context of the vibrational eigenvalues on each of these surfaces. The spectrum in the OH stretching region can then be reconstructed from the energy gaps and transition dipole moments computed for transitions between the vibrational levels supported by the adiabatic surfaces.

The GS potential within this adiabatic approximation is shown in panel B of Figure 3.8. The zero of energy for this and all of the adiabatic surfaces is taken to be the minimum of the ground-state adiabatic potential. The barrier on this surface is calculated to be ~200 cm^{-1}, giving rise to a 14.4-cm^{-1} tunneling splitting between the first two vibrational levels supported by this double-minimum potential. This value is about 5 cm^{-1} smaller than the splitting used to obtain the simulated spectrum shown in Figure 3.4 but is also within 1 cm^{-1} of the value obtained from the full-dimensional eigensolver, discussed below. To put these results in context of previous reports, Horvath et al.[8] placed the bare barrier to be about 300 cm^{-1} with a corresponding tunneling splitting of ~4 cm^{-1}. The study of Paesani,

Carrington, and co-workers,[7] on the other hand, reported a splitting of 27.05 cm^{-1} based on a fully coupled six-dimensional vibrational eigensolver calculation using the same MB-nrg potential, which exhibits a barrier along θ_{ip} of 101.63 cm^{-1}.

Excitation of the intramolecular HOH bend overtone does not appreciably change the shape of the one-dimensional adiabatic potential, as is seen by comparing the curve labelled 2HOH in Figure 3.8A (green) to the ground-state adiabatic potential in 5B (black). Conversely, the effective adiabatic barrier is significantly larger when the IHB stretching mode (blue) is excited, which is consistent with the empirically assigned quenching of the tunneling. Additionally, while the wavefunction associated with the bend overtone varies smoothly as a function of θ_{ip}, the wavefunctions assocated with states with one quantum of excitation in one of the OH oscillators show a rapid change (and avoided crossing) near $\theta_{ip} = 0$. While the nature of the vibrational states is subtler than implied by the above discussion when non-adiabatic contributions are considered,[27] the pattern of tunneling splittings for all but the FOH state is nonetheless consistent with the conclusions of the empirical analysis described above.

The fact that the $I^- \cdot H_2O$ complex contains only four atoms, and is one for which a high-accuracy potential energy surface is available,[7] raises the important question of whether computational tools are now refined to the point that observed anharmonic band patterns can be assigned from first principles. Such an advance would have a profound impact by expanding the complexity of systems amenable to experimental study without requiring the often-tedious methods of molecular spectroscopy developed over decades

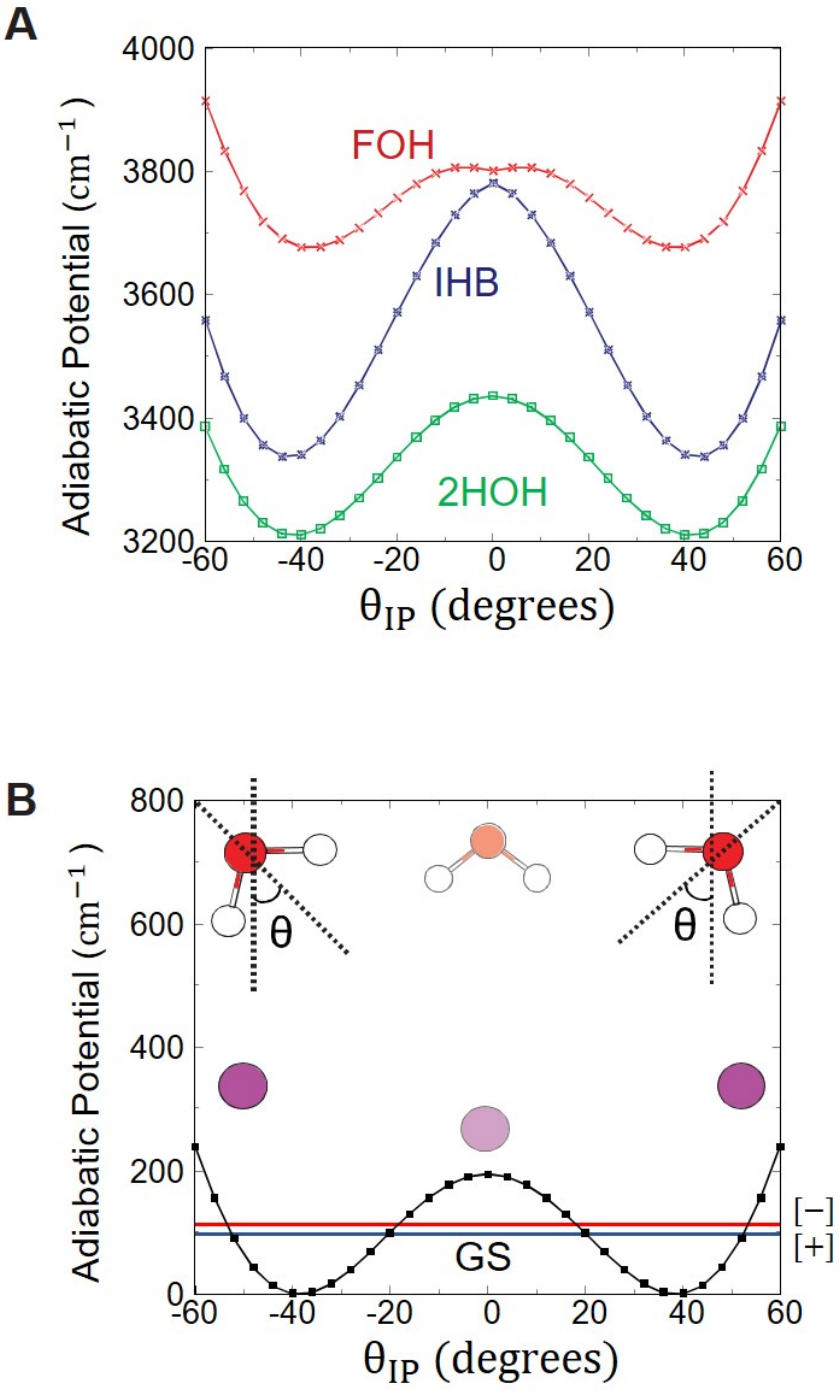

Figure 3.8: Mode-dependent tunnel splittings and adiabatic potential energy surfaces. (inset) Definition of the IP bend coordinate, along with **(B)** ZPE, **(A)** 2HOH, IHB, and FOH frequency-response curves added to the underlying double-well potential energy surface along the IP bend coordinate.

involving assignment with empirical parameters and effective Hamiltonians. To this end, the results of the fully coupled, six-dimensional calculations of the $I^- \cdot H_2O$ spectrum are examined here. Comparisons of the resulting spectra to those shown in Figure 3.5 are provided in Figure 3.9, and the corresponding transition energies are collected in Table 3.3. A complete list of the energies of relevant states, along with assignments and vibrationally averaged rotational constants, is also provided in Table 3.1.

In general, this calculated spectrum (trace 3.9B) recovers the overall character of the observed bands (trace 3.9A), including much of the rotational fine structure associated with the FOH bands and the multiplet nature of the IHB. The predicted, vibrationally averaged *A* rotational constants for the ground and excited vibrational states involved in the transitions considered above are both 17 cm^{-1}, which are in agreement with the value that was used in the empirical analysis of the spectrum (see Table 3.2 and discussion thereafter). Additionally, the calculated ground-state tunneling splitting of 15 cm^{-1} is similar to the splitting estimated with the vibrationally adiabatic approach (14.4 cm^{-1}), which highlights the accuracy of the latter method within the chosen potential energy surface. The calculated tunneling splitting for the state with two quanta in the HOH bend is 10 cm^{-1}, which yields a separation between the GS(+) and GS(-) contributions to the HOH bend overtone feature of 4.4 cm^{-1}, close to the experimentally observed value of 4 cm^{-1} (Figure 3.5). The tunneling splittings for the states with one quantum in the IHB and FOH are 6 and 4 cm^{-1}, respectively, and are significantly smaller than the ground-state tunneling splitting, as was also inferred from the simulated spectrum.

Table 3.3. Computed transition frequencies (shifted by +36 cm^{-1}), comparison with experiment, and qualitative assignments for the simulated rovibrational water-iodide spectrum at 20 K. The assignments were made by projecting the calculated states onto the basis states listed in tables 3.4 and 3.5. The || notation represents a parallel transition with $\Delta K_a = 0$.

Peak [calc]	Peak [exp]	Calculated (cm^{-1})	Experiment (cm^{-1})	Calculated Initial State	Calculated Final State	K_a
α_{1a}	--	3858	--	GS(-)	FOH+IP(+)	$0 \rightarrow 1$
α_1	β_1	3855	3855	GS(+)	FOH+IP (+)	||
α_2	β_2	3829	3831	GS(-)	FOH+IP (-)	||
α_3	β_3	3799	3815	GS(-)	FOH+IO (-)	||
α_4	β_4	3768	3763	GS(+)	FOH(-)	$1 \rightarrow 2$
α_5	β_5	3748	3744	GS(-)	FOH(+)	$1 \rightarrow 2$
α_6	β_6	3735	3729	GS(+)	FOH(-)	$0 \rightarrow 1$
α_7	β_7	3714	3714	GS(+)	FOH(+)	||
α_8	β_8	3715	3705	GS(-)	FOH(+)	$0 \rightarrow 1$
α_{8a}	--	3708	--	GS(+)	IHB+IP (-)	$1 \rightarrow 2$
α_9	β_9	3701	3695	GS(+)	FOH(-)	$1 \rightarrow 0$
α_{10b}	--	3682	--	GS(-)	FOH(+)	$1 \rightarrow 0$
α_{10a}	--	3676	--	GS(+)	IHB+IP (-)	$0 \rightarrow 1$
α_{10}	β_{10}	3668	3646	GS(+)	IHB+IP (+)	||

α_{11}	β_{11}	3642	3636	GS(+)	IHB+IP (-)	$1 \rightarrow 0$
α_{12}	β_{12}	3639	3633	GS(+)	2HOH+2IP (+)	||
α_{13}	β_{13}	3408	3438	GS(+)	IHB(+)	||
α_{14}	β_{14}	3423	3426	GS(+)	2HOH+IP (+)	||
α_{15}	β_{15}	3399	3406	GS(-)	IHB(-)	||
α_{16}	β_{16}	3355	3396	GS(+)	2HOH+IO(+)	||
α_{16a}	--	3449	--	GS(+)	2HOH+2IO(+)	||
α_{17}	β_{17}	3258	3252	GS(+)	2HOH(+)	||
α_{18}	β_{18}	3253	3248	GS(-)	2HOH(-)	||

Table 3.4: Chosen symmetry-adapted configuration state functions and symmetry labels for the basis states used in the assignment of the anharmonic six-dimensional vibrational eigenstates. The functions are constructed from harmonic oscillator basis states with the order $|\nu_{IP}, \nu_{IO}, \nu_{OOP}, \nu_{HOH}, \nu_{SS}, \nu_{AS}\rangle_{Harm}$.

Label	Symmetry	Harmonic Expansion
$GS(+)$	A_1	$\frac{1}{\sqrt{2}}\left\|0,0,0,0,0,0\right\rangle_{Harm} + \frac{1}{\sqrt{2}}\left\|2,0,0,0,0,0\right\rangle_{Harm}$
$GS(-)$	B_2	$\frac{1}{\sqrt{2}}\left\|1,0,0,0,0,0\right\rangle_{Harm} + \frac{1}{\sqrt{2}}\left\|3,0,0,0,0,0\right\rangle_{Harm}$
$IP(+)$	A_1	$\frac{1}{\sqrt{2}}\left\|0,0,0,0,0,0\right\rangle_{Harm} - \frac{1}{\sqrt{2}}\left\|2,0,0,0,0,0\right\rangle_{Harm}$
$IP(-)$	B_2	$\frac{1}{\sqrt{2}}\left\|1,0,0,0,0,0\right\rangle_{Harm} - \frac{1}{\sqrt{2}}\left\|3,0,0,0,0,0\right\rangle_{Harm}$
$IO(+)$	A_1	$\frac{1}{\sqrt{2}}\left\|0,1,0,0,0,0\right\rangle_{Harm} + \frac{1}{\sqrt{2}}\left\|2,1,0,0,0,0\right\rangle_{Harm}$
$IO(-)$	B_2	$\frac{1}{\sqrt{2}}\left\|1,1,0,0,0,0\right\rangle_{Harm} + \frac{1}{\sqrt{2}}\left\|3,1,0,0,0,0\right\rangle_{Harm}$
$IO + IP(+)$	A_1	$\frac{1}{\sqrt{2}}\left\|0,1,0,0,0,0\right\rangle_{Harm} - \frac{1}{\sqrt{2}}\left\|2,1,0,0,0,0\right\rangle_{Harm}$
$IO + IP(-)$	B_2	$\frac{1}{\sqrt{2}}\left\|1,1,0,0,0,0\right\rangle_{Harm} - \frac{1}{\sqrt{2}}\left\|3,1,0,0,0,0\right\rangle_{Harm}$
$2IO(+)$	A_1	$\frac{1}{\sqrt{2}}\left\|0,2,0,0,0,0\right\rangle_{Harm} + \frac{1}{\sqrt{2}}\left\|2,2,0,0,0,0\right\rangle_{Harm}$
$2IO(-)$	B_2	$\frac{1}{\sqrt{2}}\left\|1,2,0,0,0,0\right\rangle_{Harm} + \frac{1}{\sqrt{2}}\left\|3,2,0,0,0,0\right\rangle_{Harm}$

$2IO + IP(+)$	A_1	$\frac{1}{\sqrt{2}}\left\|0,2,0,0,0,0\right\rangle_{\mathrm{Harm}} - \frac{1}{\sqrt{2}}\left\| 2,2,0,0,0,0\right\rangle_{\mathrm{Harm}}$
$2IO + IP(-)$	B_2	$\frac{1}{\sqrt{2}}\left\|1,2,0,0,0,0\right\rangle_{\mathrm{Harm}} - \frac{1}{\sqrt{2}}\left\| 3,2,0,0,0,0\right\rangle_{\mathrm{Harm}}$
$OOP(+)$	B_1	$\frac{1}{\sqrt{2}}\left\|0,0,1,0,0,0\right\rangle_{\mathrm{Harm}} + \frac{1}{\sqrt{2}}\left\| 2,0,1,0,0,0\right\rangle_{\mathrm{Harm}}$
$OOP(-)$	A_2	$\frac{1}{\sqrt{2}}\left\|1,0,1,0,0,0\right\rangle_{\mathrm{Harm}} + \frac{1}{\sqrt{2}}\left\| 3,0,1,0,0,0\right\rangle_{\mathrm{Harm}}$
$OOP + IP(+)$	B_1	$\frac{1}{\sqrt{2}}\left\|0,0,1,0,0,0\right\rangle_{\mathrm{Harm}} - \frac{1}{\sqrt{2}}\left\| 2,0,1,0,0,0\right\rangle_{\mathrm{Harm}}$
$OOP + IP(-)$	A_2	$\frac{1}{\sqrt{2}}\left\|1,0,1,0,0,0\right\rangle_{\mathrm{Harm}} - \frac{1}{\sqrt{2}}\left\| 3,0,1,0,0,0\right\rangle_{\mathrm{Harm}}$
$2OOP(+)$	A_1	$\frac{1}{\sqrt{2}}\left\|0,0,2,0,0,0\right\rangle_{\mathrm{Harm}} + \frac{1}{\sqrt{2}}\left\| 2,0,2,0,0,0\right\rangle_{\mathrm{Harm}}$
$2OOP(-)$	B_2	$\frac{1}{\sqrt{2}}\left\|1,0,2,0,0,0\right\rangle_{\mathrm{Harm}} + \frac{1}{\sqrt{2}}\left\| 3,0,2,0,0,0\right\rangle_{\mathrm{Harm}}$
$2OOP + IP(+)$	A_1	$\frac{1}{\sqrt{2}}\left\|0,0,2,0,0,0\right\rangle_{\mathrm{Harm}} - \frac{1}{\sqrt{2}}\left\| 2,0,2,0,0,0\right\rangle_{\mathrm{Harm}}$
$2OOP + IP(-)$	B_2	$\frac{1}{\sqrt{2}}\left\|1,0,2,0,0,0\right\rangle_{\mathrm{Harm}} - \frac{1}{\sqrt{2}}\left\| 3,0,2,0,0,0\right\rangle_{\mathrm{Harm}}$
$HOH(+)$	A_1	$\frac{1}{\sqrt{2}}\left\|0,0,0,1,0,0\right\rangle_{\mathrm{Harm}} + \frac{1}{\sqrt{2}}\left\| 2,0,0,1,0,0\right\rangle_{\mathrm{Harm}}$
$HOH(-)$	B_2	$\frac{1}{\sqrt{2}}\left\|1,0,0,1,0,0\right\rangle_{\mathrm{Harm}} + \frac{1}{\sqrt{2}}\left\| 3,0,0,1,0,0\right\rangle_{\mathrm{Harm}}$
$HOH + IP(+)$	A_1	$\frac{1}{\sqrt{2}}\left\|0,0,0,1,0,0\right\rangle_{\mathrm{Harm}} - \frac{1}{\sqrt{2}}\left\| 2,0,0,1,0,0\right\rangle_{\mathrm{Harm}}$
$HOH + IP(-)$	B_2	$\frac{1}{\sqrt{2}}\left\|1,0,0,1,0,0\right\rangle_{\mathrm{Harm}} - \frac{1}{\sqrt{2}}\left\| 3,0,0,1,0,0\right\rangle_{\mathrm{Harm}}$

2HOH(+)	A_1	$\frac{1}{\sqrt{2}}\left\|0,0,0,2,0,0\right\rangle_{\mathrm{Harm}} + \frac{1}{\sqrt{2}}\left\| 2,0,0,2,0,0\right\rangle_{\mathrm{Harm}}$
2HOH(−)	B_2	$\frac{1}{\sqrt{2}}\left\|1,0,0,2,0,0\right\rangle_{\mathrm{Harm}} + \frac{1}{\sqrt{2}}\left\| 3,0,0,2,0,0\right\rangle_{\mathrm{Harm}}$
2HOH + IP(+)	A_1	$\frac{1}{\sqrt{2}}\left\|0,0,0,2,0,0\right\rangle_{\mathrm{Harm}} - \frac{1}{\sqrt{2}}\left\| 2,0,0,2,0,0\right\rangle_{\mathrm{Harm}}$
2HOH + IP(−)	B_2	$\frac{1}{\sqrt{2}}\left\|1,0,0,2,0,0\right\rangle_{\mathrm{Harm}} - \frac{1}{\sqrt{2}}\left\| 3,0,0,2,0,0\right\rangle_{\mathrm{Harm}}$
2HOH + 2IP(+)	A_1	$\frac{1}{\sqrt{3}}\left\|0,0,0,2,0,0\right\rangle_{\mathrm{Harm}} - \frac{1}{\sqrt{3}}\left\| 2,0,0,2,0,0\right\rangle_{\mathrm{Harm}} + \frac{1}{\sqrt{3}}\left\|4,0,0,2,0,0\right\rangle_{\mathrm{Harm}}$
SS(+)	A_1	$\frac{1}{\sqrt{2}}\left\|0,0,0,0,1,0\right\rangle_{\mathrm{Harm}} + \frac{1}{\sqrt{2}}\left\| 2,0,0,0,1,0\right\rangle_{\mathrm{Harm}}$
SS(−)	B_2	$\frac{1}{\sqrt{2}}\left\|1,0,0,0,1,0\right\rangle_{\mathrm{Harm}} + \frac{1}{\sqrt{2}}\left\| 3,0,0,0,1,0\right\rangle_{\mathrm{Harm}}$
SS + IP(+)	A_1	$\frac{1}{\sqrt{2}}\left\|0,0,0,0,1,0\right\rangle_{\mathrm{Harm}} - \frac{1}{\sqrt{2}}\left\| 2,0,0,0,1,0\right\rangle_{\mathrm{Harm}}$
SS + IP(−)	B_2	$\frac{1}{\sqrt{2}}\left\|1,0,0,0,1,0\right\rangle_{\mathrm{Harm}} - \frac{1}{\sqrt{2}}\left\| 3,0,0,0,1,0\right\rangle_{\mathrm{Harm}}$
AS(+)	B_2	$\frac{1}{\sqrt{2}}\left\|0,0,0,0,0,1\right\rangle_{\mathrm{Harm}} + \frac{1}{\sqrt{2}}\left\| 2,0,0,0,0,1\right\rangle_{\mathrm{Harm}}$
AS(−)	A_1	$\frac{1}{\sqrt{2}}\left\|1,0,0,0,0,1\right\rangle_{\mathrm{Harm}} + \frac{1}{\sqrt{2}}\left\| 3,0,0,0,0,1\right\rangle_{\mathrm{Harm}}$
AS + IP(+)	B_2	$\frac{1}{\sqrt{2}}\left\|0,0,0,0,0,1\right\rangle_{\mathrm{Harm}} - \frac{1}{\sqrt{2}}\left\| 2,0,0,0,0,1\right\rangle_{\mathrm{Harm}}$
AS + IP(−)	A_1	$\frac{1}{\sqrt{2}}\left\|1,0,0,0,0,1\right\rangle_{\mathrm{Harm}} - \frac{1}{\sqrt{2}}\left\| 3,0,0,0,0,1\right\rangle_{\mathrm{Harm}}$

Table 3.5: Corresponding SA-CSF's for the ion-hydrogen and free-OH basis states expressed as a linear combination of the symmetric and antisymmetric stretch SA-CSF's.

Label	Symmetry	SA-CSF Expansion
$\mathrm{IHB}(+)$	$\mathrm{A_1}$	$\frac{1}{\sqrt{2}}\mathrm{AS}(-)-\frac{1}{\sqrt{2}}\mathrm{SS}(+)$
$\mathrm{IHB}(-)$	$\mathrm{B_2}$	$\frac{1}{\sqrt{2}}\mathrm{AS}(+)-\frac{1}{\sqrt{2}}\mathrm{SS}(-)$
$\mathrm{IHB}+\mathrm{IP}(+)$	$\mathrm{A_1}$	$\frac{1}{\sqrt{2}}\mathrm{AS}(1-)-\frac{1}{\sqrt{2}}\mathrm{SS}(1+)$
$\mathrm{IHB}+\mathrm{IP}(-)$	$\mathrm{B_2}$	$\frac{1}{\sqrt{2}}\mathrm{AS}(1+)-\frac{1}{\sqrt{2}}\mathrm{SS}(1-)$
$\mathrm{FOH}(+)$	$\mathrm{A_1}$	$\frac{1}{\sqrt{2}}\mathrm{AS}(-)+\frac{1}{\sqrt{2}}\mathrm{SS}(+)$
$\mathrm{FOH}(-)$	$\mathrm{B_2}$	$\frac{1}{\sqrt{2}}\mathrm{AS}(+)+\frac{1}{\sqrt{2}}\mathrm{SS}(-)$
$\mathrm{FOH}+\mathrm{IP}(+)$	$\mathrm{A_1}$	$\frac{1}{\sqrt{2}}\mathrm{AS}(1-)+\frac{1}{\sqrt{2}}\mathrm{SS}(1+)$
$\mathrm{FOH}+\mathrm{IP}(-)$	$\mathrm{B_2}$	$\frac{1}{\sqrt{2}}\mathrm{AS}(1+)+\frac{1}{\sqrt{2}}\mathrm{SS}(1-)$

The calculated spectrum also explains the origin of the β_2 feature in the measured spectrum, which was left unassigned in the analysis of the rotational contour of the FOH fundamental. The calculations predict that this band arises from a transition between the upper member of the tunneling doublet [GS(-)] and the state with one quantum in the FOH mode and one quantum in the in-plane bend, denoted as FOH+IP(-). This assignment thus

accounts for the fact that setting the probe laser at this transition effectively isolated the bands arising from the GS(-) level in Figure 3.5E.

The more complete six-dimensional (plus rotation) calculations also allow for the reconstruction of the spectrum from the contributions of specific symmetry and K rotational levels in the ground state. The simulated dip spectra from specific lower-state levels are displayed in panels C, E, and G of Figure 3.9. For example, the results shown in trace 3.9G support the assignment scheme in which the aforementioned β_2 transition originates from GS(-) $K_a = 0$, and trace 3.9E is consistent with the conclusion that the β_4 probe corresponds specifically to a transition originating from the $K_a = 1$ state of GS(+). The calculated spectra for both of these state-specific cases are generally in excellent agreement with the experimental dip spectra, including the subtle shifts observed in the $\beta_{17,18}$ and $\beta_{7,8}$ pairs. The calculated spectra do not reproduce the intensity pattern in the IHB quartet or bend overtone regions of the double-resonance experiments. This result is likely a consequence the high laser power (and likely multi-photon behavior) used for these experiments, however, and the calculated linear spectrum should not be expected to capture these effects. Both the calculations and the above rotational analysis predict that the relatively bright $\beta_{7,8}$ feature arises from overlapping transitions and accidental coincidence of the tunneling splitting and the A rotation constant. The double-resonance experiment, with the probe laser frequency set within this peak, provides an opportunity to test these predictions. In calculated trace 3.9C, transitions originating from GS(+) with $K_a = 1$ and GS(-) with $K_a = 0$ are included with their intensities provided in a 2.7:1 ratio, based on the experimental analysis of the bend overtone contributions. The calculated spectrum is in reasonable agreement, although the intensities in the FOH region from the GS(+)

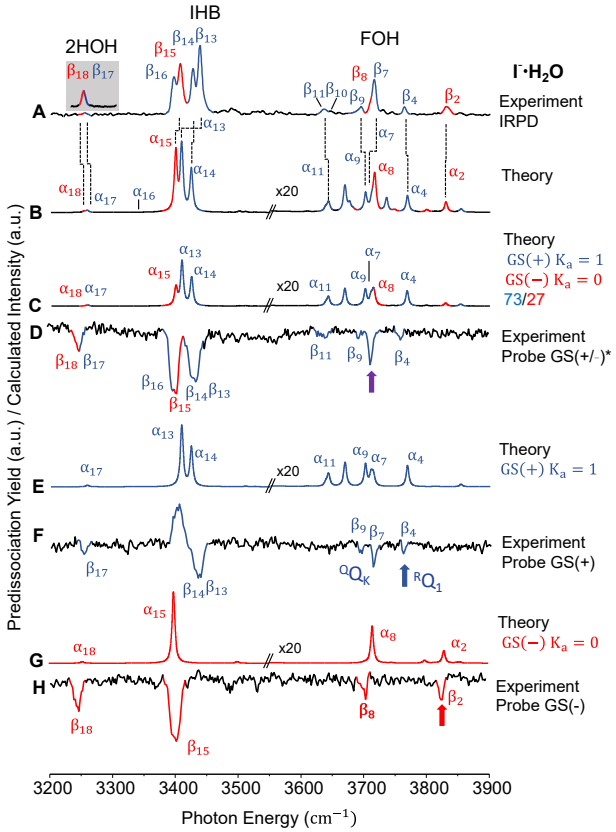

Figure 3.9: Comparison between the state-specific experimental spectra and the calculated infrared spectrum. (A) Linear infrared photodissociation spectra obtained with low laser power (1 mJ/pulse, 8 ns pulse width, 5 mm beam diameter) at 20 K. **(B)** Calculated rovibrational spectrum at 20K. **(C)** Calculated spectrum initiated from both members of the ground-state tunneling pair, with the intensity scaled by 73% for GS(+) $K_a = 1$ and 27% for GS(-) $K_a = 0$. **(D)** Experimental state-specific, double-resonance spectra obtained by probing the peak indicated by the purple arrow, which includes population from both GS(+) and GS(-). **(E, G)** Calculated spectrum with the initial state being GS(+) and GS(-), respectively. **(F, H)** Double-resonance spectra obtained by probing the peaks indicated by the color-coded arrows, which reflect the GS(+) and GS(-) population, correspondingly. All calculated traces **(B,C,E,G)** in the FOH region are magnified ×20.

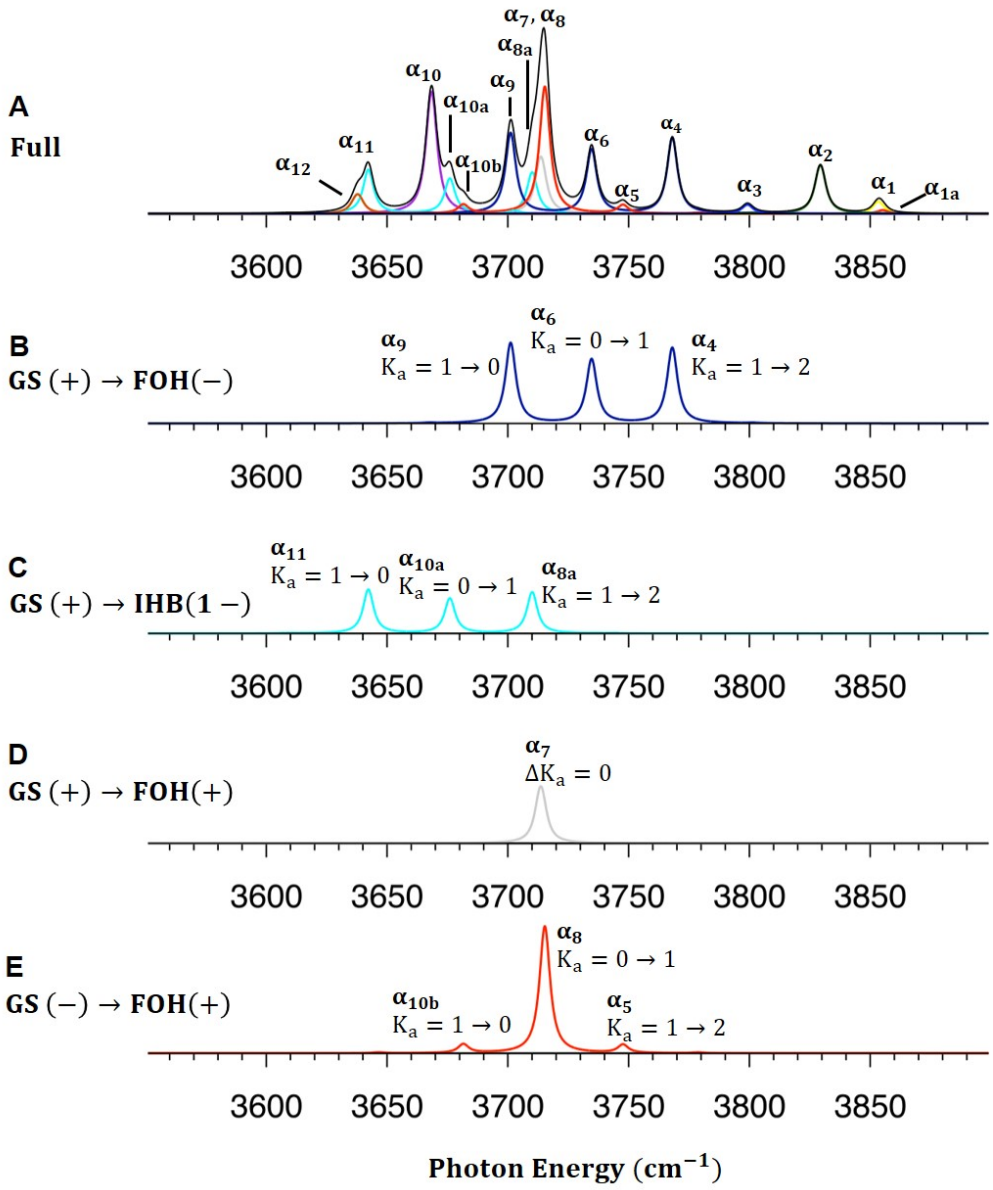

Figure 3.10: Decomposition of the main transitions underlying the FOH band. The calculated line widths have been homogeneously broadened by a Lorentzian line shape with a width of 5 cm^{-1}. The calculated spectrum has been shifted by $+36\ cm^{-1}$ to compare with the experiment. **(A)** Full decomposition of the calculated FOH band. **(B)** Perpendicular band out of GS(+). **(C)** Perpendicular band out of GS(+). **(D)** Parallel band out of GS(+). **(E)** Perpendicular band out of GS(-).

contribution are predicted to be larger. This behavior is also curiously inconsistent with a more detailed decomposition of the $\alpha_{7,8}$ band, shown in Figure 3.10. At the position of the probe laser, excitation of α_8, rather than α_7, would be predicted to dominate in trace C/D, based on the calculated spectra. Very subtle shifts of only a few wavenumbers intransitions α_7, α_{8a}, and α_8 could be enough to shift these predictions, however. Accordingly, future experiments (possibly with higher-resolution lasers) that further disentangle the several, potentially overlapping transitions in this region are recommended.

Important discrepancies between the six-dimensional prediction and the observed spectra were also observed. For example, a transition in the calculated spectrum was observed between features α_9 and α_{11}, which is not evident in the experimental spectrum. This feature is assigned to transitions from GS(+) to levels with one quantum of excitation in the IHB and one quantum of excitation in the in-plane bend [IHB+IP(-) $K_a = 1 \leftarrow 0$]. In the region of the IHB quartet, the calculated linear spectrum additionally shows only three peaks—two originating from GS(+) and one from GS(-)—that carry intensity, along with additional features that are close in energy. These and other smaller differences between the experimental and calculated spectrum likely reflect the sensitivity of the intensities of transitions to accidental resonances, which are, in turn, similarly sensitive to subtle features of the potential surface. In general, both the empirical analysis and the "ab initio" eigensolver approach were necessary in order to assign the rovibrational fine structure and line intensities. These reference comparisons, however, establish important constraints that could perhaps be used to guide the continued feedback loop required for refinement of potential energy surface development.

3.1.5 Conclusions

The origins of the unexpected quartet in the 3400 cm^{-1} region of the $I^- \cdot H_2O$ vibrational predissociation spectrum, which has alluded even qualitative assignment for nearly 25 years, were explored in the present study. New experimental approaches allowed for the resolution and assignment of the rotational structure in the FOH region of the spectrum. These assignments enabled the determination of the ground-state tunneling splitting directly from the experimental spectrum to be roughly 20 cm^{-1}. This information, along with knowledge of the fundamental frequencies of all six normal modes, was used to provide tentative assignments of the four members of the quartet, including tunneling-split bands nominally associated with the bound-OH stretch fundamentals as well as "extra" bands arising from coupling to nominally forbidden background states based on the v=2 level of the HOH intramolecular bending mode. The intensity in each of the pairs of peaks is carried by the transitions from the two members of the ground-state tunneling doublet to states with one quantum of excitation in the IHB (the "bright states"), for which the tunneling splitting in the upper level is mostly quenched. The remaining two weaker features reflect transitions involving combination bands with two quanta in the HOH bend along with excitation of single quanta in the in-plane bending or IO stretching modes. These findings were supported by two-color, IR-IR double-resonance experiments, which allowed for the separation of contributions to the spectrum from different symmetry classes of initial states. Finally, the spectra were compared to the results of high-level calculations of the rovibrational spectrum coupled with a recently available potential surface for $I^- \cdot H_2O$.

The many near-degeneracies in the spectrum of $I^- \cdot H_2O$, particularly in the region of the quartet, place considerable spectroscopic demands on any potential energy surface—well beyond commonly accepted bounds for computed or measured thermochemical quantities. In addition, the prediction of experimental rovibrational spectra requires accurate treatment of the potential and dipole moment surfaces that govern the observed spectral patterns. The present attempt to generate the observed spectrum from first principles indicates that the existing halide-water potential perhaps needs refinement to achieve spectroscopic accuracy. Such refinements likely reflect the performance of the underlying quantum chemistry methods (section S1.1) that were used in the development of the many-body potential surface and not in the underlying model used to fit this potential. Nonetheless, the band pattern predicted by the full-dimensional eigensolver approach accurately recovered much of the character of the states that give rise to the observed multiplet fine structure in the experimental linear and state-specific double-resonance spectra. This combined effort involving application of advanced theoretical and experimental methods has thus unraveled the key, quantum mechanical motions at the heart of this long-standing spectroscopic puzzle in the microhydration of the iodide ion.

3.2 Infrared spectroscopy of vibrationally excited iodide-water complex: a stringent test for vibrational state assignments and their anharmonicities

3.2.1 Introduction

Vibrational spectroscopy of isolated gas phase molecules and ions has been instrumental for calibrating theoretical construction of potential energy surfaces which

are the basis of computational chemistry since the early days when the concept of quantum mechanics is introduced to describe molecules. Early developments of laser spectroscopy coupled with mass spectrometry opened up the opportunities to obtain spectra of a specific species of ion that is mass selected.[29-32] Among the early vibrational spectroscopic studies of ion-molecule complexes, the vibrational spectrum of the iodide-water binary complex, $I^-\cdot H_2O$, was the first of this class of halide monohydrate ions to be reported in 1996 by Okumura and co-workers.[1] This study marks the beginning of a new field that has shaped our understanding of ion solvation.[1-2] Subsequent studies of the $X^-\cdot H_2O$ (X= F, Cl, Br, I) systems and their deuterated isotopologues, over the expanded frequency range of 600-4000 cm^{-1} made possible by the messenger tagging technique,[32-33] have provided a details about their vibrational level structures. The energy levels at single cm^{-1} accuracy gave stringent constraints on the potential energy surfaces that drive halide ion hydration, which are central to the recent development of high accuracy ion-water many body potentials.[3-13] The $I^-\cdot H_2O$ spectrum is especially complicated since it involves rotational structures, tunneling splitting, Fermi resonances as well as nuclear spin statistics and these features are extremely sensitive to the shape of the potential energy surface as discussed in Chapter 3.1. Thus, reproducing the experimental spectrum with state-of-the-art theoretical toolsets are still challenging. Recent study has refined the band assignments taking all the effects mentioned above into consideration and assignments when several possible transitions are nearly degenerate are particularly challenging since the accuracy of the calculated transition frequency does not allow definitive distinction of bands that are several wavenumbers from each other and has similar intensity. However, selectively exciting the nearly degenerate transitions and investigating the spectra of each

excited states results in clearly distinguishable excited state spectra which can then be used to aid the assignment of these congested bands.

3.2.2 Results and Discussion

We first investigate the I^-·HDO system which is free of the complexity caused by tunneling, Fermi resonance, and nuclear spin statistics. There are two isotopomers for the I^-·HDO isotopologue (structures in Fig. 3.11), one where the OH resides on the free OH (F_{OH}) position and results in a free OH transition and an ion-hydrogen-bonded OD (IDB) transition, and another where the OH resides in the ion-hydrogen-bonded OH (IHB) position and the OD assumes the free (F_{OD}) position. The free transitions are very week and essentially unobservable in the Ar predissociation spectra (Fig. 3.11A). The IRPD spectra (Fig. 3.11B) displays IHB, IDB and free OH transitions whereas the free OD is still too low in intensity to be observed. The IDB and F_{OD} transition in this case requires two photon absorption to detect HDO loss which results in lower fragment yield due to limitation in laser power. And the F_{OH} transition displays many peaks around the free OH frequency which is a result of the rotational pattern. Such pattern could serve as a temperature gauge for the ion, when the ion temperature is raised, the higher rotational levels are populated and the transitions spreads towards both sides around the free OH $\Delta K_a=0$ transition (Fig.3.11B-D).

Experimentally, the excited state spectra can be obtained by exciting the ion packet with a laser (excitation laser) whose frequency is fixed on one known transition below the water molecule's binding energy. After the excitation, the ions that absorbed two photons quickly dissociates (in tens of microseconds) and are then mass separated

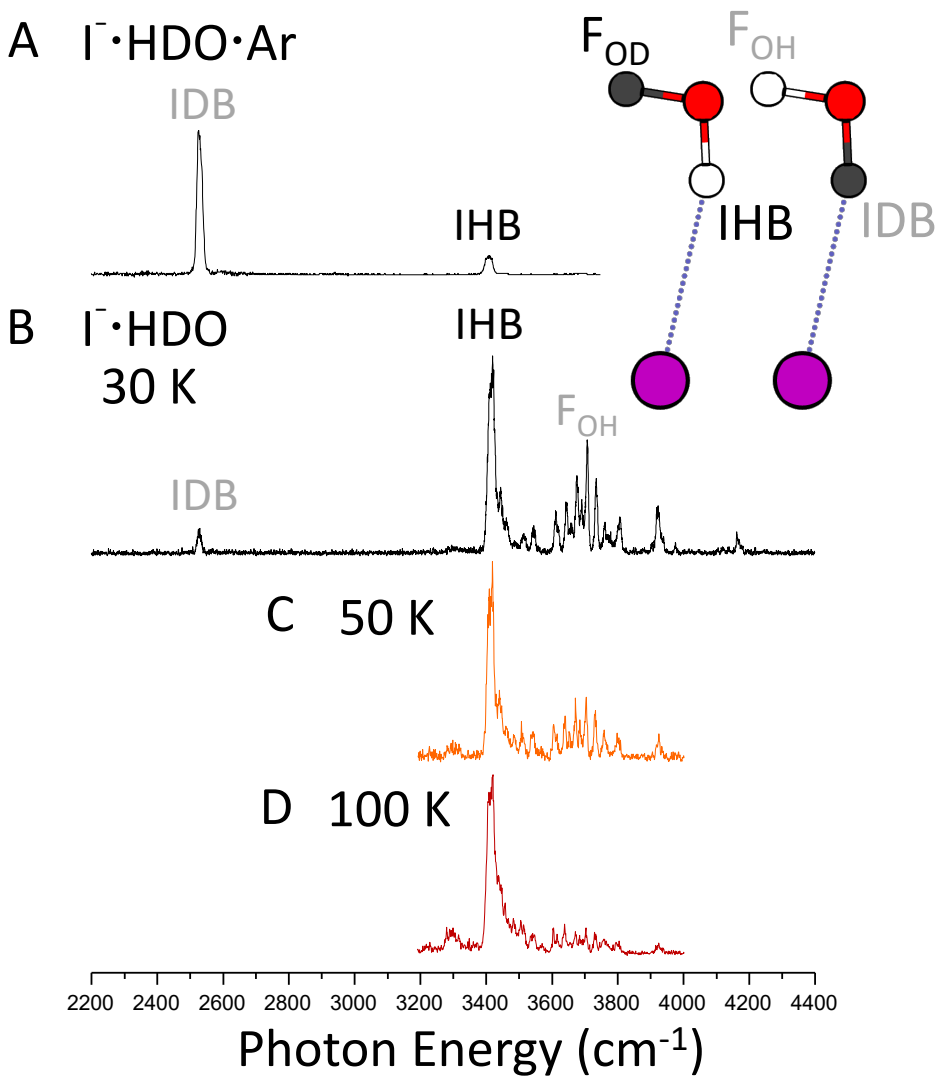

Figure 3.11: Asymmetric minimum-energy structure of I⁻·HDO and its vibrational predissociation spectrum at different temperatures. (A) Vibrational predissociation spectrum obtained using weakly bound Ar as messenger tag. On the right is the minimum-energy structures of the two isotopomers of I⁻·HDO from the MB-nrg potential (ref. 7) **(B)** IRPD spectrum of I⁻·HDO at 30 K, the IDB feature is observed through two photon absorption process. **(C,D)** IRPD spectrum of I⁻·HDO at 50 K and 100 K.

before the next laser interaction to ensure the detection of ions that absorbed one photon or no photon only. Then the second laser (probe laser) is scanned to obtain the spectra of the excited ions together with the ions that did not absorb any photon. The two laser interactions and the detection of the ions are carried out in high vacuum (10^{-8} Torr) within 100 μs time interval hence essentially collision free. The excitation laser is toggled on and off to allow the determination of the net effect of the one photon excitation. After subtracting the "excitation off" signal from the "excitation on" signal, the new transitions induced by the vibrational excitation manifest as positive signal (colored orange in Fig. 3.11B) and the bleaching of the ground state transitions appears as negative signals (colored blue in Fig. 11B). When exciting the IDB transition of the I^-·HOD isotopomer, the transitions initiated in the vibrational ground state including the F_{OH} and the IDB (vanishing blue arrow in Fig. 3.11D) transitions are bleached whereas the IDB 2←1 (orange arrow in Fig. 3.11D) appear as the dominating transition initiated from the IDB(v=1) state. The IDB 2←1 transition is redshifted (by 141 cm^{-1}) from the fundamental due to anharmonic effect and the anharmonicity ($\omega_e x_e$= 23.5 cm^{-1}) can be directly obtained. Similarly, when exciting the IHB transition of the I^-·DOH isotopomer, the IHB fundamental is bleached whereas the IHB 2←1 transition is redshifted (by 256 cm^{-1}) with an anharmonicity of $\omega_e x_e$= 42.7 cm^{-1}. Interestingly there are other weaker features accompanying the IHB 2←1 transition. Those could be other states that are accessible from the IHB(v=1) level with absorption of an infrared photon (dashed arrow in Panel I of Figure. 3.13A) due to anharmonic coupling, or a result of intramolecular vibrational energy

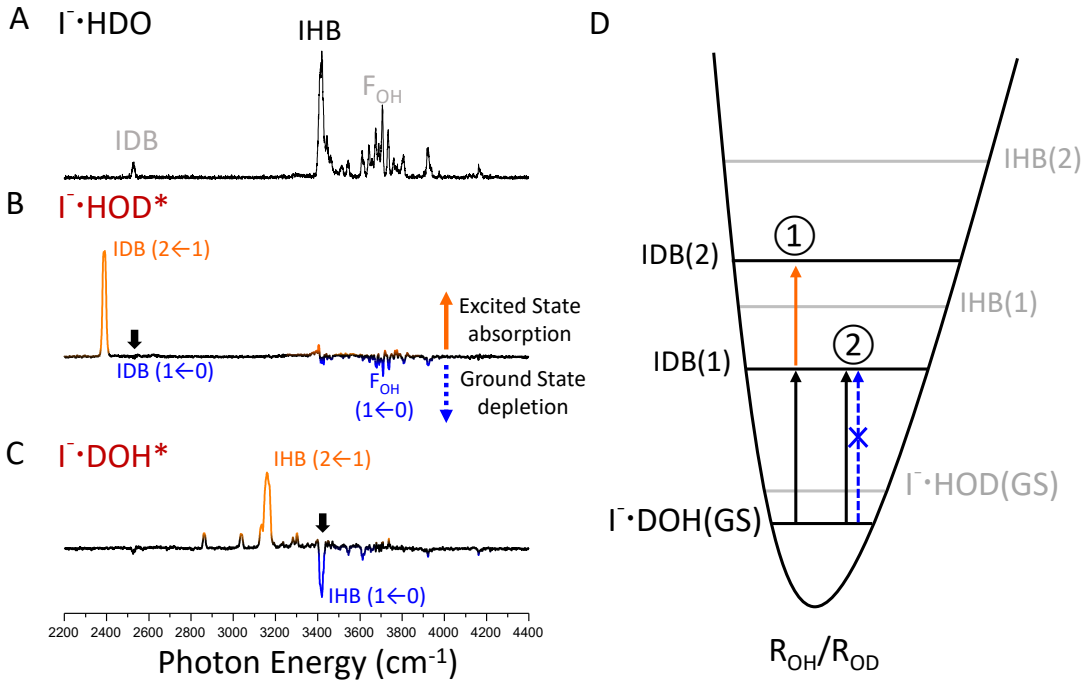

Figure 3.12: Excited state spectra of I⁻·HDO exciting the bound OH/OD band. **(A)** IRPD spectrum of I⁻·HDO at 30 K, the IDB feature is observed through two photon absorption process. **(B, C)** excited state spectra with the IDB(v=1) and IHB(v=1) as initial states, respectively. **(D)** Initial excitation of the vibrational levels of the two isotopomers where GS denotes the ground state and (1) and (2) denotes the first and second vibrational levels.

redistribution (IVR) where the energy flows into other states of similar energies and results in many other available transitions (regime II in Fig. 3.13A). In the limit of no IVR and minor anharmonic coupling to other normal modes, the excited state spectra should be denominated by the enharmonically shifted 2←1 transition (solid stick and arrow in regime I in Fig. 3.13) and other weaker transitions could appear (dashed stick and arrow in regime I in Fig. 3.13) similar to a combination band situation. In the scenario where partial IVR could appear, many other transitions (regime II in Fig. 3.13) could be allowed initiating from the so called 'first tier states'.[34] And in the situation where rapid IVR thermalize the excitation energy the spectra of the hot clusters should display broadened feature near the excited fundamental as a result of the relaxation of the initial excitation (regime III in Fig. 3.13). The experimental results suggest regime I behavior with minor regime II behavior possible. Note that the energy redistribution happens within each cluster but the overall energy distribution of the clusters does not reproduce the internal energy distribution of a thermally equilibrated hot clusters at an elevated temperature since there is no coupling between the clusters or with the bath due to the collision free condition. The ion packet's total energy distribution takes the shape of that of the initial cold clusters but shifted up in energy by one photon energy. The result is a collection of microcanonical (NVE) ensembles that assumes the energy distribution described above. However, since the ion packet started at low temperature the energy distribution is rather narrow, thus the resulted ion packet could be classified as a microcanonical ensemble with finite width (NVEω).

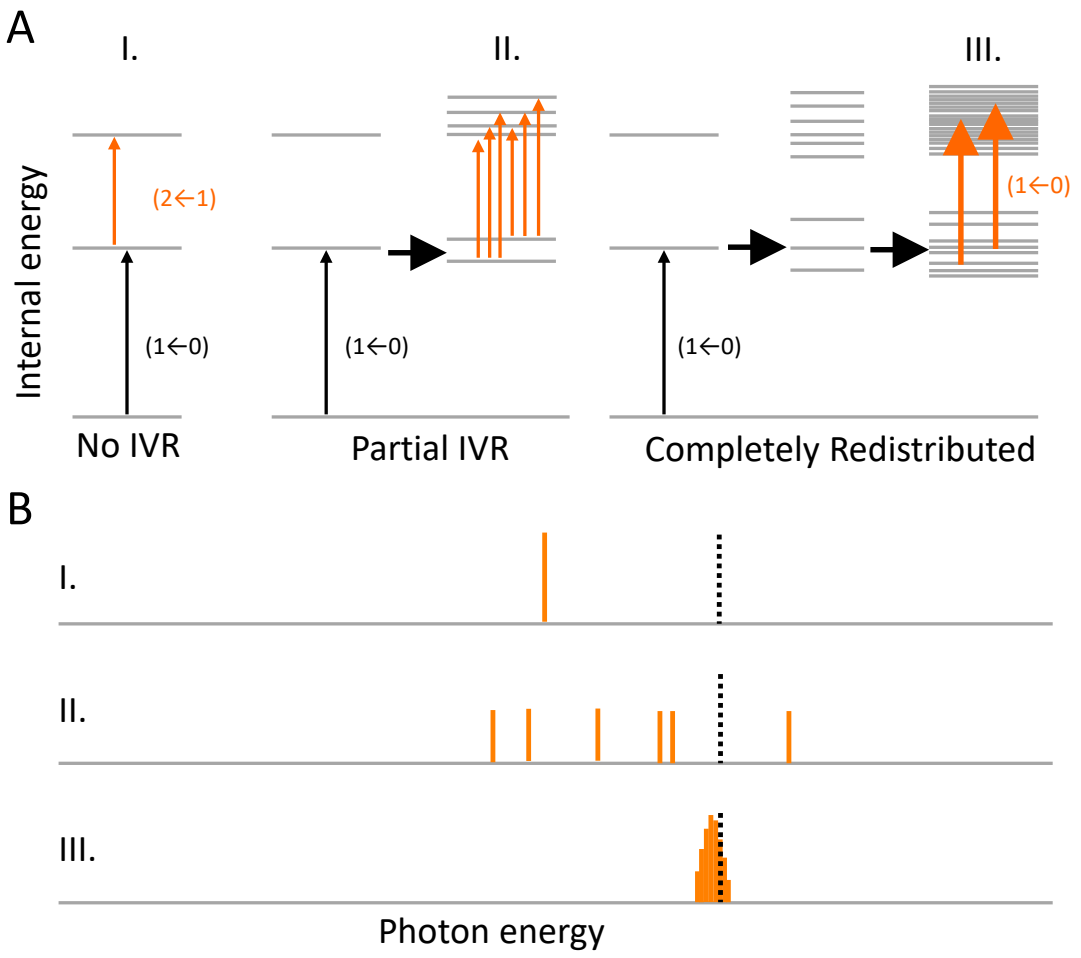

Figure 3.13: Energy level diagrams for different regimes in the excited state spectra's behaviors. Regime I is when the excitation connects two stationary states and no IVR can happen, the strongest contribution will arise from the 1 to 2 transition. Regime II is when IVR rate is slow (in other words, density of state or coupling is low) and only a few energy levels are populated close to the transition energy, several transitions can arise from those states results in a spectrum that has finite features. Regime III is when the density of state is high and IVR rate is fast, the original excitation quickly relaxes and energy is redistributed into low frequency modes, the spectra would appear as a broadened peak around the frequency of the 0 to 1 transition.

The I^-·HDO system significantly reduced the complexity of the vibrational spectra as well as the excited state spectra. The I^-·H_2O system where many states are close in energy which then allows them to couple and mix would display more complex behavior and the excited state spectra is instrumental in dissecting the origin of nearly degenerate transitions. To obtain a more complete view of the complicated system, the excitation laser are fixed at many equally spaced frequencies spanning the entire OH region of the spectra. That allows us to obtain a 2D excited state spectra where one axis is the excitation frequency and the other is the probe frequency (Fig. 3.14B). Similar to the traces displayed in figure 3.12, the new transitions induced by the excitation is colored orange on the contour map whereas the negative signal resulted from the ground state bleaching is colored blue (Fig. 3.14B). The IRPD spectra of the ground state molecule is displayed in figure 4a where the bend overtone ($2\nu_{HOH}$) transition is labeled as ①, the 2HOH+2IO(+), IHB(-), 2HOH+IP(+) and IHB(+), are labeled ②, ③, ④, and⑤ respectively. The assignments were discussed in Chapter 3.1. Additionally, in the higher energy region there are the free OH transitions with rotational fine structures which are also extensively discussed in Chapter 3.1. At a glance each excitation frequency results in many new features that are significantly different from those resulted from other excitation frequencies that is promising for using the excited state spectra as a way to distinguish and assign nearly degenerate transitions such as peak 2-5 in figure 3.14A. A close inspection of the map with respect to the excitation frequency axis reveals that the difference spectra has responses only when the excitation is on resonance (dotted line

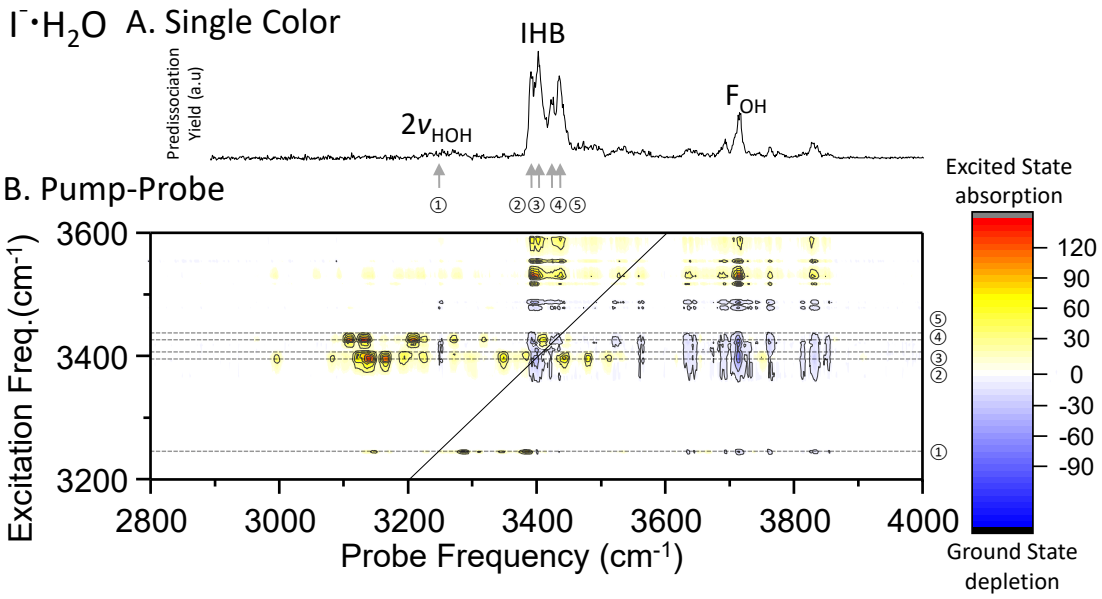

Figure 3.14: Two-dimensional map of the pump-probe spectra. (A) Displays the single laser one color spectra of $I^{-}\cdot H_2O$. **(B)** Displays the 2D map where the pump and probe lasers are fixed at two frequencies and the time delay between the two lasers is fixed at 30 microseconds. The diagonal line labels the points where the pump and the probe lasers are at the same frequency. The dotted lines are the slices at specific pump frequencies labeled by number 1-5.

labeled as ①, ②, ③, ④, and⑤ in Fig.3.14B). This is because the excitation here is incoherent hence the signal only reflects population movement.

The excited state spectra at peak 1-5 can be extracted and compared with theoretically calculated excited state spectra (Fig. 3.15). The theoretical spectra is obtained using the same method as that described in Chapter 3.1. The full dimensional calculation produces eigen states that contains multiple excitations in various normal modes and by setting one of the vibrational excited state as the initial state, the transition probability to other states can be evaluated.

The calculated spectra agree with the experiment well in the bending region but cannot fully reproduce the complexity displayed in the bend overtone and OH stretch region. Part of the reason for the less than satisfactory performance of the calculated spectra is due to the high sensitivity of the vibrational levels to the shape of the potential energy surface. The calculation even at its high level still cannot fully reproduce the levels initiated in the ground state due to the extreme precision required, as discussed in Chapter 3.1. And basing off those vibrational levels and accessing the quantum states higher up in the potential energy surface posts even more stringent requirements to the precision of the PES. In that sense such experimental data really does provide a great bench mark for developing high precision interaction potential for ion water complexes. Such experimental technique can also be adapted to monitor the time dependence of the excited state spectra and could provide insight into the IVR process in a state resolved fashion.

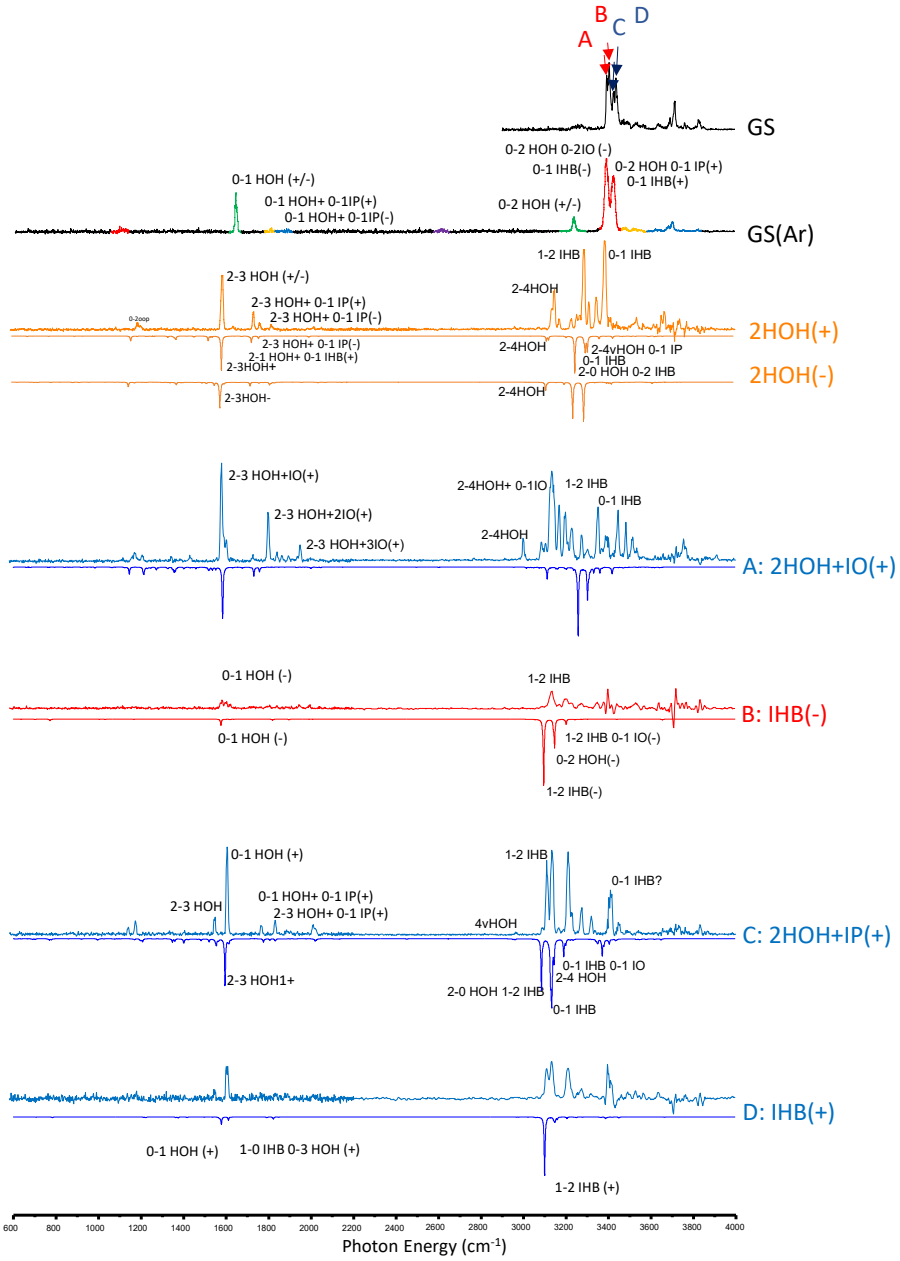

Figure 3.15: Excited state spectra of $I^-\cdot H_2O$ at various pump frequencies. The experimental spectra (upwards) and the calculated spectra (downwards) color coded by their initial states are displayed together. GS represents grounds state and GS(Ar) represents the ground state of the Ar tagged $I^-\cdot H_2O$ complex. The quantum state labeling scheme is the same as that in the Chapter 3.1.

3.3 References

1. Johnson, M. S.; Kuwata, K. T.; Wong, C.-K.; Okumura, M. Vibrational spectrum of $I^-(H_2O)$. *Chemical Physics Letters* **1996,** *260* (5-6), 551-557.

2. Robertson, W. H.; Johnson, M. A. Molecular aspects of halide ion hydration: The cluster approach. *Annual Review of Physical Chemistry* **2003,** *54* (1), 173-213.

3. Arismendi-Arrieta, D. J.; Riera, M.; Bajaj, P.; Prosmiti, R.; Paesani, F. I-TTM model for ab initio-based ion–water interaction potentials. 1. Halide–water potential energy functions. *The Journal of Physical Chemistry B* **2015,** *120* (8), 1822-1832.

4. Ayala, R.; Martınez, J. M.; Pappalardo, R. R.; Sánchez Marcos, E. On the halide hydration study: development of first-principles halide ion-water interaction potential based on a polarizable model. *The Journal of Chemical Physics* **2003,** *119* (18), 9538-9548.

5. Ayotte, P.; Weddle, G. H.; Kim, J.; Johnson, M. A. Vibrational Spectroscopy of the Ionic Hydrogen Bond: Fermi Resonances and Ion− Molecule Stretching Frequencies in the Binary $X^-\cdot H_2O$ (X= Cl, Br, I) Complexes via Argon Predissociation Spectroscopy. *Journal of the American Chemical Society* **1998,** *120* (47), 12361-12362.

6. Bailey, C. G.; Kim, J.; Dessent, C. E.; Johnson, M. A. Vibrational predissociation spectra of $I^-\cdot(H_2O)$: isotopic labels and weakly bound complexes with Ar and N_2. *Chemical Physics Letters* **1997,** *269* (1-2), 122-127.

7. Bajaj, P.; Wang, X.-G.; Carrington Jr, T.; Paesani, F. Vibrational spectra of halide-water dimers: Insights on ion hydration from full-dimensional quantum calculations on many-body potential energy surfaces. *The Journal of Chemical Physics* **2018,** *148* (10), 102321.

8. Horvath, S.; McCoy, A. B.; Elliott, B. M.; Weddle, G. H.; Roscioli, J. R.; Johnson, M. A. Anharmonicities and isotopic effects in the vibrational spectra of $X^-\cdot H_2O$,· HDO, and· D_2O [X= Cl, Br, and I] binary complexes. *The Journal of Physical Chemistry A* **2009,** *114* (3), 1556-1568.

9. Rheinecker, J. L.; Bowman, J. M. The calculated infrared spectrum of Cl^-H_2O using a full dimensional ab initio potential surface and dipole moment surface. *The Journal of Chemical Physics* **2006,** *125*, 133206.

10. Roscioli, J. R.; Diken, E. G.; Johnson, M. A.; Horvath, S.; McCoy, A. B. Prying Apart a Water Molecule with Anionic H-Bonding: A Comparative Spectroscopic Study of the $X^-\cdot H_2O$ (X= OH, O, F, Cl, and Br) Binary Complexes in the 600-3800 cm^{-1} Region. *The Journal of Physical Chemistry A* **2006,** *110* (15), 4943-4952.

11. Sarka, J.; Lauvergnat, D.; Brites, V.; Császár, A. G.; Léonard, C. Rovibrational energy levels of the $F^-(H_2O)$ and $F^-(D_2O)$ complexes. *Physical Chemistry Chemical Physics* **2016,** *18* (26), 17678-17690.

12. Thompson, W. H.; Hynes, J. T. Frequency shifts in the hydrogen-bonded OH stretch in halide-water clusters. The importance of charge transfer. *Journal of the American Chemical Society* **2000,** *122* (26), 6278-6286.

13. Wolke, C. T.; Menges, F. S.; Tötsch, N.; Gorlova, O.; Fournier, J. A.; Weddle, G. H.; Johnson, M. A.; Heine, N.; Esser, T. K.; Knorke, H. Thermodynamics of water dimer dissociation in the primary hydration shell of the iodide ion with temperature-dependent vibrational predissociation spectroscopy. *The Journal of Physical Chemistry A* **2015,** *119* (10), 1859-1866.

14. Lee, H. M.; Kim, K. S. Structures and spectra of iodide–water clusters $I^-(H_2O)_{n=1-6}$: An ab initio study. *The Journal of Chemical Physics* **2001,** *114* (10), 4461-4471.

15. Yang, N.; Duong, C. H.; Kelleher, P. J.; Johnson, M. A.; McCoy, A. B. Isolation of site-specific anharmonicities of individual water molecules in the $I^-\cdot(H_2O)_2$ complex using tag-free, isotopomer selective IR-IR double resonance. *Chemical Physics Letters* **2017,** *690*, 159-171.

16. McCoy, A. B.; Guasco, T. L.; Leavitt, C. M.; Olesen, S. G.; Johnson, M. A. Vibrational manifestations of strong non-Condon effects in the $H_3O^+\cdot X_3$ (X= Ar, N_2, CH_4, H_2O) complexes: A possible explanation for the intensity in the "association band" in the vibrational spectrum of water. *Physical Chemistry Chemical Physics* **2012,** *14* (20), 7205-7214.

17. Shao, Y.; Gan, Z.; Epifanovsky, E.; Gilbert, A. T.; Wormit, M.; Kussmann, J.; Lange, A. W.; Behn, A.; Deng, J.; Feng, X. Advances in molecular quantum chemistry contained in the Q-Chem 4 program package. *Molecular Physics* **2015,** *113* (2), 184-215.

18. Stathopoulos, A.; McCombs, J. R. PRIMME: preconditioned iterative multimethod eigensolver—methods and software description. *ACM Transactions on Mathematical Software (TOMS)* **2010,** *37* (2), 21.

19. Talbot, J. J.; Cheng, X.; Herr, J. D.; Steele, R. P. Vibrational signatures of electronic properties in oxidized water: unraveling the anomalous spectrum of the water dimer cation. *Journal of the American Chemical Society* **2016,** *138* (36), 11936-11945.

20. Wolk, A. B.; Leavitt, C. M.; Garand, E.; Johnson, M. A. Cryogenic Ion Chemistry and Spectroscopy. *Accounts of Chemical Research* **2014,** *47* (1), 202-210.

21. Schlicht, F.; Entfellner, M.; Boesl, U. Anion ZEKE-Spectroscopy of the Weakly Bound Iodine Water Complex. *The Journal of Physical Chemistry A* **2010,** *114* (42), 11125-11132.

22. Olkhov, R. V.; Nizkorodov, S. A.; Dopfer, O. Infrared photodissociation spectra of CH_3+-Ar_n complexes (n = 1-8). *J Chem Phys* **1998,** *108* (24), 10046-10060.

23. Bajaj, P.; Gotz, A. W.; Paesani, F. Toward chemical accuracy in the description of ion–water interactions through many-body representations. I. Halide–water dimer potential energy surfaces. *Journal of Chemical Theory and Computation* **2016,** *12* (6), 2698-2705.

24. Peterson, K. A.; Shepler, B. C.; Figgen, D.; Stoll, H. On the spectroscopic and thermochemical properties of ClO, BrO, IO, and their anions. *J Phys Chem A* **2006,** *110* (51), 13877-83.

25. Zare, R. N. *Angular momentum: understanding spatial aspects in chemistry and physics*. J. Wiley & Sons: 1988.

26. Western, C. M. PGOPHER: A program for simulating rotational, vibrational and electronic spectra. *Journal of Quantitative Spectroscopy and Radiative Transfer* **2017,** *186*, 221-242.

27. Hamm, P.; Stock, G. Nonadiabatic vibrational dynamics in the HCO_2^-·H_2O complex. *The Journal of Chemical Physics* **2015,** *143* (13), 134308.

28. Pitzer, K. S.; Gwinn, W. D. Energy levels and thermodynamic functions for molecules with internal rotation I. Rigid frame with attached tops. *The Journal of Chemical Physics* **1942,** *10* (7), 428-440.

29. Okumura, M.; Yeh, L. I.; Myers, J. D.; Lee, Y. T. Infrared Spectra of the Cluster Ions $H_7O_3^+ \cdot H_2$ and $H_9O_4^+ \cdot H_2$. *J. Chem. Phys.* **1986,** *85*, 2328-2329.

30. Bailey, C. G.; Kim, J.; Johnson, M. A. Infrared spectroscopy of the hydrated electron clusters $(H_2O)_n^-$, n=6, 7: Evidence for hydrogen bonding to the excess electron. *J. Phys. Chem.* **1996,** *100*, 16782.

31. Bailey, C. G.; Kim, J.; Dessent, C. E. H.; Johnson, M. A. Vibrational Predissociation Spectra of $I^- \cdot (H_2O)$: Isotopic Labels and Weakly Bound Complexes with Ar and N_2. *Chem. Phys. Lett.* **1997,** *269*, 122-127.

32. Ayotte, P.; Bailey, C. G.; Kim, J.; Johnson, M. A. Vibrational predissociation spectroscopy of the $(H_2O)_6^- \cdot Ar_n$, n>6, clusters. *J. Chem. Phys.* **1998,** *108*, 444-448.

33. Ayotte, P.; Weddle, G. H.; Kim, J.; Johnson, M. A. Mass-Selected "Matrix Isolation" Infrared Spectroscopy of the $I^- \cdot (H_2O)_2$ Complex: Making and Breaking the Inter-Water Hydrogen-Bond. *Chem. Phys.* **1998,** *239*, 485-491.

34. Yamada, Y.; Okano, J.-i.; Mikami, N.; Ebata, T. Picosecond time-resolved study on the intramolecular vibrational energy redistribution of NH stretching vibration of jet-cooled aniline and its isotopomer. *Chem. Phys. Lett.* **2006,** *432* (4-6), 421-425.

CHAPTER 4

Development of Various Generic Two Laser Experiments and Isolation of Site-specific Anharmonicities of Individual Water Molecules in the $I^-\cdot(H_2O)_2$ Complex Using Tag-free, Isotopomer Selective IR-IR Double Resonance

The material in this chapter is adapted with permission from Yang, Nan, Chinh H. Duong, Patrick J. Kelleher, Mark A. Johnson, and Anne B. McCoy. "Isolation of site-specific anharmonicities of individual water molecules in the $I^-\cdot(H_2O)_2$ complex using tag-free, isotopomer selective IR-IR double resonance." Chemical Physics Letters 690 (2017): 159-171.

4.1. Introduction

In Chapter 3, we explored the spectra of the iodide water binary complex. The small system turned out to be very challenging to interpret due to its highly quantum nature, anharmonicity, resonances, tunneling, nuclear spin statistics and rovibrational features are all present in the system. The excited state spectra is state dependent (non-ergodic) due to the low density of state. These behaviors are not generic for larger water clusters, in this chapter we add one additional water molecule to the iodide water binary complex to form $I^-\cdot(H_2O)_2$. The additional water significantly increase the density of state and makes the system more ergodic upon one photon excitation. In addition the suppression of rotational and tunneling features significantly reduces the spectral complexity. Here we focus mainly on the H-bond environment specific anharmonicity and Fermi resonance behaviors that is more important in the larger water clusters.

The characterization of the primary hydration shell around halide ions has undergone a renaissance over the past twenty years through a series of increasingly sophisticated spectroscopic investigations of the cold, size-selected cluster ions.[1-20] Important early advances exploited Ar and H_2-tagging [1, 21-23] as means of establishing the overall band patterns associated with small water networks.[2, 24] These structures generally feature water molecules in the primary hydration shell bound to the ion with one OH group (denoted the single ionic H-bond or IHB motif), leaving the partner OH free to H-bond with neighboring water molecules (here denoted IH, or inter-water H-bond). The simplest example of this is found in the $I^-\cdot(H_2O)_2$ ternary cluster, with the calculated structure indicated in Fig. 4.1a and corresponding band pattern obtained by D_2 messenger tagging spectroscopy in the OH stretching region in Fig. 4.1b. The two water molecules

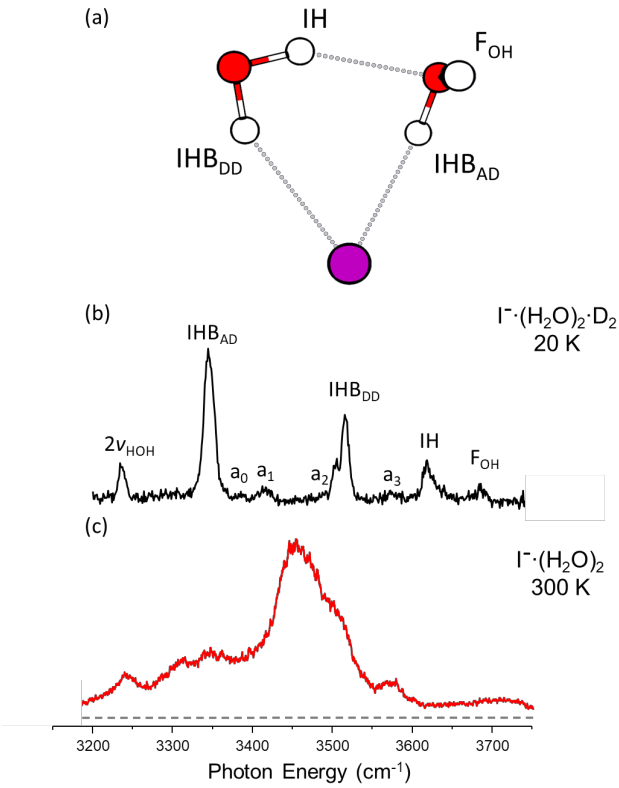

Figure 4.1: (a) Calculated minimum energy structure of $I^-\cdot(H_2O)_2$ at the MP2/aug-cc-pVTZ-PP level of theory [31] and (b) D_2-predissociation spectrum of $I^-\cdot(H_2O)_2\cdot D_2$ at a trap temperature of 20 K. The main OH stretching fundamentals are identified by their dominant contributions to the displacement vectors at the harmonic level: the free OH (F_{OH}), inter-water hydrogen bonded OH group (IH), ionic H-bonded (IHB) OH group on the AD water (IHB_{AD}), and the corresponding IHB on the DD water (IHB_{DD}). The HOH bend overtone ($2\nu_{HOH}$) is also identified, [32,33] along with several weaker transitions (denoted a_n) with energies and assignments included in Table 1. (c) Infrared photo- dissociation (IRPD) spectrum of $I^-\cdot(H_2O)_2$ at 300 K trap temperature. The baseline is indicated by the gray dashed line. The loss of the pattern of four fundamentals in (b) is interpreted to indicate that the H-bond between the two water molecules is broken in the hot ensemble. [30]

are distinguished by their DD and AD (A = acceptor and D = donor) H-bonding environments. This structure accounts for the four bands that are nominally associated with the four unique OH positions in the cyclic ground state structure, as indicated by the assignment scheme in Fig. 4.1b. These features systematically increase in intensity with increasing red-shift, in keeping with the usual spectroscopic propensity rules for H-bonds.[25-28] Subsequent studies[29-30] followed the temperature dependent breakup of the water dimer motif by monitoring the disappearance of the four-band pattern and emergence of a broad feature (300 K spectrum displayed in Fig. 4.1c) near the midpoint of the two IHB bands in the cold cluster spectrum, consistent with the presence of two asymmetrically bound water molecules (on average) undergoing largely independent, high amplitude displacements in the field of the ion.

In this study, we isolate the individual contributions of the DD and AD water molecules to the overall pattern, with specific attention to the origin of the weaker bands (a_n in Fig. 4.1b). This involves establishing the extent to which the excited state vibrational levels of the two water molecules are coupled to each other, as well as the site-dependence of the coupling between the two OH groups on the same water molecule. We obtain this information through several advances in photodissociation mass spectrometry. In order to quantify the expectedly small extent of inter-molecular coupling, we acquired the spectra of the cold ion using a two-color IR-IR photodissociation strategy that does not require a messenger tag, and thus reveals the intrinsic locations of the various bands. Second, we exploit the IR-IR method's capability of isolating the spectra of the isotopomers created upon partial isotopic labeling among the two water molecules. Theoretical analysis of the band evolution upon isotopic

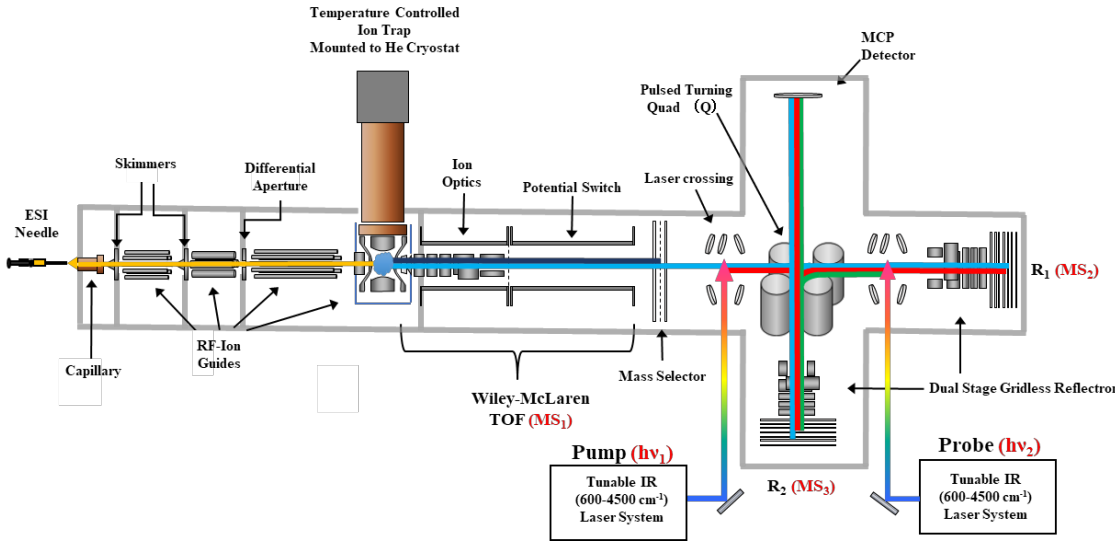

Figure 4.2: Diagram of the temperature controlled cryogenic ion vibrational spectrometer with two laser capabilities at Yale. The mass selected ions intersect the first laser crossing (pump, $h\nu_1$), yielding photo excited ions and/or photofragments. Parent and fragment ions, together with metastable decay products, are separated by the Zajfman-inspired[34], coaxial, dual-stage gridless retro-reflectron (R_1) and intersect with the second laser crossing (probe, $h\nu_2$) where either parent or fragment ions can be irradiated. The ion beam is then turned 90° by the pulsed DC turning quad (Q) into the second reflectron (R_2) to separate photofragments produced by the probe laser. Lastly, the ion beam emerging from R_2 crosses the main ion beam axis at 90° and moves toward the MCP detector where parent, pump laser fragments and probe laser fragments appear at different arrival times. This design offers great versatility by allowing the probe laser to interact with the ion packet either before or after mass separation by R_1 by simply changing the timing sequence. In particular, one can obtain isotopomer-selective dip spectra (Fig. 4.3e),[35] tag-free linear spectra by two-color IR-IR photodissociation of bare ions (Fig. 4.3d), or the spectrum of the excited clusters generated by resonant excitation of cold clusters by the pump laser below their dissociation thresholds (Fig. 4.3c). Finally, spectra of tagged clusters (Fig. 4.3a) can be obtained with very low background in a single laser mode where the probe laser interacts with parent ions after mass selection by R_1 to isolate them from fragments arising from metastable decay along the flight tube en route to R_1. Details about these components and their design are discussed in Chapter 2.

substitution then yields an unprecedented picture of the spectral behavior associated with the two binding motifs (AD and DD) from both the intra- and inter-molecular perspectives.

4.2. Implementation of the IR-IR scheme in a new triple focusing TOF photofragmentation mass spectrometer

As discussed previously,[36] the isotopomer (or conformer)-selective IR-IR method requires three stages of mass separation and two laser interaction regions (Fig. 4.2), hence denoted as an IR^2MS^3 class of secondary mass analysis.[37-38] In essence, IR^2MS^3 is a photochemical hole-burning approach that exploits sequential removal of population from all conformers by a powerful pump laser ($h\nu_1$) that is scanned through the spectrum, while a second probe laser ($h\nu_2$) monitors the population of a particular conformer in the usual predissociation scheme. The first mass spectrometer (MS_1) isolates a particular m/z for laser excitation by the pump ($h\nu_1$). A second stage of mass selection (MS_2) separates non-dissociated parent ions from the photofragments. The ions that are not dissociated by $h\nu_1$ are then irradiated by a probe laser ($h\nu_2$) which is fixed to a transition unique to a single conformer, resulting in fragments that are separated by a third stage of mass selection (MS_3). Thus, the entire spectrum of the conformer selected by the probe laser ($h\nu_2$) appears as a series of dips in the otherwise constant signal obtained by monitoring the probe fragment yield as the pump laser ($h\nu_1$) is scanned through transitions associated with the same conformer (Fig. 4.3e). This method is particularly useful when applied in a messenger tagging mode, as all resonant excitations lead to photofragmentation.

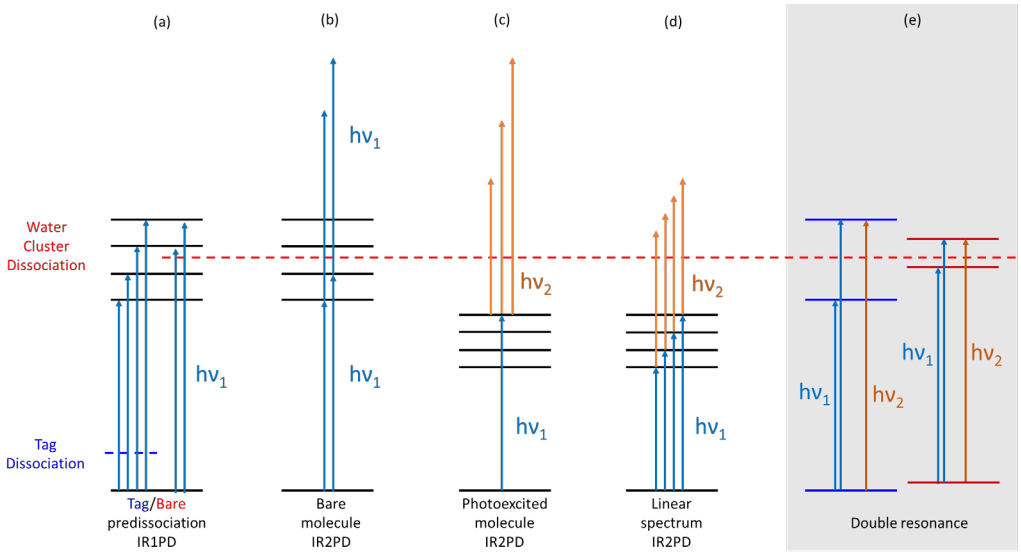

Figure 4.3: Schematics for various experiments that can be executed on the platform introduced in Fig. 4.2. including schemes for obtaining (a) tag predissociation (denoted IR1PD for single-color, one photon) spectra where the tag is chosen to have a low binding energy (blue dotted line) such as D_2 in this specific case, and bare (i.e. tag free) predissociation IR1PD spectra above the water cluster binding energy (red dashed line); (b) single-color IR two photon dissociation (IR2PD) spectra of the bare molecule below the water cluster dissociation energy by sequential absorption of two photons of the same color before dissociation; (c) two-color IR2PD spectra of photoexcited molecules obtained by fixing the first laser ($h\nu_1$) on a strong transition below the dissociation threshold and scanning the second laser ($h\nu_2$); (d) two-color IR2PD linear spectra of the cold molecules obtained by fixing the second laser ($h\nu_2$) on a transition unique to the excited state molecule and scanning the first laser ($h\nu_1$); and (e) double resonance depletion spectra obtained by fixing the second laser ($h\nu_2$) on a transition unique to one of the isomers and removing population from the ground state using the first laser (scanned). The difference in ground state energy of the two isomers in (e) is governed by zero-point energy.

In this work, we have implemented the IR-IR scheme in a modified format with the schematic layout in Fig. 4.2, which was designed to optimize the resolution of the second mass isolation stage (MS_2) by incorporating aspects of the IR^2MS^2 scheme employed by the Asmis group.[38] This was accomplished by replacing the original co-axial time of flight component[39] with a dual-stage retro-reflectron (R_1). The first laser interaction occurs as before at the transient focus of the Wiley-McLaren[40] extraction optics from the ion source. The second laser interaction occurs at the transient focal plane of the first reflectron (R_1), which reflects the beam directly back on the initial drift axis. The second laser can then easily probe either undissociated parents or the fragment ions generated by the first laser. Photofragments from the second laser are then separated from parents by turning the retro-reflected ion beam 90° into a second reflectron (R_2) using a pulsed DC quadrupole, Q, which is briefly switched on after the ions have passed through to the probe laser interaction region. Q is then switched off while the ions are dispersed in R_2 so that they then travel back orthogonal to the main ion beam and are detected by a microchannel plate (MCP) detector (Photonis) at the focal plane of R_2. The improvement of the mass separation step over the previous arrangement[35] is about a factor of 10, allowing us to work with lighter messenger tags such as H_2 (the previous version was designed for Ar tagging).

4.3. Applications of two-color IR-IR photofragmentation to isotopologues of $I^-\cdot(H_2O)_2$

4.3.1. Tag-free detection of the linear absorption spectrum: $I^-\cdot(D_2O)_2$

As a first application of IR-IR methods to the $I^-\cdot(D_2O)_2$ system, we quantify the perturbation by the D_2/H_2 messenger tag (see Fig. 4.3a), which was used in our prior study (and found to be quite similar to that recorded with Ar tagging[30, 41]) to obtain the

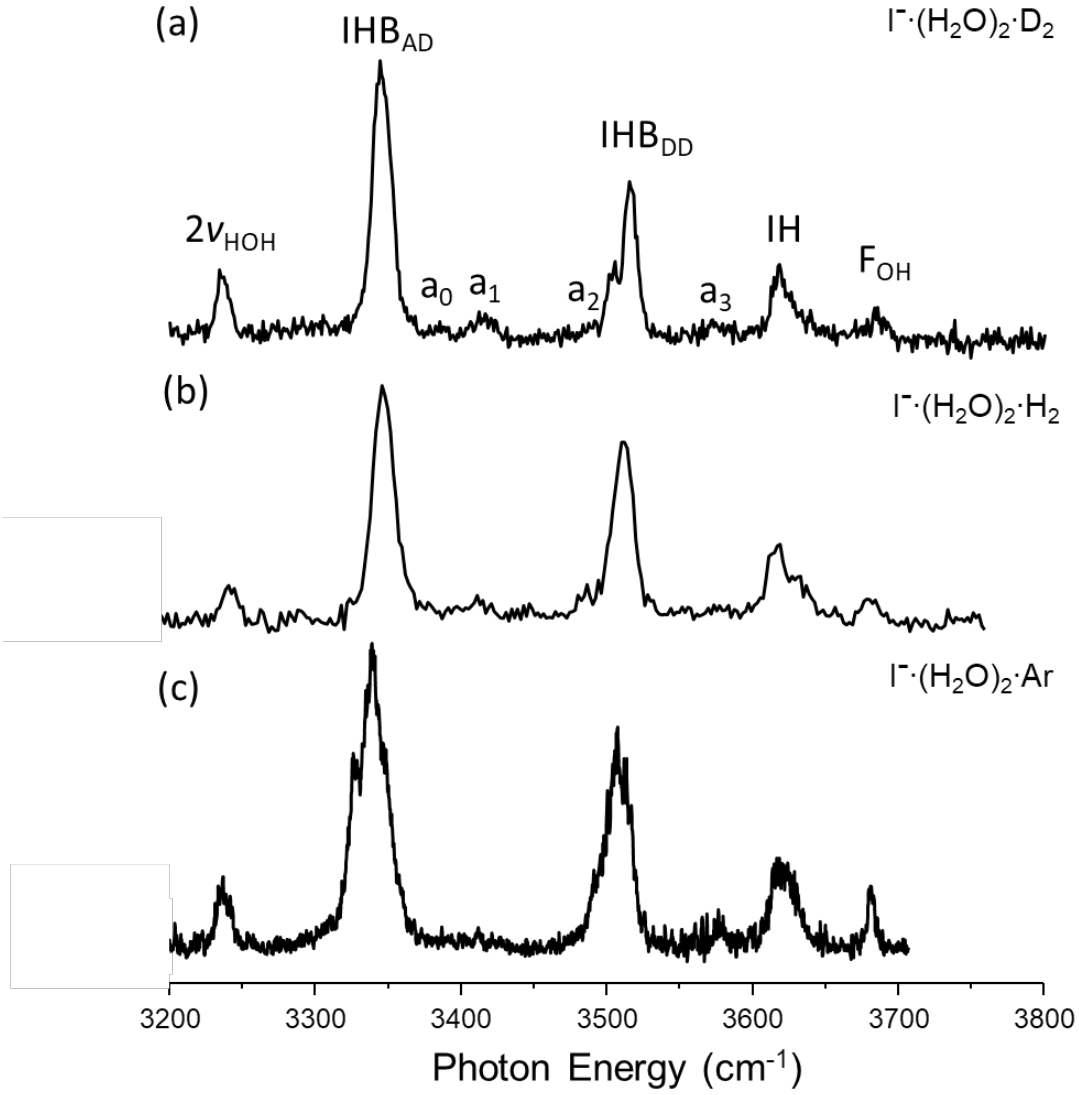

Figure 4.4: Comparison between the predissociation spectra of $I^-\cdot(H_2O)_2$ obtained with (a) D_2, (b) H_2, and (c) Ar tags.

vibrational spectra of the cold ion (Fig. 4.4). The main challenge in measuring the spectrum of the bare ion is that the dissociation energy estimated from thermochemistry to be about 3500 cm^{-1},[42-43] which lies above the OD stretching region. In the commonly used infrared multiple photon dissociation (IRMPD) approach, this issue is overcome in a scheme where resonant excitation is followed by sequential (incoherent) absorption of a sufficient number of additional photons (at the same energy) to fragment the ion.[44-45] This method has the drawback, however, that the absorption spectrum of the excited ion, $\sigma_{ex}(\nu)$, can differ substantially from that corresponding to the cold ion, $\sigma_0(\nu)$, leading to "IRMPD transparent" features.[46] In the case of water clusters, only two photons in the OD stretching region are required to achieve dissociation (henceforth denoted IR2PD) as indicated by Eqs. 4.1 and 4.2:

$$I^-\cdot(D_2O)_2 + h\nu_1 \rightarrow [I^-\cdot(D_2O)_2]^* \qquad \text{(Eq. 4.1)}$$

$$[I^-\cdot(D_2O)_2]^* + h\nu_2 \rightarrow I^-\cdot(D_2O) + D_2O. \qquad \text{(Eq. 4.2)}$$

This enables an alternative scheme where the second photon energy, $h\nu_2$, can be tuned to optimize photodissociation (Eq. 4.2) for all the excited states $[I^-\cdot(D_2O)_2]^*$ reached by resonant excitation with $h\nu_1$ (Eq. 4.1).

Based on our earlier work,[30] the $I^-\cdot(H_2O)_2$ ion represents a dramatic case of band suppression in single-color ($h\nu_1 = h\nu_2$) IR2PD (see Fig. 4.3b) spectroscopy because the spectrum changes qualitatively above about 125 K, as illustrated in the change from Fig. 4.1b to 4.1c. The present IR-IR scheme exploits this disadvantage of single-color IR2PD to provide a rational scheme for acquiring linear spectra of cold ions in the spectral energy range below the dissociation limit. This can be accomplished by first directly measuring the spectrum $[\sigma_{ex}(\nu)]$ of the $[I^-\cdot(D_2O)_2]^*$ cluster (i.e., after it has been excited

at resonance by the first laser ($h\nu_1$)). In this mode (see Fig. 4.3c), the second laser, $h\nu_2$, is scanned over an energy range such that $h\nu_1+h\nu_2>D_o$. Then, by fixing the second laser at an energy where the cold ions do not absorb, but the hot $[I^-\cdot(D_2O)_2]^*$ clusters have substantial cross-section, one can obtain the linear spectrum of the cold molecule by scanning $h\nu_1$ (see Fig. 4.3d). This general approach has been reported by Niedner-Schatteburg and co-workers[47] in an application to more complex ions at 300 K, and here we extend the approach to the cryogenically cooled ion regime. We note also that the two-color schemes are well developed since the earliest days of IRPD spectroscopy, first by Lee and co-workers[22] and then Rizzo and co-workers[48] in a variation where selective IRMPD of excited molecules with a CO_2 laser (and hence many photons) was used to obtain the linear spectrum.

The energetic profile describing the two-color IR2PD method to the $I^-\cdot(D_2O)_2$ system is illustrated in Fig. 4.5. Excitation of a sharp resonance associated with the shallow minimum (I) by $h\nu_1$ creates an ensemble of ions in region (II) where the water dimer has (on average) broken apart, but the two water molecules remain attached to the ion. Fig. 4.6 presents the spectra of these $[I^-\cdot(D_2O)_2]^*$ ions prepared by photoexcitation of the cold ion (Figs. 4.6b,c,d) at three of the strong resonances identified by D_2 predissociation of $I^-\cdot(D_2O)_2\cdot D_2$ (Fig. 4.6a), which corresponds to the scheme in Fig. 4.3c. We also compare these spectra with those of the thermally excited ions (Figs. 4.6e,f) obtained at trap temperatures of 160 and 300 K using IR1PD (see Fig. 4.3a). Note that the three spectra of the resonantly excited ions are quite similar to each other, consistent with rapid intracluster vibrational energy redistribution (IVR)[49] upon excitation at about 60% of the dissociation energy (~3500 cm^{-1}).[42]

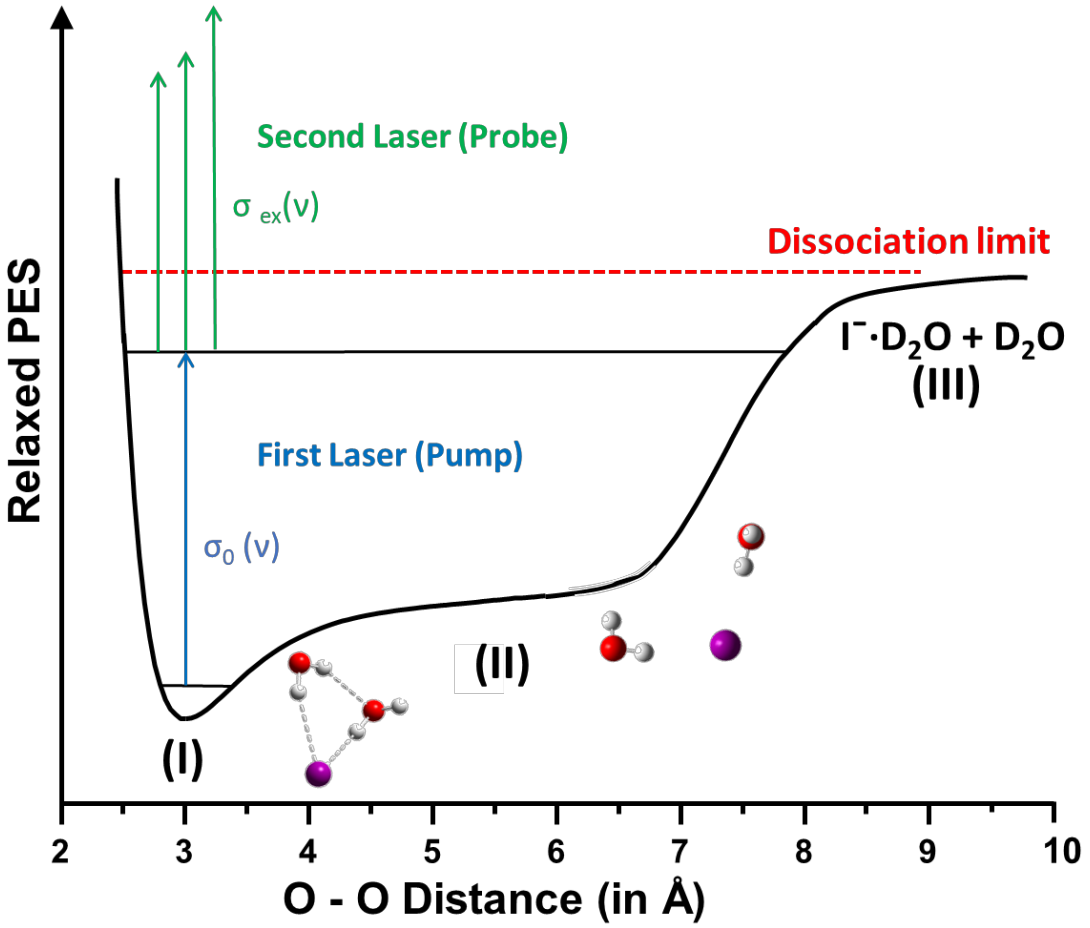

Figure 4.5: The black curve is the calculated (MP2/aug-cc-pVTZ-PP) potential energy as a function of the O-O distance in the $I^-\cdot(D_2O)_2$ cluster with other parameters relaxed, where region (I) corresponds to the cyclic ring structure at the global minimum, region (II) indicates more open structures where the inter water H-bond is broken to yield freely rotating water monomers, and (III) refers to dissociation of a water monomer.[30] The blue arrow represents the pump laser fixed on a known transition while the green arrows represent the scanning probe laser. $\sigma_0(\nu)$ and $\sigma_{ex}(\nu)$ are the ground state and excited state absorption cross sections as functions of photon energy, respectively.

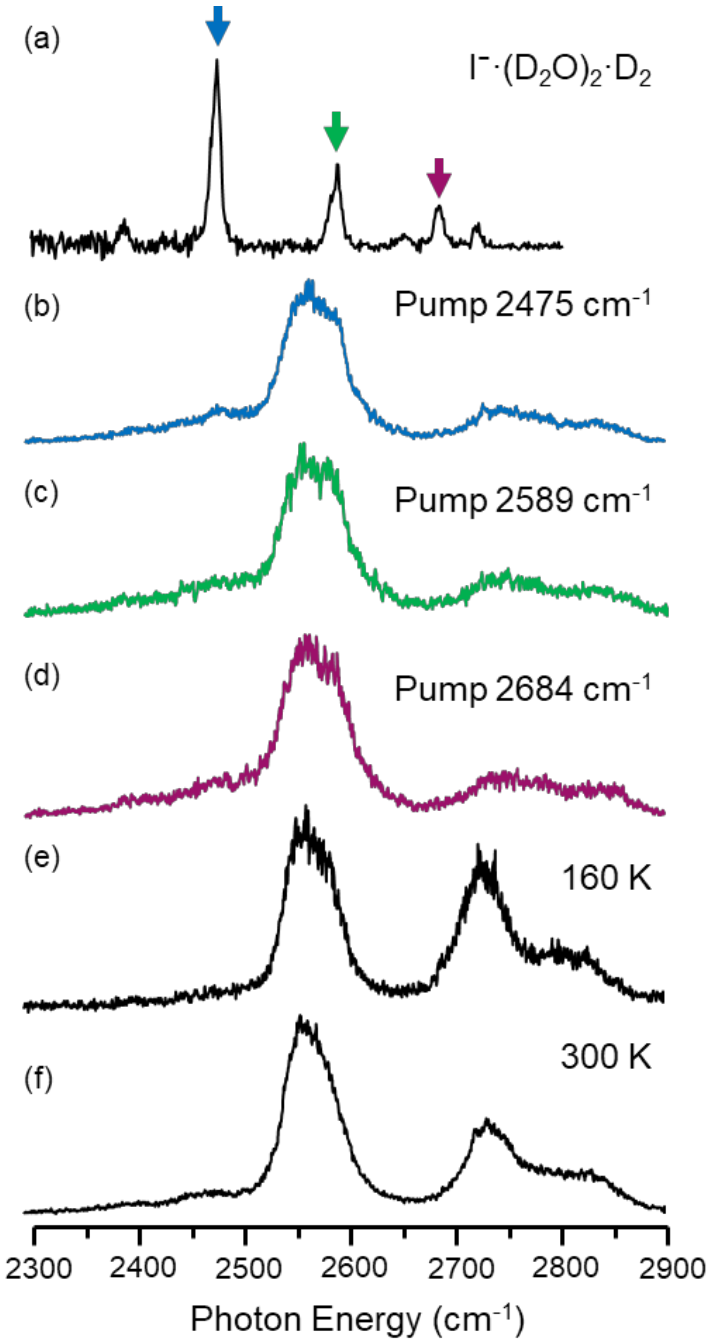

Figure 4.6: (a) IR1PD D_2 predissociation spectrum of D_2 tagged $I^-\cdot(D_2O)_2$. The color-coded arrows indicate the pump laser ($h\nu_1$) energies leading to excited ions with the photodissociation spectra displayed in traces (b), (c), (d), (more pump frequencies are shown in Fig. 4.7). In addition, traces (e) and (f) are single laser IR1PD spectra of bare $I^-\cdot(D_2O)_2$ at trap temperatures of 160 and 300 K, respectively.

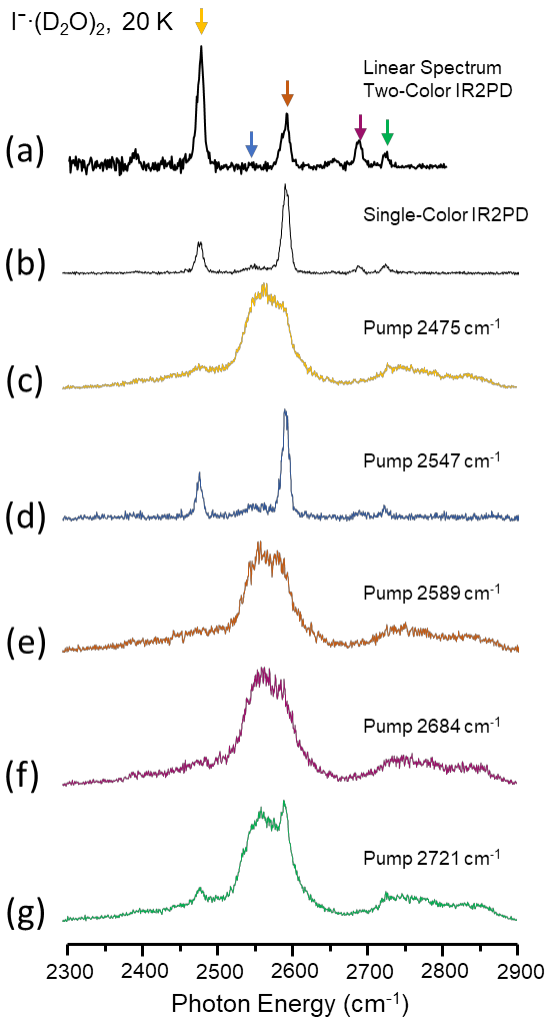

Figure 4.7: The (a) two-color IR2PD (probe at 2589 cm^{-1}) and (b) single-color IR2PD spectra obtained by the methods described in Fig. 3d and Fig. 3b, respectively. The colored spectra were gathered by the method outlined in Fig. 3c where the pump laser was parked at (c) 2475 cm^{-1}, (d) 2547 cm^{-1}, (e) 2589 cm^{-1}, (f) 2685 cm^{-1}, and (g) 2721 cm^{-1}. When there is no absorption (blue arrow) the probe laser (hv_2) simply reproduces the single color IR2PD spectra (d). When the cross section for absorption of the pump laser is low (e.g., at 2721 cm^{-1}), the probe laser sees a distribution of both photoexcited and ground state ions. The resulting spectrum (g) therefore resembles a composite of the single- and two-color IR2PD spectra (e.g., b + c).

The suppression of the band around 2750 cm^{-1} with increasing temperature suggests that photoexcited ions behave as would be anticipated for an effective temperature above 300 K, which is the highest temperature available with our current apparatus. Of course, photoexcitation of initially cold ions creates a condition closer to a microcanonical ensemble. To obtain even a rough estimate of the effective temperature achieved by absorption of a photon around 3500 cm^{-1}, one would need the heat capacity of a system undergoing very large amplitude motion as it evolves from the cyclic ground state structure to the open condition of two independently orbiting water molecules. As this involves intra-cluster dissociation of the water dimer, a process akin to a microscopic "phase transition,"[50] we simply remark here that the photoexcited ions behave as a thermal ensemble with an internal temperature greater than 300 K. Quantifying the connection between internal energy and effective temperature appears to be a very productive avenue for future work, however, where one can envision measuring the energy dependent phase space available to an extremely anharmonic motion.[51]

The fact that excitation of all three bands yields hot clusters with very similar photodissociation spectra (Figs. 4.6b,c,d), but which are dramatically different from that of the cold cluster (Fig. 4.6a), creates a very favorable scenario for detection of the linear spectrum of the cold ions using two-color IR2PD. Fig. 4.8a (black trace) compares the spectrum obtained using single color IR2PD (see Fig. 4.3b) with that obtained with D_2-tagging (4.8c), and two-color IR2PD (see Fig. 4.8b) in which $h\nu_1$ is scanned through the spectrum while $h\nu_2$ is held fixed at 2550 cm^{-1} (arrow in 4.8a). The spectrum of the cluster after excitation at the IDB_{DD} transition at 2589 cm^{-1} is reproduced from Fig. 4.6c in the green trace of Fig. 4.8a. Note that the two-color IR2PD linear spectrum (4.8b) is

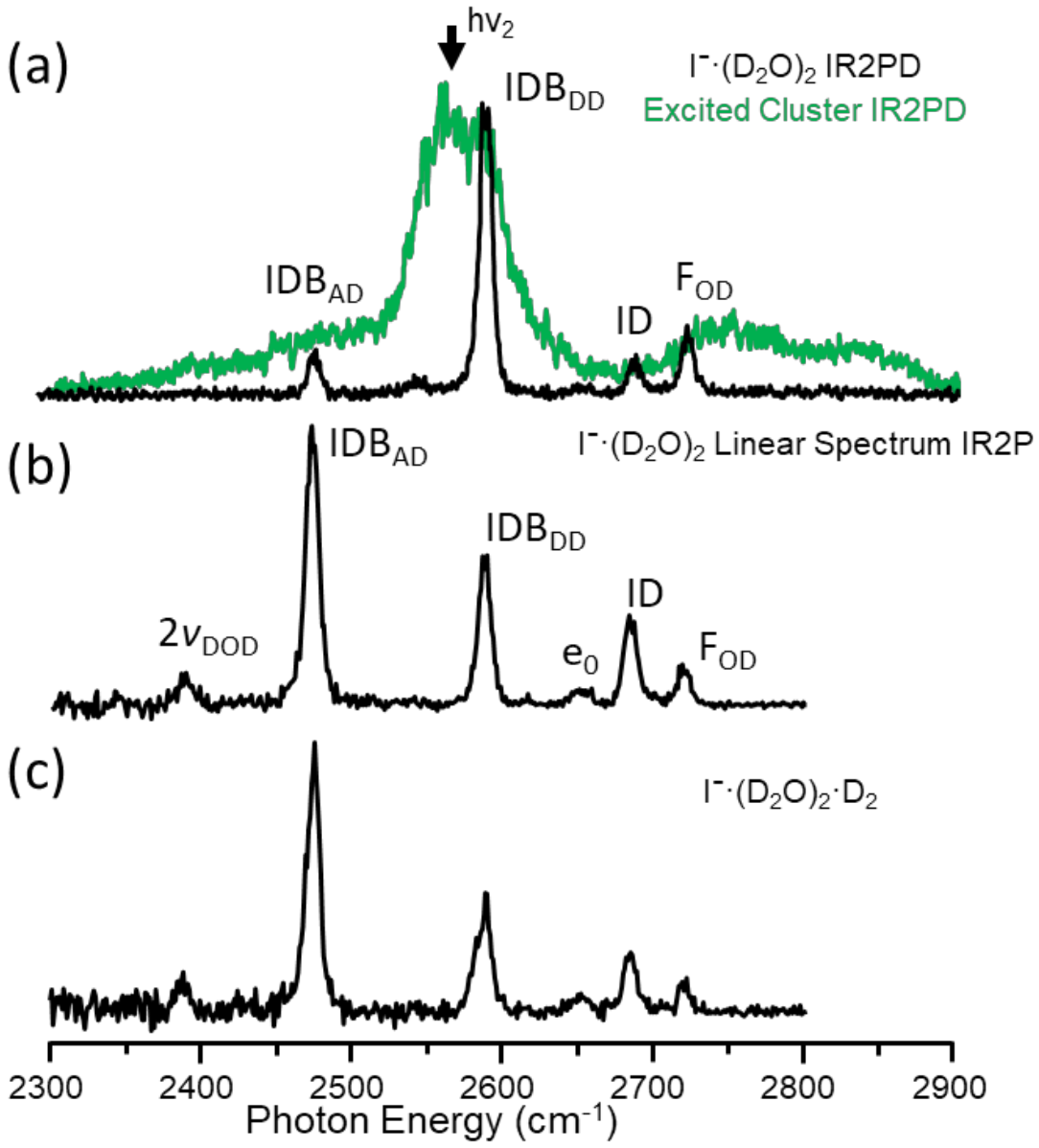

Figure 4.8: (a) The black trace is the single color IR2PD spectra of $I^-\cdot(D_2O)_2$ [see Fig. 4.3b], while the green trace is the spectrum of the cluster after excitation at 2589 cm^{-1} [see Fig. 4.3c]. The arrow in (a) indicates the probe laser position used to obtain the two-color IR2PD spectrum (b). (c) is the predissociation spectrum of D_2 tagged $I^-\cdot(D_2O)_2$. $2\nu_{DOD}$ is the D_2O bend overtone. IDB, ID and F_{OD} are the OD stretch frequencies which can be found in Table 4.1 together with the assignment of combination band e_0.

essentially identical to that obtained with D_2 tagging (4.8c), thus establishing that, in this case, the tag effect is negligible (shifts <1 cm^{-1}). This result is somewhat surprising as a number of reports have recently appeared raising caution about the distortion of the spectra obtained using the tagging method.[52-55] This minimal tag effect is consistent, however, with the small observed red shift of the D_2 stretch[56] (37 cm^{-1}, see Fig. 4.9) and calculated D_2 docking configuration, which is directly to the ion in a position rather distant from both water molecules as indicated in Fig. 4.10.

It is interesting to note that the distorted intensity profile in the single color IR2PD spectrum (4.8a, black trace) can be readily understood as a consequence of the different cross sections that govern the absorption of the first (Fig. 4.8b) and second (green overlay in 4.8a) photons. Thus, the IDB_{AD}, ID, and $2\nu_{DOD}$ bands are suppressed in the single-color, IR2PD spectrum (black trace in Fig. 4.8a) as these frequencies have low cross sections in the dissociation spectrum of the hot cluster (green trace in Fig. 4.8a). The two-color scheme overcomes this difficulty by forcing photodissociation to occur through absorption of a second photon that is fixed at an energy where all photoexcited clusters have similar cross sections, regardless of the transition excited in the linear OD stretching region. It is also useful to emphasize that the protocol at play in the experimental layout (Fig. 4.2) suppresses unwanted background from single-color IR2PD produced by the scanning laser, since these fragments are rejected before the undissociated parents are excited by the second laser, $h\nu_2$.

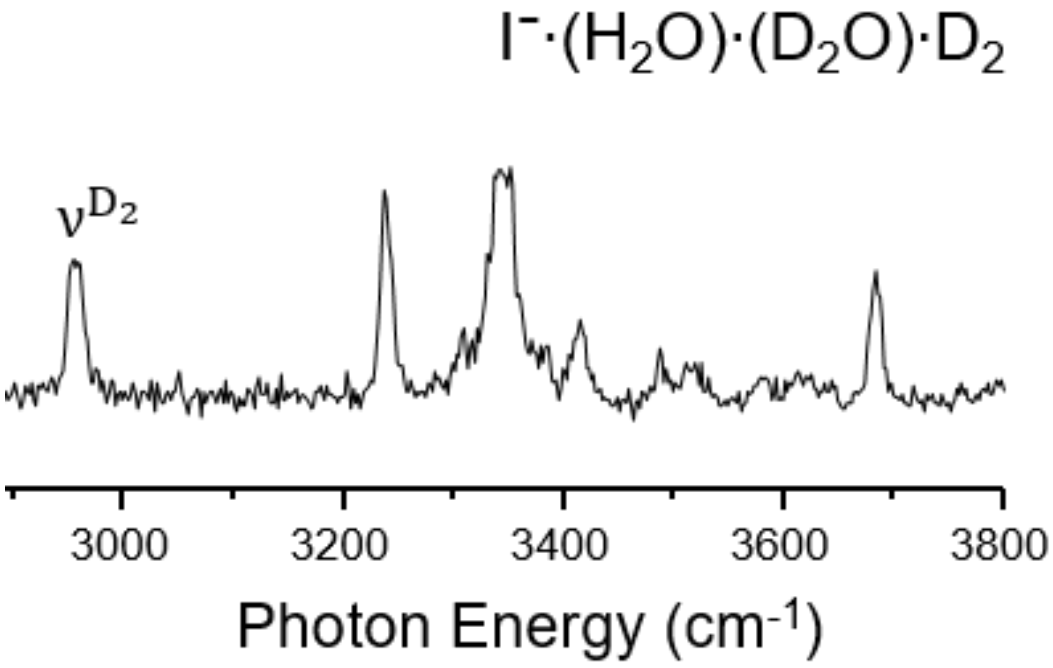

Figure 4.9: D_2-predissociation spectrum of $I^-\cdot(H_2O)(D_2O)$. The position of the D_2 transition is indicated by ν^{D_2}, which appears at 2957 cm^{-1} as opposed to the unperturbed position at 2993.6 cm^{-1}.

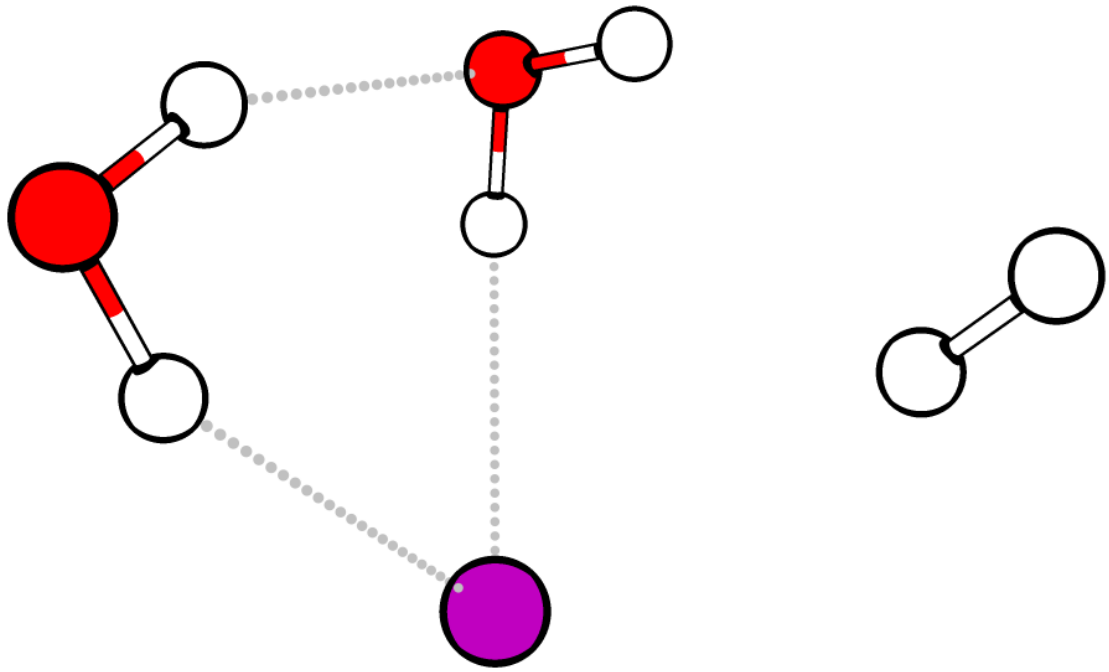

Figure 4.10: Calculated minimal energy structure of $I^-\cdot(H_2O)_2\cdot D_2$ using VPT2 at the MP2/aug-cc-pVTZ-PP level of theory.

So far, the system shown here are all well below the dissociation limit with absorption of one IR photon. We also demonstrate the case where the pump laser energy exceeds the dissociation energy threshold which results in rapid dissociation of the excited clusters before interacting with the second laser. Such process leaves only the clusters that did not absorb any photon behind and the second laser detects the same spectra as if the pump laser was never turned on (Fig. 4.11 g-k). On the other hand, when the pump laser photon energy is below the dissociation energy (~3500 cm^{-1}), the laser irradiated ion packet shows similar behavior to the case shown before (Fig 4.7b-g) where a fraction of the ions absorbs one photon while others do not (Fig. 4.11a-f), depending on the cross section at the excitation frequency. The clusters that have absorbed a photon displays broad features and the clusters that did not absorb any photon shows sharp features same as those in the cold cluster spectra, the ion packet as a whole has features from both of them (Fig. 4.11a-f). To confirm that the resulted excited state spectra with both the broad and the sharp feature is truly a mixture of cold and hot clusters instead of mode dependent non-ergodic behavior similar to that displayed by the $I^-\cdot(H_2O)$ complex discussed in Chapter 3.2, we picked one transition and took excited state spectra at various positions on the shoulder of that peak. Such operation allows us to tune the fraction of clusters that is being excited by the first laser and the result indeed suggests that the spectra contain two separate contribution from hot and cold clusters (Fig 4.12). The higher the cross section (closer to the maxima of the peak) the more intense is the broad feature suggesting more of the cold clusters are absorbing a photon. At the maximum cross section frequency, all clusters absorb at least one photon hence the sharp features completely disappears and the resulted spectra only has contribution from

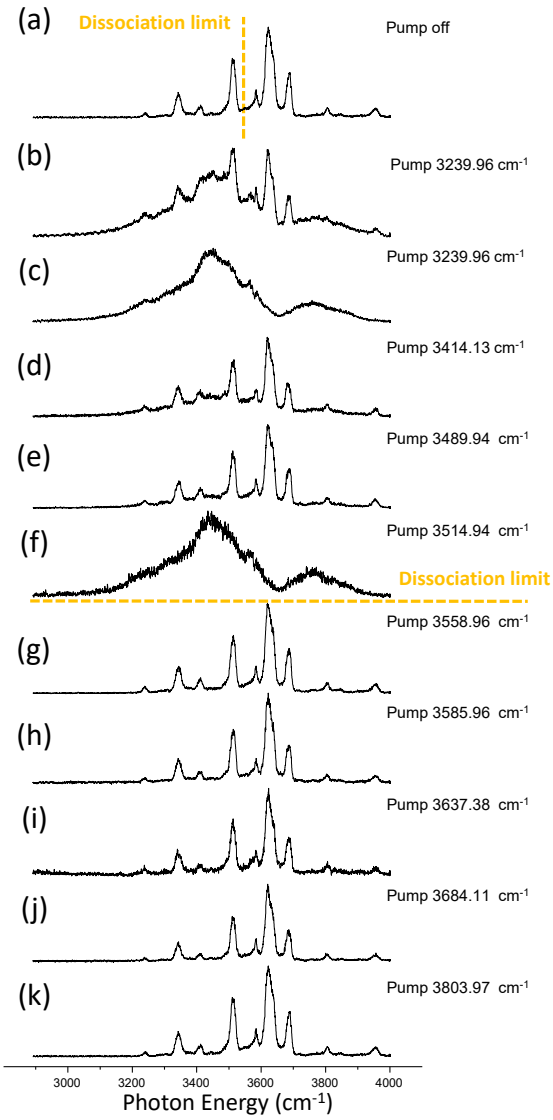

Figure 4.11: (a) Single laser IRPD spectra of $I^-\cdot(H_2O)_2$ at trap temperature 15 K. The yellow dotted line indicates the dissociation energy, above this line the spectrum is an IR1PD spectra and below this line the spectra is a IR2PD spectrum. (b-k) are the two laser spectra obtained by fixing the first laser (pump) at a specific frequency and scanning the second laser, the second laser detects both the clusters that absorbed one photon and do not dissociate and the clusters that did not absorb any photon and remains cold.

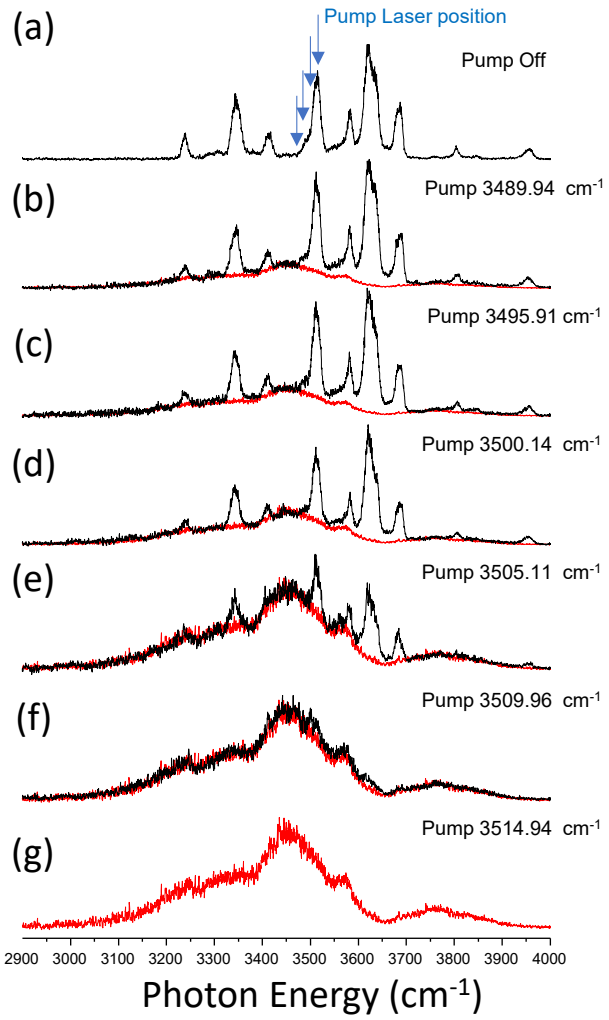

Figure 4.12: (a) Single laser IRPD spectra of $I^{-}\cdot(H_2O)_2$ at trap temperature 15 K. The yellow dotted line indicates the dissociation energy, above this line the spectrum is an IR1PD spectra and below this line the spectra is a IR2PD spectrum. (b-k) are the two laser spectra obtained by fixing the first laser (pump) at a specific frequency indicated by the blue arrows in (a) and scanning the second laser, the second laser detects both the clusters that absorbed one photon and do not dissociate (red trace) and the clusters that did not absorb any photon and remains cold (sharp features). The overall spectra are displayed as black traces.

the excited clusters. It is important to notice that the clusters could absorb two photons when irradiated by the first laser, however that results in an internal energy almost double the dissociation limit, and as shown in Fig 4.11 those clusters rapidly dissociate before interacting with the second laser and do not results in extra complexities in the excited state spectra.

To further exam the proposed two photon scheme in Fig.4.5, we can simulate the expected behavior when laser power of the first and second lasers are varied independently with our measured cross sections at both the grounds state and the excited state. We derive the cross-section formula for gas phase action spectroscopy from Beer's Law:

$$I(\nu) = I_0(\nu)e^{-\sigma(\nu)nl} \qquad \text{(Eq. 4.3)}$$

Where I is the intensity of light after crossing the medium, I_0 is the initial light intensity, ν is the frequency, σ is the cross section, n is the number density of the absorbing molecule in the medium and l is the path length. This assumes that the absorbing molecules do not get consumed whereas the light is getting absorbed. However, in gas phase ion action spectroscopy, the number of photon (~10^{16}-10^{17}) overwhelms the number of ions (~10^{3}-10^{4}) hence the photon can be treated as a constant number density reagent and the ions gets consumed in a pseudo-first order manor. That is essentially switching the absorbing molecule's number density (n) with the light intensity (I) in Beer's law. The resulted equation is similar where the number density of ions that did not absorb a photon (analog of the transmitted light intensity in Beer's law) is expressed as:

$$N_{trans}(\nu) = N_0 e^{-\sigma(\nu)F(\nu)} \qquad \text{(Eq. 4.4)}$$

and the ions that absorbed a photon is:

$$N_{absor}(\nu) = N_0(1 - e^{-\sigma(\nu)F(\nu)}) \qquad \text{(Eq. 4.5)}$$

where Fluence F (photons/cm^2) can be expressed in averaged laser power P_{avg} which can be measured experimentally:

$$F(\nu) = \frac{\int P(\nu,t)dt}{A\,h\nu} = \frac{P_{avg}(\nu)t_{width}}{h\nu} \qquad \text{(Eq. 4.6)}$$

A is the laser beam area and t is time. Assume that beam area A and laser pulse width t_{width} and temporal profile $P(t)$ is stable, the equation can be rewritten as:

$$Abs(\nu) = \frac{N_{absor}(\nu)}{N_0} = (1 - e^{-\frac{\sigma(\nu)P_{avg}(\nu)t_{width}}{\nu A}}) \qquad \text{(Eq. 4.7)}$$

Where Abs(ν) is the fraction of absorption which can be experimentally measured. And the cross section can be expressed as:

$$\sigma(\nu) = -ln\frac{Parent-Fragment}{Parent} \cdot \frac{Ah\nu}{P(\nu)} \qquad \text{(Eq. 4.8)}$$

Now consider the simple case of single color IR2PD. The power of the first laser at a certain frequency ν_1 is the same, noted as $P_1(\nu_1)$. In this case it is the IHB_{AD} that is probed, ν_1 = 3345 cm^{-1}. For the ground state cold molecule the cross section at this frequency is $\sigma_g(\nu_1)$, . For the excited state hot molecule the cross section at this frequency is $\sigma_{ex}(\nu_1)$. The probability of absorbing two photons at ν_1 and leads to dissociation is: absorption rate of the ground state times absorption rate at the excited state $Abs(\sigma_g, \nu_1) \cdot Abs(\sigma_{ex}, \nu_1)$. The fraction of ions undergoes IR2PD (Fig 4.13c) can be expressed as:

$$IR2PD(\nu_1) = \frac{Fragment(\nu_1)}{Parent} = \left((1 - e)^{-\frac{\sigma_g(\nu_1)P(\nu_1)t}{\nu_1 A}}\right)\left((1 - e)^{-\frac{\sigma_{ex}(\nu_1)P(\nu_1)t}{\nu_1 A}}\right) \qquad \text{(Eq. 4.9)}$$

For the $I^-\cdot(H_2O)_2$ system, the IR2PD yield increases with laser power which is expected. However, the trend seems deceptively linear due to the low cross section in for

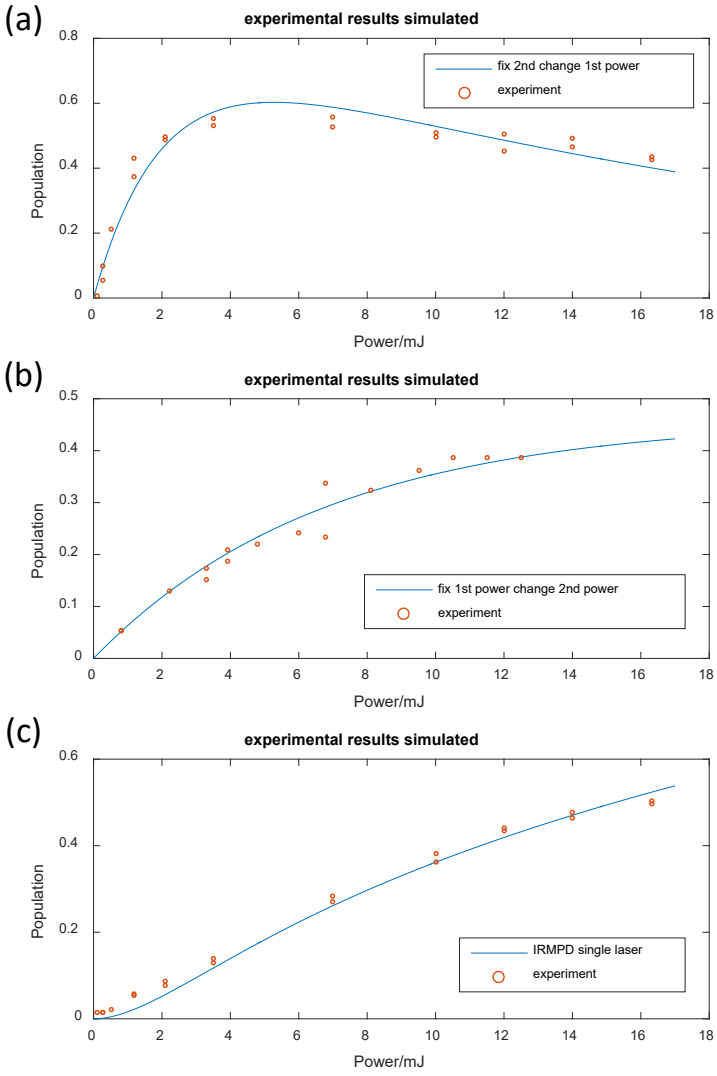

Figure 4.13: Experimental data (orange points) and simulated curves (blue) of the laser power dependence of the cluster population that absorbs only one photon (a), the excited cluster population that already absorbed one photon absorbing a second photon (b), and the cluster population that absorbs two photons at the same frequency when interacting with one single laser (c).

the second photon relative to the first photon absorption, the first photon absorption quickly saturates (Fig 4.13a) and only the second photon absorption (Fig. 4.13b) controls the overall fragment yield of the IR2PD process which results in a one-photon-absorption like behavior.

To obtain the power dependence of the first photon absorption, the second laser is fixed at 17 mJ/pulse on ν_2 (3450 cm^{-1}, Fig 4.12g) where only the excited state molecule absorbs and first laser is varied in power, noted as $P(\nu_1)$, at ν_1 (3340 cm^{-1}, IHB_{AD} in Fig 4.12a). This way only the population that absorbed one photon is detected with the second laser. The relative population of the excited molecule equals to the probability of absorbing one photon subtracts the probability of absorbing two photons and dissociating. The fraction of excited cluster that only absorbed one photon can be expressed as:

$$\frac{N_{ex}(\nu_1)}{N_{init}} = Abs(\sigma_g, \nu_1) - Abs(\sigma_g, \nu_1) \cdot Abs(\sigma_{ex}, \nu_1)$$

$$= \left((1-e)^{-\frac{\sigma g(\nu_1)P(\nu_1)t}{\nu_1 A}}\right) \cdot \left(1-(1-e)^{-\frac{\sigma ex(\nu_1)P(\nu_1)t}{\nu_1 A}}\right) \qquad \text{(Eq. 4.10)}$$

The single photon absorption at ν_1 increase linearly at lower power and quickly saturates (nearly 100% absorption), then the increase in the second photon absorption removes population from these singly excited clusters as power is increased (Fig 4.13a).

Finally, to study the power dependence of the second photon absorption, the first laser is fixed at 17 mJ on ν_1 (3340 cm^{-1}, IHB_{AD} in Fig 4.13a) and 2nd laser is varied in power, noted as $P(\nu_2)$, at a frequency ν_2 (3450 cm^{-1}, Fig 4.12g) where only the excited state molecule absorbs. The resulting signal can be expressed as:

$$\frac{N_{h\nu_2}}{N_{init}} = \frac{N_{ex}(\nu_1)}{N_{init}} \cdot Abs(\sigma_{ex}, \nu_2, P(\nu_2))$$

$$= (Abs(\sigma_g, \nu_1) - Abs(\sigma_g, \nu_1) \cdot Abs(\sigma_{ex}, \nu_1)) \cdot Abs(\sigma_{ex}, \nu_2, P(\nu_2)) \quad \text{(Eq. 4.11)}$$

The second photon absorption's power dependence behaves as a single photon absorption with low cross section, only 40% of the population absorbs even at 12 mJ/pulse (Fig. 4.13b). The simulated traces matches the experimental data points well in all three cases above indicating the two photon model proposed in Fig.4.5 is valid.

4.3.2. Intermolecular coupling and soft mode activity in the DD and AD binding sites through isotopomer selective spectroscopy of the $I^-\cdot(H_2O)\cdot(D_2O)$ isotopomers

A second powerful application of two-color IR2PD linear spectroscopy is its ability to extract the spectra of individual isotopomers in mixed H/D isotopologues. We have previously exploited this to confirm band assignments in the $Cs^+\cdot(H_2O)_6$, and $(H_2O)_6^-$ clusters,[57-58] which had been heretofore based on comparisons of calculated *overall* (rather than isotopomer specific) patterns of OH stretching and HOH bending fundamentals with observed spectra. Here, in addition to identifying the fundamentals associated with water molecules in the DD and AD binding sites, we address the more subtle issues regarding the cross coupling of OH stretching modes between the two water molecules and the coupling between the two OH oscillators on the same water molecule in the two binding sites.

The D_2-predissociation spectrum of the $I^-\cdot(H_2O)\cdot(D_2O)$ isotopologue is presented in Fig. 4.14b, along with that of the $I^-\cdot(H_2O)_2$ cluster in Fig. 4.14a. Interestingly, while the locations of the various bands very similar in the two cases (see Table 4.1), their intensity profiles are dramatically different. This presumably occurs because the

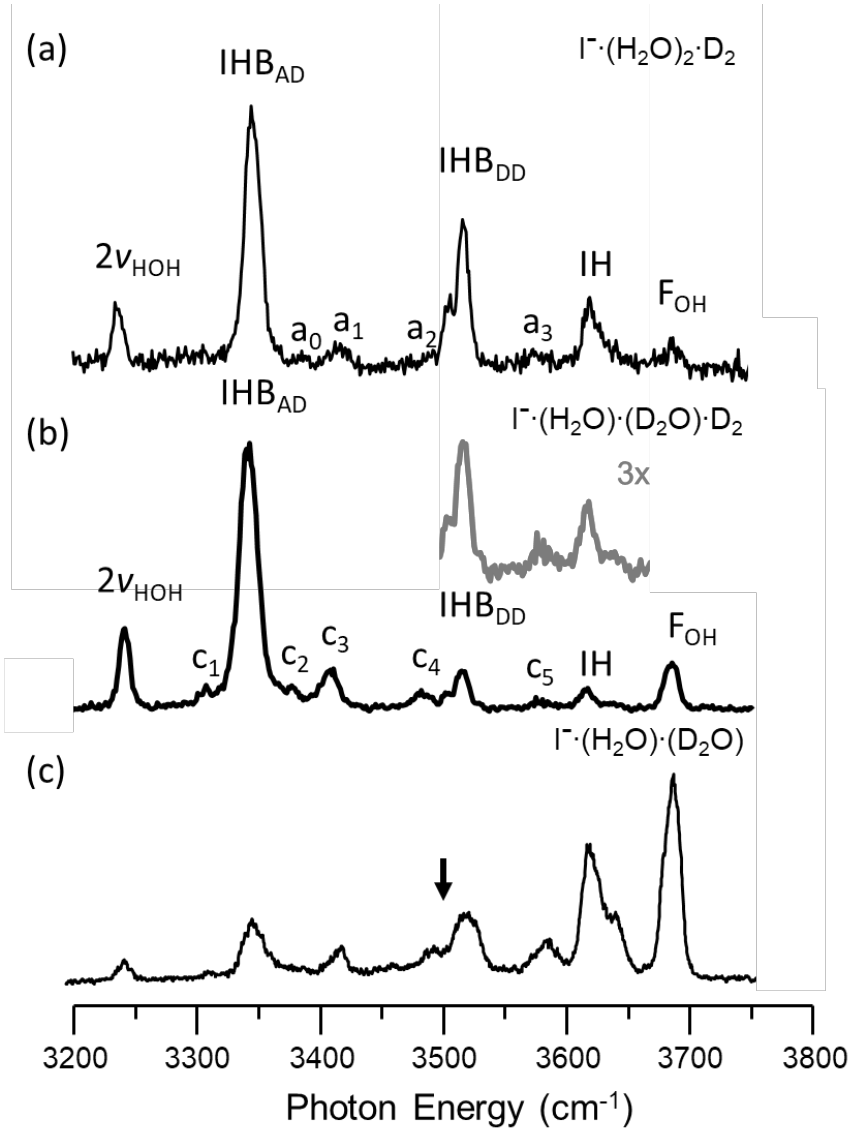

Figure 4.14: The IR dissociation spectra of (a) D_2 tagged $I^-\cdot(H_2O)_2$, (b) D_2 tagged $I^-\cdot(H_2O)\cdot(D_2O)$, and (c) bare $I^-\cdot(H_2O)\cdot(D_2O)$, where the black arrow indicates the thermochemical dissociation enthalpy.[42] Trace (c) is a hybrid spectrum where bands below D_o are single color IR2PD (Fig. 4.3b) while above D_o they are obtained by IR1PD (Fig. 4.3a). The gray trace in (b) is 3 times magnified in intensity. See Fig. 4.1 caption for labeling scheme. All labeled transitions can be found in Table 4.1. The shoulder on the IHB_{DD} band (*) was traced to a D_2 tag effect as illustrated in Fig. 4.15.

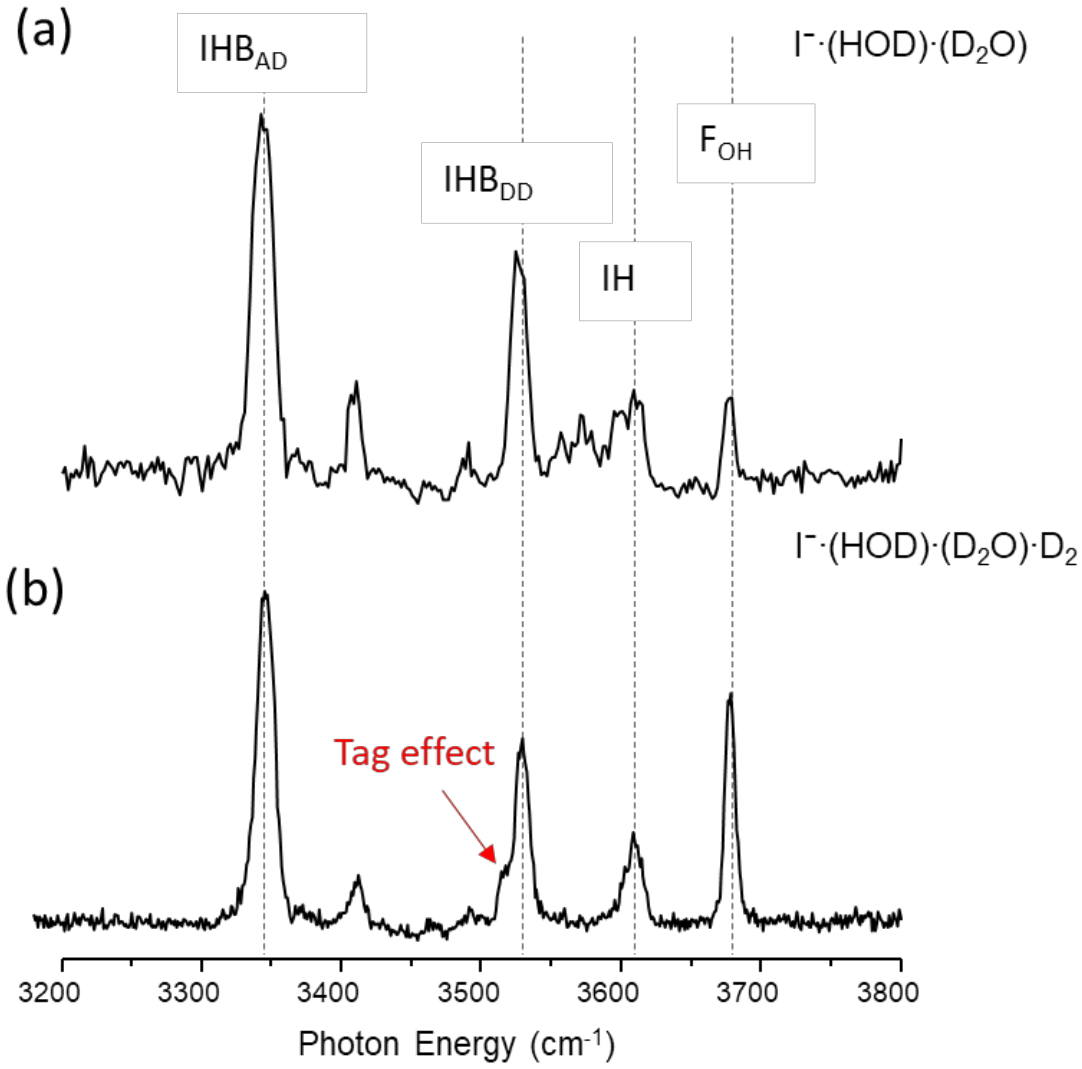

Figure 4.15: (a) IR2PD spectrum of $I^-\cdot(HOD)\cdot(D_2O)$ obtained by scanning the pump and probe on 3458 cm^{-1} (Fig 4.3d) which is unique to the photoexcited molecule cluster compared with (b) the D_2 tagged predissociation spectrum.

$I^-\cdot(H_2O)\cdot(D_2O)$ pattern is the superposition of two independent spectra associated with the two isotopomers that differ according to whether the H_2O molecule resides in the DD or AD site (see structure in Fig. 4.1a). These individual spectra can be isolated using the two-color IR-IR scheme shown in Fig. 4.3e in which the probe laser is placed on a transition unique to one of the isotopomers, while the pump laser is scanned through the entire OH region. Our previous applications of isotopomer-selective spectroscopy in ion micro-hydration[35] have been limited to tagged clusters. We next illustrate how, using the results of the two-color IR2PD method in the configuration illustrated in Fig. 4.3c, we can carry out isotopomer selective spectroscopy on the bare clusters. The challenge in this regime is that the binding energy leading to water loss is sufficiently large that many of the transitions in the linear absorption spectrum occur to levels in the vicinity of the dissection energy. This presents a photophysical challenge due to complications arising from the competition between hot band excitation and two-photon dissociation, as discussed at length by Wolke et al.[59] Because the F and IH bands lie well above the dissociation energy, they can be used to monitor the population of the H_2O molecule in the AD and DD sites, respectively. Fig. 4.16c presents the dip spectrum obtained by setting the probe at the free OH stretch at 3686 cm^{-1} (blue arrow in Fig. 4.16a) and scanning the pump, which indeed *quantitatively* recovers the features in the overall spectrum arising from the H_2O molecule residing in the AD location, as illustrated in the overlay of the dip spectrum with the D_2 tagged spectrum in Fig. 4.17. Fig. 4.16b presents the dip spectrum obtained by setting the probe on the IH transition at 3619 cm^{-1}, which again quantitatively isolates the features associated with the H_2O molecule in the DD location.

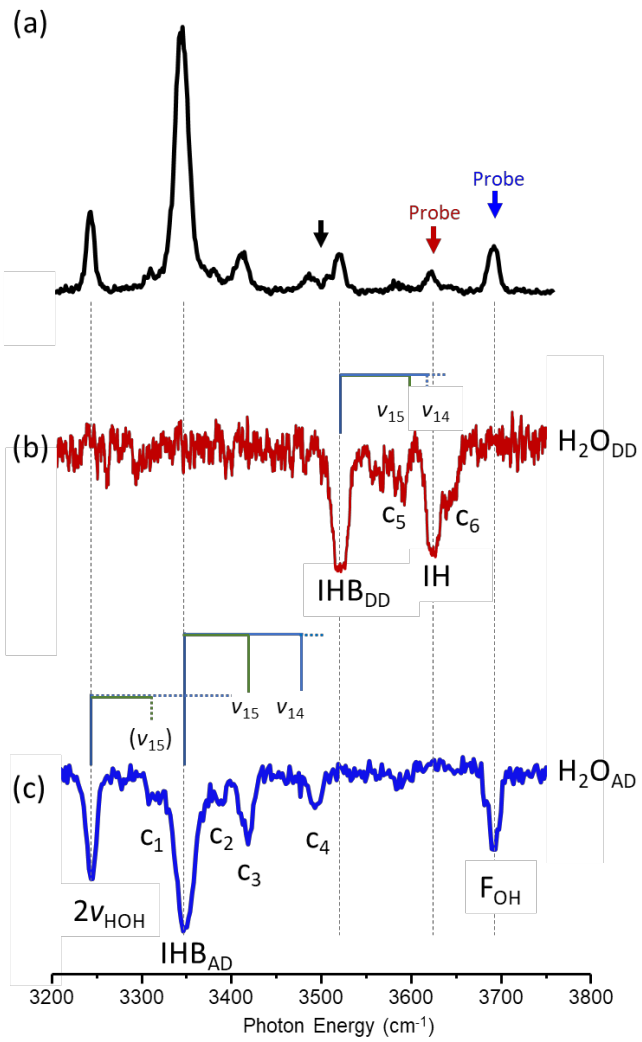

Figure 4.16: (a) The black trace is the D_2-predissociation spectrum of both isotopomers of $I^-\cdot(H_2O)\cdot(D_2O)$. The isotopomer-specific dip spectra are presented for the bare $I^-\cdot(H_2O)\cdot(D_2O)$ complex with the H_2O molecule at (b) the DD position (H_2O_{DD}), obtained by probing on the IH transition (red arrow), and (c) the AD position (H_2O_{AD}), obtained by probing on free OH (blue arrow). The black arrow is reproduced from Fig. 4.14c. The brackets represent calculated (VPT2, MP2/aug-cc-pVTZ-PP) combination bands with intensities greater than 1 km/mol, which are discussed in the text. Assignments and peak positions are collected in Table 4.1.

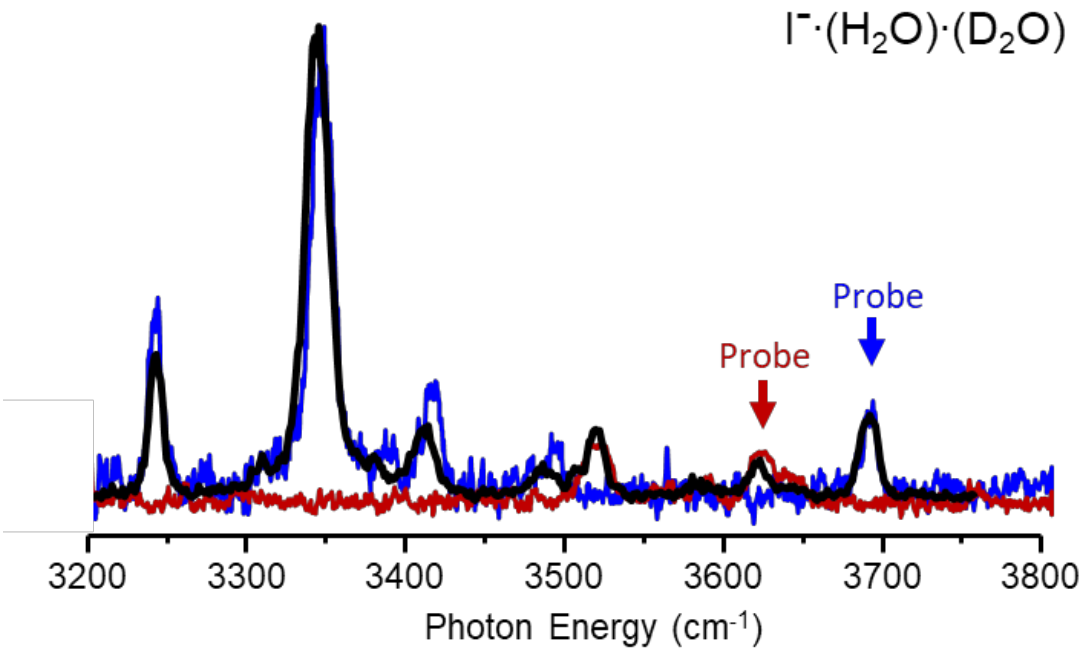

Figure 4.17: The black trace shows the relative cross section of $I^-\cdot(H_2O)_2\cdot D_2$ (obtained using single-color IR1PD Fig. 4.3a), while the blue trace displays the relative cross section of $I^-\cdot(H_2O)\cdot(D_2O)$ with the H_2O molecule on the AD position obtained by probing the free OH transition indicated by the blue arrow (described further in Fig. 4.3e) and the red trace is for the H_2O molecule on the DD position. The blue and red traces are inverted and normalized to the peak intensities of the probe position peaks in the black trace to show that these features recovered from the double resonance experiments (when combined) closely match the spectra of the two isotopomers (black trace).

Table 4.1. This table includes the experimentally observed frequencies in various isotopologues of the iodide water dimer and their assignments. For some isotopologues there are multiple isotopomers and the contribution is attributed in the isotopomer column in which case a range of frequency is reported to cover different frequencies for various isotopomers. Calculated frequencies were obtained from VPT2 calculations with the MP2/aug-cc-pVTZ-PP level of theory and basis function.

$I^-\cdot(H_2O)_2$						
Label	**[a]Experimental photon energy (cm^{-1})**	**Shift from fundamental (cm^{-1})**	**Assignment**	**Theoretical photon energy (cm^{-1})**	**Shift from fundamental (cm^{-1})**	**Isotopomer**
F_{OH}	3684		Free OH	3693		
IH	3619		Inter-water H-bonded OH	3612		
IHB_{DD}	3504 3516		Ionic H-bonded OH on DD water	3464		
IHB_{AD}	3344		Ionic H-bonded OH on AD water	3243		
$2\nu_{HOH}$	3237		H_2O bend overtone	3199		

a_0	3386		Not assigned			
a_1	3416	72	IHB_{AD}+ [c] ν_{15}	3319	76	
a_2	3490	146	IHB_{AD}+ν_{14}	3380	137	
a_3	3573	57	IHB_{DD}+ν_{15}	3542	78	
I^-·(DOH)·(H_2O)						
Label	**Experimental photon energy (cm^{-1})**	**Shift from fundamental (cm^{-1})**	**Assignment**	**Theoretical photon energy[d] (cm^{-1})**	**Shift from fundamental (cm^{-1})**	**Isotopomer**
F_{OH}	3679		Free OH	3693-3686		D on ID,IDB_{AD}, IDB_{DD}
IH	3617		Inter-water H-bonded OH	3607-3610		F_{OD}, IDB_{AD}, IDB_{DD}
IHB_{DD}	3518		Ionic H-bonded OH on DD water	3464-3468		F_{OD},ID, IDB_{AD}
IHB_{AD}	3345		Ionic H-bonded OH on AD water	3240-3245		F_{OD},ID, IDB_{DD}
F_{OD}	Not populated		Free OD	2713		F_{OD}
ID	2657		Inter-water H-	2642		ID

			bonded OD			
IDB_{DD}	2596		Ionic H-bonded OD on DD water	2555		IDB_{DD}
IDB_{AD}	2478		Ionic H-bonded OD on AD water	2404		IDB_{AD}
$2v_{HOH}$	3241		H_2O bend overtone	3198		ID,IDB_{AD}
b_0	2543	65	$IDB_{AD} + v_{15}$	2581	76	IDB_{AD}
b_1	3414	69	$IHB_{AD} + v_{15}$	3316-3421	75	F_{OD},ID, IDB_{DD}
b_3	3489	144	$IHB_{AD} + v_{14}$	3356-3378	135	F_{OD},ID, IDB_{DD}
			$I^-\cdot(H_2O)\cdot(D_2O)$			
Label	**Experimental photon energy (cm^{-1})**	**Shift from fundamental (cm^{-1})**	**Assignment**	**Theoretical photon energy (cm^{-1})**	**Shift from fundamental (cm^{-1})**	**Isotopomer**
F_{OH}	3685		Free OH	3693		H_2O on AD
IH	3615		Inter-water H-bonded OH	3610		DD

IHB_{DD}	3514		Ionic H-bonded OH on DD water	3465		DD
IHB_{AD}	3339		Ionic H-bonded OH on AD water	3243		DD
F_{OD}	2718		Free OD	2724		AD
ID	2685		Inter-water H-bonded OD	2671		DD
IDB_{DD}	2587		Ionic H-bonded OD on DD water	2551		AD
IDB_{AD}	2477		Ionic H-bonded OD on AD water	2403		AD
$2v_{HOH}$	3241		H_2O bend overtone	3198		DD
c_0	2653	66	$IDB_{DD}+v_{15}$	2626	75	AD
c_1	3308	67	$2v_2+v_{15}$			AD
c_2	3388		Not assigned			AD
c_3	3414	75	$IHB_{AD}+v_{15}$	3318	75	AD
c_4	3490	151	$IHB_{AD}+v_{14}$	3377	134	AD

c_5	3585	69	$IHB_{DD}+\nu_{15}$	3543	78	AD
c_6	3638	122	$(IHB_{DD}+\nu_{14})$	3562	97	DD

$I^-\cdot(HOD)\cdot(D_2O)$						
Label	**Experimental photon energy (cm^{-1})**	**Shift from fundamental (cm^{-1})**	**Assignment**	**Theoretical photon energy[d] (cm^{-1})**	**Shift from fundamental (cm^{-1})**	**Isotopomer**
F_{OH}	3678		Free OH	3682		H on F_{OH}
IH	3609		Inter-water H-bonded OH	3604		IH
IHB_{DD}	3517 3529		Ionic H-bonded OH on DD water	3469		IHB_{DD} IHB_{DD}
IHB_{AD}	3345		Ionic H-bonded OH on AD water	3245		IHB_{AD}
F_{OD}	2719		Free OD	2720-2723		IH,IHB_{AD}, IHB_{DD}
ID	2684		Inter-water H-bonded OD	2650-2671		F_{OH}, IHB_{AD}, IHB_{DD}

IDB_{DD}	2586		Ionic H-bonded OD on DD water	2552-2557		F_{OH},IH, IHB_{AD}
IDB_{AD}	2475		Ionic H-bonded OD on AD water	2516-2523		F_{OH},IH, IHB_{DD}
$2v_{DOD}$	2427		D_2O bend overtone	2356-2358		IH,IHB_{AD}
d_1	2540	65	$IDB_{AD}+v_{15}$	2476-2479	76	F_{OH},IH, IHB_{DD}
d_2	2651	65	$IDB_{DD}+v_{15}$	2626-2628	76	F_{OH},IH, IHB_{AD}
d_3	3370	25	Not assigned			
d_4	3412	67	$IHB_{AD}+V_{15}$	3321	76	IHB_{AD}
d_5	3464	119	$IHB_{AD}+v_{14}$	3355	110	IHB_{AD}
d_6	3491	146	$(IHB_{AD}+ {}^{e}v_{13})$	3387	142	IHB_{AD}
			$I^-\cdot(D_2O)_2$			
Label	**Experimental photon energy (cm^{-1})**	**Shift from fundamental (cm^{-1})**	**Assignment**	**Theoretical photon energy (cm^{-1})**	**Shift from fundamental (cm^{-1})**	**Isotopomer**
F_{OD}	2719		Free OD	2723		
ID	2684		Inter-water H-	2670		

			bonded OD		
			Ionic H-bonded		
IDB_{DD}	2589		OD on DD water	2552	
			Ionic H-bonded		
IDB_{AD}	2280		OD on AD water	2401	
$2\nu_{DOD}$	2388		D_2O bend overtone	2356	
e_0	2651	62	$IDB_{DD}+\nu_{15}$	2626	74

[a] Experimental frequencies are accurate within ±4 cm^{-1}.

[b] ν_{14} Antisymmetric O-I-O stretch with rock action centered on AD water molecule. Tentative assignments are indicated in parentheses.

[c] ν_{15} Antisymmetric O-I-O stretch with rock action centered on DD water molecule.

[d] In cases where a transition exists in multiple isotopomers the range of theoretical photon energies is reported.

[e] ν_{13} is the symmetric O-I-O stretch.

Having identified the contributions from each isotopomer to the overall (i.e., D_2 tagged) spectrum (Fig. 4.16a), it is clear that the H_2O_{DD} form is much less abundant than

the H_2O_{AD} form in the $I^-\cdot(H_2O)\cdot(D_2O)$ isotopologue. This strong fractionation of the light isotope to the AD position under the conditions of D_2 tagging (around 20 K trap temperature) is readily understandable given the expected difference in zero-point energies between the two isotopomers, with the H_2O_{AD} form calculated at the harmonic level to lie lower in energy by 41 cm^{-1}. An equilibrium ensemble at 20 K, for example, would be expected to accommodate 95% of the H_2O molecules in the AD site. We note that this likely sets an upper limit on the cluster temperature due to the barriers for interconversion between the DD and AD sites, which have been estimated to be at least ~70 cm^{-1} based on the calculated[59] temperature (~100 K) for the onset of interconversion between the two sites in $I^-\cdot(H_2O)_2$. We note that the isobaric $I^-\cdot(HOD)_2$ cluster does not complicate these measurements because we exclusively monitor either $I^-\cdot H_2O$ or $I^-\cdot D_2O$ fragments. We have also determined the spectrum of the $I^-\cdot(HOD)_2$ isotopologue, however, by monitoring the $I^-\cdot$HOD fragment, which is presented in Fig. 4.18.

The fine structure associated with each pattern is of interest, as it directly encodes site-specific anharmonic coupling to other vibrational modes. This is especially true because, although the intensities reflect the isotopomer populations, the band positions themselves are essentially unaffected when the neighboring H_2O is replaced by a D_2O. This behavior immediately establishes that the degree of coupling between the water molecules is minimal. Such a scenario was also encountered in the $Cs^+\cdot(H_2O)_6$ case,[58] and is not surprising when the fundamentals associated with the two sites are so widely split apart. Furthermore, the AD water molecule is identified to be exclusively

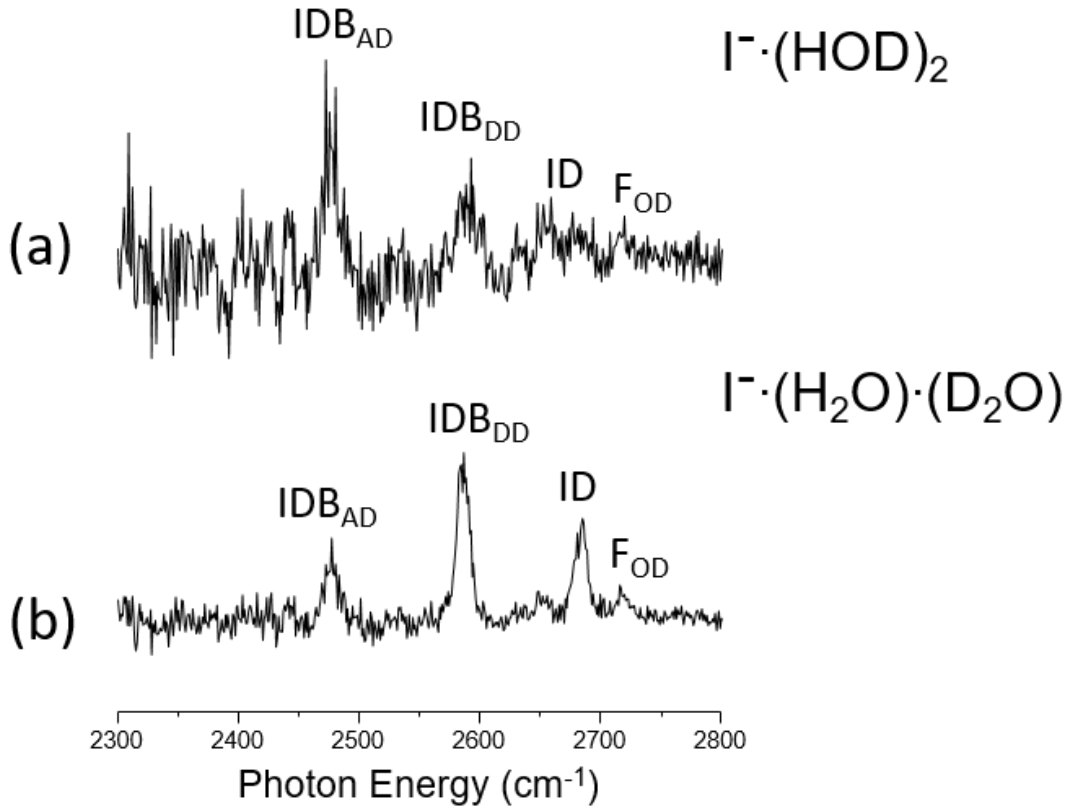

Figure 4.18: IR2PD spectra of (a) $I^-\cdot(HOD)_2$ and (b) $I^-\cdot(H_2O)\cdot(D_2O)$, the difference in fragment masses enabled selective detection of one isotopologue or the other. All peak positions can be found in Table 4.1.

responsible for the appearance of the bend overtone ($2\nu_{HOH}$) at 3240 cm^{-1}, as expected for the ~33 cm^{-1} bend-stretch mixing matrix element for the Fermi resonance.[32] Specifically, only the most red shifted IHB_{AD} band can couple strongly to the v=2 level of the bend and lend oscillator strength to the nominally forbidden IR 0→2 transition. The two features above the strong IHB_{AD} band, c_3 and c_4, can be assigned with the aid of anharmonic (VPT2) calculations (Table 4.1) as combination bands built on the IHB_{AD} transition involving two soft modes, ν_{14} and ν_{15}, with the displacement vectors of these modes displayed in Fig. 4.19. One of these is the asymmetric O-I-O stretching mode (ν_{15} at 88 cm^{-1}), with rock action centered on the DD water molecule that acts to break the weak bond between the water molecules, while the other (ν_{14} at 145 cm^{-1}) involves the asymmetric O-I-O stretch with rock action centered on the AD water molecule. Note that these modes also account for the combination bands built on the bend overtone (c_1 and c_2).

The H_2O_{DD} spectrum (Fig. 4.16b) also displays a multiplet of features around the fundamentals, c_5 and c_6, where the latter appears as a high energy shoulder on the IH feature. The 69 cm^{-1} displacement of the c_5 band relative to the IHB_{DD} is very close to the calculated (VPT2) ν_{15} (78 cm^{-1}) for this isotopomer. The situation regarding c_6 is less certain, as it corresponds to a splitting of (122 cm^{-1}), which is significantly larger than the predicted (97 cm^{-1}) displacement of the ν_{14} combination band with IHB_{DD}. This ability to define the site-specific coupling to soft modes provides a qualitatively new way to unravel the contributions of the excited state dynamics to the overall breadth of the OH stretching manifolds of H-bonded manifolds.

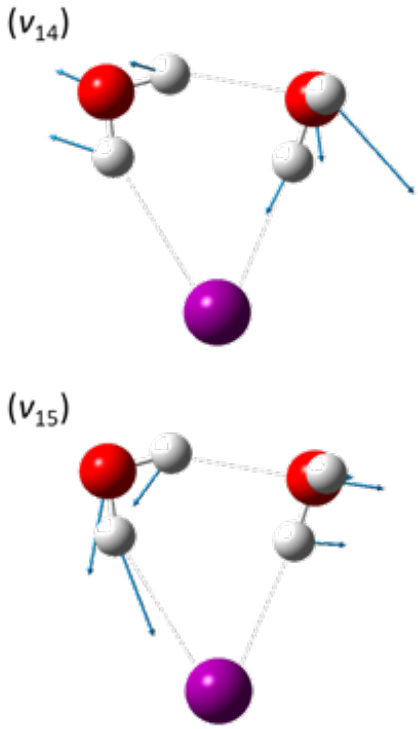

Figure 4.19: Displacement vectors (MP2/aug-cc-pVTZ-PP) of (v_{14}) antisymmetric O-I-O stretch with rock action centered on AD water molecule. (v_{14}) antisymmetric O-I-O stretch with rock action centered on DD water molecule. The band numbering scheme is based on Herzberg notation. [60]

4.3.3. Determination of the local vs normal mode character of the OH stretches in the $I^-\cdot(HOD)\cdot(D_2O)$ and $I^-\cdot(DOH)\cdot(H_2O)$ isotopologues

We next address the site-dependence of the coupling between the two OH oscillators within the same water molecule, and the soft mode activity associated with a single OH group in each of the four positions in the cyclic structure. This information can be obtained from the spectrum of the D_2 tagged $I^-\cdot(HOD)\cdot(D_2O)$ isotopologue, which is displayed in Fig. 20c. The spectral properties of the isolated OH groups are important because they encode the degree to which the two OH groups can be viewed in the context of a local oscillator picture.[61-67] In an isolated water molecule, for example, the observed splitting of 99 cm^{-1} between the symmetric and antisymmetric collective OH stretches can be recovered in a local mode picture by considering a simple 2×2 Hamiltonian in which the degenerate, local OH energies appear on the diagonal, and are mixed through an off diagonal coupling matrix element of about 50 cm^{-1}. The analogous matrix element for D_2O is about 60 cm^{-1}.

When a water molecule is placed in an H-bonding environment, however, the local OH oscillators shift in energy according to the strengths of their individual H-bonding environments, effectively lifting their degeneracy. The observed fundamentals and relative contributions of the normal mode displacements to the molecular eigenstates can then be derived by introducing an effective coupling matrix element between the non-degenerate local states to recover the observed splitting. This basic phenomenon accounts for the fact that formation of an H-bond to one of the two OH groups of a dangling water molecule red-shifts both bands nominally assigned to the symmetric and

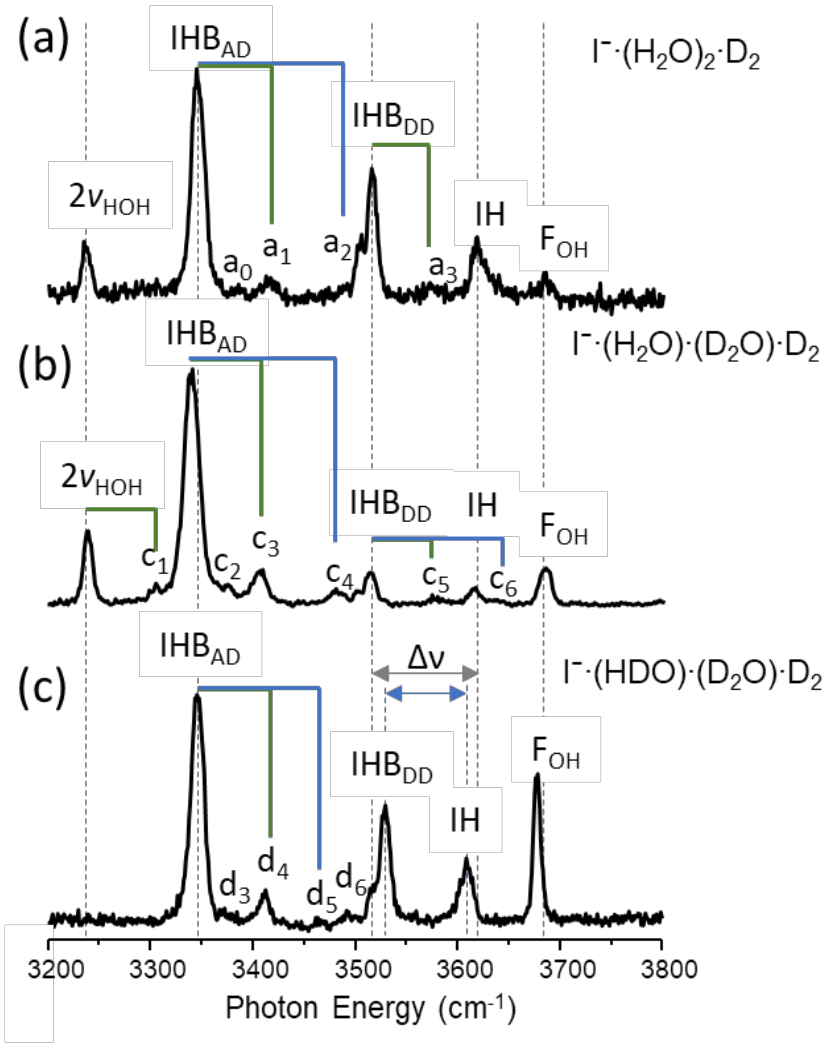

Figure 4.20: (a) is the predissociation spectrum of D_2 tagged $I^-\cdot(H_2O)\cdot(D_2O)$. (b) is the predissociation spectrum of D_2 tagged $I^-\cdot(HOD)\cdot(D_2O)$. The dotted lines indicate the peak position for those in the $I^-\cdot(H_2O)_2$ case. The brackets indicate the combination bands of the IHB_{AD} and IHB_{DD} fundamentals with ν_{15} (green), and ν_{14} (blue), which are displayed in Fig. 4.19. Peak positions and assignments are collected in Table 4.1. The blue and gray arrows in (c) indicate the splitting between the IHB_{DD} and IH band in $I^-\cdot(HOD)\cdot(D_2O)$ and $I^-\cdot(H_2O)\cdot(D_2O)$, respectively. The difference between these values ($\Delta\nu$) reflects the strength of coupling between the two OH oscillators, as discussed further in the text.

antisymmetric stretch, and in fact their character slowly evolves into decoupled motions as the strength of the interaction increases.[68]

In the cases of $I^-\cdot(H_2O)_2$ and $I^-\cdot(D_2O)_2$, the extreme splitting of the two fundamentals associated with the AD molecule (322 and 241 cm^{-1} for the H_2O and D_2O complexes, respectively) compared to the intrinsic (~50 cm^{-1} and 60 cm^{-1} for isolated H_2O and D_2O, respectively) coupling matrix elements clearly dictates that the two bands are accurately described as two local OH(D) stretches: the free OH and the ion-bound IHB. And indeed, the observed IHB_{AD}/IHB_{DD} and free features in the $I^-\cdot(HOD)\cdot(D_2O)$ and $I^-\cdot(DOH)\cdot(H_2O)$ spectra (Figs. 4.20a and 4.21, respectively) are nearly identical (to within 1 cm^{-1}) to those in the homogeneous isotopologues. The IHB_{DD} and IH bands in $I^-\cdot(H_2O)_2$ (and in $I^-\cdot(H_2O)\cdot(D_2O)$) are more interesting, however, because they appear with a 103 cm^{-1} splitting (Fig. 4.20b), which is close to that found in the isolated H_2O molecule (99 cm^{-1}). Because of the similar splitting, it would naively appear that the motions involved in the DD fundamentals should be regarded as collective normal modes associated with the symmetric and antisymmetric OH stretches, similar to those in play in the bare molecules. The single H(D) isotopologue spectra, however, establishes the locations of the two local OH(D) oscillators, and they are split by about 80(61) cm^{-1} in the absence of coupling! This scenario is actually analogous to that found in the analysis of the coupling between OH groups in hexagonal ice,[66] where the splittings observed in the spectra are again accidentally close to that of a bare water molecule, but are actually split apart not due to coupling, but rather as a result of the different local OH(D) environments.

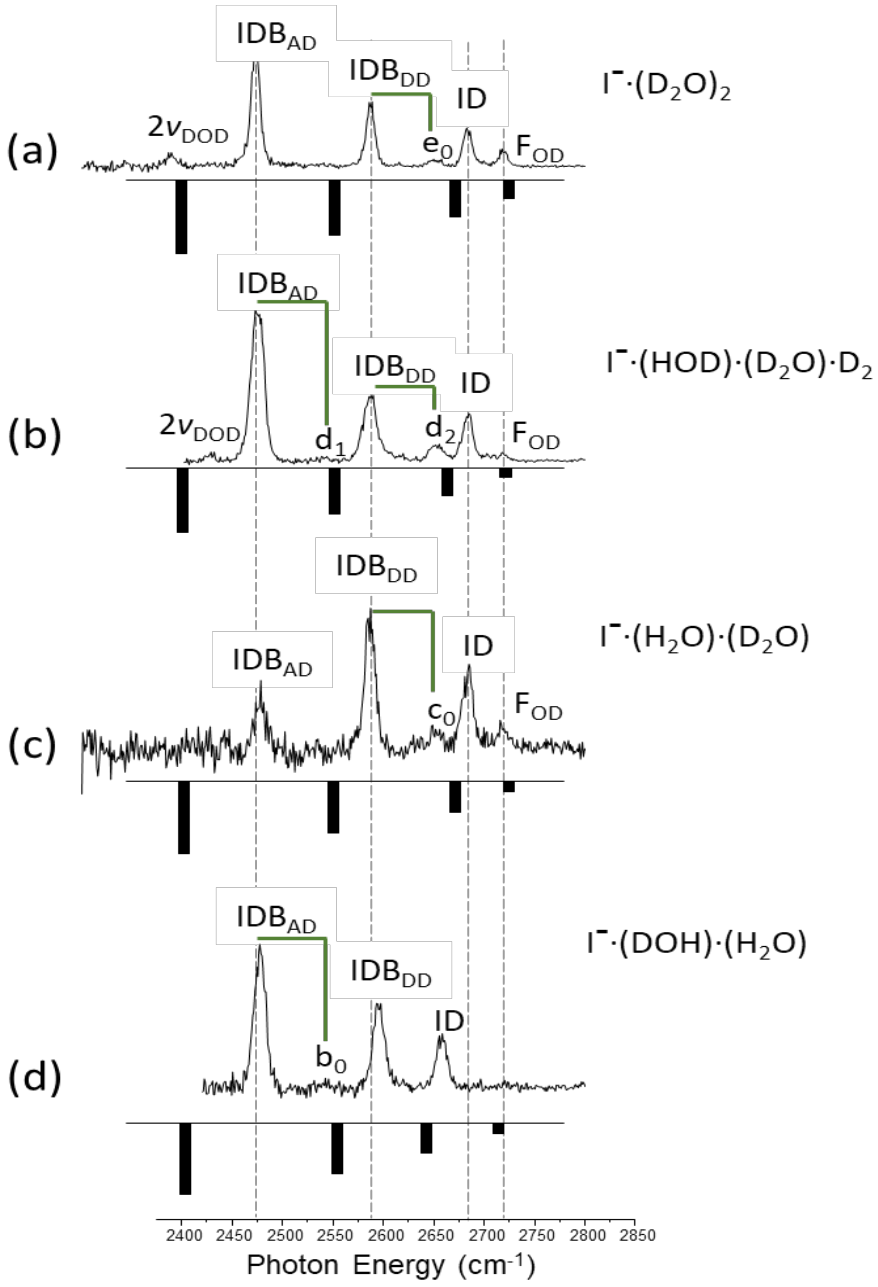

Figure 4.21: The linear spectra of (a) $I^-\cdot(D_2O)_2$, (c) $I^-\cdot(H_2O)\cdot(D_2O)$, (d) $I^-\cdot(DOH)\cdot(H_2O)$ obtained by two-color IR2PD (Fig. 4.3d) and (b) D_2 tagged spectra of $I^-\cdot(HOD\cdot(D_2O)\cdot D_2$ compared with their calculated frequencies (inverted stick spectra) using VPT2 at the MP2/aug-cc-pVTZ-PP level of theory. All labeled transitions can be found in Table 4.1.

To estimate the residual coupling between the OH(D) groups in the DD water molecule, we take the observed positions in the $I^-\cdot(HOD)\cdot(D_2O)$ and $I^-\cdot(DOH)\cdot(H_2O)$ spectra (listed in Table 4.1) as the uncoupled energies of the local OH(D) groups. We can then recover the observed band locations in the H_2O and D_2O isotopologues by introducing an empirical coupling matrix element of 32.5 cm^{-1} for OH and 38.5 cm^{-1} for OD, which are indeed significantly less than those found for the isolated water isotopologues. With this coupling parameter in hand, we can diagonalize the 2×2 matrix to estimate the contribution of each decoupled OH(D) oscillator to the two bands associated with the H_2O and D_2O molecules in the DD site. For the H_2O case, this results in the superpositions:

$$\Phi_{sym} = 0.94\ \psi_{IHB} - 0.33\ \psi_{IH} \quad \text{(Eq. 4.12)}$$

$$\Phi_{asym} = 0.33\ \psi_{IHB} + 0.94\ \psi_{IH} \quad \text{(Eq. 4.13)}$$

of the observed molecular eigenstates in the local basis. This indicates that the motions are, in fact, remarkably local, with only about a 10% contribution from the other OH group. In the OD case, the coupling between the two OD oscillators in the DD site is 38.5 cm^{-1} which suggests a stronger mixing, resulting in a 20% contribution from the partner OD group when the bands are nominally assigned to local IDB and ID motions. In either case, however, the IHB and IH labels are shown to be appropriate descriptors of the dominant vibrational motions responsible for the transitions.

Similar behavior is found when we perform a harmonic analysis on the two OH (or OD) oscillators in the DD water molecule. In an isolated H_2O, the calculated coupling between these oscillators is roughly 60 cm^{-1}, but drops to 30 cm^{-1} in $I^-\cdot(H_2O)_2$. This calculation also allows us to explore the relative contributions of kinetic and potential

couplings between the two oscillators to the observed splitting. While the kinetic coupling is decreased in the complex relative to an isolated water molecule (due to a decrease in the HOH bond angle) the dominant contribution comes from the decrease in the potential coupling between the oscillators. Specifically, the potential contribution is reduced by a factor of 0.28 in $I^-\cdot(H_2O)_2$ compared to H_2O, when calculated at the MP2/aug-cc-pVTZ(-PP) level of theory/basis set. Physically, this reflects a situation where the hydrogen atoms on H_2O_{DD} are attracted to both the acceptor water molecule and the ion. Consequently, the net force on one OH group is not strongly modulated by changes in the length of the other OH bond. This effect appears to be a general feature displayed by H_2O_{DD} molecules in a variety of environments, and we are continuing to explore this phenomenon in the microhydration regime.

Turning to the anharmonic features associated with each OH(D) binding site, we note that the $2\nu_{HOH}$ and c_1 features (Fig. 4.20b) disappear in the $I^-\cdot(HOD)\cdot(D_2O)$ isotopomer, (Fig. 4.20c) confirming the assignments indicated in Table 4.1 and Fig. 4.16. The situation regarding the d_3 band is less clear as the peak merges with residual absorption in this region above the IHB_{AD}. The c_3 band in the H_2O_{AD} (Fig. 4.16) is retained (labeled d_4 in Fig. 4.20b), while absorption near c_4 splits into two peaks, denoted d_5 and d_6.

4.3.4. Temperature-dependent spectral diffusion as a probe of large amplitude motion

In our earlier interpretation of the dramatic changes in the $I^-\cdot(H_2O)_2$ spectrum with increasing temperature (Fig. 4.1), we considered the changes in the spectrum to indicate the break-up of the water dimer into two essentially independent water molecules

orbiting the ion at around 125 K. [30] The two-color, isotopomer-selective methods we have demonstrated here enable a more detailed view of these intra-cluster dynamics. One way to illustrate this is through the $I^-\cdot(H_2O)\cdot(D_2O)$ isotopomer, which we have shown is "locked" (i.e., the AD and DD sites do not interconvert) by obtaining the site-specific, isotopomer-selective spectra using IR-IR hole burning (Fig. 4.16). Now consider the case where the energy of the system is systematically increased to the point where the two water molecules break apart. At high energy, the overall spectrum changes as the ensemble is mostly composed of separated water molecules. But there should be an intermediate regime where the basic structure of the dimer is intact, but undergoes slower interconversion between the two sites. When these large amplitude excursions are infrequent, the overall spectrum should still display the four-band pattern characteristic of the cyclic structure so that these dynamics are "hidden" in the linear spectrum. Isotopomer-selective spectroscopy, on the other hand, can reveal these slow dynamics associated with isotopomer interconversion:

$$H_2O_{AD} \leftrightarrow H_2O_{DD} \qquad \text{(Eq. 4.14)}$$

by probing a particular location characteristic of one of the sites (e.g., the H_2O molecule in the AD position by probing the F_{OH} transition). When the pump laser is scanned through the spectrum, it removes population of any species that absorbs at a particular frequency. If the sites interconvert, then the characteristic bands of one site will appear as dips when probing a feature nominally associated with the other. We have observed the related phenomenon of isomer interconversion in photoexcited clusters earlier[69] using complimentary methods, but here we illustrate how these dynamics can be revealed with

temperature-dependent, two-color, IR-IR double resonance (Fig. 4.3e) on the $I^-\cdot(H_2O)\cdot(D_2O)$ isotopomer.

Fig. 4.22a displays the linear spectrum of the cold cluster, while the lower traces (Figs. 4.22b-g) present the IR-IR double resonance spectra arising from probing the free OH (blue) and IH (red) bands at three different temperatures. At low temperature (50 K), we recover the independent spectra of the two sites discussed at length above (Figs. 4.22b,c). At 100 K, however, which is just below the temperature (125 K) identified earlier [30] where the dimer motif is broken apart, broad features begin to appear (Figs. 4.22d,e) near those associated with the site that is not selected by the probe. By 150 K, probing the IH transition (Fig. 4.22f) results in strong dips across all four of the features associated with the two sites, indicating that the two water molecules are efficiently interconverting between the two sites on the timescale (30 microseconds) of the pump-probe experiment. Although the isotopomer method explores somewhat different mechanics than that of the homogeneous system due to the strong zero-point energy effects on the shape of the intermolecular potential energy surface, the calling card of the breakup in the 100-150 K range is entirely consistent with the behavior of $I^-\cdot(H_2O)_2$ reported earlier. [30] This approach thus appears to be a viable way to explore spectral diffusion in more complex environments, creating a microscopic analogue of the methods carried out in solution using ultrafast 2DIR on isotopically labeled water in the vicinity of the BF_4^- anion.[70] More spectral diffusion experiments on this system are discussed in detail in Chapter 8.

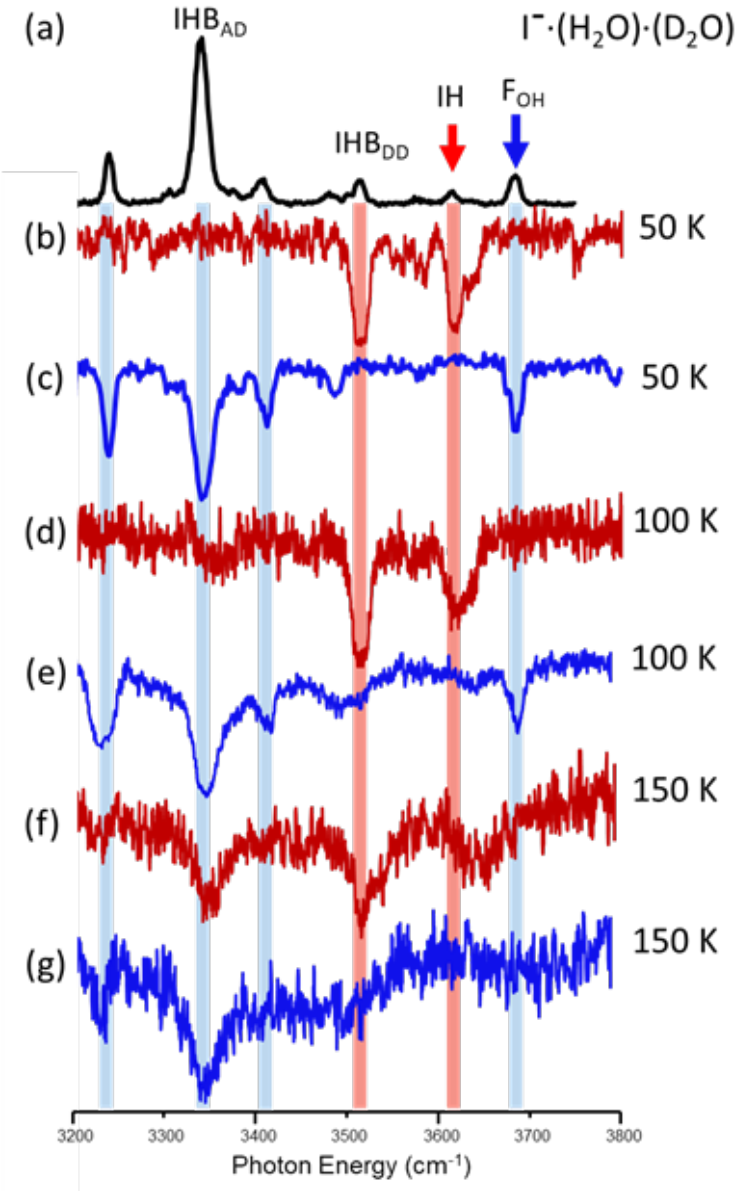

Figure 4.22. (a) Predissociation spectrum of D_2 tagged $I^-\cdot(H_2O)\cdot(D_2O)$. (b-g) Isotopomer selective double resonance dip spectra at various trap temperatures. The blue traces represent the spectra of H_2O_{AD} obtained by probing on the free OH indicted by the blue arrow in (a), while red traces represent the spectra of H_2O_{DD} acquired by probing on the IH transition labeled by the red arrow. The color-coded droplines indicate the cold cluster transition frequencies associated with each isotopomer.

4.4. Summary

We have demonstrated the spectroscopic advantages that are available through two-color, IR-IR photodissociation (IR2PD) spectroscopy of cold cluster ions through exploitation of the differences in the linear spectra and those of the cluster after excitation with a single photon in the OH/OD stretching region. These advances enable the acquisition of linear spectrum of the bare ion, thus eliminating the perturbation induced by the "messenger" tag which were, in this case, found to be surprisingly small (<1 cm^{-1}). We then demonstrated how IR-IR methods can be applied to the isotopomers arising from partial deuteration of the iodide dihydrate to isolate the spectral signatures of the two distinct binding sites, in this case the DD and AD arrangements, where A and D denote acceptor and donor H-bonding motifs. Of particular interest here is the soft mode combination band activity that is unique to each site, as well as the more subtle point regarding the coupling between the two OH(D) groups on the same water molecule. An interesting result arising from this analysis is, for example, that one cannot infer the coupling between the two OH(D) groups from the splitting between the nominally symmetric and antisymmetric stretching fundamentals when $H_2O(D_2O)$ resides in a DD binding site. We see a bright future for the application of this methodology to quantify the behavior of individual water molecules in more complex H-bonding networks, as well as to follow the spectral diffusion associated with the onset of large amplitude motion as a function of cluster internal energy and temperature.

4.5. References

1. Bailey, C. G.; Kim, J.; Dessent, C. E. H.; Johnson, M. A. Vibrational Predissociation Spectra of $I^-\cdot(H_2O)$: Isotopic Labels and Weakly Bound Complexes with Ar and N_2. *Chemical Physics Letters* **1997,** *269* (1-2), 122-127.

2. Ayotte, P.; Bailey, C. G.; Weddle, G. H.; Johnson, M. A. Vibrational Spectroscopy of Small $Br^-\cdot(H_2O)_n$ and $I^-\cdot(H_2O)_n$ Clusters: Infrared Characterization of the Ionic Hydrogen Bond. *J. Phys. Chem. A* **1998,** *102*, 3067-3071.

3. Ayotte, P.; Weddle, G. H.; Kim, J.; Johnson, M. A. Vibrational Spectroscopy of the Ionic Hydrogen Bond: Fermi Resonances and Ion-Molecule Stretching Frequencies in the Binary $X^-\cdot(H_2O)$ (X = Cl, Br, I) Complexes via Argon Predissociation Spectroscopy. *J. Am. Chem. Soc.* **1998,** *120* (47), 12361-12362.

4. Ayotte, P.; Weddle, G. H.; Kim, J.; Johnson, M. A. Mass-Selected "Matrix Isolation" Infrared Spectroscopy of the $I^-\cdot(H_2O)_2$ Complex: Making and Breaking the Inter-Water Hydrogen-Bond. *Chem. Phys.* **1998,** *239* (1-3), 485-491.

5. Cabarcos, O. M.; Weinheimer, C. J.; Lisy, J. M.; Xantheas, S. S. Microscopic Hydration of the Fluoride Anion. *J. Chem. Phys.* **1999,** *110*, 5-8.

6. Bryce, R. A.; Vincent, M. A.; Hillier, I. H. Binding Energy of $F^-\cdot H_2O$ and the Simulation of Fluoride Water Clusters using a Hybrid QM MM (Fluctuating Charge) Potential. *J. Phys. Chem. A* **1999,** *103*, 4094-4100.

7. Ayotte, P.; Nielsen, S. B.; Weddle, G. H.; Johnson, M. A.; Xantheas, S. S. Spectroscopic Observation of Ion-Induced Water Dimer Dissociation in the $X^-\cdot(H_2O)_2$ (X = F, Cl, Br, I) Clusters. *Journal of Physical Chemistry A* **1999,** *103* (50), 10665-10669.

8. Irle, S.; Bowman, J. M. Direct ab initio Variational Calculation of Vibrational Energies of the $H_2O\cdots Cl^-$ Complex and Resolution of Experimental Differences. *J. Chem. Phys.* **2000,** *113*, 8401-8403.

9. Lee, H. M.; Kim, K. S. Structures and Spectra of Iodide-Water Clusters $I^-(H_2O)_{1-6}$: an ab initio Study. *J. Chem. Phys.* **2001,** *114*, 4461-4471.

10. Bowman, J. M.; Xantheas, S. S. "Morphing" of ab initio-Based Interaction Potentials to Spectroscopic Accuracy: Application to $Cl^-(H_2O)$. *Pure Appl. Chem.* **2004,** *76* (1), 29-35.

11. Robertson, W. H.; Johnson, M. A. Molecular Aspects of Halide Ion Hydration: The Cluster Approach. *Annu. Rev. Phys. Chem.* **2003,** *54*, 173-213.

12. Price, E. A.; Hammer, N. I.; Johnson, M. A. A Cluster Study of Cl_2^- Microhydration: Size-Dependent Competition between Symmetrical H-Bonding to the Anion and the Formation of Cyclic Water Networks in the $Cl_2^-\cdot 1\text{-}5(H_2O)$ Series. *Journal of Physical Chemistry A* **2004,** *108* (18), 3910-3915.

13. Diken, E. G.; Headrick, J. M.; Roscioli, J. R.; Bopp, J. C.; Johnson, M. A.; McCoy, A. B.; Huang, X.; Carter, S.; Bowman, J. M. Argon Predissociation Spectroscopy of the $OH^-\cdot H_2O$ and $Cl^-\cdot H_2O$ Complexes in the 1000 - 1900 cm^{-1} Region: Intramolecular Bending Transitions and the Search for the Shared Proton Fundamental in the Hydroxide Monohydrate. *J. Phys. Chem. A* **2005,** *109* (4), 571-575.

14. Kammrath, A.; Verlet, J. R. R.; Bragg, A. E.; Griffin, G. B.; Neumark, D. M. Dynamics of Charge-Transfer-to-Solvent Precursor States in $I^-(H_2O)_n$ (n=3-10) Clusters Studied with Photoelectron Imaging. *J. Phys. Chem. A* **2005,** *109* (50), 11475-11483.

15. Rheinecker, J. L.; Bowman, J. M. The Calculated Infrared Spectrum of Cl^-H_2O using a Full Dimensional ab initio Potential Surface and Dipole Moment Surface. *J. Chem. Phys.* **2006,** *124* (13), 131102.

16. Roscioli, J. R.; Diken, E. G.; Johnson, M. A.; Horvath, S.; McCoy, A. B. Prying Apart a Water Molecule with Anionic H-Bonding: A Comparative Spectroscopic Study of the $X^-\cdot H_2O$ (X = OH, O, F, Cl, and Br) Binary Complexes in the 600-3800 cm^{-1} Region. *J. Phys. Chem. A* **2006,** *110* (15), 4943-4952.

17. Huang, X. C.; Habershon, S.; Bowman, J. M. Comparison of Quantum, Classical, and Ring-Polymer Molecular Dynamics Infra-red Spectra of $Cl^-(H_2O)$ and $H^+(H_2O)_2$. *Chem. Phys. Lett.* **2008,** *450* (4-6), 253-257.

18. Beck, J. P.; Lisy, J. M. Cooperatively Enhanced Ionic Hydrogen Bonds in $Cl^-(CH_3OH)$(1-3)Ar Clusters. *J. Phys. Chem. A* **2010,** *114* (37), 10011-10015.

19. Horvath, S.; Mccoy, A. B.; Elliott, B. M.; Weddle, G. H.; Roscioli, J. R.; Johnson, M. A. Anharmonicities and Isotopic Effects in the Vibrational Spectra of X^-H_2O, $\cdot HDO$, and $\cdot D_2O$ [X = Cl, Br, and I] Binary Complexes. *Journal of Physical Chemistry A* **2010,** *114* (3), 1556-1568.

20. Bajaj, P.; Gotz, A. W.; Paesani, F. Toward Chemical Accuracy in the Description of Ion-Water Interactions through Many-Body Representations. I. Halide-Water Dimer Potential Energy Surfaces. *J. Chem. Theory Comput.* **2016,** *12* (6), 2698-2705.

21. Okumura, M.; Yeh, L. I.; Myers, J. D.; Lee, Y. T. Infrared Spectra of the Cluster Ions $H_7O_3^+\cdot H_2$ and $H_9O_4^+\cdot H_2$. *J. Chem. Phys.* **1986,** *85*, 2328-2329.

22. Yeh, L. I.; Okumura, M.; Myers, J. D.; Price, J. M.; Lee, Y. T. Vibrational Spectroscopy of the Hydrated Hydronium Cluster Ions $H_3O^+ \cdot (H_2O)_n$ (n=1,2,3). *J. Chem. Phys.* **1989,** *91* (12), 7319-7330.

23. Okumura, M.; Yeh, L. I.; Myers, J. D.; Lee, Y. T. Infrared-Spectra of the Solvated Hydronium Ion: Vibrational Predissociation Spectroscopy of Mass-Selected $H_3O^+ \cdot (H_2O)_n \cdot (H_2)_m$. *J. Phys. Chem.* **1990,** *94*, 3416-3427.

24. Bailey, C. G.; Kim, J.; Dessent, C. E. H.; Johnson, M. A. Vibrational Predissociation Spectra of $I^- \cdot (H_2O)$: Isotopic Labels and Weakly Bound Complexes with Ar and N_2. *Chem. Phys. Lett.* **1997,** *269*, 122-127.

25. Ratajczak, H.; Oswal, S. L. Charge-Transfer Properties of Hydrogen-Bond. I. Theory of Enhancement of Dipole-Moment of Hydrogen-Bonded Systems. *J Phys Chem-Us* **1972,** *76* (21), 3000-+.

26. Ratajczak, H.; Orvillet.Wj. Charge-Transfer Properties of Hydrogen-Bonds. III. Charge-Transfer Theory and Relation between Energy and Enhancement of Dipole-Moment of Hydrogen-Bonded Complexes. *Journal of Chemical Physics* **1973,** *58* (3), 911-919.

27. Ratajczak, H.; Orvillethomas, W. J. Charge-Transfer Properties of Hydrogen-Bond. VI. Charge-Transfer Theory and Dipole-Moments of Hydrogen-Bonded Complexes. *Journal of Molecular Structure* **1975,** *26* (2), 387-391.

28. Ratajczak, H.; Orvillethomas, W. J.; Rao, C. N. R. Charge-Transfer Theory of Hydrogen-Bonds - Relations between Vibrational-Spectra and Energy of Hydrogen-Bonds. *Chem Phys* **1976,** *17* (2), 197-216.

29. Dorsett, H. E.; Watts, R. O.; Xantheas, S. S. Probing Temperature Effects on the Hydrogen Bonding Network of the $Cl^-(H_2O)_2$ Cluster. *Journal of Physical Chemistry A* **1999,** *103* (18), 3351-3355.

30. Wolke, C. T.; Menges, F. S.; Totsch, N.; Gorlova, O.; Fournier, J. A.; Weddle, G. H.; Johnson, M. A.; Heine, N.; Esser, T. K.; Knorke, H.; Asmis, K. R.; McCoy, A. B.; Arismendi-Arrieta, D. J.; Prosmiti, R.; Paesani, F. Thermodynamics of Water Dimer Dissociation in the Primary Hydration Shell of the Iodide Ion with Temperature-Dependent Vibrational Predissociation Spectroscopy. *J. Phys. Chem. A* **2015,** *119* (10), 1859-1866.

31. Peterson, K. A.; Shepler, B. C.; Figgen, D.; Stoll, H. On the Spectroscopic and Thermochemical Properties of ClO, BrO, IO, and Their Anions. *J. Phys. Chem. A* **2006,** *110*, 13877-13883.

32. Robertson, W. H.; Weddle, G. H.; Kelley, J. A.; Johnson, M. A. Solvation of the $Cl^-\cdot H_2O$ Complex in CCl_4 Clusters: The Effect of Solvent-Mediated Charge Redistribution on the Ionic H-Bond. *J. Phys. Chem. A* **2002,** *106*, 1205-1209.

33. Horvath, S.; McCoy, A. B.; Elliott, B. M.; Weddle, G. H.; Roscioli, J. R.; Johnson, M. A. Anharmonicities and Isotopic Effects in the Vibrational Spectra of $X^-\cdot H_2O$, $\cdot HDO$, and $\cdot D_2O$ [X = Cl, Br, and I] Binary Complexes. *J. Phys. Chem. A* **2010,** *114* (3), 1556-1568.

34. Zajfman, D.; Rudich, Y.; Sagi, I.; Strasser, D.; Savin, D. W.; Goldberg, S.; Rappaport, M.; Heber, O. High Resolution Mass Spectrometry using a Linear Electrostatic Ion Beam Trap. *Int. J. Mass Spectrom.* **2003,** *229* (1-2), 55-60.

35. Elliott, B. M.; Relph, R. A.; Roscioli, J. R.; Bopp, J. C.; Gardenier, G. H.; Guasco, T. L.; Johnson, M. A. Isolating the Spectra of Cluster Ion Isomers Using Ar-"tag" -mediated IR-IR Double Resonance Within the Vibrational Manifolds: Application to $NO_2^- \cdot H_2O$. *J. Chem. Phys.* **2008,** *129* (9), 094303.

36. Leavitt, C. M.; Wolk, A. B.; Fournier, J. A.; Kamrath, M. Z.; Garand, E.; Van Stipdonk, M. J.; Johnson, M. A. Isomer-Specific IR-IR Double Resonance Spectroscopy of D_2 Tagged Protonated Dipeptides Prepared in a Cryogenic Ion Trap. *J. Phys. Chem. Lett.* **2012,** *3* (9), 1099-1105.

37. Wolk, A. B.; Leavitt, C. M.; Garand, E.; Johnson, M. A. Cryogenic Ion Chemistry and Spectroscopy. *Accounts Chem Res* **2014,** *47* (1), 202-210.

38. Yacovitch, T. I.; Heine, N.; Brieger, C.; Wende, T.; Hock, C.; Neumark, D. M.; Asmis, K. R. Vibrational Spectroscopy of Bisulfate/Sulfuric Acid/Water Clusters: Structure, Stability, and Infrared Multiple-Photon Dissociation Intensities. *J. Phys. Chem. A* **2013,** *117* (32), 7081-7090.

39. Kamrath, M. Z.; Relph, R. A.; Guasco, T. L.; Leavitt, C. M.; Johnson, M. A. Vibrational Predissociation Spectroscopy of the H_2-Tagged Mono- and Dicarboxylate Anions of Dodecanedioic Acid. *Int. J. Mass Spectrom.* **2011,** *300* (2-3), 91-98.

40. Wiley, W. C.; McLaren, I. H. Time-of-Flight Mass Spectrometer with Improved Resolution. *Rev. Sci. Instrum.* **1955,** *26*, 1150-1157.

41. Ayotte, P.; Weddle, G. H.; Kim, J.; Johnson, M. A. Mass-Selected "Matrix Isolation" Infrared Spectroscopy of the $I^- \cdot (H_2O)_2$ Complex: Making and Breaking the Inter-Water Hydrogen-Bond. *Chem. Phys.* **1998,** *239*, 485-491.

42. Keesee, R. G.; Castleman, A. W., Jr. Gas Phase Studies of Hydration Complexes of Cl^- and I^- and Comparison to Electrostatic Calculation in the Gas Phase. *Chem. Phys. Lett.* **1980,** *74*, 139-142.

43. Keesee, R. G.; Castleman, A. W., Jr. Thermochemical Data on Gas-Phase Ion-Molecule Association and Clustering Reactions. *J. Phys. Chem. Ref. Data* **1986,** *15*, 1011-1071.

44. Putter, M.; von Helden, G.; Meijer, G. Mass Selective Infrared Spectroscopy Using a Free Electron Laser. *Chemical Physics Letters* **1996,** *258* (1-2), 118-122.

45. Asmis, K. R.; Pivonka, N. L.; Santambrogio, G.; Brummer, M.; Kaposta, C.; Neumark, D. M.; Woste, L. Gas-Phase Infrared Spectrum of the Protonated Water Dimer. *Science* **2003,** *299* (5611), 1375-1377.

46. Yacovitch, T. I.; Heine, N.; Brieger, C.; Wende, T.; Hock, C.; Neumark, D. M.; Asmis, K. R. Vibrational Spectroscopy of Bisulfate/Sulfuric Acid/Water Clusters: Structure, Stability, and Infrared Multiple-Photon Dissociation Intensities. *Journal of Physical Chemistry A* **2013,** *117* (32), 7081-7090.

47. Nosenko, Y.; Menges, F.; Riehn, C.; Niedner-Schatteburg, G. Investigation by Two-Color IR Dissociation Spectroscopy of Hoogsteen-type Binding in a Metalated Nucleobase Pair Mimic. *Phys. Chem. Chem. Phys.* **2013,** *15* (21), 8171-8178.

48. Settle, R. D. F.; Rizzo, T. R. CO_2-Laser Assisted Vibrational Overtone Spectroscopy. *J. Chem. Phys.* **1992,** *97* (4), 2823-2825.

49. Nesbitt, D. J.; Field, R. W. Vibrational Energy Flow in Highly Excited Molecules: Role of Intramolecular Vibrational Redistribution. *J. Phys. Chem.* **1996,** *100* (31), 12735-12756.

50. Schmidt, M.; Kusche, R.; von Issendorff, B.; Haberland, H. Irregular Variations in the Melting Point of Size-Selected Atomic Clusters. *Nature* **1998,** *393* (6682), 238-240.

51. Schmidt, M.; Kusche, R.; Kronmuller, W.; vonIssendorff, B.; Haberland, H. Experimental Determination of the Melting Point and Heat Capacity for a Free Cluster of 139 Sodium Atoms. *Phys Rev Lett* **1997,** *79* (1), 99-102.

52. Mizuse, K.; Fujii, A. Infrared Photodissociation Spectroscopy of $H^+(H_2O)_6 \cdot M_m$ (M = Ne, Ar, Kr, Xe, H_2, N_2, and CH_4): Messenger-Dependent Balance between H_3O^+ and $H_5O_2^+$ Core Isomers. *Physical chemistry chemical physics : PCCP* **2011,** *13* (15), 7129-7135.

53. Johnson, C. J.; Wolk, A. B.; Fournier, J. A.; Sullivan, E. N.; Weddle, G. H.; Johnson, M. A. Communication: He-Tagged Vibrational Spectra of the $SarGlyH^+$ and $H^+(H_2O)_{2,3}$ Ions: Quantifying Tag Effects in Cryogenic Ion Vibrational Predissociation (CIVP) Spectroscopy. *J. Chem. Phys.* **2014,** *140* (22), 221101.

54. Douberly, G. E.; Walters, R. S.; Cui, J.; Jordan, K. D.; Duncan, M. A. Infrared Spectroscopy of Small Protonated Water Clusters, $H^+(H_2O)_n$ (n=2-5): Isomers, Argon Tagging, and Deuteration. *J. Phys. Chem. A* **2010,** *114* (13), 4570-4579.

55. Masson, A.; Williams, E. R.; Rizzo, T. R. Molecular Hydrogen Messengers Can Lead to Structural Infidelity: A Cautionary Tale of Protonated Glycine. *Journal of Chemical Physics* **2015,** *143* (10).

56. Dickenson, G. D.; Niu, M. L.; Salumbides, E. J.; Komasa, J.; Eikema, K. S. E.; Pachucki, K.; Ubachs, W. Fundamental Vibration of Molecular Hydrogen. *Phys Rev Lett* **2013,** *110* (19), 193601.

57. Hammer, N. I.; Roscioli, J. R.; Johnson, M. A. Identification of Two Distinct Electron Binding Motifs in the Anionic Water Clusters: A Vibrational Spectroscopic Study of the $(H_2O)_6^-$ Isomers. *Journal of Physical Chemistry A* **2005,** *109* (35), 7896-7901.

58. Wolke, C. T.; Fournier, J. A.; Miliordos, E.; Kathmann, S. M.; Xantheas, S. S.; Johnson, M. A. Isotopomer-Selective Spectra of a Single Intact H_2O Molecule in the $Cs^+(D_2O)_5H_2O$ Isotopologue: Going Beyond Pattern Recognition to Harvest the Structural Information Encoded in Vibrational Spectra. *J. Chem. Phys.* **2016,** *144* (7).

59. Wolke, C. T.; Menges, F. S.; Totsch, N.; Gorlova, O.; Fournier, J. A.; Weddle, G. H.; Johnson, M. A.; Heine, N.; Esser, T. K.; Knorke, H.; Asmis, K. R.; McCoy, A. B.; Arismendi-Arrieta, D. J.; Prosmiti, R.; Paesani, F. Thermodynamics of Water Dimer Dissocation in the Primary Hydration Shell of the Iodide Ion with Temperature-Dependent Vibrational Predissociation Spectroscopy. *J. Phys. Chem. A* **2015,** *119*, 1859.

60. Herzberg, G. *Molecular-Spectra and Molecular-Structure: Infrared and Raman-Spectra of Polyatomic-Molecules*. 1988; p 16-16.

61. Sibert, E. L.; Hynes, J. T.; Reinhardt, W. P. Quantum-Mechanics of Local Mode ABA Triatomic-Molecules. *Journal of Chemical Physics* **1982,** *77* (7), 3595-3604.

62. Reimers, J. R.; Watts, R. O. A Local Mode Potential Function for the Water Molecule. *Mol Phys* **1984,** *52* (2), 357-381.

63. Low, G. R.; Kjaergaard, H. G. Calculation of OH-Stretching Band Intensities of the Water Dimer and Trimer. *Journal of Chemical Physics* **1999,** *110* (18), 9104-9115.

64. Schofield, D. P.; Kjaergaard, H. G. Calculated OH-Stretching and HOH-Bending Vibrational Transitions in the Water Dimer. *Physical chemistry chemical physics : PCCP* **2003,** *5* (15), 3100-3105.

65. Auer, B. M.; Skinner, J. L. IR and Raman Spectra of Liquid Water: Theory and Interpretation. *J. Chem. Phys.* **2008,** *128* (22).

66. Shi, L.; Gruenbaum, S. M.; Skinner, J. L. Interpretation of IR and Raman Line Shapes for H_2O and D_2O Ice Ih. *Journal of Physical Chemistry B* **2012,** *116* (47), 13821-13830.

67. Tainter, C. J.; Skinner, J. L. The Water Hexamer: Three-Body Interactions, Structures, Energetics, and OH-Stretch Spectroscopy at Finite Temperature. *Journal of Chemical Physics* **2012,** *137* (10).

68. Wolke, C. T.; Fournier, J. A.; Dzugan, L. C.; Fagiani, M. R.; Odbadrakh, T. T.; Knorke, H.; Jordan, K. D.; McCoy, A. B.; Asmis, K. R.; Johnson, M. A. Spectroscopic Snapshots of the Proton-Transfer Mechanism in Water. *Science* **2016,** *354* (6316), 1131-1135.

69. McCunn, L. R.; Gardenier, G. H.; Guasco, T. L.; Elliott, B. M.; Bopp, J. C.; Relph, R. A.; Johnson, M. A. Probing Isomer Interconversion in Anionic Water Clusters using an Ar-Mediated Pump-Probe Approach: Combining Vibrational Predissociation and Velocity-Map Photoelectron Imaging Spectroscopies. *J. Chem. Phys.* **2008,** *128* (23), 234311.

70. Moilanen, D. E.; Wong, D.; Rosenfeld, D. E.; Fenn, E. E.; Fayer, M. D. Ion-Water Hydrogen-Bond Switching Observed with 2D IR Vibrational Echo Chemical Exchange Spectroscopy. *P. Natl. Acad. Sci. USA* **2009,** *106* (2), 375-380.

CHAPTER 5

Capturing Intrinsic Site-dependent Spectral Signatures and Lifetimes of Isolated OH Oscillators in Extended Water Networks as well as Their Temperature Dependent Behavior

The material in this chapter is adapted with permission from Yang, Nan, Chinh H. Duong, Patrick J. Kelleher, and Mark A. Johnson. "Capturing intrinsic site-dependent spectral signatures and lifetimes of isolated OH oscillators in extended water networks." Nature Chemistry 12, no. 2 (2020): 159-164.

5.1 Introduction

In Chapter 3 and 4 we covered the spectral behavior of water molecules in smaller water clusters, in this chapter we make a jump to larger water clusters with around 20 water molecules where the OH stretch region of the vibrational spectra resembles that of the air-water interface. We want to exam the behavior of isolated OH oscillators inside an extended H-bond network. The smaller clusters display sharp OH features whereas the larger cluster have varying peak widths throughout the OH range.

In a broader context, the microscopic mechanics underlying the diffuse OH stretching spectrum of condensed phase water in all of its forms (liquid, solid and interface) is currently under intense study as theoretical [1-8] and experimental [9-16] advances are becoming capable of handling the cooperative interactions that drive its macroscopic behavior. Most of the breadth displayed by the OH stretching region persists even when OH oscillators are decoupled through isotopic dilution to isolate the response of HDO when surrounded by a thermally fluctuating D_2O matrix.[17] Most often, simulations of the IR spectrum adopt the ansatz that, if the surrounding local structure could be frozen in place, an isolated OH oscillator would contribute a single feature with an intrinsic width associated with the vibrational lifetime,[18] determined by the topology of the surrounding hydrogen bonding network.[19] In that case, the breadth of the OH stretching manifold can be recovered by averaging over the many different structures present in the thermal ensemble.[20] The situation in the liquid is, of course, dynamic in the sense that a single OH oscillator explores all available configurations on the very fast timescale associated with spectral diffusion.[21-22] Here we present experimental results that test two fundamental questions regarding this ansatz. The first involves the degree to which the

vibrational signature of a local oscillator is actually confined to the vibrational fundamental, and the second pertains to the dependence of the intrinsic lineshapes on their locations within the OH stretching envelope. The first issue arises because several recent studies have reported strong combination bands corresponding to excitation of soft modes along with the OH fundamentals in small cluster systems at very low temperature including those discussed in Chapter 4,[23-25] raising the question of whether such mechanics are also at play in larger networks. The second issue regards the lifetimes of the OH(v=1) excited states at 0 K and how these depend on location in the spectrum. Related aspects of these questions can be probed with two-dimensional infrared (2DIR) spectroscopy, and it is established that the lifetimes of the OH(v=1) vibrational levels (population relaxation) are on the order of ps, which sets a lower limit on the homogeneous linewidths of about 10 cm^{-1}.[15, 26-27] The timescales for spectral diffusion, on the other hand, are significantly shorter, with frequency modulations due to fluctuations in the O-O distances estimated to be about an order of magnitude faster.[6, 15, 28-29] These ultrafast processes in liquid water at high temperature obscure contributions to the broadening that are intrinsic to the local environment, i.e., that would occur even if the local surroundings were static. The goal of this study is to reveal these heretofore hidden dynamics.

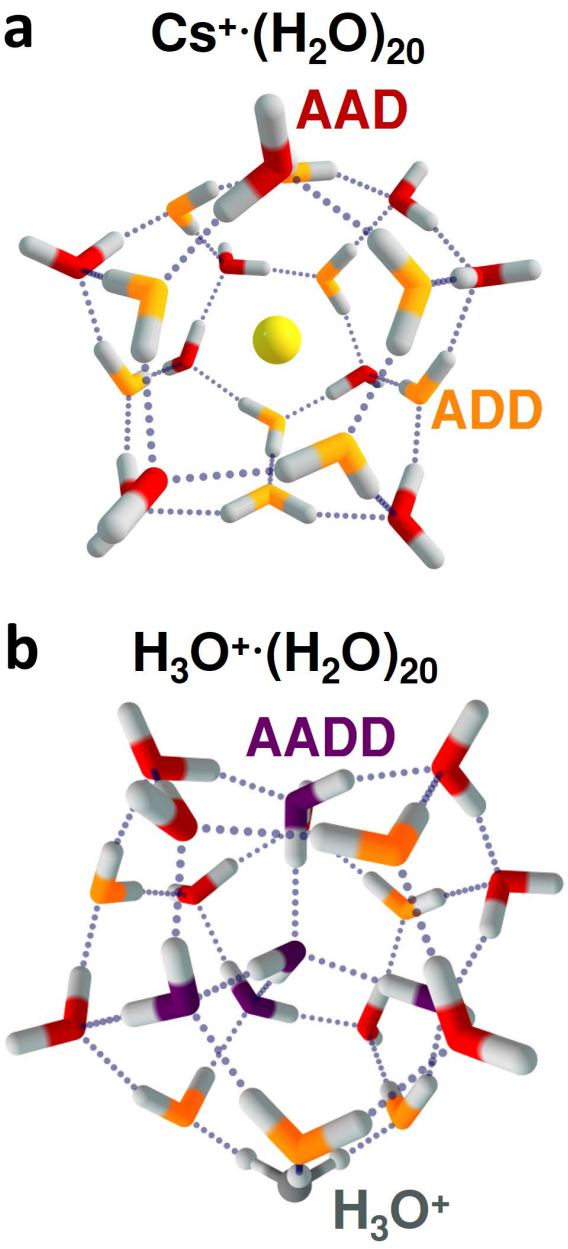

Figure 5.1: Representative structures of the pentagonal dodecahedron (PD_0) water cages. The representative $Cs^+ \cdot (H_2O)_{20}$ cluster structure [30] (a) and the minimal energy structure [31] (b) of $H_3O^+ \cdot (H_2O)_{20}$. These structures contain three classes of network sites: AAD (red), ADD (orange) and AADD (purple), that differ by the number of H-bond acceptors (A) and donors (D) associated with each water molecule.

5.2 Experimental Methods and Computational Methods

The $Cs^+(H_2O)_{20}$ cluster ions were obtained by first electrospraying 5 mM $CsNO_3$ aqueous solution in a humidity-controlled purge capsule. The $Cs^+\cdot(HDO)(D_2O)_{19}$ ions were introduced by first electrospraying a 5 mM $CsNO_3$ D_2O solution in a capsule purged with dry air and HDO/D_2O vapor mixture. Subsequently the ions are loaded into a temperature-controlled Paul trap kept at 13.5 K with 10% D_2 in He mixture as buffer gas to attach the D_2 messenger tag. The predissociation spectra were obtained by irradiating the mass selected ions with a pulsed (10 Hz, 8 ns) tunable OPO/OPA IR laser (Laservision) which results in dissociation of the messenger tag upon resonant excitation of the mass-selected ions. The fragment ion is separated from the parent ion with a secondary mass spectrometer and monitored as a function of photon energy to yield the vibrational spectrum for the ions of interest.

The isotopomer-selective two-color IR-IR double resonance hole burning dip spectra were obtained in an IR^2MS^3 instrument (Chapter 2) where mass selected ions are irradiated with the first (pump) laser and mass separated in the secondary mass spectrometer to eliminate the fragment associated with the pump laser. The remaining parent ion is then irradiated by the second (probe) laser and mass separated again in the third mass separation stage, where the fragment from the probe laser is monitored. When acquiring an isotopomer selective double resonance dip spectrum, the probe laser is fixed on a frequency that is unique to one or several similar isotopomers. The pump laser is then scanned through the entire spectrum, and when it dissociates the parent ion selected by the probe, the probe fragment signal is decreased. This depletion is recorded as a

function of pump laser frequency, and the resulting trace reveals the spectrum associated with the isotopomer selected by the probe laser.

All calculations in this paper were computed with Gaussian 09 at the B3LYP/6-31++G** level of theory and basis with the LANL2DZ pseudopotential for the Cs atom.

5.3 Results and Discussion

In this section, we demonstrate how the spectral signature of a single OH group embedded in an extended, quasi-rigid H-bond network can be experimentally determined by exploiting the unique properties of cold, size-selected cluster ions. The minimum requirement for a useful model system that can accomplish this is that it displays sufficient variation in the local binding motifs that its OH stretching fundamentals span the range observed for bulk water, and it has a high enough density of states in the 3000-4000 cm^{-1} region to provide an effective continuum of background quantum states that can interact with the excited OH group. These criteria are met by the "magic" cluster ions with the structures indicated in Fig. 5.1: $Cs^+ \cdot (H_2O)_{20}$, which encapsulates the central Cs^+ ion in a distorted pentagonal dodecahedron (hereafter denoted **PD**) cage, and $H_3O^+ \cdot (H_2O)_{20}$, which offers a radically different **PD** arrangement in which the hydronium ion resides on the surface of the cage.[30-31] Specifically, we isolate the $Cs^+ \cdot (HDO)(D_2O)_{19}$ and $D_3O^+ \cdot (HDO)(D_2O)_{20}$ isotopologues at low temperature using cryogenic mass spectrometry methods and measure the spectral signatures of a single OH group residing in each of their many topologically distinct sites. This is accomplished with the use of isotopomer-selective, two color IR-IR photofragmentation spectroscopy.[23] An important

aspect of the **PD** structures is that most (in some cases all) network sites are distinguishable in the many distinct, nearly isoenergetic H-bonding arrangements. (Note that the **PD$_0$** structure in Fig. 5.1a is the specific isomer from ref. 30.) This diversity of local environments is a useful feature when using these clusters to explore the molecular behavior of interfacial water because it enables spectroscopic characterization of their intrinsic behavior in a static ensemble. That is, the cage is structurally more similar to the liquid water surface than it is to the regular order presented by crystalline ice.[32-33] This property was recently exploited to understand the spectral signature of a single H_2O molecule trapped in each site using isotopomer-selective spectroscopy on the cryogenically cooled $Cs^+ \cdot (H_2O)(D_2O)_{19}$ clusters (also discussed in detail in Chapter 6).[34] That study revealed the site-dependence of the correlated absorptions between the two OH groups on the same water molecule. Here we are concerned with the spectroscopic signature associated with a single OH group located in each of the various sites in the **PD** structures, information that was obscured in the previous study due to complexities arising from the intramolecular coupling between the two OH groups and with the overtone of the intramolecular HOH bend.

The vibrational spectra of the cold cluster ions were obtained using the mass messenger or "tagging" technique,[35] which yields the spectrum in an action mode by resonant IR induced photoevaporation of the weakly bound D_2 molecules.[36-37] Figure 5.2b presents the $Cs^+ \cdot (HDO)(D_2O)_{19}$ spectrum in the OH stretching region, along with that of $Cs^+ \cdot (H_2O)_{20}$ in Fig. 5.2a (reproduced from ref. 34). Note that the partially resolved transitions span the range from the sharp free OH transition near 3700 cm^{-1} to about 3000 cm^{-1}, with bands dispersed throughout. This behavior indicates that the single OH group

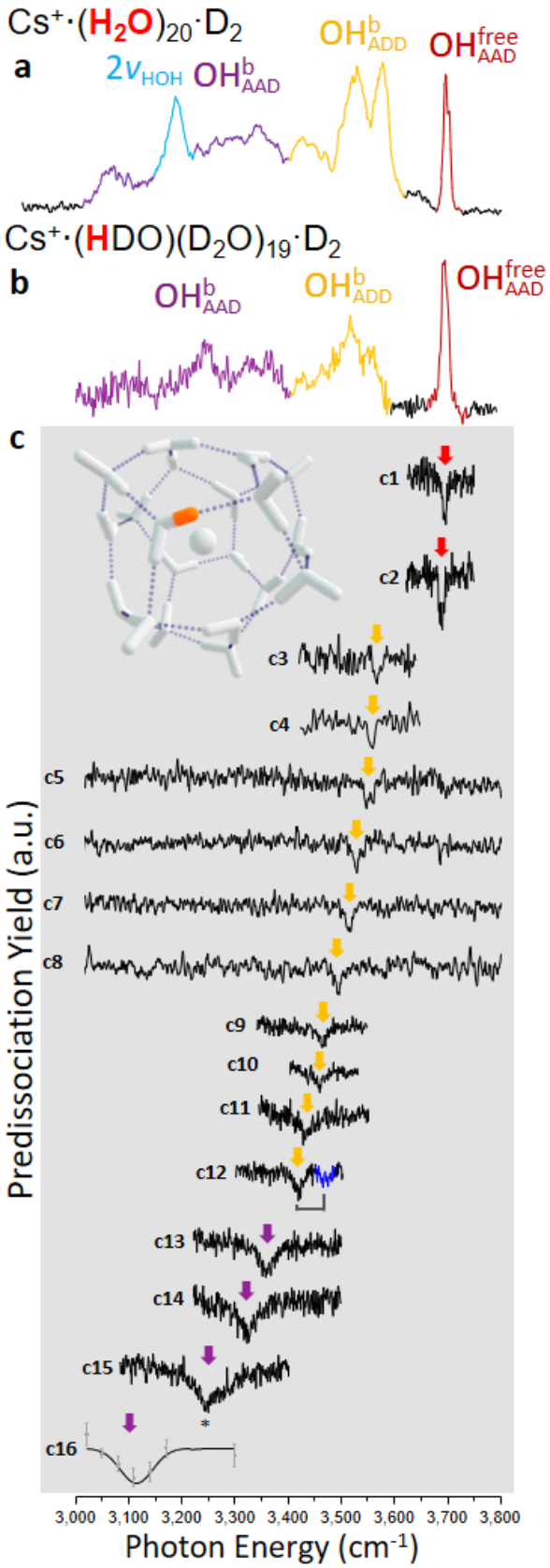
Cs+·(H2O)20·D2
a
2νHOH
OHbAAD
OHbADD
OHfreeAAD
Cs+·(HDO)(D2O)19·D2
b
OHbAAD
OHbADD
OHfreeAAD
c
c1
c2
c3
c4
c5
c6
c7
c8
c9
c10
c11
c12
c13
c14
c15
c16
*
Predissociation Yield (a.u.)
3,000 3,100 3,200 3,300 3,400 3,500 3,600 3,700 3,800
Photon Energy (cm-1)

Figure 5.2: Comparison between vibrational spectra of $Cs^+\cdot(H_2O)_{20}\cdot D_2$ and $Cs^+\cdot(HDO)(D_2O)_{19}\cdot D_2$. Displayed here are the vibrational predissociation spectra of $Cs^+\cdot(H_2O)_{20}\cdot D_2$ (a) and $Cs^+\cdot(HDO)(D_2O)_{19}\cdot D_2$ (b) and its isotopomer-specific spectra (c) where, purple, light blue and red represents the bound OH (OH^{b}_{AAD}), HOH bend overtone ($2\nu_{HOH}$) and the free OH (OH^{free}_{AAD}) on the AAD water molecules, respectively, whereas yellow labels identify the bound OH stretches (OH^{b}_{ADD}) on the ADD water molecules. Isotopomer selective spectra in the gray box (c1-c16) of $Cs^+\cdot(HDO)(D_2O)_{19}$ were obtained by probing at various locations indicated by the color-coded arrows. The structure shows one example of the single OH group that is in a configuration that contributes to one of the yellow OH^{b}_{ADD} features. Trace (c12) is expanded to show more detail in Figure 5.5. The symbol * in (c15) denotes a sharper feature that is embedded in the broader lineshape. Spectral assignments, probe positions and widths are reported in Table 5.1 and Table 5.2. Trace c16 was taken with extensive averaging at representative points due to low signal intensity in this energy range.

Table 5.1. Experimental frequencies, redshifts from the gas phase free OH frequency (±4 cm^{-1}) and FWHM of OH features in $Cs^{+}\cdot(HDO)(D_2O)_{19}$. Each row contains the features detected by fixing the probe laser on the experimental frequency except for peak 11* and 12*. Those two features where obtained when probing on peak xi and peak 12 and attributed to combination band activities, detailed explanation was included in figure 5.5. The assignments of the features are denoted such that AAD and Free refer to the bound OH and free OH on the AAD water molecules, respectively, whereas ADD refers to the bound OH groups on the ADD water molecules. Additionally, ADD combo. refers to the combination band in figure 5.2 (trace c12) and figure 5.8 (trace b12) and AAD* refers to the sharp band labeled with * in figure 5.2 (trace c15) and figure 5.8 (trace b15). The peak number corresponding to the peaks labeled in figure 5.2 (trace c1-c16) and figure 5.8 (trace b1-b16).

Experimental frequency (cm^{-1})	Peak number	Red Shift (cm^{-1})	FWHM (cm^{-1})	Confidence interval (cm^{-1})	Assignment
3691	1	15	10	±1.2	Free
3688	2	18	10	±0.9	Free
3572	3	134	12	±3.0	ADD
3560	4	146	11	±3.0	ADD
3550	5	156	11	±1.2	ADD
3528	6	178	17	±2.3	ADD
3513	7	193	15	±1.5	ADD
3495	8	211	13	±3.5	ADD
3466	9	240	20	±2.1	ADD
3457	10	249	19	±2.3	ADD
3435	11	271	22	±4.6	ADD
3455	11*	291	14	±6.6	ADD combo.
3417	12	289	20	±2.3	ADD
3468	12*	304	18	±4.2	ADD combo.
3360	13	346	33	±2.6	AAD
3321	14	385	38	±3.2	AAD
3245	15	461	65	±12	AAD
3242	15	464	10	±3.0	AAD*
3114	16	592	72	±27	AAD

Table 5.2. Experimental frequencies (±4 cm^{-1}) observed for $Cs^+(H_2O)_{20}$. Peak labels are defined in Table 5.1 and $2\nu_{HOH}$ denotes the HOH bend overtone feature.

Experimental frequency (cm^{-1})	Assignment
3704	Free
3698	Free
3579	ADD
3529	ADD
3470	ADD
3448	ADD
3430	ADD
3380	AAD
3346	AAD
3320	AAD
3300	AAD
3285	AAD
3231	$2\nu_{HOH}$
3191	$2\nu_{HOH}$
3072	AAD

can be trapped in most if not all of the spectroscopically distinct H-bonding sites available in the **PD** structure, a situation discussed at length in ref. 34 for the case of a single H_2O molecule in the otherwise perdeuterated **PD** cage. The nature of the H-bonding sites in play at various locations in the spectrum were established in the previous study of the $Cs^+ \cdot (H_2O)(D_2O)_{19}$ isotopomers,[34] which differ according to the number of donor (D) and acceptor (A) H-bonding interactions at play in each network site. Using the double resonance approach described below, [34] we determined the locations in the spectrum arising from the two OH groups on the same water molecule, as a function of the site occupied by that molecule. The AAD sites contribute the free OH bands (OH^{free}_{AAD}, red in Fig 5.2b) as well as all of the spectral features below 3450 cm^{-1}. The latter are associated with excitation of the companion OH group bound in the cage (OH^{b}_{AAD}, purple in Fig. 5.2b and Fig. 5.3). The ADD sites exclusively account for the moderately red

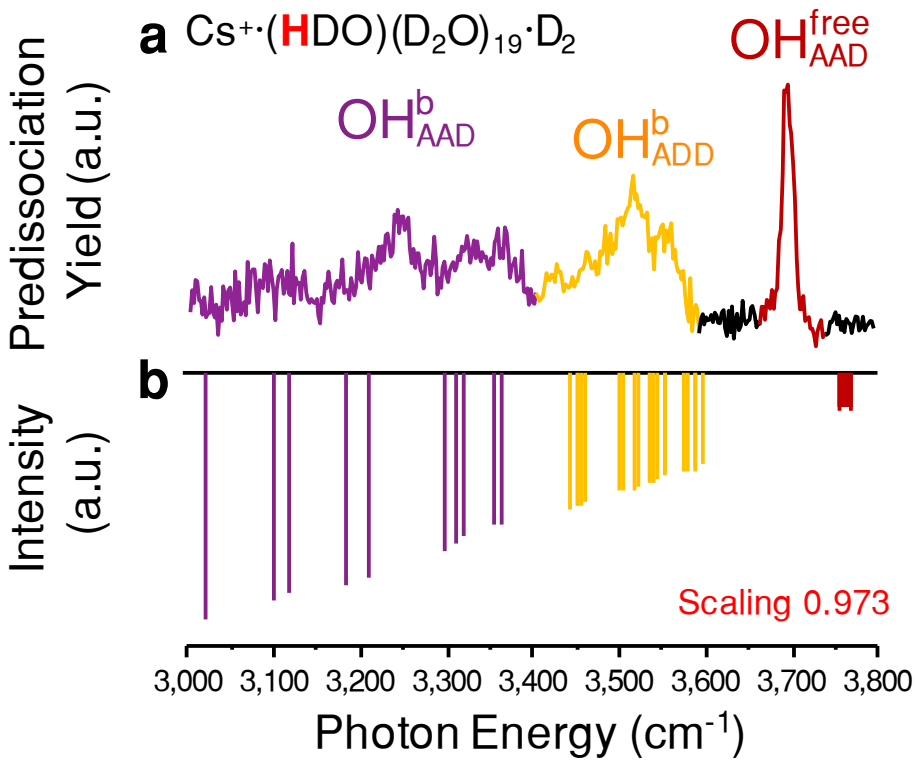

Figure 5.3: (**a**) Predissociation spectra of all isotopomers of $Cs^{+}\cdot(HDO)(D_2O)_{19}\cdot D_2$ in the OH stretching region for the structure **PD$_0$** in Fig. 5.1A. Bands colored red, orange, and purple denote the free OH stretch (OH^{free}_{AAD}), bound OH stretch on an ADD water (OH^{b}_{ADD}), and the bound OH stretch on an AAD water (OH^{b}_{AAD}), respectively. (**b**) Harmonic spectra of all isotopomers of $Cs^{+}\cdot(HDO)(D_2O)_{19}\cdot D_2$ computed at the B3LYP/6-31+G** level of theory and basis with the LANL2DZ pseudopotential for Cs scaled by a 0.973 scaling factor.

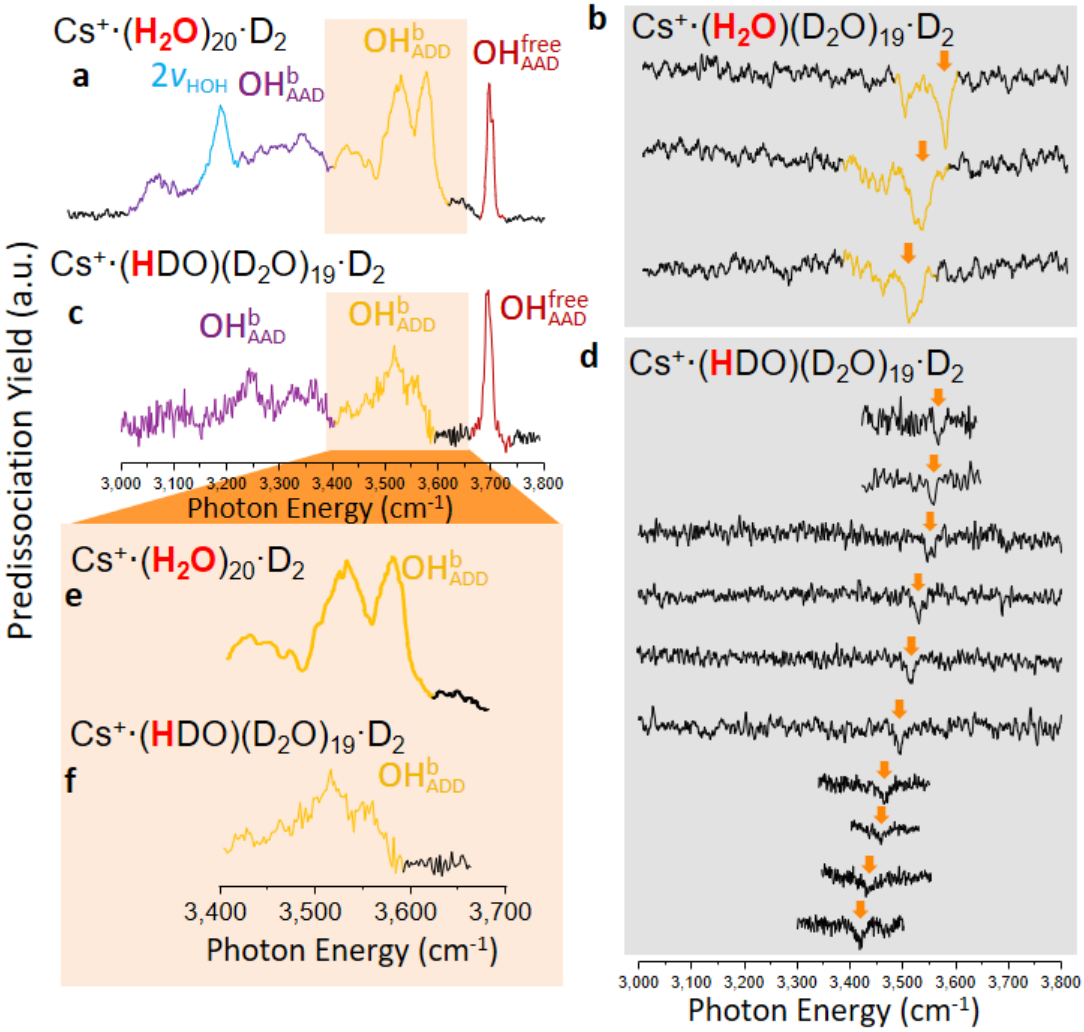

Figure 5.4: Comparison of the vibrational predissociation sepctra of $Cs^+\cdot(H_2O)_{20}\cdot D_2$ (**a**) and $Cs^+\cdot(HDO)(D_2O)_{19}\cdot D_2$ (**c**), with expanded views of the OH features associated with the ADD water molecules in (**e**) and (**f**), respectively. The spectral contribution from each single H_2O molecules can be extracted via with isotopomer selective spectroscopy of the $Cs^+\cdot(H_2O)(D_2O)_{19}\cdot D_2$ isotopologue (**b**), whereas contribution from each single OH oscillator can be extracted from the isotopomer specific spectra of $Cs^+\cdot(HDO)(D_2O)_{19}\cdot D_2$ (**d**) where intramolecular coupling between the two OH groups and the bend overtone is removed.

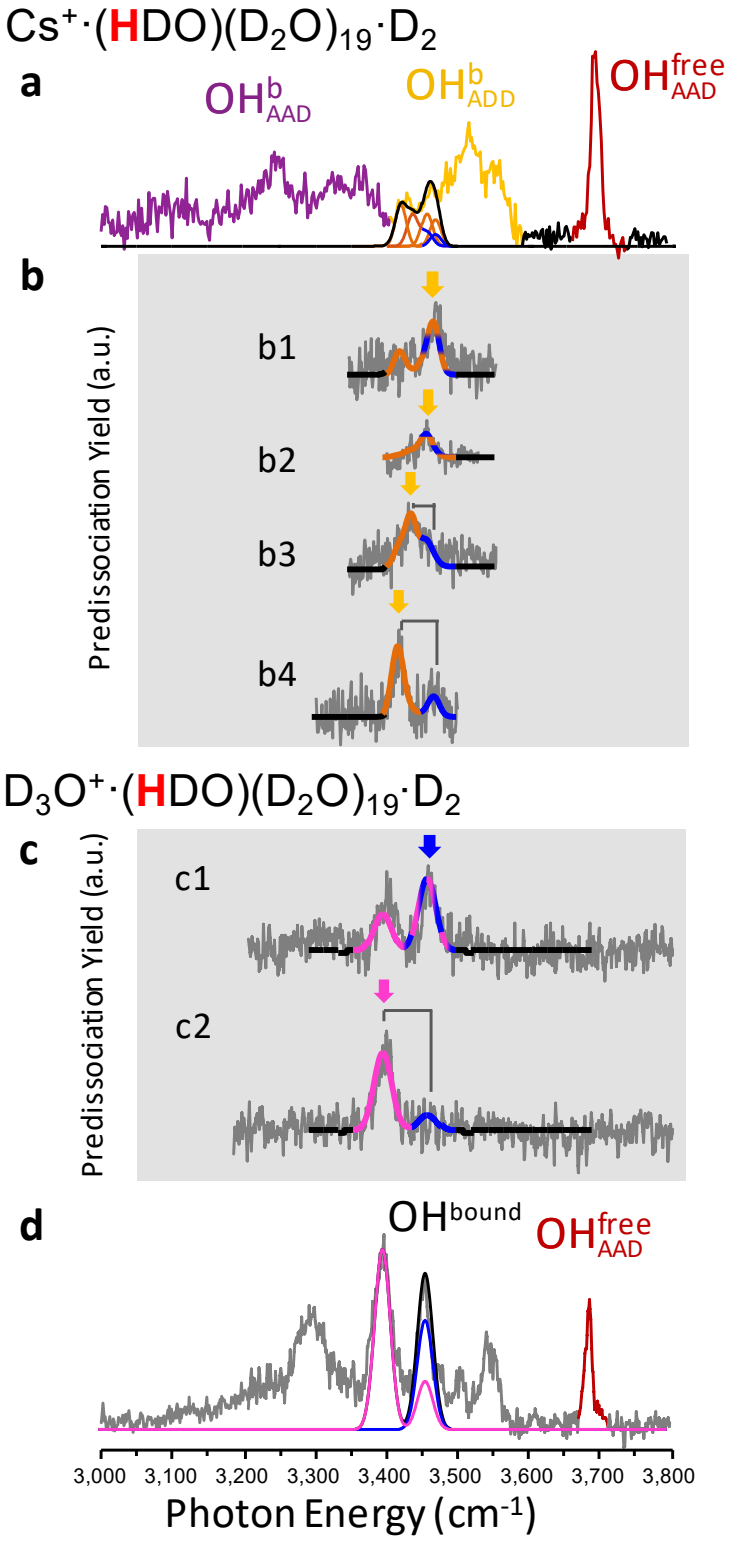
Cs+·(HDO)(D2O)19·D2
a
OHbAAD
OHbADD
OHfreeAAD
b
Predissociation Yield (a.u.)
b1
b2
b3
b4
D3O+·(HDO)(D2O)19·D2
c
Predissociation Yield (a.u.)
c1
c2
d
OHbound
OHfreeAAD
3,000 3,100 3,200 3,300 3,400 3,500 3,600 3,700 3,800
Photon Energy (cm-1)

Figure 5.5: Vibrational predissociation spectrum of $Cs^+ \cdot (HDO)(D_2O)_{19} \cdot D_2$ (**a**) and $D_3O^+ \cdot (HDO)(D_2O)_{19} \cdot D_2$ (**d**) as well as isotopomer selective spectra of them (**b, c**) respectively. Some of the lower energy OH stretches (orange feature in **b3**, **b4** and pink feature in **c2**) have combination bands built on top of them (small feature on the higher energy side indicated with the brackets). The higher energy OH stretch (blue/orange and blue/pink features on the high energy side in **b1**, **b2** and **c1**) are accidentally degenerate with the combination bands. The contribution to the predissociation spectra from the lower energy OHs and their combination bands as well as the higher energy OH stretches are depicted with smooth solid lines in (**a, d**), with the sum of the two isotopomers colored black. The higher energy features have contribution from multiple isotopomers. As a result, when the probe laser is fixed on the higher energy peaks, features from both isotopomers are detected, hence displaying a distorted intensity profile (**b1**, **b2** and **c1**). Conversely, when the probe laser is fixed on the lowest energy peak (orange arrow in **b4** and pink arrow in **c2**), only one isotopomer is detected and the intensity profile displays the typical fundamental and combination band pattern.

shifted features around 3500 cm^{-1} (yellow in Fig. 5.2b and Fig. 5.3). Note that the prominent feature (turquoise in Fig. 5.2a) at 3200 cm^{-1} in the $Cs^+ \cdot (H_2O)_{20}$ spectrum is missing in that of $Cs^+ \cdot (HDO)(D_2O)_{19}$, confirming its assignment to a Fermi resonance-activated HOH bend overtone. The suppression of this feature occurs because the bend overtone of HOD occurs at ~2800 cm^{-1}, well below the range of the OH stretching manifold. A detailed comparison of the shapes is presented in Fig. 5.4.

The key to this study is that, when the clusters are sufficiently cold to suppress migration of the isotopic label among the available sites, the ensemble of clusters is heterogeneous such that the spectral signatures arising from OH occupation in each site can be isolated. This is accomplished by carrying out two-color, IR-IR photobleaching measurements on the $Cs^+ \cdot (HDO)(D_2O)_{19}$ and $D_3O^+ \cdot (HDO)(D_2O)_{19}$ isotopologues. In that approach, a probe laser is tuned to a particular transition in the spectrum, and the population of ions responsible for that feature is monitored continuously while another, powerful pump laser is scanned through the entire spectrum upstream from the interaction with the probe laser. When the pump laser excites any transition shared by the species which is monitored by the probe frequency, the reduction in ion population yields a series of dips in the probe signal, thus revealing all the transitions and line broadening (beyond the ~5 cm^{-1} bandwidth of the IR lasers) associated with OH occupation in a particular site.[38-39]

The traces in Fig. 5.2c (gray box) present the isotopomer-selective dip spectra obtained by fixing the probe laser at the 16 different energies indicated by the arrows above the dip features in each trace. We emphasize that this behavior does not likely reflect that of a single structure, but rather of an ensemble consisting of many **PD** isomers

that are structurally similar and close in energy.[30] Note that most of the dips appear as single features centered about the probe laser energy, thus establishing that the spectrum of the $Cs^+ \cdot (HDO)(D_2O)_{19}$ isotopologue (Fig. 5.2b) is indeed heterogeneous at 20 K. It is significant, however, that the transition probed at 3415 cm^{-1} (Fig. 5.2 (trace c12) and Fig. 5.5) yields a pronounced second feature (indicated by a bracket), displaced from the fundamental by 51 cm^{-1}.

To gauge whether the doublet structure in the spectrum of the $Cs^+ \cdot (HDO)(D_2O)_{19}$ isotopomer with an OH fundamental at 3415 cm^{-1} is representative of more general behavior, we extended the study to include several photobleaching measurements on the $D_3O^+ \cdot (HDO)(D_2O)_{19}$ cluster. That system was chosen because it introduces additional variation in the topology of the **PD** network sites, including four-coordinated AADD molecules that are calculated to yield the largest red shifts.[40] Whereas the bands at the extremes of the OH stretching manifold in the $D_3O^+ \cdot (HDO)(D_2O)_{19}$ spectrum (Fig. 5.6 trace b1 and b4) yield single OH stretching features in the photobleaching scans, probing the peak near the center of the envelope at ~3400 cm^{-1} generates two very well defined peaks with a separation (60 cm^{-1}). Note that this value is very close to that (51 cm^{-1}) observed in the $Cs^+ \cdot (HDO)(D_2O)_{19}$ case, as illustrated by the comparison displayed in Fig. 5.6c (trace b2). The appearance of multiple bands in photobleaching spectra can signal interconversion between isotopomers (i.e., spontaneous migration of the OH group between sites, discussed in detail in Chapter 8 and 9).[38] In the present case, however, the fact that the two strong dips only appear when probing the higher energy feature (traces b2 and b3 in Fig. 5.6) indicates that the upper band is due to excitation of a second transition arising from the same ground state responsible for the OH stretching

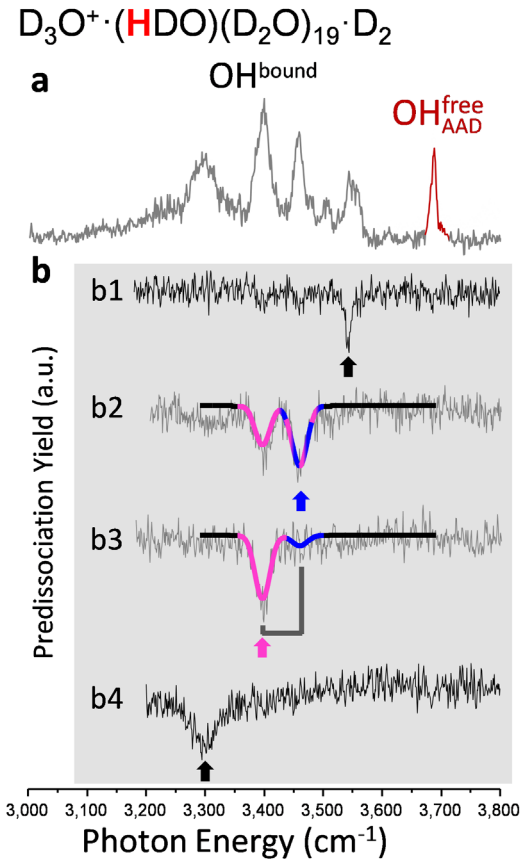

Figure 5.6: Expanded display highlighting the appearance of a second feature in the isotopomer-specific spectra of $D_3O^+\cdot(HDO)(D_2O)_{19}\cdot D_2$ with OH oscillators near 3400 cm^{-1}. Non-selective spectra are displayed in (a), while (b1-b4) are the isotopomer-selective photobleach scans obtained with the probe laser positions labeled by the arrows. The combination bands are labeled by brackets displaced from the OH stretching fundamentals on the lower energy side (b3). The simulated traces (colored in b2, b3) are overlaid on top of experimental data (gray traces), with a detailed explanation of the photoexcitation scheme included in Figure 5.5. Details about the simulation are included in the Chapter 5.4. Probe positions and widths are reported in Table 5.3.

fundamental, but displaced by 60 cm^{-1} above it. The relative intensities of the two features can be recovered in a simple model that includes the relative cross sections of the fundamental and a second, weaker band in the limit of partial optical saturation, as discussed in detail in Chapter 5.4. This is characteristic behavior for OH groups that are anharmonically coupled to soft skeletal modes of the surrounding medium (discussed in Chapter 4 where combination bands were found above the IHB OH features). [41] In that case, the second feature is due to an IR active combination band involving excitation of a soft (~60 cm^{-1}) mode along with the v=1 level of the OH stretch. It is interesting that in the case of the water cages, this soft mode activity occurs for oscillators near 3400 cm^{-1}, the spectral region that has been recently revealed (in the Cs^+ cage) to be the cross-over point for H_2O molecules residing in the AAD and ADD binding motifs (ADD above ~3400 cm^{-1} and AAD below).[34] It therefore appears that OH oscillators close to this boundary are particularly strongly coupled to soft modes of the cages in both H_3O^+ and Cs^+ systems. The appearance of such anharmonic features upon excitation of OH groups having frequencies near the center of the diffuse OH stretching band is significant because this additional complexity has not been anticipated in spectral simulations in either the cluster systems or of interfacial water.[19]

Upon closer inspection of the dip patterns in Figs. 5.2 and 5.6, it is evident that there is a systematic increase in the widths of the dips as the probe laser is tuned to increasingly red-shifted transitions in both systems. These band profiles were fit to Gaussian lineshapes (see Fig. 5.7, 5.8), with the dependence of the full widths at half maximum (FWHM) on the red shift ($\Delta\nu_{red}$, relative to the gas phase free OH fundamental at 3706 cm^{-1}) presented in Fig. 5.9 for $Cs^+ \cdot (HDO)(D_2O)_{19}$ (labeled by □)

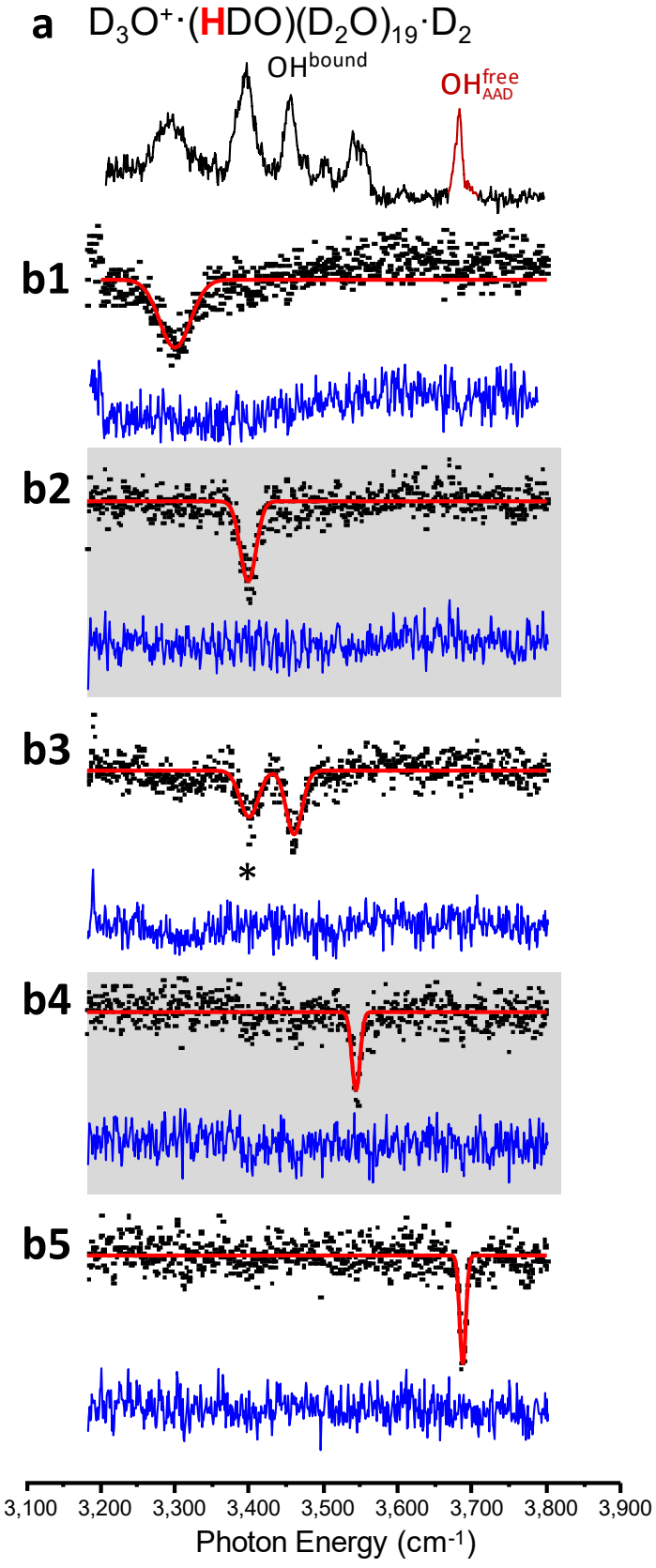
a
$D_3O^+ \cdot (HDO)(D_2O)_{19} \cdot D_2$
OH^{bound}
OH^{free}_{AAD}
b1
b2
b3
*
b4
b5
3,100
3,200
3,300
3,400
3,500
3,600
3,700
3,800
3,900
Photon Energy (cm^{-1})

Figure 5.7: Predissociation spectra (**a**) and isotopomer selective spectra (**b**) of all isotopomers of $D_3O^+ \cdot (HDO)(D_2O)_{19} \cdot D_2$ in the OH stretching region. The contribution from each OH group is isolated with isotopomer selective spectroscopy and the results are fitted with a Gaussian profile to obtain the peak position and FWHM. The residues for each fit are plotted below each trace in blue. The mean, FWHM, and error of the Gaussian fits are collected in Table 5.3. For trace **b3**, the * band is a result of the OH stretch feature in **b2** having a combination band that has the same frequency as the main feature in **b3**. Detailed analysis on the extra band in **b3** is included in figure 5.5.

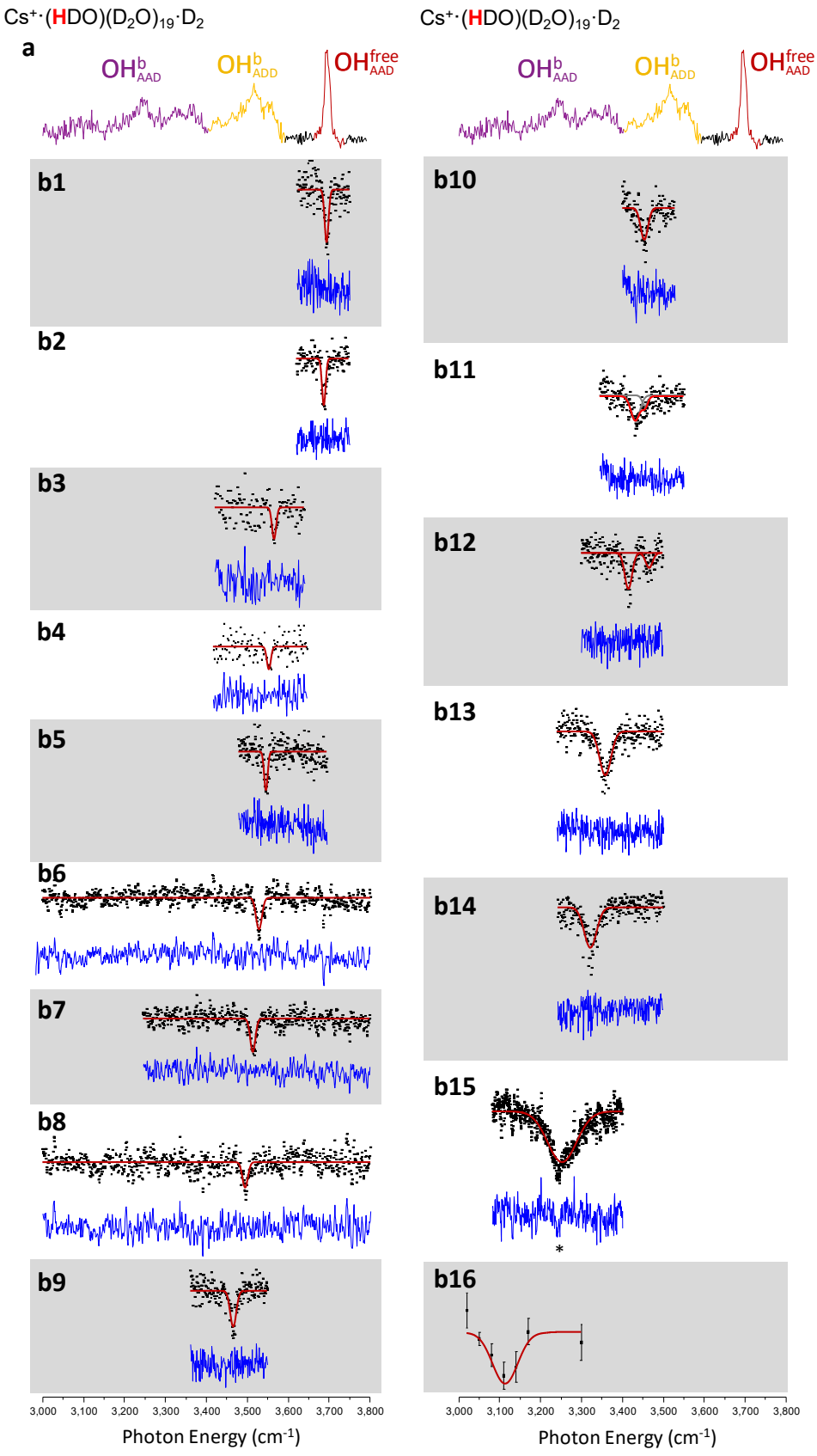
Cs⁺·(HDO)(D2O)19·D2
a
OHbAAD
OHbADD
OHfreeAAD
b1
b2
b3
b4
b5
b6
b7
b8
b9
b10
b11
b12
b13
b14
b15
b16
*
3,000 3,100 3,200 3,300 3,400 3,500 3,600 3,700 3,800
Photon Energy (cm-1)

Figure. 5.8: Predissociation spectra (**a**) and isotopomer selective spectra (**b**) of all isotopomers of $Cs^+ \cdot (HDO)(D_2O)_{19} \cdot D_2$ in the OH stretching region. The contribution from each OH group is isolated with isotopomer selective spectroscopy and the results are fitted with a Gaussian profile to obtain the peak position and FWHM. The residues for each fit are plotted below in blue. The mean, FWHM and error of the Gaussian fits are collected in Table 5.1. The * in trace **b15** (blue) indicates a sharper transition embedded in the broad feature whose assignment is not known. Spectra in **b16** was obtained by extensive averaging at several representative frequencies due to limitation in signal intensity.

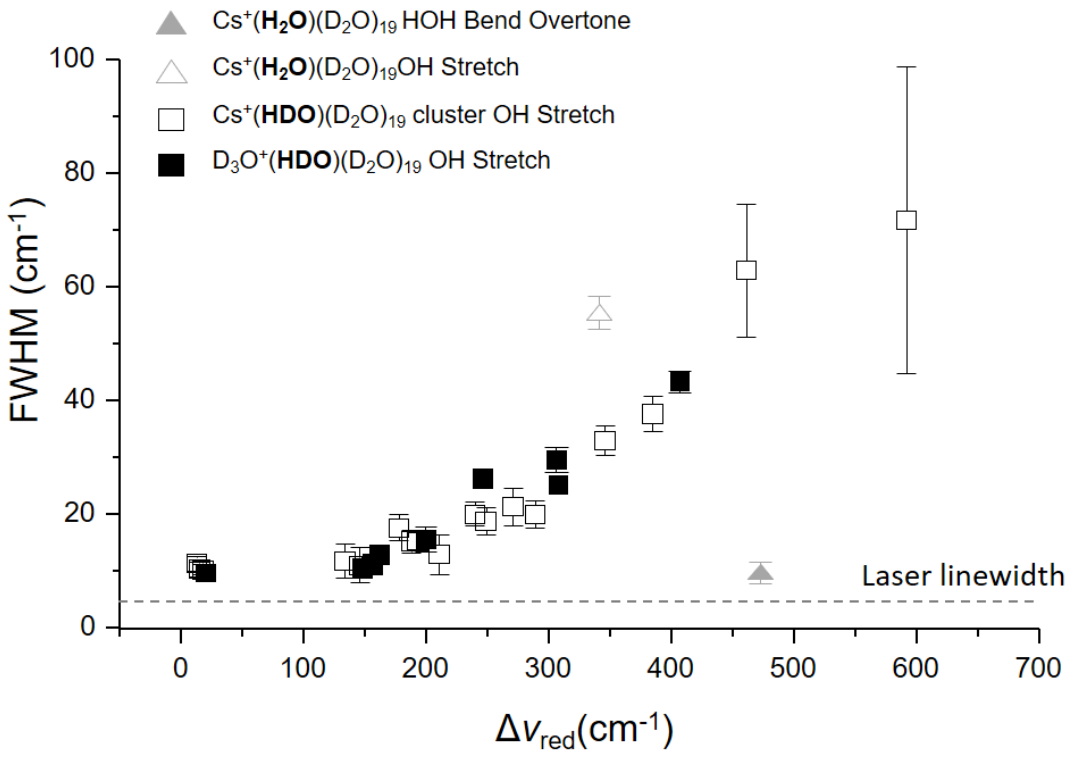

Figure 5.9: Dependence of experimental linewidths of OH stretch features on red shift. The included features can be found in figure 5.2c and figure 5.7 on the red shift of the OH frequency from the gas phase uncoupled free OH stretch value at 3607 cm^{-1}. The error bars correspond to the confidence interval associated with the Gaussian fits used to obtain the spectral width (Fig. 5.7). Triangle symbols refer to the bound OH group (△) and 0→2 overtone of the intramolecular HOH bend (▲) in $Cs^+ \cdot (H_2O)(D_2O)_{19} \cdot D_2$. The error bars are drawn at ± one standard deviation from the data points. All data are collected in Table 5.1 and 5.3.

and $D_3O^+ \cdot (HDO)(D_2O)_{19}$ (labeled by ■). We note that not all of the envelopes are Gaussian, and indeed the dip profile of the 3250 cm^{-1} feature in the $Cs^+ \cdot (HDO)(D_2O)_{19}$ spectrum is asymmetrical, with an embedded sharper feature (* in trace c15). Nonetheless, it is clear that both systems display a very similar, approximately linear systematic increase in the bandwidths for red shifts ($\Delta\nu_{red}$) above ~150 cm^{-1}. The similarity in the behavior of the two cage systems is interesting in light of the fact that the nature of the charge accommodation (surface vs internal) is quite different in each case. Nonetheless, both cages are calculated at the harmonic level to display similar overall spectral profiles, (Fig. 2 in ref. 40) with the water molecules in the cage carrying a very small percentage of the charge (< 0.02 and 0.005 e/water molecule for the H_3O^+ and Cs^+ cages, respectively).[42]

Note that asymptotic behavior at low $\Delta\nu_{red}$ is limited by the bandwidth of the IR laser (FWHM~5 cm^{-1}). The lineshapes in the $D_3O^+ \cdot (HDO)(D_2O)_{19}$ are particularly well defined as highlighted in Fig. 5.7, and are well described with a Gaussian intensity distribution far outside the instrument resolution. Unfortunately, the signal-to-noise does not allow differentiation between Gaussian and Lorentzian lineshapes. It is important to note that at the experimental temperature (20 K) the thermal fluctuation is expected to be strongly suppressed, so that the lineshapes in the cold isotopomers are dominated by the relaxation dynamics at play in the vibrationally excited states. This can be seen in the temperature dependent spectra of $D_3O^+ \cdot (HDO)(D_2O)_{19}$ where the peak widths remain constant below 60 K (Fig. 5.10). As such, this measurement provides the first determination of the intrinsic character of the vibrational excitations with minimal contributions from thermal fluctuations, and therefore sets an upper limit on the

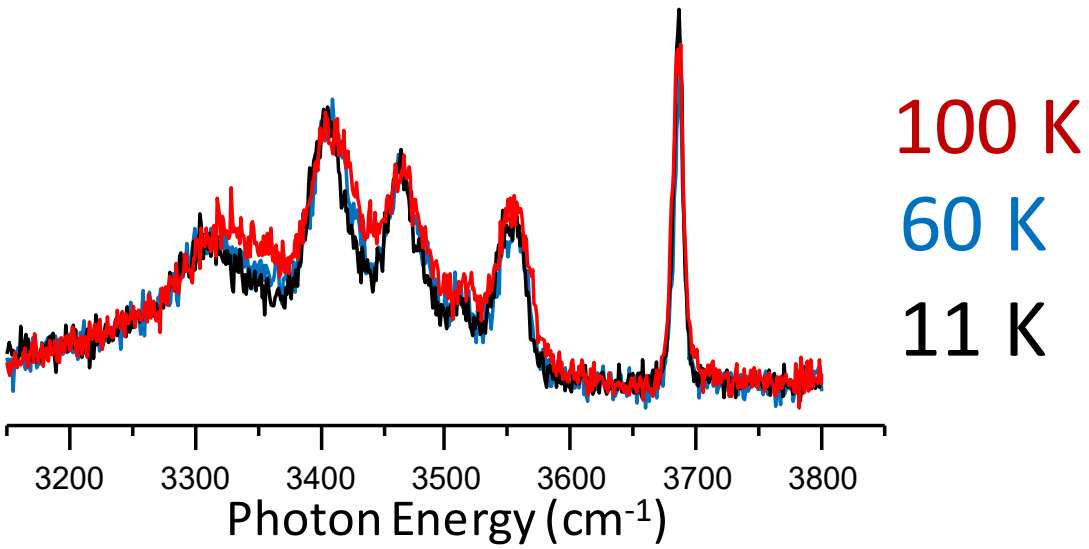

Figure 5.10: Infrared two photon dissociation (IR2PD) spectra of $D_3O^+ \cdot (HDO)(D_2O)_{19}$ at three different temperatures (11, 60 and 100 K). The spectral feature remains unchanged below 60 K. Slight broadening starts to become observable at 100 K suggesting the thermal fluctuation below 60 K is minimal.

coherence lifetimes (τ_v) of the OH stretching excitations at low temperature, as well as the inherent complexities arising from excitation of combination bands. The approximate linear increase in width with red shift indicates that $\tau_v \propto \frac{1}{\Delta\nu_{red}}$, approaching about 75 fs for the lowest frequency bands around 3100 cm^{-1}. This experimental approach cannot, however, establish the relative contributions of population relaxation (T_1) and pure dephasing (T_2) to these lifetimes.

Capturing the spectral behavior of a local OH oscillator in a well-defined network environment has the significant advantage that we can address the detailed mechanics underlying the relaxation dynamics. Moreover, the fact that most of the lineshapes are relatively smooth indicates that the background states contributing to the mixing are sufficiently dense to yield an effective continuum. This, in turn, suggests that the broadening can be addressed within the intramolecular vibrational relaxation mechanism in which the oscillator strength of a "bright" OH stretching fundamental (at zero-order) is diluted into a bath of dark states. Because the bands increasingly broaden toward lower energy, where the density of states is lower, we conclude that the main factor driving the increased widths derives from the matrix elements coupling the OH(v=1) states to the bath. We note that the broadening is indeed a property of the OH stretching degree of freedom, as evidenced by the fact that the linewidth of the HOH bend overtone (FWHM ~10 cm^{-1}, labeled by ▲ in Fig. 5.9) displayed by a single H_2O molecule in one of the $Cs^+ \cdot (H_2O)(D_2O)_{19}$ isotopomers is much narrower than that of its bound OH group (FWHM ~56 cm^{-1}, labeled by △ in Fig. 5.9). Interestingly, the broadening of the bound OH stretch in H_2O falls well *above* the trend line for the isolated OH groups (□ in Fig.

5.9), consistent with the expected acceleration in the relaxation rate due to mixing with the nearby overtone of the bend.[29]

The systematic increase in the intrinsic linewidths with red shift raises the question of whether these processes (shift and broadening) are intimately connected. At an intuitive level, it seems plausible that the more red-shifted OH oscillators are more strongly perturbed by the surrounding medium, and that this stronger coupling somehow leads to shorter lifetimes of the vibrationally excited states. This general theme has been explored earlier by Tainter et al.[19] in the context of the neutral water hexamer. They calculated how the frequencies of OH oscillators in each site are broadened by mechanical deformations in the network that are available to the cage isomer at low temperature (40 K). As such, we conclude the shifts largely reflect the local electric field along its OH bond axis, it was determined that these structural displacements yield much larger fluctuations in the local electric fields when the net field is large. This leads to a situation in which the linewidths indeed increase monotonically with red shift. That model predicts a non-linear dependence on red shift, however, with an initial rate that is substantially larger than observed here for the larger water cages, as illustrated by the comparison in Fig. 5.11. Interestingly, the values for the neutral hexamer are closest to those found in the **PD** cages for the lowest frequency oscillators. Although it is beyond the scope of this experimental report to attempt a similar theoretical simulation of the anharmonic coupling, we note that the mechanical displacements of the 20 K water cages that give rise to such fluctuations in the electric fields are likely to involve vibrational zero-point motion. [41, 43] In that case, the broadening is an unavoidable nuclear quantum

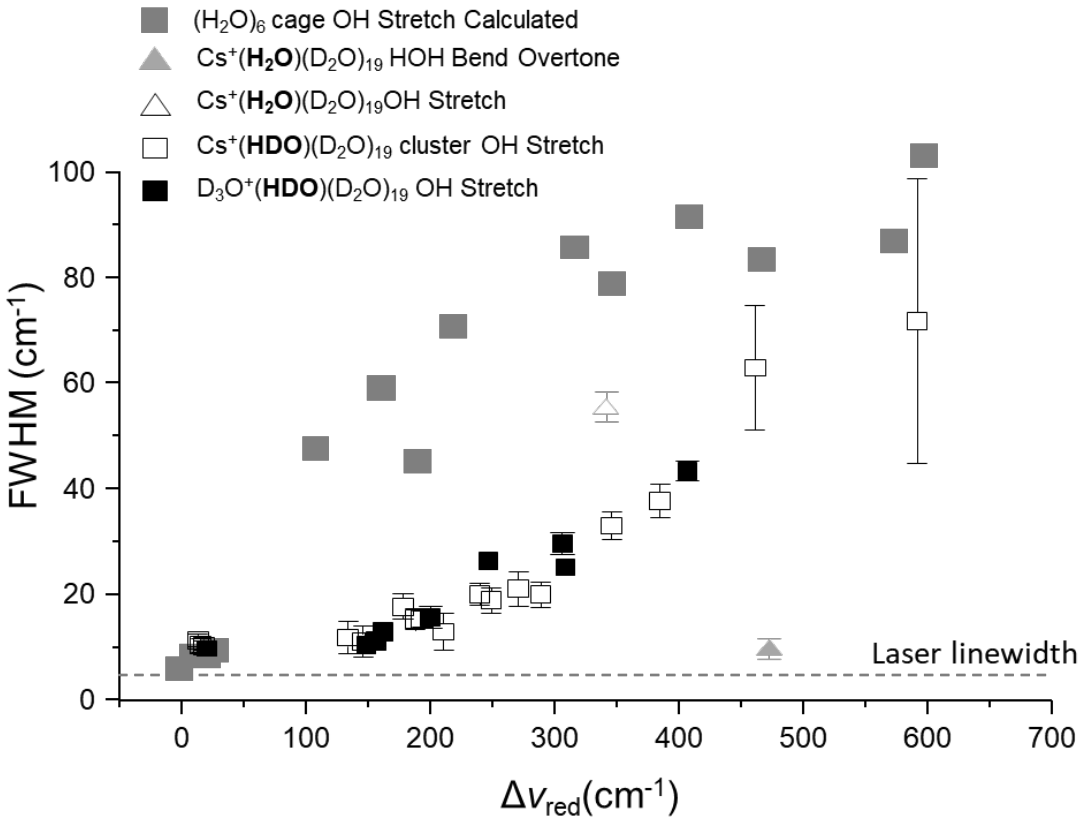

Figure 5.11: Dependence of experimental linewidths of OH stretch features on redshift in figure 5.2c and figure 5.7b, and widths of calculated frequency distributions for neutral $(H_2O)_6$ cage cluster at 40 K (ref. 18), on the red shift of the OH frequency from the gas phase uncoupled free OH stretch value at 3607 cm^{-1}. The error bars correspond to the confidence interval associated with the Gaussian fits used to obtain the spectral width (Fig. 5.7). Triangle symbols refer to the bound OH group (△) and 0→2 overtone of the intramolecular HOH bend (▲) in $Cs^+ \cdot (H_2O)(D_2O)_{19} \cdot D_2$.

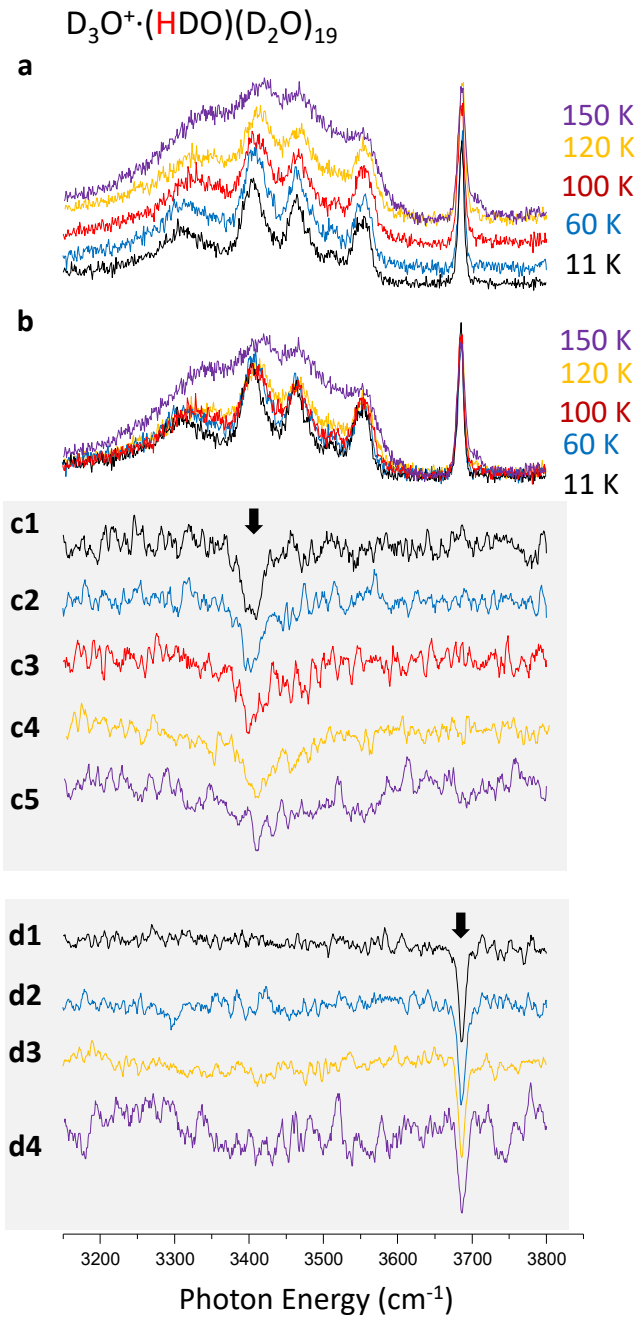

Figure 5.12: Temperature dependent OH spectra of $D_3O^+\cdot(HDO)(D_2O)_{19}$. Temperature dependent vibrational spectra of $D_3O^+\cdot(HDO)(D_2O)_{19}$ with temperature color coded (a,b). Isotopomer selective spectra of $D_3O^+\cdot(HDO)(D_2O)_{19}$ at various temperatures with the same coloring scheme (c.d).

effect that is intrinsic to the system, a phenomenon that has been well documented in a number of H-bonded cluster systems at low temperature. [43-44]

With the low temperature spectral behavior established, the cluster is heated to observe the temperature dependent effect on the OH spectral features. First of all, the overall spectra broadens towards the higher frequency side as temperature increases (Fig.5.12a,b). This is consistent with the gradual weakening of the hydrogen bond upon heating and increase in available large amplitude motions. Below 120 K the OH features are still distinguishable as they broaden, isotopomer specific spectra (Fig.5.12c,d) shows the OH feature remains as one single feature up to 120 K broadening with higher temperature. Signs of spectral diffusion is observed at 150 K and 40 microsecond delay time (discussed in detail in Chapter 9), the short delay time here was picked to minimize effect of slow spectral diffusion (ms time scale) and capture only the OH feature of the isotopomer under investigation. The free OH feature is less influenced by the rise in temperature compared with the bound OH feature that is expected since the bond OH frequency is much more sensitive on the local H-bond environment. In contrast to the gradual change below 120 K, the overall spectra changes dramatically at 150 K where the bound OH features became one broad feature. The $H_3O^+ \cdot (H_2O)_{20}$ cluster is observed to have a turning point on the calorimetry curve at about 135 K where some of the H-bonds break before evaporation can happen at higher temperature (discussed in detail in Chapter 9). Such deformation of the cage structure allows many large amplitude motions and significantly broadens the OH spectra to the point where the bond OH features almost become indistinguishable (150 K spectra in Fig.5.12a). In addition, the shoulder to the right of the free OH feature at 3700 cm^{-1} shows up at 150 K signaling the appearance of

two coordinated acceptor-donor (AD) water molecules which comes from AAD water molecule losing one H-bond as a result of deformation of the cage structure through H-bond breaking.

5.4 Fit and Simulation Methods

All the isotopomer specific dip spectra were fit to Gaussian line shapes and Lorentzian line shapes. The resulting fits have very similar shape, however, and the noise in the data does not allow us to differentiate between them. Only the gaussian line shapes are displayed in figure 5.7 and 5.8.

For the OH oscillators that are accompanied by combination bands (Fig. 5.6 trace b2, b3 and Fig. 5.5 trace b, c), a more sophisticated model that includes the oscillator strengths, oscillator frequencies, and population of the isotopomers was used to fit the data. The model first generates a spectrum (denoted as $S(\nu)_i$) for each isotopomer (denoted as i) with center frequency, peak width, and predissociation yield of both the OH fundamental and possible combination band. For example, the pink trace in Fig. 5.5d was generated with a fundamental OH feature on the lower energy side and a combination band on the higher energy side. Then the contributions from all isotopomers were summed together to yield the total predissociation spectrum (Fig. 5.5 trace a and d):

$$F(\nu)_{total} = \sum_i F(\nu)_i = \sum_i S(\nu)_i \times P_i^0$$

where F_i, S_i and P_i^0 are the fragment yield, absorption spectrum (expressed in percent yield) and population for each isotopomer, respectively, and ν is the frequency. Then the model simulates the probe laser signal:

$$F_{probe} = F(\nu_{probe})_{total} = \sum_i S(\nu_{probe})_i \times P_i^0$$

by summing over contributions from all isotopomers, which are calculated by their population multiplied by the predissociation yield at the probe frequency ν_{probe}. For instance, when the probe laser is fixed on the position indicated by the blue arrow in Fig. 5.5 trace ci, the probe laser detects both the pink and the blue isotopomers since they both have absorption at the probe frequency. The blue band contributes more to the probe signal because its oscillator strength, $S(\nu_{probe})_{blue}$, is larger and the populations of both isotopomers are similar. Then the model generates the hole-burning spectra (Fig. 5.5 colored trace ci) by adding the population weighted depletion spectra together. The hole-burning spectra can be expressed as:

$$F_{probe}(\nu_{pump}) = \sum_i S(\nu_{probe})_i \times P_i(\nu_{pump})$$

where ν_{pump} is the pump laser frequency which is being scanned and $P_i(\nu_{pump})$ is the remaining population of isomer *i* after the pump laser interaction. In this case the pump laser creates a population depletion in each isotopomer and the leftover population can be expressed as:

$$P_i(\nu_{pump}) = P_i^0 \times [1 - S(\nu_{pump})_i]$$

Then the shapes of the $F_{probe}(\nu_{pump})$ spectra were fit to the data to obtain the peak positions, relative intensities and peak widths for both the OH fundamentals and combination bands. The fit parameters were constrained since the isotopomers that have OH stretch fundamental from 3400 to 3600 cm^{-1} have similar oscillator strengths (within 20% of each other) and because the vibrational zero-point energies are similar (within 10

cm^{-1}), the populations of the isotopomers are similar. The simulated curves are displayed in Fig. 5.5.

5.5 Summary

Summarizing, we have experimentally determined the spectral signatures of isolated OH groups embedded in an extended water network at low and higher temperature. These transitions explore the full frequency range displayed by condensed phase and interfacial water. Double resonance methods reveal the intrinsic lineshapes associated with each site, which appear as single features at the extremes of the diffuse OH envelope, but display doublet structure near the center of it, which are assigned to combination bands derived from excitation of soft modes of the cage. The fundamentals generally appear as bell shaped distributions with widths that monotonically increase with the red shift in the centroid of the peak. These results establish upper bounds on the lifetimes of the OH(v=1) states prepared by impulsive (coherent) excitation, which are on the order of 75 fs for the most red-shifted bands around (3100 cm^{-1}). This general trend can be rationalized by considering the strength of the local electric field at each site and the variation in this field caused by distortions of the cage, pointing the way for more advanced theoretical treatments of these processes. In addition, all the peaks broadens and blue shifts at higher temperature which is consistent with the weakening hydrogen bond and increasing large amplitude motion in the warmer cluster.

5.6 References

1. Paesani, F.; Xantheas, S. S.; Voth, G. A. Infrared Spectroscopy and Hydrogen-Bond Dynamics of Liquid Water from Centroid Molecular Dynamics with an Ab Initio-Based Force Field. *J. Phys. Chem. B* **2009,** *113* (39), 13118-13130.

2. Reddy, S. K.; Moberg, D. R.; Straight, S. C.; Paesani, F. Temperature-dependent vibrational spectra and structure of liquid water from classical and quantum simulations with the MB-pol potential energy function. *Journal of Chemical Physics* **2017,** *147* (24).

3. Auer, B. M.; Skinner, J. L. IR and Raman Spectra of Liquid Water: Theory and Interpretation. *Journal of Chemical Physics* **2008,** *128* (22), 224511.

4. Skinner, J. L.; Pieniazek, P. A.; Gruenbaum, S. M. Vibrational Spectroscopy of Water at Interfaces. *Accounts Chem Res* **2012,** *45* (1), 93-100.

5. Ni, Y. C.; Gruenbaum, S. M.; Skinner, J. L. Slow hydrogen-bond switching dynamics at the water surface revealed by theoretical two-dimensional sum-frequency spectroscopy. *Proc. Natl. Acad. Sci. USA* **2013,** *110* (6), 1992-1998.

6. Nicodemus, R. A.; Corcelli, S. A.; Skinner, J. L.; Tokmakoff, A. Collective Hydrogen Bond Reorganization in Water Studied with Temperature-Dependent Ultrafast Infrared Spectroscopy. *J. Phys. Chem. B* **2011,** *115* (18), 5604-5616.

7. Laage, D.; Stirnemann, G.; Sterpone, F.; Hynes, J. T. Water Jump Reorientation: From Theoretical Prediction to Experimental Observation. *Accounts Chem Res* **2012,** *45* (1), 53-62.

8. Ashihara, S.; Huse, N.; Espagne, A.; Nibbering, E. T. J.; Elsaesser, T. Ultrafast Structural Dynamics of Water Induced by Dissipation of Vibrational Energy. *J. Phys. Chem. A* **2007,** *111* (5), 743-746.

9. Steinel, T.; Asbury, J. B.; Corcelli, S. A.; Lawrence, C. P.; Skinner, J. L.; Fayer, M. D. Water Dynamics: Dependence on Local Structure Probed with Vibrational Echo Correlation Spectroscopy. *Chem. Phys. Lett.* **2004,** *386* (4-6), 295-300.

10. De Marco, L.; Fournier, J. A.; Thamer, M.; Carpenter, W.; Tokmakoff, A. Anharmonic exciton dynamics and energy dissipation in liquid water from two-dimensional infrared spectroscopy. *Journal of Chemical Physics* **2016,** *145* (9), 094501.

11. De Marco, L.; Ramasesha, K.; Tokmakoff, A. Experimental Evidence of Fermi Resonances in Isotopically Dilute Water from Ultrafast Broadband IR Spectroscopy. *J. Phys. Chem. B* **2013,** *117* (49), 15319-15327.

12. Asbury, J. B.; Steinel, T.; Kwak, K.; Corcelli, S. A.; Lawrence, C. P.; Skinner, J. L.; Fayer, M. D. Dynamics of water probed with vibrational echo correlation spectroscopy. *J. Chem. Phys.* **2004,** *121* (24), 12431-12446.

13. Stiopkin, I. V.; Weeraman, C.; Pieniazek, P. A.; Shalhout, F. Y.; Skinner, J. L.; Benderskii, A. V. Hydrogen Bonding at the Water Surface Revealed by Isotopic Dilution Spectroscopy. *Nature* **2011,** *474* (7350), 192-195.

14. Schaefer, J.; Backus, E. H. G.; Nagata, Y.; Bonn, M. Both Inter- and Intramolecular Coupling of O-H Groups Determine the Vibrational Response of the Water/Air Interface. *J Phys Chem Lett* **2016,** *7* (22), 4591-4595.

15. van der Post, S. T.; Hsieh, C. S.; Okuno, M.; Nagata, Y.; Bakker, H. J.; Bonn, M.; Hunger, J. Strong frequency dependence of vibrational relaxation in bulk and surface water reveals sub-picosecond structural heterogeneity. *Nat Commun* **2015,** *6*.

16. van der Post, S. T.; Bakker, H. J. Femtosecond Mid-Infrared Study of the Reorientation of Weakly Hydrogen-Bonded Water Molecules. *J. Phys. Chem. B* **2014,** *118* (28), 8179-8189.

17. Bakker, H. J.; Skinner, J. L. Vibrational spectroscopy as a probe of structure and dynamics in liquid water. *Chem. Rev.* **2010,** *110* (3), 1498-1517.

18. Skinner, J. L.; Auer, B. M.; Lin, Y. S. Vibrational Line Shapes, Spectral Diffusion, and Hydrogen Bonding in Liquid Water. *Adv Chem Phys* **2009,** *142*, 59-103.

19. Tainter, C. J.; Ni, Y.; Shi, L.; Skinner, J. L. Hydrogen Bonding and OH-Stretch Spectroscopy in Water: Hexamer (Cage), Liquid Surface, Liquid, and Ice. *Journal of Physical Chemistry Letters* **2013,** *4* (1), 12-17.

20. Mallik, B. S.; Semparithi, A.; Chandra, A. Vibrational spectral diffusion and hydrogen bond dynamics in heavy water from first principles. *J. Phys. Chem. A* **2008,** *112* (23), 5104-5112.

21. Stenger, J.; Madsen, D.; Hamm, P.; Nibbering, E. T. J.; Elsaesser, T. Ultrafast vibrational dephasing of liquid water. *Phys Rev Lett* **2001,** *87* (2).

22. Asbury, J. B.; Steinel, T.; Stromberg, C.; Gaffney, K. J.; Piletic, I. R.; Goun, A.; Fayer, M. D. Ultrafast heterodyne detected infrared multidimensional vibrational stimulated echo studies of hydrogen bond dynamics. *Chemical Physics Letters* **2003,** *374* (3-4), 362-371.

23. Yang, N.; Duong, C. H.; Kelleher, P. J.; Johnson, M. A.; McCoy, A. B. Isolation of Site-Specific Anharmonicities of Individual Water Molecules in the $I^-\cdot(H_2O)_2$ Complex Using Tag-Free, Isotopomer Selective IR-IR Double Resonance. *Chem. Phys. Lett.* **2017,** *690*, 159-171.

24. Horvath, S.; Mccoy, A. B.; Elliott, B. M.; Weddle, G. H.; Roscioli, J. R.; Johnson, M. A. Anharmonicities and Isotopic Effects in the Vibrational Spectra of X^-H_2O, ·HDO, and $\cdot D_2O$ [X = Cl, Br, and I] Binary Complexes. *Journal of Physical Chemistry A* **2010,** *114* (3), 1556-1568.

25. Duong, C. H.; Gorlova, O.; Yang, N.; Kelleher, P. J.; Johnson, M. A.; McCoy, A. B.; Yu, Q.; Bowman, J. M. Disentangling the Complex Vibrational Spectrum of the Protonated Water Trimer, $H^+(H_2O)_3$, with Two-Color IR-IR Photodissociation of the Bare Ion and Anharmonic VSCF/VCI Theory. *J Phys Chem Lett* **2017,** *8* (16), 3782-3789.

26. Lawrence, C. P.; Skinner, J. L. Vibrational spectroscopy of HOD in liquid D2O. VII. Temperature and frequency dependence of the OH stretch lifetime. *Journal of Chemical Physics* **2003,** *119* (7), 3840-3848.

27. Gale, G. M.; Gallot, G.; Lascoux, N. Frequency-dependent vibrational population relaxation time of the OH stretching mode in liquid water. *Chemical Physics Letters* **1999,** *311* (3-4), 123-125.

28. Moilanen, D. E.; Fenn, E. E.; Lin, Y. S.; Skinner, J. L.; Bagchi, B.; Fayer, M. D. Water inertial reorientation: Hydrogen bond strength and the angular potential. *Proc. Natl. Acad. Sci. USA* **2008,** *105* (14), 5295-5300.

29. Imoto, S.; Xantheas, S. S.; Saito, S. Ultrafast Dynamics of Liquid Water: Energy Relaxation and Transfer Processes of the OH Stretch and the HOH Bend. *Journal of Physical Chemistry B* **2015,** *119* (34), 11068-11078.

30. Schulz, F.; Hartke, B. Dodecahedral Clathrate Structures and Magic Numbers in Alkali Cation Microhydration Clusters. *Chemphyschem* **2002,** *3* (1), 98-106.

31. Xantheas, S. S. Low-lying energy isomers and global minima of aqueous nanoclusters: Structures and spectroscopic features of the pentagonal dodecahedron (H2O)(20) and (H3O)+(H2O)(20). *Can J Chem Eng* **2012,** *90* (4), 843-851.

32. Buch, V.; Tarbuck, T.; Richmond, G. L.; Groenzin, H.; Li, H.; Shultz, M. J. The single-crystal, basal face of ice I-h investigated with sum frequency generation. *J. Chem. Phys* **2007,** *127* (21).

33. Smit, W. J.; Tang, F. J.; Sanchez, M. A.; Backus, E. H. G.; Xu, L. M.; Hasegawa, T.; Bonn, M.; Bakker, H. J.; Nagata, Y. Excess Hydrogen Bond at the Ice-Vapor Interface around 200 K. *Phys Rev Lett* **2017,** *119* (13), 133003.

34. Yang, N.; Duong, C. H.; Kelleher, P. J.; McCoy, A. B.; Johnson, M. A. Deconstructing Water's Diffuse OH Stretching Vibrational Spectrum With Cold Clusters. *Science* **2019,** *364* (6437), 275-278.

35. Bailey, C. G.; Kim, J.; Dessent, C. E. H.; Johnson, M. A. Vibrational Predissociation Spectra of $I^-\cdot(H_2O)$: Isotopic Labels and Weakly Bound Complexes with Ar and N_2. *Chem. Phys. Lett.* **1997,** *269*, 122-127.

36. Leavitt, C. M.; Wolk, A. B.; Kamrath, M. Z.; Garand, E.; Van Stipdonk, M. J.; Johnson, M. A. Characterizing the Intramolecular H-bond and Secondary Structure in Methylated $GlyGlyH^+$ with H_2 Predissociation Spectroscopy. *J. Am. Soc. Mass Spectr.* **2011,** *22* (11), 1941-1952.

37. Okumura, M.; Yeh, L. I.; Myers, J. D.; Lee, Y. T. Infrared-Spectra of the Solvated Hydronium Ion: Vibrational Predissociation Spectroscopy of Mass-Selected $H_3O^+\cdot(H_2O)_n\cdot(H_2)_m$. *J. Phys. Chem.* **1990,** *94*, 3416-3427.

38. Yang, N.; Duong, C. H.; Kelleher, P. J.; Johnson, M. A. Unmasking Rare, Large-Amplitude Motions in D_2-Tagged $I^-\cdot(H_2O)_2$ Isotopomers with Two-Color, Infrared–Infrared Vibrational Predissociation Spectroscopy. *J Phys Chem Lett* **2018,** *9* (13), 3744-3750.

39. Wolke, C. T.; Fournier, J. A.; Miliordos, E.; Kathmann, S. M.; Xantheas, S. S.; Johnson, M. A. Isotopomer-Selective Spectra of a Single Intact H_2O Molecule in the $Cs^+(D_2O)_5H_2O$ Isotopologue: Going Beyond Pattern Recognition to Harvest the Structural Information Encoded in Vibrational Spectra. *J. Chem. Phys.* **2016,** *144* (7), 074305.

40. Fournier, J. A.; Wolke, C. T.; Johnson, C. J.; Johnson, M. A.; Heine, N.; Gewinner, S.; Schollkopf, W.; Esser, T. K.; Fagiani, M. R.; Knorke, H.; Asmis, K. R. Site-Specific Vibrational Spectral Signatures of Water Molecules in the Magic $H_3O^+(H_2O)_{20}$ and $Cs^+(H_2O)_{20}$ Clusters. *Proc. Natl. Acad. Sci. U. S. A.* **2014,** *111* (51), 18132-18137.

41. Fournier, J. A.; Johnson, C. J.; Wolke, C. T.; Weddle, G. H.; Wolk, A. B.; Johnson, M. A. Vibrational Spectral Signature of the Proton Defect in the Three-Dimensional $H^+(H_2O)_{21}$ Cluster. *Science* **2014,** *344* (6187), 1009-1012.

42. Fournier, J. A.; Wolke, C. T.; Johnson, M. A.; Odbadrakh, T. T.; Jordan, K. D.; Kathmann, S. M.; Xantheas, S. S. Snapshots of Proton Accommodation at a Microscopic Water Surface: Understanding the Vibrational Spectral Signatures of the Charge Defect in Cryogenically Cooled H+(H2O)(n=2-28) Clusters. *J Phys Chem A* **2015,** *119* (36), 9425-9440.

43. Johnson, C. J.; Dzugan, L. C.; Wolk, A. B.; Leavitt, C. M.; Fournier, J. A.; McCoy, A. B.; Johnson, M. A. Microhydration of Contact Ion Pairs in $M^{2+}OH^-(H_2O)_{n=1-5}$ (M = Mg,

Ca) Clusters: Spectral Manifestations of a Mobile Proton Defect in the First Hydration Shell. *J. Phys. Chem. A* **2014,** *118* (35), 7590-7.

44. Hamm, P.; Stock, G. Nonadiabatic vibrational dynamics in the $HCO_2^{-}\cdot H_2O$ complex. *Journal of Chemical Physics* **2015,** *143* (13).

CHAPTER 6

Deconstructing Water's Diffuse OH Stretching Vibrational Spectrum with Cold Clusters: Unmasking the Factors Controlling the Anharmonic Spectral Response of a Single Water Molecule Embedded in a Two-dimensional Cage

The material in this chapter is adapted with permission from Yang, Nan, Chinh H. Duong, Patrick J. Kelleher, Anne B. McCoy, and Mark A. Johnson. "Deconstructing water's diffuse OH stretching vibrational spectrum with cold clusters." Science 364, no. 6437 (2019): 275-278.

6.1 Introduction

Building on the understanding of the behavior of isolated OH oscillator in an extended hydrogen bond network established in Chapter 5 and knowledge about isolated H_2O molecule in smaller clusters discussed in Chapter 4, we discuss the spectral signatures of intact H_2O molecules embedded in an H-bond network. Similar to the smaller cluster, Fermi resonance is observed for the OH oscillators that is close in frequency to that of the bend overtone transition. In addition, the linewidth and combination band behavior resemble that observed in HDO molecules in Chapter 5 which provides a good zeroth order basis for adding in additional interactions such as intramolecular couplings and Fermi resonances.

Relating to topics outside this thesis, understanding the transient local structures and ultrafast dynamics that account for the broad vibrational envelope displayed by water in the OH stretching region is a challenge for contemporary physical chemistry [1-3]. A common ansatz, for example, posits that, if the local network surrounding a single OH group could be frozen in place, that oscillator would yield a single absorption feature at a frequency determined by the H-bonding configurations of the neighboring water molecules [4-5]. The envelope of the observed spectrum can then be recovered by invoking rapid "spectral diffusion" arising from the thermal fluctuations in the network structure that rapidly move this transition across the spectrum [6-7]. In isotopically homogeneous water, this process is masked by the delocalized nature of the vibrational excitation among nearby, nominally equivalent OH groups (i.e. vibrational excitons). [8-9]. Although this complication can be overcome by diluting H_2O in excess D_2O, which yields a sample where the OH groups are dominated by HDO and are thus decoupled from the

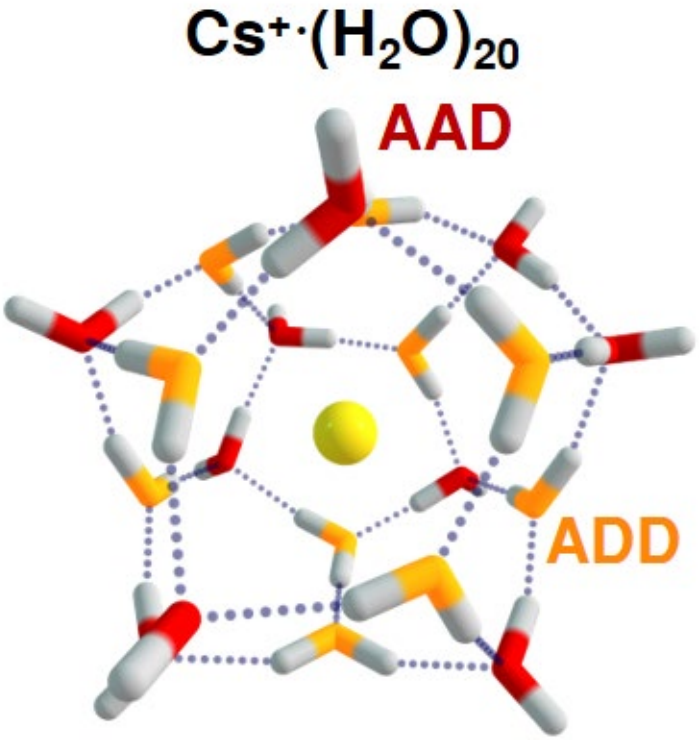

Figure 6.1: Minimum energy structure [42] of the distorted pentagonal dodecahedron (PD) cage formed by the $Cs^+\cdot(H_2O)_{20}$ cluster, denoted PD_0. On the top is a static picture of the PD_0 structure and on the bottom is an interactive 3D model which can be rotated in Adobe Reader. This structure has two classes of network sites (AAD, red and ADD, orange) that differ by the number of H-bond acceptors (A) and donors (D) associated with the water molecules at each location.

surrounding array of OD oscillators (Such as the spectra discussed in Chapter 5) [10], the resulting OH spectrum is still quite diffuse. Here we are concerned with the related situation in which a single, intact H_2O molecule is isolated in D_2O, and address how the intramolecular coupling (between the two OH groups as well as with the intramolecular bending mode) and intermolecular coupling to translational modes depends on the shape of the local H-bond network. Although such information is not available in measurements on bulk water, it can be obtained by exploiting the unique properties of size-selected and cryogenically cooled water clusters, a regime that has proven to be useful in the elucidation of the molecular-level mechanics underlying bulk behavior in a variety of contexts [11-24]. These information has also been explored for smaller water clusters in Chapter 4. This dataset provides a direct window into the degree to which excited state dynamics contribute to the structure of the diffuse spectrum.

6.2 Experimental and Computational Methods

6.2.1 Experimental Methods

The $Cs^+(H_2O)_{20}$ cluster ions were obtained by first electrospraying 5 mM $CsNO_3$ aqueous solution in a humidity-controlled purge capsule. The $Cs^+\cdot(H_2O)(D_2O)_{19}$ ions were introduced by first electrospraying an 5 mM $CsNO_3$ D_2O solution in a capsule purged with dry air and D_2O vapor mixture. The cluster ions then undergo collisional solvent exchange with H_2O in a low-pressure (~ 10^{-4} Torr) ion guide. Subsequently the ions are loaded into a temperature-controlled Paul trap kept at 13.5 K with 10% D_2 in He mixture as buffer gas to attach the D_2 messenger tag. The predissociation spectra were

obtained by irradiating the mass selected ions with a pulsed (10Hz, 8ns) tunable OPO/OPA IR laser (Laservision) which results in dissociation of the messenger tag upon resonant excitation of the mass-selected ions. The fragment ion is separated from the parent ion with a secondary mass spectrometer and detected to IR absorption by the ion of interest.

The isotopomer-selective two-color IR-IR double resonance hole burning dip spectra were carried out in an IR^2MS^3 instrument where mass selected ions are irradiated with the pump laser first and mass separated in the secondary mass spectrometer to eliminate the fragment. The remaining parent ion is then irradiated by the probe laser and mass separated again in the third mass separation stage, where the fragment from the probe laser is monitored. When acquiring an isotopomer selective double resonance dip spectrum, the probe laser is fixed on a frequency that is unique to one or several similar isotopomers. The pump laser is scanned through the entire spectrum, and when it dissociates the parent ion selected by the probe, the probe fragment signal is decreased. This depletion is recorded as a function of pump laser frequency, and the resulting trace reveals the spectrum associated with the isotopomer selected by probe.

6.2.2 Computational Methods

Unless specifically stated, all calculations in this paper were computed with Gaussian 09 [28] at the B3LYP/6-31++G** level of theory and basis with the LANL2DZ pseudopotential for the Cs atom. For comparison, in Figure 6.3, the results of calculations of the optimized structure and harmonic spectrum of Cs^+(2H,38D) are reported based on the same basis sets using CAM-B3LYP and M06-2X functionals. The

local mode treatment of the OH oscillators is based on the approach outlined by Sibert and co-workers [43]. Our implementation has been described elsewhere [47].

6.3 Results and Discussion

We specifically report the spectral signatures of individual H_2O molecules located in each of the many spectroscopically distinct sites available in the $Cs^+ \cdot (H_2O)(D_2O)_{19}$ cluster ion (denoted hereafter Cs^+(2H, 38D)). This system was selected because it adopts an arrangement in which the spherical Cs cation is encapsulated in a distorted pentagonal dodecahedral (PD) structure [25-27] at low temperature (~20 K). The reported minimum energy structure [26] of this cluster (computed with Gaussian 09 [28] at the B3LYP/6-31++G** level of theory and basis with the LANL2DZ pseudopotential for Cs), hereafter denoted **PD_0**, is depicted in Fig. 6.1, which reveals a two-dimensional sheet of networked water molecules, each in a three-coordinate H-bonding configuration. There are two general classes of H-bonding environments we hereafter classify as AAD and ADD configurations according to the number of acceptor (A) and donor (D) hydrogen bonds, respectively. The AAD class (red in Fig. 6.1) is distinguished by the free OH group (F_{OH}) that projects out from the surface, while the ADD motif (orange) is embedded roughly in the plane of the surface.

The vibrational spectra of these size-selected cluster ions were obtained using a triple-focusing, cryogenic photofragmentation mass spectrometer described in detail in Chapter 2 [29], Spectra are obtained by monitoring IR photoevaporation of weakly bound D_2 molecules in a linear action regime, which is equivalent to absorption spectra [30].

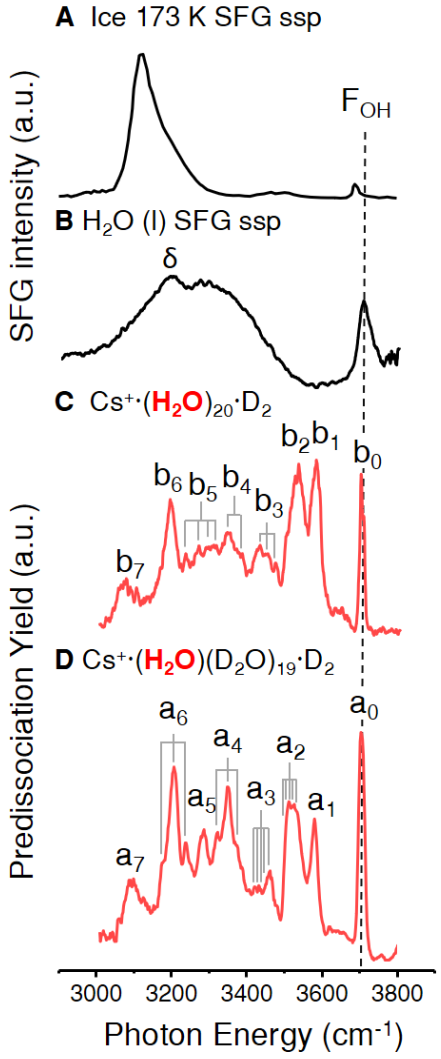

Figure 6.2: Comparison of SFG spectra from the ice and liquid water surfaces with the experimental vibrational spectra of $Cs^+(40H)\cdot D_2$ and its isotopologue incorporating an intact H_2O molecule. SFG spectra of ice-vapor (A) [34] and water-air (B) [33] interfaces (used with permission) obtained using ssp polarization combinations. (C) and (D) were obtained by predissociation of the (C) $Cs^+\cdot(H_2O)_{20}\cdot D_2$, and (D) $Cs^+\cdot(H_2O)(D_2O)_{19}\cdot D_2$ cluster ions. The δ label indicates assignment of intramolecular HOH bending overtone from the literature.[33] The frequencies of features labeled a_n and b_n are included in Tables 6.1 and 6.2.

Table 6.1. Experimental frequencies (±4 cm^{-1}) of Cs^+(2H,38D), each column contains the features detected by fixing the probe laser on the probe position (colored red with frequency listed on top of the column). The text in the cells are the assignments of the features, where AAD, F and $2\nu_{HOH}$ refer to the bound OH, free OH, and bend overtones on the AAD water molecules, respectively whereas ADD refers to the bound OH groups on the ADD waters. *Denotes multiplet structure within main peak identified in Fig. 6.2.

	Trace location	Fig 6.2H	Fig 6.2G	Fig 6.2F	Fig 6.2	Fig 6.2D	Fig 6.2C	Fig 6.2B	Fig 6.2B
	Probe Position (cm^{-1})	3082	3277	3319	3366	3505	3527	3573	3700
Peak label	Peak Position (cm^{-1})								
a_7	3082	**AAD**							AAD
a_6*	3199		AAD						AAD
	3204			$2\nu_{HOH}$					$2\nu_{HOH}$
	3231				$2\nu_{HOH}$				$2\nu_{HOH}$
a_5	3277		**$2\nu_{HOH}$**						$2\nu_{HOH}$
a_4*	3319			**AAD**					AAD
	3366				**AAD**				AAD
a_3*	3414						ADD		
	3426						ADD		
	3444						ADD		
	3454					ADD			
	3459						ADD		
a_2*	3496							ADD	
	3505					**ADD**			
	3517						ADD		
	3522						ADD		
	3527						**ADD**		
a_1	3573							**ADD**	
a_0*	3695	F							**F**
	3697				F				**F**
	3699		F						**F**
	3703			F					**F**

Table 6.2. Experimental frequencies (±4 cm^{-1}) observed for $Cs^+(40H)$. Peak labels are defined in Fig. 6.2C.

correct wavelength	assignment	Fig.6.2 label
3704	Free	b_0*
3698	Free	
3579	ADD	b_1
3529	ADD	b_2
3470	ADD	b_3*
3448	ADD	
3430	ADD	
3380	AAD	b_4*
3346	AAD	
3320	AAD	b_5*
3300	AAD	
3285	AAD	
3231	$2\nu_{HOH}$	
3191	$2\nu_{HOH}$	b_6
3072	AAD	b_7

* Denotes multiplet structure within main peak identified in Fig. 6.2.

The spectrum of the D_2-tagged $Cs^+(40H)$ cluster is presented in Fig. 6.2C. It consists of a dense series of overlapping transitions that have been discussed previously [31]. Highest in energy, the sharp feature at 3704 cm^{-1} arises from the free OH group, and its location establishes that only AAD water molecules are present. This is clear because AD sites have been observed in other cluster sizes [32] and are indicated by a higher energy transition appearing in the range 3710-3720 cm^{-1}. Although the selection rules for IR activity are different than those at play in vibrational sum frequency generation (SFG) at the air-water interface [33] and at the surface of bulk (173 K) ice [34], it is useful to compare the vibrational patterns, with representative SFG spectra presented in Figs. 6.2A and 6.2B

for ice and water, respectively.[33-34] The free OH feature (F_{OH}) is evident in all the spectra. However, in spite of the fact that the ice surface, like the PD cluster, is dominated by equal contributions from ADD and AAD sites [35] (exactly 10 each for the PD structure), the cluster spectra are actually closer to that of the liquid water surface. Where the envelope of the lower energy band extends farther toward the free OH feature. For example, the δ feature in the air-water SFG spectrum at 3200 cm^{-1} has been attributed to activity involving the bend overtone, [33] where a prominent peak (b_6) is observed in the cluster spectrum at 3191 cm^{-1}. At the same time there are significant differences; the dominant feature in the Cs^+(40H) cluster spectrum (Fig. 6.2C) occurs as a strong doublet (b_1, b_2) centered at 3554 cm^{-1}, whereas the SFG response of both phases near 3554 cm^{-1} is very weak.

The extensive range of the OH stretching bands in the Cs^+(40H) spectrum arises in part from the very large number of nearly equivalent PD structures. However, even for a single representative structure (**PD_0** in Fig. 6.1), [36-37] the calculated harmonic spectrum (Fig. 6.3) indicates that the frequency of a given H-bonded OH oscillator depends not only on the site class (ADD vs AAD), but also on the hydrogen bonding arrangements of the molecules surrounding it [38-39]. For example, the transition associated with the donor OH group is predicted to be much less redshifted when the acceptor water molecule has a free OH group. This effect has been treated in neutral water clusters by Ohno et al. [38] and later extended to the liquid, ice and interface regimes by Tainter et al. [39] When these extended patterns are included, the **PD_0** structure is quite unsymmetrical such that essentially all the bound OH groups are in topologically distinct environments. As a result, the calculated fundamentals (displayed in Fig. 6.3) are distributed over 600 cm^{-1},

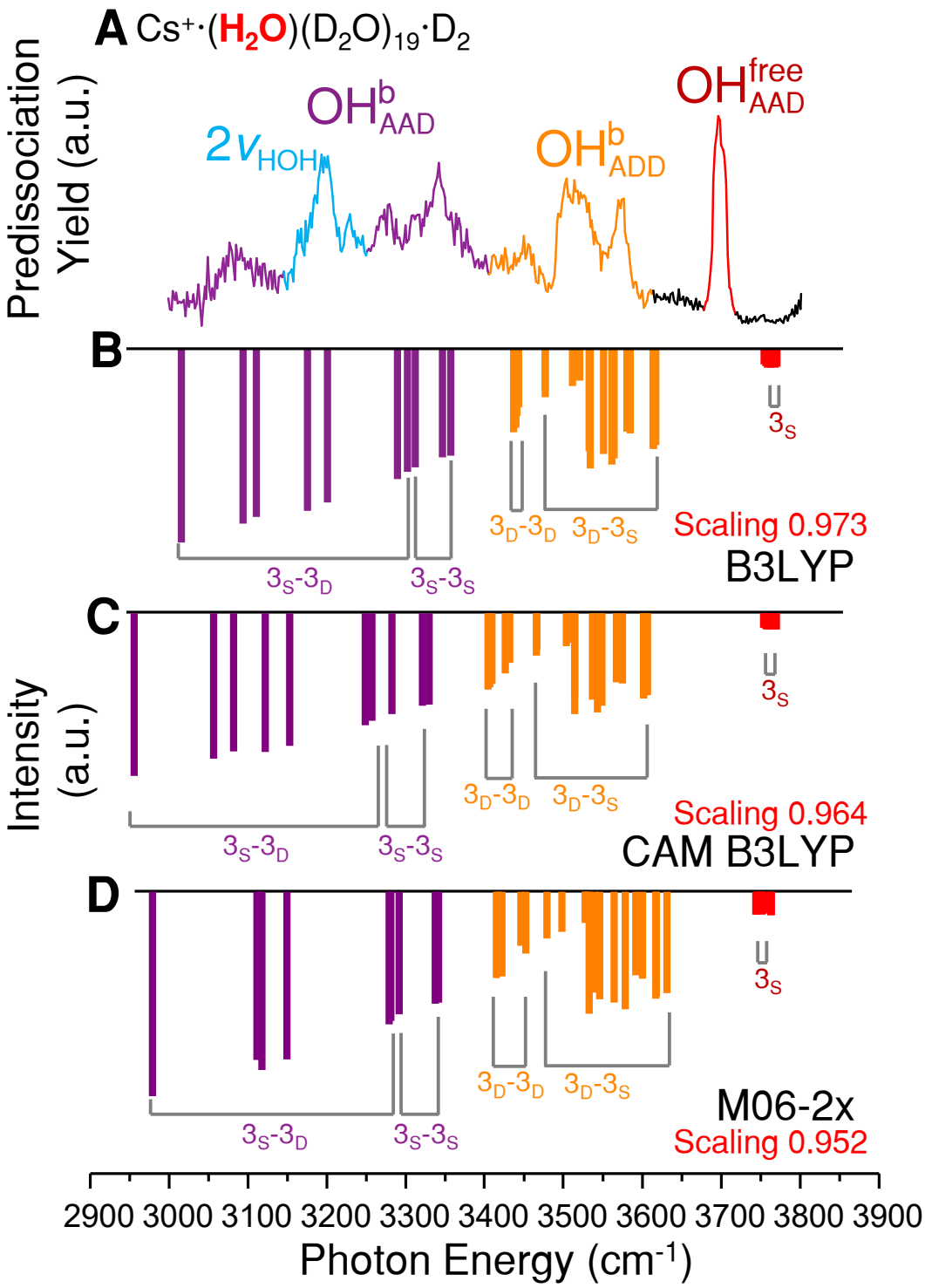
A Cs+·(H2O)(D2O)19·D2
Predissociation Yield (a.u.)
2νHOH
OHbAAD
OHbADD
OHfreeAAD
B
3S
3D-3D
3D-3S
3S-3D
3S-3S
Scaling 0.973
B3LYP
C
Intensity (a.u.)
Scaling 0.964
CAM B3LYP
D
M06-2x
Scaling 0.952
2900 3000 3100 3200 3300 3400 3500 3600 3700 3800 3900
Photon Energy (cm-1)

Figure 6.3: (**A**) Predissociation spectra of all isotopomers of $Cs^+(2H,38D)\cdot D_2$ in the OH stretching region. Bands colored red, orange, purple and blue denote the free OH stretch (OH^{free}_{AAD}), bound OH stretch on an ADD water (OH^{b}_{ADD}), bound OH stretch on an AAD water (OH^{b}_{AAD}), and the intramolecular HOH bend overtone ($2\nu_{HOH}$), respectively. Harmonic spectra of all isotopomers of $Cs^+(2H,38D)$ computed at the (**B**) B3LYP/6-31++G**, (**C**) CAM-B3LYP/6-31++G** and (**D**) M06-2X/6-31++G** levels of theory and basis with the LANL2DZ pseudopotential for Cs. The calculated transitions are categorized according to the nomenclature suggested by Skinner and coworkers [44] where the number indicates the total number of H-bonds that an individual water molecule is involved in (1-4) and the letter indicates the number of OH groups on that water molecule that are donating H-bonds (N for none, S for single and D for double). Finally, a specific OH oscillator is indicated by a pair of water molecules connected with a dash where the H-bond donor resides on the left and acceptor on the right (e.g. 3_D-3_S means the OH group on an ADD water that donates to an AAD water, see Fig. 6.4 for more examples).

and harmonic analysis of the bands arising from the various sites in the **PD$_0$** structure indicates a strong correlation between the redshift of a given site and the H-bonding index advocated by Skinner [39], as illustrated in Figs. 6.3B and 6.4.

We next describe how the local PD network sites that contribute to the pattern in Fig. 6.2C can be revealed using an isotopic labeling scheme that is only available in the cluster regime. Specifically, because chemical scrambling between the OH and OD groups is strongly suppressed in water clusters, a single, intact H_2O molecule can be incorporated into an otherwise perdeuterated assembly [40-41]. Consequently, an H_2O molecule can be integrated into the PD cage by ligand exchange, a process in which preformed $Cs^+\cdot(D_2O)_{20}$ clusters interact at low pressure with H_2O vapor as described in Chapter 6.2. This mechanism is verified by the absence of the HDO bending fundamental in the spectra of clusters with the stoichiometry $Cs^+\cdot(H_2O)(D_2O)_n$ [40] and the suppression of odd numbers of H atoms in the product ion isotopologues (see Fig. 6.5), which would reveal chemical scrambling by evaporation of HDO.

The vibrational spectrum of the D_2-tagged Cs^+(2H,38D) isotopologue is compared in Fig. 6.2D with that of Cs^+(40H) in Fig. 6.2C. Note that the overall envelope of the Cs^+(2H,38D) covers the energy range observed for the Cs^+(40H) cluster, with the positions of the labeled peaks collected in Tables 6.1 and 6.2. Because only two OH oscillators are available in the mass-selected Cs^+(2H,38D) ion, the extent of its OH stretching region must arise from H_2O occupation of many different sites within the PD structure to create a plethora of isotopomers. One important difference in the spectra of the two isotopologues is that the free OH feature in the Cs^+(2H,38D) spectrum is clearly enhanced relative to that in the Cs^+(40H) cluster, indicating that the free OH site is

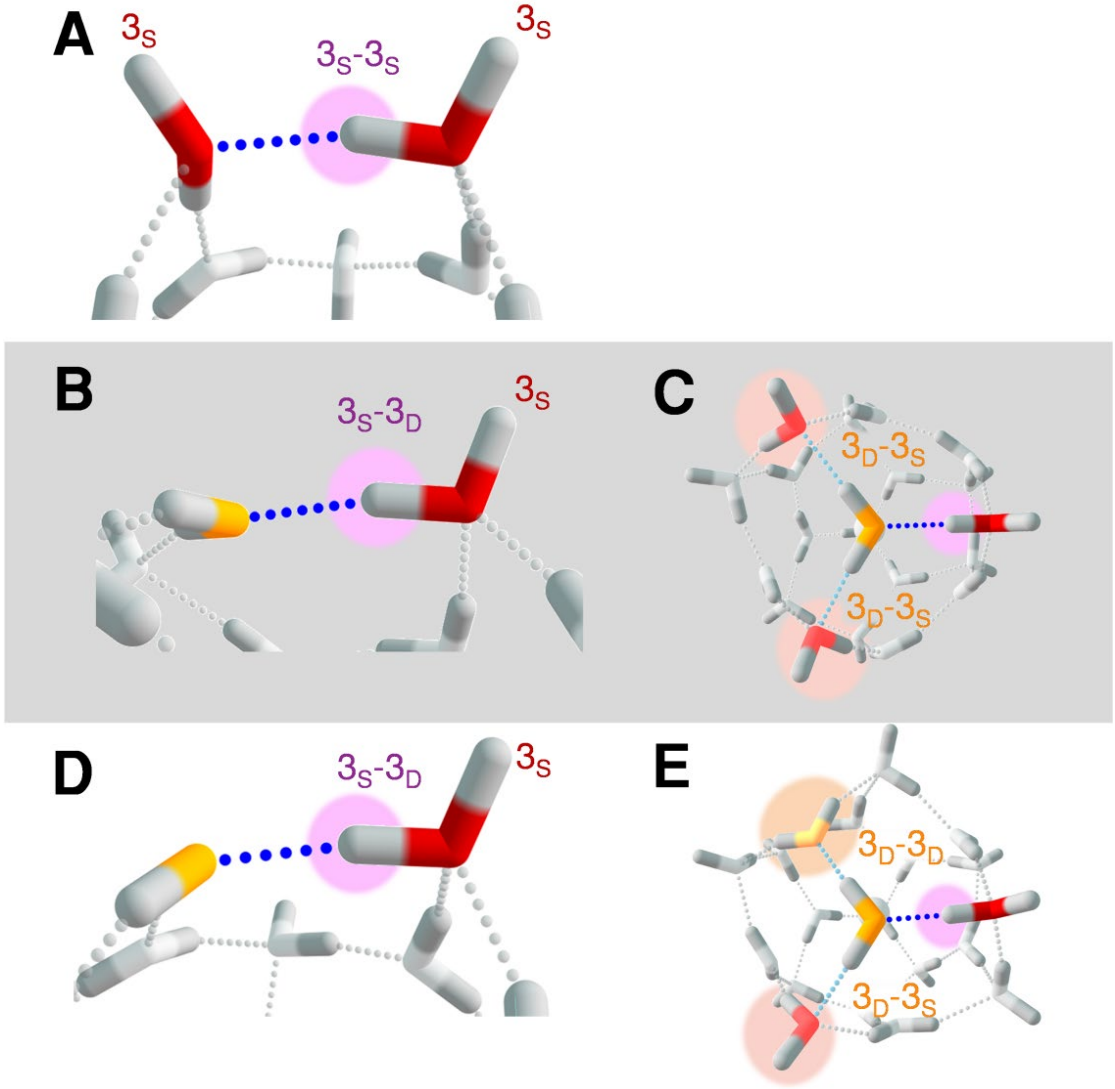
A
3S
3S-3S
3S
B
3S-3D
3S
C
3D-3S
3D-3S
D
3S-3D
3S
E
3D-3D
3D-3S

Figure 6.4: Expanded views of several donor-acceptor pairs in the calculated structure of $Cs^+(40H)$ computed at the B3LYP/6-31++G**level of theory and basis with the LANL2DZ pseudopotential for Cs. The bound OH on AAD water molecules (OH^b_{ADD}), indicated by purple halos on red molecules, can be categorized by their H-bond acceptors into two classes: 3_s-3_s with an AAD water as acceptor (**A**) and 3_s-3_d with an ADD water (Orange, (**B-E**)). The 3_s-3_d class can be further differentiated according to the types of water molecules that the acceptor ADD water binds to. The case where the acceptor ADD water binds to two AAD waters (**C**) results in the acceptor ADD water displaced slightly out of the cage towards the free OH (**B**), whereas when the acceptor ADD water binds to one AAD and one ADD water (**E**), the acceptor ADD water is displaced inward, away from the free OH (**D**). These three motifs result in different OH^b_{ADD} transition frequencies on the donor AAD water molecule. The motif in (**A**) yields the highest calculated frequency whereas that displayed in (**D,E**) results in the lowest frequency.

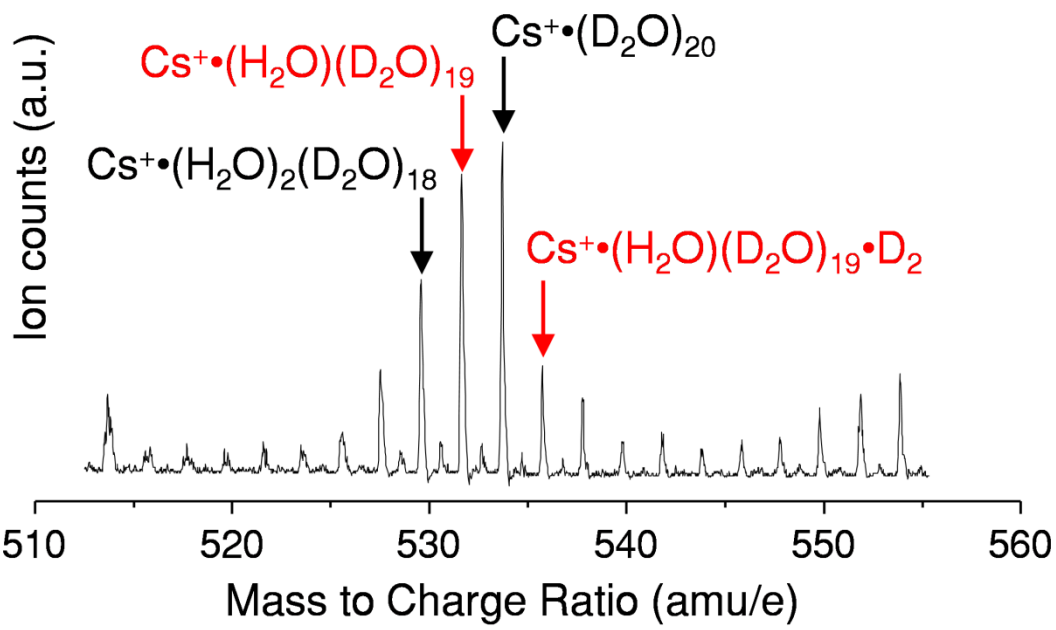

Figure 6.5: Product mass spectrum arising from condensation of H_2O molecules onto preformed $Cs^+\cdot(D_2O)_n$ clusters at an H_2O pressure of approximately 10^{-4} Torr in an octopole ion guide.

preferentially populated in the cold ensemble. This is consistent with the behavior observed at the surface of ice, where nuclear quantum effects strengthen the bonds holding D_2O molecules in ADD sties [42]. The similarities in the band shapes in Fig. 6.2C and 6.2D raises the question of whether the spectrum of the homogenous isotopologue is a simple superposition of the spectra of isolated H_2O molecules occupying the various sites, or indeed reflects coupling among nearby molecules in the PD structure. In fact, the only major differences between the two spectra are the character of the absorptions near 3350 cm^{-1} (a_4 vs b_4 in Fig. 6.2C and 6.2D), a 14 cm^{-1} redshift in the strong doublet (a_1, a_2 vs b_1,b_2 in Fig. 6.2D) below the free OH feature at ~3700 cm^{-1}, and a small (<10 cm^{-1}) redshift in the a_6-b_6, a_7-b_7 features at the lower energy end of the absorption. To put this in context, the matrix elements arising from intramolecular coupling have been considered for bulk water [1] and found to be distributed about a mean value of 27.1 cm^{-1} depending on the orientations and fundamental OH stretching frequencies of the nearby water molecules. This coupling was explored at the harmonic level using the methods developed by Sibert, [24] which involves decoupling the various OH oscillators that make up the normal modes of the **PD_o** structure [43]. The results of this analysis are provided in Table 6.3, and indicate that, for the AAD molecules, the couplings range from 33 to 45 cm^{-1}, which lead to ~5 cm^{-1} shifts in the frequencies of the OH stretching fundamentals.

Provided that the Cs^+(2H,38D) clusters are sufficiently cold to suppress spontaneous interconversion between the isotopomers that differ according to site occupation by H_2O, the spectrum is a heterogeneous superposition of their distinct spectra. As such, isotopomer-specific spectra provides a direct way to extract the spectrum of an H_2O molecule located in each site. Of particular importance, these spectra

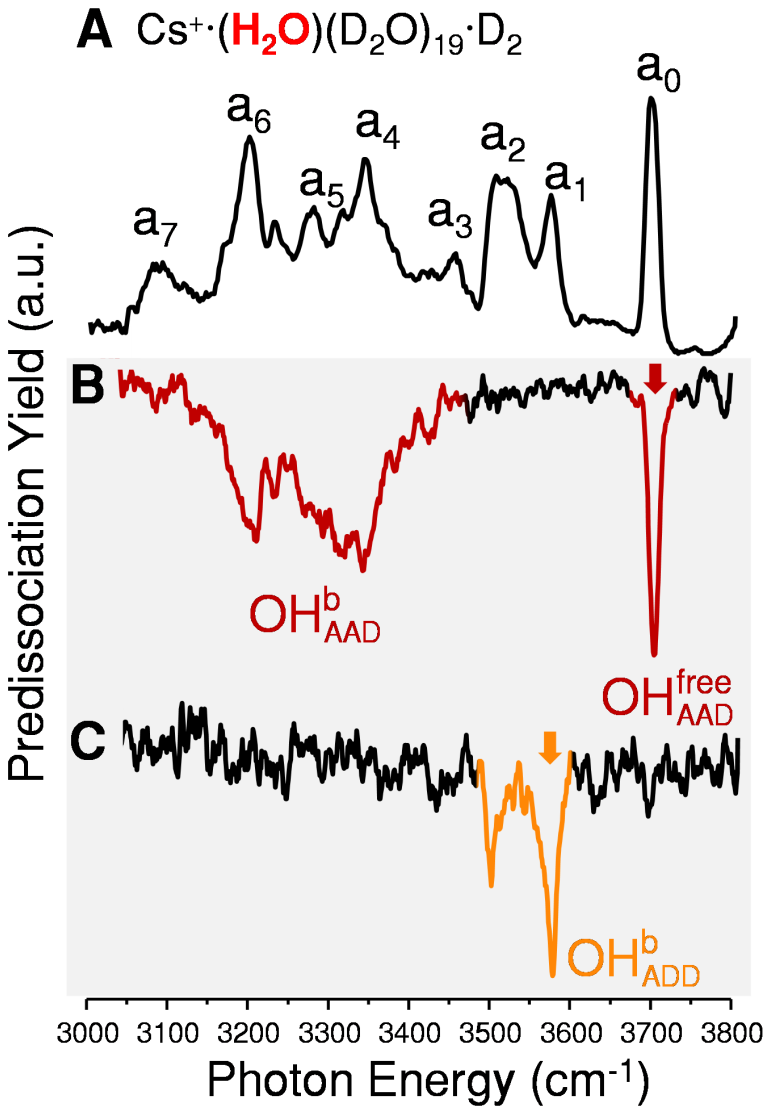

Figure 6.6: Isolation of the contributions of the AAD (red) and ADD (orange) water molecules to the spectrum of the Cs^+(2H, 38D)·D_2 isotopologue. Vibrational predissociation spectrum of (A) Cs^+·(2H,38D)·D_2 and two-color, IR-IR double resonance hole burning spectra of Cs^+·(2H,38D)·D_2 with the probe laser fixed on (B) the a_0 (red arrow) and (C) the a_1 (orange arrow) features, thus isolating the signatures of H_2O in AAD and ADD sites, respectively.

reveal the embedded correlations between transitions derived from the two OH groups that are distributed throughout the ensemble spectrum. We isolated the site-specific spectra using a two-color, IR-IR photobleaching approach described in Chapter 2 [29]. This requires three stages of mass selection and is therefore denoted a MS^3IR^2 class of secondary analysis. In this application, one IR laser is fixed on a particular probe transition while another, powerful IR laser is scanned through the entire spectrum. The photofragment yield from the probe laser then reveals the isotopomer-selective spectrum as a series of dips as the pump laser removes population from the species selected by the probe frequency.

Fig. 6.6B demonstrates how the MS^3IR^2 approach can establish the locations of the transitions arising from the bound OH companion of the free OH group on the same water molecule. This is accomplished by fixing the probe laser on the free OH band at 3699 cm^{-1} (a_0) while the pump laser is scanned across the OH region. The resulting dip spectrum (Fig. 6.6B) exhibits a very large gap between the F_{OH} band and the onset of a diffuse absorption envelope below 3400 cm^{-1}. This observation provides direct evidence that the bands in the lower energy region of the spectrum ($a_{4\text{-}7}$) are exclusively due to excitation of the bound OH group associated with H_2O molecules in AAD network sites. Consequently, the strong doublet (a_1 and a_2) centered at 3540 cm^{-1} must be exclusively derived from the ADD sites. That conclusion can again be directly tested, this time by fixing the probe laser on the dominant peak a_1 at 3573 cm^{-1} to yield the dip spectrum in Fig. 6.6C, which indeed reveals two bands spaced by ~80 cm^{-1}. The separation between these two transitions is consistent with the splitting between the two donor OH groups on the same molecule [44]. Although the splitting is close to that found for the symmetric and

antisymmetric stretches in an isolated water molecule, harmonic analysis of the couplings of the local OH oscillators in the **PD_0** structure indicates that the leading contribution to the splitting comes from differences in the environment of the two OH bonds in the various ADD sites (see Table 6.3). The traces in Fig. 6.7B and 6.7C display how this doublet evolves in the region of the a_1-a_3 peaks, demonstrating that these distinct ADD contributions are partially overlapping.

The overall behavior displayed in Fig. 6.6 is in qualitative agreement with the harmonic prediction (Fig. 6.3) that the AAD and ADD classes contribute to distinct regions of the spectrum. We next address the nature of the free OH feature and the diffuse absorption displayed by the AAD sites below 3400 cm^{-1} in the Cs^+(2H,38D) spectrum (Fig. 6.6B). Because all AAD sites necessarily display a free OH feature, further isolation of the independent contributions to the low energy envelope must be accomplished by probing various locations (indicated by purple arrows in Fig. 6.7E-H) throughout the region. As expected, all these probe positions yield a free OH band, but the isotopomer-selective spectra reveal that the feature near 3700 cm^{-1} is actually heterogeneous. Specifically, there are two even narrower (~9 cm^{-1} FWHM) components to this feature as highlighted by the expanded scan in Fig. 6.8. The MS^3IR^2 spectra in Fig. 6.7E-H establish that there are at least four distinct network sites contributing to the diffuse low energy envelope (Fig. 6.6B). These scans display an evolving multiplet substructure as the probe energy approaches a narrower band (a_6, blue) near 3200 cm^{-1}. This narrow band appears near the expected location for the v = 0→2 overtone transition arising from the HOH bending fundamental (ν_{HOH}) at ~1600 cm^{-1}, which is nominally IR forbidden in the double harmonic level approximation (i.e., normal modes coupled with a

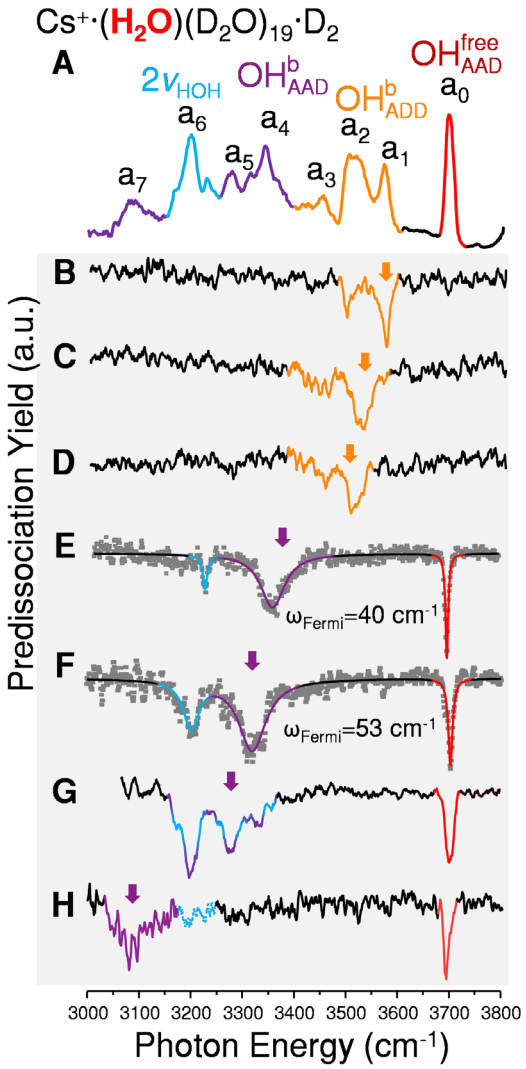

Figure 6.7: Isolation of band patterns associated with spectroscopically distinct sites occupied by an intact H_2O molecule in the $Cs^+(2H,38D)\cdot D_2$ cluster, obtained by fixing the probe laser at the photon energies indicated by downward arrows while scanning the pump laser through the OH stretching region. (A) Non-selective predissociation spectrum of $Cs^+(2H,38D)\cdot D_2$, (B-D) bands due to ADD sites (orange), (E-H) bands arising from AAD sites. The AAD contributions are further resolved into excitations of free OH (red), bound OH (purple) and intramolecular bend overtones (blue). The solid lines in (E) and (F) are fits to a 2×2 coupling scheme between the OH stretch and intramolecular bend described in detail in Fig. 6.9.

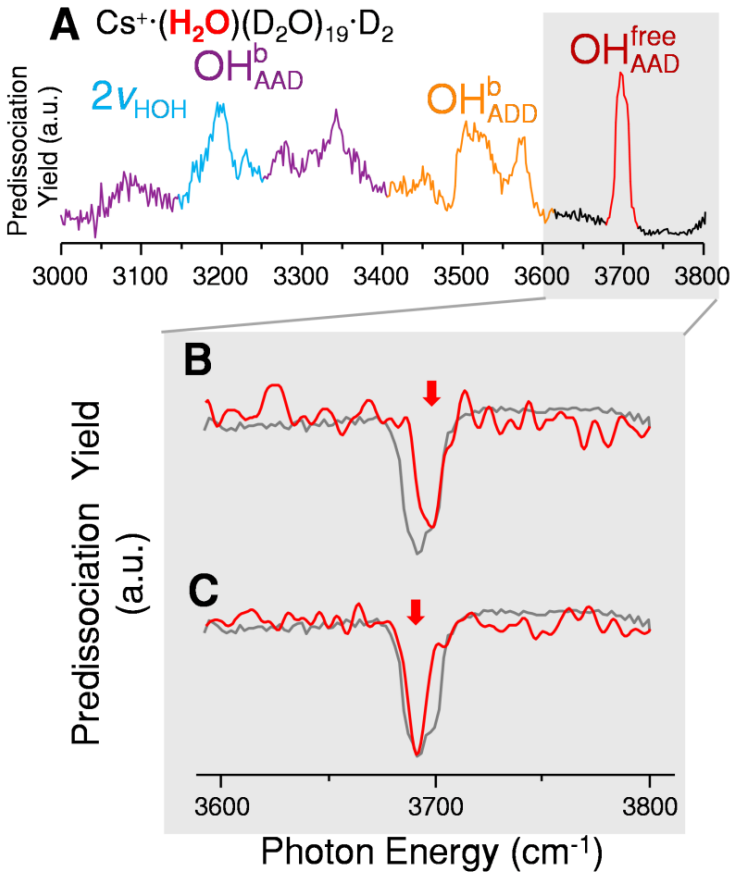

Figure 6.8: (**A**) Predissociation spectra of all isotopomers of $Cs^+(2H,38D)\cdot D_2$. . See caption in Fig. 6.3 for notation. The free OH region is expanded and presented as inverted gray traces in (**B**) and (**C**). The red depletion traces are two-color, isotopomer-selective IR-IR double resonance hole burning spectra of $Cs^+(2H,38D)\cdot D_2$ in the free OH region, obtained by probing on the position indicated by the red arrows in (**B**) and (**C**).

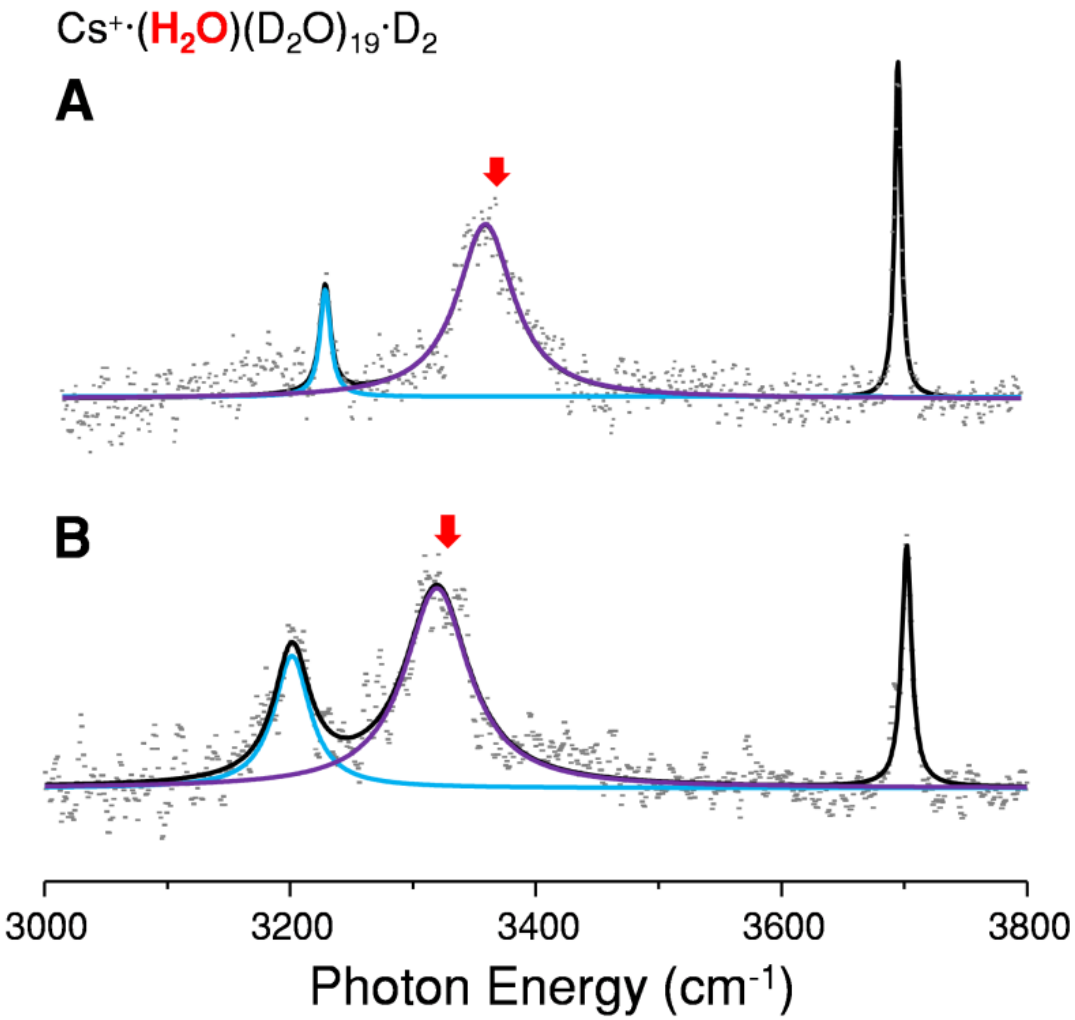
Cs+·(H2O)(D2O)19·D2
A
B
3000
3200
3400
3600
3800
Photon Energy (cm-1)

Figure 6.9: Fits (solid lines) of the multiplet structures in Figs. 6.7E (**A**) and 6.7F (**B**) to a 2×2 Fermi resonance model. Each trace displays the spectral features associated with one H_2O molecule: the free OH, the bound OH partner (purple) and the intramolecular bend overtone (turquoise). The probe positions are indicated by the red arrows. The fit results are reported below: **A**. OH^{b}_{ADD} band center (3364 ± 4 cm^{-1}) with area of 92 ± 4 a.u. and width (56 ± 3 cm^{-1}) whereas the nominal $2\nu_{HOH}$ band is centered at 3234 ± 4 cm^{-1} with area 11 ± 2 a.u. and width (10 ± 2 cm^{-1}). The fitted Lorentzians result from a coupling constant of 40 cm^{-1} between the two states. **B**. OH^{b}_{ADD} band center (3320 ± 4 cm^{-1}) with area 115 ± 5 a.u. and width (64 ± 3 cm^{-1}) whereas the nominal $2\nu_{HOH}$ band is centered at 3202 ± 4 cm^{-1} with area 58 ± 3 a.u. and width 36 ± 3 cm^{-1}. These were obtained with a coupling constant of 53 cm^{-1} between the two states. These values were obtained by solving

$$H = T^{+}\nu T$$

for the elements of *H* (e.g. the unperturbed frequencies of the OH stretch, ν^0_{str}, and the HOH bend overtone, $2\nu^0_{bnd}$, as well as the Fermi resonance coupling term, λ_{sbb}. To do this we express the three matrices as

$$H = \begin{pmatrix} 2\nu^0_{bnd} & \lambda_{sbb} \\ \lambda_{sbb} & \nu^0_{str} \end{pmatrix}, T = \begin{pmatrix} T_{11} & T_{12} \\ -T_{12} & T_{11} \end{pmatrix} \text{ and } \nu = \begin{pmatrix} \nu_L & 0 \\ 0 & \nu_H \end{pmatrix}$$

where ν_L and ν_H represent the centers of the blue and purple features in the above spectra, while T_{11} and T_{12} provide the square roots of the normalized areas under these features. The value of λ_{sbb} is obtained through simple matrix multiplication of these 2×2 matrices.

Table 6.3. Calculated frequencies of H_2O molecules in the **PD_0** structure in a 2-dimensional coupled (normal mode) and uncoupled (local mode) representation of the OH vibrations. The splittings ($\Delta\omega$) provide the frequency difference between the two OH stretch vibrations (between ω_L and ω_H or ω_1 and ω_2) on a single water molecule, when the vibrations are expressed in a normal or local mode representation, while coup. (λ_{12}) provides the intramolecular coupling between the two local mode stretches. The water molecules are classified into AAD and ADD types. All numbers are in wavenumbers (cm^{-1}).

Normal mode		**Local mode**		**Splitting**			**Coup.**	**Type**
ω_L	ω_H	ω_1	ω_2	$\Delta\omega_{Normal}$	$\Delta\omega_{Local}$	Diff.	$\lvert\lambda_{12}\rvert$	Type
3091.6	3859.2	3094.2	3856.6	767.6	762.4	5.2	44.6	AAD
3174.2	3868.8	3177.5	3865.4	694.6	687.9	6.8	48.1	
3192.0	3868.7	3195.4	3865.3	676.7	669.9	6.8	48.0	
3259.8	3861.4	3263.4	3857.8	601.7	594.5	7.2	46.4	
3286.5	3865.8	3290.5	3861.9	579.4	571.4	8.0	47.8	
3378.0	3873.5	3383.0	3868.5	495.5	485.5	10.0	49.5	
3392.3	3875.0	3397.6	3869.7	482.8	472.2	10.6	50.3	
3400.3	3866.4	3405.7	3861.0	466.0	455.3	10.6	49.6	
3436.8	3862.9	3442.5	3857.3	426.1	414.8	11.2	48.6	
3447.7	3867.1	3453.7	3861.2	419.4	407.5	12.0	49.6	
3530.2	3678.2	3538.3	3670.0	147.9	131.7	16.2	33.7	ADD
3533.5	3630.0	3544.7	3618.8	96.5	74.1	22.4	30.9	
3534.1	3683.6	3543.5	3674.2	149.5	130.8	18.8	36.2	
3534.6	3648.3	3548.3	3634.6	113.7	86.3	27.4	37.0	
3536.9	3630.9	3554.2	3613.5	94.0	59.3	34.8	36.5	
3572.3	3662.6	3594.7	3640.1	90.3	45.4	44.8	39.0	
3572.4	3658.9	3599.8	3631.5	86.5	31.7	54.8	40.2	
3607.9	3716.6	3632.0	3692.5	108.7	60.5	48.2	45.2	
3616.4	3712.9	3646.6	3682.7	96.5	36.1	60.4	44.7	
3617.7	3714.0	3648.2	3683.5	96.3	35.3	61.0	44.8	

linear expansion of the dipole surface). It is well known [45] that the OH (v=1) and ν_{HOH} (v=2) harmonic states are often anharmonically coupled in a Fermi resonance interaction, which yields two mixed states that both contribute to the IR absorption spectrum. In the model commonly used [45] to treat this effect, the intensity ratio of the two transitions depends on the energy separation between the two unperturbed levels and the matrix element that couples them. Because the bending mode is relatively insensitive to local coordination, the overtone remains relatively fixed while the OH fundamentals are incrementally red-shifted through the energy of the ν_{HOH} (v=2) level. Although the spectrum in Fig. 6.7G appears to result from the overlap of at least two distinct contributions (as evidenced by the broadening of the F_{OH} peak), the traces in Fig. 6.7E and 6.7F yield sharper F_{OH} bands and were therefore further analyzed to reveal the intramolecular coupling mechanics. The observed patterns were fit to a simple 2×2 interaction picture in which the oscillator strength of the bend overtone occurs through intensity borrowing from the nearby OH (v=1) level. This procedure indicates that Fermi coupling matrix elements of 40 and 53 cm^{-1} are required to recover the observed patterns (solid lines in traces 6.7E and 6.7F, respectively), with the width (FWHM) of the nominal OH stretching fundamental of about 60 cm^{-1} as illustrated in detail in Fig. 6.9. Note that this matrix element is larger than that (~33 cm^{-1}) reported earlier in the $X^{-}\cdot H_2O$ (X=halide) systems [45]. The width associated with the bound OH group is also of interest, as it establishes an excited state relaxation time of the OH oscillator on the order of 200 fs. Equally important is the observation that these broadened bands occur without significant excitation of combination bands involving low frequency intermolecular vibrational modes, unlike the situation encountered in the microhydration of anions [29, 46].

6.4 Summary

Summarizing, we have established that the range of frequencies exhibited by the OH oscillators of H_2O molecules occupying seven distinct sites in the $Cs^+ \cdot (H_2O)_{20}$ cluster covers that found in the SFG spectrum of the air-water interface. We further demonstrated how, by following the spectroscopic behavior of single (intact) H_2O molecules embedded in the pentagonal dodecahedron water cage surrounding the Cs^+ cation, we can unmask previously hidden mechanistic features that underlie the diffuse IR spectrum of the tri-coordinated, two-dimensional water network. The water molecules that are embedded in the cage surface by donating two H-bonds to neighbors exclusively account for the absorption in the range 3450 – 3600 cm^{-1}, while the bound OH companion of water molecules with a free OH group yield all of the more diffuse absorption below 3450 cm^{-1}. The v=1 level of the OH stretching manifold associated with that bound OH group undergoes a strong Fermi type interaction with the v=2 level of the intramolecular HOH bending mode as the former is red shifted through the zero-order location of the bend overtone near ~3200 cm^{-1} with a matrix element of ~45 cm^{-1}. These results establish the intrinsic breadths and multiplet signatures associated with excitation of a water molecule at very low temperature, which must result from anharmonic couplings among the excited vibrational states. With this information and experimental capability in hand, an exciting direction for future work will be to follow the onset of spectral diffusion in micro-canonical ensembles and thus reveal the trajectories of the large amplitude motions that underlie the rapid spectral diffusion exhibited by bulk water.

6.5 References

1. Auer, B. M.; Skinner, J. L. IR and Raman Spectra of Liquid Water: Theory and Interpretation. *Journal of Chemical Physics* **2008,** *128* (22), 224511.

2. Bakker, H. J.; Skinner, J. L. Vibrational spectroscopy as a probe of structure and dynamics in liquid water. *Chem. Rev.* **2010,** *110* (3), 1498-1517.

3. Perakis, F.; De Marco, L.; Shalit, A.; Tang, F. J.; Kann, Z. R.; Kuhne, T. D.; Torre, R.; Bonn, M.; Nagata, Y. Vibrational Spectroscopy and Dynamics of Water. *Chem Rev* **2016,** *116* (13), 7590-7607.

4. Hayashi, T.; Jansen, T. L.; Zhuang, W.; Mukamel, S. Collective solvent coordinates for the infrared spectrum of HOD in D_2O based on an ab initio electrostatic map. *Journal of Physical Chemistry A* **2005,** *109* (1), 64-82.

5. Corcelli, S. A.; Lawrence, C. P.; Skinner, J. L. Combined electronic structure/molecular dynamics approach for ultrafast infrared spectroscopy of dilute HOD in liquid H_2O and D_2O. *Journal of Chemical Physics* **2004,** *120* (17), 8107-8117.

6. Steinel, T.; Asbury, J. B.; Corcelli, S. A.; Lawrence, C. P.; Skinner, J. L.; Fayer, M. D. Water Dynamics: Dependence on Local Structure Probed with Vibrational Echo Correlation Spectroscopy. *Chem. Phys. Lett.* **2004,** *386* (4-6), 295-300.

7. Bankura, A.; Karmakar, A.; Carnevale, V.; Chandra, A.; Klein, M. L. Structure, Dynamics, and Spectral Diffusion of Water from First-Principles Molecular Dynamics. *J Phys Chem C* **2014,** *118* (50), 29401-29411.

8. Paarmann, A.; Hayashi, T.; Mukamel, S.; Miller, R. J. D. Nonlinear response of vibrational excitons: Simulating the two-dimensional infrared spectrum of liquid water. *Journal of Chemical Physics* **2009,** *130* (20), 204110.

9. De Marco, L.; Fournier, J. A.; Thamer, M.; Carpenter, W.; Tokmakoff, A. Anharmonic exciton dynamics and energy dissipation in liquid water from two-dimensional infrared spectroscopy. *Journal of Chemical Physics* **2016,** *145* (9), 094501.

10. Hornig, D. F.; White, H. F.; Reding, F. P. The Infrared Spectra of Crystalline H_2O, D_2O and HDO. *Spectrochimica Acta* **1958,** *12* (4), 338-349.

11. Hammer, N. I.; Shin, J.-W.; Headrick, J. M.; Diken, E. G.; Roscioli, J. R.; Weddle, G. H.; Johnson, M. A. How Do Small Water Clusters Bind an Excess Electron? *Science* **2004,** *306*, 675-679.

12. Young, R. M.; Neumark, D. M. Dynamics of Solvated Electrons in Clusters. *Chem Rev* **2012,** *112* (11), 5553-5577.

13. Abel, B.; Buck, U.; Sobolewski, A. L.; Domcke, W. On the nature and signatures of the solvated electron in water. *Physical chemistry chemical physics : PCCP* **2012,** *14* (1), 22-34.

14. Wolke, C. T.; Fournier, J. A.; Dzugan, L. C.; Fagiani, M. R.; Odbadrakh, T. T.; Knorke, H.; Jordan, K. D.; McCoy, A. B.; Asmis, K. R.; Johnson, M. A. Spectroscopic Snapshots of the Proton-Transfer Mechanism in Water. *Science* **2016,** *354* (6316), 1131-1135.

15. Fournier, J. A.; Johnson, C. J.; Wolke, C. T.; Weddle, G. H.; Wolk, A. B.; Johnson, M. A. Vibrational Spectral Signature of the Proton Defect in the Three-Dimensional $H^+(H_2O)_{21}$ Cluster. *Science* **2014,** *344* (6187), 1009-1012.

16. Keutsch, F. N., Saykally, R. J. Water Clusters: Untangling the mysteries of the liquid, one molecule at a time. *Proc. Natl. Acad. Sci. USA* **2001,** *98* (19), 10533-10540.

17. Smith, J. D.; Cappa, C. D.; Wilson, K. R.; Messer, B. M.; Cohen, R. C.; Saykally, R. J. Energetics of Hydrogen Bond Network Rearrangements in Liquid Water. *Science* **2004,** *306*, 851.

18. Cole, W. T. S.; Farrell, J. D.; Sheikh, A. A.; Yonder, O.; Fellers, R. S.; Viant, M. R.; Wales, D. J.; Saykally, R. J. Terahertz VRT spectroscopy of the water hexamer-d_{12} prism: Dramatic enhancement of bifurcation tunneling upon librational excitation. *Journal of Chemical Physics* **2018,** *148* (9), 094301.

19. Cole, W. T. S.; Saykally, R. J. Hydrogen bond network rearrangement dynamics in water clusters: Effects of intermolecular vibrational excitation on tunneling rates. *Journal of Chemical Physics* **2017,** *147* (6), 064301.

20. Perez, C.; Muckle, M. T.; Zaleski, D. P.; Seifert, N. A.; Temelso, B.; Shields, G. C.; Kisiel, Z.; Pate, B. H. Structures of Cage, Prism, and Book Isomers of Water Hexamer from Broadband Rotational Spectroscopy. *Science* **2012,** *336* (6083), 897-901.

21. Perez, C.; Zaleski, D. P.; Seifert, N. A.; Temelso, B.; Shields, G. C.; Kisiel, Z.; Pate, B. H. Hydrogen Bond Cooperativity and the Three-Dimensional Structures of Water Nonamers and Decamers. *Angewandte Chemie-International Edition* **2014,** *53* (52), 14368-14372.

22. Clarkson, J. R.; Baquero, E.; Shubert, V. A.; Myshakin, E. M.; Jordan, K. D.; Zwier, T. S. Laser-initiated shuttling of a water molecule between H-bonding sites. *Science* **2005,** *307*, 1443.

23. Clarkson, J. R.; Herbert, J. M.; Zwier, T. S. Infrared photodissociation of a water molecule from a flexible molecule-H_2O complex: Rates and conformational product yields following XH stretch excitation. *J. Chem. Phys.* **2007,** *126* (13), 134306.

24. Tabor, D. P.; Kusaka, R.; Walsh, P. S.; Zwier, T. S.; Sibert, E. L. Local Mode Approach to OH Stretch Spectra of Benzene-$(H_2O)_n$ Clusters, n=2-7. *Journal of Physical Chemistry A* **2015,** *119* (38), 9917-9930.

25. Cooper, R. J.; Chang, T. M.; Williams, E. R. Hydrated Alkali Metal Ions: Spectroscopic Evidence for Clathrates. *J. Phys. Chem. A* **2013,** *117* (30), 6571-6579.

26. Schulz, F.; Hartke, B. Dodecahedral Clathrate Structures and Magic Numbers in Alkali Cation Microhydration Clusters. *Chemphyschem* **2002,** *3* (1), 98-106.

27. Selinger, A.; Castleman, A. W. Evidence for the Encagement of Alkali-Metal Ions through the Formation of Gas-Phase Clathrates - Cs+ in Water Clusters. *J. Phys. Chem.* **1991,** *95* (22), 8442-8444.

28. Frisch, M. J.; Trucks, G. W.; Schlegel, H. B.; Scuseria, G. E.; Robb, M. A.; Cheeseman, J. R.; Scalmani, G.; Barone, V.; Mennucci, B.; Petersson, G. A.; Nakatsuji, H.; Caricato, M.; Li, X.; Hratchian, H. P.; Izmaylov, A. F.; Bloino, J.; Zheng, G.; Sonnenberg, J. L.; Hada, M.; Ehara, M.; Toyota, K.; Fukuda, R.; Hasegawa, J.; Ishida, M.; Nakajima, T.; Honda, Y.; Kitao, O.; Nakai, H.; Vreven, T.; J. A. Montgomery, J.; Peralta, J. E.; Ogliaro, F.; Bearpark, M.; Heyd, J. J.; Brothers, E.; Kudin, K. N.; Staroverov, V. N.; Kobayashi, R.; Normand, J.; Raghavachari, K.; Rendell, A.; Burant, J. C.; Iyengar, S. S.; Tomasi, J.; Cossi, M.; Rega, N.; Millam, J. M.; Klene, M.; Knox, J. E.; Cross, J. B.; Bakken, V.; Adamo, C.; Jaramillo, J.; Gomperts, R.; Stratmann, R. E.; Yazyev, O.; Austin, A. J.; Cammi, R.; Pomelli, C.; Ochterski, J. W.; Martin, R. L.; Morokuma, K.; Zakrzewski, V. G.; Voth, G. A.; Salvador, P.; Dannenberg, J. J.; Dapprich, S.; Daniels, A. D.; Farkas, Ö.; Foresman, J. B.; Ortiz, J. V.; Cioslowski, J.; Fox, D. J. *Gaussian 09, Revision D.01*, Gaussian, Inc.: Wallingford, CT, 2009.

29. Yang, N.; Duong, C. H.; Kelleher, P. J.; Johnson, M. A.; McCoy, A. B. Isolation of Site-Specific Anharmonicities of Individual Water Molecules in the $I^-\cdot(H_2O)_2$ Complex Using Tag-Free, Isotopomer Selective IR-IR Double Resonance. *Chem. Phys. Lett.* **2017,** *690*, 159-171.

30. Wolk, A. B.; Leavitt, C. M.; Garand, E.; Johnson, M. A. Cryogenic Ion Chemistry and Spectroscopy. *Acc. Chem. Res.* **2014,** *47* (1), 202-210.

31. Fournier, J. A.; Wolke, C. T.; Johnson, C. J.; Johnson, M. A.; Heine, N.; Gewinner, S.; Schollkopf, W.; Esser, T. K.; Fagiani, M. R.; Knorke, H.; Asmis, K. R. Site-Specific Vibrational Spectral Signatures of Water Molecules in the Magic $H_3O^+(H_2O)_{20}$ and $Cs^+(H_2O)_{20}$ Clusters. *Proc. Natl. Acad. Sci. U. S. A.* **2014,** *111* (51), 18132-18137.

32. Miyazaki, M.; Fujii, A.; Ebata, T.; Mikami, N. Infrared spectroscopic evidence for protonated water clusters forming nanoscale cages. *Science* **2004,** *304* (5674), 1134-1137.

33. Schaefer, J.; Backus, E. H. G.; Nagata, Y.; Bonn, M. Both Inter- and Intramolecular Coupling of O-H Groups Determine the Vibrational Response of the Water/Air Interface. *J Phys Chem Lett* **2016,** *7* (22), 4591-4595.

34. Wei, X.; Miranda, P. B.; Zhang, C.; Shen, Y. R. Sum-frequency spectroscopic studies of ice interfaces. *Physical Review B* **2002,** *66* (8), 085401.

35. Smit, W. J.; Tang, F. J.; Sanchez, M. A.; Backus, E. H. G.; Xu, L. M.; Hasegawa, T.; Bonn, M.; Bakker, H. J.; Nagata, Y. Excess Hydrogen Bond at the Ice-Vapor Interface around 200 K. *Phys Rev Lett* **2017,** *119* (13), 133003.

36. Schulz, F.; Hartke, B. Structural information on alkali cation microhydration clusters from infrared spectra. *Phys. Chem. Chem. Phys.* **2003,** *5* (22), 5021-5030.

37. Anick, D. J. Topology-energy relationships and lowest energy configurations for pentagonal dodecahedral, (H2O)(20)X clusters, X=empty, H2O, NH3, H3O+: The importance of O-topology. *Journal of Chemical Physics* **2010,** *132* (16), 164311.

38. Ohno, K.; Okimura, M.; Akai, N.; Katsumoto, Y. The effect of cooperative hydrogen bonding on the OH stretching-band shift for water clusters studied by matrix-isolation infrared spectroscopy and density functional theory. *Physical chemistry chemical physics : PCCP* **2005,** *7* (16), 3005-3014.

39. Tainter, C. J.; Ni, Y.; Shi, L.; Skinner, J. L. Hydrogen Bonding and OH-Stretch Spectroscopy in Water: Hexamer (Cage), Liquid Surface, Liquid, and Ice. *Journal of Physical Chemistry Letters* **2013,** *4* (1), 12-17.

40. Wolke, C. T.; Fournier, J. A.; Miliordos, E.; Kathmann, S. M.; Xantheas, S. S.; Johnson, M. A. Isotopomer-Selective Spectra of a Single Intact H_2O Molecule in the $Cs^+(D_2O)_5H_2O$ Isotopologue: Going Beyond Pattern Recognition to Harvest the Structural Information Encoded in Vibrational Spectra. *J. Chem. Phys.* **2016,** *144* (7), 074305.

41. Zatula, A. S.; Ryding, M. J.; Andersson, P. U.; Uggerud, E. Proton Mobility and Stability of Water Clusters Containing Alkali Metal Ions. *Int. J. Mass Spec.* **2012,** *330*, 191-199.

42. Nagata, Y.; Pool, R. E.; Backus, E. H. G.; Bonn, M. Nuclear Quantum Effects Affect Bond Orientation of Water at the Water-Vapor Interface. *Phys Rev Lett* **2012,** *109* (22), 226101.

43. Sibert, E. L.; Tabor, D. P.; Kidwell, N. M.; Dean, J. C.; Zwier, T. S. Fermi Resonance Effects in the Vibrational Spectroscopy of Methyl and Methoxy Groups. *J. Phys. Chem. A* **2014,** *118* (47), 11272-11281.

44. Gruenbaum, S. M.; Tainter, C. J.; Shi, L.; Ni, Y.; Skinner, J. L. Robustness of Frequency, Transition Dipole, and Coupling Maps for Water Vibrational Spectroscopy. *Journal of Chemical Theory and Computation* **2013,** *9* (7), 3109-3117.

45. Robertson, W. H.; Weddle, G. H.; Kelley, J. A.; Johnson, M. A. Solvation of the $Cl^{-}\cdot H_2O$ Complex in CCl_4 Clusters: The Effect of Solvent-Mediated Charge Redistribution on the Ionic H-Bond. *J. Phys. Chem. A* **2002,** *106*, 1205-1209.

46. Craig, S. M.; Menges, F. S.; Duong, C. H.; Denton, J. K.; Madison, L. R.; McCoy, A. B.; Johnson, M. A. Hidden Role of Intermolecular Proton Transfer in the Anomalously Diffuse Vibrational Spectrum of a Trapped Hydronium Ion. *Proc. Natl. Acad. Sci. USA* **2017,** *114* (24), E4706-E4713.

47. Dzugan, L. C.; DiRisio, R. J.; Madison, L. R.; McCoy, A. B. Spectral signatures of proton delocalization in $H^{+}(H_2O)$(n=1-4) ions. *Faraday Discuss.* **2018,** *212*, 443-466.

CHAPTER 7

Unraveling the Controlling Factors of OH Frequency: Isolating the Contributions of Specific Network Sites to the Interfacial Vibrational Spectrum of Water with Isotopomer-Selective Spectroscopy of Cold Clusters

The material in this chapter is adapted with permission from Yang, Nan, Thien Khuu, Sayoni Mitra, Mark A. Johnson, Ryan DiRisio, Anne B. McCoy, Evangelos Miliordos, and Sotiris S. Xantheas. "Deconstructing water's diffuse OH stretching vibrational spectrum with cold clusters." The Journal of Physical Chemistry A (2020).

7.1 Introduction

In Chapter 6, we explored two types of water molecules imbedded in an extended H-bond network and their spectral features. In this Chapter, we extend that study and exploit the unique properties of water cluster cage structures, formed upon hydration of various cations including alkali metal ions, ammonium and methyl ammonium, to establish how the topology of the extended local network controls the vibrational signatures of water molecules at the interface. This involves detection of the two correlated OH stretching transitions of the same H_2O molecule embedded in cold, size-selected $Li^+ \cdot (H_2O)(D_2O)_{19}$, $Na^+ \cdot (H_2O)(D_2O)_{19}$, $Cs^+ \cdot (H_2O)(D_2O)_{19}$, $CH_3NH_3^+ \cdot (H_2O)(D_2O)_{20}$ and $NH_4^+ \cdot (H_2O)(D_2O)_{22}$ clusters with isotopomer-selective two-color, IR-IR photodissociation spectroscopy. The different cage structures adopted by this series sample great variety of H-bonding network sites hence allowing direct observation of the spectral signatures of all types of water molecules present on the interface as well as comparison between the same type of water molecules that are residing in slightly different H-bond environments. Such observations allow us to establish a frequency map for each type of water molecules as well as rules for determining the OH frequencies based on its H-bond network. With the aid of theoretical calculations, we propose a qualitative scheme for predicting the OH frequency according to its first and second shell hydrogen bond partners.

The molecular nature of the water surface is an important feature of interfacial chemistry ranging from that of aerosols in the troposphere to the acceleration of reactions in mesoscopic droplets.[1] Spectroscopic probes of the interfacial water structure are available using infrared sum-frequency generation (SFG)[2] which has been recently

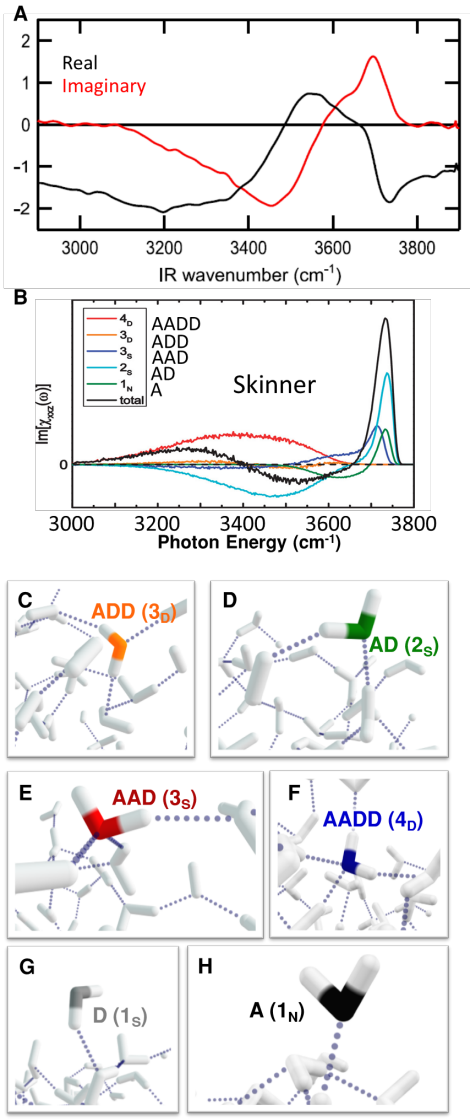

Figure 7.1: Theoretical decomposition of the SFG $\chi^{(2)}$ spectrum of the air-water interface to reveal the contributions of water molecules in specific local network sites. (A) Complex $\chi^{(2)}$ spectra of water with the real part in black and imaginary part in red, reproduced from ref.19 with permission. (B) Theoretical analysis of contribution from different types of water to $\chi^{(2)}$ spectra's the imaginary part reproduced from ref.8 with permission. (C-H) example structures of different types of water molecules on the interface where A denotes H-bond acceptor and D denotes H-bond donor.

enhanced using optical heterodyne detection[3-6] of the up-conversion signal to yield the phase of the polarization response across the spectrum. This information has provided important benchmarks for theoretical simulations of the spectrum, which in turn yield local, molecular level pictures for the sites that contribute to various regions across the spectrum.[7-8] Recent advances in SFG spectroscopy allowed accurate determination of the complex $\chi^{(2)}$ spectrum of the air water interface.[9] Figure 7.1 includes a summary of experimental complex SFG spectra (Fig. 7.1A) and the theoretical imaginary spectrum (black trace in Fig. 7.1B) where the sign of the Im $\chi^{(2)}$ spectra encodes frequency and orientation of the involved OH oscillators. The theoretical effort from Skinner and coworkers further dissects the contributions from various types of water molecules on the air-water interface classified according to their hydrogen bond acceptor (A) and donor (D) numbers. Each type of water molecule (Representative structures of all types of water molecules present at the interface are displayed in Figure 7.1C-H.) displays different spectral signatures which illustrates the heterogeneous nature of the diffuse absorptions. The sharp band around 3700 cm^{-1} can be readily assigned to the free OH feature arising from three possible candidates (A, AD, and AAD) whereas the assignments of their corresponding bound OH's frequencies remains unknown. The assignments of different parts of the bound OH region in the SFG spectrum is under active discussion and the interpretation of the spectra shapes are even more challenging compare to bulk water due to possible signal cancelation arising from positive and negative features at the same frequency from different types of water molecules. For example, the assignment of the 3500cm^{-1} region as well as the difference between the region below and above it and their influence on the intensity profile as well as spectral dynamics remains controversial.[4, 10-13]

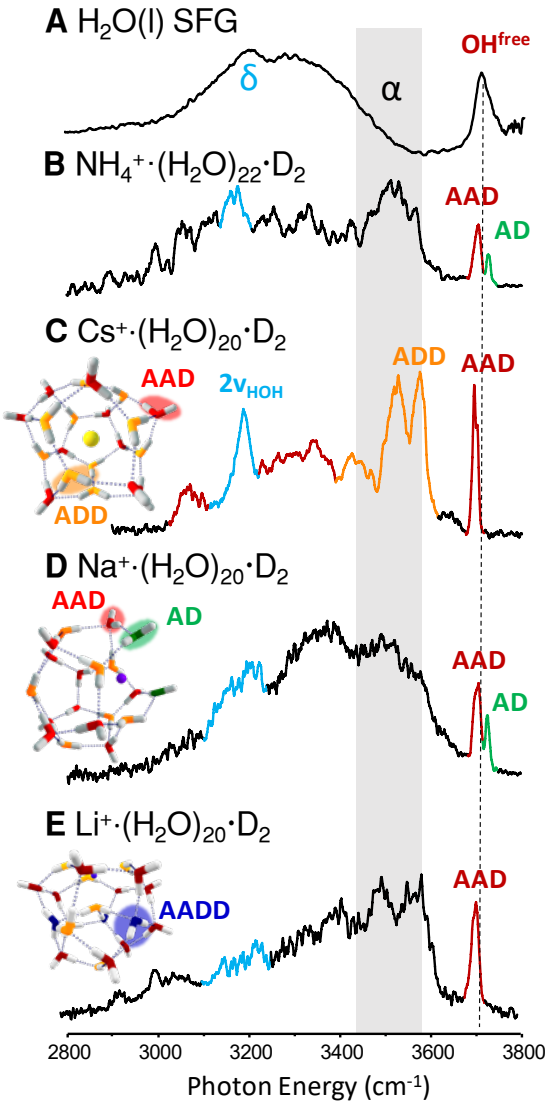

Figure 7.2: SFG intensity spectra of the air water interface compared to the spectra of various water clusters in the OH region. (A) SFG intensity ($|\chi^{(2)}|^2$) spectra of water reproduced from ref.5 with permission. δ denotes the bend overtone ($2\nu_{HOH}$) transition and α denotes the controversial 3500 cm^{-1} region. (B-E) Vibrational predissociation spectra recorded with an D_2 messenger tag and representative structures of $NH_4^+\cdot(H_2O)_{22}$, $Cs^+\cdot(H_2O)_{20}$, $Na^+\cdot(H_2O)_{20}$, and $Li^+\cdot(H_2O)_{20}$. OH bands and water molecules in the structures are color coded according to their types.

Experimental spectra of all types of water molecules presence at the interface can be especially useful for interpreting the structural information contained in the interfacial vibrational spectra.

Complimentary to the theoretical effort to disentangle contributions from different types of water molecules to the interface spectra of water, cryogenically cooled ionic water clusters provide the unique opportunity to reveal the spectral features of an intact H_2O molecule imbedded in a heavy water hydrogen bond network. The isotopic scrambling that produces HDO in the bulk isotope dilution experiments are suppressed even at room temperature due to the absence of excess proton.[14-15] This removes the intermolecular coupling which causes diffusive excitonic behaviors[16] that blurs out site specific spectral contributions while preserving the correlated absorption as well as the intramolecular coupling of the two OH oscillators on the same water molecule. Such capability was demonstrated previously on Cs water clusters where the spectral signatures of single H_2O molecules occupying different H-bonding sites on isotopically labeled water clusters were isolated with IR-IR double resonance hole-burning technique using a triple-focusing, cryogenic photofragmentation mass spectrometer.[17-18]. The previous study isolated spectral signatures of the OH groups on AAD and ADD water molecules as well as the contribution from the bend overtone (Fig. 7.2C). It does not, however, contain other types of water molecules such as AD and AADD, which also contribute significantly to the SFG spectra of water air interface (Fig. 7.2A) [5, 19] according to the theoretical analysis reproduced in figure 7.1A[8, 20].

7.2 Results and Discussion

In this study, we explore various different charge carrier ions in different size water clusters to provide a variety of H-bond network structures (Fig. 7.2B-E structure inserts) which encompass a collection of A, D, AD, ADD, AAD, and AADD type water molecules embedded in different hydrogen bond environments. Within each ionic species, there are various isomers that share the same oxygen atom framework and differ only in the H-bond topology in terms of where the OH donor points to.[21] These isomers are close in energy and are present under our experimental conditions, hence providing even greater variety of H-bond environments that closely resemble those experienced by interfacial water molecules in liquid or amorphous ice. As a result, these different water cages all display a similar pattern to that of the interface, namely free OH features and a broad bound OH envelope (Fig. 7.2B-E) that spans the entire OH region of the SFG spectra. In addition, the bend overtone features observed in the SFG spectra (δ band, Fig. 7.2A) are also present in the all H_2O cluster species (turquoise bands, Fig. 7.2). Therefore, they serve as microscopic models for the interface due to similar disruption of continuous H-bond network at the boundary and great variety of H-bond arrangements.[18, 22] In addition to the previously determined features for the AAD and ADD types of water molecules, the $NH_4^+ \cdot (H_2O)_{22}$ and $Na^+ \cdot (H_2O)_{20}$ spectra (Fig. 7.2 B, D green) display an extra free OH feature at higher frequency than the AAD water molecules' free OH, which signals the existence of AD water molecules.[23] The companion bound OH feature on the same AD water molecule can be obtained through isotopomer specific double resonance hole burning experiment on the $NH_4^+ \cdot (H_2O)(D_2O)_{21}$ and $Na^+ \cdot (H_2O)(D_2O)_{19}$ isotopologues by fixing the probe laser on the free OH transition associated with the AD water (green

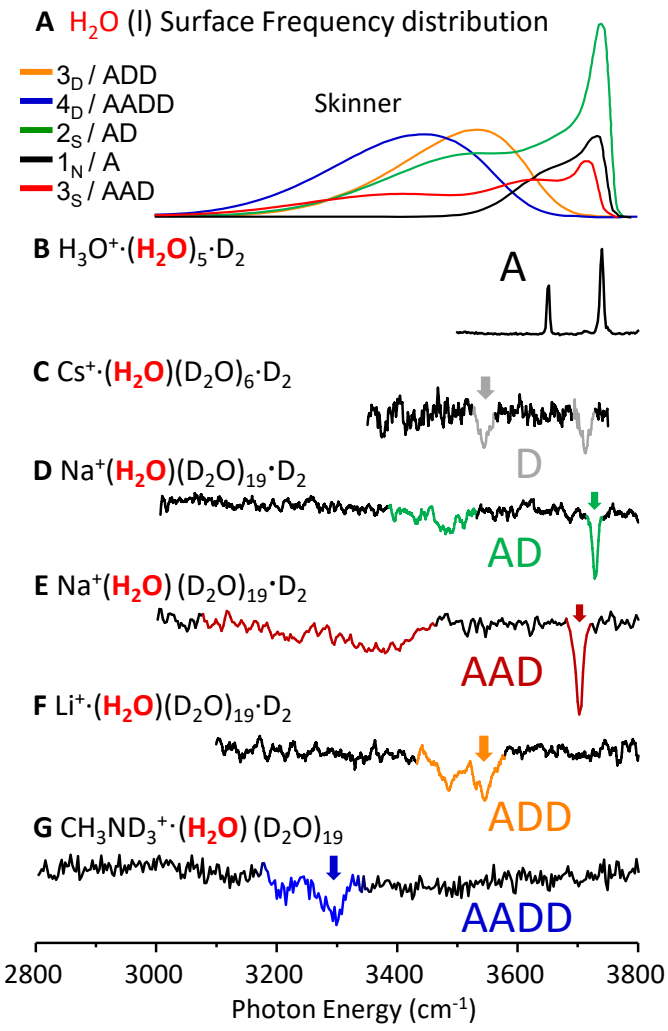

Figure 7.3: Theoretically calculated OH frequency distribution at the air water interface compared with examples of each type of water molecule's spectra obtained with finite size water clusters. (A) OH frequency distribution at the surface reproduced from ref.8 with permission. (B) Vibrational predissociation spectra of $H_3O^+\cdot(H_2O)_5$. (C-G) Spectra of each type of water molecules present on the surface obtained with isotopomer selective double resonance hole burning technique applied to various water clusters with the probe laser position labeled with the colored arrows.

features in Fig. 7.2) and scanning a bleaching laser upstream. When the bleaching laser is on resonance with the isotopomer population with an H_2O molecule in the AD site, it depletes the population via photodissociation and results in a decrease or dip in the probe laser signal. More experimental details are included in Chapter 2 and 6. Figure 7.3 contains examples from each type of water molecules with different H-bonding environments. The hole-burning spectra probing the AD water molecule is displayed in figure 7.3D. A clear bound OH feature is detected around 3500 cm^{-1} in addition to the tell-tale AD free OH feature. This bound OH frequency falls in the same region as the ADD water molecules (Fig. 7.3F) and provides an additional possible assignment for the interfacial spectra at this region.

The single-acceptor (A type) dangling water molecule displays the typical symmetric/antisymmetric OH stretch pattern that is present in many smaller cationic water clusters.[24-25] Since these small water clusters usually only have A type water molecules, the only feature in the free OH region is the symmetric and asymmetric OH stretches. The two free OH features in Fig. 3B agree well with the theoretical prediction of the frequency distribution of the interfacial A type water (Fig. 7.3A, black trace). Note that even though SFG spectra's intensity patterns are governed by different rules than the linear vibrational spectra, the underlying OH oscillator frequency distribution is influenced in the same manner by the H-bonding environments. Hence, we focus here on the comparison between our experimental results with the computed OH frequency distribution on the interface. The correlated OH absorption of all other types of water molecules are isolated with isotopomer specific hole burning technique described above (Fig. 7.3C-G). The observed spectral features fall within the envelope predicted by

Skinner and coworkers. [8, 20] However the theoretically predicted frequency distribution of AD and AAD seems to have an additional collection of frequencies around 3610 cm^{-1} compared with the site-specific spectra (Fig. 7.3D,E). These frequencies is located between the free OH and bound OH features observed in the site-specific spectra and corresponds to the low intensity region in the SFG intensity spectra which could be attributed to either signal cancelation or absence of OH oscillators in the frequency range. In general, the A, D, AD, and AAD types account for the free OH features whereas the bound OH region has contributions from all types of water molecules excluding the A type. An interesting effect is that accepting an extra H-bond (D vs. AD, AD vs. AAD, ADD vs. AADD) redshifts the bound OH feature, which signifies reinforcement of the hydrogen bond through cooperativity effect. Another phenomenon worth noticing is that the four coordinated water's (AADD) features are higher in frequency compared to those observed in crystalline ice, ice interface, and ice-like water nanodroplets.[26-30] This can be attributed to the lack of ice-like structure around the AADD water, which is expected in these systems where the AADD water molecules are at or near the cluster boundary. Meanwhile, the significantly broader envelope in the theoretical frequency distribution can be attributed to thermal broadening and the distribution of slightly different H-bond environments experienced by the same type of water molecules. For example, depending on what type of water molecule the AAD water's bound OH is donating to or accepting from, the frequency of the OH feature can appear anywhere from 2800 to 3400 cm^{-1}. To explore the effect of the H-bond environments, we isolated the spectral features of many of the same type water molecules situated in slightly different H-bond environments

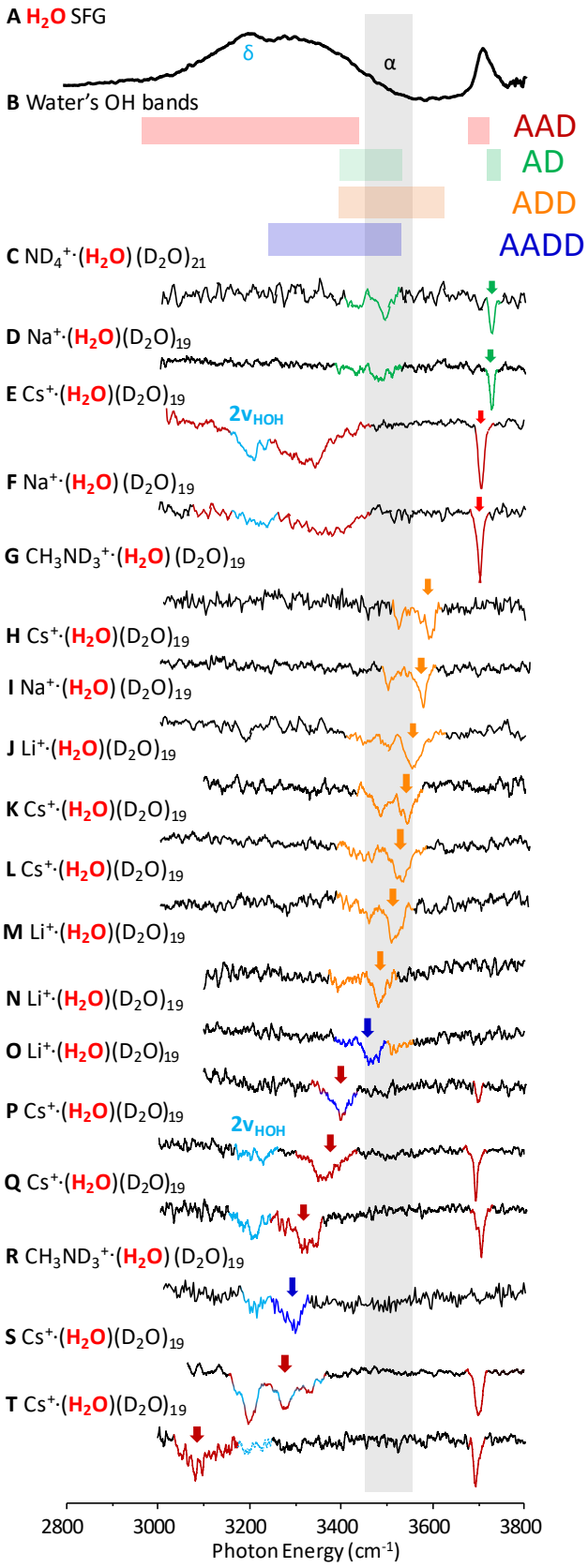
A H2O SFG
δ
α
B Water's OH bands
AAD
AD
ADD
AADD
C ND4+·(H2O) (D2O)21
D Na+·(H2O)(D2O)19
E Cs+·(H2O)(D2O)19
2νHOH
F Na+·(H2O) (D2O)19
G CH3ND3+·(H2O) (D2O)19
H Cs+·(H2O)(D2O)19
I Na+·(H2O) (D2O)19
J Li+·(H2O)(D2O)19
K Cs+·(H2O)(D2O)19
L Cs+·(H2O)(D2O)19
M Li+·(H2O)(D2O)19
N Li+·(H2O)(D2O)19
O Li+·(H2O)(D2O)19
P Cs+·(H2O)(D2O)19
2νHOH
Q Cs+·(H2O)(D2O)19
R CH3ND3+·(H2O) (D2O)19
S Cs+·(H2O)(D2O)19
T Cs+·(H2O)(D2O)19
2800
3000
3200
3400
3600
3800
Photon Energy (cm-1)

Figure 7.4: SFG intensity spectra compared with various types of water molecule's spectra obtained with finite size water clusters. (A) OH frequency distribution at the surface. (B) OH band regions divided by types of water molecules summarized from the isotopomer specific hole burning spectra in (C-T). (C-T) Spectra of various types of water molecules imbedded in various water clusters with the probe laser position labeled with colored arrows. Bands are colored according to the water molecule's types and mixing color indicates mixed feature from different origins.

(Fig.7.4). The comparison between calculated frequencies and experimentally observed frequencies in these cluster ions are included in figure 7.5-7.9.

The frequencies of the OH oscillators on the AD water are robust regardless of their H-bond environments (Fig. 7.4 C,D). When the AD water accepts an additional hydrogen bond and becomes an AAD water, the bound OH frequency and free OH frequency both redshift with the bound OH being significantly more sensitive to the H-bond environment (Fig. 7.4 E,F). The spectra in figure 7.4 E and F are obtained by probing the free OH features which are common to many different AAD water molecules that have significantly different bound OH frequencies (Fig. 7.4 P, Q, S, and T). Probing on the overlapping free OH features result in a dip spectrum that encompasses bound OH features displayed by all the corresponding AAD water molecules present in the cluster ensemble. The contribution from each different AAD water molecule can be further separated by probing on the bound OH region. Interestingly, in addition to the bound OH feature, there is another feature in the same frequency range which is a result of the Fermi resonance between the OH stretch and the HOH bend overtone on the same water molecule. The bend overtone band is observed in the SFG spectra as well and has significant consequences in the relaxation dynamics of the bound OH oscillators [11, 31]. As mentioned before, the variation in H-bond environment of the first shell water molecules connected to the OH oscillators of interest have significant effects on the bound OH frequencies. For example, when the AAD water molecule's OH donates to an ADD water molecule, the donor OH frequency is more redshifted compare to the case where the OH donates to an AAD molecule (Chapter 6, Figure 6.3).[18] One example is the OH frequencies sorted by their first shell water type displayed in Fig. 7.6. We propose a

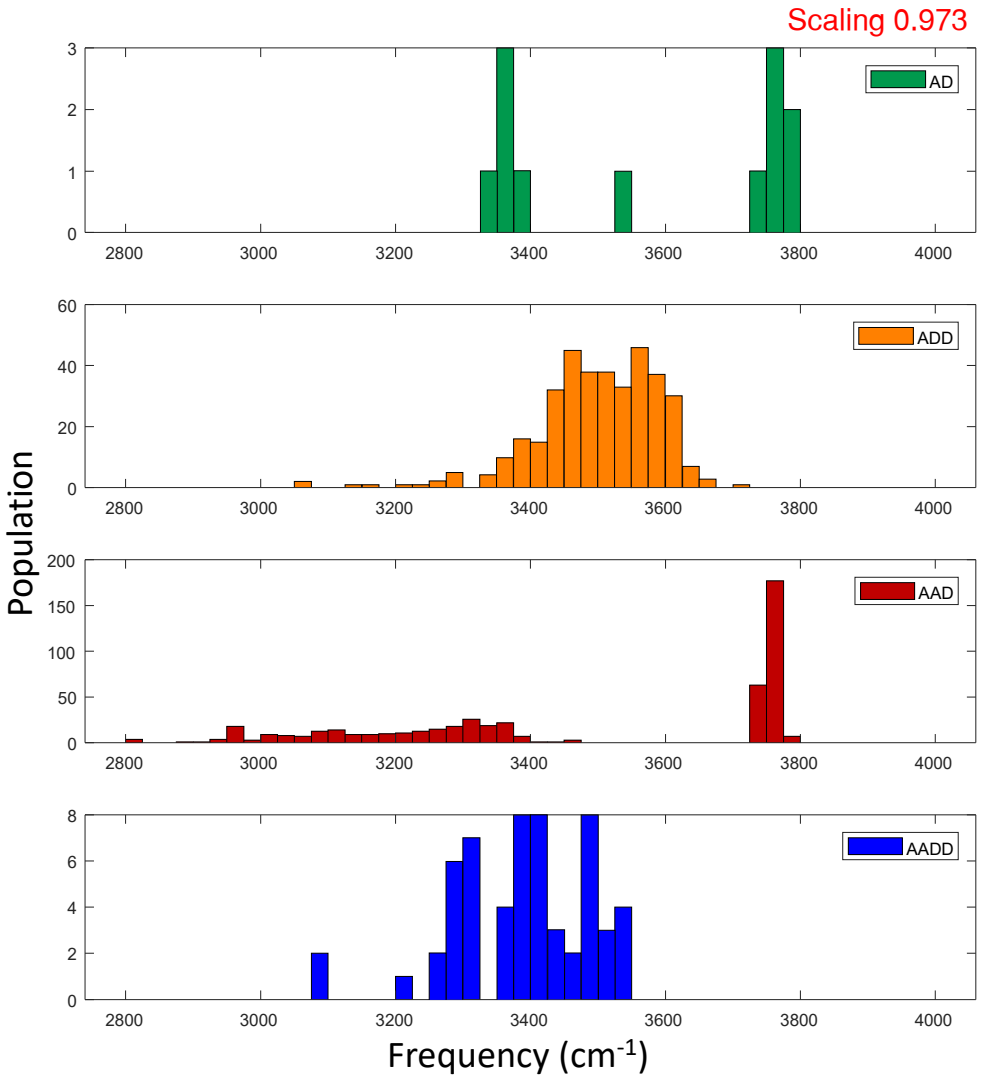

Figure 7.5: Frequency distribution of different types of H_2O molecules imbedded in $(D_2O)n$ cages. The harmonic frequencies of all isotopomers of $Li^+\cdot(H_2O)(D_2O)_{19}$, $Na^+\cdot(H_2O)(D_2O)_{19}$, $Cs^+\cdot(H_2O)(D_2O)_{19}$, and $CH_3NH_3^+\cdot(H_2O)(D_2O)_{20}$ are calculated at the B3LYP/6-31++G** level of theory and basis with the LANL2DZ pseudopotential for the Cs atom. The calculated frequencies are scaled by a 0.973 scaling factor. Multiple structural isomers are included for some of the species. Details of the harmonic frequencies for each cluster are displayed in Fig. 7.6-7.9.

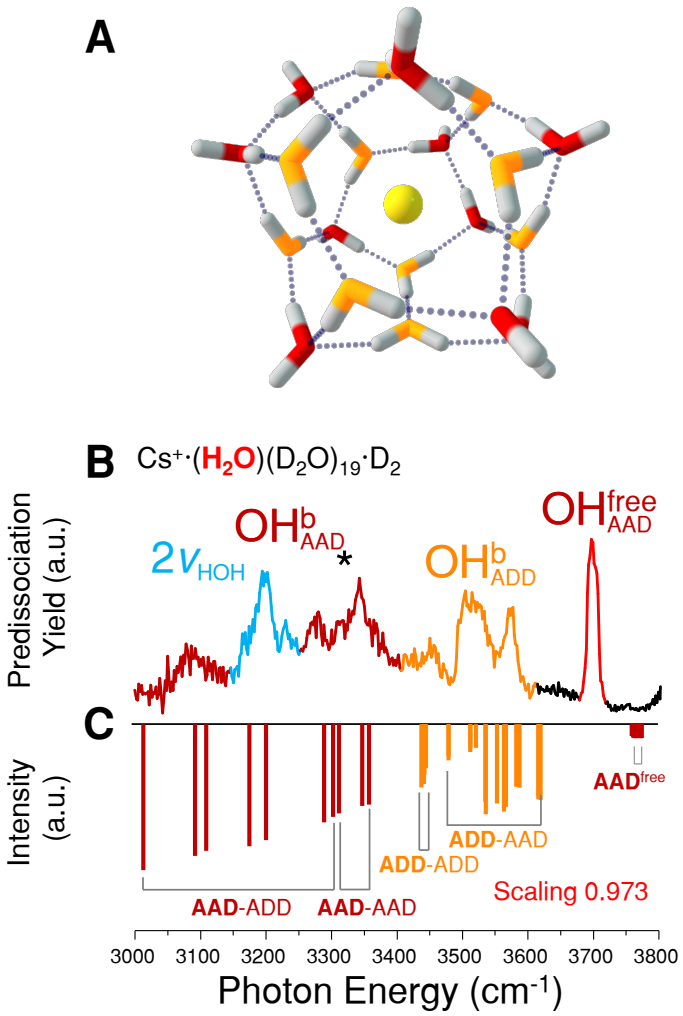

Figure 7.6: Comparison between the experimental and theoretical vibrational spectra of $Cs^+\cdot(H_2O)(D_2O)_{19}$. (A) Representative low energy structure of $Cs^+\cdot(H_2O)_{20}$ (B)Single laser vibrational predissociation spectra of all isotopomers of the $Cs^+\cdot(H_2O)(D_2O)_{19}$. (C)Harmonic spectra calculated at the B3LYP/6-31++G** level of theory and basis with the LANL2DZ pseudopotential for the Cs atom. The calculated frequencies are scaled by a 0.973 scaling factor. The labels consist of the water molecule type the OH group of interest is residing on and the water molecule's type that the OH group of interest is donating to. For example, **AAD**-ADD denotes the OH group on an AAD molecule donating to an AAD molecule.

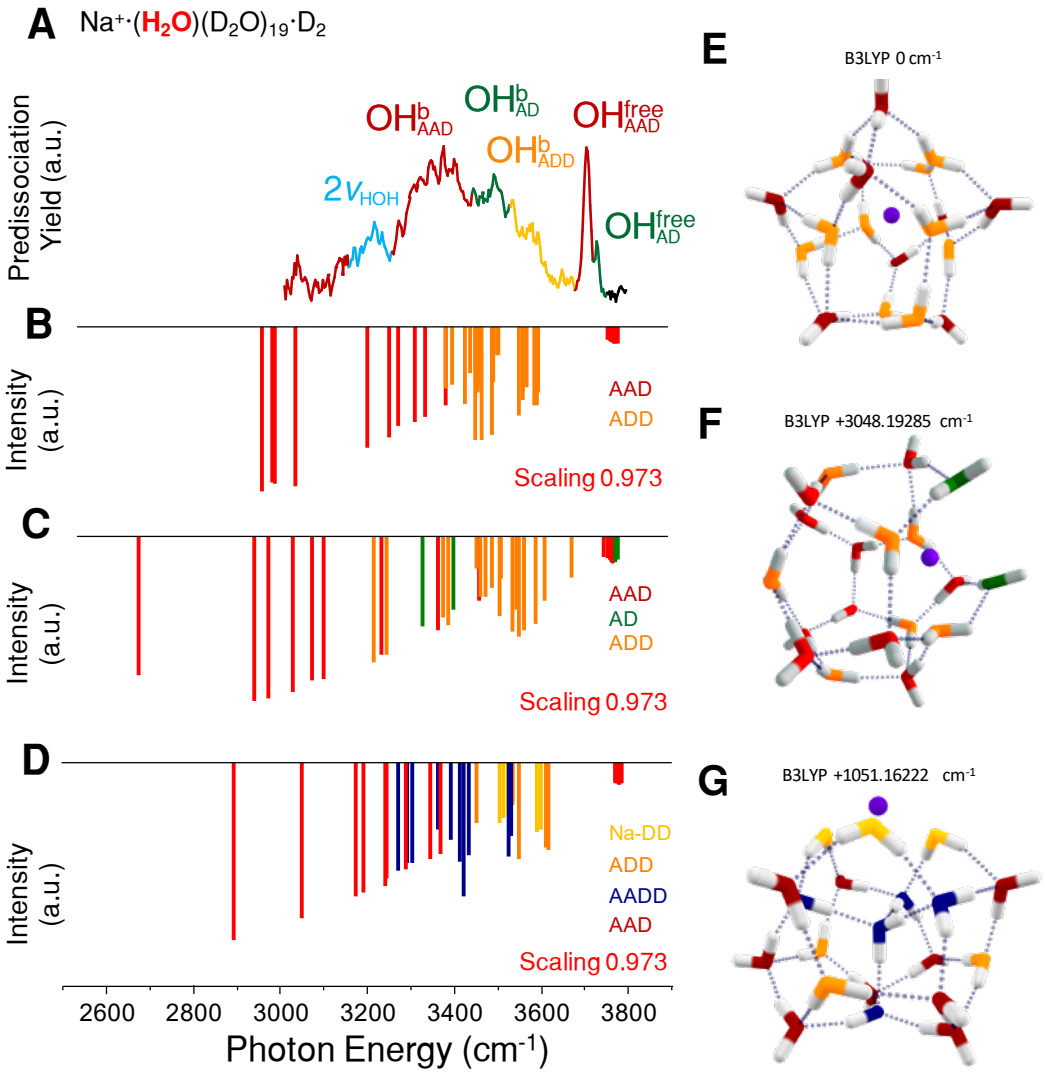

Figure 7.7: Comparison between the experimental and theoretical vibrational spectra of $Na^+·(H_2O)(D_2O)_{19}$. (A)Single laser vibrational predissociation spectra of all isotopomers of the $Na^+·(H_2O)(D_2O)_{19}$. (B-D) Harmonic spectra calculated at the B3LYP/6-31++G** level of theory and basis. The calculated frequencies are scaled by a 0.973 scaling factor. (E-G) Representative structures of $Na^+·(H_2O)_{20}$ with their relative energies. The spectrum in (B) corresponds to the structure displayed in (E), the spectrum in (C) corresponds to the structure in (F) and the spectrum in (D) corresponds to the structure in (G).

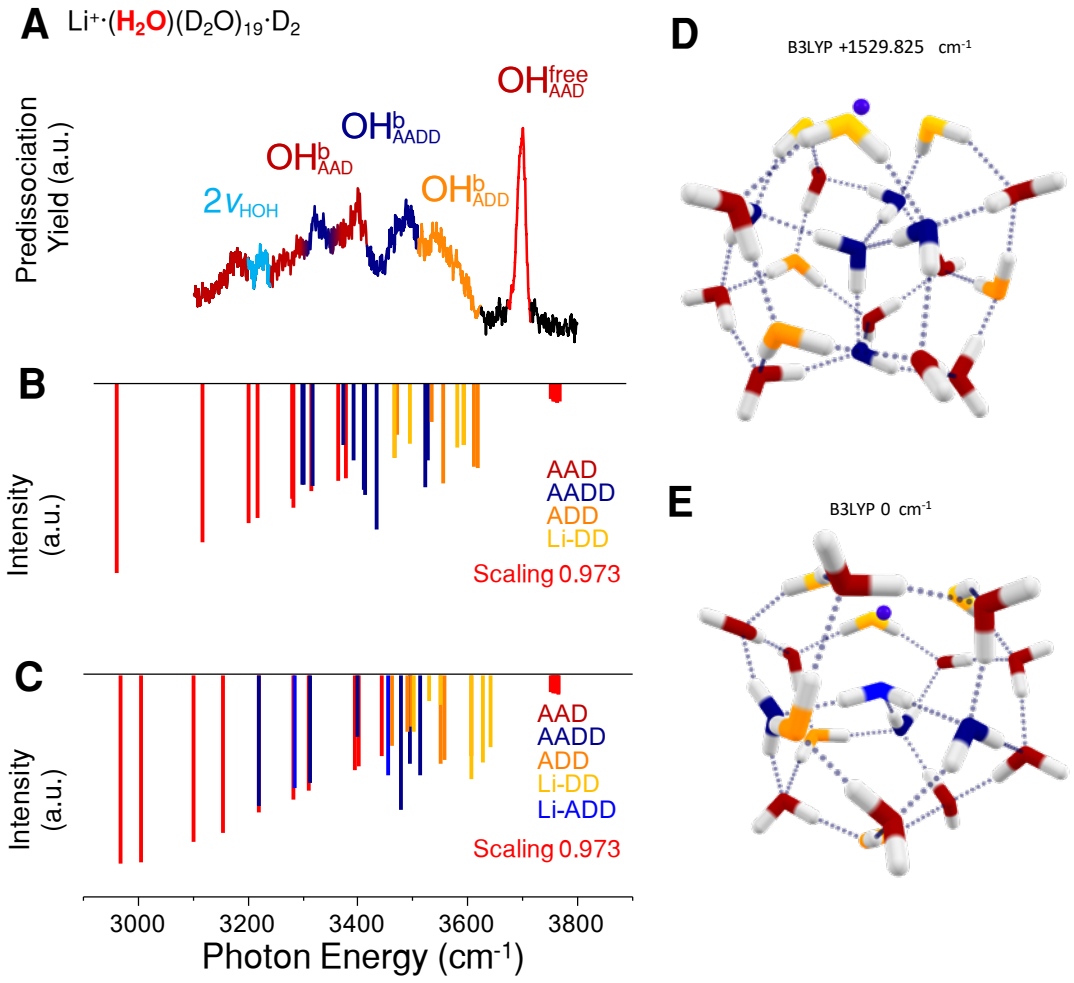

Figure 7.8: Comparison between the experimental and theoretical vibrational spectra of $Li^+\cdot(H_2O)(D_2O)_{19}$. (A)Single laser vibrational predissociation spectra of all isotopomers of the $Li^+\cdot(H_2O)(D_2O)_{19}$. (B,C) Harmonic spectra calculated at the B3LYP/6-31++G** level of theory and basis. The calculated frequencies are scaled by a 0.973 scaling factor. (D,E) Representative structures of $Li^+\cdot(H_2O)_{20}$ with their relative energies. The spectrum in (B) corresponds to the structure displayed in (D), and the spectrum in (C) corresponds to the structure in (E).

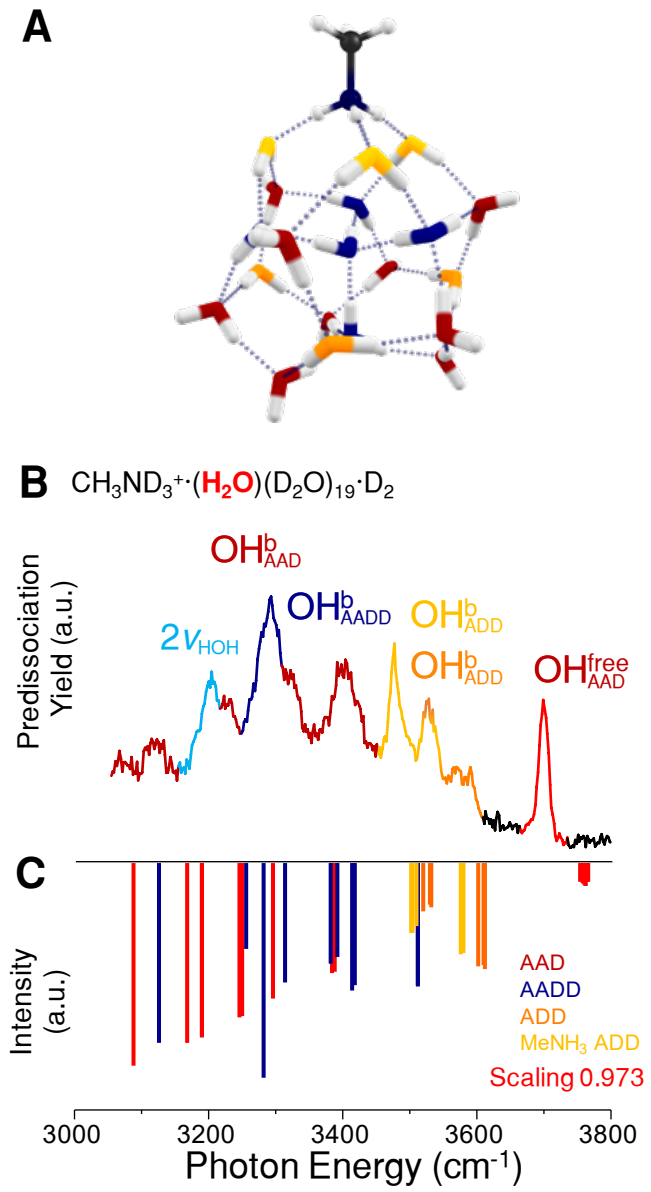

Figure 7.9: Comparison between the experimental and theoretical vibrational spectra of $CH_3ND_3^+\cdot(H_2O)(D_2O)_{19}$. (A) Representative low energy structure of $CH_3NH_3^+\cdot(H_2O)_{20}$ (B)Single laser vibrational predissociation spectra of all isotopomers of the $CH_3ND_3^+\cdot(H_2O)(D_2O)_{19}$. (C)Harmonic spectra calculated at the B3LYP/6-31++G** level of theory and basis. The calculated frequencies are scaled by a 0.973 scaling factor.

qualitative model for predicting the OH frequency according to its type, in other words the number of acceptor/donor hydrogen bond it is making (Fig. 7.10). In general, when an OH group approach an lone pair on another water molecule's oxygen, the electron pulls on the hydrogen and causing the OH bond of interest to elongate and red shift in frequency, for example in the D water in Fig S8, the bound OH (horizontal OH) is redshifted compare to the free OH (the black dots indicates the frequency of the OH oscillators with top being the highest frequency or bluest and the bottom being the lowest frequency or reddest). On top of that, when the OH group's oxygen atom accepts an hydrogen bond (the D water molecule turns into an AD water molecule by accepting the hydrogen bond), the first shell donor OH 'pushes' the hydrogen on the OH group of interest and causing it to elongate and red shift in frequency, that scheme is depicted as red arrows in the AD case in Fig. 7.10 where the gray OH on the left donates to the OH of interest and pushes the H atom away (red arrow pointing to the right on top of the OH bond). Furthermore, accepting another hydrogen bond, which turns AD into AAD in Fig. 7.10, will have an additional 'push' on the OH of interest and elongate the OH bond and redshift the frequency even more, which is depicted by the double red arrow on the OH bond of interest. Similar trend also applies when comparing the ADD and AADD water molecules, accepting an additional hydrogen bond in general pushes the H atoms away from the oxygen and redshifts the OH oscillator on the acceptor water molecule. On the other hand if the OH group's partner OH on the same water molecule forms a new H-bond by donating to another water molecule, the acceptor water molecule pulls on the H atom on the partner which also causes a pull on the OH of interest causing it to contract and blueshift in frequency (depicted as left going arrow in the ADD and AADD water

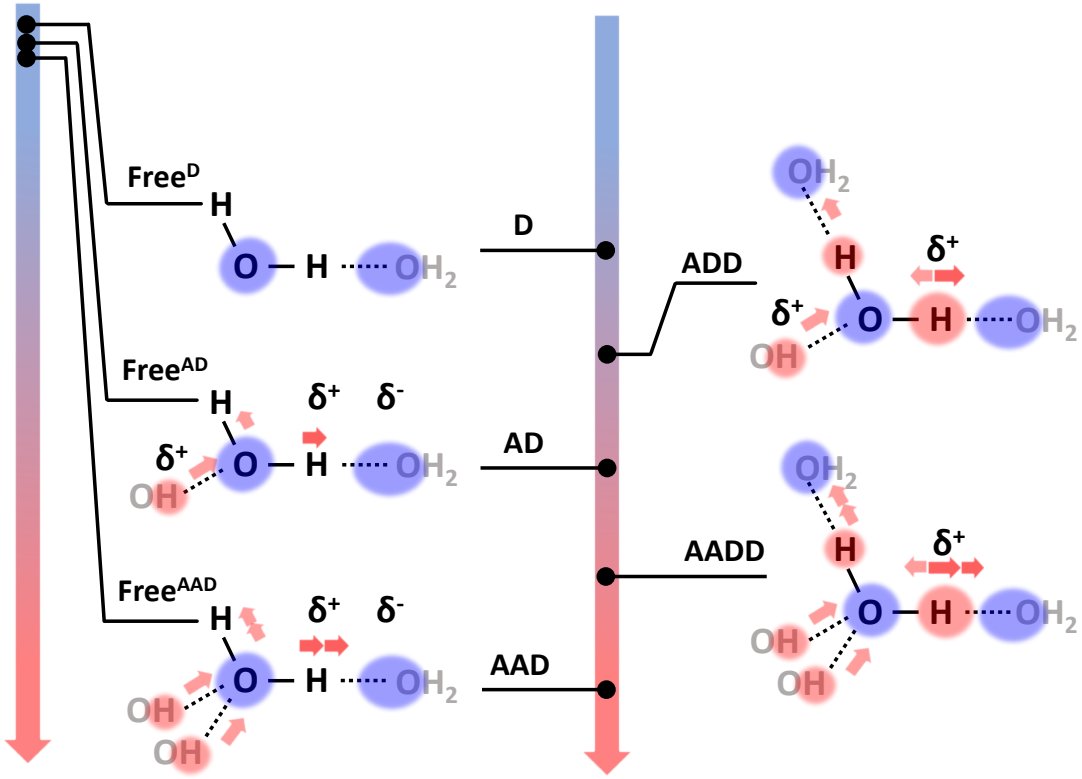

Figure7.10: Dependence of OH oscillator's frequency on the H-bond environments. The OH of interest is labeled by solid O-H bond. The black dots indicate frequency of the OH oscillator where bottom is lowest frequency and top is the highest frequency. The small red arrows are the direction of the hydrogen pushing.

molecules in Fig. 7.10). With that in mind we can predict the AADD water molecule's bond OH is blue shifted relative to that on the AAD molecule, and similarly ADD is blue shifted relative to AD by letting the partner OH donate to another water molecule. Note that the pull and push language applied to the H atom is for the ease of visualization, the electron density plays a role as well by shifting in the opposite direction relative to the H atom, for example, when we use the language of an OH donor approaches the O atom of the OH of interest and pushes the H away, what really happens is the proximity of the OH donor attracts the electron on the oxygen and decreases the electron density on the OH bond of interest hence weakening the OH bond, which has the net effect of elongating the OH bond of interest as if it is pushing the H atom's partial positive charge with its own partial positive charge. At last we can also to the 'hydrogen pushing' analysis on the free OH groups on D, AD and AAD water molecules, when the OH of interest accepts additional H-bonds it pushes the H atom and elongates the free OH bond which results in redshift of the AAD relative to AD then to D water molecules. Summary of the effects of the first shell water molecule's type on the OH frequency is included in Fig. 7.11.

Having established the qualitative 'Hydrogen pushing' model of the first shell environment's influence on the OH stretch frequency, we extend this model to look at the effects of the second shell solvation environments. For example, when an AAD water molecule's bond OH donates to an ADD water molecule vs. an AAD water molecule (Fig. 7.6), the bond OH frequency is influenced by the first shell acceptor water molecule's hydrogen bonds to the second shell water molecules. Specifically, we have established that when an OH bond donates to another water molecule it pulls on the H atom and elongates the OH bond, on top of that effect if the acceptor water (first shell)

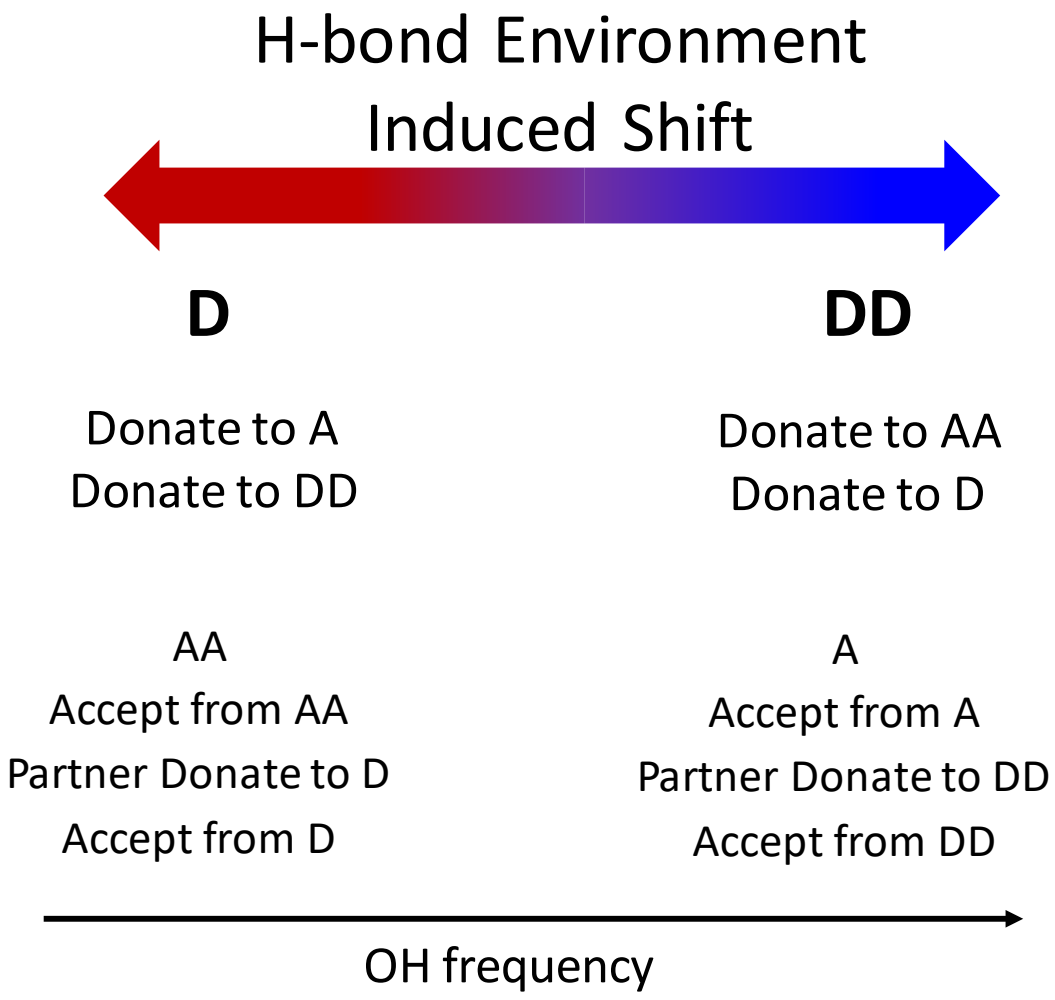

Figure 7.11: Dependency of OH frequency on the H-bonding environment. The colored arrow indicates blue shift and red shift, the A and D labels the type of the water molecule that the OH is residing on. For example, a single donor (D) water's OH stretch is generally lower in frequency compared to the double donor (DD) water molecule. The 'donate to' and 'accept from' labels denote the type of water molecule the OH group of interest is connected to. And the 'partner donates to' labels the H-bond environment the other OH group on the same water molecule is residing in.

donates to another water (second shell), the second shell acceptor pulls on the first shell acceptor which then relays the pulling effect to the OH of interest (Fig. 7.12). Thus, having additional acceptor waters in the second shell makes the first shell acceptor a better acceptor and redshifts the OH of interest, for example donating to an ADD water molecule which has two second shell acceptor water molecules maximizes the redshift (Fig. 7.12) of the OH oscillator under investigation. Similarly when the first shell water accepts an additional hydrogen bond, the additional second shell donor OH pushes the H atom in the opposite direction causing opposite effect (depicted by left going arrow in the AA case in figure 7.13) and causing the OH bond of interest to contract (AA compared with A in figure 7.13). Finally, we exam the first shell donor water molecule and its second shell H-bond partners (Fig. 7.14). Again by applying the same hydrogen pushing scheme when the first shell donor water molecule accepts additional hydrogen bonds it pushes the the H atom on the first shell donor OH towards the OH of interest making it a better donor hence further pushes the H on the OH group of interest away causing more redshift (connected red arrows in Fig. 7.14). With these in mind the most redshifted OH group should be on an AAD water molecule where it accepts from two other AAD water molecules and donates to an ADD water molecules, such scenario would give the most push on the donor side first shell water and the most pull on the acceptor side first shell water. However, it is more complicated when there are effects going in the opposite direction since the extend of pushing or pulling are different, in those cases one needs to carefully chose the reference points by varying one factor at a time to try to predict the OH frequency. These rules are sorted into three tiers by their influence on the OH of interest and summarized in figure 7.11, for example having the partner OH on the same

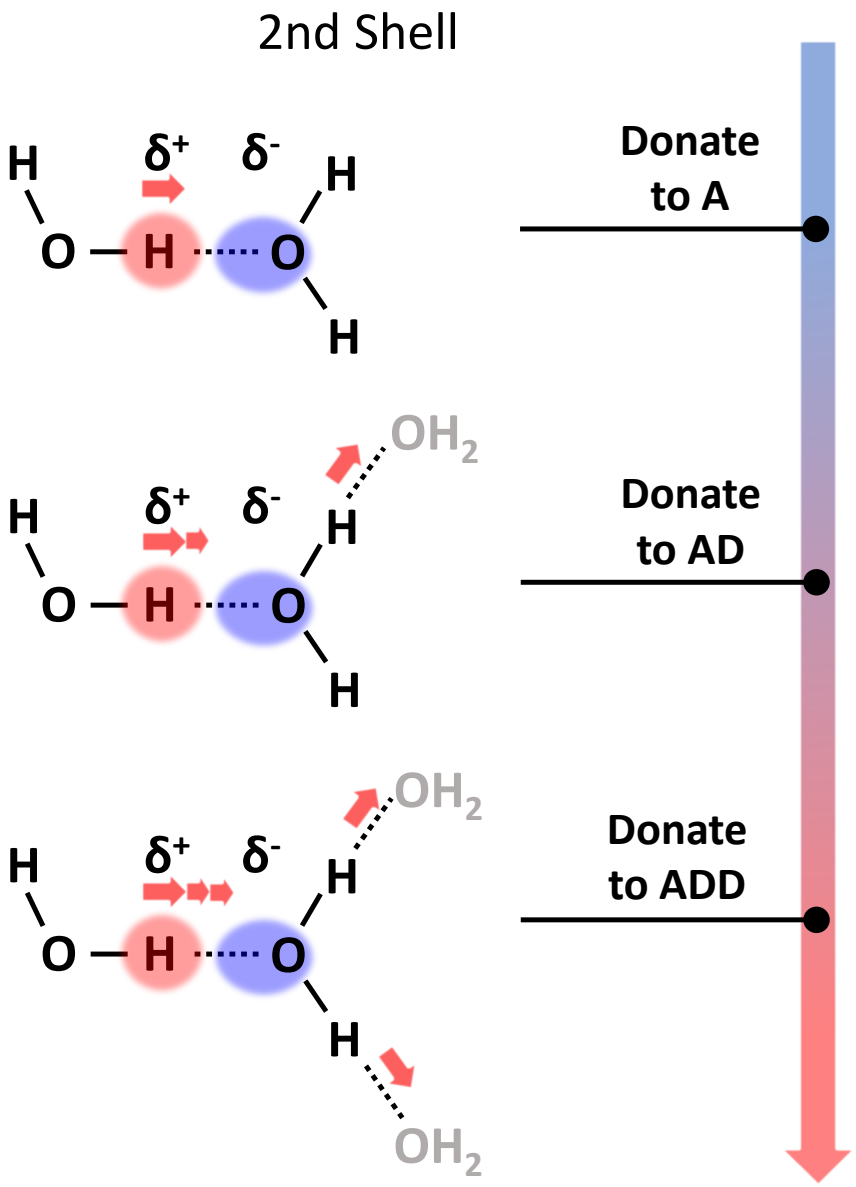

Figure 7.12: Dependence of OH oscillator's frequency on the second shell water H-bond environments. The OH of interest is labeled by solid O-H bond with H highlighted in red spherical shade. The first shell water molecule is also in black whereas the second shell water molecules are in gray. The black dots indicate frequency of the OH oscillator where bottom is lowest frequency and top is the highest frequency. The small red arrows are the direction of the hydrogen pushing.

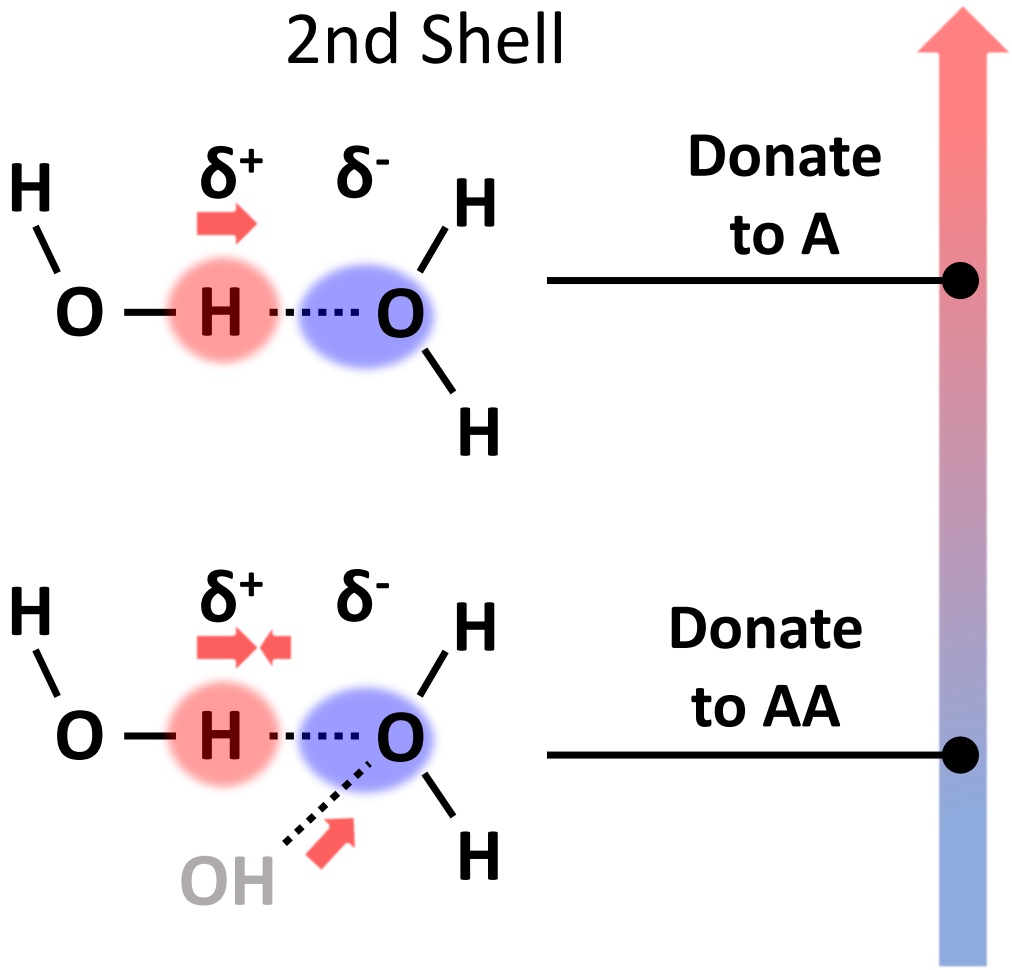

Figure 7.13: Dependence of OH oscillator's frequency on the second shell water H-bond environments. The OH of interest is labeled by solid O-H bond with H highlighted in red spherical shade. The first shell water molecule is also in black whereas the second shell water molecules are in gray. The black dots indicate frequency of the OH oscillator where top is lowest frequency and bottom is the highest frequency. The small red arrows are the direction of the hydrogen pushing.

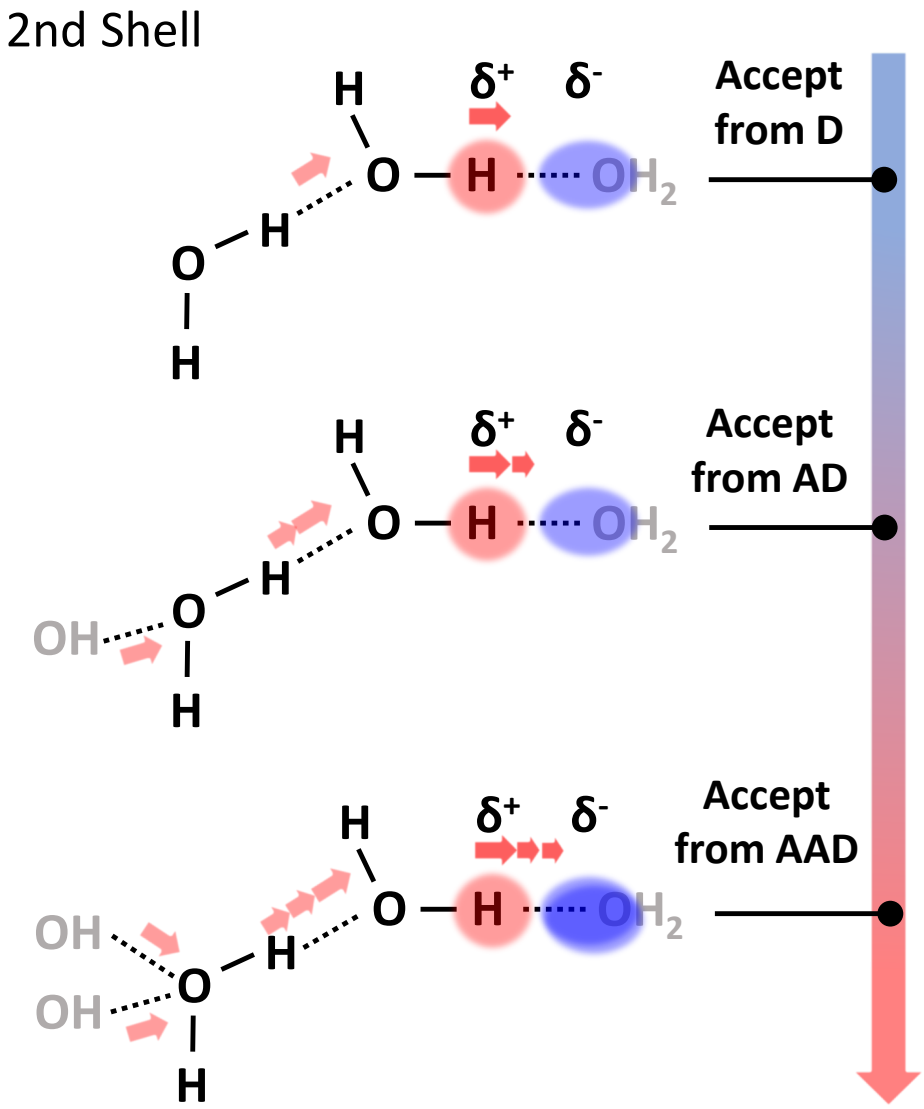

Figure 7.14: Dependence of OH oscillator's frequency on the second shell water H-bond environments. The OH of interest is labeled by solid O-H bond with H highlighted in red spherical shade. The first shell water molecule is also in black whereas the second shell water molecules are in gray. The black dots indicate frequency of the OH oscillator where bottom is lowest frequency and top is the highest frequency. The small red arrows are the direction of the hydrogen pushing.

water molecule forming an additional H bond as a donor (DD compare to D) blueshifts the OH frequency the most compare to other factors that are listed lower, whereas donating to A vs. AA or DD vs. D have comparable effects on the OH frequency of interest. In addition to the qualitative analysis, we also ran a regression tree analysis on the OH frequencies embedded in a large number of different environments (about 200 clusters, 4000 different OH oscillators) which could give a rough estimate of the OH frequency depending on its first and second shell environment (Fig. 7.15). The regression tree agrees with the qualitative rules established in Fig. 7.11.

In addition to the OH features, the variation in H-bond environments is enough to 'tune' the frequency of the OH oscillators around the bend overtone frequency and demonstrates the relation between intensity borrowing and the frequency difference between the OH stretch and the bend overtone. As the OH stretch frequency approaches the bend overtone (~3200 cm^{-1}) the bend overtone intensity increase (Fig. 7.4 O-T), and OH stretches more than 150 cm^{-1} away do not display a significant bend overtone feature, which is consistent with the previously determined coupling constant ~40 cm^{-1} [18]. In addition to AAD water molecules, the ADD water molecule's bound OH frequencies are also subjected to the surrounding water molecule's types. The frequencies of the ADD water molecules can appear anywhere in the 3400-3620 cm^{-1} interval with the two OH stretches ~80 cm^{-1} from each other, which is similar to the expected splitting between two intramolecularly-coupled, near-degenerate OH oscillators. Similar to AD vs. AAD water molecules, when an ADD water molecule accepts an additional H-bond and become an AADD water molecule, the OH frequency redshifts. The four-coordinated water displays similar frequency to those of ADD water molecules when resting on the surface of the

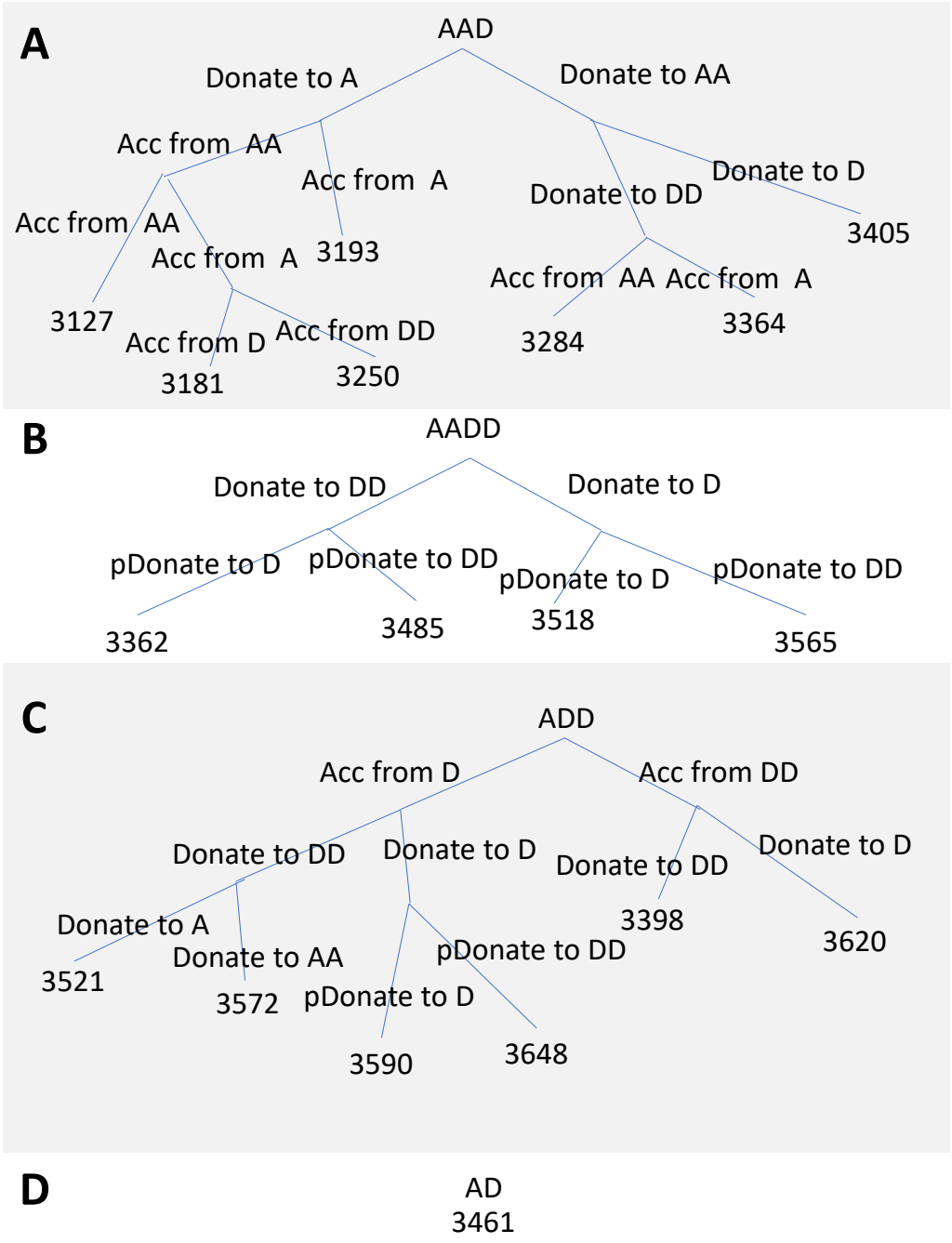

Figure 7.15: Regression tree of OH oscillator's frequency on the H-bond environments. The frequencies are in cm^{-1}.

cage (Fig. 7.4 N, O) consistent with the trend in the harmonic spectra (Fig. 7.8 and 7.9). The extra feature (orange, Fig. 7.4N) is resulted from overlap between the weak OH feature in one of the ADD water molecule (Fig. 7.4J) and the strong OH feature of the AADD water molecule (Fig. 7.4N) in the $Li^+ \cdot (H_2O)(D_2O)_{19}$ cage. The bound OH feature in figure 7.4O is assigned to both the bound OH of the AAD water molecule and the bound OH in the AADD water molecule due to intensity discrepancy between the free OH and the bound OH groups. Normally, the AAD water molecule has a weaker free OH feature and a stronger bound OH that is then broadened and display similar or lower amplitude compare to the free OH at a single frequency. This trend can be seen in all other AAD water molecules (i.e. Fig 4. P, T). Hence, the bound OH feature in figure 7.4O is too strong to be just AAD and therefore assigned to both AAD and AADD water molecules. The higher frequency AADD water molecules likely rest on the surface, whereas the AADD molecule that resides in the center of the cage (Fig. 7.4R) is lower in frequency. Note that the frequencies of these water molecules are high compare to that observed in crystalline ice (~3200 cm^{-1}) and can be explained again by the topology of the first shell water molecules: the close vicinity to the surface boundary disrupts the H-bond network and weakens the H-bonds for the AADD water molecules, whereas residing deeper inside the H-bond network puts less geometric strain on the H-bonds and thus allows it to approach the optimal geometry for four-coordinated water. With these experimental site-specific spectra of water molecules available, an assignment scheme can be established outlining the possible frequency regions for each type of water molecules (Fig. 7.4B). The 3500 cm^{-1} region marks the most complicated region, where OH oscillators from AD, ADD, and AADD water molecules all present. The presence of

four coordinated water's OH stretches in the region as high as 3500 cm^{-1} is especially interesting since the AADD water is not usually discussed in the context of interfacial water spectroscopy and their dynamics.

7.3 Summary

In summary, vibrational spectra of an H_2O molecule residing in various hydrogen bonding environments are isolated by applying trace isotope dilution and isotopomer-specific double-resonance spectroscopy to a collection of cationic water clusters. The number of acceptors and donors on one water molecule has a dominating effect on the frequency of the OH oscillators on that molecule due to cooperativity effects. Additionally, the OH frequency also depends on the type (for example AD type or AADD type) of the first shell water molecules that are in direct contact with the OH group of interest. Specifically, the four-coordinated water molecules display blueshifted frequencies relative to the value found in crystalline ice, likely due to closer proximity to the surface boundary of the H-bond network, thus providing an additional possibility for assigning the interfacial water's spectra. Overall, the comprehensive collection of the spectra of all types of water molecules on the H-bond network boundary provides insights for the interpretation of SFG spectra of water and sets an unambiguous benchmark for the correlated OH absorption frequencies as well as the bend overtone intensity for theoretical predictions. And a hydrogen pushing model for qualitatively predicting the OH frequency is established and a regression tree model is trained to quantitatively predict the OH frequency with information about its first and second shell hydration environments.

7.4 References:

1. Yan, X.; Bain, R. M.; Cooks, R. G. Organic Reactions in Microdroplets: Reaction Acceleration Revealed by Mass Spectrometry. *Angewandte Chemie-International Edition* **2016,** *55* (42), 12960-12972.

2. Wei, X.; Shen, Y. R. Motional effect in surface sum-frequency vibrational spectroscopy. *Phys Rev Lett* **2001,** *86* (21), 4799-4802.

3. Shen, Y. R. Phase-Sensitive Sum-Frequency Spectroscopy. *Annu Rev Phys Chem* **2013,** *64*, 129-150.

4. Hsieh, C. S.; Okuno, M.; Hunger, J.; Backus, E. H. G.; Nagata, Y.; Bonn, M. Aqueous Heterogeneity at the Air/Water Interface Revealed by 2D-HD-SFG Spectroscopy. *Angewandte Chemie-International Edition* **2014,** *53* (31), 8146-8149.

5. Nihonyanagi, S.; Kusaka, R.; Inoue, K.; Adhikari, A.; Yamaguchi, S.; Tahara, T. Accurate determination of complex c(2) spectrum of the air/water interface. *Journal of Chemical Physics* **2015,** *143* (12).

6. Vinaykin, M.; Benderskii, A. V. Vibrational Sum-Frequency Spectrum of the Water Bend at the Air/Water Interface. *Journal of Physical Chemistry Letters* **2012,** *3* (22), 3348-3352.

7. Ni, Y. C.; Skinner, J. L. IR and SFG vibrational spectroscopy of the water bend in the bulk liquid and at the liquid-vapor interface, respectively. *J. Chem. Phys.* **2015,** *143* (1).

8. Tainter, C. J.; Ni, Y.; Shi, L.; Skinner, J. L. Hydrogen Bonding and OH-Stretch Spectroscopy in Water: Hexamer (Cage), Liquid Surface, Liquid, and Ice. *Journal of Physical Chemistry Letters* **2013,** *4* (1), 12-17.

9. Nihonyanagi, S.; Kusaka, R.; Inoue, K.; Adhikari, A.; Yamaguchi, S.; Tahara, T. Accurate determination of complex chi((2)) spectrum of the air/water interface. *Journal of Chemical Physics* **2015,** *143* (12).

10. Hsieh, C. S.; Campen, R. K.; Okuno, M.; Backus, E. H. G.; Nagata, Y.; Bonn, M. Mechanism of vibrational energy dissipation of free OH groups at the air-water interface. *P. Natl. Acad. Sci. USA* **2013,** *110* (47), 18780-18785.

11. Bonn, M.; Nagata, Y.; Backus, E. H. G. Molecular Structure and Dynamics of Water at the Water-Air Interface Studied with Surface-Specific Vibrational Spectroscopy. *Angewandte Chemie-International Edition* **2015,** *54* (19), 5560-5576.

12. Inoue, K.; Ishiyama, T.; Nihonyanagi, S.; Yamaguchi, S.; Morita, A.; Tahara, T. Efficient Spectral Diffusion at the Air/Water Interface Revealed by Femtosecond Time-Resolved Heterodyne-Detected Vibrational Sum Frequency Generation Spectroscopy. *Journal of Physical Chemistry Letters* **2016,** *7* (10), 1811-1815.

13. Seki, T.; Sun, S. M.; Zhong, K.; Yu, C. C.; Machel, K.; Dreier, L. B.; Backus, E. H. G.; Bonn, M.; Nagata, Y. Unveiling Heterogeneity of Interfacial Water through the Water Bending Mode. *Journal of Physical Chemistry Letters* **2019,** *10* (21), 6936-6941.

14. Zatula, A. S.; Ryding, M. J.; Andersson, P. U.; Uggerud, E. Proton Mobility and Stability of Water Clusters Containing Alkali Metal Ions. *Int. J. Mass Spec.* **2012,** *330*, 191-199.

15. Ryding, M. J.; Zatula, A. S.; Andersson, P. U.; Uggerud, E. Isotope exchange in reactions between D2O and size-selected ionic water clusters containing pyridine, H+(pyridine)(m)(H2O)(n). *Physical chemistry chemical physics : PCCP* **2011,** *13* (4), 1356-1367.

16. De Marco, L.; Fournier, J. A.; Thamer, M.; Carpenter, W.; Tokmakoff, A. Anharmonic exciton dynamics and energy dissipation in liquid water from two-dimensional infrared spectroscopy. *Journal of Chemical Physics* **2016,** *145* (9).

17. Yang, N.; Duong, C. H.; Kelleher, P. J.; Johnson, M. A.; McCoy, A. B. Isolation of Site-Specific Anharmonicities of Individual Water Molecules in the $I^-\cdot(H_2O)_2$ Complex Using Tag-Free, Isotopomer Selective IR-IR Double Resonance. *Chem. Phys. Lett.* **2017,** *690*, 159-171.

18. Yang, N.; Duong, C. H.; Kelleher, P. J.; McCoy, A. B.; Johnson, M. A. Deconstructing Water's Diffuse OH Stretching Vibrational Spectrum With Cold Clusters. *Science* **2019,** *364* (6437), 275-278.

19. Schaefer, J.; Backus, E. H. G.; Nagata, Y.; Bonn, M. Both Inter- and Intramolecular Coupling of O-H Groups Determine the Vibrational Response of the Water/Air Interface. *J Phys Chem Lett* **2016,** *7* (22), 4591-4595.

20. Skinner, J. L.; Pieniazek, P. A.; Gruenbaum, S. M. Vibrational Spectroscopy of Water at Interfaces. *Accounts Chem Res* **2012,** *45* (1), 93-100.

21. Kirov, M. V.; Fanourgakis, G. S.; Xantheas, S. S. Identifying the most stable networks in polyhedral water clusters. *Chemical Physics Letters* **2008,** *461* (4), 180-188.

22. Yang, N.; Duong, C. H.; Kelleher, P. J.; Johnson, M. A. Capturing Intrinsic Site-Dependent Spectral Signatures and Lifetimes of Isolated OH Oscillators in Extended Water Networks. *Nat. Chem.* **2020,** *12*, 159-164.

23. Miyazaki, M.; Fujii, A.; Ebata, T.; Mikami, N. Infrared spectroscopic evidence for protonated water clusters forming nanoscale cages. *Science* **2004,** *304* (5674), 1134-1137.

24. Fournier, J. A.; Wolke, C. T.; Johnson, M. A.; Odbadrakh, T. T.; Jordan, K. D.; Kathmann, S. M.; Xantheas, S. S. Snapshots of Proton Accommodation at a Microscopic Water Surface: Understanding the Vibrational Spectral Signatures of the Charge Defect in Cryogenically Cooled $H^+(H_2O)_{n=2-28}$ Clusters. *J. Phys. Chem. A* **2015,** *119* (36), 9425-9440.

25. Walters, R. S.; Pillai, E. D.; Duncan, M. A. Solvation dynamics in $Ni^+(H_2O)_n$ clusters probed with infrared spectroscopy. *J. Am. Chem. Soc.* **2005,** *127* (47), 16599-16610.

26. Moberg, D. R.; Becker, D.; Dierking, C. W.; Zurheide, F.; Bandow, B.; Buck, U.; Hudait, A.; Molinero, V.; Paesani, F.; Zeuch, T. The End of Ice I. *Proc. Natl. Acad. Sci.* **2019,** *116* (49), 24413-24419.

27. Pradzynski, C. C.; Forck, R. M.; Zeuch, T.; Slavicek, P.; Buck, U. A Fully Size-Resolved Perspective on the Crystallization of Water Clusters. *Science* **2012,** *337* (6101), 1529-1532.

28. Buch, V.; Tarbuck, T.; Richmond, G. L.; Groenzin, H.; Li, I.; Shultz, M. J. Sum frequency generation surface spectra of ice, water, and acid solution investigated by an exciton model. *J. Chem. Phys.* **2007,** *127* (20), 204710.

29. Wei, X.; Miranda, P. B.; Zhang, C.; Shen, Y. R. Sum-frequency spectroscopic studies of ice interfaces. *Physical Review B* **2002,** *66* (8), 085401.

30. Smit, W. J.; Tang, F. J.; Sanchez, M. A.; Backus, E. H. G.; Xu, L. M.; Hasegawa, T.; Bonn, M.; Bakker, H. J.; Nagata, Y. Excess Hydrogen Bond at the Ice-Vapor Interface around 200 K. *Phys Rev Lett* **2017,** *119* (13), 133003.

31. van der Post, S. T.; Hsieh, C. S.; Okuno, M.; Nagata, Y.; Bakker, H. J.; Bonn, M.; Hunger, J. Strong frequency dependence of vibrational relaxation in bulk and surface water reveals sub-picosecond structural heterogeneity. *Nat Commun* **2015,** *6*.

CHAPTER 8

Demonstration of Temperature Dependent Spectral Diffusion Experiment: Unmasking Rare, Large-Amplitude Motions in $I^-\cdot(H_2O)_2$ Isotopomers

The material in this chapter is adapted with permission Yang, Nan, Chinh H. Duong, Patrick J. Kelleher, and Mark A. Johnson. "Unmasking Rare, Large-Amplitude Motions in D_2-Tagged $I^-\cdot(H_2O)_2$ Isotopomers with Two-Color, Infrared–Infrared Vibrational Predissociation Spectroscopy." The Journal of Physical Chemistry Letters 9, no. 13 (2018): 3744-3750.

8.1 Introduction

At the end of Chapter 4 we briefly metioned the first observation of temperature depedent onset of spectral diffusion cuased by large amplitude hydrogen bond rearragement in the $I^-\cdot(H_2O)\cdot(D_2O)$ cluster. We discuss the temperature depdent experiment probing spectral diffusion in detail in this chapter. Specifically, we describe a two-color, isotopomer-selective IR-IR population labeling method that can monitor very slow spectral diffusion of OH oscillators in H-bonded networks and apply it to the $I^-\cdot(HDO)\cdot(D_2O)$ and $I^-\cdot(H_2O)\cdot(D_2O)$ systems, cryogenically cooled and D_2-tagged at an ion trap temperature of 15 K. These measurements reveal very large (>400 cm^{-1}), spontaneous spectral shifts despite the fact that the predissociation spectra in the OH stretching region of both isotopologues are sharp and readily assigned to four fundamentals of largely decoupled OH oscillators held in a cyclic H-bonded network. This spectral diffusion is not observed in the untagged isotopologues of the dihydrate clusters that are generated under the same source conditions in 40 microseconds delay, but does become apparent at about 75 K. All the results in this chapter are at a fixed delay time of 40 microseconds between the first and second laser interaction, the time depedent experiments are discussed in Chapter 9.

The mechanics underlying spectral diffusion in the OH stretching region of strongly H-bonded systems (e.g. water) have been subjected to intense study through the application of ultrafast IR spectroscopy and molecular-level theoretical simulations.[1-8] In water, the timescales are remarkably fast (<200 fs),[4] even when processes such as the formation of spatially extended vibrational excitons are quenched by isolating OH oscillators using dilute HDO in perdeuterated water.[1-6, 8] This behavior raises important

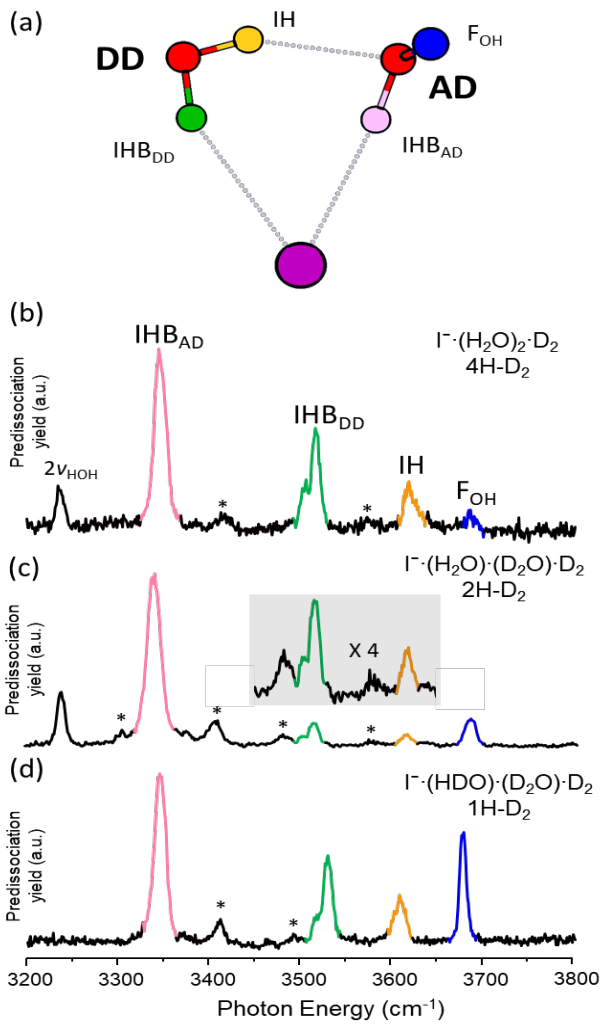

Figure 8.1: (a) Calculated (MP2/aug-cc-pVTZ-PP, ref. 20) minimum energy structure of $I^-\cdot(H_2O)_2$ and D_2-predissociation spectra of (b) $I^-\cdot(H_2O)_2\cdot D_2$, (c) $I^-\cdot(H_2O)\cdot(D_2O)\cdot D_2$ and (d) $I^-\cdot(HDO)\cdot(D_2O)\cdot D_2$. The H atoms and the vibrational bands are color coded according to the corresponding local OH oscillators, denoted free OH (F_{OH}, blue), inter-water hydrogen bonded OH (IH, yellow), ionic H-bonded (IHB) OH on the AD water (IHB_{AD}, pink), and the corresponding IHB on the DD water (IHB_{DD}, green). The HOH bend overtone ($2\nu_{HOH}$) is also identified, which disappears in the $I^-\cdot(HDO)\cdot(D_2O)$ isotopologue, while (*) identifies combination bands involving soft modes of the complex (ref. 25). Traces b, c and d are adapted from data in Chapter 4 or ref. 25.

questions about the relaxation mechanisms at play in the room temperature liquid. In this regard, Laage and Hynes pointed out an interesting aspect of H-bond reorientation dynamics in which the network structure remains relatively intact most of the time, but donor-acceptor pairs infrequently switch on a fast timescale from one configuration to the next.[9-12] In contrast to diffusive orientational relaxation that characterizes solutes in more weakly interacting solvents,[8, 13-17] this so-called "jump" mechanism is purported to be a generic feature of H-bonded systems, both in homogenous media such as water, and in the context of the hydration of solute neutrals and ions.[7, 18-19] Here we explore this phenomenon in a microscopic system where the spectral dynamics can be traced to particular oscillators in a well-defined structure: the $I^-\cdot(H_2O)_2$ cluster ion with the asymmetric structure (MP2/aug-cc-pVTZ-PP level of theory)[20] indicated in Fig. 8.1a.

8.2 Experimental Details

Ions were extracted from 1-ethyl-3-methylimidazolium iodide acetonitrile solution by electrospray ionization (ESI) in wet air and injected into the source region of a custom tandem time of flight photofragmentation mass spectrometer (Fig. 8.2).[1] Acetonitrile was used as the spray solvent because of its superior performance in generating stable ions, while 1-ethyl-3-methylimidazolium iodide (EMIM/I) was simply convenient as the $EMIM^+$ cation is routinely used in our apparatus to optimize ion yields. Isotope substitution can either be achieved through exposing the ESI source to mixed isotope water vapor or by solvent exchange in the ion guides. Solvent exchange of the $I^-\cdot(H_2O)_2$ cluster with pure D_2O vapor under low pressure yields $I^-\cdot(H_2O)\cdot(D_2O)$ without formation of the $I^-\cdot(HDO)_2$ cluster. The ions were then transported through RF ion guides through several stages of differential pumping and loaded into a 3-D Paul trap (Jordan TOF, Inc)

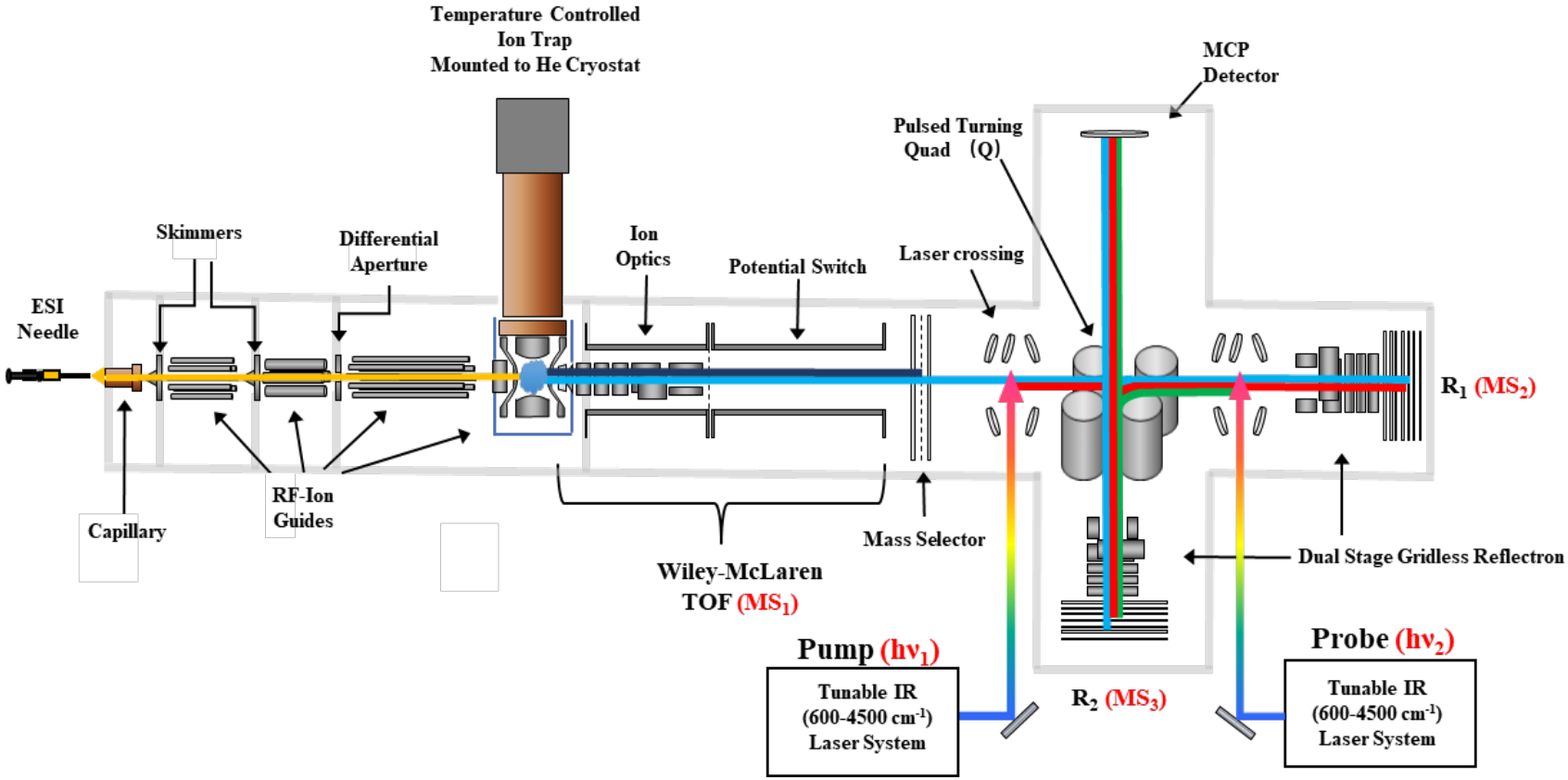
Temperature Controlled
Ion Trap
Mounted to He Cryostat
MCP
Detector
Pulsed Turning
Quad (Q)
Skimmers
Differential
Aperture
Ion
Optics
Potential Switch
Laser crossing
ESI
Needle
R1 (MS2)
RF-Ion
Guides
Capillary
Mass Selector
Dual Stage Gridless Reflectron
Wiley-McLaren
TOF (MS1)
Pump (hν1)
Probe (hν2)
Tunable IR
(600-4500 cm-1)
Laser System
R2 (MS3)
Tunable IR
(600-4500 cm-1)
Laser System

Figure 8.2: Diagram of the temperature controlled cryogenic ion vibrational spectrometer with two laser capabilities at Yale. The mass selected ions are intersected by the pump laser ($h\nu_1$) at the first laser crossing, yielding photo excited ions and/or photofragments while depleting the ground state parent ion. Parent and fragment ions are separated by the coaxial, dual-stage gridless retro-reflectron (R_1) and intersected by the probe laser ($h\nu_2$) at the second laser crossing where a certain isomer/isotopomer within the parent ions is interrogated by the probe laser. The ion beam is then turned 90^o by the pulsed DC turning quad (Q) into the second reflectron (R_2) to separate photofragments from the probe laser interaction. Lastly, the ion beam emerging from R_2 crosses the main ion beam axis at 90^o and moves toward the MCP detector where parent, pump laser fragments and probe laser fragments appear at different arrival times. By scanning the pump laser and fixing the probe laser on a transition unique to one of the isotopomers and monitoring the photofragment signal which exclusively reflects the population in the selected isotopomer, one can obtain isotopomer selective dip spectra. In addition, spectra of tagged clusters can be obtained with very low background in a single laser mode where the probe laser interacts with parent ions after mass selection by R_1 to isolate them from fragments arising from metastable decay along the flight tube en route to R_1. The schematic is reproduced from the work by Yang et al (ref.1).

which is mounted to a temperature-controlled helium cryostat. The ions were stored in the ion trap for 95 ms. During this time they were cooled to close to the trap temperature by pulsed helium buffer gas. For the messenger tag experiments, He buffer gas containing 10% D_2 at 15 K trap temperature was used to generate tagged cluster ions. The tagged clusters were then extracted out of the Paul trap and into the acceleration region of the tandem time of flight photodissociation mass spectrometer where they were later mass-selected by a pulsed reflector. The ions were then intersected by a tunable OPO/OPA infrared laser (LaserVision) to photoevaporate the D_2 tag and yield a vibrational predissociation spectrum. In the double resonance hole burning experiment, two tunable IR lasers were used where the ions were first intersected by the pump laser and mass separated in the first reflectron (R_1 in Fig. 8.2). Then the unfragmented parent ion interacts with the probe laser and the fragments and parents were again separated in the second reflectron (R_2 in Fig. 8.2). The fragments from the pump laser and the probe laser and the parent arrives at the detector at different timing and the double resonance dip spectra were obtained by monitoring the probe laser signal against pump laser frequency. Single laser scans were carried out with 2 mJ/pulse laser energy in about ~0.5 cm diameter spot, while the two laser scans were carried out under saturation conditions for both lasers (18 mJ/pulse in each laser). Details of the role of multiple photon processes in the application of IR-IR to the bare complex are discussed in ref. 1. The possible interference from clusters excited by one photon below the dissociation limit has been addressed by direct determination of the cross sections for excited state absorption at probe wavelengths. The spectroscopic behavior of this complex yields a favorable

scenario that suppresses probe at F_{OH} and IH absorptions by clusters excited near the dissociation limit.

8.3 Results and Discussion

Previous spectroscopic studies and Chapter 4 [21-25] have confirmed that the dominant, four band vibrational pattern (Fig. 8.1b) displayed by both the D_2-tagged (hereafter denoted 4H-D_2) and that of the cryogenically cooled $I^-\cdot(H_2O)_2$ cluster (4H), [25] is assigned to largely decoupled OH oscillators as indicated by the color coding in Figs. 8.1a and 8.1b. A temperature dependent study[21] in 2015 established that this pattern is broadened and finally lost at around 125 K, which was interpreted with the aid of theoretical simulations to indicate the breakup of the water dimer motif into two largely independent water molecules orbiting the ion below the dissociation threshold. Interestingly, however, it was also predicted that there are rare, large amplitude "switching" motions that leave the cyclic structure intact.[21] Specifically, it was proposed that the two water molecules could change roles from H-bond acceptor-donor (AD) to double donor (DD) by flipping the outer free OH group into the bound (IH) position over a low (~274 cm^{-1}) barrier, which is shown schematically in Fig. 8.3a. These large amplitude motions could not be probed by monitoring changes in the 4H spectrum, however, because the pattern remains the same after such an event. To address this behavior experimentally, we introduced an IR-IR double resonance hole-burning method with the layout described in Fig. 8.2 and Chapter 2. This technique is capable of tracking the spectral evolution of OH groups in mixed isotopologues where D atoms occupy two or three of the available sites.[25] Application of this method to the bare $I^-\cdot(H_2O)\cdot(D_2O)$ system (2H)[25] demonstrated that the two isotopomers (formed by occupation of either the

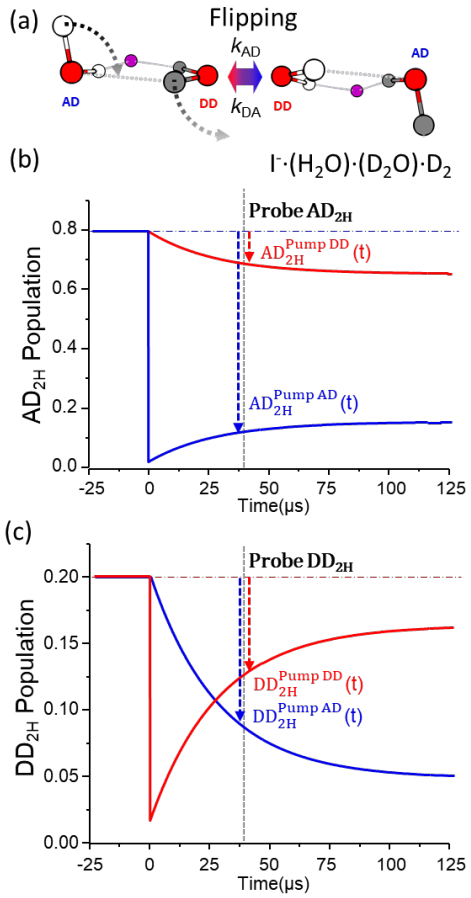

Figure 8.3: (a) Schematic of the flip motion that exchanges the DD_{2H} and AD_{2H} sites, where the gray atoms label the deuterated positions; (b) and (c) are the calculated time-dependent population changes in the 2H-D_2 (b) AD_{2H} and (c) DD_{2H} sites in the regime II limit under the condition that the pump laser completely removes the local population in one of the two sites (see text) at t=0. The horizontal lines indicate the equilibrium population before interaction with the pump laser. The displacements between the dotted horizontal lines and the solid traces correspond to the expected time-dependent population changes. The traces are color coded according to the pump laser excitation of AD_{2H} (blue) and DD_{2H} (red). The population changes at the probe timing (vertical dashed gray line in (b) and (c)) are plotted as dashed drop arrows. See text for numerical values used in the simulation.

AD or DD site by an intact H_2O molecule) begin to interconvert above about 100 K (Fig. 8.4). Note that the isobaric species $I^-\cdot(HDO)_2$ can be suppressed using ligand switching reactions as described in the previous work.[25] The spectra were observed to broaden considerably near the onset of interconversion, indicating that this process is driven by thermal activation of the soft modes that manifest as hot band structure and lead to dissociation of the inter-water H-bond (IH). Similar results on the 1H system were obtained in the context of this study and presented in Fig. 8.5. Here we extend that study to the 1H-D_2 and 2H-D_2 systems, and demonstrate that the D_2-tagged clusters undergo large amplitude rearrangements in spite of the fact that the band patterns obtained at ion trap temperature of 15 K are sharp. These measurements also establish that this spectral migration occurs on a very long (~40 μs) timescale, qualitatively consistent with an extreme example of the rare event "jump" mechanism described above.[9, 11]

A survey of the potential energy barriers for interconversion of the sites indicates that there are two low lying paths: a "rocking" motion leading to exchange of the free OH and IHB position of the AD molecule, and a "flipping" motion discussed in the earlier report [25] where the free OH displaces the inter-water H-bond. The barriers for these are on the order of 180 cm^{-1} for the rock and 274 cm^{-1} for the flip, as estimated by relaxed scans of the potential energy surface plotted in Fig. 8.6.

The D_2 tag molecule is calculated to bind close to the free OH group above the plane defined by the heavy atoms with the bond axis oriented toward the iodide, as displayed in Fig. 8.7. The D_2 stretching fundamental appears in the spectrum and is red-shifted by 37 cm^{-1} compared to that of the isolated molecule.[26] The binding energy of D_2 to cluster ions with similar shifts are on the order of 500-600 cm^{-1}.[27-28] The OH/OD

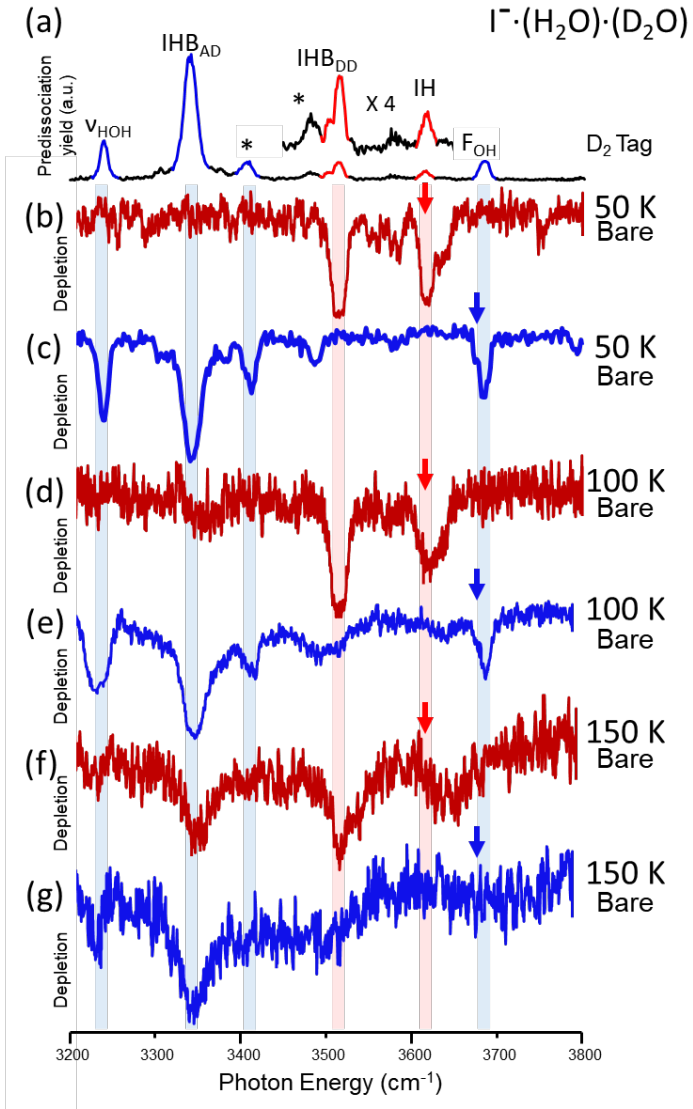

Figure 8.4: (a) The predissociation spectrum of D_2 tagged $I^-\cdot(H_2O)\cdot(D_2O)$. (b) through (g) are the double resonance hole burning experiment spectra of bare $I^-\cdot(H_2O)\cdot(D_2O)$ at various trap temperatures. The blue traces represent the spectra of AD_{2H} obtained by probing on the free OH indicted by the blue arrow in (c,e,g), while red traces represent the spectra of DD_{2H} acquired by probing on the IH transition labeled by the red arrow. The color-coded droplines indicate the cold cluster transition frequencies associated with each isotopomer. The traces are reproduced from the work by Yang et al (ref.1).

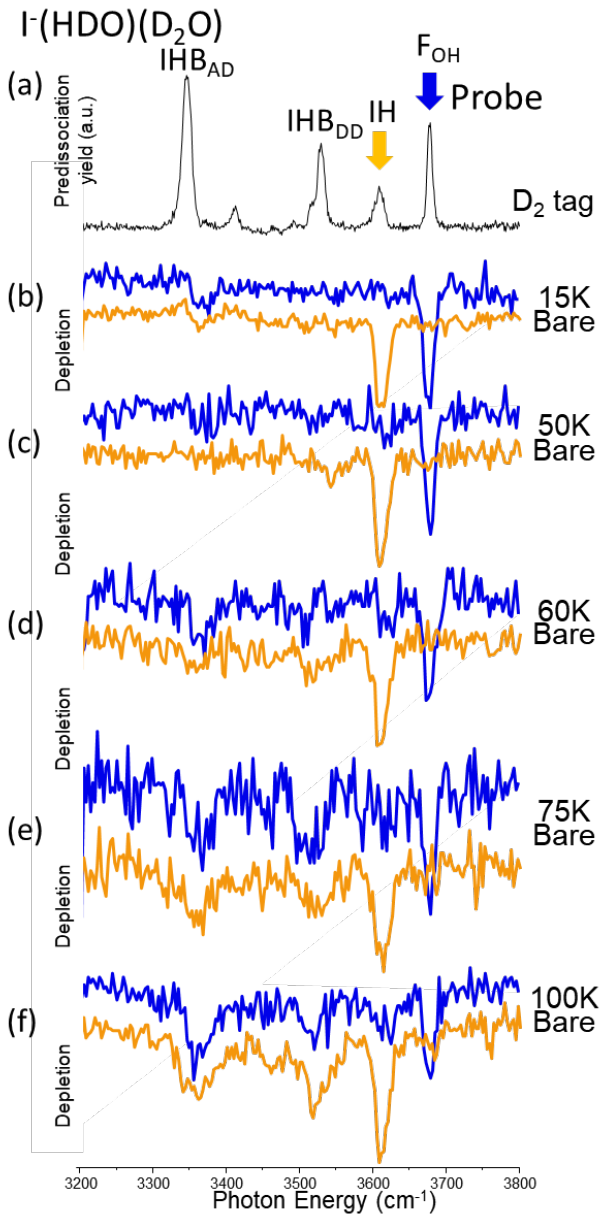

Figure 8.5: (a) D_2-predissociation spectrum of all four isotopomers of $I^-\cdot(HDO)(D_2O)\cdot D_2$. (b-f) Double resonance hole burning dip spectra of bare $I^-\cdot(HDO)(D_2O)$ at various temperatures. The traces are color coded according to the probe position: yellow corresponds to probing the IH position and blue corresponds to probing the free OH position. Dips other than the probe position indicates the H atom migrated during the time between pump and probe laser. The migration happens around 60-75 K.

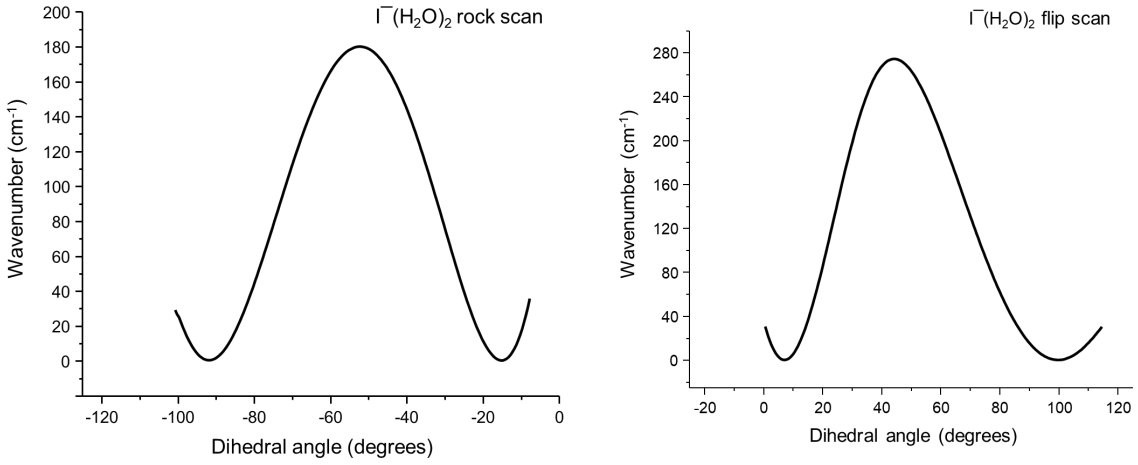

Figure 8.6: Calculated (MP2/aug-cc-pVTZ-PP, ref.2) relaxed potential energy scan along the (right) flipping (Fig. 8.13f) coordinate and the (left) rocking (Fig. S8.13g) coordinate for $I^{-}\cdot(H_2O)_2$. These are generated by rotating the AD water molecule through a C_{2v} geometry to exchange protons bound to the ion in the rocking pathway and moving the free OH into the IH position for the flipping pathway. The two minima resemble the minimal energy structure in Fig. S8.13h whereas the peak height in the center represents the barrier height of the two pathways as described in the main text. Note that in the deuterated systems tunneling is not possible due to the isotopic substitution.

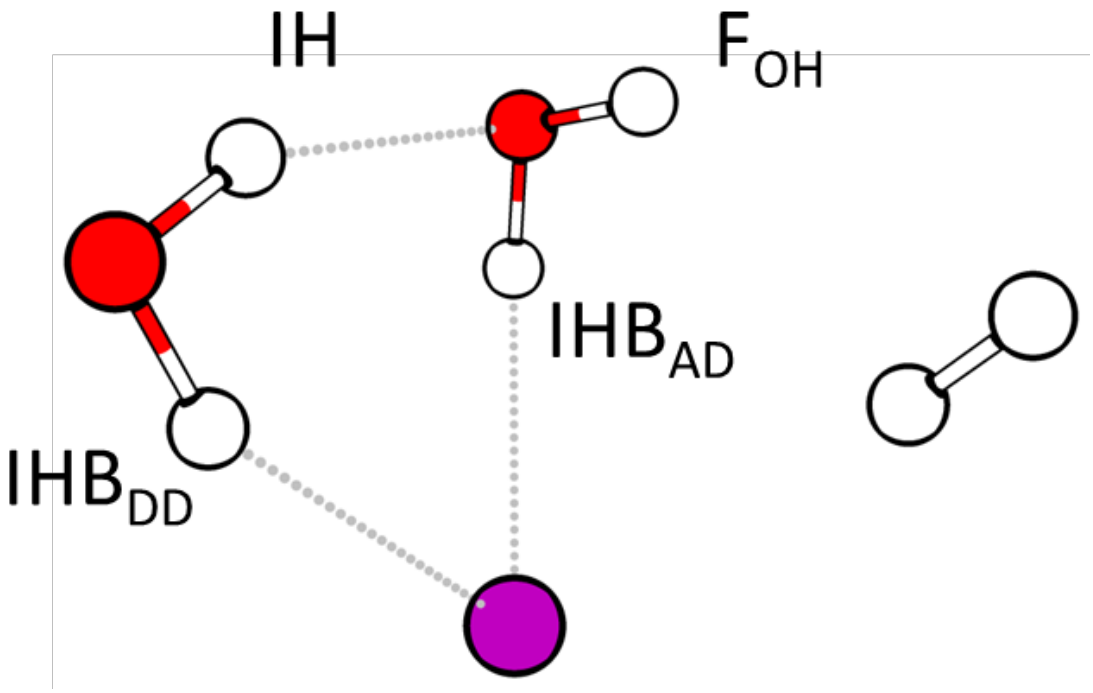

Figure 8.7: Rotatable PDF on the previous page displays the calculated structure of $I^{-}\cdot(H_2O)_2\cdot D_2$ at the MP2/aug-cc-pVTZ-PP level of theory and basis function (ref. 2). A static version is displayed on this page.

features in the D_2-tagged spectra of all isotopomers were demonstrated to be within 4 cm^{-1} of those in the bare clusters, which were obtained using another variation of the IR-IR two color photodissociation scheme.[25] The D_2 tag was found to optimize at a trap temperature 15 K.

The 1H-D_2 and 2H-D_2 spectra are presented in Figs. 8.1d and 8.1c, respectively. They both exhibit four fundamentals close to those in the 4H-D_2 system (Fig. 8.1b), but with very different intensity profiles. Weaker bands (*) are also evident that have previously been analyzed and assigned to soft mode combination bands.[25] The isotope dependence of the band intensities is readily understood as a consequence of the relative populations of the isotopomers that contribute to the overall spectrum. In the case of 1H, the unique OH group can reside in each of the four distinct sites in the cyclic structure, while the 2H system has two configurations depending on whether the intact H_2O occupies the AD or DD position (AD_{2H} and DD_{2H}, respectively). The energies of the isotopomers differ according to their vibrational zero-point energy (ZPE) contributions, and the calculated anharmonic (VPT2) values (MP2/aug-cc-pVTZ-PP) are collected in Table 8.1. The observed band intensities are determined by the population of an OH group at each site and the relative oscillator strengths of the associated vibrational fundamentals. The latter are also included in Table 8.1 and plotted in Fig. 8.8a for 2H. For 1H, the free OH isotopomer is the lowest in energy, while the other three locations (IHB_{AD}, IHB_{DD}, and IH in Fig. 8.1a) are closer in energy, ranging from 33 to 38 cm^{-1} above the free OH, with the IH position being most unfavorable. The observed 1H-D_2 spectrum (Fig. 8.1d) is qualitatively consistent with the expected fractionation among the

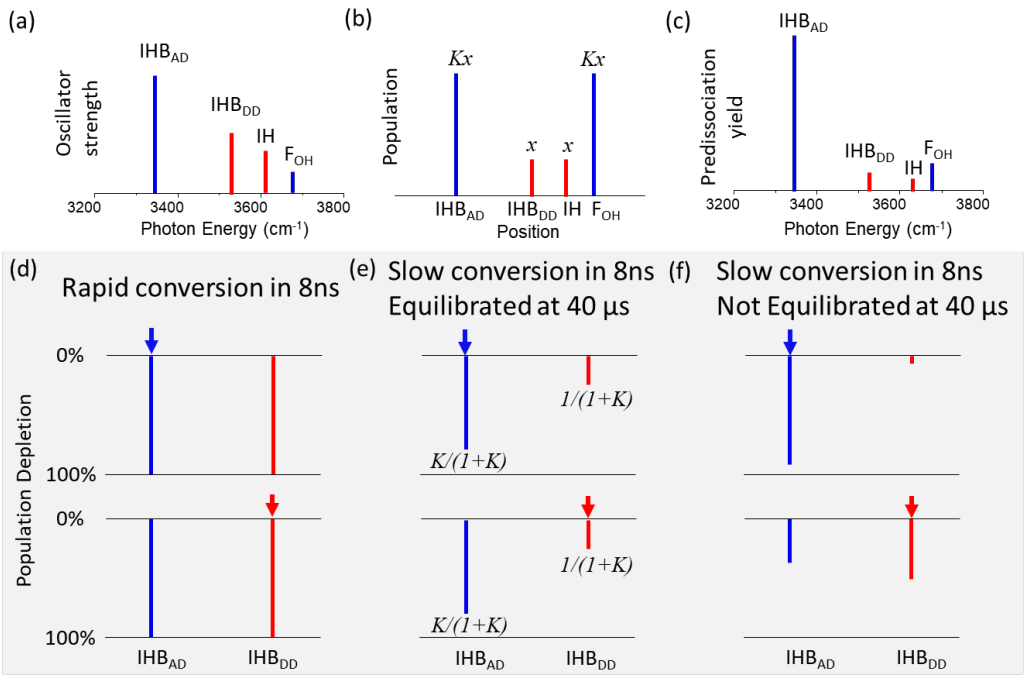

Figure 8.8: (a) calculated (MP2/aug-cc-pVTZ-PP, ref. 2) fundamental intensities of the four OH oscillators in the two $I^-\cdot(H_2O)(D_2O)$ isotopomers according to whether the H_2O molecule resides in the AD (AD_{2H}, blue) or DD (DD_{2H}, red) positions, (b) calculated population ratio of the four OH oscillators which reflects population of the two isotopomers at 30 K, 'x' here is the population of the less dominant DD_{2H} isotopomer and K here is the equilibrium constant of the $DD_{2H} \rightleftharpoons AD_{2H}$ reaction. (c) Calculated predissociation yield obtained by multiplying oscillator strength by population for each OH oscillator. (d,e,f) Demonstrations of double resonance hole burning spectra under different regimes when probing on a specific isotopomer, where probe positions are indicated by the colored arrows. The two oscillators chosen have high oscillator strength hence insure 100% dissociation upon excitation. Conversion refers to the interchange of the H_2O molecule between the AD and DD sites, $\tau_L =$ 8 ns is the pump laser pulse width and $\tau_w =$ 40 µs is the time delay between pump and probe laser and K is the same equilibrium constant as the one in (b).

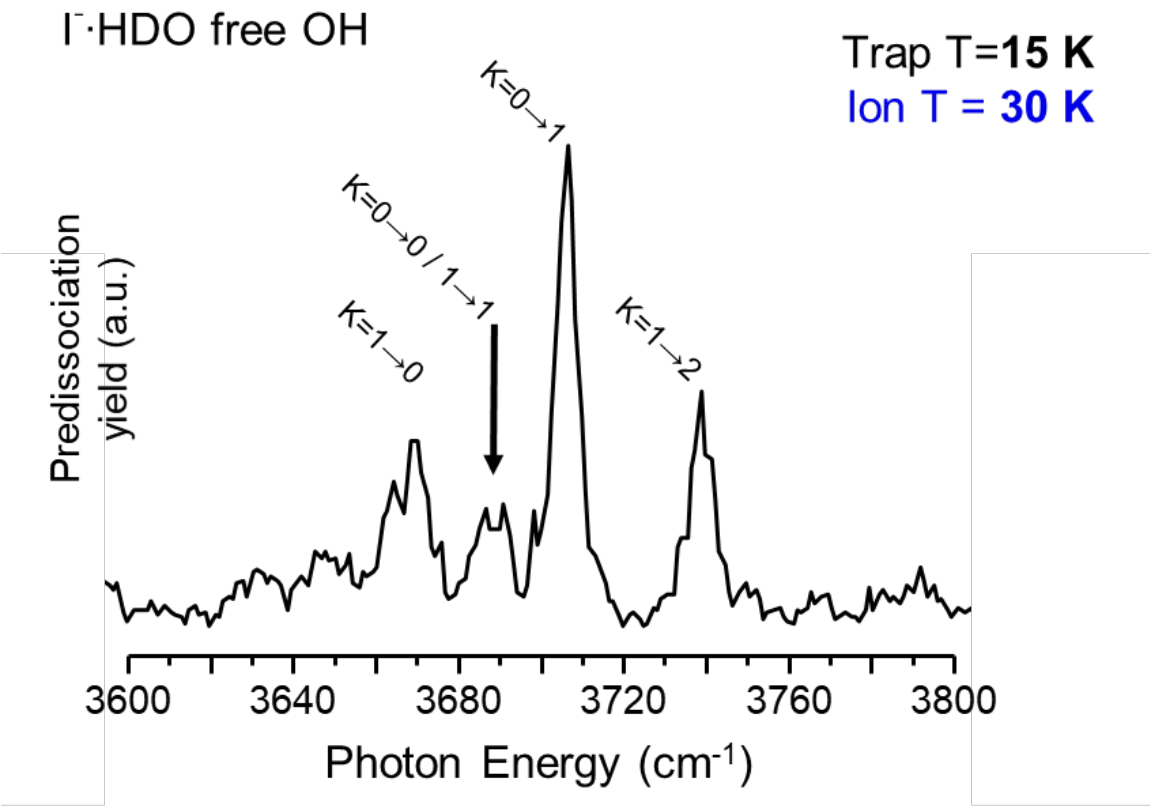

Figure 8.9: Vibrational predissociation spectrum of I^{-}·HDO at trap temperature 15K. The features are the rotational K transitions on the free OH fundamental and they are assigned according to the calculated (MP2/aug-cc-pVTZ-PP, ref. 2) rotational constants and vibrational fundamental. Temperature was extracted using Boltzmann factor between population in the K= 0 and K= 1 state which can be obtained by integrating the peak area of the K= 0 → 1 and K= 1 → 2 transitions and correcting for the difference in transition moments (ref.3).

sites for a thermal population distribution at low temperature, i.e., such that the free OH stretch is strongly enhanced while the other three (IHB_{AD}, IHB_{DD}, and IH) display a similar profile to that of the 4H-D_2 isotopologue (Fig. 8.1b). The temperature of the ions in the trap were estimated by measuring the rotational temperature of the bare $I^-\cdot HOD$ ion (Fig. 8.9), which has an open K-stack structure involving rotation of the free OH group about the axis connecting the heavy atoms. This method yields an ion temperature of ~30 K for a trap temperature of 15 K, where the elevated ion temperature is consistent with other measurements carried out in a variety of trapping configurations.[29-35] The small shifts in the band positions when the OH groups are decoupled in the 1H isotopomer have been discussed in detail in an earlier report.[25] Similarly strong isotope fractionation between DD and AD sites is apparent in the 2H-D_2 case (Fig. 8.1c), in which the ZPE difference brings the AD_{2H} site 42 cm^{-1} lower than DD_{2H}.[25]

The fact that the overall band patterns in the 1H-D_2 and 2H-D_2 spectra are sharp and readily assigned to the cyclic structure is a key feature enabling the present experimental investigation of spectral diffusion. Specifically, the observation of absorption at one of these OH stretch frequencies reveals its occupation by an H atom, even if only transiently. In the case of a static system, the absorption spectrum of each isotopomer can be experimentally determined using an IR-IR population labeling or "hole burning" technique described in detail in earlier reports.[21, 25, 36-39] This method exploits the photodissociation action mode by which mass-selected ion spectra are typically obtained as a way to selectively remove population of a particular isotopomer from an ion ensemble selected by its m/z. In an isotopomer-selective mode, two

Table 8.1. Experimentally observed frequencies ($\pm 4\ cm^{-1}$) for the four OH sites in the $I^-\cdot(HDO)\cdot(D_2O)$ and $I^-\cdot(H_2O)\cdot(D_2O)$ cluster ions along with their vibrational zero point energies. Calculated frequencies were obtained from VPT2 calculations with the MP2/aug-cc-pVTZ-PP level of theory and basis function as reported in Ref. 1, which did not include the ZPE values.

$I^-\cdot(HDO)\cdot(D_2O)$								
H Position	**Harmonic Vibrational ZPE (cm^{-1})**	**Harmonic Relative VZPE (cm^{-1})**	**Anharmonic Vibrational ZPE (cm^{-1})**	**Anharmonic Relative VZPE (cm^{-1})**	**Calculated harmonic frequency (cm^{-1})**	**Calculated anharmonic frequency (cm^{-1})**	**Calculated Intensity**	**Experimental frequency (cm^{-1})**
IHB_{AD}	8466	38	8306	33	3475	3245	841	3346
IHB_{DD}	8463	35	8307	35	3687	3469	363	3528
IH	8474	46	8310	38	3765	3604	92	3608
F_{OH}	8428	0	8272	0	3872	3682	21	3676
$I^-\cdot(H_2O)\cdot(D_2O)$								
H Position	**Harmonic Vibrational ZPE (cm^{-1})**	**Harmonic Relative VZPE (cm^{-1})**	**Anharmonic Vibrational ZPE (cm^{-1})**	**Anharmonic Relative VZPE (cm^{-1})**	**Calculated harmonic frequency (cm^{-1})**	**Calculated anharmonic frequency (cm^{-1})**	**Calculated Intensity**	**Experimental frequency (cm^{-1})**
IHB_{AD}	9143	0	8957	0	3468	3243	729	3344
$F_{OH(AD)}$	9143	0	8957	0	3876	3693	38	3686
IHB_{DD}	9188	44	8998	42	3675	3465	380	3516
$IH_{(DD)}$	9188	44	8998	42	3777	3610	92	3619,3638

independently tuned IR lasers are employed: One of them (the probe) is fixed on a transition associated with a particular isotopomer, while the other (the pump) excites the same ion packet upstream and is scanned through the entire vibrational spectrum. When the pump laser excites any transition associated with the species interrogated by the probe, photodissociation removes that contribution to the tagged ion packet before it interacts with the probe laser, thus reducing the probe laser photofragment yield. As such, the entire spectrum of that particular isotopomer can be revealed by a series of "dips" in the probe signal. Implementation of this strategy requires three stages of mass selection as shown in Fig. 8.2, and is thus termed an MS^3IR^2 class of secondary ion analysis.[40]

Here we use the MS^3IR^2 scheme to reveal the migration of the OH group between sites on the timescale between the pump and probe lasers. Specifically, by observing the fragmentation signal arising from fixing the probe laser on the OH fundamental associated with a particular site, dips will appear in this signal when the pump laser excites transitions arising from H atom occupation in *other sites by the same cluster*. It is important to emphasize that this experimental approach probes the population transfer that occurs spontaneously on the timescale (denoted here as the waiting time, τ_w) between pump and probe pulses. This approach can be regarded as a cluster variation of the classic "T-jump" experiments in the 1950s, where a dynamic equilibrium is abruptly interrupted to reveal the underlying kinetics through the transient response in the populations of reactants and products as equilibrium is restored.[41] We note that cluster-based population transfer experiments relying on buffer gas cooling has been demonstrated earlier by the Zwier group,[42-44] and photo-induced, large amplitude motion

in isolated clusters has also been explored on picosecond time scale by Fuji and coworkers.[45-49]

To illustrate the essential features of our approach, consider a dynamic two-state system such as that at play (vide infra) in the 2H-D_2 cluster. In this case, the 2H-D_2 predissociation spectrum (Fig. 8.1c) reflects the steady state populations of the two states (AD_{2H} and DD_{2H} modified by the oscillator strengths of the various bands (Fig. 8.8)). Note that the calculated oscillator strengths exhibit a nearly linear increase with increasing red-shift of the OH band relative to that of the free OH. As such, photodepletion is most efficient when pumping the two lower energy IHB bands. The two timescales of importance in this experiment are the duration of the pump pulse ($\tau_L \sim$ 8 ns) and the waiting time between the pump and probe lasers, τ_w, which in this case is very long ($\sim$ 40 μs) due to the time required for intermediate mass isolation of the ion packet that was interrogated by the pump. Three limits of kinetic response are in play according to the characteristic time for exchange, τ_{ex}:

I. Static ensemble; $\tau_{ex} \gg \tau_w$

II. Slow exchange; $\tau_w > \tau_{ex} > \tau_L$

III. Fast exchange; $\tau_L \gg \tau_{ex}$

Regime I is in effect for the implementation of isotopomer-selective spectroscopy,[21, 25, 36-39] while regime III corresponds to rapid site exchange on the timescale of the pump laser. In regime III, excitation of the strong IHB transitions can be carried out to saturation which will, in turn, completely deplete the ion ensemble by removing both isotopomers

upon excitation of either one of the IHB bands. We are primarily interested in regime II, where the pump laser only depletes the steady state population in a particular site at the instant of excitation, but the slow kinetics of the site exchange allows partial re-equilibration of the populations during the waiting time, τ_w. In that case, the probe signal cannot be completely depleted by the pump laser on any transition, but dips will appear according to the local population destroyed by the pump laser in each site and the recovery kinetics that replenish this population. If we further assume that the observed steady state population ($\frac{AD_{2H}}{DD_{2H}} \sim 4$) is dynamic and controlled by an effective equilibrium constant, K_{eq}, for the unimolecular reaction:

$$AD_{2H} \rightleftharpoons DD_{2H}, \qquad \text{Eq. 8.1}$$

then the forward (k_f) and reverse (k_r) unimolecular reaction rates that govern the exchange kinetics follow the usual constraint: $K_{eq} = \frac{k_f}{k_r} = \frac{DD_{2H}}{AD_{2H}}$. Solving the kinetic response equations[50] yields the predicted time-dependent populations of the two sites in Fig. 8.3. These curves describe the limiting regime II case where the local population in one site is completely removed by the pump laser, and is then partially restored as the remaining ion ensemble relaxes back to steady state. This model leads to the time evolution of the reactant population *AD(t)* :

$$\Delta AD(t) = \Delta AD(0)e^{-(k_f+k_r)(t)}, \quad \text{Eq. 8.2}$$

where $\Delta AD(t) = AD(t) - AD(\infty)$. $AD(0)$ is the population immediately after depletion by the pump, and $AD(\infty)$ denotes that upon re-equilibration.[50]

Qualitatively, the curves in Fig. 8.3 indicate that pumping the IHB_{AD} band should yield large changes in both (DD and AD) site populations (blue traces in Figs. 8.3b and 8.3c). This occurs because the initial DD_{2H} population is transferred back to the AD_{2H} site to restore equilibrium when the (initially) larger AD_{2H} population is removed by the pump. This is in contrast to the response upon saturation of the IHB_{DD} band (red traces in Figs. 8.3b and 8.3c), where a minor change relative to the large reservoir of AD_{2H} population can effectively repopulate the steady state DD_{2H} population, leading to a small change in AD_{2H} relative to that of the DD_{2H} site. The same data are organized in a different manner in Fig. 8.10 to emphasize the time evolution of the relative populations.

We begin by applying the MS^3IR^2 method to the (bare) 2H cluster cooled in a 15 K ion trap. Because two of the four bands (F_{OH} and IH) lead to excited vibrational levels that lie above the dissociation limit ($D_0 \sim 3500$ cm^{-1}),[21] probing these features monitors the populations in each site without requiring the tag protocol. The isotopomer-selective spectra are reproduced from Chapter 4 (ref. 25) in Figs. 8.11b and 8.11d, which are generated by probing the OH group in the free and IH positions, respectively. Both probe transitions yield dips isolated to the transitions of the two sites in the MS^3IR^2 spectra, thus confirming that the cold bare ensemble conforms to regime I kinetics, where occupation of the AD and DD positions persists longer that the 40 μs waiting time (τ_w) between the pump and probe lasers.

With the behavior of the bare ion in mind, we next explored the onset of spectral diffusion in the 2H-D_2 cluster. In the tagged system, all four transitions can be probed in

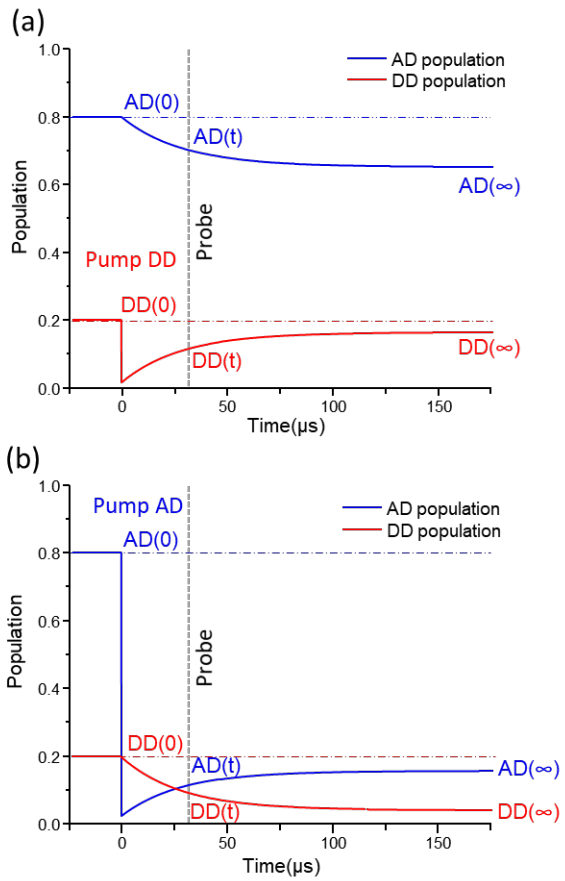

Figure 8.10: (a) and (b) are the time-dependent population changes at the AD and DD sites in the regime II limit under the condition that the pump laser removes the local population in one of the two sites. The population time behavior was simulated with reversible unimolecular kinetics. Panel (a) applies to the case where the pump laser removes population from the DD site, and (b) pertains to the case when the pump laser removes population from the AD site. AD(0) and DD(0) are the populations before the pump laser interaction, which reflect steady state equilibration before excitation by the pump laser. The displacements between the dotted horizontal lines and the solid lines correspond to the expected time-dependent population changes. AD(t) and DD(t) are the populations obtained by the probe laser at time t after the pump, while AD(∞) and DD(∞) are the populations when the equilibrium is re-established.

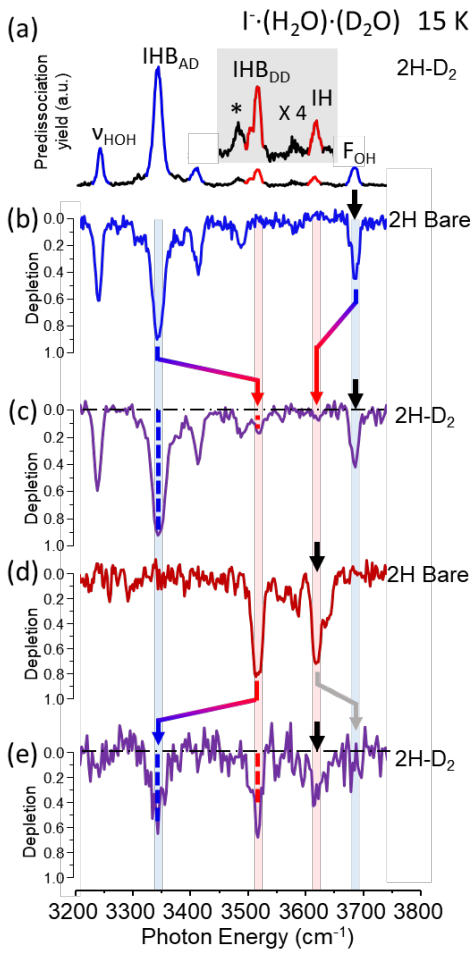

Figure 8.11 (a) D_2-predissociation spectrum of the two $I^-\cdot(H_2O)\cdot(D_2O)\cdot D_2$ isotopomers. The features associated with the AD_{2H} isotopomer are colored blue and those associated with DD_{2H} are colored red. (b) and (d) are MS^3IR^2 dip spectra obtained by probing on the bare $I^-\cdot(H_2O)\cdot(D_2O)$ ion at the positions indicated by the black arrows, while (c) and (e) are obtained by probing on the D_2 tagged $I^-\cdot(H_2O)\cdot(D_2O)$ ion at the positions indicated by the black arrows. The colored arrows indicate the H migration that causes the extra dip features in the spectra and the gray arrow indicates that the expected feature was not resolved at the current signal to noise. The dashed drop lines indicate the depletions predicted by the first order unimolecular kinetics model in Fig 8.3. See text for numerical values used in the simulation.

the linear action regime, and Figs. 8.11c and 8.11e display the MS^3IR^2 dip spectra associated with probing the AD_{2H} and DD_{2H} sites, respectively, which were monitored by probing the F_{OH} and IH transitions (black arrows) that are exclusive to each site. The downward pointing colored arrows indicate features in the spectrum that arise from H_2O occupation in the site that is *not* monitored by the probe. Surprisingly, in contrast to the behavior of the bare 2H cluster, dip features appear at all four fundamentals, thus establishing that exchange between sites in the D_2-tagged cluster does occur at a trap temperature of 15 K. The pathway that connects the DD_{2H} and AD_{2H} states of the 2H cluster is the concerted flipping motion (illustrated in Fig. 8.3a) predicted in Chapter 4.[25] The dip pattern in Fig. 8.11e is most pronounced, which records the DD_{2H} population response to depletion of the AD_{2H} population. Specifically, about 50% of the DD_{2H} molecules can be removed by pumping the IHB_{AD} band at 3344 cm^{-1}. This is in contrast to the AD_{2H} population (Fig. 8.11c), which is efficiently depleted by pumping the IHB_{AD} band on resonance, but only exhibits ~5% reduction when the IHB_{DD} is pumped at 3516 cm^{-1}. Since both IHB transitions can drive >90% reduction of the population in the case of the bare 2H ion, the fact that only partial depletions are obtained in the 2H-D_2 case rules out regime I kinetics, thus placing the system in the regime II class of dynamic systems.

To understand the kinetic implications of the observed dip pattern in the MS^3IR^2 spectra of the 2H-D_2 system, we appeal to the idealized equilibrium model for the kinetics of the forward and reverse reactions described above and illustrated in Fig. 8.3. Those curves were generated with rate constants $k_f = (7\pm3) \times 10^3$ s^{-1} and $k_r = (3\pm1) \times 10^4$ s^{-1}, which are consistent with the equilibrium constant $K_{eq} = 0.25 \pm 0.05$ obtained from

the observed isotope fractionation ratio. This model predicts the dip patterns in the DD_{2H} and AD_{2H} populations given by the vertical dashed arrows in Fig. 8.3 and dashed vertical lines in Figs. 3c and 3e, which indeed recover the observed behavior. We emphasize that, without explicit measurement of the time evolution of the system, we cannot confirm that the simple kinetic model accurately describes the situation in the microscopic cluster regime. The fact that the population response can be understood in this context does, however, provide a qualitative estimate to the time scales involved, which are remarkably slow.

The 2H-D_2 study addressed the kinetics of the flipping motion and illustrated in Fig. 8.3a. As discussed above, however, there should be another low energy rocking pathway (Fig. 8.12a) that leads to interchange of the two OH groups on the AD water molecule, which cannot be addressed in the 2H system. We therefore turn to the 1H-D_2 cluster to explore this motion, since the key bands associated with H occupation of the two sites are the widely spaced free OH (blue) and IHB_{AD} (pink) features. The dip pattern observed for this system is reported in Fig. 8.12b, and like the 2H-D_2 case, this system is dynamic (in contrast to the behavior of the bare 1H) under the same trapping conditions (see Fig. 8.5b). Most importantly, the trace in Fig. 8.12b, which was obtained by probing the free OH site (solid blue start of arrow), displays a prominent dip upon pump excitation of the IHB_{AD} band (pink vertical arrowhead). This confirms the migration of the OH group between free and IHB_{AD} positions, which corresponds to the rocking pathway (Fig. 8.12a).

Probing all four positions in the 1H-D_2 system yields dip patterns (see Fig. 8.13) indicating that all four sites are exchanging. The interpretation of these dip patterns in the

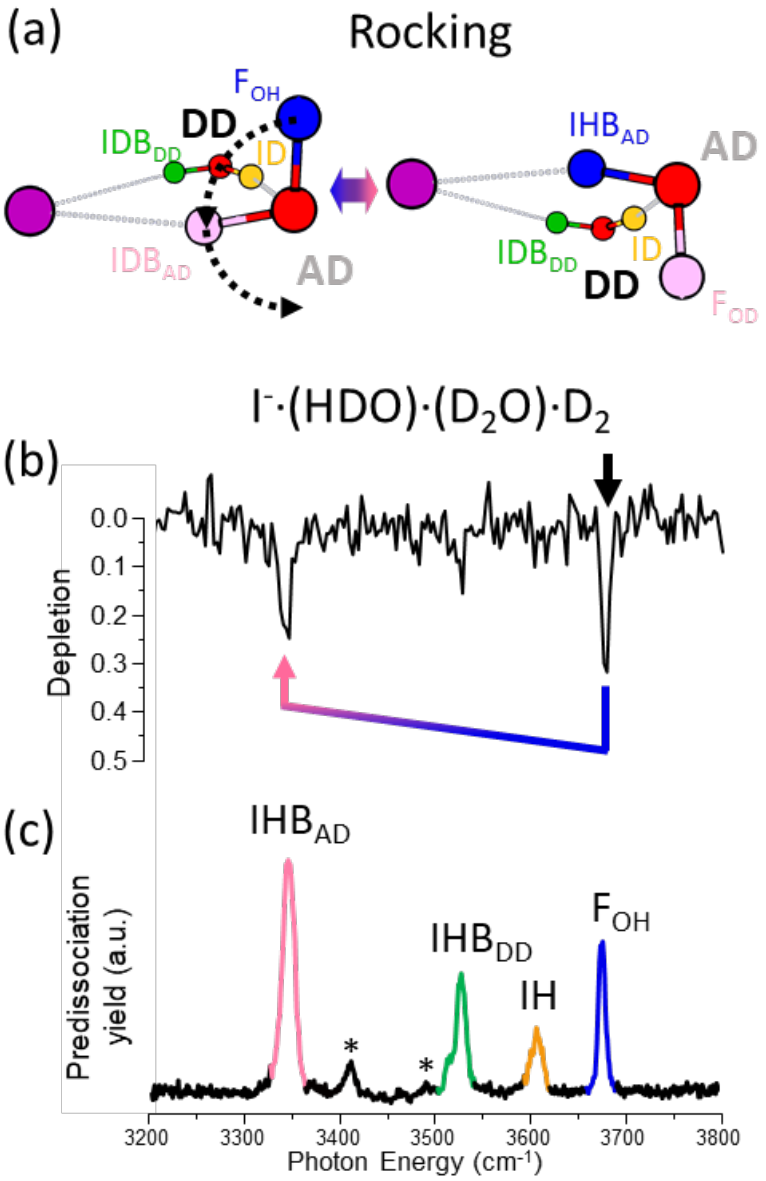

Figure 8.12. (a) Schematic of the rocking pathway for H migration. (b) MS^3IR^2 dip spectra of $I^-\cdot(HDO)\cdot(D_2O)\cdot D_2$ obtained by probing on free OH position. The black arrow labels the probe laser position and the colored arrow indicates the H migration to yield absorption at the IHB_{AD} site. (c) D_2-predissociation spectrum of all four $I^-\cdot(HDO)\cdot(D_2O)\cdot D_2$ isotopomers. Features are color-coded by the H sites (see caption Fig. 8.1).

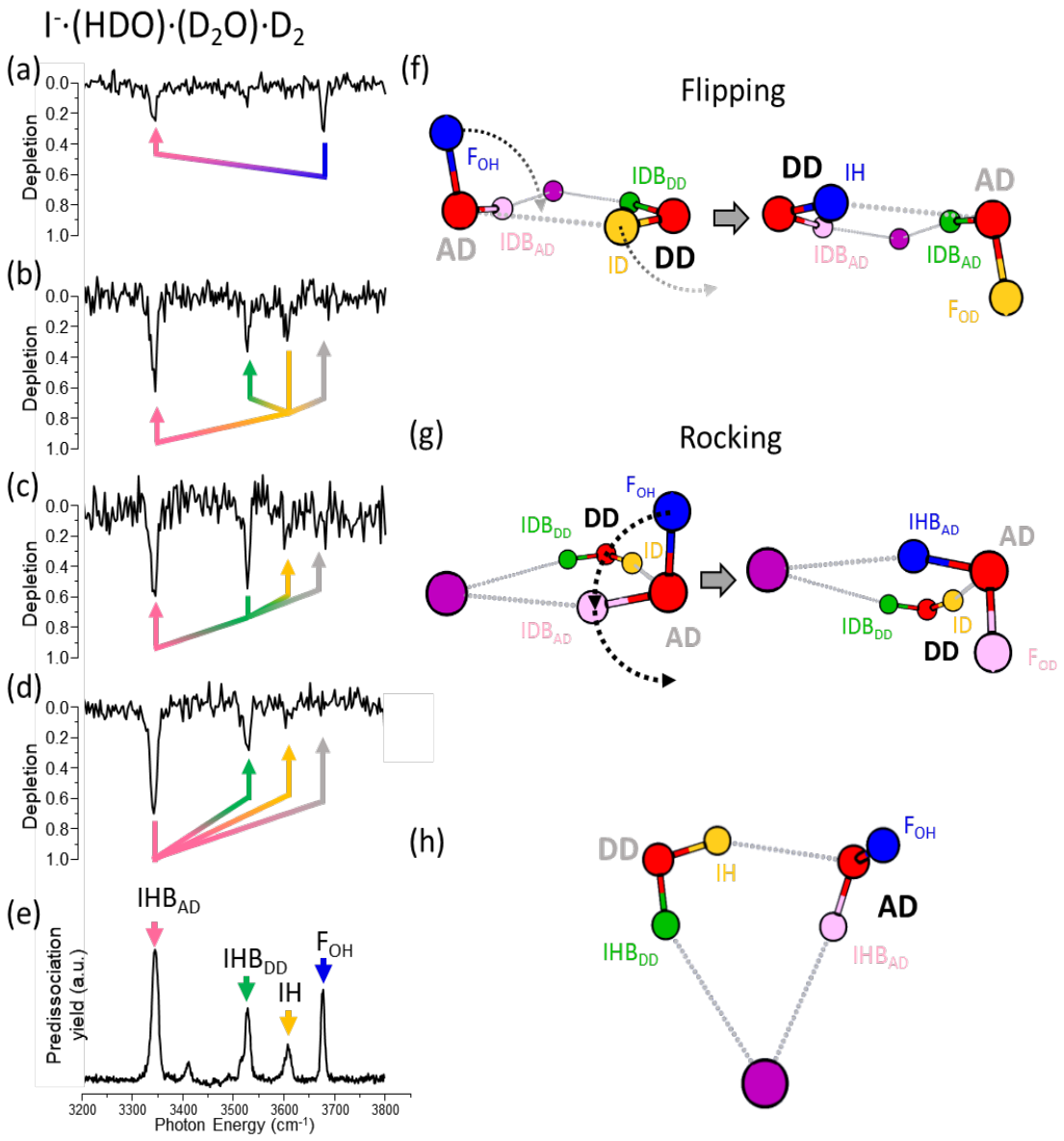

Figure 8.13: (a,b,c,d) Double resonance hole burning dip spectra of $I^-\cdot(HDO)(D_2O)\cdot D_2$ obtained by probing on four different OH positions. The tails of the arrows label the probe laser position and arrow heads indicate the H migrations. Arrows are color coded by the H sites and gray means the signal to noise was not enough to resolve the feature. (e) D_2-predissociation spectrum of all four isotopomers of $I^-\cdot(HDO)(D_2O)\cdot D_2$. (f,g) Schematics of the possible pathway for H migration. (h) Minimum energy (MP2/aug-cc-pVTZ-PP, ref. 2) structure of $I^-\cdot(HDO)(D_2O)$.

context of the simple kinetic model is not straightforward, however, as it appears that some of the population in the most stable free OH site is static, while higher energy components are dynamic. It is also possible that this system displays partial regime I kinetics for some of the site exchanges. Detailed analysis of this more complex situation will require determination of the internal energy distribution of the 1H-D_2 ion ensemble and likely involve experimental advances such as interrogation of the kinetics with shorter laser pulses, both of which are beyond the scope of this work. The main focus here is to report the fact that the D_2 tagged cluster ions display observable migration among the sites, which in the case of the 2H system occurs on an extremely slow time scale. In this regard, it is interesting that the bare 1H and 2H cluster ions are static while the D_2-tagged systems are dynamic under the same (15 K) trapping conditions. The static behaviors of the bare ions establish that the barriers to exchange are sufficiently large to suppress tunneling or thermally activated exchange even on the long timescale of the measurement. The D_2 molecule thus appears to enable exchange, possibly by lowering these barriers or by providing an energy reservoir that yields larger internal energy content at the same temperature (Fig. 8.14). The latter scenario presents an interesting possibility where the D_2 molecule plays the role of a solvent in that energy is exchanged between internal motions of the tightly bound cluster ion and the soft modes associated with the weakly bound tag.

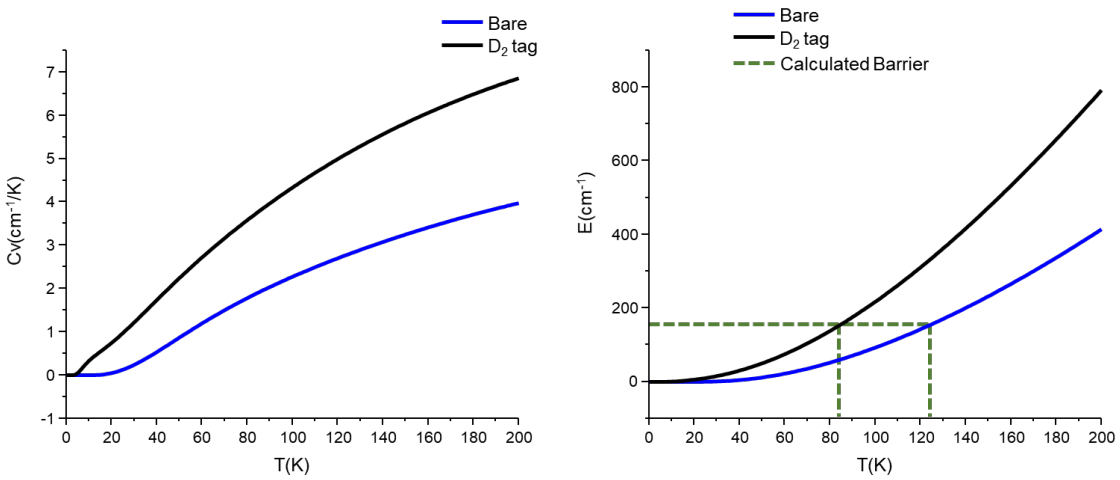

Figure 8.14: On the left is the heat capacity of $I^{-}\cdot(H_2O)_2$ (blue) and $I^{-}\cdot(H_2O)_2\cdot D_2$ (black) calculated from harmonic frequencies obtained with the MP2/aug-cc-pVTZ-PP level of theory and basis function (ref. 2). The addition of the weakly bonded D_2 molecule increase the low energy degrees of freedom hence increase the heat capacity significantly. On the right is the internal energy obtained by integrating the heat capacity over temperature. Th green dash indicates the calculated barrier and corresponding Boltzmann temperatures of the flip motion. The calculation using harmonic oscillator partition function will underestimate the heat capacity but it provides a qualitative sense of the effect of D_2 tag molecule on the internal energy of the system.

8.4 Summary

Summarizing, we have used a two-color IR-IR pump-probe scheme with a long (40 μs) delay between pulses to directly observe slow spectral diffusion arising from interconversion among the isotopomers of the D_2-tagged $I^-\cdot(HDO)\cdot(D_2O)$ and $I^-\cdot(H_2O)\cdot(D_2O)$ systems at a trap temperature of 15 K. These dynamics occur despite the patterns of sharp resonances in the D_2-tagged spectra, indicating that the site-to-site migrations must be rare events in the sense that the lifetime in each site is much longer than the time required to migrate between them. This is indeed a cluster regime signature of the infrequent jump mechanism discussed above in the context of the H-bonding dynamics at play in liquids. [9, 11-12] Efforts are now underway to better characterize the time evolution of the slow spectral diffusion and follow its dependence on the nature of the tagging species as well as cluster ion temperature.

8.5 References

(1) Woutersen, S.; Emmerichs, U.; Bakker, H. J. Femtosecond Mid-IR Pump-Probe Spectroscopy of Liquid Water: Evidence for a Two-Component Structure. *Science* **1997,** *278*, 658-660.

(2) Stenger, J.; Madsen, D.; Hamm, P.; Nibbering, E. T. J.; Elsaesser, T. Ultrafast Vibrational Dephasing of Liquid Water. *Phys. Rev. Lett.* **2001,** *87*.

(3) Laenen, R.; Simeonidis, K.; Laubereau, A. Subpicosecond Spectroscopy of Liquid Water in the Infrared: Effect of Deuteration on the Structural and Vibrational Dynamics. *J. Phys. Chem. B* **2002,** *106*, 408-417.

(4) Fecko, C. J.; Eaves, J. D.; Loparo, J. J.; Tokmakoff, A.; Geissler, P. L. Ultrafast Hydrogen-Bond Dynamics in the Infrared Spectroscopy of Water. *Science* **2003,** *301*, 1698-1702.

(5) Yeremenko, S.; Pshenichnikov, M. S.; Wiersma, D. A. Hydrogen-Bond Dynamics in Water Explored by Heterodyne-Detected Photon Echo. *Chem. Phys. Lett.* **2003,** *369*, 107-113.

(6) Lawrence, C. P.; Skinner, J. L. Vibrational Spectroscopy of Hod in Liquid D_2o. Iii. Spectral Diffusion, and Hydrogen-Bonding and Rotational Dynamics. *J. Chem. Phys.* **2003,** *118*, 264-272.

(7) Laage, D.; Hynes, J. T. Reorientional Dynamics of Water Molecules in Anionic Hydration Shells. *Proc. Natl. Acad. Sci. USA* **2007,** *104*, 11167-11172.

(8) Moilanen, D. E.; Wong, D.; Rosenfeld, D. E.; Fenn, E. E.; Fayer, M. D. Ion-Water Hydrogen-Bond Switching Observed with 2D IR Vibrational Echo Chemical Exchange Spectroscopy. *Proc. Natl. Acad. Sci. U. S. A.* **2009,** *106*, 375-380.

(9) Laage, D.; Stirnemann, G.; Sterpone, F.; Rey, R.; Hynes, J. T. Reorientation and Allied Dynamics in Water and Aqueous Solutions. *Ann. Rev. Phys. Chem.* **2011,** *62*, 395-416.

(10) Laage, D.; Hynes, J. T. On the Molecular Mechanism of Water Reorientation. *J. Phys. Chem. B* **2008,** *112*, 14230-14242.

(11) Laage, D.; Hynes, J. T. A Molecular Jump Mechanism of Water Reorientation. *Science* **2006,** *311*, 832-835.

(12) Laage, D.; Stirnemann, G.; Sterpone, F.; Hynes, J. T. Water Jump Reorientation: From Theoretical Prediction to Experimental Observation. *Acc. Chem. Res.* **2012,** *45*, 53-62.

(13) Piletic, I. R.; Gaffney, K. J.; Fayer, M. D. Structural Dynamics of Hydrogen Bonded Methanol Oligomers: Vibrational Transient Hole Burning Studies of Spectral Diffusion. *J. Chem. Phys.* **2003,** *119*, 423-434.

(14) Park, S.; Fayer, M. D. Hydrogen Bond Dynamics in Aqueous NaBr Solutions. *Proc. Natl. Acad. Sci. U. S. A.* **2007,** *104*, 16731-16738.

(15) Lee, M. W.; Carr, J. K.; Gollner, M.; Hamm, P.; Meuwly, M. 2d Ir Spectra of Cyanide in Water Investigated by Molecular Dynamics Simulations. *J. Chem. Phys.* **2013,** *139*.

(16) Kozinski, M.; Garrett-Roe, S.; Hamm, P. Vibrational Spectral Diffusion of CN^- in Water. *Chem. Phys.* **2007,** *341*, 5-10.

(17) Laage, D.; Hynes, J. T. Do More Strongly Hydrogen-Bonded Water Molecules Reorient More Slowly ? *Chem. Phys. Lett.* **2006,** *433*, 80-85.

(18) Kropman, M. F.; Bakker, H. J. Femtosecond Mid-Infrared Spectroscopy of Aqueous Solvation Shells. *J. Chem. Phys.* **2001,** *115*, 8942-8948.

(19) Nigro, B.; Re, S.; Laage, D.; Rey, R.; Hynes, J. T. On the Ultrafast Infrared Spectroscopy of Anion Hydration Shell Hydrogen Bond Dynamics. *J. Phys. Chem. A* **2006,** *110*, 11237-11243.

(20) Peterson, K. A.; Shepler, B. C.; Figgen, D.; Stoll, H. On the Spectroscopic and Thermochemical Properties of Clo, Bro, Io, and Their Anions. *J. Phys. Chem. A* **2006,** *110*, 13877-13883.

(21) Wolke, C. T.; Menges, F. S.; Totsch, N.; Gorlova, O.; Fournier, J. A.; Weddle, G. H.; Johnson, M. A.; Heine, N.; Esser, T. K.; Knorke, H.; Asmis, K. R.; McCoy, A. B.; Arismendi-Arrieta, D. J.; Prosmiti, R.; Paesani, F. Thermodynamics of Water Dimer Dissociation in the Primary Hydration Shell of the Iodide Ion with Temperature-Dependent Vibrational Predissociation Spectroscopy. *J. Phys. Chem. A* **2015,** *119*, 1859-1866.

(22) Ayotte, P.; Nielsen, S. B.; Weddle, G. H.; Johnson, M. A.; Xantheas, S. S. Spectroscopic Observation of Ion-Induced Water Dimer Dissociation in the $X^-\cdot(H_2O)_2$ (X = F, Cl, Br, I) Clusters. *J. Phys. Chem. A* **1999,** *103*, 10665-10669.

(23) Ayotte, P.; Weddle, G. H.; Kim, J.; Kelley, J.; Johnson, M. A. A Cluster Study of Anionic Hydration: Spectroscopic Characterization of the $I^-\cdot W_n$, $1 \leq N \leq 3$, Supramolecular Complexes at the Primary Steps of Solvation. *J. Phys. Chem. A* **1999,** *103*, 443-447.

(24) Ayotte, P.; Weddle, G. H.; Kim, J.; Johnson, M. A. Mass-Selected "Matrix Isolation" Infrared Spectroscopy of the $I^-\cdot(H_2O)_2$ Complex: Making and Breaking the Inter-Water Hydrogen-Bond. *Chem. Phys.* **1998,** *239*, 485-491.

(25) Yang, N.; Duong, C. H.; Kelleher, P. J.; Johnson, M. A.; McCoy, A. B. Isolation of Site-Specific Anharmonicities of Individual Water Molecules in the $I^-\cdot(H_2O)_2$ Complex Using Tag-Free, Isotopomer Selective Ir-Ir Double Resonance. *Chem. Phys. Lett.* **2017,** *690*, 159-171.

(26) Dickenson, G. D.; Niu, M. L.; Salumbides, E. J.; Komasa, J.; Eikema, K. S. E.; Pachucki, K.; Ubachs, W. Fundamental Vibration of Molecular Hydrogen. *Phys. Rev. Lett.* **2013,** *110*, 193601.

(27) Kamrath, M. Z.; Relph, R. A.; Guasco, T. L.; Leavitt, C. M.; Johnson, M. A. Vibrational Predissociation Spectroscopy of the H_2-Tagged Mono- and Dicarboxylate Anions of Dodecanedioic Acid. *Int. J. Mass Spectrom.* **2011,** *300*, 91-98.

(28) Kamrath, M. Z.; Garand, E.; Jordan, P. A.; Leavitt, C. M.; Wolk, A. B.; Van Stipdonk, M. J.; Miller, S. J.; Johnson, M. A. Vibrational Characterization of Simple Peptides Using Cryogenic Infrared Photodissociation of H_2-Tagged, Mass-Selected Ions. *J. Am. Chem. Soc.* **2011,** *133*, 6440-6448.

(29) Kelleher, P. J.; Johnson, C. J.; Fournier, J. A.; Johnson, M. A.; McCoy, A. B. Persistence of Dual Free Internal Rotation in $NH_4^+(H_2O)\cdot He_{n=0-3}$ Ion–Molecule Complexes: Expanding the Case for Quantum Delocalization in He Tagging. *J. Phys. Chem. A* **2015,** *119*, 4170-4176.

(30) Rizzo, T. R.; Boyarkin, O. V. Cryogenic Methods for the Spectroscopy of Large, Biomolecular Ions. *Gas-Phase Ir Spectroscopy and Structure of Biological Molecules* **2015,** *364*, 43-97.

(31) Choi, C. M.; Choi, D. H.; Kim, N. J.; Heo, J. Effective Temperature of Protonated Tyrosine Ions in a Cold Quadrupole Ion Trap. *Int. J. Mass Spectrom.* **2012,** *314*, 18-21.

(32) Boyarkin, O. V.; Mercier, S. R.; Kamariotis, A.; Rizzo, T. R. Electronic Spectroscopy of Cold, Protonated Tryptophan and Tyrosine. *J. Am. Chem. Soc.* **2006,** *128*, 2816-2817.

(33) Redwine, J. G.; Davis, Z. A.; Burke, N. L.; Oglesbee, R. A.; McLuckey, S. A.; Zwier, T. S. A Novel Ion Trap Based Tandem Mass Spectrometer for the Spectroscopic Study of Cold Gas Phase Polyatomic Ions. *Int. J. Mass Spectrom.* **2013,** *348*, 9-14.

(34) Chakrabarty, S.; Holz, M.; Campbell, E. K.; Banerjee, A.; Gerlich, D.; Maier, J. P. A Novel Method to Measure Electronic Spectra of Cold Molecular Ions. *J. Phys. Chem. Lett.* **2013,** *4*, 4051-4054.

(35) Endres, E. S.; Egger, G.; Lee, S.; Lakhmanskaya, O.; Simpson, M.; Wester, R. Incomplete Rotational Cooling in a 22-Pole Ion Trap. *J. Mol. Spectrosc.* **2017,** *332*, 134-138.

(36) Heine, N.; Fagiani, M. R.; Rossi, M.; Wende, T.; Berden, G.; Blum, V.; Asmis, K. R. Isomer-Selective Detection of Hydrogen-Bond Vibrations in the Protonated Water Hexamer. *J. Am. Chem. Soc.* **2013,** *135*, 8266-8273.

(37) McCunn, L. R.; Headrick, J.; Johnson, M. A. Site-Specific Addition of D_2O to the $(H_2O)_6^-$ "Hydrated Electron" Cluster: Isomer Interconversion and Substitution at the Double H-Bond Acceptor (Aa) Electron-Binding Site. *Phys. Chem. Chem. Phys.* **2008,** *10*, 3118-3123.

(38) Guasco, T. L.; Johnson, M. A.; McCoy, A. B. Unraveling Anharmonic Effects in the Vibrational Predissociation Spectra of $H_5o_2^+$ and Its Deuterated Analogues. *J. Phys. Chem. A* **2011,** *115*, 5847-5858.

(39) Wolke, C. T.; Fournier, J. A.; Miliordos, E.; Kathmann, S. M.; Xantheas, S. S.; Johnson, M. A. Isotopomer-Selective Spectra of a Single Intact H_2O Molecule in the $Cs^+(D_2O)_5H_2O$ Isotopologue: Going Beyond Pattern Recognition to Harvest the Structural Information Encoded in Vibrational Spectra. *J. Chem. Phys.* **2016,** *144*, 074305.

(40) Relph, R. A.; Elliott, B. M.; Weddle, G. H.; Johnson, M. A.; Ding, J.; Jordan, K. D. Vibrationally-Induced Interconversion of H-Bonded $NO_2^-{\cdot}H_2O$ Isomers within

$NO_2^-{\cdot}H_2O{\cdot}Ar_m$ Clusters Using IR-IR Pump-Probe through the OH and NO Stretching Vibrations. *J. Phys. Chem. A.* **2009,** *113*, 975-981.

(41) Eigen, M.; Demaeyer, L. Self-Dissociation and Protonic Charge Transport in Water and Ice. *Proc R Soc Lon Ser-A* **1958,** *247*, 505-533.

(42) Harrilal, C. P.; DeBlase, A. F.; Fischer, J. L.; Lawler, J. T.; McLuckey, S. A.; Zwier, T. S. Infrared Population Transfer Spectroscopy of Cryo-Cooled Ions: Quantitative Tests of the Effects of Collisional Cooling on the Room Temperature Conformer Populations. *J. Phys. Chem. A* **2018,** *122*, 2096-2107.

(43) Dian, B. C.; Longarte, A.; Winter, P. R.; Zwier, T. S. The Dynamics of Conformational Isomerization in Flexible Biomolecules. I. Hole-Filling Spectroscopy of N-Acetyl Tryptophan Methyl Amide and N-Acetyl Tryptophan Amide. *J. Chem. Phys.* **2004,** *120*, 133-147.

(44) Dian, B. C.; Longarte, A.; Zwier, T. S. Conformational Dynamics in a Dipeptide after Single-Mode Vibrational Excitation. *Science* **2002,** *296*, 2369-2373.

(45) Fujii, M.; Dopfer, O. Ionisation-Induced Site Switching Dynamics in Solvated Aromatic Clusters: Phenol-$(Rare\ Gas)_N$ Clusters as Prototypical Example. *Int. Rev. Phys. Chem.* **2012,** *31*, 131-173.

(46) Tanabe, K.; Miyazaki, M.; Schmies, M.; Patzer, A.; Schutz, M.; Sekiya, H.; Sakai, M.; Dopfer, O.; Fujii, M. Watching Water Migration around a Peptide Bond. *Angew Chem Int Edit* **2012,** *51*, 6604-6607.

(47) Nakamura, T.; Schmies, M.; Patzer, A.; Miyazaki, M.; Ishiuchi, S.; Weiler, M.; Dopfer, O.; Fujii, M. Solvent Migration in Microhydrated Aromatic Aggregates:

Ionization-Induced Site Switching in the 4-Aminobenzonitrile-Water Cluster. *Chem-Eur J* **2014,** *20*, 2031-2039.

(48) Miyazaki, M.; Nakamura, T.; Wohlgemuth, M.; Mitric, R.; Dopfer, O.; Fujii, M. Single Water Solvation Dynamics in the 4-Aminobenzonitrile-Water Cluster Cation Revealed by Picosecond Time-Resolved Infrared Spectroscopy. *Phys. Chem. Chem. Phys.* **2015,** *17*, 29969-29977.

(49) Dopfer, O.; Fujii, M. Probing Solvation Dynamics around Aromatic and Biological Review Molecules at the Single-Molecular Level. *Chem. Rev. (Washington, DC, U. S.)* **2016,** *116*, 5432-5463.

(50) Aguda, B. D.; Pritchard, H. O. Reversible and Irreversible Formulation of Unimolecular Reactions. *J. Chem. Phys.* **1992,** *96*, 5908-5914.

CHAPTER 9

From Temperature Dependent Spectral Diffusion to Time Dependent Kinetics Measurements: Mapping the Temperature-Dependent and Network-site-specific Onset of Hydrogen Bond Rearrangement a Water Cluster Nano-cage

The material in this chapter is adapted with permission Yang, Nan, Sean C. Edington, Tae Hoon Choi, Elva V. Henderson, Joseph P. Heindel, Sotiris S. Xantheas, Kenneth D. Jordan, and Mark A. Johnson. "Mapping the temperature-dependent and network-site-specific onset of spectral diffusion in a water cluster nanocage" Proceedings of the National Academy of Sciences 117, no. 42 (2020): 26047-26052.

9.1 Introduction

In previous Chapters we have established the static spectral behavior of single OH oscillator as well as intact H_2O molecules in various sites of extended hydrogen bond networks. We also explored spectral diffusion in small water clusters with short, fixed delay time between the lasers. In this Chapter we use a new experimental scheme that allows time dependent measurements where the laser delay time can be varied from microseconds to hundreds of milliseconds. Such capability allows direct measurement of reaction rates inside a temperature-controlled cluster and has many potential applications in studying reaction mechanisms by mapping out the activation energies in a finitely solvated reactive system. Specifically, in this chapter we explore the kinetic processes that sustain equilibrium in a microscopic, finite system, namely a water cluster ion held in an ion trap. This is accomplished by monitoring the spontaneous, time-dependent frequency evolution (the frequency autocorrelation) of a single OH oscillator, embedded in a "droplet-like" water cluster as a function of temperature. The measurements are carried out by applying two-color, IR-IR photodissociation mass spectrometry to the $D_3O^+ \cdot (HDO)(D_2O)_{19}$ isotopologue of the "magic number" protonated water cluster, $H^+ \cdot (H_2O)_{21}$. The OH frequency is observed to evolve over tens of milliseconds in the temperature range (90-120 K) such that large (~300 cm^{-1}) "jumps" appear first, and are traced to rare, site-to-site migrations of local OH oscillators that preserve the cage's overall structure. The hydrogen bonded network rearranges through low-barrier pathways involving the rotation of an acceptor-acceptor-donor (AAD) surface water molecule that is associated with a weaker hydrogen bond to its neighbors. One important advantage of this approach is that it provides a new insight into the molecular-level processes that

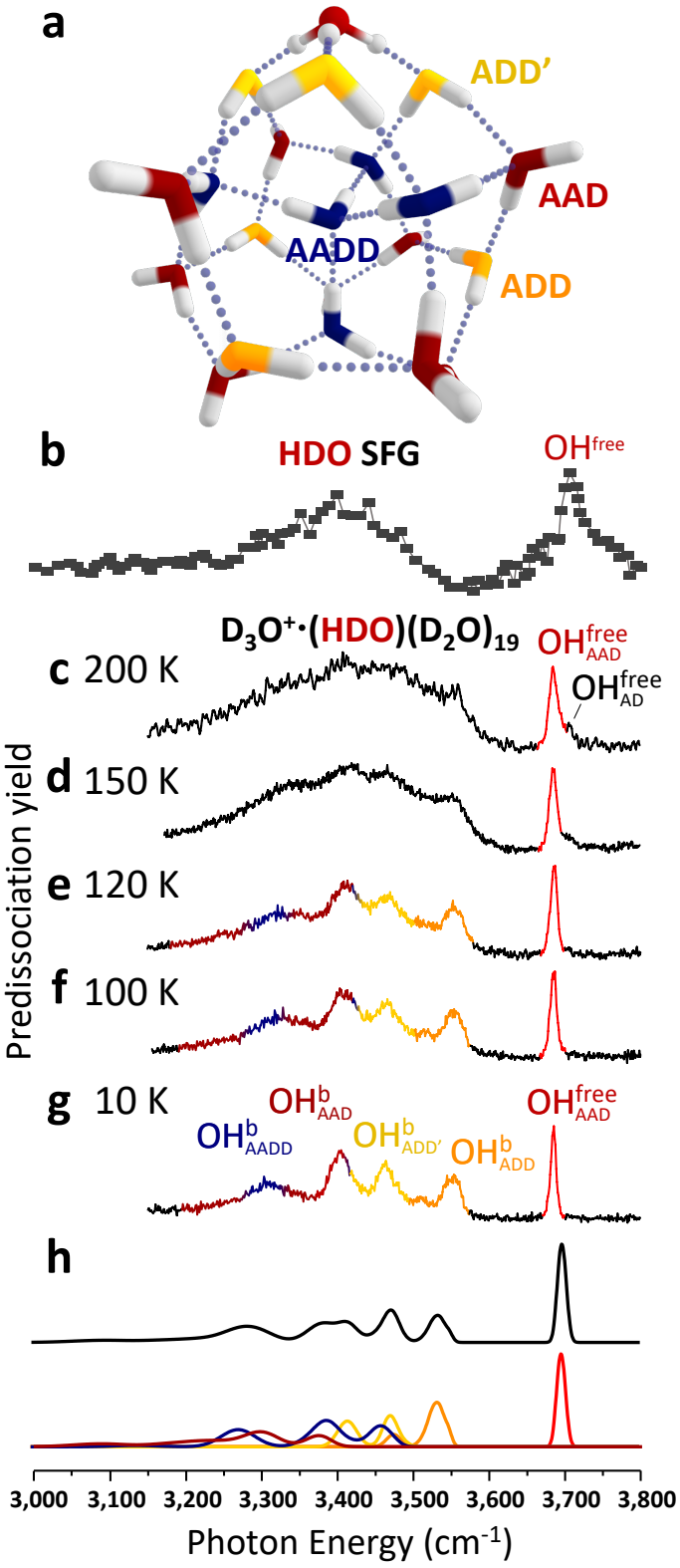
a
ADD'
AAD
AADD
ADD
b
HDO SFG
OH^free
D3O+·(HDO)(D2O)19
c 200 K
OH^free_AAD
OH^free_AD
d 150 K
e 120 K
f 100 K
g 10 K
OH^b_AAD
OH^b_AADD
OH^b_ADD'
OH^b_ADD
OH^free_AAD
h
Predissociation yield
3,000 3,100 3,200 3,300 3,400 3,500 3,600 3,700 3,800
Photon Energy (cm-1)

Figure 9.1: Comparison of the isotope-diluted SFG spectrum of the air-water interface with vibrational predissociation spectra of $D_3O^+ \cdot (HDO)(D_2O)_{19}$ at temperatures in the range 10-200 K. (a) Representative low-energy structure of the $H_3O^+ \cdot (H_2O)_{20}$ cluster. The stick spectra of the clusters with the OH group in each of the possible sites of the cluster are included in Supplementary Fig. 9.14. (b) SFG spectrum of HDO at the water-air interface (*4*) reproduced with permission. (c-g) Vibrational spectra of $D_3O^+ \cdot (HDO)(D_2O)_{19}$ from 200 to 10 K. OH^b and OH^{free} represent hydrogen bonded OH and free OH. The A/D notation labels the number of hydrogen bond acceptors and donors on one water molecule. (h) displays the calculated spectrum based on 400 isotopomers of the 10 lowest energy structural isomers of the $D_3O^+ \cdot (HDO)(D_2O)_{19}$ cluster. The contribution from each type of water molecule (or site) is displayed as a color-coded trace.

drive spectral diffusion in a fully connected, extended network of water molecules. This demonstration opens the way for wide-ranging applications where thermally activated chemical transformations are unraveled in the context of both solvent and solute contributions in a regime where every atom counts.

Chemical systems maintain equilibrium through kinetic processes that balance the populations of reactants and products. In solution, these processes involve energy exchange with the solvent, and simulations of chemical processes in solution often involve a hierarchy of methods. For example, local interactions involving the solute and first-shell solvent molecules might be treated with accurate quantum chemical methods, while the effects of the more distant solvent are included using simpler models.[1, 2] In this report, we introduce an experimental approach that exploits temperature-controlled molecular clusters to provide a well-defined system in which to monitor the dynamic behavior of a simple reversible chemical process as a function of temperature. With the aid of theory, we identify the low energy pathways that are associated with the onset of the observed spectral patterns and further interpret the role of the local environment in promoting these molecular-level processes.

Specifically, gas phase cluster ions are equilibrated through collisions with a low-pressure buffer gas and interaction with blackbody radiation, and hence can be viewed as being weakly coupled to a heat bath.[3] We specifically consider the "droplet-like" water cluster formed upon hydration of an "excess proton" by 21 water molecules, with a representative low-energy structure[4] shown in Fig. 9.1a. Note that its vibrational spectrum (Fig. 9.1c) strongly resembles that of the air-water interface (*cf.* Fig. 9.1b).[5]

9.2 Experimental and Computational Methods

9.2.1 Experimental Methods

The $D_3O^+ \cdot (HDO)(D_2O)_{19}$ cluster ions were obtained by first electrospraying 10 mM D_2SO_4 aqueous solution in a humidity-controlled purge capsule filled with HDO:D_2O 1:20 mixture. The ions so generated were loaded into a temperature-controlled Paul trap kept at the experiment temperature (10-200 K in this study) with He as buffer gas to equilibrate the temperature of the ions to that of the trap. The instrument diagram is displayed in Fig. 9.2. The experiment duty cycle (100 ms duration) starts with a buffer gas pulse which resides in the trap for about 20 ms before being evacuated. Note that if the ion is injected constantly, there will be constant ion loading and will defeat the mass selection by loading more unwanted ions in after the mass selection pulse. This suggests there is still enough buffer gas (at least 10^{-4} Torr) to trap the ions even 50 ms after the buffer gas pulse. Such observation is consistent with experiment done on similar instrument which indicated that the residual buffer gas pressure is sufficient to maintain canonical behavior even at ~70 ms after the gas pulse.[28] During this time window, an ion packet stored in the second ion guide is injected into the trap. The gas pressure as a function of time, as well as the ion loading window, is illustrated in Fig. 9.3a. After the ion is loaded and cooled, an amplitude-modulated frequency sweep (1-200 kHz, 2 V amplitude) is applied to one of the end caps of the Paul trap.[32] When the frequency waveform matches the secular frequency of a certain mass ion (in this case m/z=421), it will be ejected or collided onto the trap electrode. In-trap mass selection can be achieved through amplitude modulation (AM) of the frequency sweep, specifically by setting the waveform amplitude to zero when its frequency is near the secular frequency of the

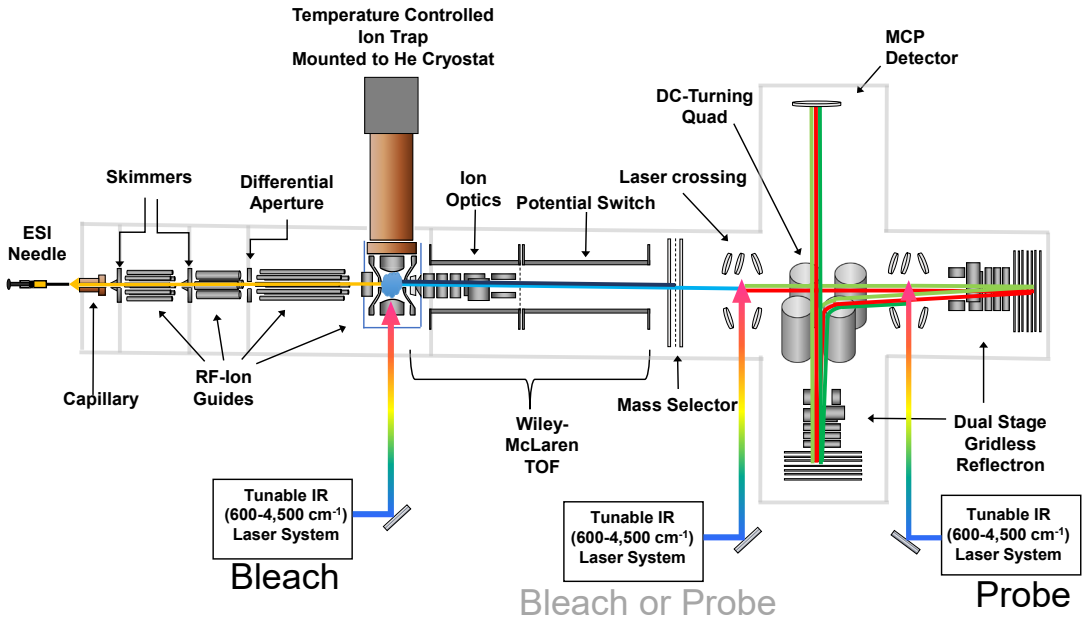

Figure 9.2: MS^4IR^3 Instrument for the temperature controlled variable delay time hole burning experiment. The second ion guide is capable of storing ions and ejecting them as an ion packet into the Paul trap in which the secular frequency mass selection (MS^1) is performed. The bleach laser (IR^1) is introduced into the ion trap after ion cooling and mass selection. The bleached ion ensemble is stored for a variable delay time, then mass selected again with a TOF mass selection (MS^2). In the TOF region there are two additional stages of mass selection with two reflectrons (MS^3 and MS^4). In between $MS^{2,3 \text{ and } 4}$ there are two IR lasers that can serve as the probe laser (IR^2 and IR^3). In this study, we use the in-trap laser and the third laser as the bleach and probe laser, respectively.

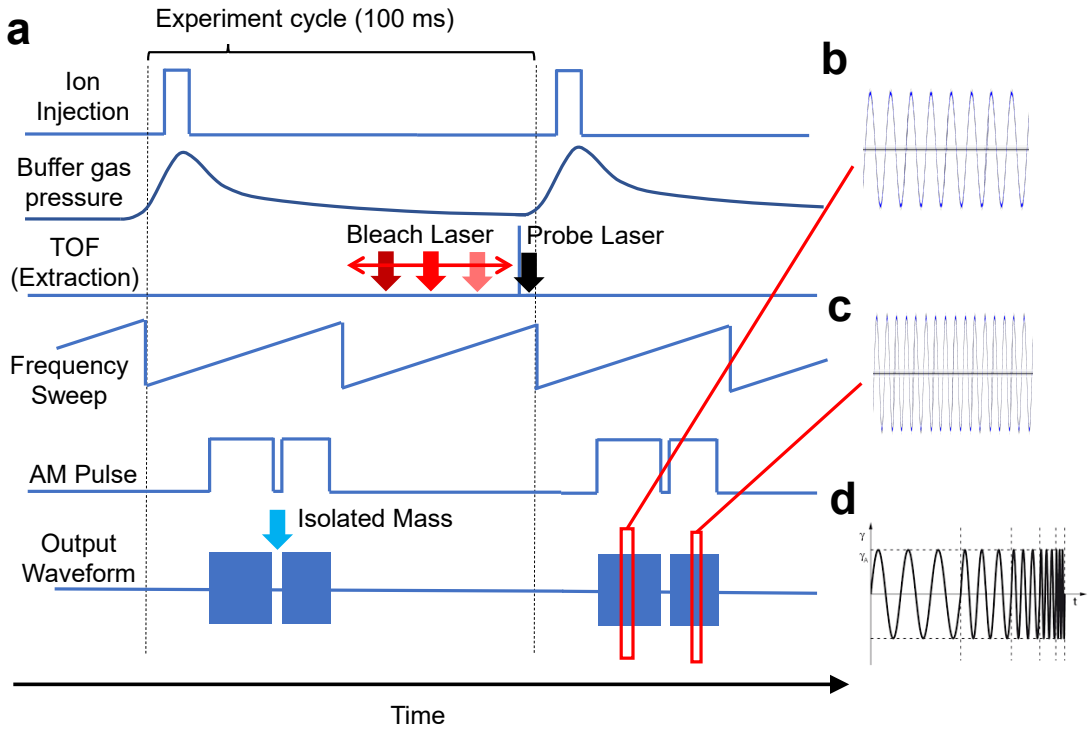

Figure 9.3: Time sequence for the in-trap mass selection and variable delay two laser experiment. (a) The experiment starts with pulsed buffer gas and ion injection. After the ions are introduced and cooled in the Paul trap, an amplitude-modulated frequency sweep in the ion secular frequency range is introduced to select the desired mass. The frequency sweep (d) starts from low frequency that corresponds to the higher masses (b) and sweeps to high frequency (c) that removes the lower masses. The output waveform is modulated to zero when the frequency matches the desired mass to allow the target species to remain in the trap. After mass selection, the bleach laser is introduced to the trap at variable delay time. Finally, the ions are extracted from the ion trap for TOF mass analysis and probe laser detection.

desired mass, and turning it back on after it passes the mass to be preserved (The frequency as a function of time, the AM pulse, and the output waveform are displayed in Fig.9.3a). After mass isolation of the $D_3O^+ \cdot (HDO)(D_2O)_{19}$ species, the ions are stored in the ion trap until the beginning of the time of flight (TOF) mass analysis, at which time the ions are extracted out of the Paul trap into the TOF region.

In a typical single laser experiment where the predissociation yield of all mass degenerate isotopomers is recorded, the mass-selected ions are irradiated with a pulsed (10 Hz, 8 ns) tunable OPO/OPA IR laser (LaserVision) which results in dissociation of the cluster ion through water loss upon resonant excitation of the mass-selected ions. The fragment ion is separated from the parent ion with a secondary mass spectrometer and used as a channel for detection of IR absorption by the ion of interest.

The isotopomer-selective, two-color, IR-IR double resonance, hole burning dip spectra were acquired by first irradiating mass-selected ions in the ion trap with the bleach laser which will result in mass change through water evaporation when the cluster absorbs a photon. Mass separation in the first stage of the TOF mass spectrometer was used to eliminate the resulting fragments. The remaining parent ions are then irradiated by the probe laser and mass separated again in the second and third mass separation stages, where the photofragment from the probe laser is monitored. When acquiring an isotopomer-selective double resonance dip spectrum, the probe laser is fixed on a frequency unique to one or several similar isotopomers with absorptions at the same frequency. The bleach laser is scanned through the entire spectrum. When the bleach laser dissociates the parent ion selected by the probe, the probe fragment signal is attenuated (bleached). This depletion is recorded as a function of bleach laser frequency,

and the resulting trace reveals the spectrum associated with the isotopomer selected by the probe. Irradiating the ions inside the ion trap allows us to vary the time delay between the bleach and the probe lasers and record reaction kinetics of the system of interest. The key is that both bleach and probe lasers remove ground state population by photodissociation (evaporation of a water molecule in this case, since bare clusters are excited in contrast to the typical "tagging" method that involves photodissociation of a weakly bound adduct like H_2 or Ar). [23]

For example, at cold temperature when the isotopomers do not interconvert, the population depletion caused by the bleach laser remains the same over time (Fig. 9.4a, b). Thus, photodepletion of isotopomer B's population does not influence the population in A whereas photodepletion of A results in decrease in isotopomer A's population. When the probe laser is fixed on A and the bleach laser is scanned through the entire spectrum, there will only be a dip feature at the frequency corresponding to A. The time-dependent population change is thus essentially zero (Fig. 9.4c). Now consider the case at elevated temperature where interconversion between isotopomers A and B can occur: bleaching B will now result in a decrease in B's population that gets refilled by exchange with A's population. This ultimately results in depletion in the population of both A and B (Fig. S8d). Similarly, photodepletion of A's population results in decrease of both the population of A and B over time (Fig. 9.4e). In that case, the hole-burning spectra at longer delay times display dip features at frequencies corresponding to both the A and B isotopomers (Fig. 9.4f) and the time dependence of the populations reveals the interconversion kinetics.

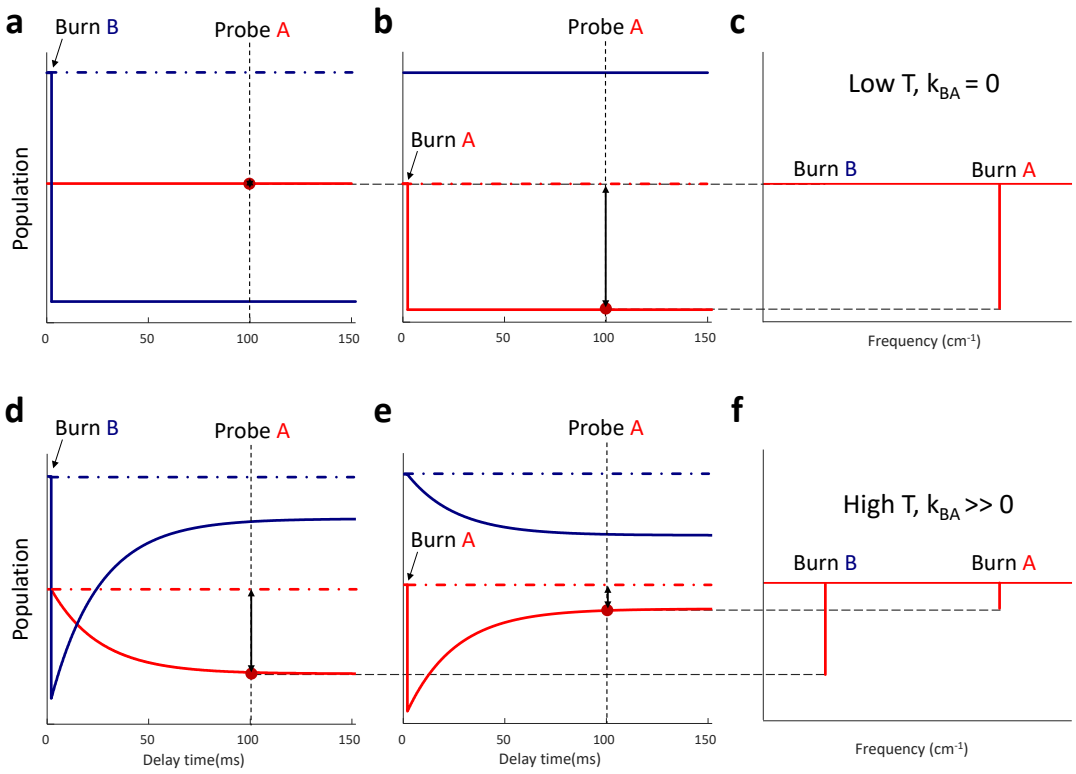

Figure 9.4: Time dependent population behavior of a two isotopomer system at two different temperatures. (a-c) At low temperature, bleaching isotopomer B does not influence the population in A whereas bleaching A results in depletion of A's population at the frequency corresponding to A. (d-f) At higher temperatures where interconversion between the two isotopomers can happen, bleaching B will result in a decrease in A's population over time to refill the hole burned in B. Bleaching A will result in a large initial depletion in A, which is then refilled by B. This behavior manifests in the hole-burning spectra of A as two dips at both A's and B's positions.

The kinetics observed here reflect the ensemble behavior of many clusters trapped in the ion trap and equilibrated with the trap wall through collisions with the buffer gas where the cluster ions display canonical behavior. For individual cluster ions, there are rare large amplitude motions that rearrange the hydrogen bond network and result in interconversion between different isotopomers. If we consider the model system where type A and type B isotopomers interconvert with each other, we can follow the behavior of individual clusters (Fig. 9.5b). At the beginning (t=0), the system is in equilibrium and there are 3 clusters of the type A isotopomer and 6 of type B. This corresponds to an equilibrium constant of 2 for the A↔B interconversion. As time passes, some of the type A isotopomers spontaneously become type B - and some type B become type A - through H-bond switching. The overall population ratio remains the same since the system remains in equilibrium. Then, at t=15 ms, the bleach laser dissociates all clusters of type A and leaves behind 6 type B clusters. As the equilibrium condition is compromised, it becomes more probable, overall, for type B clusters to convert into type A clusters. Thus, the population of B is gradually depleted and the population of A is partially restored (the cluster types statistically fluctuate, but on average some of the type B population is converted to type A). After a long waiting time, a new equilibrium is reached and the 6 remaining clusters are fractionated into 4 of type B and 2 of type A, preserving the same equilibrium constant of 2. The ensemble average of population displays first order kinetics that can be expressed as an exponential decay of the difference between the old equilibrium population and the new equilibrium population (Fig. 9.5a).

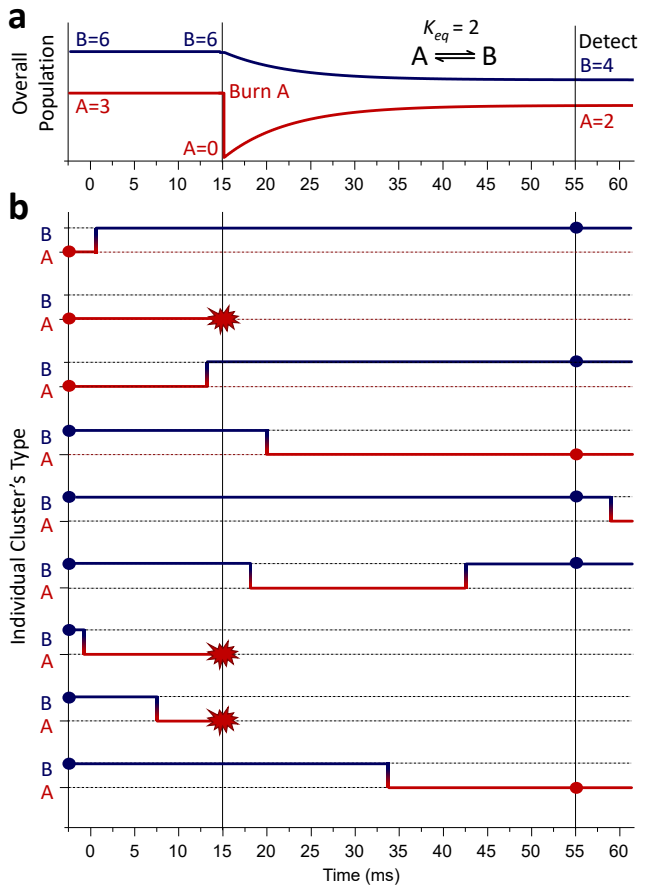

Figure 9.5: Comparison between the ensemble behavior and the individual cluster ion's behavior at elevated temperature where interconversion between two isotopomers is possible. (a) The overall behavior of the ensemble including population in A and B isotopomers with an equilibrium constant of 2, which results in an equilibrium population ratio of 1:2 for A:B. (b) Behavior of individual clusters where interconversion between A and B can happen. The identity of the cluster is traced over time. Interconversion is depicted as a sudden jump from dotted line labeled A to B or vice versa. At t=15 ms, a bleach laser pulse is introduced at a frequency corresponding to absorption in isotopomer A, which destroys all instantaneous population in isotopomer A. At t=55 ms, the probe laser can be introduced to count the population in A or B isotopomers.

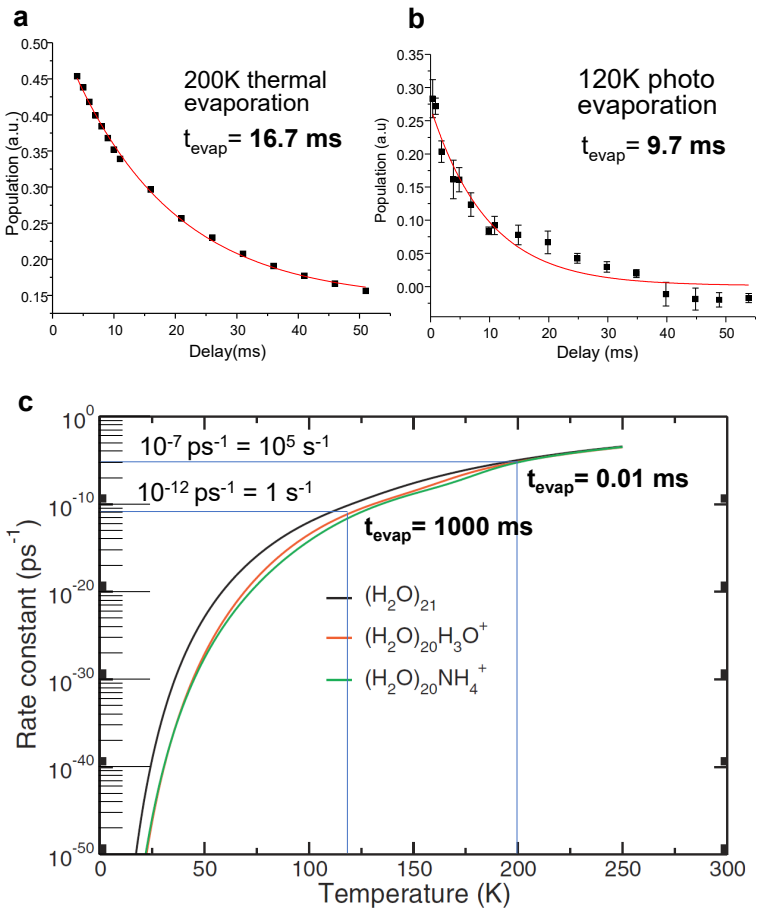

Figure 9.6: Thermal and photo induced evaporation kinetics of the D_3O^+·(HDO)$(D_2O)_{19}$ clusters. (a) Thermal evaporation kinetics at 200 K measured in the Paul trap held at 200 K. The evaporation time is about 16.7ms. The exponential behavior indicates a canonical condition in the ion trap. (b) Photoinduced evaporation kinetics at 120 K with a vibrational excitation at 3,686 cm^{-1} measured in the Paul trap held at 120 K. The evaporation time is about 450 ms without laser excitation and 9.7 ms with the laser excitation. The vibrational excitation heats the cluster to about 200 K considering the harmonic heat capacity (Figure 9.5). The experimentally measured rates agree with the theoretically calculated rate constants (c) at 200 K [14]. Panel (c) is reproduced with permission.

Beside the laser experiments, the thermal evaporation kinetics can also be measured. After in-trap mass selection, the ions are stored in vacuum inside the Paul-trap. The delay time between the mass selection and the TOF mass analysis can be varied. The populations of the parent ion and the evaporation product ion (smaller water clusters) as a function of time reveal the evaporation kinetics of water clusters (Fig. 9.6a). Such experiments can be done at various temperatures to determine the temperature-dependent evaporation rates. Yet another type of experiment can be done by applying a laser pulse immediately following mass selection. The absorption of a photon will result in a well-defined temperature jump in the cluster and acceleration of evaporation. One can prepare clusters with the same internal energy through either thermal heating or laser excitation. These methods should yield similar evaporation kinetics since IVR occurs on a timescale much faster than that of evaporation (Fig. 9.6b). Population decays in Figure 9.6 and Figure 9.17 are fitted with a single exponential function of the form $(t) = P_{eq} + \left(P(0) - P_{eq}\right)e^{-\frac{t}{\tau}}$, where P_{eq} is the equilibrium population at $t = \infty$, P(0) is the initial population at $t = 0$, and τ is the characteristic time constant.

9.2.2 Computational Methods for the Structures and Vibrational Frequencies of $H^+(D_2O)_{21}$

Detailed calculations on different H-bonding arrangements of $H_3O^+ \cdot (H_2O)_{20}$ with a pentagonal dodecahedral structure identify 10 structurally similar, low-energy isomers that are very close in energy (Fig. 9.7). These structures minimize the number of dangling hydrogens on adjacent water monomers while having no dangling hydrogens adjacent to the H_3O^+ monomer. Seven of these isomers are known from earlier studies.[33, 34]

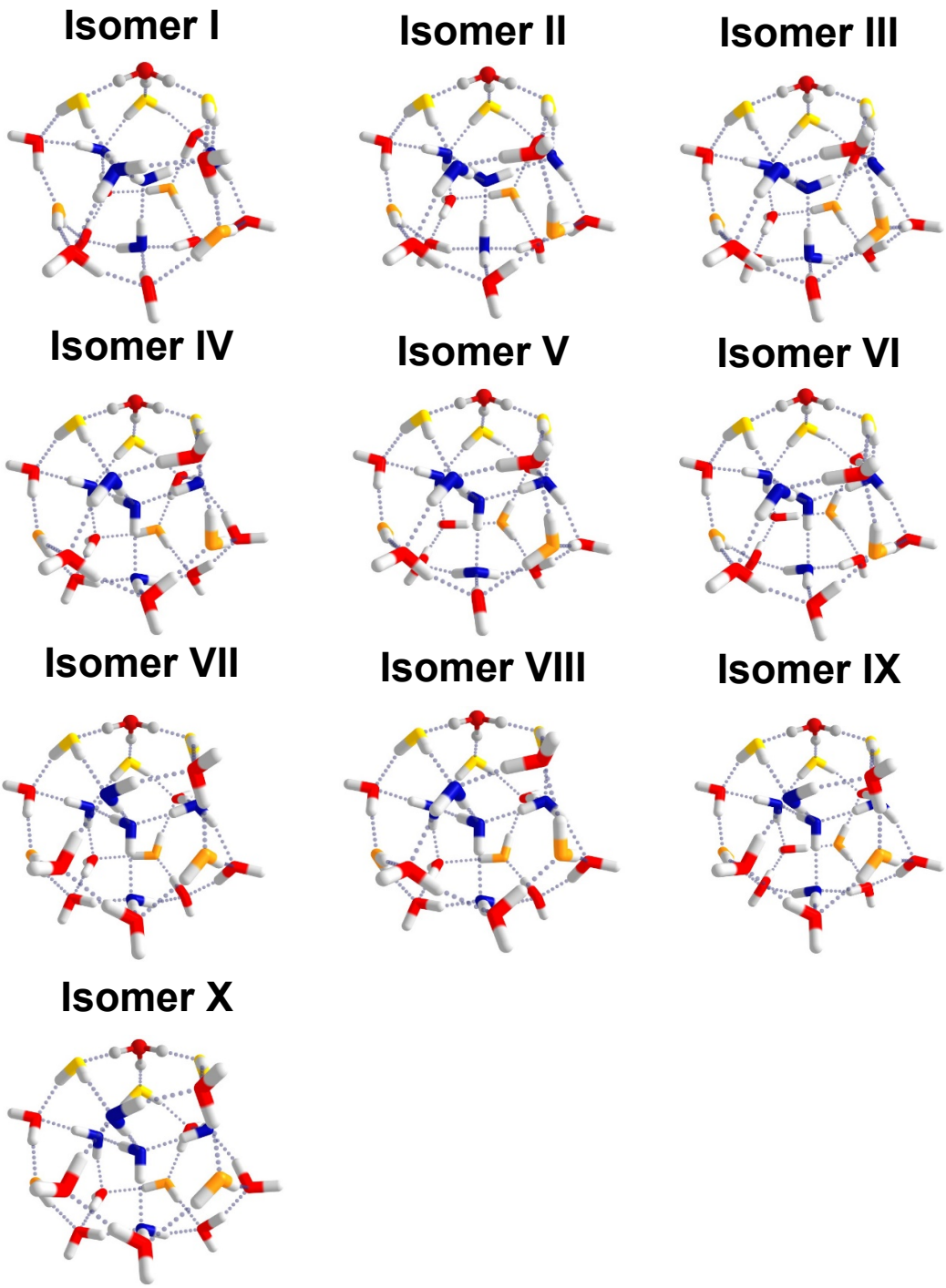

Figure 9.7: Structure of all 10 low energy isomers of the $H_3O^+ \cdot (H_2O)_{20}$ species.

These geometries are optimized at the DF-MP2/aug-cc-pVTZ level. The relative energies are included in Table 9.1.

Optimizations of the structures of the ten low-energy isomers were performed using the DF-MP2 method,[35-40] where the "DF" indicates the use of density fitting, in conjunction with the aug-cc-pVDZ basis set.[41-46] The DF-MP2/aug-cc-pVDZ optimized structures were used to calculate harmonic vibrational frequencies and intensities at the same level of theory.[12] The geometries were then reoptimized at the DF-MP2/aug-cc-pVTZ[41-46] level, with the resulting structures being used for subsequent single-point calculations at the DF-MP2/aug-cc-pVQZ[41-46] level of theory. All calculations were done using the Molpro 2018 package.[48,49] Table 9.1 lists the relative energies of the ten isomers calculated at the DF-MP2/aug-cc-pVQZ level of theory.

Table 9.1. Relative energies of the lowest energy isomers of $H_3O^+ \cdot (D_2O)_{20}$. Energies are calculated at the DF-MP2/aug-cc-pVQZ level of theory, using geometries optimized at the DF-MP2/aug-cc-pVTZ level.

Isomer	Relative energy (kcal/mol)
1	0.082
2	0.049
3	0.029
4	**0.000**
5	0.021
6	0.075
7	0.137
8	0.034
9	0.134
10	0.161

Vibrational frequencies were calculated for all 43 possible locations of H on each isomer, including on the hydronium monomer, for a total of 430 sets of frequencies. For

the individual structural isomers, the spread in the relative zero-point energies (ZPEs) for the different isotopomers is only about 70 cm^{-1}, or 0.2 kcal/mol. This is close to the differences in the relative ZPEs of the ten $H_3O^+ \cdot (H_2O)_{20}$ isomers considered here.

In generating the calculated spectra reported in the main body of the text and in Fig. 9.7, the frequencies were scaled by a factor of 0.96, which brings the calculated frequencies of the free OH transitions into close agreement with experiment. The OH stretch frequencies where the H atom is located on the hydronium monomer are ~400 cm^{-1} lower in energy than the lowest frequency HOD OH stretch vibrations, and thus are not included in the calculated spectra used for comparison with experiment. The spectra from the remaining 400 isotopomers are given equal weight. Given their closeness in energy this should be a reasonable assumption for clusters at temperatures near or above 100 K.

9.3 Results and Discussion

The specific dynamical processes at play here are the temperature-dependent pathways for migration of a single H atom through the various distinct sites in an otherwise perdeuterated cage. This is accomplished by following how the frequency of the OH oscillator evolves in time as the temperature is systematically raised to enable large amplitude motion of the water molecules. We specifically monitor the migration of the OH oscillator among the various spectroscopically distinct sites (labeled by different colors in the structure and spectra in Fig.9.1) in the structure after a sudden disruption of the equilibrium population. That is, the steady-state populations in the various network sites, constrained by the equilibrium constant (K_{eq}) in a thermal ensemble, are sustained through steady-state, site-to-site interconversion kinetics. We remark that these

rearrangements are closely related to those that drive ultrafast "spectral diffusion" in bulk and interfacial water. [6, 7, 8, 9, 10]

Our experimental approach to measuring the spontaneous kinetic processes in clusters is motivated by the classic "T-jump" approach pioneered by Eigen in the 1950s, who demonstrated a way to determine the rates of the fast reactions that sustain a macroscopic equilibrium state. That method involved quickly displacing the system away from equilibrium and then observing the time response of the populations as a new equilibrium condition is established.[11] Here, we employ a variation of this scheme in which we remove the population in one of the sites in an ensemble of clusters held at constant temperature and observe the system moving toward the new equilibrium population distribution.

The structure displayed in Fig. 9.1a (denoted PD_0) is one of many arrangements with similar oxygen atom cages but different topologies of the extended H-bonding network (see the ten low lying isomers in Fig. 9.7).[4, 12, 13] We introduce a single H atom into the perdeuterated isotopologue, which is isolated and studied using photofragmentation mass spectrometry as detailed in the Chapter 8.2 and Chapter 2. These isotopologues occur in two classes according to whether the H isotope is sequestered in the hydronium ion or resides in the surrounding neutral water cage. We are here concerned with only the $D_3O^+ \cdot (HDO)(D_2O)_{19}$ type (hereafter denoted PD_{OH}) because the OH stretches of the embedded hydronium are known to lie near 2000 cm^{-1} and do not contribute to the spectra in the OH stretching region. The PD_{OH} class occurs with many spectroscopically distinct isotopomers at low temperature according to the location of the unique OH group in the PD structure. This spectral variation occurs

because the water molecule with the OH group is differentiated according to the number of H-bond donors (D) and acceptors (A) at play in each site, as well as the H-bonding topology of the more distant molecules in the network. We note that, because both inter- and intra-molecular coupling are suppressed in the OH stretching spectrum of the PD_{OH} isotopomer, the resulting bands are dramatically simplified compared to those displayed by the homogeneous $H_3O^+ \cdot (H_2O)_{20}$ isotopologue (Fig. 9.8a,b).[14] There are five clearly distinct OH bands in the PD_{OH} spectrum that are color-coded in Fig. 9.1g (full spectrum in Fig. 9.9) according to the specific sites that are calculated to yield fundamentals in the observed locations (Fig. 9.10).

At low temperature, the spectrum of the mass-selected ion packet consists of a heterogeneous contribution from the spectra of individual isotopomers, each of which can be isolated using isotopomer-selective vibrational spectroscopic methods as discussed at length in previous studies. [15, 16, 17, 18] Isotopomer selection is achieved by sequentially removing each isotopomer from the ion packet through IR photodissociation at each of the five band positions with an initial IR laser with pulse width ~8 ns (hereafter denoted the bleach laser). Features in the spectrum that are modulated by the bleach are revealed by interrogating the same ion packet with a second IR laser pulse (~8 ns pulse width, hereafter denoted the probe laser) that follows the bleach pulse after a delay time, Δt. Site-specific spectra for the five sites were reported previously and are reproduced in Fig. 9.8. The assignments of the five sites are not exactly trivial due to overlapping contributions from different types of water molecules as seen in the theoretical and experimental spectra comparison in Fig. 9.10. The technique of isolating an intact H_2O molecule and determining the correlated absorptions of the two OH oscillators can be

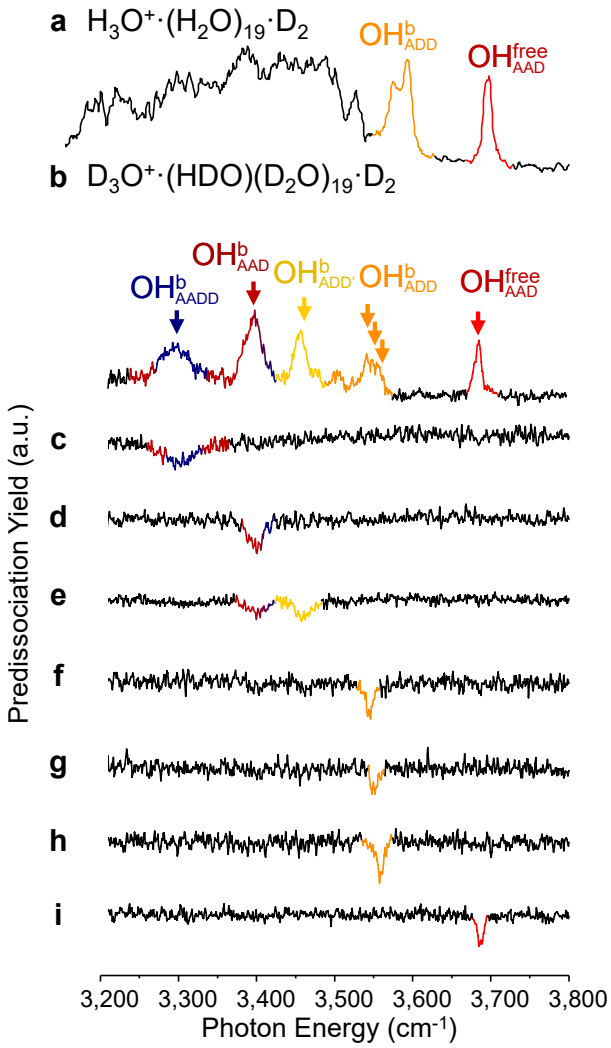

Figure 9.8: Comparison between the vibrational spectra of $H_3O^+\cdot(H_2O)_{20}$ and $D_3O^+\cdot(HDO)(D_2O)_{19}$. Single laser vibrational predissociation spectra of the all-H isotopologue (a) and the $D_3O^+\cdot(HDO)(D_2O)_{19}$ isotopologue (b) obtained with the D_2 messenger tagging technique at 13.5 K. The single laser spectrum in (b) contains contributions from various isotopomers that are isolated with the isotopomer-specific double resonance hole burning technique and displayed in (c-i) where the probe position is listed in (b) and color coded in the same scheme as other figures. The appearance of the lower energy feature in (e) was discussed previously in ref. 28 and attributed to combination band activity.

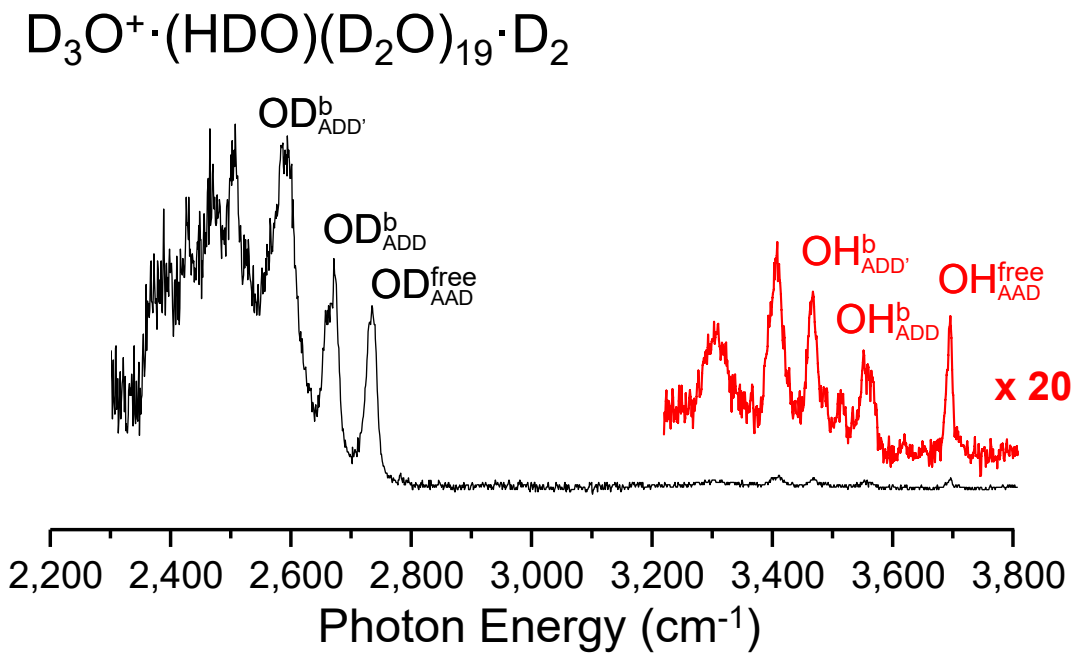

Figure 9.9: Comparison of OD and OH intensities of the $D_3O^+\cdot(HDO)(D_2O)_{19}$ cluster. The red trace is a scaled up (by 20 times) version of the black trace in the OH region. The low intensity in the OH region is caused by isotopic dilution. As a result, each individual cluster displays 42 OD features and only one OH feature.

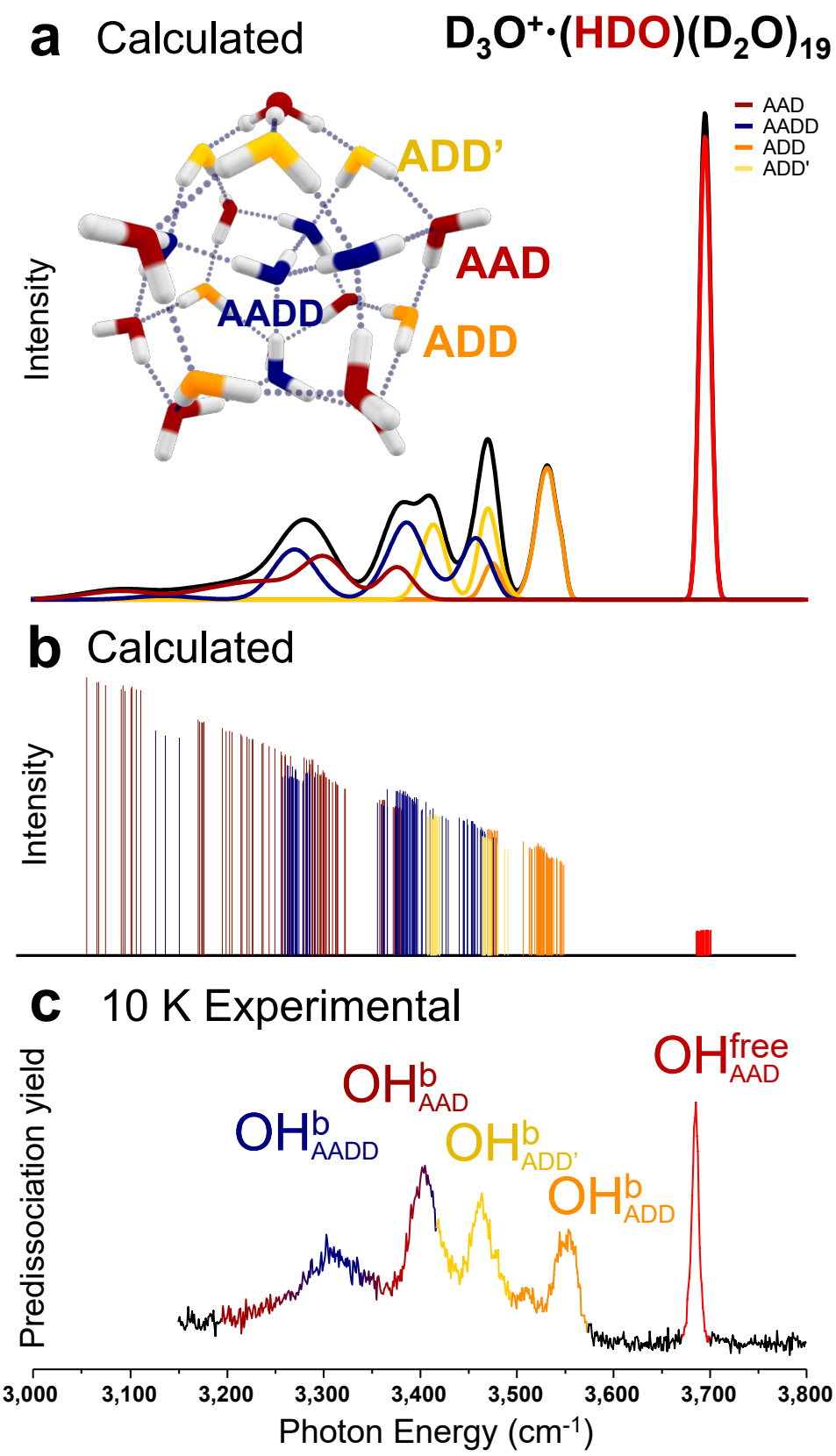
a Calculated
$D_3O^+ \cdot (HDO)(D_2O)_{19}$
AAD
AADD
ADD
ADD'
ADD'
AAD
AADD
ADD
Intensity
b Calculated
Intensity
c 10 K Experimental
OH^{free}_{AAD}
OH^{b}_{AAD}
OH^{b}_{AADD}
$OH^{b}_{ADD'}$
OH^{b}_{ADD}
Predissociation yield
3,000
3,100
3,200
3,300
3,400
3,500
3,600
3,700
3,800
Photon Energy (cm^{-1})

Figure 9.10: Comparison between calculated and experimental vibrational spectra of all isotopomers of the $D_3O^+ \cdot (HDO)(D_2O)_{19}$ isotopologue. (a) Calculated spectra including summed contributions (black trace) from all 400 isotopomers of the 10 low energy structural isomers shown in Figure 9.7 where scaled (0.96 scaling factor) harmonic frequencies are convolved with experimentally determined linewidths (28). Contributions from the various types of water molecules are displayed in color coded traces that corresponds to the scheme depicted in the representative structure. (b) Calculated stick spectra. (c) Experimental spectra at 10 K including contributions of all isotopomers present.

very helpful for assigning bands associated with different types of water molecules as illustrated in Chapter 6 and Chapter 7. However, such experiment is not available for protonated water clusters due to the proton transfer reaction at room temperature which would turn the intact H_2O molecule in to HDO molecules. Here we utilize the structural similarity between $CH_3NH_3^+(H_2O)_{20}$ and $H_3O^+(H_2O)_{20}$ (Fig. 9.11 a and b) and $CH_3NH_2^+(H_2O)_{20}$'s lack of mobile proton to preserve the intact H_2O molecule embedded in the same cage structure. The structural similarity is confirmed spectroscopically in figure 9.11 c and d where the five OH band pattern and position is preserved from the D_3O^+ cluster to the $MeND_3^+$ cluster with slight change in the AAD region. The extra peaks around 3000 cm^{-1} are caused by the CH stretches on the methyl group. With the structural similarity confirmed we investigates the spectral feature of intact H_2O molecules in the $CH_3ND_3^+\cdot(H_2O)(D_2O)_{19}$ cluster (Fig. 9.12). The most noticeable change going from the $CH_3ND_3^+\cdot(HDO)(D_2O)_{19}$ cluster to the $CH_3ND_3^+\cdot(H_2O)(D_2O)_{19}$ cluster is the appearance of the bend overtone Fermi resonance feature ($2\nu_{HOH}$) around 3200 cm^{-1} (Fig. 9.12b). Other bands remain mostly the same with some minor shifts caused by intramolecular coupling between the two OH oscillators on the same water molecule. There are four types of water molecules and all their features can be readily assigned by comparing the double resonance dip spectra to the theoretically calculated spectra (Fig. 9.12 c-k). Such results help confirm the assignment scheme used in the $D_3O^+\cdot(HDO)(D_2O)_{19}$ spectra. The only thing that needs extra attention are the ADD' band positions due to their direct connection with the positive charge carrier ion (D_3O^+ or $MeND_3^+$), the reduced acidity of $MeND_3^+$ compared with the hydronium ion is expected to cause a blue shift in the ADD' OH frequencies. That can be considered in terms of the

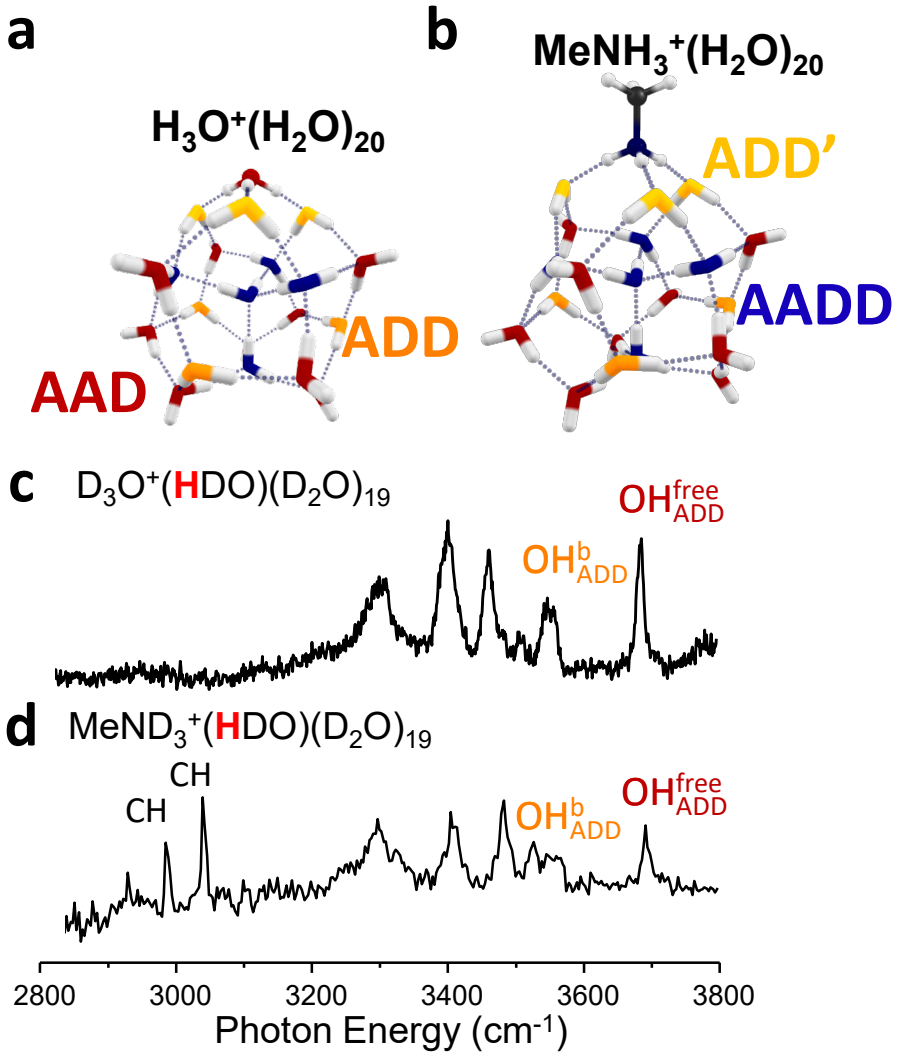

Figure 9.11: Structures and vibrational predissociation spectra of $D_3O^+\cdot(HDO)(D_2O)_{19}$ and $CH_3ND_3^+\cdot(HDO)(D_2O)_{19}$. Representative low energy structure of (a) $D_3O^+\cdot(HDO)(D_2O)_{19}$ and (b) $CH_3ND_3^+\cdot(HDO)(D_2O)_{19}$. Vibrational predissociation spectra of D_2 tagged (c) $D_3O^+\cdot(HDO)(D_2O)_{19}$ and (d) $CH_3ND_3^+\cdot(HDO)(D_2O)_{19}$.

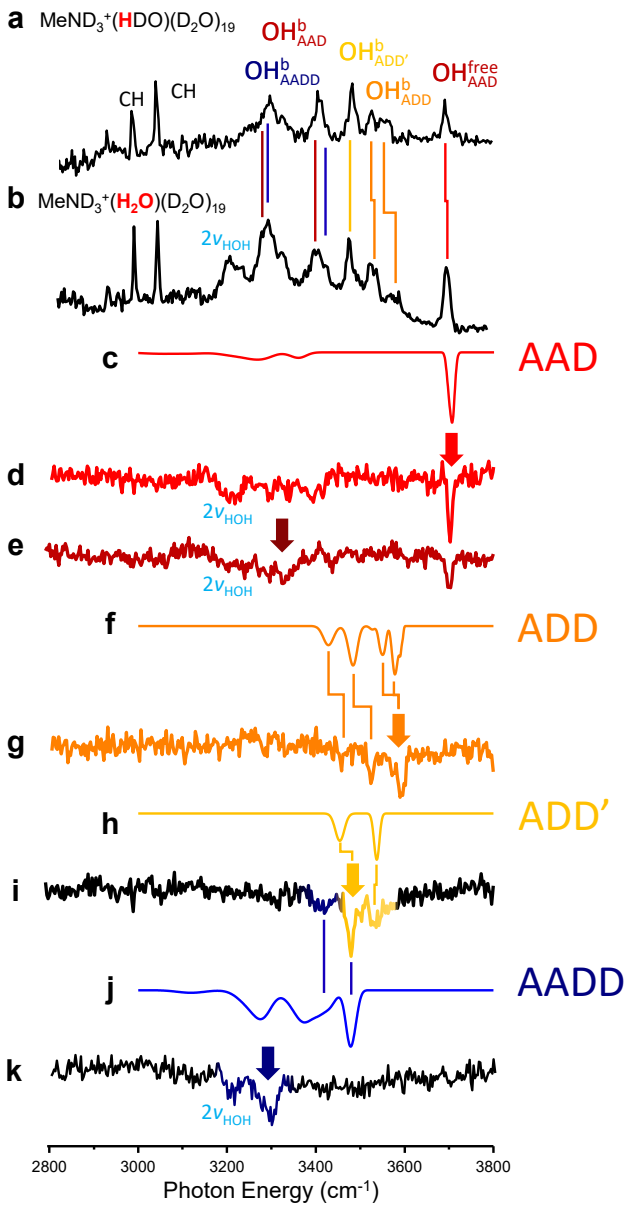

Figure 9.12: Vibrational spectra of $CH_3ND_3^+ \cdot (H_2O)(D_2O)_{19}$ and $CH_3ND_3^+ \cdot (HDO)(D_2O)_{19}$. Vibrational spectra of D_2 tagged (a) $CH_3ND_3^+ \cdot (HDO)(D_2O)_{19}$ and (c) $CH_3ND_3^+ \cdot (H_2O)(D_2O)_{19}$. Double resonance spectra (d,e,g,i,k) and calculated spectra (c,f,h,j) of) $CH_3ND_3^+ \cdot (H_2O)(D_2O)_{19}$ probing various positions indicated by the color coded arrow. Some has contribution from more than one type of water molecule (g has ADD and ADD', i has ADD' and AADD).

hydrogen pushing model established in Chapter 7, the stronger acidity D_3O^+ ion is a better donor and pushes harder on the ADD' OH bonds hence elongating them more and causes more red shift whereas the weaker push caused by the $MeND_3^+$ ion will induce less redshift on the ADD' OH. Such prediction matches the computed results (Fig. 9.13f-i). The overall assignment scheme in Figs.9.14 and 9.10 is supported by the methyl ammonium study summarized in Fig. 9.13.

The cold (T = 10 K) ensemble is static, such that photodestruction of an isotopomer permanently removes this species even when the ion packet is stored for long holding times (up to 1 s in the present study) in an ion trap. In this report, we explore the situation in which, as the temperature is elevated, the OH group is observed to spontaneously migrate from one site to another.

The strategy of our experimental approach is illustrated schematically in Fig. 9.14, where each circle represents the population in one of the spectroscopically distinct sites with the appropriate color as defined in Figs. 9.1a and 9.1g. The low temperature case, which we exploited earlier to obtain the spectral signatures of OH in each site, is diagrammed in the top panel. Removal of population in the red sites by photodissociation leaves a static ensemble of the remaining ions. When the second laser probes the populations of the various other isomers at time Δt later, the four other features appear unaffected by the selective population removal by the first laser. As the temperature is increased, however, the OH group can migrate between sites. In the simplest case where only two sites interconvert (red and brown in Fig. 9.14b), and the bleach laser's pulse width is short compared to the site-to-site exchange rate, the red population can be initially completely removed. But then this population partially recovers over time, while

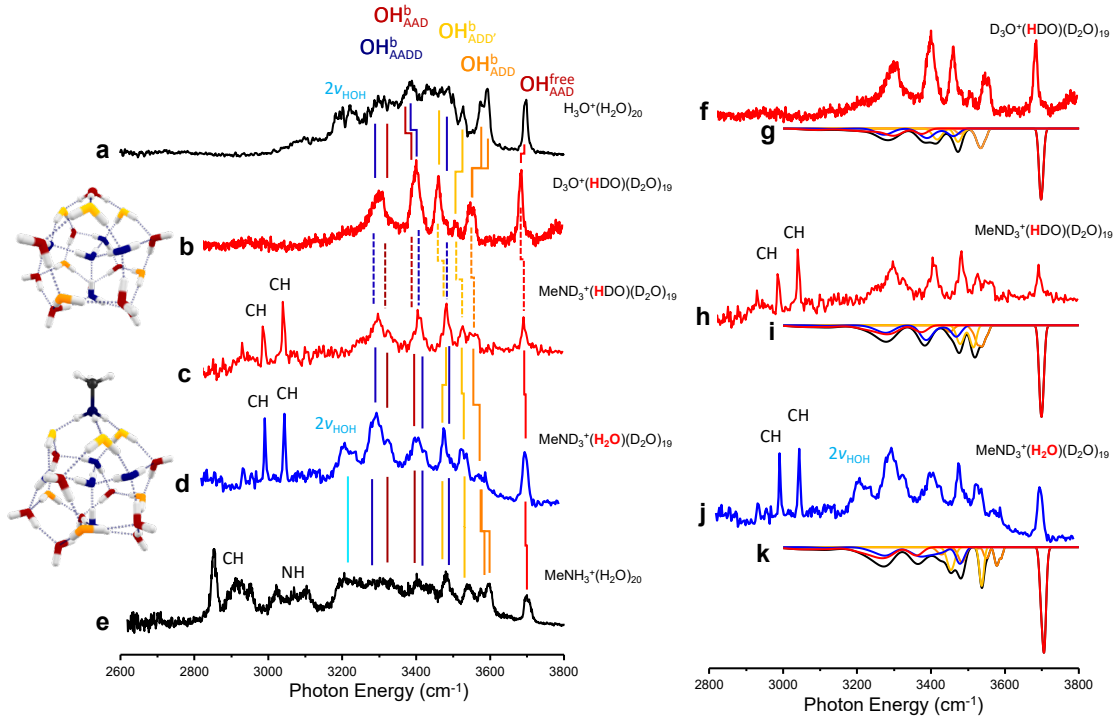

Figure 9.13: Overall assignment scheme of $CH_3NH_3^+\cdot(H_2O)_{20}$ and $H_3O^+\cdot(H_2O)_{20}$ cluster and their isotopologues containing one HDO or one H_2O molecules.

Vibrational spectra of (a) $H_3O^+\cdot(H_2O)_{20}$, (b) $D_3O^+\cdot(HDO)(D_2O)_{19}$, (c) $CH_3ND_3^+\cdot(HDO)(D_2O)_{19}$, (d) $CH_3ND_3^+\cdot(H_2O)(D_2O)_{19}$ and (e) $CH_3NH_3^+\cdot(H_2O)_{20}$ where vertical lines indicates how peaks of the same assignments (color coded) shifts from one species to another. The two structures are reproduced from figure 9.11. Comparison between calculated spectra (g,i,k) with contributions from each type of water molecules color coded and the experimental spectra (f,h,j) of $D_3O^+\cdot(HDO)(D_2O)_{19}$, $CH_3ND_3^+\cdot(HDO)(D_2O)_{19}$, and $CH_3ND_3^+\cdot(H_2O)(D_2O)_{19}$.

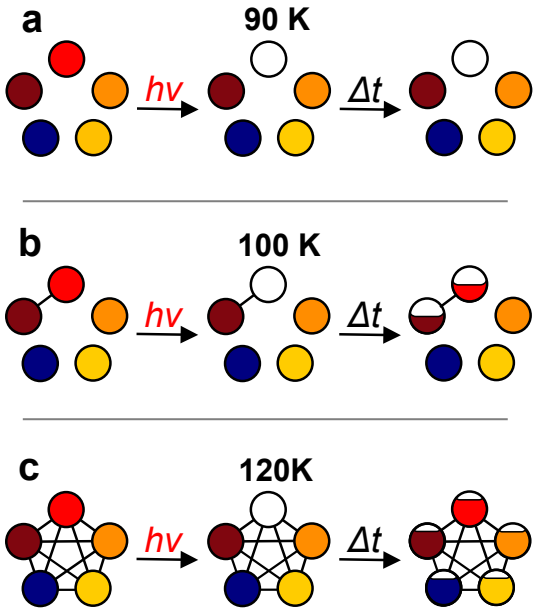

Figure 9.14: Scheme describing the onset of spectral diffusion by site exchange in a temperature controlled, cluster using selective photodissociation. The populations in the five spectroscopically distinct sites, color coded to match those identified in Fig. 9.1g and 9.1h, are indicated by the fractional filling of the circles. The panels correspond to three temperature regimes: (a) a low temperature, static ensemble in which the red isotopomer is removed at t=0, and subsequent interrogation of the ensemble after a delay time Δt reveals persistent removal of the red species from the ion packet, (b) an intermediate temperature where only two sites, red and brown, undergo interconversion on the timescale of the experiment. In this case, initial depletion of the red species, and hence its vibrational signature band, partially recovers after time Δt while the population of the brown isotopomer decreases to restore equilibrium with red, and (c) a sufficiently high temperature that all sites interconvert after initial depletion of red such that, after delay Δt, the red population is largely restored while those in the other four sites exhibit minor depletions upon returning to steady state.

the population in the brown state is reduced to achieve the ratio of populations in the two states dictated by the equilibrium constant. When steady state is restored at sufficiently long delay times, Δt, the populations of both red and brown sites will be reduced by half (assuming $\underline{K_{eq}}$=1), while those in the other three sites are unaffected. This site-specific population redistribution scenario is depicted by partial refilling of the bleached circle after a delay time Δt in Fig. 9.14b. The effect is observable in an experiment that monitors the modulations in the probe laser IR band intensities (and hence site populations) by the action of the bleach, which would yield diminution of the red and brown bands in the OH stretching region. The case where all sites interconvert at high temperature is diagrammed in Fig. 9.14c. The initially depleted red site is repopulated by site-exchange with all other four sites, yielding strong initial depletion of the red band followed by nearly complete recovery. All other bands are reduced to a lesser extent over time. In this case, the IR spectrum for the ensemble would appear exactly the same as that before the depletion laser, but with all bands attenuated by the fraction of total red site population removed at t=0.

The temperature dependent measurements are carried out using a two-color, IR-IR photodissociation scheme. The experimental layout (Fig. 9.2) and details of the experimental approach are included in Chapter 8.2. Because this system is relatively large, the unimolecular rates for laser-induced evaporation are on the order of several milliseconds, which dictates the time delay between bleach and probe such that the clusters excited by the bleach laser are efficiently removed from the ion packet before it is explored by the probe. In that case, when the scanning bleach laser excites any transition that modulates the population of the site interrogated by the probe, that change

is registered as a depletion or dip in the probe signal. We note that because the evaporation rates and spectral dynamics are so slow, excitation by the bleach laser is carried out while the ions are held in the temperature controlled, 3D RF ion trap, which enables trapping for long periods without loss.

To apply the temperature dependent IR-IR photobleaching method to the PD_{OH} clusters, it is important to first establish the temperature dependence of the linear IR spectrum, which is displayed in Fig. 9.1. At 10 K, the spectrum is remarkably simple, featuring a well-resolved grouping of five bands. These have been traced to the various classes of H-bonding arrangements color-coded with structural assignments in Fig. 9.1. Interestingly, this five-band pattern persists up to 120 K before it recedes into a continuum background by 200 K, a temperature at which the clusters are unstable with respect to evaporation on the ms timescale of the mass spectrometer. For reference, the evaporation time ($1/k_{evap}$) is measured to be ~17 ms at 200 K as described in detail in Fig. 9.6. We note that the observed evolution of the spectra with temperature is consistent with nano-calorimetric measurements reported earlier on $H_3O^+ \cdot (H_2O)_{20}$. In that case, an inflection in the caloric curve near 135 K was interpreted to signal the cluster analogue of a melting transition,[19] which occurs below the onset of evaporation at around 150 K. [19, 20, 21, 22, 23] We note also that recent molecular dynamics simulations of $H_3O^+ \cdot (H_2O)_{20}$ by Kseniia et al. [24] confirm that the melting transition occurs over the 130-149 K range, and, moreover, show that although the PD structure dominates up to the melting region, starting at about 130 K, cage structures containing four-membered rings begin to appear. This is consistent with our temperature-dependent spectra, which display significant broadening of the bands as they are overcome by a diffuse background absorption

between 120 K and 150 K (Fig. 9.1d, e). Additionally, a shoulder appears about 18 cm^{-1} above the OH_{AAD}^{free} feature at 150 K, which signals the presence of AD water molecules and the disruption of the PD cage motif. Meanwhile, the persistence of the telltale bands presented by the PD structure at 120 K establishes the integrity of this arrangement even when the clusters have substantial internal energy. For example, an estimate of the heat capacity at 120 K at the harmonic level (Figs. 9.15 and 9.16) indicates that the average internal energy is ~2400 cm^{-1}, which corresponds to about 2/3 of the energy required to dissociate a water molecule from the cluster (3742 cm^{-1}).[25, 26] The internal energy distribution and the heat capacity curve are calculated with harmonic frequencies and using grand vibrational partition function as well as random sampling. We note that there is a rather broad expected distribution of energies (ΔE~1200 cm^{-1}) in an ensemble of ions held at constant T=120 K (Fig. 9.16). It is likely that this temperature is maintained by collisions with the residual He buffer gas in the trap,[27, 28] which we estimate to be on the order of 10^{-4} Torr at 120 K.

The top panel in Fig. 9.17 presents the time dependence of the two color, IR-IR spectra of the PD_{OH} cluster at 120 K. The upper trace (Fig. 9.17a) displays the changes in the OH_{AAD}^{free} site population, obtained by monitoring the probe laser fragment 40 μs after the bleach laser removes populations that have resonances at various energies along the course of the scan. The only dip feature occurs when the bleach laser excites the red (OH_{AAD}^{free}) transition, which is the behavior expected for a static, heterogeneous ensemble. Under exactly the same conditions of excitation, however, the response of the probe laser fragment yield is dramatically different after a time delay of 50 ms between the two lasers, with the result displayed in Fig. 9.17b. Indeed, depletion of red population is now

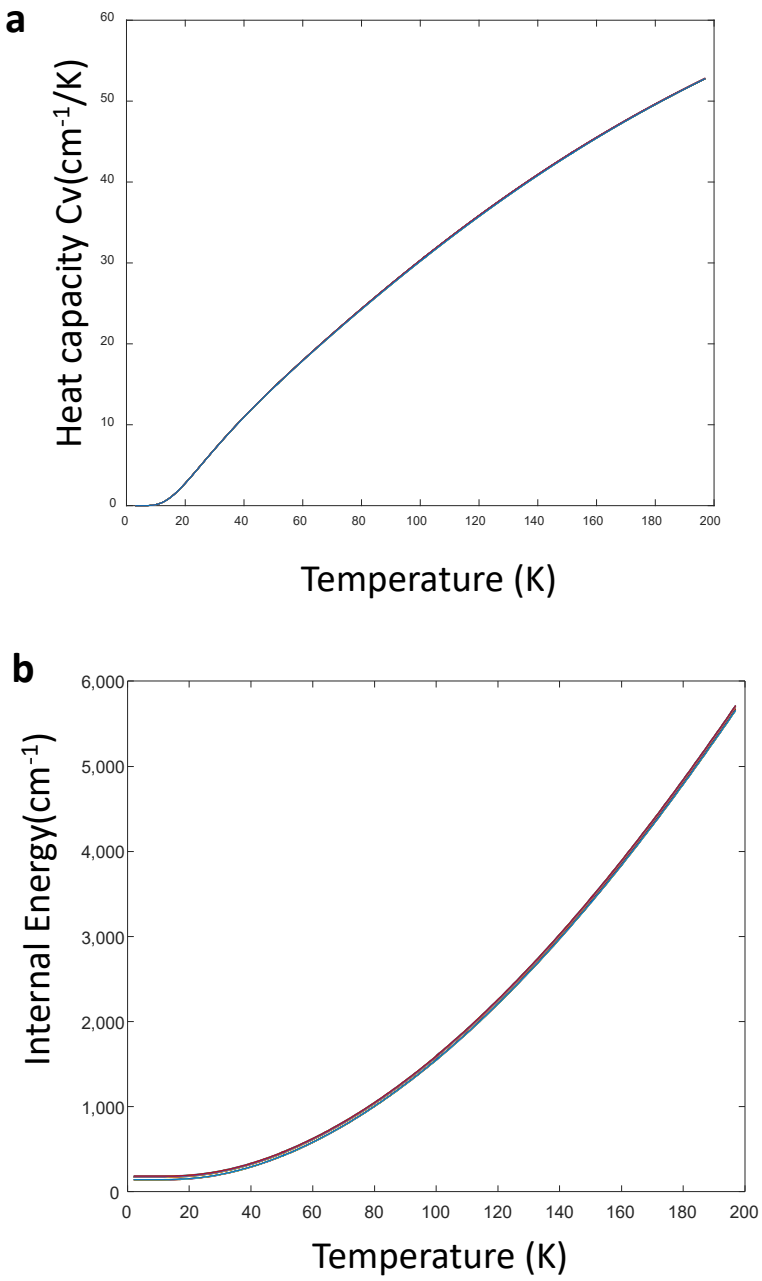

Figure 9.15: Harmonic heat capacity curve and internal energy as a function of temperature of all isotopomers of D_3O^+·(HDO)(D_2O)$_{19}$. The heat capacity (a) and internal energy (b) are similar among all isotopomers.

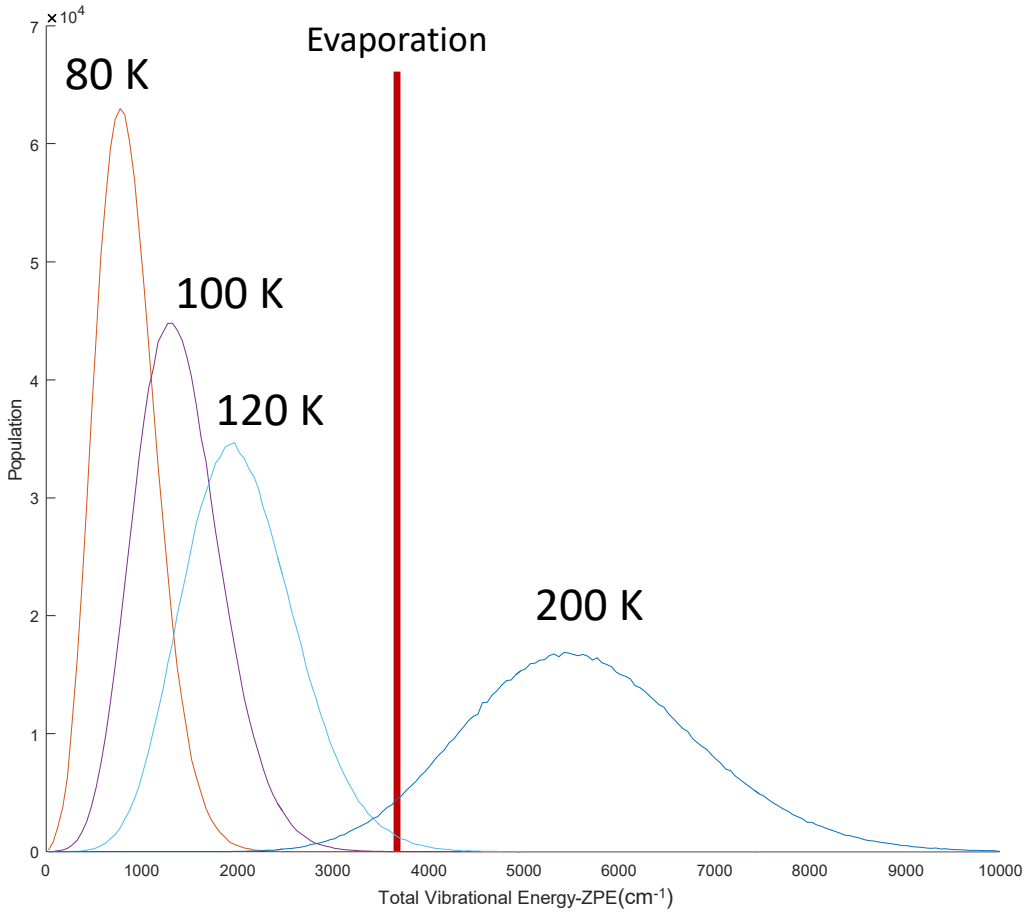

Figure 9.16 Vibrational Internal energy distribution of $D_3O^+ \cdot (HDO)(D_2O)_{19}$. The internal energy distribution is obtained by random sampling of all he normal modes harmonically following Boltzmann distribution. The ZPE is subtracted such that the ground state energy is at 0.

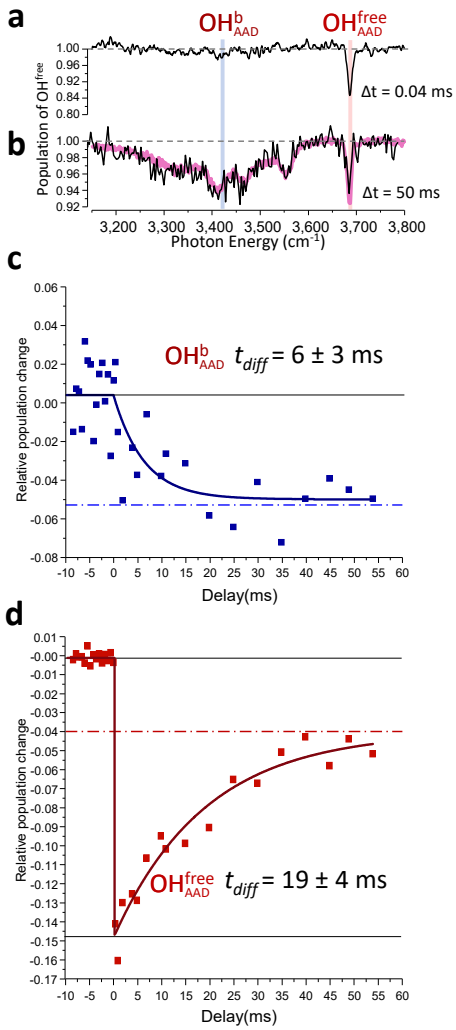

Figure 9.17: Time dependence of the PD_{OH} IR spectrum following photodepletion of the isotopomer with the isotopically labeled OH group in the non-bonded (red) site (OH^{free}_{AAD}) at T = 120 K. Double resonance spectra were obtained at bleach-probe delay times of: (a) 0.04 ms, and (b) 50 ms. The purple trace in (b) closely reproduces the single laser spectrum of the entire isotopologue (all sites occupied) from Fig. 1e. The time evolutions of the OH^{free}_{AAD} population modulation by the bleach laser at two frequencies (OH^{b}_{AAD} and OH^{free}_{AAD} in (a)) are presented in (c) and (d), respectively. The time constants t_{diff} were extracted from exponential fits to the observed data. Negative delay times in (c) and (d) correspond to experiments with the bleach laser off.

obtained upon excitation of all five OH sites, with the result that the dip trace appears essentially the same as the linear spectrum of the entire ion isotopologue (purple lines through the points from the IR-IR scan in Fig. 9.17b, reproduced from Fig. 9.1e). This behavior is conclusive evidence that the spectrum associated with a single site at t=0 evolves over time to encompass the contributions of all sites, which in turn establishes that the OH group migrates among all five locations. It is important to emphasize that this occurs while the overall spectrum retains the telltale bands of the PD cage. This implies that the migration is a rare event in the sense that the OH isotopic label almost always occupies a well-defined position in the cage. This general behavior was reported earlier in our initial study of temperature dependent hole burning spectra of the much simpler $I^-\cdot(H_2O)_2$ system.[29]

The two lower panels in Fig. 9.17 (c and d) present the time evolution of the depleted populations at two sites, one corresponding to the free OH (labeled OH_{AAD}^{free}), probed at 3686 cm^{-1}, red, 9.17d) and the other associated with OH occupation at the bound AAD site (labeled OH_{AAD}^{b}, and probed at 3407 cm^{-1}, blue, 9.17c). The different responses of these traces conform to the scenario outlined in Fig. 9.14. Specifically, the large depletion initially present in the population of the red OH_{AAD}^{free} site is gradually restored with a characteristic time constant of 19 ms, whereas a much smaller depletion in the population of site OH_{AAD}^{b} occurs over similar time range (Fig. 9.17c) as these OH groups migrate to the free OH site. Note that, although we have focused on only two positions in this discussion, at T = 120 K all sites are interchanging with the red site, as evidenced by the extensive dip pattern in Fig. 9.17b. As such, the final fractional depletion in OH_{AAD}^{free} (5%) is much smaller than the initial depletion (15%) since the other

four sites contribute to compensate for the loss due to the bleach of the initial free OH site population.

The spectral evolution at 120 K is well described in the scheme where slow migration of the OH groups re-equilibrate the populations in the ion packet on the 50 ms time scale. This raises the question, however, of whether the pathways that are available for this migration depend on the temperature of the ensemble. This might be anticipated, for example, if the free energy barriers are different for the rearrangements necessary for the OH to migrate between the various sites. We therefore determined the temperature dependence of the IR-IR dip spectra. A summary of the results is presented in Fig. 9.18. At 90 K, the spectrum is dominated by a strong dip at the probe frequency, but by 100 K, there is a clear appearance of a weak, *isolated* second depletion feature near 3350 cm^{-1}, about 300 cm^{-1} from the red band. Interestingly, the heat capacity curve observed with nanocalorimetry on the same cluster has a minor inflection point around 90 K.[19] This is consistent with the increase in phase space volume allowed by the onset of H-bond switching between the free OH and the bound OH on the same AAD water molecule that is implied here. Upon increasing the temperature to 110 K, it is clear that many more sites are exchanging with the probed red site, as the dip pattern (Fig. 9.18e) includes many of the most red-shifted OH groups. This behavior is significant because it emphasizes that the frequency of an OH oscillator does not gradually broaden with time about the original location, but instead abruptly changes to another, distant frequency. The experimental results, discussed above, are consistent with a low barrier isomerization process initiated at T ~ 100 K, and higher barrier processes being engaged above T = 120 K. We examine the barriers for rotation of a HOD molecule in the various sites of a $HDO(D_2O)_{20}$ cluster

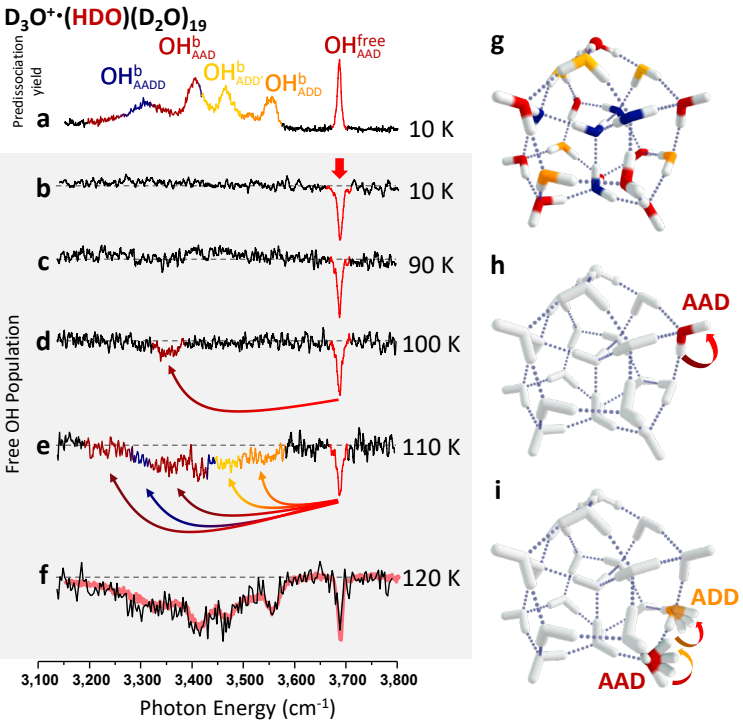

Figure 9.18: Temperature dependent evolution of the photobleaching spectra corresponding to a bleach-probe delay of 50 ms and fixing the probe laser to monitor population of the isotopomer with isotopically labeled OH group in the non-bonded (red) site ($\mathbf{OH_{AAD}^{free}}$). (a) Vibrational spectrum of all isotopomers at 10 K and (b)-(f) hole burning spectra at 10-120 K. The red trace in (f) reproduces the single laser spectrum of the entire isotopologue (all sites occupied) from Fig. 1e. The vertical red arrow in (b) indicates the probe laser frequency, whereas the curved arrows in (d) and (e) indicate that the appearance of additional dips arise from OH migration from the OH_{AAD}^{free} site to various other sites when their populations are depleted by the bleach laser, (g) a representative low energy PD structure, (h) a possible pathway for OH migration at 100 K, and (i) schematic illustration of more complex pathways that likely operate at higher temperatures, where the ribbon arrows indicate the directions of OH group rotations.

comprised of a hydrogen bonding network that mimics that of the $H_3O^+ \cdot (H_2O)_{20}$ cluster.[30] We focus on the neutral rather than the protonated cluster because of the availability of highly accurate force fields for the former. The lowest barrier pathway for rotation of a water molecule involves an AAD water donating an H-bond to an adjacent AAD molecule (Fig. 9.19, Water 3). The lowest barrier associated with the AAD-AAD pair is consistent with its classification as a "weak" hydrogen bond on the surface of polyhedral water clusters.[31] As shown in the Fig. 9.20, this isomerization process is highly cooperative, involving the motion of several water molecules in the cluster. In addition, it proceeds through a stable intermediate with two 4-membered and one 3-membered ring, and a five-coordinated water molecule. The calculated vibrational frequencies of the HOD molecule in this site are in close agreement with those for the water molecule involved in the isomerization process that turns on at T = 110 K in the $D_3O^+ \cdot (HDO)(D_2O)_{19}$ cluster. Note that the bound OH stretching band associated with AAD water molecules that donate to another AAD molecule were observed to be ~ 3350 cm^{-1} in previous study (Fig. 7.6), [15] which is indeed close to observed exchange feature that appears at 100 K (Fig. 9.18d). The barriers for rotating the other water molecules are >1.3 kcal/mol higher in energy than the one for the low energy pathway described above, a fact that is consistent with the more extensive isomerization observed experimentally at temperatures above 120 K as well as the ~1.8 kcal/mol difference in activation energy obtained experimentally (Fig. 9.21).

The temperature dependent fractional depletion in figure 9.18 is fitted in figure 9.21, assuming first order kinetics and the Arrhenius rate equation. First the rate constant depends on the Arrhenius equation $k(T) = Ae^{-\frac{E_0}{k_B T}}$ where k is the temperature-dependent

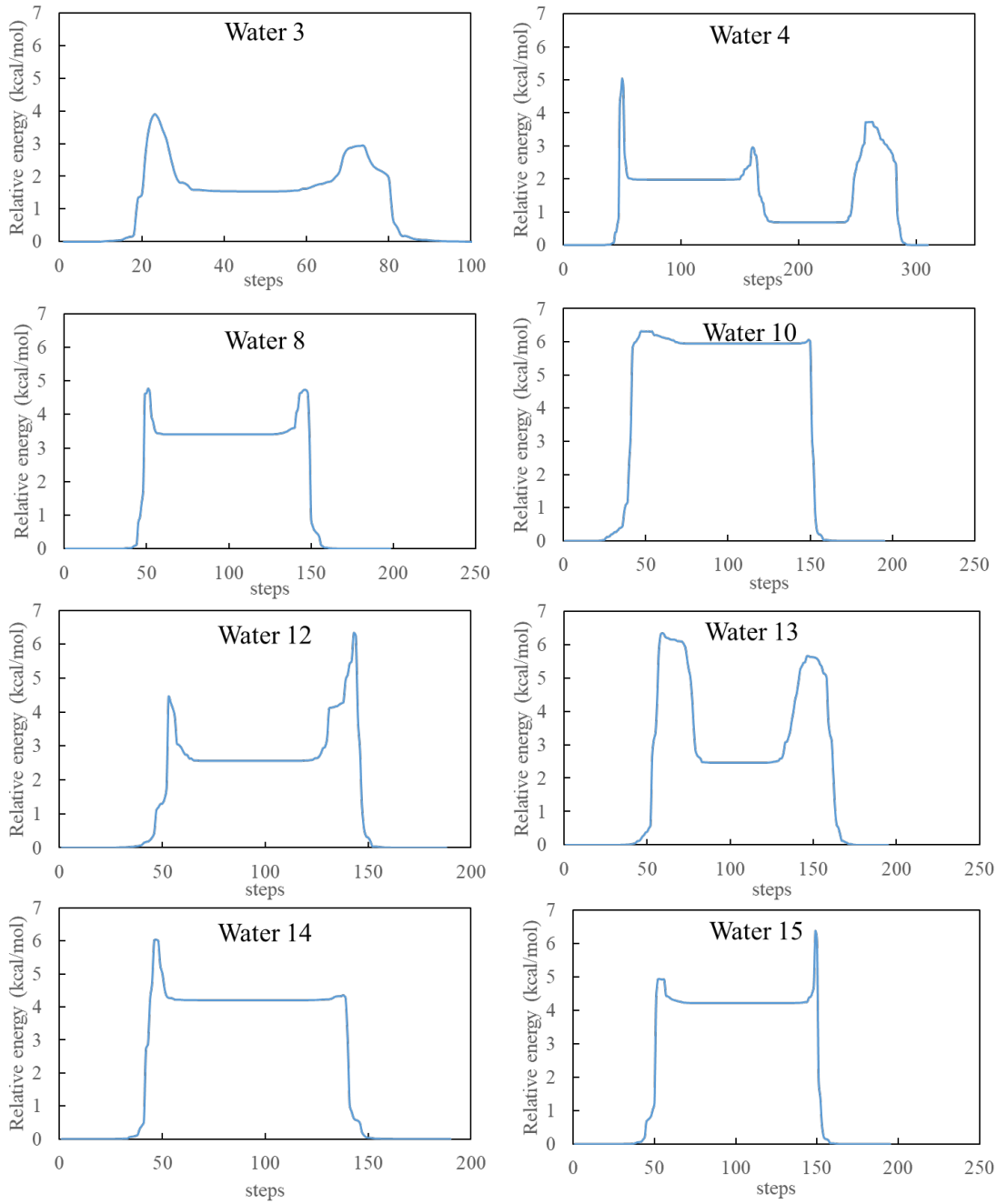

Figure 9.19: The lowest energy pathways for rotation of each of the AAD molecules of $(H_2O)_{21}$. The relative energies are calculated with MBPol. The barrier heights are included in Table 9.2.

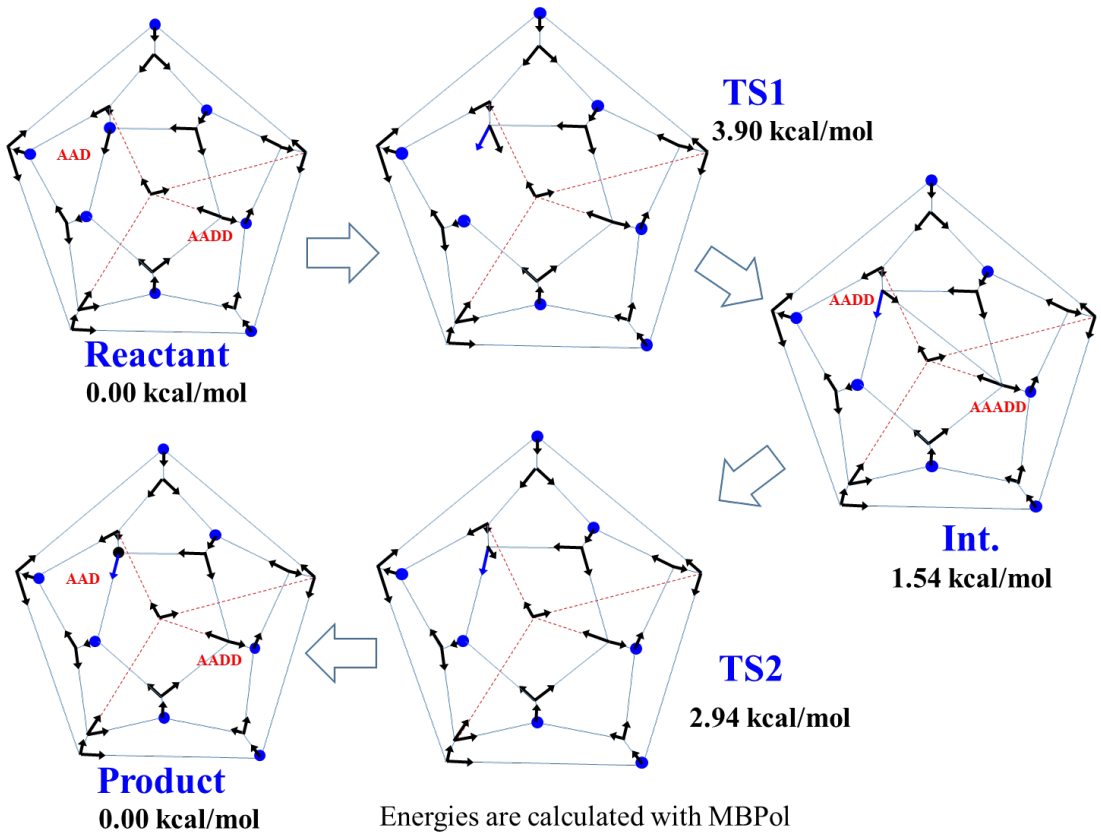

Figure 9.20: Schlegel diagrams for the lowest energy rotational pathway of water 3 of $(H_2O)_{21}$. The blue dots denote the water molecules with a free OH group, the arrows labels the OH groups and the thinner lines represents hydrogen bonds. The water molecule labeled AAD in the reactant panel is the water molecule of interest that is involved in the rearrangement that exchange the free OH with its bound OH group. One of the original AAD water molecule's OH (black arrow) forms an additional hydrogen bond to the original AADD water molecule to form a four-membered ring involving a five coordinated AAADD water molecule.

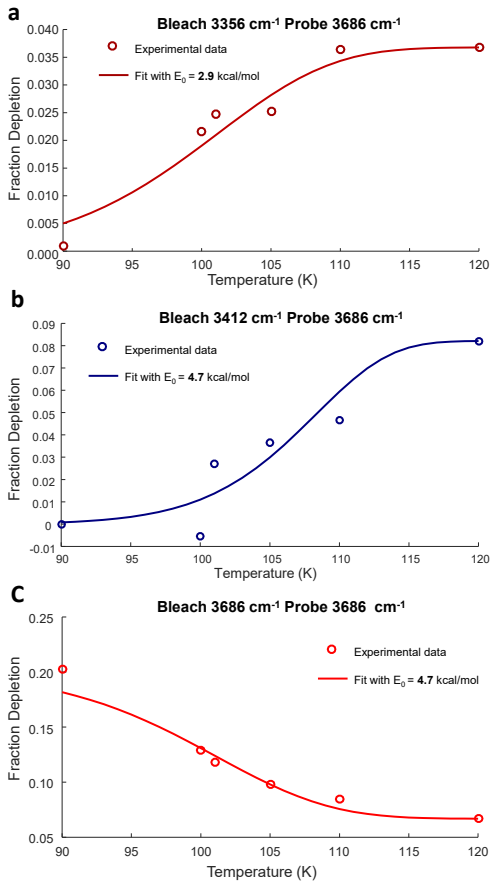

Figure 9.21: Fractional depletion obtained at specific bleach-probe frequencies as a function of temperature. (a)Temperature dependent fractional depletion obtained at 50 ms delay time by probing the free OH position (3686 cm^{-1}) and bleaching the bound OH position of one of the AAD water molecule. This position has the lowest onset temperature for H-bond rearrangement and yield an apparent activation energy (E_0) of 2.9 kcal/mol (1000 cm^{-1}). (b, c) Temperature dependent fractional depletion obtained at 50 ms delay time by probing the free OH position (3686 cm^{-1}) and bleaching the bound OH position of one of the AADD water molecule (b) and bleaching the free OH position of all AAD water molecules (c). Both results yield apparent activation energy (E_0) about 4.7 kcal/mol (1670 cm^{-1}) which is consistent with the higher onset temperature (120 K) for all the other rearrangement pathways.

Table 9.2. Energies (kcal/mol) of transition states and intermediates for rotating the water molecules of $(H_2O)_{21}$ with a free OH group. Energies are referenced relative to the global minimum.

Pathway	Method	TS 1	Int. 1	TS 2	Int. 2	TS 3
Water 3	TTM	4.73	1.50	2.70	-	-
	TTM + ZPE	3.61	0.78	2.08	-	-
	MBPol	3.90	1.54	2.94	-	-
	MBPol + ZPE	3.56	1.56	2.71	-	-
	MP2/AVDZ	-	2.20	-	-	-
Water 4	TTM	4.39	0.65	2.46	1.84	5.50
	TTM + ZPE	3.30	0.51	2.07	1.44	5.33
	MBPol	3.73	0.69	2.96	1.98	5.04
	MBPol + ZPE	3.35	0.70	2.78	2.11	4.69
	MP2/AVDZ	-	0.80	-	2.19	-
Water 8	TTM	6.06	2.92	4.00	-	-
	TTM + ZPE	4.78	2.85	3.37	-	-
	MBPol	4.77	3.41	4.73	-	-
	MBPol + ZPE	4.47	3.41	4.38	-	-
	MP2/AVDZ	-	3.57	-	-	-
Water 10	TTM	6.63	5.19	6.84	-	-
	TTM + ZPE	5.39	4.75	6.07	-	-
	MBPol	6.06	5.95	6.32	-	-
	MBPol + ZPE	5.75	5.74	5.90	-	-
	MP2/AVDZ	-	5.47	-	-	-
Water 12	TTM	5.31	2.45	5.00	4.75	5.46
	TTM + ZPE	4.32	2.03	4.99	4.81	5.35
	MBPol	6.34	2.56	4.14	4.03	4.46
	MBPol + ZPE	5.91	2.71	3.95	3.89	4.09
	MP2/AVDZ	-	3.29	-	4.77	-
Water 13	TTM	7.00	2.20	7.00	-	-
	TTM + ZPE	5.76	1.52	6.36	-	-

	MBPol	5.66	2.46	6.34	-	-
	MBPol + ZPE	5.12	2.44	5.98	-	-
	MP2/AVDZ	-	2.48	-	-	-
Water 14	TTM	4.90	3.88	4.91	-	-
	TTM + ZPE	3.69	3.20	4.57	-	-
	MBPol	6.04	4.21	4.36	-	-
	MBPol + ZPE	5.73	4.04	4.00	-	-
	MP2/AVDZ	-	4.93	-	-	-
Water 15	TTM	7.06	3.84	4.38	-	-
	TTM + ZPE	5.68	3.39	4.37	-	-
	MBPol	6.38	4.22	4.94	-	-
	MBPol + ZPE	5.95	4.15	4.61	-	-
`	MP2/AVDZ	-	4.64	-	-	

first order rate constant, A is the pre-exponential factor (experimentally determined by measuring the rate constant at a known temperature), E_0 is the activation energy and k_B is the Boltzmann constant. Then the population over time can be calculated with the equation $P(t) = P_{eq} + \left(P(0) - P_{eq}\right)e^{-k(T)t}$ and the fractional depletion is $f = \frac{P(t)}{P_{pre}}$, where P_{pre} denotes the population before the bleach laser interaction.

Qualitatively, this large jump in frequencies at the onset of large amplitude motion is consistent with models in which spectral diffusion reflects infrequent, but large structural rearrangements rather than diffusive fluctuation about an initial configuration.[6] We also emphasize that the 120 K dip spectrum, displayed in Fig. 9.18f, is effectively an inverted presentation of the linear spectrum of the entire ensemble at this temperature. The arrows in Fig. 9.18 indicate the direction of population transfer responsible for the diminution of absorption at the probe (red) frequency. In this way, we reveal the hierarchy of site-to-site interconversions that are accessible with increasing temperature. A particularly interesting feature in this regard involves the band associated with water molecules that are directly attached to the hydronium ion core (labeled as ADD'), which begin to undergo exchange with the free OH site at 110 K. This is significant because transfer of these OH sites to those associated with more remote locations in the cage requires migration of the hydronium. As such, we conclude that 110 K also marks the onset of charge translocation across the cluster surface.

Furthermore, we carried out similar experiments on the $Cs^+ \cdot (HDO)(D_2O)_{19}$ cluster where only two types of water molecules are present (ADD and AAD). The absence of the central AADD water molecule prohibits the formation of 5-membered ring which lowers the activation energy of H-bond rearrangement. Such condition should rise the

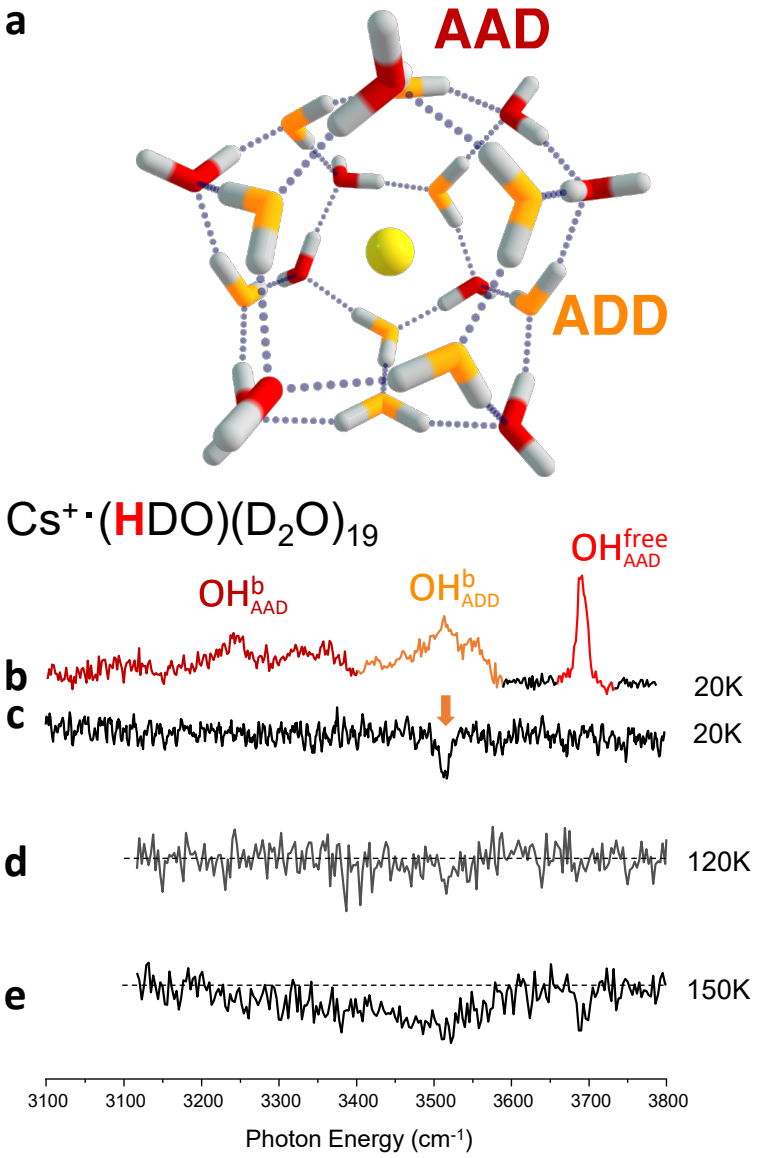

Figure 9.22: Temperature dependent evolution of the photobleaching spectra corresponding to a bleach-probe delay of 50 ms and fixing the probe laser to monitor population of the isotopomer of $Cs^+\cdot(HDO)(D_2O)_{19}$ with isotopically labeled OH group in the AAD (orange) site (OH_{ADD}^{free}). (a) Representative minimal energy structure of $Cs^+\cdot(H_2O)_{20}$. (b) Vibrational spectrum of all isotopomers at 10 K and (c)-(e) hole burning spectra at 20-150 K.

activation energy of the spectral diffusion. The preliminary results (Fig. 9.22) obtained by probing one of the ADD water molecule's OH group suggests that at 120 K there is still no obvious signs of spectral diffusion, the spectral diffusion become apparent at 150 K which significantly higher than that of the protonated water cluster (110 K). Such results open possibility for many follow-on experiments on various water clusters sampling all types of hydrogen bond environment and solvent ions that could reveal the hydrogen bond rearrangement pathway's dependence on the hydrogen bond environments.

9.4 Summary

In summary, we have demonstrated a new type of experiment that captures the hierarchical, detailed molecular motions that contribute to spontaneous spectral diffusion in a finite system as a function of temperature. This is applied to follow the time dependence of a single OH oscillator embedded in the surface of the droplet-like structure adopted by 20 water molecules upon accommodation of the hydronium ion. Although the telltale vibrational signature of the cluster remains intact up to 120 K, the frequency of the OH group is observed to change in time, revealing migration between spectroscopically distinct sites. The time scale of this motion is on the order of tens of milliseconds, indicating that the rearrangements occur as very rare events. The onset for dynamics is close to 100 K, at which point the absorption occurs at two local features separated by about 300 cm^{-1}. All sites are interchanged on this timescale by 120 K, a significantly lower temperature than that at which the well-defined cluster structure is lost. This ability to monitor equilibrium processes in the cluster regime opens the way for wide-ranging applications where thermally activated chemical transformations are

unraveled in the context of both solvent and solute contributions at the molecular level. New experiments probing the dynamics of proton transfer reactions between two protonation sites on an organic framework is underway.

9.5 References

1. Brancato G, Rega N, Barone V. A hybrid explicit/implicit solvation method for first-principle molecular dynamics simulations. *Journal of Chemical Physics* 2008, **128**(14).

2. Fattebert JL, Lau EY, Bennion BJ, Huang P, Lightstone FC. Large-Scale First-Principles Molecular Dynamics Simulations with Electrostatic Embedding: Application to Acetylcholinesterase Catalysis. *Journal of Chemical Theory and Computation* 2015, **11**(12)**:** 5688-5695.

3. Price WD, Schnier PD, Jockusch RA, Strittmatter EF, Williams ER. Unimolecular reaction kinetics in the high-pressure limit without collisions. *J Am Chem Soc* 1996, **118**(43)**:** 10640-10644.

4. Xantheas SS. Low-lying energy isomers and global minima of aqueous nanoclusters: Structures and spectroscopic features of the pentagonal dodecahedron $(H_2O)_{20}$ and $H_3O^+(H_2O)_{20}$. *Can J Chem Eng* 2012, **90**(4)**:** 843-851.

5. Tian CS, Shen YR. Isotopic Dilution Study of the Water/Vapor Interface by Phase-Sensitive Sum-Frequency Vibrational Spectroscopy. *J Am Chem Soc* 2009, **131**(8)**:** 2790-2791.

6. Laage D, Stirnemann G, Sterpone F, Hynes JT. Water Jump Reorientation: From Theoretical Prediction to Experimental Observation. *Accounts Chem Res* 2012, **45**(1)**:** 53-62.

7. Ni YC, Gruenbaum SM, Skinner JL. Slow hydrogen-bond switching dynamics at the water surface revealed by theoretical two-dimensional sum-frequency spectroscopy. *Proc Natl Acad Sci USA* 2013, **110**(6)**:** 1992-1998.

8. Ojha D, Kaliannan NK, Kuhne TD. Time-dependent vibrational sum-frequency generation spectroscopy of the air-water interface. *Commun Chem* 2019, **2**.

9. Inoue K, Nihonyanagi S, Singh PC, Yamaguchi S, Tahara T. 2D heterodyne-detected sum frequency generation study on the ultrafast vibrational dynamics of H_2O and HOD water at charged interfaces. *Journal of Chemical Physics* 2015, **142**(21).

10. Cyran JD, Backus EHG, Nagata Y, Bonn M. Structure from Dynamics: Vibrational Dynamics of Interfacial Water as a Probe of Aqueous Heterogeneity. *Journal of Physical Chemistry B* 2018, **122**(14)**:** 3667-3679.

11. Eigen M. Immeasurably Fast Reactions. *Nobel Lecture* 1967, **11:** 1963-1979.

12. Kirov MV. Atlas of optimal proton configurations of water clusters in the form of gas hydrate cavities. *J Struct Chem*+ 2002, **43**(5)**:** 790-797.

13. Yu Q., Bowman JM. Tracking Hydronium/Water Stretches in Magic $H_3O^+(H_2O)_{20}$ Clusters through High-level Quantum VSCF/VCI Calculations. *J Phys Chem A* 2020, **124**(6)**:** 1167-1175.

14. Fournier JA, Johnson CJ, Wolke CT, Weddle GH, Wolk AB, Johnson MA. Vibrational Spectral Signature of the Proton Defect in the Three-Dimensional $H^+(H_2O)_{21}$ Cluster. *Science* 2014, **344**(6187)**:** 1009-1012.

15. Yang N, Duong CH, Kelleher PJ, McCoy AB, Johnson MA. Deconstructing Water's Diffuse OH Stretching Vibrational Spectrum With Cold Clusters. *Science* 2019, **364**(6437)**:** 275-278.

16. Yang N, Duong CH, Kelleher PJ, Johnson MA. Capturing Intrinsic Site-Dependent Spectral Signatures and Lifetimes of Isolated OH Oscillators in Extended Water Networks. *Nature Chem* 2019.

17. Yang N, Duong CH, Kelleher PJ, Johnson MA, McCoy AB. Isolation of Site-Specific Anharmonicities of Individual Water Molecules in the $I^-\cdot(H_2O)_2$ Complex Using Tag-Free, Isotopomer Selective IR-IR Double Resonance. *Chem Phys Lett* 2017, **690:** 159-171.

18. Wolke CT, Fournier JA, Miliordos E, Kathmann SM, Xantheas SS, Johnson MA. Isotopomer-Selective Spectra of a Single Intact H_2O Molecule in the $Cs^+(D_2O)_5H_2O$ Isotopologue: Going Beyond Pattern Recognition to Harvest the Structural Information Encoded in Vibrational Spectra. *J Chem Phys* 2016, **144**(7)**:** 074305.

19. Boulon J, Braud I, Zamith S, Labastie P, L'Hermite JM. Experimental nanocalorimetry of protonated and deprotonated water clusters. *J Chem Phys* 2014, **140**(16).

20. Calvo F, Douady J, Spiegelman F. Accurate evaporation rates of pure and doped water clusters in vacuum: A statistico-dynamical approach. *J Chem Phys* 2010, **132**(2).

21. Dunbar RC. BIRD (blackbody infrared radiative dissociation): Evolution, principles, and applications. *Mass Spectrom Rev* 2004, **23**(2)**:** 127-158.

22. Niedner-Schatteburg G, Bondybey VE. FT-ICR studies of solvation effects in ionic water cluster reactions. *Chem Rev* 2000, **100**(11)**:** 4059-4086.

23. Schmidt M, von Issendorff B. Gas-phase calorimetry of protonated water clusters. *Journal of Chemical Physics* 2012, **136**(16).

24. Korchagina K, Simon A, Rapacioli M, Spiegelman F, L'Hermite JM, Braud I*, et al.* Theoretical Investigation of the Solid–Liquid Phase Transition in Protonated Water Clusters. *Phys Chem Chem Phys* 2017, **19**(40)**:** 27288-27298.

25. Magnera TF, David DE, Michl J. The 1st 28 Gas-Phase Proton Hydration Energies. *Chem Phys Lett* 1991, **182**(3-4)**:** 363-370.

26. Shi Z, Ford JV, Wei S, Castleman AW, Jr. Water Clusters: Contributions of Binding Energy and Entropy to Stability. *J Chem Phys* 1993, **99**(10)**:** 8009-8015.

27. Vazquez T, Taylor C, Evans-Nguyen T. Ion-Trap-Performance Enhancement Utilizing Pulsed Buffer-Gas Introduction. *Anal Chem* 2018, **90**(17)**:** 10600-10606.

28. Harrilal CP, DeBlase AF, Fischer JL, Lawler JT, McLuckey SA, Zwier TS. Infrared Population Transfer Spectroscopy of Cryo-Cooled Ions: Quantitative Tests of the Effects of Collisional Cooling on the Room Temperature Conformer Populations. *J Phys Chem A* 2018, **122**(8)**:** 2096-2107.

29. Yang N, Duong CH, Kelleher PJ, Johnson MA. Unmasking Rare, Large-Amplitude Motions in D_2-Tagged $I^-\cdot(H_2O)_2$ Isotopomers with Two-Color, Infrared–Infrared Vibrational Predissociation Spectroscopy. *J Phys Chem Lett* 2018, **9**(13)**:** 3744-3750.

30. Rakshit A, Bandyopadhyay P, Heindel JP, Xantheas SS. Atlas of putative minima and low-lying energy networks of water clusters n = 3-25. *J Chem Phys* 2019, **151**(21)**:** 214307.

31. Kirov MV, Fanourgakis GS, Xantheas SS. Identifying the most stable networks in polyhedral water clusters. *Chemical Physics Letters* 2008, **461**(4-6)**:** 180-188.

32. March R.E. An introduction to quadrupole ion trap mass spectrometry. J Mass Spectrom , **32**(4), 351-369 (1997).

33. Xantheas S. S., Low-lying energy isomers and global minima of aqueous nanoclusters: Structures and spectroscopic features of the pentagonal dodecahedron $(H_2O)_{20}$ and $(H_3O)^+(H_2O)_{20}$. *Can. J. Chem. Eng.* **90**, 843-851 (2012).

34. Hodges M. P., Wales D. J., Global minima of protonated water clusters. *Chem. Phys. Lett.* **324**, 279-288 (2000).

35. Schütz M., Lindh R., Werner H. J., Integral-direct electron correlation methods. *Mol. Phys.* **96**, 719 (1999).

36. Azhary A. El, Rauhut G., Pulay P., Werner H. J., Analytical energy gradients for local second-order Møller-Plesset perturbation theory. *J. Chem. Phys.* **108**, 5185 (1998).

37. Werner H. J., Manby F. R., Knowles P. J., Fast linear scaling second-order Møller-Plesset perturbation theory (MP2) using local and density fitting approximations. *J. Chem. Phys.* **118**, 8149 (2003).

38. Polly R., Werner H. J., Manby F. R., Knowles Peter J., Fast Hartree-Fock theory using local density fitting approximations. *Mol. Phys.* **102**, 2311 (2004).

39. Møller C., Plesset M. S., Note on an approximation treatment for many-electron systems. *Phys. Rev.* **46**, 618– 622 (1934).

40. Eckert F., Pulay P., Werner H. J., *Ab initio* geometry optimization for large molecules. *J. Comp. Chem.* **18**, 1473 (1997).

41. Dunning T. H., Gaussian basis sets for use in correlated molecular calculations. I. The atoms boron through neon and hydrogen. *J. Chem. Phys.* **90**, 1007– 1023 (1989).

42. Kendall R. A., Dunning T. H., Harrison R. J., Electron affinities of the first-row atoms revisited. Systematic basis sets and wave functions. *J. Chem. Phys.* **96**, 6796– 6806 (1992).

43. Eichkorn K., Treutler O., Öhm H., Häser M., Ahlrichs R., Auxiliary basis sets to approximate Coulomb potentials. *Chem. Phys. Lett.* **240**, 283– 290 (1995).

44. Eichkorn K., Weigend F., Treutler O., Ahlrichs R., Auxiliary basis sets for main row atoms and transition metals and their use to approximate Coulomb potentials. *Theor. Chem. Acc.* **97**, 119– 124 (1997).

45. Eichkorn K., Treutler O., Oehm H., Häser M., Ahlrichs R., Auxiliary basis sets to approximate Coulomb potentials. *Chem. Phys. Lett.* **240**, 283– 290 (1995).

46. Weigend F., Accurate Coulomb-fitting basis sets for H to Rn. *Phys. Chem. Chem. Phys.* **8**, 1057– 1065 (2006).

47. Hrenar T., Rauhut G., Werner H. J., Impact of local and density fitting approximations on harmonic vibrational frequencies. *J. Phys. Chem. A* **110**, 2060 (2006).

48. Werner H. J., Knowles P. J., Knizia G., Manby F. Schutz R., M., Molpro: a general-purpose quantum chemistry program package. WIREs Comput. *Mol. Sci*. **2**, 242– 253. (2012).

49. Werner H. J., Knowles P. J., Knizia G., Manby F. R., Schütz M., Celani P., Györffy W., Kats D., Korona T., Lindh R., MOLPRO, version 2019.1, a package of ab initio programs. (2019).

48. Lagutchenkov A., Fanourgakis G. S., Xantheas S. S., *J. Chem. Phys.* **122**, 194310 (2005).

49. Schlegel, Verh. Kais. Leopold.-Carolin V. . *Dtsch. Akad. Naturforsch* **44**, 343 (1883).

50. Babin, V., Leforestier, C. & Paesani, F. Development of a “First Principles” Water Potential with Flexible Monomers: Dimer Potential Energy Surface, VRT Spectrum, and Second Virial Coefficient. *Journal of Chemical Theory and Computation* **9**, 5395-5403 (2013).

51. Wales, D., private communication.

52. Wales, D. OPTIM: A program for optimizing geometries and calculating reaction pathways, http://www-wales.ch.cam.ac.uk/OPTIM/.

53. Fanourgakis, G. S. & Xantheas, S. S. The flexible, polarizable, Thole-type interaction potential for water (TTM2-F) revisited. *J. Phys. Chem. A* **110**, 4100-4106 (2006).